



Book of Abstracts

# 10<sup>th</sup> ECCOMAS Thematic Conference on MULTIBODY DYNAMICS December 12 - 15, 2021



<https://eccomasmultibody2021.mm.bme.hu>



Budapest University of Technology and Economics  
Faculty of Mechanical Engineering

**Book of Abstracts of the  
10<sup>th</sup> ECCOMAS Thematic Conference on MULTIBODY DYNAMICS**

**Edited by**

József Kövecses,  
Gábor Stépán,  
Ambrus Zelei

**Contact**

Department of Applied Mechanics,  
Budapest University of Technology and Economics,  
Műgyetem rkp 5., Budapest, H-1111, Hungary.

**Publisher**

Budapest University of Technology and Economics

ISBN 978-963-421-869-2

Budapest, 2021.



## About the conference

### Organizing Committee

Gábor Stépán, Chair, Budapest University of Technology and Economics, Hungary  
József Kövecses, Co-Chair, McGill University, Canada  
Tamás Insperger, Budapest University of Technology and Economics, Hungary  
László Bencsik, Secretary, Budapest University of Technology and Economics, Hungary  
Ambrus Zelei, Budapest University of Technology and Economics, Hungary

### Scientific Committee

Ambrósio J. (Portugal)	Goicolea J. (Spain)	Schiehlen W. (Germany)
Amirouche F. M. L. (USA)	González Varela F. J. (Spain)	Schwab A. (Netherlands)
Anderson K. (USA)	Ibrahimbegovic A. (France)	Seifried R. (Germany)
Arnold M. (Germany)	Jonker B. (Netherlands)	Shabana A. (USA)
Bauchau O. (USA)	Kecskeméthy A. (Germany)	Sharp R. S. (UK)
Bencsik L. (Hungary)	Kim S. (Korea)	Sika Z. (Czech Republic)
Berbyuk V. (Sweden)	Kövecses J. (Canada)	da Silva M. M. (Brazil)
Betsch P. (Germany)	Lankarani H. (USA)	Silva M. T. (Portugal)
Blajer W. (Poland)	Liu C. (China)	Sinatra R. (Italy)
Bottasso C. (Germany)	McPhee J. (Canada)	Stépán G. (Hungary)
Brüls O. (Belgium)	Mikkola A. (Finland)	Suda Y. (Japan)
Choi J. H. (Korea)	Müller A. (Austria)	Terumichi Y. (Japan)
Cuadrado J. (Spain)	Negrut D. (USA)	Terze Z. (Croatia)
Eberhard P. (Germany)	Nikravesh P. (USA)	Valásek M. (Czech Republic)
Fisette P. (Belgium)	Pennestrí E. (Italy)	Verlinden O. (Belgium)
Font-Llagunes J. M. (Spain)	Pfeiffer F. (Germany)	Woernle C. (Germany)
Flores P. (Portugal)	Pogorelov D. (Russia)	Wojtyra M. (Poland)
Frączek J. (Poland)	Polach P. (Czech Republic)	Zelei A. (Hungary)
García Orden J. (Spain)	Raison M. (Canada)	
Gerstmayr J. (Austria)	Saha S. (India)	

### Supporting Organizations



Budapest University of Technology and Economics



Hungarian Academy of Sciences



The Academy of Europe, Budapest Knowledge Hub

### Industrial Support



Knorr-Bremse Hungary

## Welcome message

Welcome to the 10<sup>th</sup> ECCOMAS Thematic Conference on Multibody Dynamics!

The conference series has a remarkable history. It is home to professionals specialized in different technologies and applications of multibody dynamics not only from Europe, but from all over the world. Our conference will be the 10th in a successful series of meetings held in Lisbon (2003), Madrid (2005), Milan (2007), Warsaw (2009), Brussels (2011), Zagreb (2013), Barcelona (2015), Prague (2017), Duisburg (2019). The organizers are grateful for the opportunity of organizing the ECCOMAS Thematic Conference on Multibody Dynamics in 2021 in Budapest. In spite of the difficulties caused by the pandemic, we managed to keep the biannual structure of the conference series.

Multibody dynamics plays a central role in the modeling, analysis, simulation and optimization of mechanical systems with a large variety of engineering applications. The conference serves as an excellent opportunity for researchers worldwide to exchange ideas in multibody dynamics concerning theoretical and application aspects such as multibody kinematics, formalisms and efficient numerical methods developed for multibody problems, dynamics of flexible multibody systems, slender structures, contact problems and impacts, mechatronics, robotics and control, vehicle dynamics, aerospace dynamics, system identification, optimization and sensitivity analysis, validation, software development, biomechanics, gait analysis and education. The conference also provides a platform for sharing novel ideas within the continuously growing multibody research community.

We faced major and unique challenges with the organization of the conference. As you know, the event was originally planned to take place in the summer of 2021 in Budapest. However, due to the unforeseen, special circumstances of the last two years imposed on us by the pandemic, we had to move the conference to the end of the year 2021, and eventually, we had to decide to go with a fully online event. Despite the online nature of the conference, the number of presentations, abstracts and papers is still high, which shows the activity and enthusiasm of the researchers in the multibody community.

The organizers are especially thankful for the contribution of the members of the Scientific Committee during the thorough review process of the abstracts and the full papers.

Despite the challenges and the alternative form of the conference, we hope that you enjoy the event and find the Proceedings as a valuable professional material when studying in details the background of the lectures of your interest.

Gábor Stépán, József Kövecses (chair and co-chair of the conference)  
and the Organizing Team of the  
10<sup>th</sup> ECCOMAS Thematic Conference on MULTIBODY DYNAMICS

## Table of Contents

<b>KEYNOTE LECTURES</b>	10
The Tippedisk: an archetype for a friction-induced inversion phenomenon	
<i>Leine, Remco; Sailer, Simon</i>	11
On the Simulation of Autonomous Agents and Human-Autonomous Agent Interaction	
<i>Negrut, Dan</i>	12
The Use of Multibody System Dynamics in Different Product Processes	
<i>Mikkola, Aki</i>	13
 <b>APPLIED BIOMECHANICS AND GAIT ANALYSIS (APPBIO)</b>	14
Extended Kalman Filter for Real-Time, Full-Body Motion Capture and Driving Efforts Estimation (ID: 238)	
<i>Pérez-Soto, Manuel; Luján, Urbano; Sanjurjo, Emilio; Cuadrado, Javier</i>	15
Numerical stability analysis of the conservative SLIP model with a Hill-type muscle (ID: 234)	
<i>Patko, Dora; Zelei, Ambrus</i>	17
Child Gait Predictive Dynamic Simulation (ID: 133)	
<i>Ezati, Mahdokht; McPhee, John</i>	19
Statistical Analysis of Performance Measures During Acceleration and Deceleration in Overground Running (ID: 247)	
<i>Zajcsuk, Liliána; Zelei, Ambrus</i>	21
Efficient Walking Of A Discrete Simple Biped With a Torso (ID: 116)	
<i>Gismelseed, Sarra Abbasher; Al Yahmedi, Amur Salim; Zaier, Riadh; Bait Bahadur, Issam; Al-Ouakad, Hassan</i>	23
Use of a Multibody Model for Determination of the 3D Human Spine Posture from Wearable Inertial Sensors (ID: 123)	
<i>Michaud, Florian; Luján, Urbano; Cuadrado, Javier; Castaño, David</i>	25
 <b>BIOMECHANICS (BIOMECH-1-2-3)</b>	27
A new method for feedback and feedforward decomposition of human postural control: application to single-leg Yoga postures (ID: 132)	
<i>Menegaldo, Luciano L.; Pinto, Dafne P.; Moreira, Pedro S.</i>	28
Estimation of the Reaction Time During Balancing on Rolling Balance Board in the Frontal Plane (ID: 221)	
<i>Molnar, Csenge A.; Insperger, Tamas</i>	30
Biomechanical Modeling and Examination of Effects of Ankle Sprain Orthoses (ID: 246)	
<i>Reymundo, Pedro; Hakansson, Nils; Lankarani, Hamid</i>	32
Kinematic Analysis of Planar Biomechanical Models using Mixed Coordinates (ID: 245)	
<i>Roupa, Ivo; Gonçalves, Sérgio; Silva, Miguel Tavares</i>	34
Sars Covid19 main protease mutation analysis via a kinematic method (ID: 215)	
<i>Chen, Xiyu; Leyendecker, Sigrid; van den Bedem, Henry</i>	36
Assisted Walking with Hybrid Orthosis Using Functional Electrical Stimulation (ID: 272)	
<i>Peiret, Albert; Jane, Marcel; Pamies-Vila, Rosa; Font-Llagunes, Josep M</i>	38
Biomechanics of Swimmers: A Multibody Inverse Dynamics Approach (ID: 270)	
<i>Simões, Francisca; Sequeira, Mariana; Quental, Carlos; Ambrosio, Jorge; Vilas-Boas, João Paulo</i>	40
Forward Dynamic Simulations of the Temporomandibular Joint based on Subject-Specific Data (ID: 142)	
<i>Guo, Jianqiao; Chen, Junpeng; Wang, Jing; Ren, Gexue; Tian, Qiang</i>	42
Long Term Simulation of Stem Cell Nucleus During Adipogenesis (ID: 147)	
<i>Rabiei, Manoochehr; McColloch, Andrew; Cho, Michael; Bowling, Alan</i>	44
Analytical solutions of the electromechanical middle ear model with an implantable hearing device (ID: 195)	
<i>Weremczuk, Andrzej; Rusinek, Rafal</i>	46
Control concepts for human motion control during balancing an inverted pendulum (ID: 208)	
<i>Nagy, Dalma J.; Insperger, Tamás</i>	48
Optimal control of a human driver in highly dynamic driving scenarios (ID: 188)	
<i>Roller, Michael; Björkenstam, Staffan; Dörlich, Vanessa; Harant, Monika; Leyendecker, Sigrid; Linn, Joachim</i>	50
Optimization and Evaluation of Spinal Exoskeleton Design Concepts using Optimal Control (ID: 235)	
<i>Harant, Monika; Näf, Matthias Basil; Mombaur, Katja</i>	52
Towards Compliant Human-Exoskeleton Interactions Within Multibody Dynamics Simulations of Assisted Human Mo-	



tor Control (ID: 191)	
<i>Inkol, Keaton A; McPhee, John</i>	54
Rehabilitation of Musculoskeletal Models Using Deep Reinforcement Learning (ID: 269)	
<i>Madorell Batlle, Queral; Peiret Gimenez, Albert; Font Llagunes, Josep Maria</i>	56
Estimation of Intervertebral Efforts via an EMG-driven Multibody Model of the Sorensen Test (ID: 126)	
<i>Hinneken, Simon; Detrembleur, Christine; Mahaudens, Philippe; Fisette, Paul</i>	58
<b>CONTACT, IMPACT AND CONSTRAINTS (CONTACT-1-2-3)</b>	60
Model-based Co-simulation of Non-smooth Mechanical Systems (ID: 256)	
<i>Raoofian, Ali; Peiret, Albert; Kövecses, József; Teichmann, Marek</i>	61
Further investigation on LuGre friction force model under normal load variation (ID: 225)	
<i>Marques, Filipe; Woliński, Łukasz; Wojtyra, Marek; Flores, Paulo; Lankarani, Hamid M.</i>	63
Multibody fatigue assessment in industrial mechanisms considering wear in revolute joints (ID: 252)	
<i>López-Lombartero, Mario; Remírez, Adrián; Cabello, Mario; Cuadrado, Javier</i>	65
The Tippedisk: a minimal model for friction-induced inversion (ID: 113)	
<i>Sailer, Simon; Eugster, Simon; Leine, Remco</i>	67
Do we need to impose constraints at acceleration level in the nonsmooth generalized-alpha method? (ID: 261)	
<i>Cosimo, Alejandro; Cavalieri, Federico; Cardona, Alberto; Bruls, Olivier</i>	69
Planar Wrapping and Stretching of a Thick Strand on a Surface by Continuous Integration (ID: 183)	
<i>Müller, Katharina; Kecskemethy, Andres</i>	71
Train Bogie Dynamics Modeling with an Emphasis on Contact Mechanics in a Multibody Model (ID: 262)	
<i>Vermaut, Martijn; Bentefrit, Mohamed; Naets, Frank; Desmet, Wim</i>	73
Efficient impact simulation using the flexible natural coordinate formulation and pinball model (ID: 266)	
<i>Peeters, Jari; Zapata, Luis; Vermaut, Martijn; Naets, Frank</i>	75
Long-term rolling motions of a basketball on the rim (ID: 241)	
<i>Antali, Máté; Havas, Vince; Stépán, Gábor; Hogan, S. John</i>	77
Numerical Analysis of Contact-Impact Problems using Finite Element Method (ID: 124)	
<i>Serfőző, Dániel; Pere, Balázs</i>	79
Port crane guidance dynamics analysed via the Multibody approach (ID: 214)	
<i>Acosta Suárez, Raúl; Fisette, Paul; Docquier, Nicolas</i>	81
A Nonsmooth Dynamics Perspective on State Observer Design for Mechanical Systems with Unilateral Constraints (ID: 140)	
<i>Preiswerk, Pascal V.; Leine, Remco I.</i>	83
Non-smooth numerical solution for Coulomb friction and rolling resistance (ID: 267)	
<i>Sanchez, Eliana; Cosimo, Alejandro; Cardona, Alberto; Bruls, Olivier; Cavalieri, Federico</i>	85
On the simulation of freewheels using the methods of non-smooth dynamics (ID: 217)	
<i>Tasora, Alessandro; Mangoni, Dario; Robuschi, Nicolò</i>	87
Manufacturing tolerance optimization of circuit breaker mechanism using Multibody Dynamic simulation (ID: 259)	
<i>Akhadkar, Narendra; Porwal, Gitesh</i>	89
3D LuGre model for multibody systems involving contacts with stick-slip (ID: 175)	
<i>Colantonio, Lorenzo; Dehombreux, Pierre; Hajžman, Michal; Verlinden, Olivier</i>	91
An impact model of three-dimensional rigid rocking blocks (ID: 150)	
<i>Varkonyi, Peter L.; Ther, Tamas</i>	93
Synchronous Contact/Impact Events Modelling With A Smooth-Based Approach (ID: 114)	
<i>Gismeros Moreno, Raúl; Corral Abad, Eduardo; Meneses Alonso, Jesús; Gómez García, María Jesús; Castejón Sisamón, Cristina</i>	95
<b>EDUCATION, VALIDATION AND SOFTWARE DEVELOPMENT (EDU)</b>	97
Demystifying the Mechanical and Numerical Concepts Underlying Multibody System Dynamics: Development of an International MOOC (ID: 194)	
<i>Fisette, Paul; Hinneken, Simon; Moreau, Emile; Raison, Maxime</i>	98
Validation of MBD-CFD Co-Simulation for Corrugating Machine (ID: 115)	
<i>Arora, Rohit; Nakagawa, Atsushi; Takata, Tomoshige; Akaki, Tomohiro; Kanazawa, Hiroyuki</i>	100

Development of a Cyber-Physical Test Bench for E-Powertrain Components (ID: 119)	
<i>Rodríguez Frade, Borja; Rodríguez González, Antonio Joaquín; Maceira Muñios, Diego; Bottero, Francisco; Sanjurjo Maroño, Emilio; Lugrís Armesto, Urbano; Naya Villaverde, Miguel Ángel; González Varela, Francisco Javier; Cuadrado Aranda, Francisco Javier</i>	102
<b>FLEXIBLE MULTIBODY DYNAMICS (FLEX-1-2-3)</b>	104
An improved absolute coordinate formulation (ACF) for flexible multibody dynamics (ID: 134)	
<i>Zwölfer, Andreas; Gerstmayr, Johannes</i>	105
Computation of internal forces in beam elements with constraint torsional warping (ID: 218)	
<i>Dwarshuis, Koen; Aarts, Ronald; Ellenbroek, Marcel; Brouwer, Dannis</i>	107
Modelling of dielectric elastomer actuated flexible multibody dynamics (ID: 135)	
<i>Huang, Dengpeng; Leyendecker, Sigrid</i>	109
Sloshing Dynamics Estimation for Liquid-filled Containers under 2-Dimensional Excitation (ID: 274)	
<i>Di Leva, Roberto; Carricato, Marco; Gattringer, Hubert; Müller, Andreas</i>	111
Eigenfrequency assignment to flexible-link multibody systems using Taylor expansion of a parametric modal model (ID: 236)	
<i>Belotti, Roberto; Palomba, Ilaria; Wehrle, Erich; Vidoni, Renato</i>	113
Satisfying floating frame constraints in an absolute interface coordinates floating frame formulation (ID: 197)	
<i>Schilder, Jurnan; Ellenbroek, Marcel</i>	115
Flexible Multibody Dynamics and Sensitivity Analysis in the Design of a Morphing Leading Edge for High-Performance Sailplanes (ID: 203)	
<i>Gufler, Veit; Wehrle, Erich; Achleitner, Johannes; Vidoni, Renato</i>	117
Simultaneous Space-Time Discretization for Controlling the Motion of Rigid Bodies Actuated Through Elastic Ropes (ID: 153)	
<i>Ströhle, Timo; Betsch, Peter</i>	119
Multipoint Constraints for Interface Reduction in Flexible Multibody Systems (ID: 205)	
<i>Cammarata, Alessandro; Sinatra, Rosario; Maddio, Pietro Davide</i>	121
Influence of the Flexibility of the Railway Locomotive Bogies Components on its Dynamics (ID: 273)	
<i>Pagaimo, João; Millan, Pedro; Costa, João; Ambrósio, Jorge</i>	123
Flexible Multibody Impact Simulations of Hierarchically Refined Isogeometric Models (ID: 131)	
<i>Rückwald, Tobias; Held, Alexander; Seifried, Robert</i>	125
A toolkit of componets to design a soft gripper (ID: 186)	
<i>Grube, Malte; Velichkova, Hristiana; Wieck, Jan Christian; Fiedler, Bodo; Seifried, Robert</i>	127
Adjoint optimisation of worm-like body locomotion (ID: 248)	
<i>Munoz, Jose J; Bijalwan, Ashutosh</i>	129
Topology Optimization for Eigenfrequencies of a Flexible Multibody System (ID: 184)	
<i>Sun, Jialiang; Tian, Qiang; Hu, Haiyan</i>	131
<b>DYNAMIC ANALYSIS OF AN INTERNAL TURNING TOOL WITH ELASTIC FOUNDATION (WINKLER MODEL) (ID: 222)</b>	
<i>Alves da Silva, Wallyson Thomas; Rostamian, Rouben; Szilagyi, Attila</i>	133
Non-linear beam formulation with NURBS interpolation for the simulation of sliding contacts (ID: 181)	
<i>Wasmer, Paul; Betsch, Peter</i>	135
Coupled multibody model of industrial robot with milling simulator for trajectory compensation (ID: 139)	
<i>Dambly, Valentin; Huynh, Hoai Nam; Verlinden, Olivier; Rivière-Lorphèvre, Édouard</i>	137
<b>FORMALISMS AND NUMERICAL METHODS (FORM-1-2-3)</b>	139
Tensorial deformation measures for the floating frame of reference formulation (ID: 159)	
<i>Sonneville, Valentin; Géraudin, Michel</i>	140
Direct Sensitivity Analysis of Spatial Multibody Systems with Friction using Penalty Formulation (ID: 260)	
<i>Verulkar, Adwait; Sandu, Corina; Dopico, Daniel; Sandu, Adrian</i>	142
An iterative procedure for dynamic integrity assessment (ID: 179)	
<i>Habib, Giuseppe</i>	144
Hamiltonian-based Optimal Control of Multibody Systems in the Presence of Artificial Discontinuities (ID: 198)	

<i>Pikuliński, Maciej; Malczyk, Paweł</i> .....	146
A system identification procedure for multibody system dynamics (ID: 146)	
<i>Askari, Ehsan; Crevecoeur, Guillaume</i> .....	148
Sparse Identification of Open-Loop Multibody System Dynamics (ID: 276)	
<i>Malczyk, Paweł; Frączek, Janusz</i> .....	150
Cutting the knot: Critical features of Centrifugal Vibration Absorbers Modeling (ID: 165)	
<i>Pennestri', Ettore; Cera, Mattia; Valentini, Pier Paolo; Cirelli, Marco</i> .....	152
GENERIC-Based Integration of Constrained Dissipative Mechanical Systems (ID: 163)	
<i>Valdes y Beck, Vanessa; Betsch, Peter</i> .....	154
On Modeling Joint Friction Forces in the Constrained Hamiltonian Formulation (ID: 193)	
<i>Malczyk, Paweł; Wojtyra, Marek</i> .....	156
Efficient earthquake simulation of stiff and high DOF Bridge Expansion Joint models with Python (ID: 196)	
<i>Tahedl, Michael; Borchsenius, Fredrik; Taras, Andreas</i> .....	158
Projection Continuation for Minimal Coordinate Set Dynamics of Constrained Systems (ID: 166)	
<i>Zhou, Ping; Masarati, Pierangelo; Zaroni, Andrea</i> .....	160
The GGL Variational Principle for Constrained Mechanical Systems (ID: 125)	
<i>Kinon, Philipp L.; Betsch, Peter</i> .....	162
Combined Inverse Dynamics and Constraint Force Analysis of Parallel Kinematic Machines (ID: 137)	
<i>Gnad, Daniel; Gattringer, Hubert; Müller, Andreas</i> .....	164
Kane's Equations for Nonholonomic Systems in Bond-Graph-Compatible Velocity and Momentum Forms (ID: 171)	
<i>Phillips, James R.; Amirouche, Farid</i> .....	166
Cable-actuated soft finger modeling using an ALE approach (ID: 122)	
<i>Devigne, Olivier; Cosimo, Alejandro; Brüls, Olivier</i> .....	168
Rotational Component and Translational Component in a Measured Velocity Data (ID: 141)	
<i>Yoo, Wan Suk; Kim, Jae Yeon; Kim, Soo Jin</i> .....	170
An Efficient Algorithm for Solving Time Optimal Control Problems in Multibody Dynamics (ID: 118)	
<i>Eichmeir, Philipp; Steiner, Wolfgang</i> .....	172
<b>MULTIBODY KINEMATICS (KIN)</b> .....	174
A Set of Generalized Coordinates and Their Influence on System Dynamics (ID: 112)	
<i>Zhakatayev, Altay; Rogovchenko, Yuriy; Pätzold, Matthias</i> .....	175
Effects for Reduction of Computational Effort in Multibody Dynamic Models – A Case Study (ID: 254)	
<i>Sun, Chiyu; Shen, Huiping; Kecskemethy, Andres</i> .....	177
Optimal Design of Multibody Systems Using Independent Adjoint Variables (ID: 160)	
<i>Maciag, Paweł Wojciech; Malczyk, Paweł; Frączek, Janusz</i> .....	179
Quaternion Spline Interpolation for Suspension Kinematics and Dynamics (ID: 212)	
<i>Houdek, Václav; Hajžman, Michal; Verlinden, Olivier</i> .....	181
Design Optimization of Quality Inspection Robots for Particle Accelerator Components (ID: 173)	
<i>Gamper, Hannes; Luthi, Adrien; Gattringer, Hubert; Mueller, Andreas; Di Castro, Mario</i> .....	183
Analytical port inversion for a flexible beam model in the Two-Input Two-Output Port approach (ID: 206)	
<i>Finozzi, Antonio; Alazard, Daniel; Sanfedino, Francesco</i> .....	185
<b>MECHATRONICS, ROBOTICS AND CONTROL (MECHATR-1-2-3)</b> .....	187
A compliant and redundantly actuated 2-DOF 3RRR PKM: Less is more (ID: 164)	
<i>Berendsen, Dustin; Sridhar, Aditya; Aarts, Ronald</i> .....	188
Simulation of the Dynamics of the 3-CRS Parallel Robot with a Bond Graph Approach (ID: 192)	
<i>Boudon, Benjamin; Malafosse, Pierre; Guigon, Louis; Margetts, Rebecca; Bouzgarrou, Chedli; Dang, Thu-Thuy; Bouton, Nicolas</i> .....	190
Motion Control of a Crane-like Manipulator Relying on the HTC Vive - Precision and Accuracy of the Pose Estimation (ID: 231)	
<i>Zana, Roland Reginald; Zelei, Ambrus</i> .....	192
State estimation of a hydraulically driven multibody system using the unscented Kalman filter (ID: 189)	
<i>Khadim, Qasim; Hag, Yashar Shabbouei; Jaiswal, Suraj; Matikainen, Marko K.; Mikkola, Aki; Handroos, Heikki</i> ..	194



Synthesis of Trajectory of Underactuated Multibody System (ID: 244)	
<i>Valasek, Michael</i> .....	196
Extending the admissible control-loop delay for the inverted pendulum subject to PDA feedback by detuning the delays (ID: 230)	
<i>Balogh, Tamas; Varszegi, Balazs; Insperger, Tamas</i> .....	198
Robust motion planning for underactuated multibody systems through a variational approach (ID: 168)	
<i>Boscariol, Paolo; Richiedei, Dario</i> .....	200
Uni-frequency 6 DOF Active Dynamic Absorber for Spatial Mechanisms (ID: 210)	
<i>Šika, Zbyněk; Krivošej, Jan; Vyhlídal, Tomáš</i> .....	202
Synthesis of an Extended Kalman Filter for Cable-Driven Parallel Robots (ID: 199)	
<i>Boschetti, Giovanni; González, Francisco; Piva, Giulio; Richiedei, Dario; Rodríguez Frade, Borja; Trevisani, Alberto</i>	204
Path tracking in cable suspended parallel robots through position-dependent Model Predictive Control with embedded integrator (ID: 201)	
<i>Bettega, Jason; Richiedei, Dario; Trevisani, Alberto</i> .....	206
A Heuristic Sequencing Method for Time Optimal Tracking of Open and Closed Paths (ID: 138)	
<i>Zauner, Christian; Gattringer, Hubert; Müller, Andreas; Jörgl, Matthias</i> .....	208
Delayed control of an unstable chain of integrator: The relation between the system parameter and the admissible time delay (ID: 167)	
<i>Kovacs, Balazs; Insperger, Tamas</i> .....	210
Reinforcement Learning Assisted Robotic Contact Tasks (ID: 265)	
<i>Arbatani, Siamak; Kovecses, Jozsef; Teichmann, Marek</i> .....	212
Motion Capture Based Model Identification of the Humanoid Robot REEM-C using Static Poses (ID: 233)	
<i>Aller, Felix; Harant, Monika; Mombaur, Katja</i> .....	214
High-Speed Trajectory Tracking on Robotic Arm by Learning the Dynamic Response of the PID Controller with a Neural Network (ID: 227)	
<i>Toussaint, Baptiste; Raison, Maxime</i> .....	216
A Recursive Dynamics Algorithm for Soft Robotic Manipulators Made of Viscoelastic Material (ID: 257)	
<i>Iwamura, Makoto; Hirata, Kento; Maeda, Yoshiki; Oto, Kyuji</i> .....	218
Mathematical Model and Control Simulation of Hexapod Robot Locomotion in Tripod Gait (ID: 152)	
<i>Osman, Krešimir</i> .....	220
<b>OPTIMIZATION, SENSITIVITY ANALYSIS, AND PARAMETER IDENTIFICATION (OPTIM-1-2) .....</b>	<b>222</b>
Sensitivity analysis for thermohydrodynamic models: uncertainty analysis and parameter estimation (ID: 136)	
<i>Puscas, Maria Adela; Fiorini, Camilla; Després, Bruno</i> .....	223
On the Role of Adjoint Gradients in Time-Optimal Control Problems under Final Constraints (ID: 182)	
<i>Lichtenecker, Daniel; Eichmeir, Philipp; Nachbagauer, Karin</i> .....	225
Discrete adjoint method for the sensitivity analysis of an augmented Lagrangian Index-3 formulation with projections (ID: 224)	
<i>López Varela, Álvaro; Dopico Dopico, Daniel; Luaces Fernandez, Alberto</i> .....	227
Input optimization for flexible multibody systems using the Adjoint Variable Method and the Flexible Natural Coordinate Formulation (ID: 268)	
<i>Vanpaemel, Simon; Naets, Frank; Desmet, Wim</i> .....	229
Shape optimization in time variant system through multibody dynamics analysis (ID: 155)	
<i>Akeno, Koki; Arora, Rohit; Kanazawa, Hiroyuki</i> .....	231
Optimization of a three wheeled tilting vehicle. (ID: 249)	
<i>Dopico Dopico, Daniel; López Varela, Álvaro; Luaces Fernández, Alberto</i> .....	233
A Gradient-Based Computation of Time Optimal Bang-Bang Controls (ID: 220)	
<i>Eichmeir, Philipp; Nachbagauer, Karin; Steiner, Wolfgang</i> .....	235
Topology Optimization Procedure for Flexible Multibody Systems with Augmented Standard Input Data (ID: 154)	
<i>Held, Alexander; Rückwald, Tobias</i> .....	237
On the Dynamics and Optimal Control of Constrained Mechanical Systems (ID: 130)	
<i>Schneider, Simeon; Betsch, Peter</i> .....	239
Nonlinear Optimal Control of Underactuated Mechanical Systems (ID: 250)	
<i>Bodor, Bálint; Bencsik, László</i> .....	241

Stability chart of a multiple spring-mass system subjected to delayed collocated control (ID: 178)	
<i>Szaksz, Bence Mate; Stepan, Gabor</i>	243
<b>EFFICIENT NUMERICAL ALGORITHMS (REALTIME)</b>	245
Reduced Order Interface Modelling for Haptic Simulation and Interfacing (ID: 263)	
<i>Kerr, Liam Peter; Kövecses, József</i>	246
Rod-removal technique for flexible-rods in the framework of semi-recursive multibody formulation (ID: 128)	
<i>Pan, Yongjun; Huang, Liming; Yu, Xinxin; Mikkola, Aki</i>	248
Enabling Artificial Intelligence Studies in Off-Road Mobility Through Physics-Based Simulation of Multi-Agent Scenarios (ID: 162)	
<i>Young, Aaron; Benatti, Simone; Taves, Jay; Elmquist, Asher; Serban, Radu; Negrut, Dan</i>	250
Comparing Semi-recursive Multibody Formulations for Hydraulically Driven Mechanisms (ID: 177)	
<i>Jaiswal, Suraj; Rahikainen, Jarkko; Khadim, Qasim; Sopanen, Jussi; Mikkola, Aki</i>	252
Assessment of Variable Step-Size Integration of Multibody Systems (ID: 172)	
<i>Ruggiu, Maurizio; González, Francisco</i>	254
<b>SLENDER STRUCTURES (THREAD-1-2-3)</b>	256
A One-Dimensional Model for Developable Flexible Elastic Strips with Isogeometric Discretisation (ID: 226)	
<i>Bauer, Benjamin; Roller, Michael; Linn, Joachim; Simeon, Bernd</i>	257
Effective inelastic bending behavior of multi-wire cables using Finite Elements accounting for wire contact (ID: 144)	
<i>Hawwash, Muhannad; Dörlich, Vanessa; Linn, Joachim; Müller, Ralf; Keller, Roger</i>	259
Stability of coarse grid discretisations for dissipative systems: numerical experiments for a test problem (ID: 148)	
<i>Tumiotto, Denise; Arnold, Martin</i>	261
Dynamics of Axially Moving Beams with Transported Discrete Masses and Contact (ID: 151)	
<i>Ntarladima, Konstantina; Pieber, Michael; Gerstmayr, Johannes</i>	263
A nonsmooth approach to frictionless beam-to-beam contact (ID: 145)	
<i>Bosten, Armin; Cosimo, Alejandro; Linn, Joachim; Bröls, Olivier</i>	265
Tensegrity Based Spatial Serial Robots (ID: 219)	
<i>Zavřel, Jan; Kaňka, Tomáš; Halamka, Vojtěch; Valášek, Michael; Šika, Zbyněk</i>	267
Analysis of beam-to-beam contact using mortar method (ID: 143)	
<i>Tomec, Jan; Jelenić, Gordan</i>	269
First steps in data based constitutive modelling of inelastic effects in composite cables using Preisach hysteresis operators (ID: 156)	
<i>Manfredo, Davide; Dörlich, Vanessa; Linn, Joachim; Arnold, Martin</i>	271
Nonlinear Cosserat rod statics using homogenized constitutive properties of multi-layered cross-sections (ID: 232)	
<i>Stavole, Martina; Leyendecker, Sigrid</i>	273
Velocity based elements in the analysis post-critical behaviour of spatial frames (ID: 204)	
<i>Kusuma Chandrashekhara, Sudhanva; Zupan, Dejan</i>	275
Modeling the rotary inertia of sheaves with the Arbitrary Lagrangian-Eulerian Modal approach (ID: 120)	
<i>Escalona, Jose Luis; Mohammadi, Narges</i>	277
Optimized tensegrity structures for the usage in robotics (ID: 240)	
<i>Hajžman, Michal; Bulín, Radek; Hrabáčka, Martin; Polach, Pavel; Byrtus, Miroslav</i>	279
Realistic parameters for dynamic simulation of composite cables using a damped Cosserat rod model (ID: 207)	
<i>Jungkenn, Dominik; Schneider, Fabio; Andersson, Fredrik; Linn, Joachim</i>	281
On the modelling of flexible slender structures guided through narrow space (ID: 174)	
<i>Bulín, Radek; Dyk, Štěpán; Hajžman, Michal</i>	283
Modeling of spiral strands using 1D finite strain beam model: role of frictional contact interactions in the bending behavior (ID: 190)	
<i>Saadat, Mohammad Ali; Durville, Damien</i>	285
<b>VEHICLE DYNAMICS AND AEROSPACE APPLICATIONS (VEH-1-2-3)</b>	287
Simplified mechanical model for balancing a motorbike with steering at zero speed (ID: 229)	

<i>Szabó, András; Horváth, Hanna Zs.; Takács, Dénes</i> .....	288
Handling Evaluation of Tractor-semitrailer with Split Fifth Wheel Coupling Undergoing an ISO Double Lane Change Manoeuvre (ID: 251)	
<i>Jogi, Ajith; Chandramohan, Sujatha; Dash, Sabyasachi</i> .....	290
Development of steering laws to assist the driving of a of a 4-wheel steering vehicle (ID: 223)	
<i>Dambacher, Louis; Boudon, Benjamin; Bouton, Nicolas; Lot, Roberto; Lalande, Nicolas; Lenain, Roland</i> .....	292
Multibody Dynamic Approach to Risk Analysis of Autonomous Driving Test Scenario (ID: 255)	
<i>Zhang, Sheng-peng; Choi, Ji-yoon; Won, Sung-hyuk; Heo, Dong-hoe; Tak, Tae-oh</i> .....	294
Modeling and Simulation of a High-speed Maglev Vehicle on an Infinite Elastic Guideway (ID: 161)	
<i>Schneider, Georg; Schmid, Patrick; Dignath, Florian; Eberhard, Peter</i> .....	296
Analysis of the dynamic behavior of a counterbalance forklift truck through multibody modelling and simulation (ID: 170)	
<i>Pinelli, Marco; Giovannucci, Monica; Martini, Alberto</i> .....	298
Reversing a truck-full trailer combination in the presence of feedback delay (ID: 200)	
<i>Mihályi, Levente; Vörös, Illés; Várszegi, Balázs; Takács, Dénes</i> .....	300
Flexible Multibody Dynamic Analysis for a 23-g Flapping Wing Micro Aerial Vehicle (ID: 185)	
<i>Choi, JaeWon; Gong, DuHyun; Im, ByeongUk; Shin, SangJoon</i> .....	302
Numerical analysis of the linearization of the railway multibody equations of motion with moving reference frames (ID: 127)	
<i>Aceituno, Javier F.; Escalona, José L.</i> .....	304
Influence of the Friction Model on the Dynamics of Railway Freight Vehicles (ID: 271)	
<i>Millan, Pedro; Pagaimo, João; Ambrosio, Jorge; Magalhães, Hugo; Antunes, Pedro</i> .....	306
Multi-Stage MBS and FE Simulation Strategy to Design a Safe Motorcycle (ID: 202)	
<i>Maier, Steffen; Fehr, Jörg</i> .....	308
Optimization of flapping wing dynamics for Martian atmosphere via DMOC approach (ID: 275)	
<i>Terze, Zdravko; Pandža, Viktor; Kasalo, Marko; Zlatar, Dario</i> .....	310
Adaptive techniques for Kalman filter estimation based on multibody models (ID: 209)	
<i>Rodríguez, Antonio J.; Sanjurjo, Emilio; Naya, Miguel Ángel</i> .....	312
Survey of the Use of Multibody Simulations in the Development of Trolleybuses (ID: 187)	
<i>Polach, Pavel; Hajžman, Michal</i> .....	314
Surface Error Correction of a Mesh Deployable Reflector (ID: 258)	
<i>Maddio, Pietro Davide; Salvini, Pietro; Sinatra, Rosario; Cammarata, Alessandro</i> .....	316
Model Order Reduction for Elastic Multibody Systems with Fast Rotating Flexible Bodies (ID: 121)	
<i>Frie, Lennart; Dieterich, Oliver; Eberhard, Peter</i> .....	318
Author index .....	320



**Section**

**KEYNOTE LECTURES**

KEYNOTE

## Keynote Lecture

### The Tippedisk: an archetype for a friction-induced inversion phenomenon

Remco Leine, Simon Sailer

Institute for Nonlinear Mechanics  
University of Stuttgart  
Pfaffenwaldring 9, 70569 Stuttgart, Germany  
[leine, sailer]@inm.uni-stuttgart.de

#### ABSTRACT

Nonlinear phenomena are studied in a variety of different engineering applications, ranging from stick-slip vibrations in oilwell drillstrings to subharmonic resonances of AFM microcantilevers. These systems are extremely complex and have a very rich dynamic behavior. Correspondingly, modeling of such systems is far from trivial, models are of large state dimension and can only be reduced to small dimensions through the adoption of a large number of simplifying modeling assumptions. Although this paradigm is inevitable to solve engineering problems, it is cumbersome for fundamental research on specific nonlinear phenomena. Moreover, the application of methods in nonlinear dynamics is still restricted to a few state dimensions. In academics, there is a need for relatively simple systems which can well be modeled with a few degrees of freedom and only show one particular nonlinear phenomenon. For this reason, a number of science toys (e.g. the Euler disk, the tippetop, the rattleback) have been taken up by the research community as archetypes for nonlinear phenomena, such as finite-time singularities or friction-induced instabilities. In this talk, we will bring a new archetype for friction-induced inversion to the scientific playground: the tippedisk, being an inhomogeneous disk spun on a support around an in-plane axis. Similar to the tippetop, the tippedisk inverts its orientation when spun rapidly. However, unlike the tippetop, the body has neither rotational symmetry in geometry, complicating its interaction with the supporting hyperplane, nor in its principal moments of inertia, leading to additional gyroscopic terms. We will present an adequate numerical model and use singular perturbation theory to describe and understand the inversion phenomenon globally on a two dimensional submanifold. Furthermore, we will compare the low dimensional analysis with laboratory experiments. The tippedisk proves to be an excellent real-life system which can easily be modeled and experimentally tested and which allows to use the whole toolbox of nonlinear dynamics to analyze its global dynamics.

#### BIOGRAPHY



Remco Leine is Full Professor for Nonlinear Mechanics and director of the Institute for Nonlinear Mechanics at the University of Stuttgart. He received the M.Sc. degree from Delft University of Technology and the Ph.D. degree from Eindhoven University of Technology, The Netherlands, in 1996 and 2000, respectively. In 2007 he obtained the Habilitation degree from the ETH Zurich and became Titularprofessor in 2012 before he joined the University of Stuttgart in 2014.

Remco Leine's research is focused on the intersection of nonsmooth dynamics and nonlinear dynamics. In particular, he is interested in the nonsmooth dynamics of multibody systems with impact and friction and is continuously working on a stability and bifurcation theory for nonsmooth dynamical systems.

He is co-founder of the European Network for Nonsmooth Dynamics and is regularly organizing mini-symposia on nonsmooth dynamics at international conferences and won the Best ENOC Minisymposium Prize in 2008. During the past years, he has published three books on nonsmooth dynamics and over 49 journal papers. Recently, he joined the scientific advisory board of the Journal of Theoretical, Computational and Applied Mechanics (JTCAM).

## Keynote Lecture

### On the Simulation of Autonomous Agents & Human-Autonomous Agent Interaction

Dan Negrut

NVIDIA Fellow

Bernard A. and Frances M. Weideman Professor of Mechanical Engineering  
University of Wisconsin-Madison

#### ABSTRACT

This talk outlines efforts in the Simulation-Based Engineering lab at the University of Wisconsin-Madison to create a simulation environment that can be used to understand and shape the dynamics of autonomous mechatronics agents such as vehicles, robots, rovers, etc. I will describe a software infrastructure called Chrono that we have been augmenting for more than one decade and which seeks to support tasks such as assessing the operation safety of autonomous agents (AAs), improving this safety, reducing cost to market, and compressing the engineering design cycle. I will also highlight ongoing efforts in which we support projects aimed at characterizing the human-AA interaction. The talk will touch on the equations governing the dynamics of these agents (the physics of the agents), as well as the simulation of sensors and virtual worlds. Quick comments will be made on the question of whether control policies learned through simulation transfer to the real world, i.e., addressing the so-called sim-to-reality gap.

#### BIOGRAPHY



Dan Negrut received his Mechanical Engineering Ph.D. in 1998 from the University of Iowa under the supervision of Professor Edward J. Haug. He spent six years working for Mechanical Dynamics, Inc., a software company in Ann Arbor, Michigan. In 2004 he served as an Adjunct Assistant Professor in the Department of Mathematics at the University of Michigan, Ann Arbor. He spent 2005 as a Visiting Scientist at Argonne National Laboratory in the Mathematics and Computer Science Division. At the end of 2005 Dan joined the Mechanical Engineering faculty at the University of Wisconsin-Madison. His interests are in Computational Science and he leads the Simulation-Based Engineering Lab (<http://sbel.wisc.edu>). Lab sponsors include NASA, US Army Research Office, Department of Transportation, and National Science Foundation. The lab's projects focus on high performance computing, computational dynamics, terramechanics, simulation-in-robotics, and fluid-solid interaction problems. Dan received a National Science Foundation Career Award in 2009. Since 2010 he is an NVIDIA CUDA Fellow. He is one of the technical leads of Project Chrono, an open source physics-based simulation engine (<http://www.projectchrono.org/>).



## Keynote Lecture

### The Use of Multibody System Dynamics in Different Product Processes

Aki Mikkola

LUT University, Department of Mechanical Engineering  
P.O. Box 20,  
53851 Lappeenranta, Finland,  
aki.mikkola@lut.fi

#### ABSTRACT

Globally, digitalization is revolutionizing industry, and traditional business models based on material flow processing are being replaced by models based on data and knowledge processing. A data and knowledge processing business, i.e., a software-based business, seems complementary to even traditional economic theories.

This presents an opportunity for multibody-based simulation. On the process level, multibody modelling and multibody-based twinning is enabling transparent monitoring of and accurate adjustment and control over production processes. Virtual processes can be rapidly and thoroughly tested in parallel with and as changes are made to the virtual product. This makes it possible to optimize and adjust processes to achieve ever higher environmental, economic, and operational efficiencies without ambiguity and free of 'process inertia'. Being able to effectively model products, equipment, people, environments, and both intended and causal interactions, i.e., by analyzing reality through simulation, enables industrial companies to better drive sustainable growth. This sustainability, which is comprised of environmental, technical, economic, social, and individual dimensions, can be addressed by implementing multibody-based twinning over the entire product or production system lifecycle.

This paper introduces a number of cases where multibody-based models are used in different product processes. Example cases touch on (1) gamification-based product development, (2) new concepts in preventive maintenance that combine real-life data and simulation enabled by pervasive communication networks, (3) autonomous machinery, and (4) the adaptive optimization of manufacturing through applications of artificial intelligence.

#### BIOGRAPHY



Aki Mikkola received a Ph.D. degree in the field of machine design in 1997. Since 2002, he has been working as a Professor in the Department of Mechanical Engineering at LUT University, Finland. Currently, Mikkola leads the research team of the Laboratory of Machine Design. He has been awarded five patents, has contributed to more than 130 peer-reviewed journal papers and has presented more than 100 conference articles. His major research activities are related to flexible multibody dynamics, rotating structures, and biomechanics. Mikkola has served on several occasions as session organizer for international conferences. In the First Joint International Conference on Multibody System Dynamics that was organized in Finland during 2010, Mikkola served as Chair, together with Prof. Werner Schiehlen. He is currently Editor-in-Chief of the Journal of Multibody System Dynamics (Springer).

**Section**

**APPLIED BIOMECHANICS AND GAIT ANALYSIS**

APPBIO

# Extended Kalman Filter for Real-Time, Full-Body Motion Capture and Driving Efforts Estimation

Manuel Pérez-Soto<sup>1</sup>, Urbano Lúgrís<sup>1</sup>, Emilio Sanjurjo<sup>1</sup>, Javier Cuadrado<sup>1</sup>

<sup>1</sup> Laboratory of Mechanical Engineering  
University of La Coruña  
Mendizábal, s/n, 15403 Ferrol, Spain  
urbano.lugris@udc.es

## EXTENDED ABSTRACT

### 1 Introduction

Real-time biofeedback has been used for years as a powerful rehabilitation tool. Many studies show that rehabilitation results can be improved with the aid of motion capture systems, force plates, electromyography probes, inertial measurement units, and other types of sensors, by allowing a patient to better adapt the movement to any kind of specified requirements through visual, auditory or haptic feedback [1].

By using complex biomechanical models, it is possible to combine the sensor measurements in order to obtain advanced biofeedback systems, even allowing to estimate muscle efforts in real time [2]. In this work, an Extended Kalman Filter (EKF) for real-time estimation of the motion and its driving forces and torques is developed. The filter is based on a previous EKF designed for real-time motion capture, using a kinematic model [3], but in this case the system dynamics are also included. Therefore, the new EKF allows to generate feedback in real time from the estimated ground reactions and joint torques, and, as an additional benefit, the motion reconstruction is improved, since the dynamics of the multibody system are now taken into account.

### 2 Multibody model

The EKF proposed in this work is based on a multibody model representing the musculoskeletal system [3], as shown in Figure 1. The model consists of 18 rigid bodies, mostly constrained by spherical joints, with a total of 52 degrees of freedom, grouped into a vector of independent coordinates  $\mathbf{z}$ .

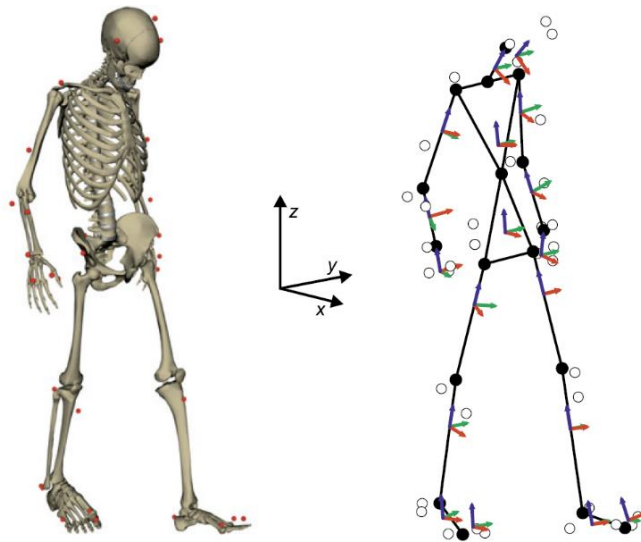


Figure 1: Multibody model

The equations of motion of the multibody system have the following form:

$$\mathbf{M}(\mathbf{z})\ddot{\mathbf{z}} = \mathbf{Q}(\mathbf{z}, \dot{\mathbf{z}}) + \mathbf{B}(\mathbf{z})\mathbf{F}_e \quad (1)$$

where  $\mathbf{M}$  is the mass matrix,  $\mathbf{Q}$  contains the gravitational, centrifugal and Coriolis forces,  $\mathbf{F}_e$  are the estimated joint torques and ground reaction forces, and  $\mathbf{B}$  is a matrix that transforms the latter into generalized forces.

### 3 Extended Kalman Filter

The state vector of the Kalman filter,  $\mathbf{x}$ , comprises the independent coordinates of the model  $\mathbf{z}$ , their first time derivatives  $\dot{\mathbf{z}}$ , and the estimated applied forces  $\mathbf{F}_e$ . In order to express the state propagation model in a linear state-space form, the first step is to

solve the ODE system (1) for the accelerations [4]:

$$\ddot{\mathbf{z}} = \mathbf{M}^{-1}(\mathbf{Q} + \mathbf{B}\mathbf{F}_e) \quad (2)$$

Then, the resulting equations can be linearized about a reference state, and written in linear state–space form:

$$\begin{bmatrix} \delta\dot{\mathbf{z}} \\ \delta\ddot{\mathbf{z}} \\ \delta\dot{\mathbf{F}}_e \end{bmatrix} = \begin{bmatrix} \mathbf{0} & \mathbf{I} & \mathbf{0} \\ \frac{\partial\ddot{\mathbf{z}}}{\partial\mathbf{z}} & \frac{\partial\ddot{\mathbf{z}}}{\partial\dot{\mathbf{z}}} & \frac{\partial\ddot{\mathbf{z}}}{\partial\mathbf{F}_e} \\ \mathbf{0} & \mathbf{0} & \mathbf{0} \end{bmatrix} \begin{bmatrix} \delta\mathbf{z} \\ \delta\dot{\mathbf{z}} \\ \delta\mathbf{F}_e \end{bmatrix} + \begin{bmatrix} \mathbf{0} \\ \mathbf{0} \\ \dot{\mathbf{w}} \end{bmatrix} \quad (3)$$

where  $\delta$  denotes the increment of the corresponding state variable. In this filter,  $\delta\mathbf{F}_e$  will be considered as a Wiener process, so its derivative consists of continuous–time zero–mean white noise  $\dot{\mathbf{w}}$ , which is introduced in the model as plant noise. By following the standard procedure to derive a discrete EKF from a continuous model, this ODE system can be discretized in time, thus providing the state transition and noise covariance matrices of the filter.

In this implementation, the system observation is carried out by two sets of sensors: 36 optical markers placed at anatomical landmarks, and two force plates, as shown in Figure 2. The observation function  $\mathbf{h}(\mathbf{x})$ , which provides the sensor values as a function of the state, is also nonlinear, so its Jacobian matrix must be computed in order to obtain the observation matrix  $\mathbf{H}(\mathbf{x})$  of the filter.

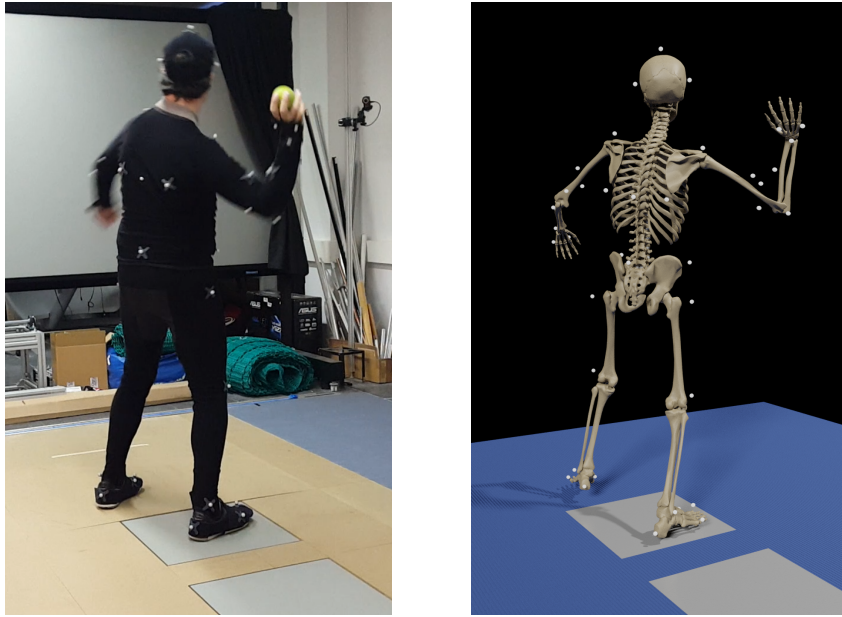


Figure 2: Motion capture using optical sensors

#### 4 Conclusion

After tuning the plant and sensor noise parameters, the filter provides robust motion capture and reconstruction, while estimating joint torques and ground reactions on the fly, without the need of further post–processing. However, since the filter uses mostly position sensors, the estimation of those efforts that are not being directly measured (i.e., the joint torques) is delayed in time. The amount of delay may or may not be acceptable, depending on the biofeedback application, but it can be greatly reduced by adding gyroscopes or accelerometers to the filter, as shown in [4].

#### References

- [1] O.M. Giggins, U. M. Persson, B. Caulfield. Biofeedback in Rehabilitation. *Journal of Neuroengineering and Rehabilitation*, 10:60, 2013.
- [2] G. Durandau, D. Farina, M. Sartori. Robust Real–Time Musculoskeletal Modeling Driven by Electromyograms. *IEEE Transactions on Biomedical Engineering*, 65:556–564, 2018.
- [3] J. Cuadrado, F. Michaud, U. Lúgrís, M. Pérez–Soto. Using Accelerometer Data to Tune the Parameters of an Extended Kalman Filter for Optical Motion Capture: Preliminary Application to Gait Analysis. *Sensors*, 21:427, 2021.
- [4] E. Sanjurjo, D. Dopico, A. Luaces, M.A. Naya. State and Force Observers based on Multibody Models and the Indirect Kalman Filter. *Mechanical Systems and Signal Processing*, 106:210–228, 2018.

# Numerical Stability Analysis of the Conservative SLIP Model with a Hill-Type Muscle

Dóra Patkó<sup>1</sup>, Ambrus Zelei<sup>2</sup>

<sup>1</sup>Faculty of Mechanical Engineering  
Budapest University of Technology and Economics  
Muegyetem rkp. 3-5, Budapest, Hungary  
dora.patko@mm.bme.hu

<sup>2</sup>MTA-BME Research Group on Dynamics of  
Machines and Vehicles  
Muegyetem rkp. 3-5, Budapest, Hungary  
zelei@mm.bme.hu

## EXTENDED ABSTRACT

### 1 Introduction

The human balancing process is an interesting research topic which requires multidisciplinary knowledge. Various models are used to analyze the hopping, running movements and the underlying causes of its stability in case of humans, animals and biomimetic robots. Several types of muscle models can be used to consider the non-linearities of the muscle system.

### 2 Mechanical model

We study the spring-loaded inverted pendulum (SLIP) model [1]. However instead of the spring, we attached a simplified Hill-type muscle to the point-mass, which consists of the active element only. Note that since the muscle can only exert pulling force, we need to invert the muscle model such as in the work of Häufle et al. [2], where they analyzed a similar model for a vertical hopping. However, we consider running movement assuming stability arises from this kind of movement. Let us denote the state variables of the system as  $\mathbf{x}$ :

$$\mathbf{x} = [x, y, \dot{x}, \dot{y}]^T, \quad (1)$$

where  $x, y$  are the Cartesian-coordinates of the point-mass. The intrinsic properties of the muscle model can be considered in different complexities. At this point, we consider conservative autonomous systems only. Hence we neglect the force-velocity relation of the active element of the muscle so that we assume the relation is constant, moreover we assume constant maximal muscle activation such as in [2]. Three alternative force-length relation is studied: constant, linear and non-linear Hill-type.

### 3 Methods

The system is non-smooth, and it is capable to move on a periodic trajectory, which consists of a flight and a stance phase. The flight phase equation of motion can be solved in closed form, but the stance phase equation of motion cannot be due to the geometric nonlinearities. First let us choose a Poincaré-section, for convenience let it be the apex point of the flight phase, when  $\dot{y}$  is zero. The  $x$  variable is a quasi-cyclic coordinate since it has no effect on the motion in the flight phase. However, it appears in the equations regarding the stance phase, but only its relative position matters from the ground attachment point. In case of periodic motion with time period  $T$  the solution coincides the Poincaré-section at the same point. Therefore, if we treat the behavior of the system as a black box between  $t_0$  and  $t_0 + T$ , where  $\mathbf{x}(t_0)$  is on the Poincaré section, only two variables affect the stability of the system,  $y$  and  $\dot{x}$ . Note that at this point we only consider autonomous conservative systems, therefore if we fix the mechanical energy of the system, we can express one of these variables as the function of the other. Therefore, the stability of the system can be analyzed via a 1D return map, as shown in Figure 1.

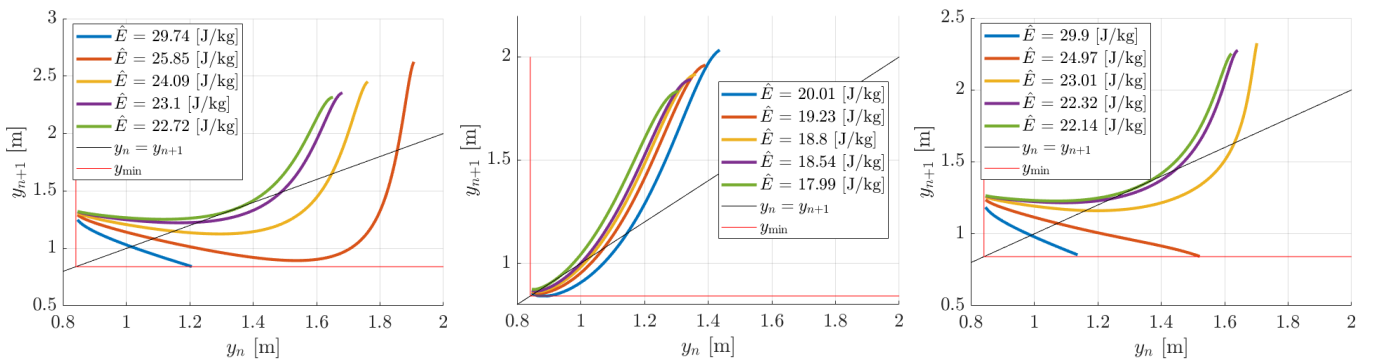


Figure 1: 1D return maps of the system from left to right the force-length relation is: constant, linear, non-linear Hill-type

According to this method, we can conclude that with all the three force-length relations orbital asymptotic stability can be achieved within a mechanical energy range. Moreover, the basin of attraction and bifurcations can also be determined from these maps. In every mechanical energy level where stable hopping is possible, the system has an unstable periodic trajectory too. The stable hopping is associated with lower jumping heights but faster running velocities. As the mechanical energy level is

increasing, these two fix points grow apart, and since the upper limit of the basin of attraction (BoA) is the jumping height of the corresponding unstable motion, the BoA is increasing. However, the BoA size can shrink abruptly, because high energy curves intersect the limiting minimal jumping height, which results in a fall-over since the system is not able to take off at the end of the stance phase. Another interesting phenomenon can be observed; there is a lower energy limit for periodic orbits connected with a saddle-node bifurcation.

The question arises; what happens when the system meets with a disturbance that causes it to change its mechanical energy level? For this kind of analysis, the 1D return map is not appropriate. We should find the monodromy matrix  $\mathbf{C}$  of the system, which is constructed numerically via the help of the fundamental matrices  $\Phi$  of each phase and the saltation matrices  $\mathbf{S}$  connecting these phases [3]. In our case, since the Poincaré-section is in the middle of the flight phase, the principal matrix is as follows:

$$\mathbf{C} = \Phi_F(t_{\text{apex}})\mathbf{S}_{S2F}(t_{S2F})\Phi_S(t_{S2F})\mathbf{S}_{F2S}(t_{F2S})\Phi_F(t_{F2S}). \quad (2)$$

The construction of the matrices in (2) is detailed in the work of Piiroinen et al. [3]. The indexes S and F denote the stance and flight phases respectively. S2F denotes the phase change from stance to flight and vice versa. According to the Floquet theory, the eigenvalues of the principal matrix determine the stability of a solution. In our case, we have two eigenvalues with the value 1, one zero Floquet multiplier and one which depends on the initial conditions. Since the system is autonomous, one of the 1-valued eigenvalue is the trivial one associated with the trivial eigenvector. The zero multiplier is associated with the  $x$  direction, since the  $x$  coordinate is quasi-cyclic it is projected in every stance phase such a way that the attachment point to the ground is in the origin. The initial condition dependent multiplier is the same as one can determine from the 1D return maps. The remaining 1-valued multiplier suggests that the system can only achieve neutral stability for all force-length complexities in case of arbitrary disturbance. This finding is in correspondence with the fact that the system is conservative, therefore cannot change its mechanical energy level on its own. Therefore, a perturbed solution will converge to the periodic solution on a given iso-energy surface and since the initial conditions which result in periodic motions are continuous, some of the error between the original and the new trajectory will disappear, but if the mechanical energy have changed, a remaining difference can be observed; as shown for dimensionless generalized coordinates in Figure 2.

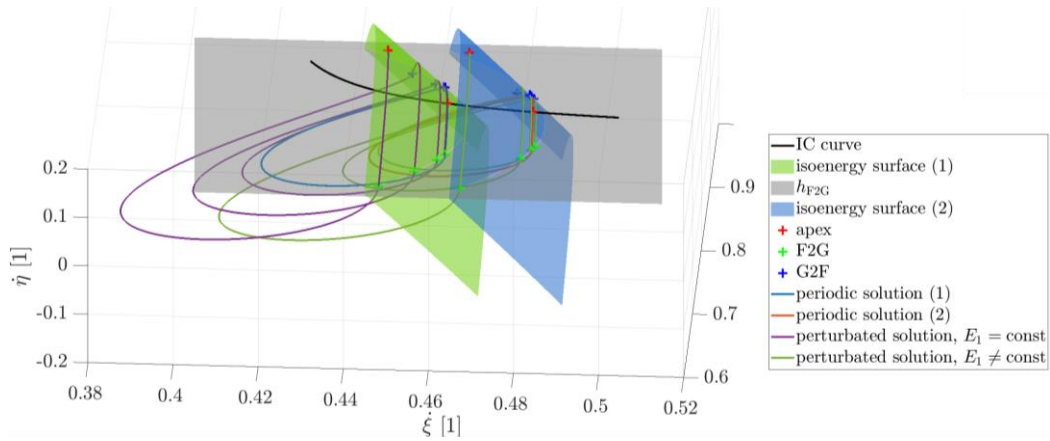


Figure 2: Relation between the iso-energy surfaces and trajectories,  $h$  is the switching function

## 4 Conclusion

For energy conserving perturbations, orbital asymptotic stability can be achieved by a conservative autonomous SLIP model with a simple Hill-type muscle using any of the three (constant, linear and non-linear Hill-type) intrinsic force-length relations. Therefore, running movement provide stability in contrast to vertical hopping, where orbital asymptotic stability cannot be achieved unless at least linear force-velocity relation was considered, and the system lost its conservatism [2].

## Acknowledgments

The research reported in this paper and carried out at BME has been supported by the NRDI Fund (TKP2020 IES, Grant No. BME-IE-BIO and TKP2020 NC, Grant No. BME-NC) based on the charter of bolster issued by the NRDI Office under the auspices of the Ministry for Innovation and Technology and by the Hungarian National Research, Development and Innovation Office (Grant no. NKFI-FK18 128636).

## References

- [1] Blickhan, R. et al. “Intelligence by mechanics.” *The Royal Society* 365(1850):199–220 (2007).
- [2] Haeufle, D., Grimmer, S., and Seyfarth, A. “The role of intrinsic muscle properties for stable hopping - stability is achieved by the force-velocity relation.” *Bioinspiration & Biomimetics* 5(1):016004 (2010).
- [3] Piiroinen, P.T, Dankowicz, J. “Low-Cost Control of Repetitive Gait in Passive Bipedal Walkers.” *International Journal of Bifurcation and Chaos* 15(6): 1959-1973 (2005).

# Child Gait Predictive Dynamic Simulation

Mahdokht Ezati<sup>1</sup> and John McPhee<sup>2</sup>

<sup>1</sup>Systems Design Engineering  
University of Waterloo  
Waterloo, Ontario, Canada  
mezati@uwaterloo.ca

<sup>2</sup>Systems Design Engineering  
University of Waterloo  
Waterloo, Ontario, Canada  
mcphee@uwaterloo.ca

## EXTENDED ABSTRACT

### 1 Introduction

Most recent predictive gait simulations focused on adults and older people, but clinical centers working on treatments of child gait disorders prefer to rely more on pediatric gait simulations than adult gait simulations. Recent predictive gait simulations used an anatomically-detailed muscle model (i.e., Hill-type muscle model) to simulate the muscles, but it is challenging to fit an anatomically-detailed muscle model to specific subjects due to computational and modeling challenges. In this research, we developed computationally-efficient and physiologically-meaningful musculoskeletal (MSK) and neuromusculoskeletal (NMSK) models to simulate natural, slow, and fast gaits for children using muscle-torque-generators (MTGs). MTGs fit specific subjects more easily than anatomically-detailed muscle models. We also evaluated the effect of different optimization cost terms on the accuracy of the predicted results by developing a wide range of child natural-gait simulations, ranging from fully-data-tracking to fully-predictive.

### 2 Methods

We developed a 2-dimensional 11-degree-of-freedom (11-DOF) child model in contact with the ground through a 3-dimensional ellipsoidal volumetric foot-ground contact model [1]. The model includes 3-DOF HAT-to-ground joint (HAT: head-arms-trunk segment), 1-DOF hip joints, 1-DOF knee joints, 1-DOF ankle joints, and 1-DOF metatarsal joints. The metatarsal joints are torque-driven, and the hip, knee, and ankle joints are actuated by pairs of agonist and antagonist MTGs proposed by [2]. The parameters of the MTGs were fitted to our child gait model using a parameter identification done by direct collocation optimal control in which the mean experimental gait motion data of 20 healthy children were tracked. The subjects were 9 males and 11 females with an age of  $10.8 \pm 3.2$  years, a mass of  $41.4 \pm 15.5$  kg, and a height of  $1.47 \pm 0.2$  m [3].

To generate natural, slow, and fast gait simulations, we used two separate direct collocation optimal controls: “MSK-model optimization” and “NMSK-model optimization”. In the MSK-model optimization, the musculoskeletal geometry and muscle contraction dynamics were represented by MTGs and the control inputs are 12 MTG activations, considering 6 MTGs for each leg. In the NMSK-model optimization, the MSK model along with muscle activation dynamics were used and the control inputs are 16 muscle excitations, considering 8 muscles for each leg. We used the MSK-model and NMSK-model optimizations to predict five different-speed gaits, including very slow walking at 0.9 m/s (XS), slow walking at 1.09 m/s (S), natural walking at 1.26 m/s (M), fast walking at 1.29 m/s (L), and very fast walking at 1.58 m/s (XL).

To simulate the XS, S, L, and XL gaits, the final times of the optimizations and the bounds on the states and control inputs were defined based on the experimental data of the corresponding slow and fast gaits extracted from [3]. The cost function consists of: (1) three dynamic-based cost terms (DYN), minimizing joint jerks and residual loads and solving motion dynamics implicitly, (2) a stability-based cost term (STB), controlling the motion of the center of mass, (3) three human-criteria-based cost terms (HC), minimizing MTG activations for the MSK model, and muscle activations and metabolic energy consumption for the NMSK model, and (4) three data-tracking cost terms (DT), tracking the experimental joint angles (Ang), torques (Trq), and ground reaction forces (GRF) of the natural gait (i.e., the M walking) scaled (stretched/compressed) with respect to the cycle time of the gait we wanted to predict.

To simulate the M walking, we implemented different gait simulations, ranging from fully-tracking to fully-predictive, using the proposed MSK and NMSK models. For each model’s optimization, we investigated eight cost functions composed of the cost terms DYN, STB, HC, and DT cost terms (Table 1). The cost terms, specified by a checkmark in each row of Table 1, were first multiplied by weighting factors and then summed together to form the cost function named at the beginning of the row. In cost function #1, fully-data-tracking (FDT), all three DT cost terms were used. In cost functions #2-4, semi-data-tracking (SDT), two of the DT cost terms were used and in cost functions #5-7, semi-predictive (SP), only one of the DT cost terms was used. In cost function #8, fully-predictive (FP), there is no DT cost term.

### 3 Results

According to the findings from the XS, S, L, and XL gait simulations, the larger the gap between the speed of slow or fast gaits and the speed of natural gait, the longer the computational time and the less accurate the results for slow-gait or fast-gait simulations. The MSK-model and NMSK-model optimizations predicted physiologically-realistic torques, motions, and GRFs



for child slow and fast gaits. The NMSK-model predicted the joint torques for the XS, S, L, and XL gaits with normalized-root-mean-square errors (NRMSEs) of 0.10, 0.07, 0.07, and 0.10, respectively, that are 17%, 12%, 10%, and 2% more accurate than the MSK-model's resultant torques. The NRMSEs were calculated given the experimental inverse dynamic torques of child slow and fast gaits. The NMSK-model optimization also predicted cost of transport (COT) (Figure 1) and muscle excitations (Figure 2) for the different-speed gaits. The COT plot in Figure 1 follows the expected 'U'-shaped curve, where the minimum occurs at the natural speed. Most of the resultant muscle excitations were in agreement with the experimental EMG data (gray plots in Figure 2).

According to the findings from the M gait simulations with different cost functions, the NMSK-model optimizations converged roughly 2.5 times faster than MSK-model optimizations since the control inputs of the NMSK-model optimizations were muscle excitations, the initial guess of which were set to EMG data. The NMSK-model optimization with the SDT3 cost function predicted the most accurate muscle excitations. With the FP cost function, the NMSK-model optimization predicted angles, torques, tangential, and normal GRFs with root-mean-square errors (RMSEs) of 5.8 degree, 7.5 N.m, 15.8 N, and 62 N, respectively, which are 20%, 16%, 10%, and 8% more accurate than the MSK-model optimization's results. The NMSK-model optimization with the FP cost function predicted muscle excitations with an RMSE of 0.06, 12% more accurate than NMSK-model optimization's muscle excitations with the FDT cost function.

Table 1. The configurations of cost functions.

#	cost function	cost term					
		DYN	STB	HC	DT		
					Trq	Ang	GRF
1	FDT	✓	✓	✓	✓	✓	✓
2	SDT1	✓	✓	✓	-	✓	✓
3	SDT2	✓	✓	✓	✓	-	✓
4	SDT3	✓	✓	✓	✓	✓	-
5	SP1	✓	✓	✓	-	-	✓
6	SP2	✓	✓	✓	-	✓	-
7	SP3	✓	✓	✓	✓	-	-
8	FP	✓	✓	✓	-	-	-

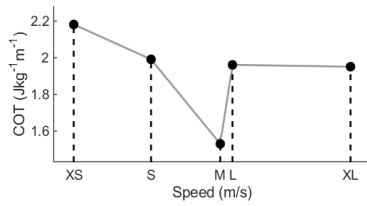


Figure 1. Predicted cost of transport vs. gait speed.

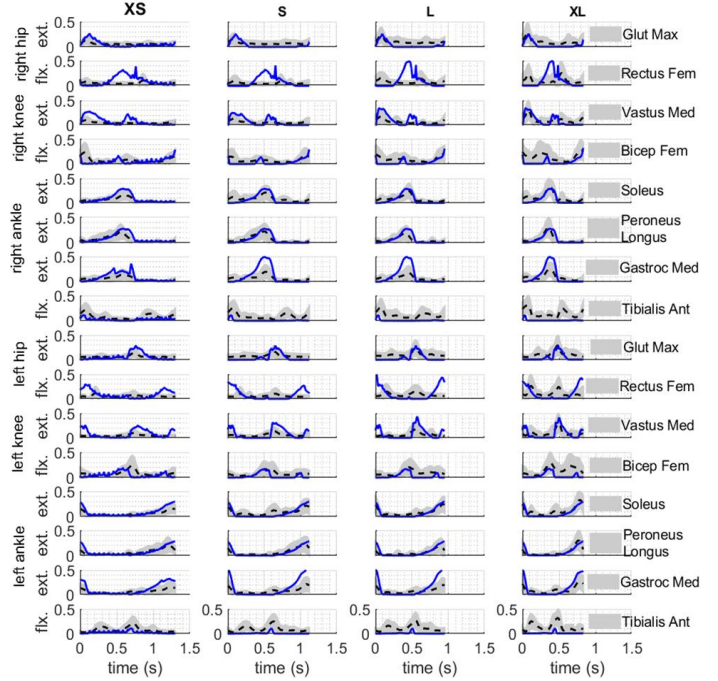


Figure 2. Predicted muscle excitations vs. time.

## 4 Conclusion

The proposed MSK-model and NMSK-model optimizations could minimize the reliance of simulations on experiments and predict dynamically-consistent and physically-realistic slow and fast gaits for children by tracking the scaled experimental data of natural-speed gait. In addition, with the fully-predictive cost function, the proposed NMSK-model could predict angles, torques, GRFs, and muscle excitations comparable with experimental data and estimate COT (1.53 J/kg-1m-1) for child natural gait.

## Acknowledgments

This research was funded by the Natural Sciences and Engineering Research Council of Canada (NSERC) and the Canada Research Chairs (CRC) program.

## References

- [1] M. Ezati, P. Brown, B. Ghannadi, and J. McPhee, "Comparison of direct collocation optimal control to trajectory optimization for parameter identification of an ellipsoidal foot-ground contact model," *Multibody Syst. Dyn.*, pp. 1–23, 2020, doi: 10.1007/s11044-020-09731-3.
- [2] M. Millard, A. L. Emonds, M. Harant, and K. Mombaur, "A reduced muscle model and planar musculoskeletal model fit for the simulation of whole-body movements," *J. Biomech.*, vol. 89, pp. 11–20, 2019, doi: 10.1016/j.jbiomech.2019.04.004.
- [3] G. Bovi, M. Rabuffetti, P. Mazzoleni, and M. Ferrarin, "A multiple-task gait analysis approach: Kinematic, kinetic and EMG reference data for healthy young and adult subjects," *Gait Posture*, vol. 33, no. 1, pp. 6–13, 2011, doi: 10.1016/j.gaitpost.2010.08.009.



# Statistical Analysis of Performance Measures During Acceleration and Deceleration in Overground Running

Liliána Zajcsuk<sup>1</sup>, Ambrus Zelei<sup>2</sup>,

<sup>1</sup> Department of Applied Mechanics  
Budapest University of Technology and Economics  
Műegyetem rkp. 5., 1111 Budapest, Hungary  
zajcsuk@mm.bme.hu

<sup>2</sup> MTA-BME Research Group  
on Dynamics of Machines and Vehicles  
Műegyetem rkp. 5., 1111 Budapest, Hungary  
zelei@mm.bme.hu

## EXTENDED ABSTRACT

### 1 Introduction

Human running has been an increasingly popular research topic over the last decades. There are plenty of open questions, especially regarding the operation of the central nervous system (CNS) and the underlying optimization principles. Based on previous studies, the description of those optimization processes is possible based on a combination of time-variant cost functions. Our long-term goal is to understand this process based on experimental evidences, related to well-defined cost functions, such as energy dissipation, energy conservation or energy accumulation. These cost functions are in analogy with deceleration, constant speed locomotion and acceleration. Numerous scientific papers provide measurement data related to acceleration in the stance phase [1, 2]. However, the literature lacks of analyses for deceleration, and particularly for the airborne phase. We think that deceleration should be investigated, since better understanding of the CNS's optimization principles become possible. Furthermore, many injuries happen during deceleration. Thus, we collected new data related to varying speed locomotion and compared constant velocity running, acceleration and deceleration.

### 2 Methods

Eight non-professional athletes (3 males, 8 females, age:  $17,9 \pm 3,9$ ; height:  $1,697 \pm 0,69$  [m]; weight:  $57,4 \pm 11,7$  [kg]) participated in the measurement. They were performing five tasks corresponding to different cost functions: 1) slow, 2) moderate, 3) high speed running, 4) acceleration to full speed and 5) deceleration from full speed. The kinematics was recorded by OptiTrack motion capture system, and we used Moticon Science Insoles to assess the foot pressure distribution. The beginning and the transition of the gait cycles (initial contact - IC and toe off - TO) were identified. Metrics characterizing the locomotion, e.g. joint/segmental angles, position of the centre of pressure (CoP) and its distance from the centre of mass (CoM) and ground reaction force components, were calculated from the raw data for every gait cycle. We also used an inverse dynamics model to evaluate the forces and moments acting on the joints.

### 3 Results

The measures  $m_i(t)$ , such as segmental angles and force data were stored as time functions. The scalar values at stance and flight transitions and extremes were extracted:  $m_i(t_{IC})$  at IC,  $m_i(t_{TO})$  at TO,  $\max(m_i(t))$  and  $\min(m_i(t))$ . The average and the confidence interval (significance level  $p=0.95$ ) were calculated to visualize the data. The most used visualization techniques are collected in Fig. 1. Wilcoxon signed-rank test was used to identify the metrics, which could identify the cost-functions for the different tasks. We also made a correlation analysis to determine, whether there is a correlation between the speed and measures (for constant velocity running) or between the running type (deceleration, constant speed and acceleration) and the measures. Fig. 2 shows plots related to the data analysis. Based on the results of the Wilcoxon signed-rank test, we can state that there is a significant difference in case of the relative and absolute segment angles, total force, angular velocity of the foot and distance between the centre of pressure and centre of mass. Those differences are also visible on the time-functions. For constant speed running, we found that there is a strong correlation between the velocity of the participants and the elevation of the toe and the ankle, therefore the foot, shank, thigh and knee angles also show correlation. Angular acceleration and the CoP-CoM distance also correlate with the velocity. For the deceleration-constant speed running-acceleration comparison there is a strong correlation between the running types and the thigh angle, trunk angle and the  $x$ -components of the forces acting in the joints ( $x$  axis shows the direction of the locomotion).

### 4 Conclusions

Metrics, taken from the literature, were used to observe quantitative changes caused by different cost functions in case of different velocities, acceleration or deceleration. We could also observe some trends regarding the changes caused by the different locomotion types or velocity difference. These results help us to create predictive models of human gait and kinematics reproduction. Functional role and movement strategy of each joint would be identified [2, 3] and included into the models in future work.

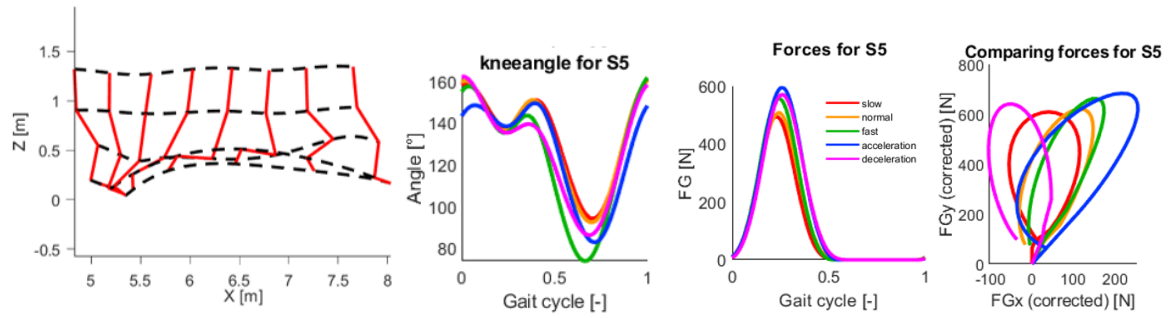


Figure 1: Tools for data visualisation and statistics: stroboscopic visualization of the motion (first panel); knee angle changes during a gait cycle; measured vertical ground reaction force (third panel); path of the ground-reaction force vector [1] (fourth panel).

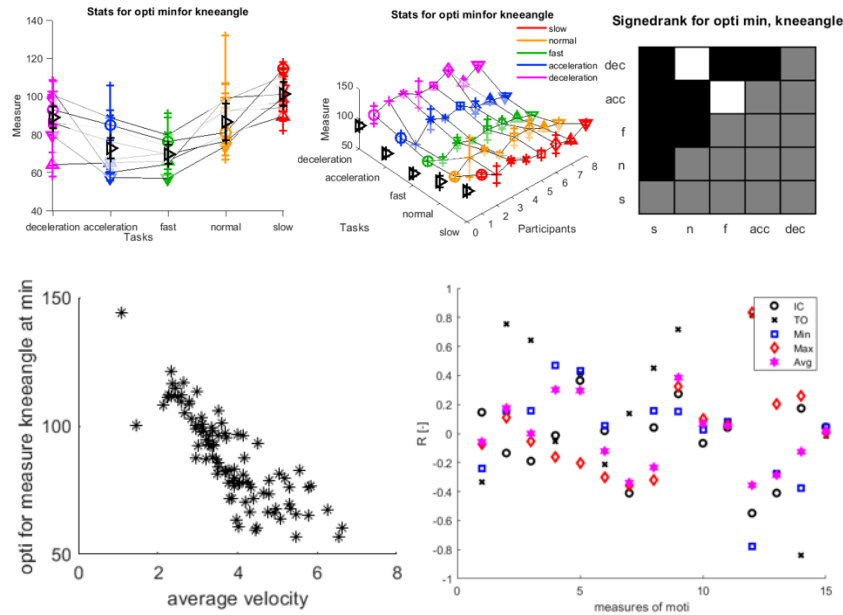


Figure 2: Tools for statistics: confidence intervals for each task in case of each scalar measure (top left panel); confidence intervals for each task and each subject in case of each scalar measure (top middle panel); matrix plot of the signed-rank test, where black / white tiles indicate significant difference / not proven difference for each scalar measure (top right panel); example data plotted for the knee angle minimum to calculate correlation (bottom left panel); correlation coefficients for the measures taken from Moticon (bottom right panel).

## Acknowledgments

The research reported in this paper and carried out at BME has been supported by the NRDI Fund (TKP2020 IES, Grant No. BME-IE-BIO and TKP2020 NC, Grant No. BME-NC) based on the charter of bolster issued by the NRDI Office under the auspices of the Ministry for Innovation and Technology and by the Hungarian National Research, Development and Innovation Office (Grant no. NKFI-FK18 128636).

## References

- [1] van Caekenberghe I., Segers V., Aerts P., Willems P., de Clerq D.: Joint kinematics and kinetics of overground accelerated running versus running on an accelerated treadmill. *Journal of The Royal Society Interface* 2013, 10(84): 20130222.
- [2] Farris D.J., Raitter B.J.: Modulation of leg joint function to produce emulated acceleration during walking and running in humans. *Royal Society Open Science* 2017, 4(3): 160901.
- [3] Jin L., Hahn M.E.: Modulation of lower extremity joint stiffness, work and power at different walking and running speeds. *Human Movement Science* 2018, 58: 1-9.

# An Efficient Discrete Model of a Simple Biped with a Torso

Sarra Gismelseed<sup>1</sup>, Amur Al Yahmedi<sup>2</sup>, Riadh Zaier<sup>2</sup>, Hassen M. Ouakad<sup>2</sup>, Issam Bahadur<sup>2</sup>

<sup>1</sup>Department of Mechanical & Industrial  
Engineering  
Sultan Qaboos University  
Khoud, Muscat, Oman  
sarraabbasher@gmail.com

<sup>2</sup>Department of Mechanical & Industrial Engineering  
Sultan Qaboos University  
Khoud, Muscat, Oman  
[amery, zaier, houakad,  
bahdoor@squ.edu.om]

## EXTENDED ABSTRACT

### 1 Introduction

Many researchers have studied human gait by modeling human body as a simple mechanical system represented mathematically as biped models that can describe the basics of human motion. Many studies in the literature on humanoid robots have focused in deriving the model using standard continuous-time mechanics. In [1], a gait trajectory of biped model in continuous time domain has been provided using simple technique that is based on the symmetric features in the dynamics of this compass-type model. The motion obtained by their technique resembles the phenomenon of a passive dynamic walking, since the motion contains swing phase and a foot collision taking place one after another. Srinivasan et. al., [2] have simulated human gait using an inverted pendulum model with the assumption of a rigid human body and massless legs. The model in [2] generated the energy-based optimal gait of three distinct types of human gait that are; i) walking, ii) inverted pendulum run, and iii) running. The discrete mechanics, on the other hand, have been recently applied to derive biped models. Compass-type biped model and discrete mechanics are used in [3] to formulate a gait generation problem. They have verified the generation of a stable gait by formulating a constrained nonlinear optimization problem in which the model minimizes the angular velocities using both impact and swing phases models. In 2015, Sun et. al. [4] have studied periodic gait optimization problem of the bipedal walking robot using discrete mechanics. Their study has shown that the algorithm can converge to a stable gait cycle by selecting a proper initial guess of the gait [4]. The paper gives a brief introduction about Discrete Euler Lagrange Formulation and how to derive the system dynamics using this method. Then, an optimization problem is formulated to generate the optimal gait for the biped base on minimum cost function.

### 2 Mathematical Model and Problem Formulation

The proposed model consists of two point masses, one represents the rigid torso and the other one represents the hip, and two massless legs. The hip mass  $m_H$  is at a position  $(x_H, y_H)$  at time  $t$ , and the torso mass  $m_T$  is at a position  $(x_T, y_T)$ . The torque  $\tau(t)$  controls the torso between the stance leg and the torso. The fluctuations of the leg length  $q(t)$  due to flexion of the hip, knee and ankle are incorporated in a single telescopic axial actuator that carries a compressive time varying force  $F(t)$ .

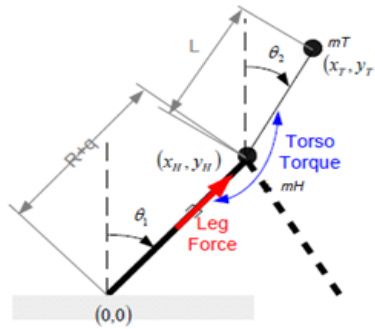


Figure 1: Biped Model with a Torso

The formula of discrete Lagrangian is obtained by estimating the integral of the continuous-time Lagrangian over a small interval of time  $h$  using the midpoint rule [5].

$$\mathcal{L}_d(q_k, q_{k+1}) = \int_{t_k}^{t_{k+1}} \mathcal{L}(q, \dot{q}) dt = h \mathcal{L}\left(\frac{q_{k+1} + q_k}{2}, \frac{q_{k+1} - q_k}{h}\right)$$

The equations of motion are derived using Discrete Euler Lagrange formulation by assuming the two legs are identical and only one-foot contacts the ground.

$$D_1 \mathcal{L}_d(\theta_{1k}, \theta_{1k+1}, \theta_{2k}, \theta_{2k+1}, q_k, q_{k+1}) + f_d^-(\theta_{1k}, \theta_{1k+1}, \theta_{2k}, \theta_{2k+1}, q_k, q_{k+1}) \\ + D_2 \mathcal{L}_d(\theta_{1k-1}, \theta_{1k}, \theta_{2k-1}, \theta_{2k}, q_{k-1}, q_k) + f_d^+(\theta_{1k-1}, \theta_{1k}, \theta_{2k-1}, \theta_{2k}, q_{k-1}, q_k) = 0 \quad (1)$$

Given a specific  $d$ , assuming that the biped starts its step with the nominal leg length ( $R + q(1) = R$ ); we seek the control strategy; that minimizes the cost of transport

$$J = \sum_{k=1}^N h \cdot \frac{|F_k(t)(\frac{q_{k+1}-q_k}{h})| + |T_k(\frac{\theta_{1,k+1}-\theta_{1,k}}{h}, \frac{\theta_{2,k+1}-\theta_{2,k}}{h})|}{2mgd} \quad (2)$$

Subject to dynamics constraints given in equation (1) and satisfying periodicity constraints of the gait:

- Same position and velocity of the torso before and after the step.
- Same velocity of the hip in both X and Y direction before and after the step.
- Same position of the hip in Y direction before and after the step.
- The difference between the final and initial positions of the hip is the step length  $d$ .

In addition to the pervious constraints, the maximum length is constrained to be 10% of the nominal length of the leg [6].

### 3 Simulation Results

In each trial, the optimizer started with different initial conditions. The optimizer will seek solutions as the two parameters step size  $d$  and speed  $v$  are varied. It converges to a unique solution that determines the optimal gait for this speed and step length. The following figures show the gait pattern for 0.6 m step size with velocity of 1.566 m/s. The optimal gait for these parameters, based on the minimum cost of transport, is walking.

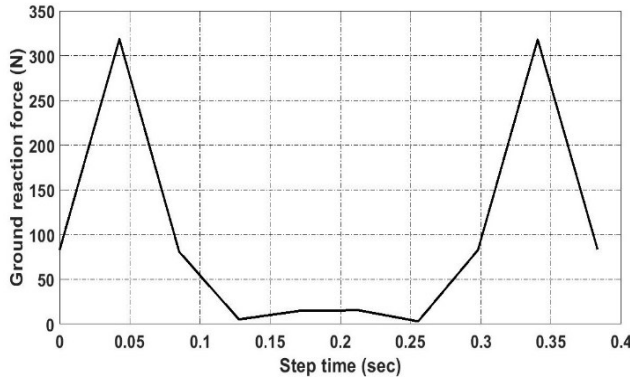


Figure 2: Ground reaction force profile during walking

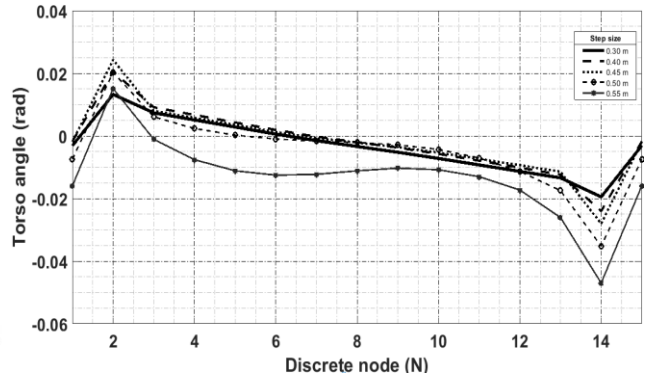


Figure 3: Torso angle at different step sizes

### 4 Conclusion

Despite the fact that the model used is simple and lacking many features of human walking like knee flexion and ankle joint, the gait optimization for this simple model predicts many features of human locomotion. The results show that the movement of torso changes with changing the step size and walking speed.

### References

- [1] Morita S, Fujii H, Kobiki T, Minami S, Ohtsuka T. Gait generation method for a compass type walking machine using dynamical symmetry, 2004 IEEE/RSJ International Conference on Intelligent Robots and Systems (IROS)(IEEE Cat. No. 04CH37566) 2004 Oct (Vol. 3, pp. 2825-2830). IEEE.
- [2] Srinivasan, M., 2006. Why Walk and Run: Energetic Costs and Energetic Optimality in Simple Mechanics-Based Models of a Bipedal Animal, New York: Cornell University.
- [3] Kai T, Shintani T. A discrete mechanics approach to gait generation on periodically unlevel grounds for the compass-type biped robot. International Journal of Advanced Research in Artificial Intelligence. 2013 Sep;2(9):43-51.
- [4] Sun, Z., Tian, Y., Li, H. and Wang, J., 2016. A superlinear convergence feasible sequential quadratic programming algorithm for bipedal dynamic walking robot via discrete mechanics and optimal control. Optimal Control Applications and Methods, 37(6), pp.1139-1161.
- [5] AlYahmedi, A. & Sayari, M., 2014. Efficient Walking Of A Simple Biped With a Torso. Qatar, Middle East Conference on Biomedical Engineering (MECBME), pp. pp. 382-384.
- [6] Kraus, M. (2013). "Variational integrators in plasma physics." [arXiv preprint arXiv:1307.5665](https://arxiv.org/abs/1307.5665).

# Use of a Multibody Model for Determination of the 3D Human Spine Posture from Wearable Inertial Sensors

Florian Michaud<sup>1</sup>, Urbano Luguís<sup>1</sup>, Javier Cuadrado<sup>1</sup>, David Castaño<sup>2</sup>

<sup>1</sup>Lab. of Mechanical Engineering  
University of La Coruña  
Mendizabal s/n, 15403 Ferrol, Spain  
florian.michaud@udc.es

<sup>2</sup>North Physio  
Avda. Rosalia de Castro 34, bajo B  
15701 Santiago de Comp., Spain  
david.castano.tamayo@gmail.com

## EXTENDED ABSTRACT

Because spine curvature influences vertebral loading and factor-of-risk patterns for neutral standing and other activities [1], determination of the correct location and orientation of the spine bodies is essential for effective prevention, evaluation and treatment of spinal disorders. In this field, the X-ray image is still used as “gold standard”, and remains an essential tool for the diagnosis of spinal abnormalities/deformities, as it accurately reveals the degree and severity of the problem. However, this technology is not accessible for most clinicians, and diagnostic X-ray exposure increases the risk of cancer [2]. Nowadays, there is a wide range of spine posture and motion assessment tools available for clinical use [3]. Even if optoelectronic systems can yield very accurate results, surface markers usually do not offer information on spine rotations. Recent developments in microelectromechanical systems (MEMS) have caused a renewed interest in the use of Inertial Measurement Units (IMUs) to record three-dimensional (3D) human posture and motion [4].

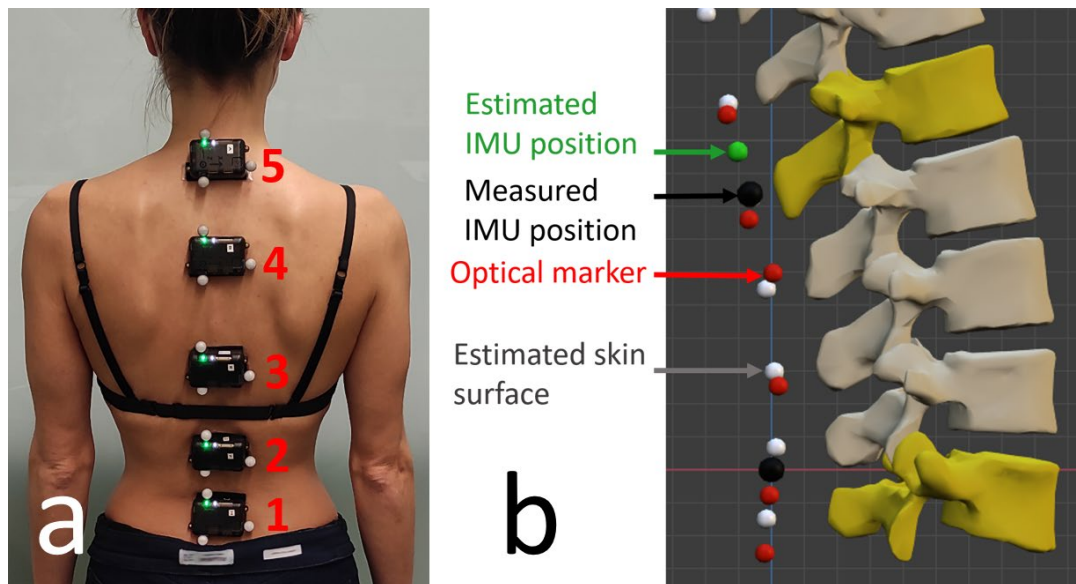


Figure 1: a) IMUs attached to the subject's body and markers attached to the IMUs; b) Multibody model of the spine.

IMUs estimate their own orientation within an Earth-fixed frame by using sensor fusion algorithms, such as Madgwick's algorithm [5] or the extended Kalman filter (EKF). These algorithms provide an estimate of the orientation by combining the information coming from the triaxial accelerometers, gyroscopes and magnetometers present in the IMU. Because the spinal curvature is soft, i.e. it can be approximated using a cubic spline [6], and the relative orientations of vertebrae are limited by anatomical restrictions, a reduced number of sensors can be used to estimate a higher number of vertebral orientations by extrapolation with the help of a multibody model of the spine. In this work, the location and orientation of the 17 vertebrae constituting the thoracolumbar region of the spine were estimated and compared from different sensor configurations (varying the number of sensors from 3 to 5). Calibration of the IMUs, angular offsets, gender differences and scaling difficulties were addressed in this study to achieve an accurate 3D-representation of the spine. To validate the approach and evaluate the accuracy and consistency issues due to IMU measurements, closely related to sensor calibration and magnetometer sensitivity [7], [8], three optical reflective markers were attached to each inertial sensor (Fig. 1a). The locations of the IMUs provided by the optical motion capture system (OPT) were compared with their estimated locations based on the readings from the IMUs and the spine multibody model. Additionally, the proposed method can be applied by using the orientations obtained from the markers instead of those obtained from the IMUs themselves, thus offering both an evaluation of the orientations provided by the IMUs and a new configuration of markers to estimate the missing information on spine rotations observed by using other skin-attached marker configurations.



To validate the approach and the correct location of the bodies, the estimated positions of the sensors using the multibody model (green dots in Fig. 1b) and the inertial measurement system were compared with those obtained from the optical system (black dots in Fig. 1b) using the three markers attached to each IMU (red dots in Fig. 1b). The position of IMU #1 was set as the origin of the two systems, and the position errors corresponding to IMUs #2, #3, #4 and #5, four control points of the 3D spline defined by the spine, were determined for nine healthy subjects with the two motion capture systems (IMU and OPT) and the several sensor configurations (Fig. 2).

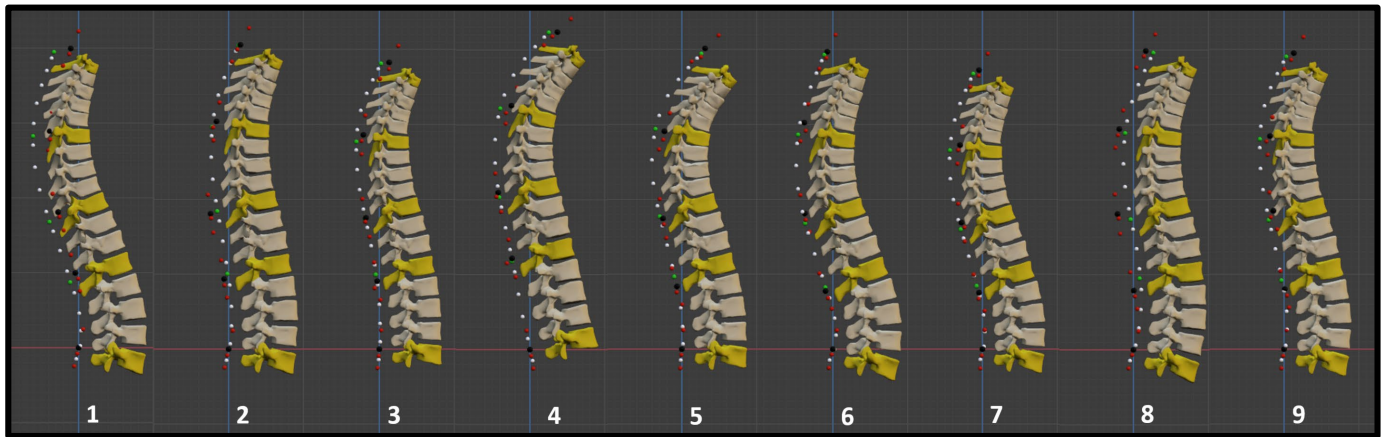


Figure 2: Lateral view of the nine 3D spine postures obtained with the inertial system and five sensors.

Obtaining the sensor orientations from the optical system, the mean errors were 1.05 cm using 4 or 5 sensors, and 1.53 cm using 3 sensors. Obtaining the sensor orientations from the inertial system, the errors showed slightly higher values, with a minimum mean error of 1.23 cm using 4 IMUs, and mean errors of 1.40 cm using 5 IMUs and 1.31 cm using 3 IMUs. The mean error in the location of vertebra T1, the last body of the open kinematic chain, was 0.84 cm using 5 IMUs and the optical system. With the other configurations (either with OPT or IMU), the error at T1 was found to be between 1.0 cm and 1.37 cm. The mean length of the spine measured along the skin of the subjects was 40.8 cm.

## References

- [1] A. G. Bruno, K. Burkhart, B. Allaire, D. E. Anderson, and M. L. Bouxsein, "Spinal Loading Patterns From Biomechanical Modeling Explain the High Incidence of Vertebral Fractures in the Thoracolumbar Region," *J. Bone Miner. Res.*, vol. 32, no. 6, pp. 1282–1290, 2017, doi: 10.1002/jbmr.3113.
- [2] Y. Zhang *et al.*, "Diagnostic radiography exposure increases the risk for thyroid microcarcinoma," *Eur. J. Cancer Prev.*, vol. 24, no. 5, pp. 439–446, Sep. 2015, doi: 10.1097/CEJ.0000000000000169.
- [3] E. Digo, G. Pierro, S. Pastorelli, and L. Gastaldi, "Evaluation of spinal posture during gait with inertial measurement units," *Proc. Inst. Mech. Eng. Part H J. Eng. Med.*, vol. 234, no. 10, pp. 1094–1105, Oct. 2020, doi: 10.1177/0954411920940830.
- [4] G. D. Voinea, S. Butnariu, and G. Mogan, "Measurement and geometric modelling of human spine posture for medical rehabilitation purposes using a wearable monitoring system based on inertial sensors," *Sensors (Switzerland)*, vol. 17, no. 1, 2017, doi: 10.3390/s17010003.
- [5] S. O. H. Madgwick, A. J. L. Harrison, and R. Vaidyanathan, "Estimation of IMU and MARG orientation using a gradient descent algorithm," in *2011 IEEE International Conference on Rehabilitation Robotics*, Jun. 2011, pp. 1–7, doi: 10.1109/ICORR.2011.5975346.
- [6] D. D. Bethune, L. H. Broekhoven, E. Kung, and D. G. Snewing, "Statistical method for evaluating human thoracolumbar spinal curves in the sagittal plane: a preliminary report," *Arch. Phys. Med. Rehabil.*, vol. 67, no. 9, pp. 590–594, Sep. 1986.
- [7] M. A. Brodie, A. Walmsley, and W. Page, "Dynamic accuracy of inertial measurement units during simple pendulum motion," *Comput. Methods Biomech. Biomed. Engin.*, vol. 11, no. 3, pp. 235–242, 2008, doi: 10.1080/10255840802125526.
- [8] J. Cuadrado, F. Michaud, U. Lugrís, and M. Pérez Soto, "Using Accelerometer Data to Tune the Parameters of an Extended Kalman Filter for Optical Motion Capture: Preliminary Application to Gait Analysis," *Sensors*, vol. 21, no. 2, p. 427, Jan. 2021, doi: 10.3390/s21020427.

**Section**  
**BIOMECHANICS**

**BIOMECH-1-2-3**

# A New Method for Feedback and Feedforward Decomposition of Human Postural Control: Application to Single-Leg Yoga Postures

Luciano Menegaldo, Dafne Pires Pinto, Pedro Sarmet Moreira

Biomedical Engineering Program  
Federal University of Rio de Janeiro  
Av. Horácio Macedo 2030,  
21941-914, Rio de Janeiro, Brazil  
lmeneg@peb.ufrj.br

## EXTENDED ABSTRACT

### 1 Introduction

Human postural control requires integrating several control strategies associated with exploring passive joint limits in a mixed feedback-feedforward control [1]. Zatsiorsky and Duarte [2, 3] proposed the Rambling (RM) and Trembling (TR) decomposition of the Center of Pressure (COP) trajectory, in quiet bipedal standing, for assessing feedforward (rambling) and feedback (trembling) mechanisms acting to maintain an upright posture. Rambling represents a slowly moving equilibrium feedforward reference point, mediated mainly by the brain cortex. The trembling part is associated with faster peripheral, spinal reflex feedback control mechanisms, which try to follow or restore the body trajectory toward the reference point [4, 5]. The primary outcome variables of rambling/trembling decomposition are the variability, expressed by the standard deviation, and speed of the decomposed COP trajectories. Here, we investigate whether Yoga practice can induce motor control adaptations at the cortical or spinal levels, comparing RM and TR trajectories of Yoga practitioners (YG) and non-practitioners (CG) while performing two single-leg support Yoga postures, the Vrksasana (tree posture) and Natarajasana (dancer posture).

The original RM/TR decomposition algorithm [2, 3] is based on the subsampling of COP trajectory at the instant equilibrium points (IEP), which are the timestamps when the horizontal force, measured by the force platform, equals zero. These points are the knots for generating interpolating cubic splines that define the RM trajectory. TR is the difference between COP and RM. The original algorithm did not apply to our data because horizontal forces rarely crossed zero while performing the Yoga postures. Additionally, the small horizontal postural forces rely usually over the same magnitude of some force plates accuracy, while low-cost game-designed force platforms, such as the Wii-Board, does not measure horizontal forces. Zatsiorsky and Duarte [2] suggest that RM and TR can be defined, alternatively, by selecting different parts of the COP Power Spectrum Density (PSD). Based on this idea, we introduced a new method to perform the RM/TR decomposition using a genetic algorithm optimization for adjusting the parameters of a Savitzky-Golay (SG) polynomial smoothing filter. SG is a generalized Low-pass finite impulse response filter that preserves signal tendency by fitting data in a moving window with successive low-order polynomials. Here, we have applied this method to Yoga postural data and compared the RM and TR trajectories between YG and CG.

### 2 Methods

Ten yoga practitioners (YG: Yoga Group; three men;  $37.2 \pm 8.7$  years;  $1.66 \pm 0.1$  m;  $63 \pm 10.2$  Kg) and ten non-practitioners (CG: Control Group; four men;  $34.7 \pm 8.6$  years;  $1.67 \pm 0.09$  m;  $69 \pm 15.4$  Kg) participated on the study, which was approved by the Institution's Ethics Committee. The volunteers were instructed to maintain the body as stable as possible while performing the single-leg postures Vrksasana and Natarajasana. Healthy non-yoga practitioners can perform such postures without significant difficulties. A 20-seconds stable stretch of the signal was considered, after the volunteers stabilized the Yoga posture departing from bipedal quiet standing. The biomechanical signals were captured using a BTS Smart-D system (BTS® Bioengineering, Italy) comprising eight infrared cameras sampled at 250 Hz and two P-6000 force platforms (40cmx60cm) sampled at 1000 Hz. Thirty-three reflective markers were placed on specific anatomical body parts. Full-body kinematics and inverse dynamics were reconstructed using the 37 DOF OpenSim Lai-Arnold (<https://simtk.org/projects/model-high-flex>) multibody model. Kinematics, COP and ground reaction forces were filtered by a Butterworth 4th-order zero-lag low-pass filter with the cut-off frequency of 6 Hz. Examples of OpenSim reconstructed postures are illustrated by the videos: Vrksasana <https://doi.org/10.6084/m9.figshare.11529369> and Natarajasana <https://doi.org/10.6084/m9.figshare.11529507>. COP parameters in the anteroposterior (AP) and mediolateral (ML) directions were analyzed separately.

As mentioned above, the original RM/TR algorithm does not apply to our data, and a criterion based on COP PSD was used. The average mean frequency from Zatsiorsky and Duarte [2] data for the RM was  $0.16 \pm 0.03$  Hz and TR  $0.67 \pm 0.12$  Hz, such that the decomposition works approximately as a low/high-pass filter. A genetic algorithm was used to adjust the order (O)  $\in \mathbb{N}$  and the frame length (FL)  $\in \mathbb{N}_{odd}$  of a Savitzky-Golay (SG) polynomial smoothing filter. The genetic algorithm optimization problem was formulated as follows. For each trial, Find O and FL that minimize the cost function  $J$

$$J = \int_{f=0}^{f=0.32} [S_{xx}(COP)^2 - S_{xx}(RM)^2]^{0.5} df + \int_{f=0.48}^{f=2} [S_{xx}(COP)^2 - S_{xx}(TR)^2]^{0.5} df \quad (1)$$



$$RM = SG_{O,FL}(COP) \quad (2)$$

$$TR = COP - RM \quad (3)$$

$$\text{subject to} \quad \begin{aligned} 4 &\geq O \geq 2 \\ 900 &> FL > 100 \end{aligned} \quad (4)$$

PSD ( $S_{xx}$ ) was determined by the Welch periodogram. The genetic algorithm (Matlab ga.m) converged in about one minute for each trial (in an I7-5500U Windows Notebook). Output variables were SD (standard deviation) and SP (speed) for both RM and TR. Speed was calculated as the arclength of RM or TR excursion divided by time (20s).

### 3 Results and discussion

Figure 1 illustrates a time series and PSD obtained with the proposed RM/TR decomposition for Vrksasana in the ML direction. The RM and TR speed and standard deviation were compared between groups using the Mann-Whitney-U test after verifying that the data was not normally distributed. RM and TR data were considered as independent observations, as well as the AP and ML directions. However, SD and SP were regarded as dependent observations, and significant  $\alpha < 0.05$  was divided by two by applying a Bonferroni correction for multiple observations. Vrksasana rambling SD in the ML axis presented statistical differences between groups (median, interquartile range), CG (4.72, 2.42), YG (3.39, 1.14), effect size  $\eta^2 = 0.532$ ,  $p = 0.011$ . Regarding angular kinematics, Yoga practitioners showed a higher lumbar bending and hip abduction angle in Vrksasana. For Natarajasana, YG presented a higher hip flexion and hip extension torque. Therefore, the proposed COP decomposition method was able to identify cortical adaptations associated with reducing rambling variability in the mediolateral axis of Vrksasana posture, suggesting the emergence of supraspinal feedforward motor learning effects mediated by Yoga training. Additionally, biomechanical adaptations were also observed in the Yoga practitioners in the control of the hip and lumbar joints.

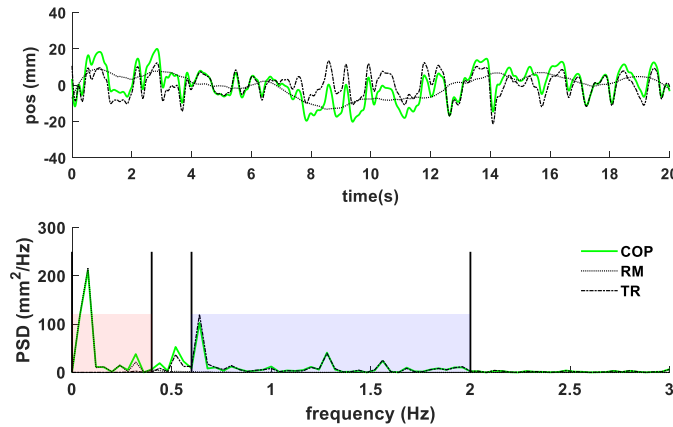


Figure 1: Upper panel, example for COP and its rambling and trembling components for Vrksasana, ML direction. Below, the Power Spectrum Density. The shaded areas correspond to the domain used to set the error integrals of the GA optimization for adjusting the Savitzky-Golay filter parameters.

### Acknowledgments

The authors are acknowledged to the Brazilian Financing Agencies CAPES, CNPq, FINEP and FAPERJ.

### References

- [1] L. A. Teixeira, N. Maia, N. Azzi, J. A. de Oliveira, C. Ribeiro de Souza, L. S. Rezende, D. Boari Coelho. Automatic postural responses are scaled from the association between online feedback and feedforward control. *European Journal of Neuroscience*, 51(10):2023-2032, 2020.
- [2] V. M. Zatsiorsky, M. Duarte. Instant equilibrium point and its migration in standing tasks: rambling and trembling components of the stabilogram. *Motor Control* 3(1):28-38, 1999.
- [3] V. M. Zatsiorsky, M. Duarte. Rambling and trembling in quiet standing. *Motor Control* 4(2):185-200, 2000.
- [4] P. A. M. Ferronato, J. A. Barela. Age-related changes in postural control: rambling and trembling trajectories. *Motor Control* 15(4):481-493, 2011.
- [5] M. B. Speedtsberg, S. B. Christensen, K. K. Andersen, J. Bencke, B. R. Jensen, D. J. Curtis. Impaired postural control in children with developmental coordination disorder is related to less efficient central as well as peripheral control. *Gait and Posture* 51:1-6, 2017

# Estimation of The Reaction Time During Balancing on Rolling Balance Board in The Frontal Plane

Csenge A. Molnar<sup>1</sup>, Tamas Insperger<sup>2</sup>,

<sup>1</sup> Department of Applied Mechanics  
Faculty of Mechanical Engineering  
Budapest University of Technology and Economics  
Muegyetem rkp 5, 1111 Budapest, Hungary  
csenge.molnar@mm.bme.hu

<sup>2</sup> Department of Applied Mechanics  
Faculty of Mechanical Engineering  
Budapest University of Technology and Economics  
Muegyetem rkp 5, 1111 Budapest, Hungary  
insperger@mm.bme.hu

## EXTENDED ABSTRACT

### 1 Introduction

The number of falls caused by loss of balance is increasing nowadays due to the aging society. The main risks of falling are the inactive lifestyle, attenuated vision, impaired medical conditions and the increased reaction time [1]. The stabilization of the human body during balancing is carried out by the central nervous system (CNS). Understanding the operation of the CNS and identifying the critical factor might help to predict and prevent the potential falls and shorten the rehabilitation period. The goal of the current research is to estimate the reaction time during standing on a rolling balance board in the frontal plane and to create a simple model of the CNS.

### 2 Methods

The rolling balance board consists of two wheels and a board made from plywood. The wheels are available with different radii  $R$ . Balancing trials at different dynamic conditions were performed by 15 healthy young adults. Six wheel radii ( $R=50, 75, 100, 125, 150, 200$  mm) and three stance widths ( $d=0.15, 0.25, 0.40$  m) were tested. First, the participants were asked to perform a response time test with the so-called complex reaction time tester (CRTT). CRTT consists of a box providing 10 randomly timed light flashes and as a response, a pedal has to be pushed with the dominant foot of the participant. The second task was to perform balancing trials on balance boards of the selected wheel radii and stance width sizes. The subjects were asked to balance for at least 30 s long with open eyes, stretched legs and arms behind the back (Fig. 1c). To avoid the effect of multiple-try learning, the participants had only one attempt for each combination of  $R$  and  $d$ , therefore a subject performed maximum  $3 \times 6 = 18$  trials. The trials were recorded with OptiTrack motion capture system and analyzed in Matlab environment. The successful  $R$  and  $d$  combinations of subject S1 are denoted by black filled marker in Fig. 2, the unsuccessful trials are shown by white marker with black edge.

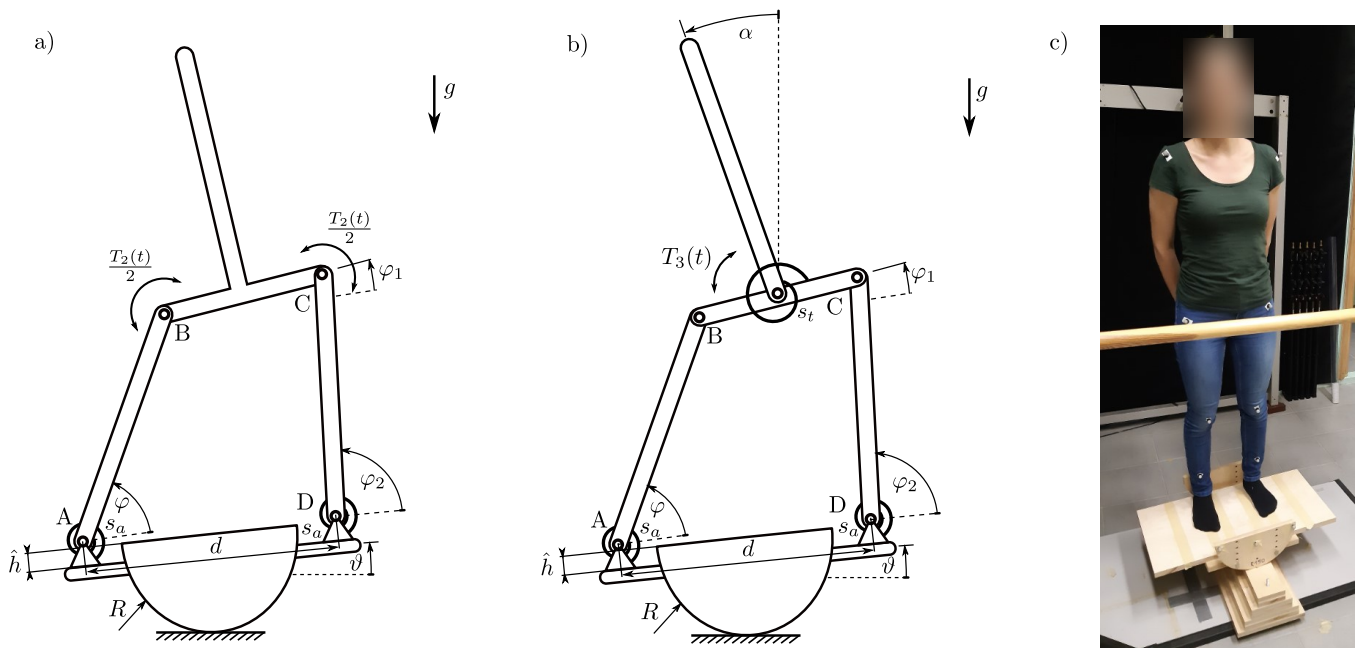


Figure 1: a) Two degree-of-freedom mechanical model of the task. b) Three degree-of-freedom mechanical model of the task. c) Standing on the rolling balance board.

Subjects found the balancing task easier for large wheel radius and small stance width and they employed ankle strategy, which corresponds to a 2-degree-of-freedom (DoF) mechanical model shown in Fig. 1a. The human body is modeled as a four-bar linkage mechanism. As the task becomes more challenging (e.g., by setting smaller wheel radius), ankle strategy is replaced by hip strategy, which can be described by the 3-DoF mechanical model shown in Fig. 1b. During the stabilization process, the receptors of the visual and vestibular sensory organs provide information about the inclination angle and angular velocity of the human body segments and the balance board. Therefore, the operation of the CNS is described by full state feedback. A feedback delay is introduced in the control loop in order to model human reaction time. For the sake of simplicity, the time delay of the visual and vestibular system is estimated with the same value,  $\tau$ .

### 3 Results and discussion

The linearized equation of motion is a system of delay-differential equations. If the data of the human subject and the balance board or equivalently, the coefficients of  $A(s)$  are fixed, then the stability of the trivial solution is affected by the control gains and the delay only. There exists a stabilizing domain of the control gains for each fixed  $\tau$  delay. The size of the domain decreases as the delay increases and completely disappears at the so-called critical feedback delay. The critical delays were calculated for different  $R$  and  $d$  pairs applying the so-called multiplicity-induced-dominance method [2]. The result, namely the stabilizability diagram is shown in Fig. 2 with gray scale.

The critical delays are related to the balancing ability of humans. If the reaction time of a subject is smaller than the critical delay associated with a certain combination of  $R$  and  $d$ , then the subject might be able to balance successfully. However, if larger than the critical delay, balancing is not possible due to the absence of the stabilizing control gains. The reaction time of the participants were estimated by comparing the stabilizability diagram and the distribution of the successful and unsuccessful trials. The reaction time is the average of the critical delays associated with the successful and unsuccessful  $R$  and  $d$  combinations next to the dashed separating line.

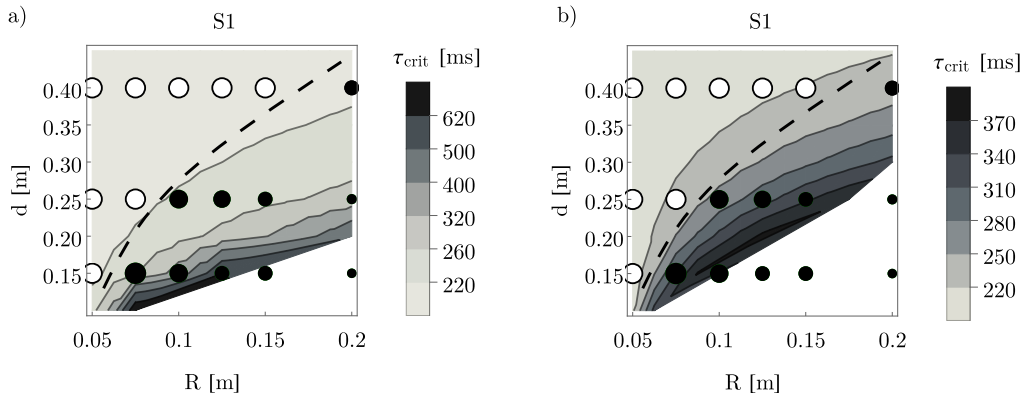


Figure 2: Stabilizability diagram.

Excluding four outlier subjects, the correlation coefficients is 0.78 between the measured response time and the estimated reaction time based on the 2-DoF model and 0.76 between the measured response time and the estimated reaction time based on the 3-DoF model. The average reaction time of the 15 subjects is 222 ms for the 2-DoF and 238 ms for the 3-DoF mechanical model. The estimated reaction times are slightly larger than the reaction time during quiet standing (90-125 ms). During standing on the balance board, more complex signals are to be processed which may require longer time interval. The correlation coefficients suggest that the full state feedback might be an appropriate model of the operation of the CNS.

### Acknowledgments

The research has been supported by the UNKP-20-3 New National Excellence Program of the Ministry for Innovation and Technology from the source of the National Research, Development and Innovation Fund.

### References

- [1] S. N. Robinovitch et al. Video capture of the circumstances of falls in elderly people residing in long-term care: an observational study. *The Lancet*, 381(9860):47–54, 2013.
- [2] C. A. Molnar et al. Calculation of the critical delay for the double inverted pendulum. *J. Vib. Control*, page 1077546320926909, 2020.
- [3] C. A. Molnar et al. Rolling balance board of adjustable geometry as a tool to assess balancing skill and to estimate reaction time delay. *J. R. Soc. Interface*, 18:20200956, 2021.

# Biomechanical Modeling and Examination of Effects of Ankle Sprain Orthoses

Pedro F. Reymundo<sup>1</sup>, Nils A. Hakansson<sup>2</sup>, Hamid Lankarani<sup>1</sup>

<sup>1</sup>Mechanical Engineering Dept.  
Wichita State University  
Wichita, Kansas 67206-0133, USA  
pfraymundo@shockers.wichita.edu

<sup>2</sup>Biomedical Engineering Dept.  
Wichita State University  
Wichita, Kansas 67206-0066, USA  
nils.hakansson@wichita.edu

<sup>1</sup>Mechanical Engineering Dept.  
Wichita State University  
Wichita, Kansas 67206-0133, USA  
hamid.lankarani@wichita.edu

## EXTENDED ABSTRACT

### 1 Introduction

Ligaments are passive structures that connect articulating bones and keep joints assembled. Mechanically they are much like muscles but with no active contractile element. When treating grade-III ankle sprains, patients are often instructed to immobilize the affected ligaments in order to allow reparative healing. However, signs of functional instability are apparent after long periods of immobilization. Several studies have compared the efficacy of controlled range of motion walker boots and braces against traditional casts in reducing muscle activity. Nevertheless, the integrity of the affected ligaments such as the anterior talofibular ligament (ATFL) during conservative and functional treatments of ankle sprains is a subject that is not yet fully understood. Therefore, the objective of this study was to use musculoskeletal dynamic simulations to study the effectiveness of functional articulated ankle foot orthoses (AFO) in providing muscle stimulation, while simultaneously protecting the affected ligaments and accelerate recovery.

### 2 Method

The methodology of the study includes both experimental protocols as well as modeling and simulation. Kinetic and kinematic data were collected from 10 healthy college-aged, consented subjects (male to female ratio 5:5) as they walked on six force plates under three walking conditions: i) regular unconstrained, ii) rigid right foot CAM Walker boot (0° plantar-flexion/dorsi-flexion), and iii) right foot CAM Walker with range of motion of 20° plantar-flexion and dorsi-flexion. Kinematic data were collected using an 11-camera video-based motion analysis system and a 27 retro-reflective marker set used to define the foot, shank, thigh, pelvis, torso, and head segments for each subject as they walked (Figure 1). Reflective markers for the heel, and lateral/medial malleolus were placed on the surface of the boot for the rigid AFO and articulated AFO conditions. EMG data were collected using surface electrodes from three superficial muscles: right tibialis anterior, right extensor digitorum longus, and right peroneus longus. Subjects performed 5 trials for each of the 3 conditions mentioned above for a total of 15 gait trials per subject.

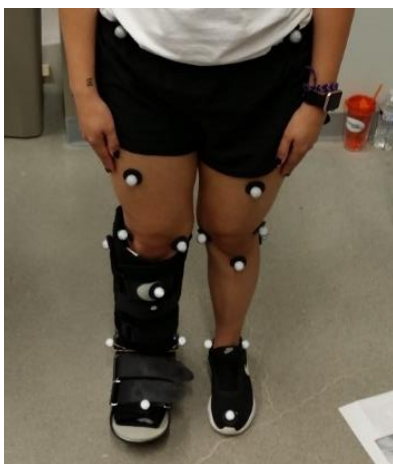


Figure 1: Lower limb marker set with AFO

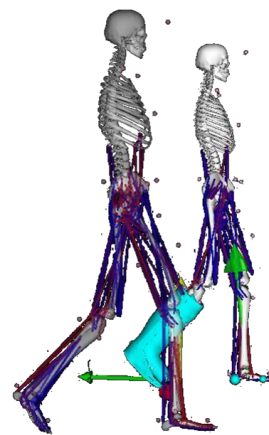


Figure 2: Lumped torso/lower limbs modeling and CMC simulation examples performed in OpenSim

Walking simulations were generated using a musculoskeletal biomechanics simulation software, OpenSim [1]. A musculoskeletal model with two legs and a lumped torso segment that includes 23 degrees-of-freedom and 92 muscle-tendon actuators was utilized in this study. The equations and parameters to model the ligament and the force-length curve are based on the study in [2], and the ligament modeling techniques used in AnyBody Modeling System [3]. To generate walking simulations, the model was scaled to best fit the subject mass and marker positions. The Inverse Kinematics tool was then used to calculate limb segment positions and joint angles based on the experimental marker position data. The resultant kinematics and experimentally measured ground reaction forces were imported into the Computed Muscle Control (CMC) tool to calculate the muscle activations, lengths, and forces for all three experimental walking conditions. Experimental EMG was used to validate the simulation-generated

muscle activity. Special attention was given to the tibialis anterior (TA), the extensor digitorum longus (EDL), and the peroneus longus (PL). Figure 2 shows examples of CMC simulations with and without the CAM Walker boot. Note, muscles in red are active and muscles in blue are inactive.

### 3 Results

Experimental TA EMG magnitudes increased when walking with the rigid AFO and increased further when walking with the articulated AFO. EDL EMG magnitudes increased only when walking with the articulated AFO. PL EMG magnitudes decreased when walking with the rigid AFO but decreased less when walking with the articulated AFO. Comparison of the experimental EMG and the simulated muscle excitations from OpenSim for the three walking conditions studied resulted in no overall significant difference for the TA and EDL muscles and a significant difference for the PL (Figure 3 shows 0° plantar-flexion/dorsi-flexion condition). High variability was encountered when comparing the collected and simulated muscle activities of the peroneus longus. For the AFO effect on ATFL force, the ankle joint exhibited natural plantarflexion during the swing phase of walking without the AFO, and little and reduced ankle range of motion with the rigid and articulated AFO, respectively, Figure 4. The simulated ATFL ligament forces decreased when wearing a rigid AFO during walking and there was little change in ATFL ligament force loads between walking with the rigid and articulated AFO, Figure 4.

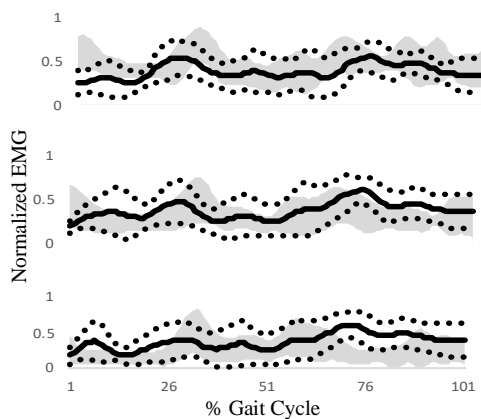


Figure 3: Subject 2 average simulated muscle activations from CMC (solid line +/- 1 SD dotted) and average experimental EMG (grey) for the right TA (top), EDL (middle), and (PL) for walking with the AFO.

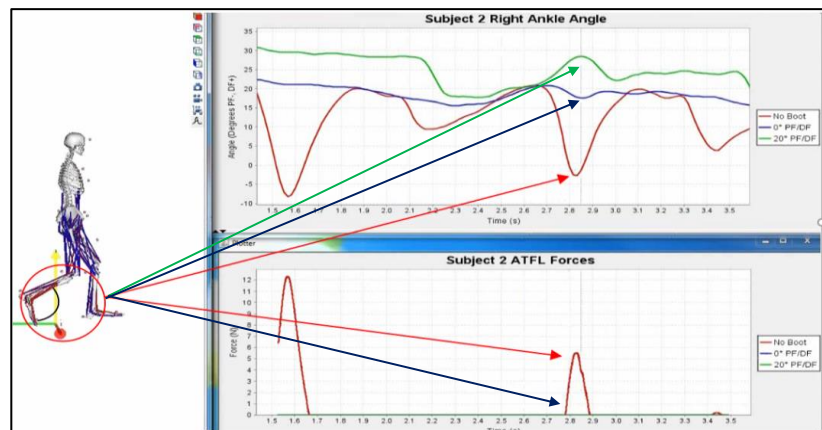


Figure 4: (Upper curves) Subject 2 CMC simulation right ankle joint kinematics for the no boot (red), rigid boot (blue), and articulated boot (green) conditions. Arrows point to the respective angle curves during the swing phase. (Lower curves) ATFL ligament force loads for walking without (red) and with the AFO (blue) are similar.

### 4 Discussion

The goal of this study was to validate the efficacy of functional articulated AFOs in providing muscle stimulation while simultaneously protecting the affected ligaments and promote a quick recovery. It can be inferred from the results that the use of an articulated walker showed a slight increase in muscle activity, which can help stimulate the muscles throughout functional treatment of ankle sprains. The ATFL forces showed a decrease with the rigid boot condition and a minor increase in these forces when range of motion was introduced. Though the study showed that muscle stimulation and ligament integrity was achieved, it was conducted with uninjured subjects, which could limit the generalizability of the results to patients with ankle instabilities.

### 5 Conclusion

The research performed in this study indicates that the use of articulated ankle foot orthoses does in fact stimulate important muscle activity necessary for proper motor control while in turn maintaining the ATFL forces at a minimal. Altogether, the results demonstrated the importance of musculoskeletal dynamic simulations and how they may serve as a tool to uncover the biomechanical causes of movement abnormalities and help design improved treatments. This study conveys evidence that functional treatment should be preferred over conservative immobilization.

### References

- [1] Delp, S. L. et al., "OpenSim: open-source software to create and analyze dynamic simulations of move-ment," IEEE Trans. Biomed. Eng., vol. 54, no. 11, Nov. 2007, pp. 1940–1950.
- [2] Silveira, A. C. P. da, "Extended Biomechanical Model of the Ankle-Foot Complex: Incorporation of Muscles and Ligaments," (Doctoral dissertation), 2015.
- [3] "Anybody Tutorials - Lesson7: Ligaments.," A/S AnyBody Technology. [Online]. Available: [http://www.anybodytech.com/fileadmin/AnyBody/Docs/Tutorials/chap5\\_Muscle\\_modeling/lesson7.html](http://www.anybodytech.com/fileadmin/AnyBody/Docs/Tutorials/chap5_Muscle_modeling/lesson7.html).

# Kinematic Analysis of Planar Biomechanical Models using Mixed Coordinates

Ivo Roupa, Sérgio Gonçalves, Miguel Tavares da Silva

IDMEC-Institute of Mechanical Engineering  
Instituto Superior Técnico, Universidade de Lisboa  
Av. Rovisco Pais 1, 1049-001 Lisboa, Portugal  
[ivo.roupa, sergio.goncalves, miguelsilva]@tecnico.ulisboa.pt

## EXTENDED ABSTRACT

### 1 Introduction

Kinematic analysis (KA) is a powerful tool used in the study of biomechanical systems, since it allows for the computation of the orientation of the model segments, trajectory of specific points, angular displacement of joints, among other variables of interest. Two approaches can be used to perform the kinematic analysis of multibody systems, namely, forward (FK) or inverse kinematics (IK). In the first case, the model is guided using linear and angular drivers calculated in a previous step. Afterwards, the consistent generalized coordinates are obtained by imposing the kinematic constraints that define the model. On the other hand, in IK the position and orientation of each segment is computed by minimizing the difference between the experimental data and a set of points belonging to the model, namely the coordinates of the system or other points of interest. This procedure allows for the fitting of the computational model to the experimental data.

In biomechanical models, FK should be applied with caution due to experimental errors associated to the measurement, in particular soft tissue artifacts (STA) [1]. The STA refers to the motion of the markers on the surface of the body with respect to the underlying bones due to inertial effects, skin deformation and sliding, gravity and muscle contraction [2]. Moreover, STA is task- and subject- dependent, which makes standard filtering techniques ineffective.

Andersen et al. (2009) showed that the use of methodologies to minimize the errors between experimental markers and model points result in significant differences in the kinematic outcomes when compared with standard methods. On its turn, these differences can lead to large errors and inconsistencies during dynamic analysis [3]. Consequently, a method that enables to adjust the model to the system in study is of particular interest for the biomechanics area, since it can minimize the errors associated to the experimental acquisition of anatomical points that constitute the biomechanical model. To address this issue, several methods have been proposed, being the most common based on optimization techniques [4].

In this work, a new approach based exclusively on kinematic constraints and least-square minimization is proposed to perform the kinematic analysis of biomechanical systems. The methodology considers the use of angular coordinates to model the kinematic drivers of the system. These coordinates are referred to as ‘mixed coordinates’ and complement the set generalized coordinates used by the Fully Cartesian Coordinates (FCC) formulation adopted [5]. This method enables to perform an IK analysis and to determine simultaneously the angular drivers of the model. It allows also for the minimization of the error between experimental and computational points, ensuring a better fit of the model to the experimental data.

### 2 Methods

The mixed coordinates (MC) formulation is defined as a combination of FCC with generalized angular coordinates. These coordinates represent the angular degrees-of-freedom of the kinematic pairs of the model, which will be calculated during the IK analysis. Therefore, MC allow for the simultaneous computation of the generalized coordinates of the biomechanical model and its joint angles.

However, this approach leads to an augmented vector of generalized coordinates of the system, since a new vector with length equal to the total number of angular degrees of freedom of the system is appended to the already existent vector of generalized coordinates. Thus, the use of additional kinematic constraint equations, which will be introduced in the form of trajectory constraints, is required. These trajectory drivers will map the experimental coordinates of points of interest of the model.

An important aspect of MC is that it only requires a change in the structure of the angular kinematic constraint equations of the FCC formulation, since the angle between the vectors of the bodies become a generalized coordinate of the system. Hence, its contribution to the Jacobian matrix of the system is different from the one in FCC, as it includes the terms dependent of the angular coordinates.

The MC were applied in the analysis of 3 gait cycles of a healthy female adult. Kinematic data were collected in the Lisbon Biomechanics Laboratory at Instituto Superior Técnico using 14 infrared Qualisys cameras with a sampling frequency of 100 Hz. The acquisition protocol was based on the PlugInGait model. The location of the hip joints was determined based on regression equations [6], whereas ankle, knee, elbow, and wrist joints were calculated based on the coordinates of the respective lateral and medial markers.



To compare the error associated with each approach, namely, FCC and FCC+MC, the root mean square errors (RMSE) between the experimental coordinates of each joint center and its estimation based on the consistent generalized coordinates of the model were computed. Additionally, the CPU time required to perform each kinematic analysis was also measured.

### 3 Results

On average, the errors associated with the position of the joints were significantly lower in the IK analysis with the FCC+MC formulation. The accuracy for the IK method was approximately 3 orders of magnitude smaller than those obtained using FK for all the joints. Regarding the CPU times, the FK analysis with FCC took 4.49s and approximately 4 iterations per time frame to obtain the solution using the Newton Raphson method. On the other hand, the IK analysis with MC required 12.95s and an average of 8 iterations. These differences may be explained by the higher dimension of the Jacobian matrix in the MC formulation (FK:  $\Phi_{q[58 \times 48]}$ , IK:  $\Phi_{q[82 \times 60]}$ ). However, it is important to note that the processing time spent to obtain the initial angular drivers in the FK case was not included, while in the IK approach the time already consider all the required steps to perform the kinematic analysis and obtain the joint angles and generalized coordinates of the system.

Table 1: Root Mean Square Error (RMSE) between the experimental coordinates of each joint center and its estimation based on the consistent generalized coordinates of the model

	RMSE (mm)												
	Neck		Shoulder		Elbow		Wrist		Hip		Knee		Ankle
Formulation	-	Right	Left	Right	Left	Right	Left	Right	Left	Left	Right	Left	Right
FCC	5.7	9.0	8.7	8.2	9.2	13.5	15.3	14.5	14.6	24.6	24.8	20.9	21.9
FCC + MC	0.005	0.007	0.007	0.005	0.005	0.004	0.004	0.009	0.004	0.006	0.006	0.015	0.017

### 4 Discussion

In general, the accuracy of the kinematic reconstruction using the FCC with MC is significantly higher than when only FCC are used. This issue is the direct result of the minimization of the distance between the model points and experimental data introduced by the method. Moreover, the IK analysis considering the FCC+MC formulation presents the advantage of computing the angular drivers that rule the system, without a preprocessing step.

The use of IK analysis enables also to reduce some of the experimental errors introduced by the use of markers to track the human body, namely the SMA. By simultaneously minimizing the distance to all joints, the method finds a position that better depict the experimental movement, correcting possible displacements of the markers. In addition, this method avoids one of the main drawbacks of the FK analysis, namely the propagation of errors along the kinematic chain, i.e., experimental errors will be passed continuously to the child bodies, resulting, in general, in higher distances between the experimental and model points in the distal joints.

### Acknowledgments

This research was supported by Fundação para a Ciência e a Tecnologia through IDMEC, under LAETA, project UIDB/50022/2020 and project ARCADE with reference PTDC/CCI-COM/30274/2017.

### References

- [1] M. S. Andersen, M. Damsgaard, and J. Rasmussen, "Kinematic analysis of over-determinate biomechanical systems," *Comput. Methods Biomech. Biomed. Engin.*, vol. 12, no. 4, pp. 371–384, 2009, doi: 10.1080/10255840802459412.
- [2] A. Cappello, P. F. La Palombara, and A. Leardini, "Optimization and smoothing techniques in movement analysis," *Int. J. Biomed. Comput.*, vol. 41, no. 3, pp. 137–151, 1996, doi: 10.1016/0020-7101(96)01167-1.
- [3] V. Camomilla, A. Cereatti, A. G. Cutti, S. Fantozzi, R. Stagni, and G. Vannozzi, "Methodological factors affecting joint moments estimation in clinical gait analysis: A systematic review," *Biomed. Eng. Online*, vol. 16, no. 1, pp. 1–27, 2017, doi: 10.1186/s12938-017-0396-x.
- [4] M. Begon, M. S. Andersen, and R. Dumas, "Multibody Kinematics Optimization for the Estimation of Upper and Lower Limb Human Joint Kinematics: A Systematized Methodological Review," *J. Biomech. Eng.*, vol. 140, no. 3, 2018, doi: 10.1115/1.4038741.
- [5] I. Roura, S. B. Gonçalves, and M. Tavares da Silva, "Dynamic Analysis of Planar Multibody Systems with Fully Cartesian Coordinates," 2018 in *Proceedings of 5th International Conference on Multibody System Dynamics*.
- [6] R. B. Davis, S. Ounpuu, D. Tyburski, and J. R. Gage, "A gait analysis data collection and reduction technique," *Hum. Mov. Sci.*, vol. 10, no. 5, pp. 575–587, 1991, doi: 10.1016/0167-9457(91)90046-Z.

# Sars Covid19 Main Protease Mutation Analysis By The Kinematic Method

Xiyu Chen<sup>1</sup>, Sigrid Leyendecker<sup>1</sup>, Henry van den Bedem<sup>2,3</sup>

<sup>1</sup> Institute of Applied Dynamics  
Friedrich-Alexander-Universität Erlangen-Nürnberg  
Immerwahrstrasse 1, 91058 Erlangen, Germany  
xiyu.chen@fau.de

<sup>2</sup> Department of Bioengineering and Therapeutic Sciences  
University of California San Francisco  
94720 San Francisco, CA, USA

<sup>3</sup>Division of Biosciences  
SLAC National Accelerator Laboratory, Stanford University  
94025 Menlo Park, CA, USA

## EXTENDED ABSTRACT

### 1 Introduction

The flexibility of protein is a significant factor for protein conformation and the ligand binding with protein modifies its flexibility. The larger flexibility causes more complex conformational properties and changes its activity. Since 2019, the new coronavirus Sars Covid19 has caused pandemics being harmful in many ways. The main protease (Mpro) of Sars Covid19 is known as one of the potential drug targets whose investigation is worthwhile for potential drug development. In particular, Mpro selecting as a target is relatively safe because it has no human homolog, which decreases the probability to target a wrong host protein [1, 2]. Three domains are contained in the Mpro protomer and the N-terminal finger (1-9) normally has a significant influence on its activity [3]. However, the conformation and the influence of the Mpro monomer are still not clear. In this work, we investigated the mutation effects of the Mpro of the new Sars coronavirus based on kinematic flexibility analysis. Compared with the possibilities of molecular dynamics investigations, our kinematic method can analyze larger molecules and requires less computational costs.

### 2 Kinematic flexibility analysis

Kinematic flexibility analysis (KFA) is an efficient, fast method to analyze the conformational flexibility and transition of 3D macromolecules and a helpful tool to investigate how their flexibility influences their function. Kinematically, hydrogen bonds and hydrophobic interactions can be modeled as holonomic constraint. KFA treats all covalent bond (dihedral angles) as degrees of freedom  $\mathbf{q}$  and the non-covalent interaction as holonomic constraints  $\Phi(\mathbf{q})=0$ , see [4]. Consistent with these holonomic constraints, the velocity constraints read  $d\Phi/dt = \mathbf{J}\dot{\mathbf{q}} = 0$ .

Through singular value decomposition of the Jacobian matrix  $\mathbf{J}$ , a basis for its nullspace can be determined. This nullspace is identical to the current conformation tangent space. The nullspace contains the admissible velocities  $\dot{\mathbf{q}}$  and it provides the required information for the molecular rigidity analysis and for conformational transitions.

### 3 Kinematic analysis of Sars Covid19 Mpro mutation

The new Sars coronavirus Mpro dimer has two protomers, as shown in the Fig. 1(A) (pdb: 6Y2E), the one protomer of Mpro is in detailed in cyan, the other one surface is shown in grey. For the catalytic activity, dimerization is a significant process. The N-finger of protomers interacts with the other protomers to stabilise the dimer. The structure of the Mpro protomer is shown in the Fig. 1(B) and Fig. 1(C). O. S. Amamuddy et al. [1] studied Sars Mpro conformation and estimated possible mutation position. Based on these mutation positions, we apply the kinematic transition method to analyze the flexibility change after the mutation. These mutation positions are: A7, G15, M17, V20, T45, D48, M49, R60, K61, A70, G71, L89, K90, P99, Y101, R105, P108, A116, A129, P132, T135, I136, N151, V157, C160, A173, P184, T190, A191, A193, T196, T198, T201, L220, L232, A234, K236, Y237, D248, A255, T259, A260, V261, A266, N274, R279 and S301L (as shown in the Fig. 1(B)). In the Sars Covid19 Mpro, each protomer contains three domains, the domain I and domain II contain the residues number 10-99 and residues number 100-182, respectively, the domain III connects with domain II by a linker loop with about 15 residues.

Different inhibitor ligands and different mutations are investigated in this work with regard to their ability to influence the flexibility of the Sars Covid19 Mpro. The pdbfile 6Y2E is Mpro without ligand binding and the other pdbfiles is Mpro with one ligand. For the flexibility, which influence the activity and conformational property of Mpro, the root mean squared fluctuation (RMSF) of the atom positions is a good indicator. Fig. 1(D) shows the ratio between the root mean squared fluctuation (RMSF) values of Mpro with ligands and without ligands. Most of the RMSF ratios are less than 1 which means that the binding of Mpro with the ligand cause the RMSF value to decrease. This indicates that the Mpro becomes more rigidified when binding with the ligand. In particular for the domain I and domain II, the pdbfile 6LU7 with inhibitor N3 shows a large decrease of the RMSF value. On the other hand, the pdbfile 5R7Z residue 214 shows an increased RMSF value and also causes the neighbouring residues to have larger RMSF values than the other regions. Another peak is shown in the N-finger region which stabilise the dimer. Fig. 1(E) shows the RMSF ratios between Mpro with mutation and without mutation. The mutation position is marked in the figure. The pdbfile 6LU7 shows a substantial increase in the RMSF value after mutation, the mutation increases the Mpro's flexibility to peak factors of three in the domain II and domain III. The pdbfile 5R81 shows largely increased RMSF values in the domain III. Also around the mutation positions, the RMSF values increase largely. Furthermore, the pdbfile 5R80 and 6Y2F show decreased RMSF values after the mutation in the domain I and II.



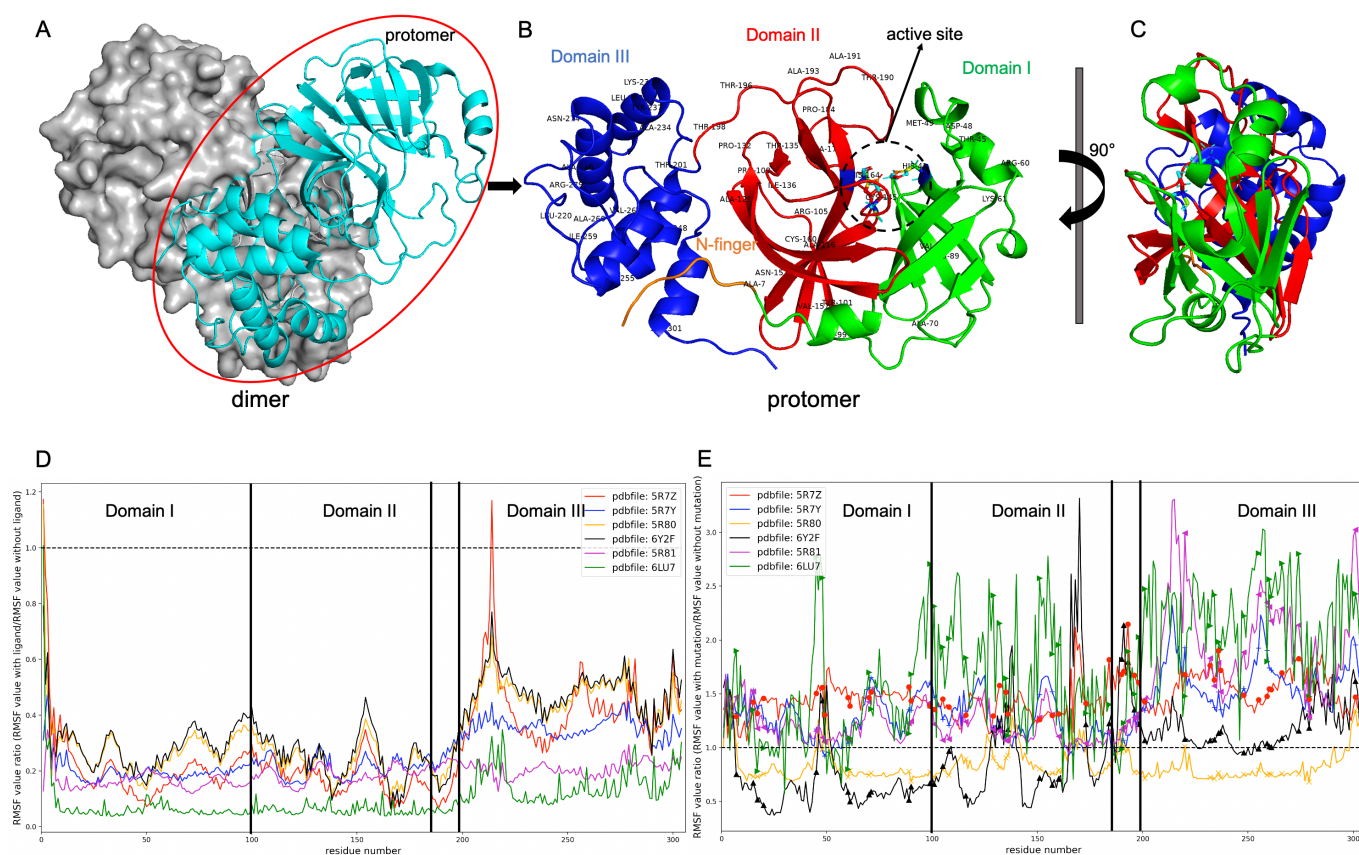


Figure 1: new coronavirus Sars Covid19 Mpro mutation analysis based on the kinematical method. (A) new coronavirus Sars Covid19 Mpro monomer(pdb: 6Y2E, Mpro without ligand binding), the one protomer of dimer is in detailed in cyan and the other one surface is in the gray. (B) each protomer contains three domains and the residue 1-7 is the N-finger (orange), the mutation position is marked with residue name and residue number. (C) The rotated view for the conformational view of the SARS-CoV-2 main protease protomer. (D) the RMSF value ratio between with ligand and without ligand for different pdbfile. (pdb: 5R7Z, 5R7Y, 5R80, 6Y2F, 5R81 and 6LU7, Mpro with ligand binding) (E) the RMSF value ratio between Mpro mutation and without mutation for different pdbfile. The positions of the residues which undergoing mutations are highlighted by the marker

In summary, based on kinematic flexibility analysis, we investigate the flexibility of new Sars Covid19 Mpro and its mutations. The Sars Covid19 Mpro has three domains, and the Mpro becomes more rigidified when it binds with ligands, in particular in the domains I and II. The flexibility decrease upon ligand binding yields potential for the development of drugs. After mutation, the pdbfile 6LU7, 5R7Y, 5R81 and 5R7Z show an increased flexibility because of the residue mutation, while the flexibility of the pdbfile 6Y2F and 5R80 is decreased in the domains I and II after mutation. The larger flexibility cause more complex conformational properties which may make it more dangerous.

## Acknowledgments

The authors gratefully acknowledge financial support by DFG grant LE 1841/5-1 to SL, and NIH award GM123159 to HvdB. HvdB is partially supported by a Mercator Fellowship from the DFG in LE 1841/5-1.

## References

- [1] O. S. Amamuddy, Gennady M. Verkhivker and Ö. T. Bishop. Impact of emerging mutations on the dynamic properties the SARS-CoV-2 main protease: an in silico investigation. *Journal of Chemical Information and Modeling*. 2021
- [2] S. Chen et al. Mutation of Gly-11 on the Dimer Interface Results in the Complete Crystallographic Dimer Dissociation of Severe Acute Respiratory Syndrome Coronavirus 3C-like Protease. *Journal of Biological Chemistry*. 283, 554–564, 2008
- [3] Kneller, D.W., Phillips, G., O'Neill, H.M. et al. Structural plasticity of SARS-CoV-2 3CL Mpro active site cavity revealed by room temperature X-ray crystallography. *Nat Commun* 11, 3202, 2020
- [4] X. Chen, S. Leyendecker, H. van den Bedem. Kinematic Flexibility Analysis of Active and Inactive Kinase Conformations *Proceedings in Applied Mathematics and Mechanics*, 2020

# Assisted Walking with Hybrid Orthosis Using Functional Electrical Stimulation

Albert Peiret<sup>1</sup>, Marcel Jané<sup>1</sup>, Rosa Pàmies-Vilà<sup>1</sup>, Josep M. Font-Llagunes<sup>1</sup>

<sup>1</sup> Department of Mechanical Engineering and Biomedical Engineering Research Centre  
Universitat Politècnica de Catalunya, Diagonal 647, 08028, Barcelona, Spain  
email1@address

## EXTENDED ABSTRACT

### 1 Introduction

Neurological disorders affect body mobility, strength and coordination, and can significantly impact the quality of life. For instance, suffering a spinal cord injury (SCI) generally result in permanent lower-limbs paralysis. Robotic assistive devices, such as lower-limb exoskeletons, can help SCI patients to recover their mobility and autonomy in everyday life. Moreover, advances in neuroprosthetics have shown that functional electrical stimulation (FES) can be used to control joint motion by inducing muscle contraction through electrical assistance [1].

Hybrid assistive devices that combine wearable robotics and neuroprosthesis present some advantages compared to robotic assistive devices. Namely, FES-induced muscle contraction activates muscle metabolism, which delays muscle atrophy and promotes cardiovascular activity. However, determining the optimal control strategy of hybrid devices is still a challenge. Here, we present an optimization framework for musculoskeletal models with hybrid assistive devices using the direct collocation method.

### 2 Methods

The direct collocation method discretizes the optimal control problem in time and formulates a nonlinear optimization problem, where the dynamic equations become the constraints in the optimization. The goal is to find the controls (i.e., device assistance and muscle excitation) and the trajectory (i.e., the state of the system at each time-step) that minimize a cost function.

The cost function can represent the muscle metabolic cost so that energy expenditure is minimized, in addition to the device assistance, and other trajectory-tracking terms. Therefore, the cost function can be written as a

$$J = \sum_{k=0}^N \left( \sum_{coord.} w_{q_i} (q_{i,k} - q_{i,k}^*)^2 + \sum_{vel.} w_{v_i} (v_{i,k} - v_{i,k}^*)^2 + \sum_{muscl.} w_{a_i} a_{i,k}^2 + \sum_{joints} w_{f_i} f_{i,k}^2 \right) \quad (1)$$

where  $q_{i,k}$  and  $v_{i,k}$  are the  $i$ -th generalized coordinate and velocity of the multibody system at the  $k$ -th time-step,  $q_{i,k}^*$  and  $v_{i,k}^*$  are their reference value obtained from experiments,  $a_{i,k} \in [0, 1]$  is the  $i$ -th muscle activation, and  $f_{i,k}$  is the  $i$ -th joint torque of the assistive device. Here, the weights were chosen to be  $w_q = w_v = 1$ , and  $w_a = w_f = 0.01$ .

A musculoskeletal model of the lower-limbs is used to determine muscle activation and optimal device assistance. The limbs are modelled with rigid bodies articulated at the joints, which are represented by ideal kinematic constraints. The model has 10 DOF's of the 2D motion in the sagittal plane, and 18 muscles with the Hill-type muscle model proposed in [2], the equations of which were smoothed to help optimization solver convergence.

The right leg was used to investigate the level of assistance needed for ankle dorsiflexion during the swing phase. Experimental data of a healthy subject was used as reference trajectory for the optimization. The foot-ground contact forces were also measured and used as externally applied forces.

The model and the optimal control problem were implemented with the software package OpenSim, which uses the software library IPOPT as interior-point optimization solver [3].

### 3 Results

Several optimal control problems were solved using different maximum values for the muscle activation of the tibialis anterior,  $a_{max} = \{1, 0.1, 0.01\}$ . These values represent different degrees of FES assistance of the muscle. Figure 1 shows the ankle angle, the muscle activation and the joint assistive torque for the optimal solutions.

Results show that a lower maximum activation requires a higher torque assistance. However, that results in a lower ankle dorsiflexion angle due to the fact that both, angle and torque, are present in the cost function. The higher the torque, the higher the cost associated to the assistance. Therefore, the cost associated with the trajectory-tracking term will only decrease until an equilibrium point in the optimization, where both terms balance each other.

Naturally, the weights of all the terms in the cost function could be adjusted so that the tracking error is minimized and higher torque values can be reached. However, it is worth noting that the physical meaning of these weights should be taken into account in order to find a meaningful optimal solution.

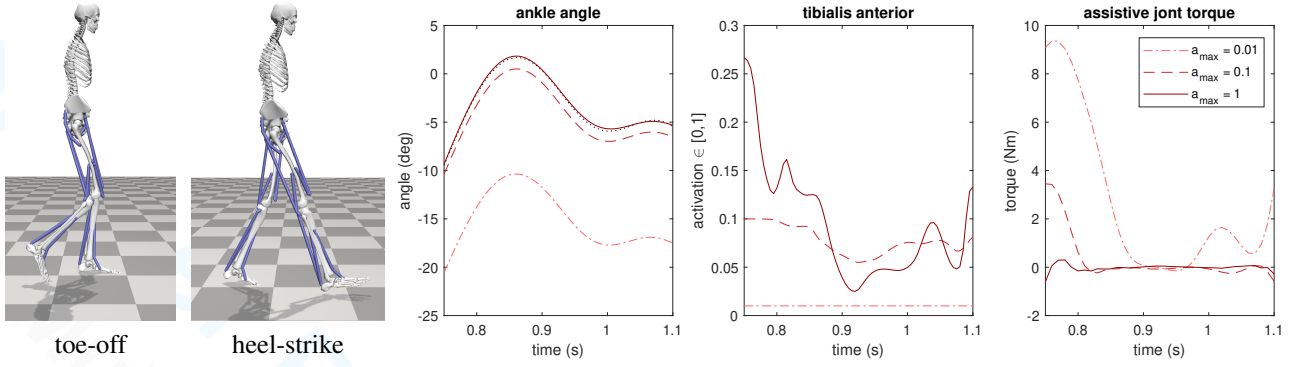


Figure 1: Optimization results for assisted ankle dorsiflexion using different values of maximum muscle activation  $a_{\max}$  of the tibialis anterior during swing, i.e., from toe-off ( $t = 0.75$  s) until heel-strike ( $t = 1.1$  s)

#### 4 Conclusions

It was shown how the assistive torque at the ankle joint increases for lower levels of tibialis anterior assistance. Combining muscle contraction and active torque assistance can help to better understand how hybrid devices can combine wearable robotics and neuroprosthesis. However, solving optimal control problems with musculoskeletal models using hybrid assistance requires some special attention when defining the weight associated to each cost, where the physical meaning of the variables shall not be ignored. In future steps, a more representative model of FES assistance will be added to the optimization.

#### References

- [1] Romero-Sánchez, F., Bermejo-García, J., Barrios-Muriel, J. and Alonso, F.J., 2019. Design of the cooperative actuation in hybrid orthoses: a theoretical approach based on muscle models. *Frontiers in neurorobotics*, 13, p.58.
- [2] De Groote, F., Kinney, A. L., Rao, A. V., Fregly, B. J. (2016). Evaluation of Direct Collocation Optimal Control Problem Formulations for Solving the Muscle Redundancy Problem. *Annals of Biomedical Engineering*, 44(10), 1–15.
- [3] Dembia, C.L., Bianco, N.A., Falisse, A., Hicks, J.L. and Delp, S.L., 2020. Opensim moco: musculoskeletal optimal control. *PLOS Computational Biology*, 16(12), p.e1008493.

# Biomechanics of Swimmers: A Multibody Inverse Dynamics Approach

Francisca Simões, Mariana Sequeira, Carlos Quental, Jorge Ambrósio<sup>1</sup>, João Paulo Vilas-Boas<sup>2</sup>

<sup>1</sup>IDMEC, Instituto Superior Técnico  
University of Lisbon  
Address, 1044-001 Lisbon, Portugal  
{franciscatsimoes, marianafsequeira, car-  
los.quental, jorge.ambrosio}@tecnico.ulisboa.pt

<sup>2</sup>Faculdade de Desporto  
University of Porto  
Address, 4200-450 Porto, Portugal  
jpvb@fade.up.pt

## EXTENDED ABSTRACT

### 1 Introduction

Human motion is one of the objects of study in biomechanics, which involves complex interactions between the neuromuscular and skeletal systems. Understanding these interactions is necessary not only for medical applications but also for sports sciences or for planning physical conditioning activities. Fundamental quantities of interest in human motion research are the intersegmental forces and moments acting at the joints, which represent the net loads that act at each biomechanical joint, and muscle forces. Computational biomechanical models based on multibody dynamics are powerful tools that enable the evaluation of these quantities in the human body, whose in vivo or in vitro measurement is, when possible, extremely difficult [1]. In the context of human swimming, current biomechanical models are mostly based on simplified models of specific parts of the human body [2]. Due to limitations on motion acquisition, especially in the air-water interface, they are kept simple and are hardly able to simulate the broad range of motion of many of the anatomical segments relevant to swimming. Another fundamental data for the evaluation of internal forces are the external forces acting on the human body during swimming, herein referred to as hydrodynamic forces. Unlike terrestrial motion where these external forces are easily measured using force platforms, the determination of the external forces in water is very difficult [2]. This work provides a methodology that allows overcoming the difficulty in obtaining the external forces acting on the swimmer, by estimating them using the Swimming Human Model computational tool, SWUM [3]. These forces distributed on the swimmer biomechanical model anatomical segments are used, together with the model kinematics whose movement is acquired experimentally in the swimming pool, to obtain the internal forces in the model, as depicted by Fig. 1.

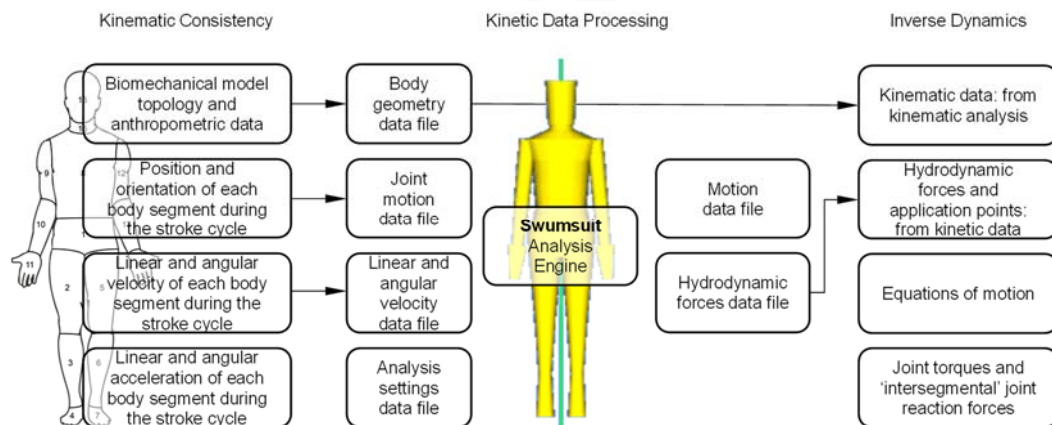


Figure 1: Flowchart for the methodology developed for the estimation of the hydrodynamic forces and their use for the inverse dynamic analysis.

### 2 Methods

The kinematic data is obtained at the Biomechanics Laboratory at University of Porto, LABIOMEUP, for a 25-year-old male swimmer with 70.3 kg, and 1.80 m. By using several underwater and above water infrared cameras the swimmer has 38 markers which allow for the reconstruction of his swimming motion. By following the dataset of Dumas et al. [4] and performing appropriate anatomical segments scaling the characteristics of the anthropometric model are a good match to those of the swimmer subject. Due to the lack of experimental methods to acquire the hydrodynamic forces, these are not obtained experimentally.

The markers spatial positions are first obtained using direct linear transformations being the trajectory of each one of them obtained after applying a double-pass Butterworth filter with appropriate cutoff frequencies. The anatomical segments geometry is scaled from the markers and the intersegmental angles variation with time is also obtained. A kinematic analysis of the biomechanical model, with the intersegmental angles driven by the data acquired is performed to obtain the model positions,



velocities and accelerations at every time instant of the complete swimming cycle. The kinematic data obtained and the anatomical segment geometric data are supplied as input files for the SWUM [3] computational tool, which is used in turn to estimate the hydrodynamic forces on the swimmer model. This tool uses the slice method to obtain forces in each slice of each biomechanical segment of the model. The set of center points for the anatomical segment slices and the distributed hydrodynamic forces constitutes the kinetic data required for the inverse dynamic analysis. The joint torques and the joint 'reaction' forces are obtained by performing the inverse dynamic analysis for which the kinematic data, obtained in the first part of the method, and the kinetic data from SWUM are the required input.

### 3 Preliminary Results

The methodology presented and discussed in this work is applied to a swimmer using a freestyle technique, crawl. In Fig. 2 two frames of an animation of the swimmer motion, in which a graphical representation of the hydrodynamic forces, obtained with SWUM, are displayed. The results obtained allow for the evaluation of the internal forces in the human body biomechanical model which are of particular interest to understand what is the contribution of each anatomical segment for the thrust of the swimmer and what are the forces required to develop such movement. In the process, the estimation of the 'joint reaction' forces allows to have an estimation of the health risks to develop this swimming technique

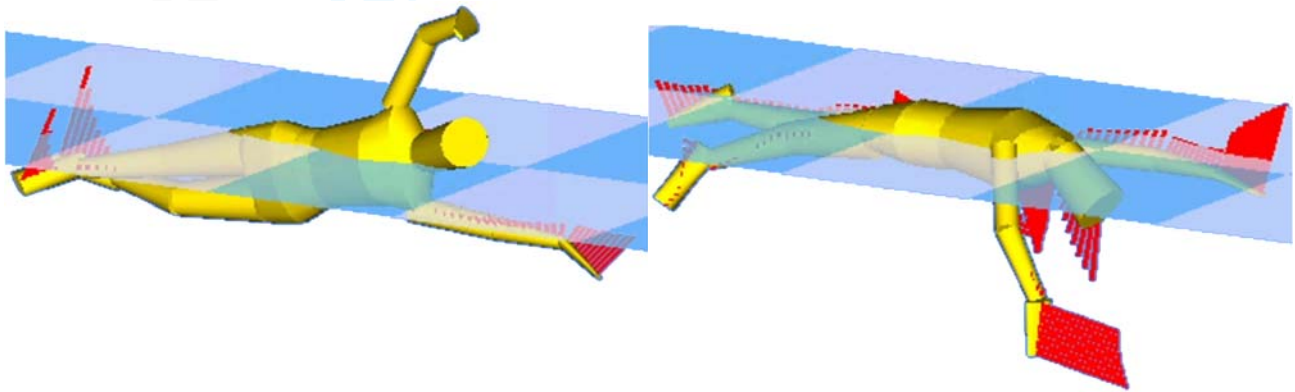


Figure 2: Frames of the model of the swimmer in crawl, as obtained in Swimsuit, with the hydrodynamic forces displayed.

The full length paper provides a more complete description of the results obtained and a critical analysis of the swimming technique used by the subject. The results also allow for planning a training programme that allows the swimmer to develop a more efficient motion or to mitigate his injury potential.

### 4 Preliminary Conclusions

A full-body model of the human body is proposed for inverse dynamic analysis of the lower limbs. To overcome the limitations on the acquisition of the external forces acting on the human body, the simulation software developed by Nakashima et al. [3] is used to determine the hydrodynamic forces, allowing the computation of the intersegmental joint forces and joint torques. The whole methodology proposed is novel and it allows for a consistent inverse dynamic analysis of biomechanical models subjected to distributed hydrodynamic forces. The results of the external hydrodynamic forces support the validity of the interface developed between Swimsuit [3] and the LHBM [2], as the dynamic response developed at the lower limbs is similar between the results obtained here and those reported, for the same swimming motion [3].

### Acknowledgments

This work was supported by FCT, through IDMEC, under LAETA project number UIDB/50022/2020.

### References

- [1] Quental, C., Folgado, J., Ambrósio, J., & Monteiro, J. (2015). Critical analysis of musculoskeletal modelling complexity in multibody biomechanical models of the upper limb. *Computer Methods in Biomechanics and Biomedical Engineering*, 18(7), 749–759. <https://doi.org/10.1080/10255842.2013.845879>.
- [2] Lauer, J., Rouard, A. H., & Vilas-Boas, J. P. (2016). Upper limb joint forces and moments during underwater cyclical movements. *Journal of Biomechanics*, 49(14), 3355–3361. <https://doi.org/10.1016/j.jbiomech.2016.08.027>.
- [3] Nakashima, M., Satou, K., & Miura, Y. (2007). Development of Swimming Human Simulation Model Considering Rigid Body Dynamics and Unsteady Fluid Force for Whole Body. *Journal of Fluid Science and Technology*, 2(1), 56–67. <https://doi.org/10.1299/jfst.2.56>.
- [4] Dumas, R., Chèze, L., & Verriest, J. P. (2007a). Adjustments to McConville et al. and Young et al. body segment inertial parameters. *Journal of Biomechanics*, 40(3), 543–553. <https://doi.org/10.1016/j.jbiomech.2006.02.013>.

# Forward Dynamic Simulations of the Temporomandibular Joint based on Subject-Specific Data

Jianqiao Guo<sup>1</sup>, Junpeng Chen<sup>2</sup>, Jing Wang<sup>2</sup>, Gexue Ren<sup>3</sup>, Qiang Tian<sup>1</sup>

<sup>1</sup>MOE Key Laboratory of Dynamics and Control of Flight Vehicle,  
School of Aerospace Engineering,  
Beijing Institute of Technology,  
Beijing, 100081, China  
guojianqiao@bit.edu.cn (J. Guo)

<sup>2</sup>Department of Oral and Maxillofacial Surgery,  
Peking University School and Hospital of Stomatology  
Beijing, 100081, China  
wjing0122@163.com (J. Wang)

<sup>3</sup> Department of Engineering Mechanics  
Tsinghua University,  
Beijing, 100084, China  
rengx@tsinghua.edu.cn

## EXTENDED ABSTRACT

### 1 Introduction

The temporomandibular joint (TMJ) is a highly active articulation during daily activities. Knowledge of the TMJ dynamics is significant for understanding the mechanism of joint instabilities and refining implant design. Musculoskeletal models provided a non-invasive tool in predicting muscle, ligament, and joint contact forces. However, most existing musculoskeletal models of the mandible were generic without correlations with subject-specific kinematic measurements [1]. To overcome this limitation, we are working on a multibody modeling approach of TMJ based on clinical experiments (ultrasound, CBCT, EMG). As a preliminary study, a CBCT-based method to obtain TMJ kinematics was introduced in this abstract. Its obtained data was then utilized to drive a musculoskeletal model of the mandible.

### 2 Anatomical and kinematic measurements

Four volunteers (3 men and 1 woman, 24-26 years old) without TMJ disorders were recruited. All these subjects provided written informed consent to participate. Their mandible anatomical data were acquired using a CBCT scanner (NewTom VG, NewTom, Italy). During the scanning process, each subject was asked to keep clenching in the intercuspal position.

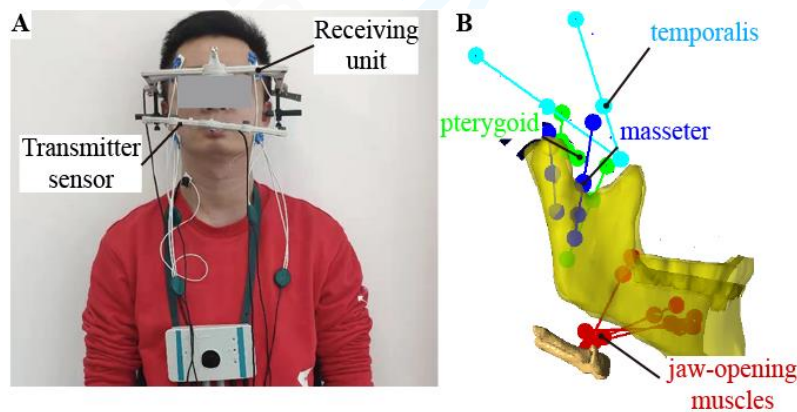


Figure 1: A. Measurements of mandibular kinematics. B. Flexible multibody modeling of the jaw muscles

The mandibular movements of each subject were then recorded using the WinJaw system (Zebris Medical GmbH, Isny, Germany), shown in Figure 1A. Before kinematic measurements, a maxillary plate with three landmarks was glued on the maxillary teeth, and a Trios intraoral scanner (3shape, Copenhagen, Denmark) was used to record its relative position to the upper dentition. The obtained geometries were then co-registered with the CBCT scans based on the anatomical markers (the point between the first upper incisors, marginal ridge, etc.). The initial positions of the lower incisor and the left/right condyle were also recorded for kinematic analysis.

Next, the volunteers were required to perform three trials of maximal opening-closing together with protrusion. Each movement started from the maximum intercuspatation position, ensuring the initial coincidence between the maxillary and mandibular coordinates. Furthermore, we assumed that there exist another three landmarks that were attached to the mandible rigid. These points were coincident with those in the maxillary plate at the beginning of each test. During the mandible movements, time-dependent positions of the virtual landmarks were recorded for further analysis. For validation, the mandible kinematics was also measured by the WinJaw system, using a mobile transmitter sensor glued to the mandibular teeth. Its position relative to the receiving unit that fixed on the head was recorded during each cycle.

Based on the obtained virtual landmark positions  $\mathbf{q}^i$  ( $i=1,2,3$ ), the translational and rotational components of mandible movements were described by a rotation matrix  $\mathbf{R}$  and a translation vector  $\mathbf{v}$ . Using the least-square method provided by Sodervist et al. [2], the problem of determining  $\mathbf{R}$  and  $\mathbf{v}$  is equivalent to minimizing the following formula:

$$\sum_{i=1}^3 (\mathbf{R}\mathbf{q}_{\text{str}}^i + \mathbf{v} - \mathbf{q}^i)^T (\mathbf{R}\mathbf{q}_{\text{str}}^i + \mathbf{v} - \mathbf{q}^i), \quad (1)$$

where  $\mathbf{q}_{\text{str}}^i$  denotes the position of each landmark in maximum intercuspation location.

### 3 Simulations of the jaw open-close movements

A three-dimensional musculoskeletal model of the human mandible was developed using our in-house multibody dynamics simulation code [3-4], shown in Figure 1B. The generic model was based on the published geometrical and physical properties [5]. With the help of CBCT scans, the modeling parameters were linearly scaled based on the distance between the TMJ condyles. The mandible model was actuated by a set of 24 Hill-type actuators, including the main fascicle groups of the masseter, temporalis, pterygoid and digastric muscles. Each muscle fascicle was discretized by the flexible cable element [3]. By this means, the muscular mass was distributed along its fibers, and its active-passive force was calculated based on a typical Hill-type relation. Each joint was modeled as a spherical condylar shape coinciding with a frictionless surface. Here, the contact surface was fitted to the first 10mm of the measured condylar path during protrusion tests.

The simulations of the jaw open-close movements were carried out following the procedure below. First, the three-dimensional rotations of the mandible rigid were applied as the kinematic inputs. The mandible motion was underactuated at this step, and its translational components were determined by the passive stiffness of the jaw-closing muscles. The forward dynamic simulations were then performed using the calculated fascicle length as the target values. Finally, the obtained incisor displacement was finally compared with experimental measurements to validate the simulation procedure.

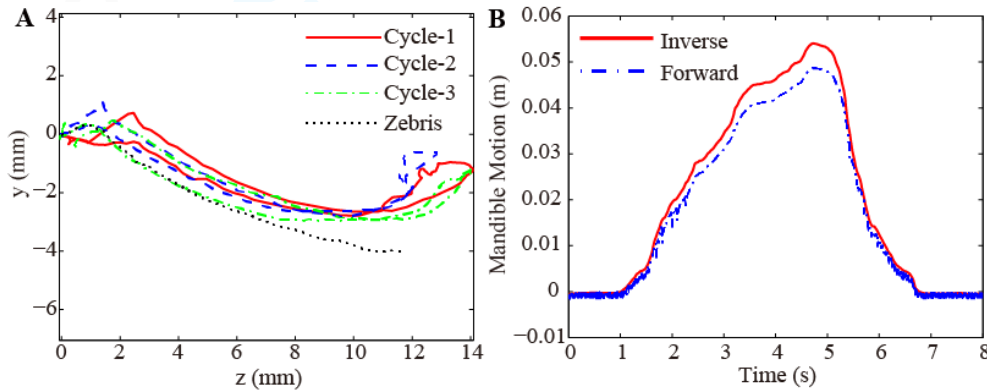


Figure 2: Comparisons of the measured condylar paths (A) and the simulated incisor movements (B) of a typical subject

### 4 Results and conclusion

As shown in Figure 2A, the TMJ pathways recorded agreed with the Zebris measurements in the first 10mm. The observed differences during the late phase of opening were mainly due to the registration error. The mandibular incisor displacements based on the forward dynamic simulations were depicted in Figure 2B. Compared with the measured incisor movements, the proposed musculoskeletal model can reproduce the mandible kinematics of each subject with the RMS error of  $3.7 \pm 1.3$ mm.

The results partially demonstrate that the proposed approach successfully depicts the subject-specific dynamic behavior of the mandatory system, suggesting its potential use in improving the diagnosis and treatment of the TMJ disorders.

### Acknowledgments

This work was supported in part by the Key Projects of International Scientific and Technological Innovation Cooperation among Governments under National Key R & D Plan (2017YFE0124500) and the China Postdoctoral Science Foundation (2020TQ0042).

### References

- [1] S. Benedikt, S.-S. Martina, P. Eva, et al. A dynamic jaw model with a finite-element temporomandibular joint. *Frontiers in Physiology*, 10: 1156, 2019.
- [2] I. Söderkvist, P. A. Wedin. Determining the movements of the skeleton using well-configured markers. *Journal of biomechanics*, 26: 1473-1477, 1993.
- [3] J. Guo, H. Huang, Y. Yu, et al. Modeling muscle wrapping and mass flow using a mass-variable multibody formulation. *Multibody System Dynamics*, 49: 315-336, 2020.
- [4] J. Guo, W. Guo, G. Ren. Embodiment of intra-abdominal pressure in a flexible multibody model of the trunk and the spinal unloading effects during static lifting tasks. *Biomechanics and Modeling in Mechanobiology*, Accepted, 2021.
- [5] M. de Zee, M. Dalstra, P. M. Cattaneo, et al. Validation of a musculo-skeletal model of the mandible and its application to mandibular distraction osteogenesis. *Journal of biomechanics*, 40: 1192-1201, 2007.

# Long Term Simulation of Stem Cell Nucleus During Adipogenesis

Manoochehr Rabiei<sup>1</sup>, Andrew McColloch<sup>2</sup>, Michael Cho<sup>2</sup>, Alan Bowling<sup>1</sup>,

<sup>1</sup> Mechanical and Aerospace Engineering Department  
University of Texas at Arlington  
500 W 1st St, Arlington, TX, 76010, USA  
manoochehr.rabiei@mavs.uta.edu  
bowling@uta.edu

<sup>2</sup> Bioengineering Department  
University of Texas at Arlington  
500 UTA Blvd, Arlington, TX, 76010, USA  
andrew.mccolloch@mavs.uta.edu  
michael.cho@uta.edu

## EXTENDED ABSTRACT

### 1 Introduction

Biomolecular simulations require extensive computational resources in all cases. Even so, simulating large time histories, in order of seconds, remain elusive even with the employment of supercomputers. The underlying biological phenomena have a multiscale nature. The processes range from atomistic to microscale. This multiscale nature infeasibly increases the computational time for acquiring the solution of the dynamic system. In this work a scaling approach, based on the method of multiple scales, is further developed to accomplish a long term simulation of a cellular system. This multiscale approach results in massive reduction in computational time. The test case is the development of a mesenchymal stem cell nucleus during the adipogenic differentiation. This process, observed in 15 days, was simulated in less than 1.5 hours on a typical desktop computer. This drastic reduction in computational time allows for the dynamic study of mechanical properties, such as nucleus membrane stiffness, that are very difficult to experimentally measure with much certainty.

### 2 Test Case and Model

The experiment consists of the induction of human bone marrow-derived mesenchymal stem cells (hMSCs) to form adipocytes using chemical factors[1]. The extent of differentiation effect on the hMSC nucleus was observed for 15 days through fluorescent imaging (Fig. 1). Following image acquisition, fluorescent images were processed for nuclei morphology and lipid production [2].

The system was modeled as one stem cell nucleus in two dimensions, owing to the two-dimensional nature of the data collected in experimental observation. Intra-nuclear particles, such as chromosomes and proteins, are coarse-grained to 250 rigid circular particles, as shown in Fig. 2. Their interactions are modeled as contacts and impacts. The membrane is modeled as one continuous elastic band under tension. The actin microfilaments are modeled as springs that provide structural support for the membrane. The effects of the viscosity of nucleoplasm is modeled as viscous damping due to drag. The random Brownian motion is included with its associated temperature based forces. The effects of lipid accumulation is modeled as external forces on the nucleus. The unscaled model have the form of

$$M(\mathbf{q}) \ddot{\mathbf{q}} = D(\mathbf{q}) \dot{\mathbf{q}} + K(\mathbf{q}) \mathbf{q} + \mathbf{\Gamma}_l \quad (1)$$

where  $K$  denotes the actin microfilament stiffness,  $D$  denotes the viscous damping, and  $\mathbf{\Gamma}_l$  denotes all other large active forces (Contact, Membrane, External, and Forces associated with Brownian motion).

The multiscale nature of this problem stems partially from the length scale, ranging from micrometers to nanometers. More importantly, it stems from the disproportionate size of the large forces to the small masses, femtograms, of the rigid spheres representing the material contained in the stem cell nucleus. The stiffness of the actin microfilaments are also orders of magnitudes larger than viscous damping of cyto- and nucleoplasm. This type of problem is notorious for the unreasonably long computational time required [3], which has made computer simulation of these phenomena over long time range infeasible[4].

Conventional methods for reducing computational time are generally of consists of two categories: coarse-graining of some

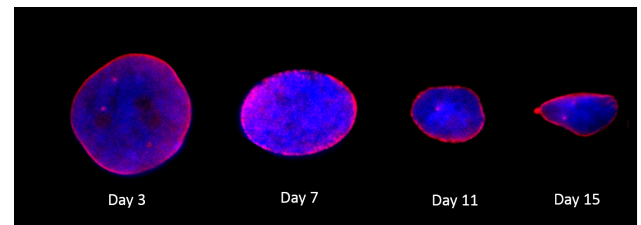


Figure 1: Composite images of nuclear remodeling. The LMAC proteins (red) and DNA (blue) in the nuclei of human MSCs were imaged at different days of adipogenic differentiation. The images were superimposed to demonstrate the distribution of the nuclear envelope proteins and reduction in size of the nuclei.

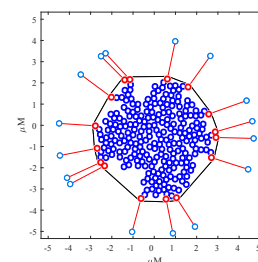


Figure 2: Nuclear model initial configuration.



form[5], or reducing the order of the differential equations [6].

However, even with these approaches, simulating a phenomenon at the nano- or microscale for a period of days cannot be attempted even by deploying supercomputers [4]. In this work, a previously developed scaling approach[7], based on method of multiple scales (MMS)[8], is further developed and used in conjunction with coarse-graining to simulate the stem cell nucleus for long time period of 15 days. By using multiple scaling factors the magnitude of small generalized active forces can be brought to the same scale as the mass term independently of the large generalized active forces [7], preserving their effects in the large time frame. Herein a new analysis of a two scaling factor approach is presented and employed to obtain the solution. Employing this scaling approach to the model in (1) results in the scaled model with the form

$$M(\mathbf{q})\ddot{\mathbf{q}} = a_2 D(\mathbf{q})\dot{\mathbf{q}} + a_2 b_2 K(\mathbf{q}) + a_2 b_2 \mathbf{\Gamma}_l \quad (2)$$

where  $a_2 = 3.2 \times 10^{-10}$  and  $b_2 = 1.6 \times 10^{-12}$  are two scaling factors.

### 3 Conclusion

With this scaling approach, it is possible to stretch the integration time step to large values. This is accomplished by choosing a large characteristic time unit. Herein the time scale of  $1ks = 1000s$  delineates the fast and slow dynamics. This allows the capture the dynamics most important over the long term. This is in extreme contrast with previous works [9, 7, 10] that did not breach the timescale of  $1ms = 10^{-3}s$ . The chosen time scale is in proportion to the observed time frame of the phenomenon of weeks. The simulation of the unscaled model requires a computational time of 1 minute per 1 nanosecond of simulation time history. Based on this estimate, the total computational time required will be on the order of  $\approx 10^{12}$  days. The scaling approach reduces these extreme computational requirements down to 1.5 hours on an HP Z230 workstation desktop with an Intel Xeon E3-1225 v3 processor. The agreement between the simulation and experimental results, as shown in Fig. 3 and discussed further in [2], validates this approach.

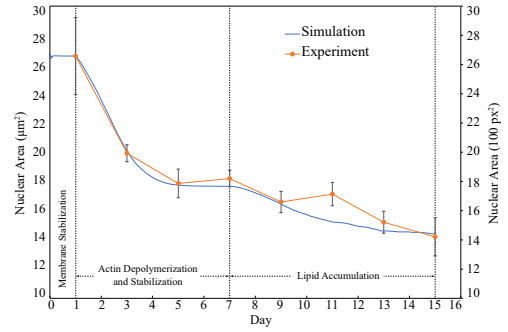


Figure 3: Different stages of the simulation corresponding with experimental data. The results show remarkable alignment between the simulation and experiment.

### References

- [1] Titushkin, I., Sun, S., Paul, A., and Cho, M., 2013. “Control of adipogenesis by ezrin, radixin and moesin-dependent biomechanics remodeling”. *Journal of biomechanics*, **46**(3), pp. 521–526.
- [2] McColloch, A., Rabiei, M., Rabbani, P., Bowling, A., and Cho, M., 2019. “correlation between nuclear morphology and adipogenic differentiation: Application of a combined experimental and computational modeling approach”. *Nature Scientific Reports*, **9**(1), pp. 1–13.
- [3] Dror, R. O., Dirks, R. M., Grossman, J., Xu, H., and Shaw, D. E., 2012. “Biomolecular simulation: a computational microscope for molecular biology”. *Annual review of biophysics*, **41**, pp. 429–452.
- [4] Lane, T. J., Shukla, D., Beauchamp, K. A., and Pande, V. S., 2013. “To milliseconds and beyond: challenges in the simulation of protein folding”. *Current Opinion in Structural Biology*, **23**(1), pp. 58–65.
- [5] Poursina, M., and Anderson, K. S., 2013. “Canonical ensemble simulation of biopolymers using a coarse-grained articulated generalized divide-and-conquer scheme”. *Computer Physics Communications*, **184**(3), 3, pp. 652–660.
- [6] Grogan, F., Lei, H., Li, X., and Baker, N. A., 2020. “Data-driven molecular modeling with the generalized langevin equation”. *Journal of Computational Physics*, **418**, p. 109633.
- [7] Haghshenas-Jaryani, M., and Bowling, A., 2015. “Modeling flexibility in myosin v using a multiscale articulated multi-rigid body approach”. *ASME Journal of Computational and Nonlinear Dynamics*, **10**(1), January, p. 011015 (11 pages).
- [8] Nayfeh, A. H., 1973. *Perturbation Methods*. Wiley.
- [9] Palanki, A., and Bowling, A., 2015. “Dynamic model of estrogen docking using multiscale analysis”. *Nonlinear Dynam.*, **79**(2), January.
- [10] Guy, A., and Bowling, A., 2018. “A multiscale formulation for reducing computation time in atomistic simulations”. *Journal of Computational and Nonlinear Dynamics*, **13**(5), p. 051002.

# Analytical Solutions of the Electromechanical Middle Ear Model with an Implantable Hearing Device

Andrzej Weremczuk<sup>1</sup>, Rafal Rusinek<sup>2</sup>

<sup>1</sup>Department of Applied Mechanics  
Lublin University of Technology  
Nadbystrzycka 38D, 20-618 Lublin,  
Poland  
a.weremczuk@pollub.pl

<sup>2</sup> Department of Applied Mechanics  
Lublin University of Technology  
Nadbystrzycka 38D, 20-618 Lublin,  
Poland  
r.rusinek@pollub.pl

## EXTENDED ABSTRACT

### 1 Introduction

The human middle ear is composed of three bones, i.e. the malleus, the incus and the stapes. These bones are the smallest in the human body and are connected to each other and to the temporal bone by means of ligaments and tendons. Since the middle ear is the smallest and one of the most complicated biomechanical structures in the human body, its modelling is especially demanding and difficult. Sometimes the middle ear has to be modified to improve the hearing process. The use of implantable middle ear hearing devices (implants) is among the most innovative methods of hearing loss treatment. The main objective of this paper is to explain the role of the active implant in the middle ear structure.

The human middle ear (HME) is usually modelled as a multi-degree-of-freedom model of lumped masses by the finite element method (FEM). This model type is more difficult to create but, on the other side, it provides deeper insight into the system dynamics. Lumped mass models with 3 [1], 4 [2] and even 6 [3] degrees of freedom (dof) are usually built to analyze sound transfer through the intact human ear. In most cases, lumped mass models are solved numerically. It is practically impossible to find in literature the description of an analytical solution for the system with more than 3dof [4].

The modelling of the middle ear with an active implant requires the use a multi-degree-of-freedom model. Such device is implanted in the human ear to treat sensorineural hearing loss. The implantable middle ear hearing device (IMEHD) is usually attached to the long process of the incus. This means that at least a 3dof model of the middle ear and a 2dof system of the IMEHD, which is an active element of the implant, are required to describe the middle ear implant (MEI).

### 2 Electromechanical model of implanted middle ear

The proposed model of the middle ear (Figure. 1) consists of three masses: the malleus ( $m_M$ ), the incus ( $m_I$ ) and the stapes ( $m_S$ ) that are connected to each other and to the temporal bone by the incudo-malleal joint (IMJ), incudo-stapedial joint (ISJ) and ligaments: the anterior malleal ligament (AML), the posterior incudal ligament (PIL) and the annular ligament (AL).

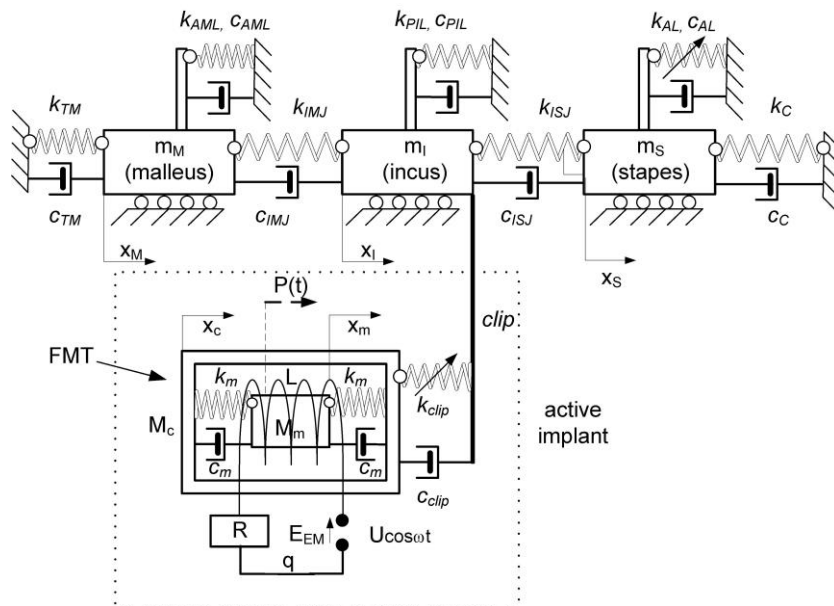


Figure 1: 6dof model of the middle ear with an active implant

Damping and stiffness properties of the elements are denoted as  $c$  and  $k$ , respectively. In the model, the AL has nonlinear stiffness characteristics. Stapes motion is excited by an active implant whose a floating mass transducer (FMT) is the main part.

The FMT consists of a magnet ( $m_m$ ) suspended in a metal case ( $m_c$ ) with dashpots ( $c_m$ ) and springs ( $k_m$ ). The magnet is moved by electromagnetic field generated by an electrical circuit with resistance  $R$  and conductance  $L$  supplied by a voltage source.  $E_{EM}$  denotes the electromotive force that generates an electro-dynamic force ( $P(t)$ ) acting in the mechanical subsystem. The FMT is fixed to the incus long process with a clip whose linear damping and stiffness coefficients are denoted as  $c_{clip}$ ,  $k_{clip}$ . Moreover, nonlinear stiffness is introduced with the coefficients  $k_{clip2}$  and  $k_{clip3}$  to model characteristics of couplers various designs. The governing differential equations of the implanted middle ear (IME) in a dimensional form are as follows:

$$\begin{aligned}
\ddot{x}_M m_M + \tilde{k}_{11} x_M + \tilde{k}_{12} x_I + \tilde{c}_{11} \dot{x}_M + \tilde{c}_{12} \dot{x}_I &= 0 \\
\ddot{x}_I m_I + \tilde{k}_{21} x_M + \tilde{k}_{22} x_I + \tilde{k}_{23} x_S + \tilde{k}_{24} x_c + \tilde{\beta}_{24} (x_I - x_c)^2 + \tilde{\gamma}_{24} (x_I - x_c)^3 + \tilde{c}_{21} \dot{x}_M + \tilde{c}_{22} \dot{x}_I + \tilde{c}_{23} \dot{x}_S + \tilde{c}_{24} \dot{x}_c &= 0 \\
\ddot{x}_S m_S + \tilde{k}_{32} x_I + \tilde{k}_{33} x_S + \tilde{c}_{32} \dot{x}_I + \tilde{c}_{33} \dot{x}_S + \tilde{\gamma}_3 x_S^3 &= 0 \\
\ddot{x}_c M_c + \tilde{k}_{42} x_I + \tilde{k}_{44} x_c + \tilde{k}_{45} x_m - \tilde{\beta}_{24} (x_I - x_c)^2 - \tilde{\gamma}_{24} (x_I - x_c)^3 + \tilde{c}_{42} \dot{x}_I + \tilde{c}_{44} \dot{x}_c + \tilde{c}_{45} \dot{x}_m &= 0 \\
\ddot{x}_m M_m + \tilde{k}_{54} x_c + \tilde{k}_{55} x_m + \tilde{c}_{54} \dot{x}_c + \tilde{c}_{55} \dot{x}_m &= \alpha_0 \dot{q} \\
\ddot{q} L + R \dot{q} + \alpha_0 (x_c - x_m) &= U \cos(\omega t),
\end{aligned} \tag{1}$$

where:  $x$  and  $q$  denote the mechanical coordinates and the electrical charge, respectively. Moreover, the system coefficients are defined as follows:

$$\begin{aligned}
\tilde{k}_{11} &= k_{TM} + k_{AML} + k_{IMJ}, \quad \tilde{k}_{12} = -k_{IMJ}, \quad \tilde{k}_{21} = \tilde{k}_{12}, \quad \tilde{k}_{22} = k_{PIL} + k_{ISJ} + k_{IMJ} + k_{clip}, \quad \tilde{k}_{23} = -k_{ISJ}, \quad \tilde{k}_{24} = -k_{clip}, \quad \tilde{k}_{32} = \tilde{k}_{23}, \\
\tilde{k}_{33} &= k_{AL} + k_{ISJ} + k_C, \quad \tilde{k}_{24} = \tilde{k}_{42}, \quad \tilde{k}_{44} = k_{clip} + k_m, \quad \tilde{k}_{45} = -k_m, \quad \tilde{k}_{54} = \tilde{k}_{45}, \quad \tilde{k}_{55} = -\tilde{k}_{54} = k_m, \quad \tilde{\beta}_{24} = k_{clip2}, \quad \tilde{\gamma}_{24} = k_{clip3}, \quad \tilde{\gamma}_3 = k_{AL3}, \\
\tilde{c}_{11} &= c_{TM} + c_{AML} + c_{IMJ}, \quad \tilde{c}_{21} = -c_{IMJ}, \quad \tilde{c}_{22} = c_{PIL} + c_{ISJ} + c_{IMJ} + c_{clip}, \quad \tilde{c}_{23} = -c_{ISJ}, \quad \tilde{c}_{24} = -c_{clip}, \quad \tilde{c}_{32} = \tilde{c}_{23}, \\
\tilde{c}_{33} &= c_{AL} + c_{ISJ} + c_C, \quad \tilde{c}_{24} = \tilde{c}_{42}, \quad \tilde{c}_{44} = c_{clip} + c_m, \quad \tilde{c}_{45} = \tilde{c}_{54}, \quad \tilde{c}_{55} = -\tilde{c}_{54} = c_m.
\end{aligned} \tag{2}$$

Then the model described by equation (1) was transformed into a dimensionless form, which was solved analytically with the help of the multiple time scale method [5]. As a solution, modulation equations were obtained, which were used to analyze the influence of parameters on the dynamics of the system. The obtained results were verified with the use of a numerical model.

### 3 Summary

A multi-degree-of-freedom nonlinear biomechanical model of the middle ear should generate interesting nonlinear phenomena, especially when the system is coupled to the electrical system of the implant. The interaction between the mechanical and the electrical system will additionally give rise to new phenomena that have not yet been described in literature. The coupling coefficient defined as a constant or nonlinear relation plays the main role in the system dynamics. This paper investigates periodic solutions of a nonlinear model of the middle ear with an active implant. A multi-degree-of-freedom model is used to obtain a solution near the first resonance. The model is solved analytically by the multiple time scales method. Next, the stability of periodic solutions is analyzed in order to determine the influence of parameters on the dynamics of the middle ear with the active implant. Moreover, some parameters of the middle ear structure are investigated with respect to their impact on periodic solutions.

### Acknowledgments

The research was financed in the framework of the project Nonlinear effect in middle ear with active implant, no.2018/29/B/ST 8/01293, funded by the National Science Centre, Poland.

### References

- [1] M. E. Ravicz, W. T. Peake, H. H. Nakajima, S. N. Merchant, and J. J. Rosowski, Modeling flexibility in the human ossicular chain: comparison to ossicular fixation data, Middle Ear Mechanics in Research and Otology (K. Gyo and H. Wada, eds.), Word Scientific, Singapore, 2004. W. Schiehlen. Multibody system dynamics: Roots and perspectives. Multibody System Dynamics, 1:149-188, 1997.
- [2] H. H. Nakajima, M. E. Ravicz, S. N. Merchant, W. T. Peake, and J. J. Rosowski, Experimental ossicular fixations and the middle ears response to sound: Evidence for a flexible ossicular chain, Hearing research 204 (2005), 60–77.
- [3] B. Feng and R. Z. Gan, A lumped-parameter mechanical model of human ear for sound transmission, Second Joint Embs-Bmes Conference 2002, Vol. 1-3, Conference Proceedings (2002), 267–268.
- [4] R. Rusinek, J. Warminski, M. Zadrozniak, and M. Szymanski, Nonlinear approach to modelling of otosclerosis in a human middle ear, Differential Equations and Dynamical Systems 21 (2013), no. 1-2, 45–57.
- [5] A. H. Nayfeh, C. M. Chin, J. Pratt. Perturbation Methods in Nonlinear Dynamics - Applications to Machining Dynamics. Journal of Manufacturing Science and Engineering, 119:485-493, 1997.

# Control Concepts for Human Motion Control During Balancing an Inverted Pendulum

Dalma J. Nagy<sup>1,2</sup>, Tamás Insperger<sup>1,2</sup>

<sup>1</sup> Department of Applied Mechanics  
Budapest University of Technology and Economics  
Műegyetem rkp. 5, H-1111 Budapest, Hungary

<sup>2</sup> MTA-BME Lendület Human Balancing Research Group  
Műegyetem rkp. 5, H-1111 Budapest, Hungary  
[dalma.nagy, insperger]@mm.bme.hu

## EXTENDED ABSTRACT

### 1 Introduction

Control of balance is one of the most important motor skills, which is necessary in almost all every-day activities. Several factors influence an individual's ability to balance, for example genetics, age, emotional state, strength, muscle coordination and flexibility, and training status. The majority of the above mentioned factors can be associated to two important features of balancing, namely, the reaction delay of human nervous systems and to the sensory dead zones of human perception. In the mechanical models of balancing, the corresponding controller is an event-driven intermittent time-delayed control.

The principles of general human balancing tasks is often aimed to understand through stick balancing on the fingertip. In this paper, human stick balancing is investigated in terms of reaction time delay and sensory dead zones for position and velocity perception using a special combination of delayed state feedback and mismatched predictor feedback as control model.

### 2 Control force models

The mechanical model of stick balancing is derived in the anterior-posterior plane of the balancing subject, which is equivalent to the mechanical model of the inverted pendulum-cart system. The inertia of the arm segments is modeled with a cart of equivalent mass  $m_e$ , whereas the mass of stick is  $m$ , its length is  $l$ . The stick is connected to the cart via a planar joint in the model, and the subject exerts the control force  $F$  on the cart in order to stabilize the stick in the upward vertical position. The governing equation was derived using the generalized coordinates  $x$  and  $\varphi$ . Since  $x$  is a cyclic coordinate, it can be eliminated from the equation and one gets

$$\ddot{\varphi} - \frac{6mgl(m + m_e) - 3m^2l^2\dot{\varphi}^2 \cos \varphi}{4ml^2(m + m_e) - 3m^2l^2 \cos^2 \varphi} \sin \varphi = -\frac{6ml \cos \varphi}{4ml^2(m + m_e) - 3m^2l^2 \cos^2 \varphi} F. \quad (1)$$

Several control concepts have appeared in the literature to model the control action during stick balancing. We consider two main concepts: state feedback and predictor feedback, and the combination of these. The simplest state feedback takes the form of a delayed proportional-derivative (PD) controller, which uses the stick angle and stick angular velocity in the feedback loop [1]. Therefore, the control force depends on the delayed state variables of the stick, namely  $\varphi(t - \tau)$  and  $\dot{\varphi}(t - \tau)$ , where  $\tau$  is the delay. The delayed PD controller without sensory dead zone describes human balancing on a global scale well, however, sensory dead zones play an important role in the local dynamics. Here, dead zones are applied for each feedback variable and the control force switches on and off according to whether the state variable(s) is (are) in or out of the dead zone(s).  $\Pi_\varphi$  is the threshold for angular position perception  $\varphi$ , and  $\Pi_{\dot{\varphi}}$  is the threshold for angular velocity perception  $\dot{\varphi}$ .

Research projects on human motion control have also investigated whether the central nervous system employs internal models in motor control [2, 3] to predict the actual state of the balanced object. Results support the existence of such a forward model in the sensory preprocessing control loop. In case of perfect predictor feedback, the feedback loop has zero delay, however, the switching of the control force when state variables exit the dead zone occurs with a delay since within the dead zone the actual state of the stick is unknown and hence no prediction can be made.

An intermediate model between delayed PD and perfect predictor feedback with sensory dead zone is the case when the control force has nonzero delay, which is smaller than the delay of the switching. This can also be interpreted as an imperfect predictor with delay mismatch. The imperfection of the predictor is described by the parameter *delay mismatch*, which provides a transition between perfect predictor feedback (zero delay mismatch) and delayed state feedback (mismatch equal to switching delay).

### 3 Methods

The above explained control models are investigated numerically for a  $l = 40$  cm stick, and the maximum admissible switching delay (critical delay) is determined based on a practical stabilizability concept. Milton et al. [4] performed blank-out tests during stick balancing and showed that the time delay between the offset of the blank-out and the first corrective movement is about 230 ms (range: 220-240 ms for three expert stick balancers). Based on the available results in the literature, we take the reference reaction time delay during stick balancing to  $\tau_{\text{ref}} = 230$  ms, which just coincides with  $\tau_{\text{crit,PD}}$  associated to delayed PD feedback without sensory dead zone for  $l = 40$  cm [5]. In what follows,  $\tau_{\text{ref}} = 230$  ms is compared to the critical delay obtained by numerical analysis of the different mechanical models.

## 4 Results

The solution of the governing equation for delayed PD feedback subject to sensory dead zones resembles to the swirling motion of measured time signals. Still, this model fails in the sense that when more realistic delays are used ( $> 220$  ms) then no stable solution can be found for stick length  $l = 40$  cm.

The stabilizability diagrams are shown in Fig. 1a) for the perfect, and in Fig. 1b-d) for the imperfect predictor feedback with different feedback delays. The critical delays for the perfect predictor feedback model are significantly larger than  $\tau_{\text{ref}}$ . This suggests the perfect predictor feedback may not model well human stick balancing.

When imperfections are introduced in the model by increasing the delay of the control force, then the critical delay becomes smaller. The region of physiologically possible sensory thresholds that yield critical delay close to the reference value  $\tau_{\text{ref}}$  can be determined as the intersection of the  $\tau_{\text{crit}}$  surface and the red plane  $\tau_{\text{ref}} = 230$  ms. Additionally, the solution of the equation of motion for particular parameter combinations again resemble to the seemingly chaotic motion observed in measured time signals.

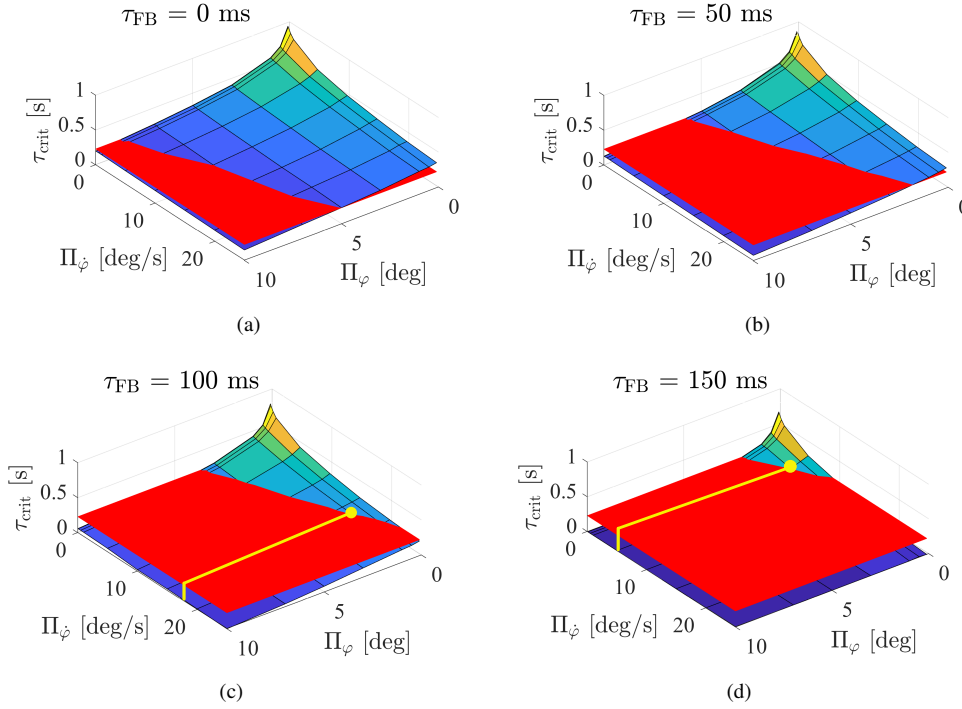


Figure 1: Critical time delays for the perfect a) and imperfect b-d) predictor feedback control models of a  $l = 40$  cm long inverted pendulum as function of sensory thresholds, where  $\tau_{\text{FB}}$  stands for delay in the feedback. Intersection with the red plane  $\tau_{\text{ref}} = 230$  ms marked with yellow dots shows physiologically possible sensory threshold values.

## Acknowledgments

The research reported in this paper and carried out at BME has been supported by the NRDIFund (TKP2020 IES, Grant No. BME-IE-BIO and TKP2020 NC, Grant No. BME-NC) based on the charter of bolster issued by the NRDIFund Office under the auspices of the Ministry for Innovation and Technology.

## References

- [1] J. Milton, J. L. Cabrera, T. Ohira, S. Tajima, Y. Tonosaki, C. W. Eurich and S. A. Campbell. The time-delayed inverted pendulum: Implications for human balance control. *Chaos: An Interdisciplinary Journal of Nonlinear Science*, 19(2):026110, 2009.
- [2] M. Kawato. Internal models for motor control and trajectory planning. *Current Opinion in Neurobiology*, 9(6):718-727, 1999.
- [3] B. Mehta and S. Schaal. Forward models in visuomotor control. *Journal of Neurophysiology*, 88(2):942-953, 2002.
- [4] J. Milton, R. Meyer, M. Zhvanetsky, S. Ridge and T. Insperger, Control at stability's edge minimizes energetic costs: expert stick balancing. *Journal of the Royal Society Interface*, 13(119):20160212, 2016.
- [5] G. Stepan. Delay effects in the human sensory system during balancing. *Philosophical Transactions of the Royal Society A*, 367:1195-1212, 2009.

# Optimal control of a human driver in highly dynamic driving scenarios

Michael Roller<sup>1</sup>, Staffan Björkenstam<sup>2</sup>, Vanessa Dörlich<sup>1</sup>, Monika Harant<sup>1</sup>, Marius Obentheuer<sup>1</sup>, Sigrid Leyendecker<sup>3</sup>, Joachim Linn<sup>1</sup>

<sup>1</sup> Mathematics for the Digital Factory  
Fraunhofer ITWM

Fraunhofer-Platz 1, 67663 Kaiserslautern, Germany

[michael.roller,vanessa.doerlich,monika.harant,marius.obentheuer,jochim.linn]@itwm.fraunhofer.de

<sup>2</sup> Geometry and Motion Planning

Fraunhofer-Chalmers Centre

Chalmers Science Park, 412 88 Gothenburg, Sweden

staffan.bjorkenstam@fcc.chalmers.se

<sup>3</sup> Institute of Applied Dynamics

Friedrich–Alexander University Erlangen–Nürnberg

Immerwahrstrasse 1, 91058 Erlangen, Germany

sigrid.leyendecker@fau.de

## EXTENDED ABSTRACT

### 1 Introduction

To simulate the human driver in early stages of product development, digital human models (DHM) are widely used in automotive industry. Detailed finite element (FE) models of the human body are used to simulate the highly dynamic impact and resulting injuries in the human body in crash simulations [1]. DHM based on multibody system (MBS) kinematics are widely applied in reachability investigations and ergonomic assessment of the driver [2]. These types of models are only used in (quasi-)static scenarios, where the car is standing or driving with constant velocity. In dynamic driving maneuvers like cornering, sudden braking or lane change and pre-crash scenarios, neither FE nor simple MBS kinematic models are applicable. On one hand, FE models are comparatively difficult to control and the simulation times are too long. Simulation times for dynamic driving maneuvers are in the range of seconds, while in crash simulations only milliseconds are computed. On the other hand, purely kinematic MBS models are not able to take dynamic loads and contact forces into account. Furthermore, the motion generation is complicated, because these models are usually based on forward or inverse kinematics.

### 2 Methods

In this work, we will present an approach for the enhancement of a multibody based DHM to generate human like motions for a highly dynamic impact simulation. The human is modelled as a multibody system, where the limbs are rigid bodies and connected via joints. Hill muscles are used to implement digital versions of the real muscles in the human body and to actuate the multibody system. An optimal control algorithm, which is able to handle opening and closing of contacts, is developed in order to generate the dynamic human motion. It allows for the simulation of dynamic interactions of the DHM with the car interior such as the seat, pedals or the steering wheel as well as the impact of the car. In this approach, only some basic boundary conditions have to be prescribed. These include the sitting posture of the human at starting time with two hands on the steering wheel and the trajectory of the car. Using a certain objective function, the optimal control approach generates the desired control (muscle actuation) and the human motion. This approach has already been applied successfully to simulate dynamic motions of workers [3, 4]. A time continuous optimal control problem with two phases  $\alpha \in \{1, 2\}$  is defined abstractly by the following formulas

$$\min_{\mathbf{q}, \mathbf{u}} J = \int_{t_0}^{t_2} \phi(\mathbf{q}, \dot{\mathbf{q}}, \mathbf{u}, \dot{\mathbf{u}}) dt \quad (1)$$

s.t.

$$\frac{\partial L}{\partial \mathbf{q}}(\mathbf{q}, \dot{\mathbf{q}}) - \frac{d}{dt} \frac{\partial L}{\partial \dot{\mathbf{q}}}(\mathbf{q}, \dot{\mathbf{q}}) + \mathbf{F}(\mathbf{q}, \dot{\mathbf{q}}, \mathbf{u}) + \mathbf{G}^T(\mathbf{q}) \boldsymbol{\lambda} + \mathbf{H}_\alpha^T(\mathbf{q}) \mu_\alpha = 0 \quad t \in [t_{\alpha-1}, t_\alpha] \quad \alpha \in \{1, 2\}, \quad (2)$$

$$\mathbf{g}(\mathbf{q}) = 0 \quad t \in [t_0, t_2], \quad (3)$$

$$\mathbf{h}_\alpha(\mathbf{q}) = 0 \quad t \in [t_{\alpha-1}, t_\alpha] \quad \alpha \in \{1, 2\}, \quad (4)$$

The variable  $\mathbf{q}$  represents the temporal trajectory of the MBS between the starting time  $t_0$  and the end time  $t_2$ . The control signals for the muscles and the joint torques are combined in the variable  $\mathbf{u}$ . In (1), the objective function  $J$  is introduced, where  $\phi$  is a measure for the state of the system. As a side constraint, the constrained Euler-Lagrange equations (2)-(4) have to be fulfilled, where the function  $L$  represents the Lagrangian of the system. The function  $\mathbf{g}$  summarizes the constraints and the variable  $\boldsymbol{\lambda}$  is the corresponding Lagrangian multiplier. Both are active across both phases, while the function  $\mathbf{h}_\alpha$  and the corresponding Lagrangian multiplier  $\mu_\alpha$  are only active in one of the phases. Additional equality and inequality constraints can be included in the optimal control problem as boundary conditions. Altogether, the optimal control problem is an optimization problem and the solutions are temporal trajectories of the MBS  $\mathbf{q}$ , the control signals  $\mathbf{u}$  and the Lagrangian multipliers  $\boldsymbol{\lambda}, \mu_\alpha$ . In order to solve the optimal control problem, the continuous problem (1)-(4) is discretised into a non-linear programming problem using discrete mechanics, see [6] for more details. This approach is called DMOCC (discrete mechanics and optimal control with constraints).

The discrete equations of motion derived in this way have been shown to be superior to standard discretisations since they preserve characteristics of the continuous system such as conservation of momentum and a good energy behaviour. This results in very stable integrators, which in practice allows for the use of large time steps when solving the problems. However, additional technical difficulties had to be solved [4, 5] in order to include the correct behavior at the phase transition in the discrete domain.

### 3 Application

As application case we investigate the dynamic scenario of sudden impact of a car with the DHM as the driver. The DHM is a MBS, which is able to translate and rotate freely in space and is actuated mostly by joint torques, while the arms are actuated by Hill muscles. The constraint function (3), which acts across both phases, fixes the hands to the steering wheel, the feet to the pedals and the hip to the seat. The simulation is split in two phases, as defined in (2). In the first phase ( $\alpha = 1$ ) the car is accelerated from starting at standstill. No additional constraint function (4) is needed. At the beginning of the second phase ( $\alpha = 2$ ), the car stops immediately to simulate the impact by adding an additional dynamic constraint  $\mathbf{h}_2$ . Therefore, the kinetic energy of the car is absorbed completely by a phase specific constraint force. The DHM has to use the muscle and control torques to eliminate the kinetic energy during the second phase as there are no additional constraint forces. In Figure 1, a posture of

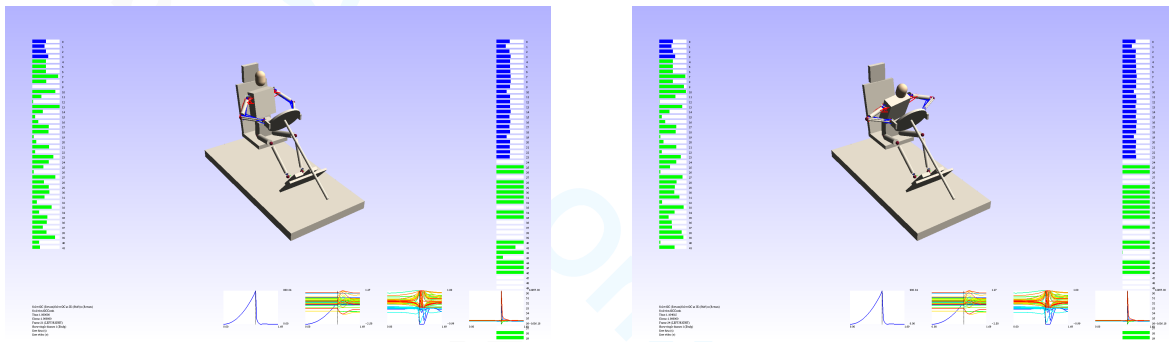


Figure 1: Shows two snapshots of the optimized motion, one before and one shortly after impact.

the manikin in the second phase shortly after the impact is visualized. It can be observed that the upper body of the manikin is moving towards the steering wheel at the beginning of the simulation. This is caused by a lack of strength of the muscles in the arms and the control torques in the lower back to eliminate the remaining kinetic energy immediately.

### 4 Discussion

In this work we present a method to include dynamic impact scenarios in a discrete optimal control framework based on DMOCC. It has to be noted that the motion was generated by the DMOCC method using only the constraints described in section 3. Thus, no tedious and time-consuming forward kinematic positioning of the manikin has to be performed. Additionally, all specified muscle forces and actuation signals are computed by this method as a by-product, which can be used in a further physiological evaluation.

### References

- [1] Iwamoto M, Kisanuki Y, Watanabe I, Furusu K, Miki K, Hasegawa J. Development of a finite element model of the total human model for safety (THUMS) and application to injury reconstruction. In: Proceedings of the international IRCOBI Conference; 2002.
- [2] Hanson L, Högberg D, Carlson JS, Delfs N, Brodin E, Mårdberg P, et al. Industrial Path Solutions—Intelligently Moving Manikins. In: DHM and Posturography. Elsevier; 2019. p. 115–124.
- [3] Björkenstam S, Leyendecker S, Linn J, Carlson JS, Lennartson B. Inverse Dynamics for Discrete Geometric Mechanics of Multibody Systems With Application to Direct Optimal Control. Journal of Computational and Nonlinear Dynamics. 2018;13(10):101001.
- [4] Roller M, Björkenstam S, Linn J, Leyendecker S. Optimal control of a biomechanical multibody model for the dynamic simulation of working tasks. In: Proceeding of the 8th ECCOMAS Thematic Conference on Multibody Dynamics; 2017. In: IFToMM World Congress on Mechanism and Machine Science. Springer; 2019. p. 26–33.
- [5] Koch M, Leyendecker S. Structure preserving optimal control of a three-dimensional upright gait. In: Multibody Dynamics. Springer; 2016. p. 115–146.
- [6] Leyendecker S, Ober-Blöbaum S, Marsden JE, Ortiz M. Discrete mechanics and optimal control for constrained systems. Optimal Control Applications and Methods. 2010;31(6):505–528.



# Optimization and Evaluation of Spinal Exoskeleton Design Concepts using Optimal Control

Monika Harant<sup>1</sup>, Matthias B. Naf<sup>2</sup>, Katja Mombaur<sup>3</sup>

<sup>1</sup> Mathematics for the Digital Factory  
Fraunhofer Institute for Industrial Mathematics  
Fraunhofer-Platz 1, 67663 Kaiserslautern, Germany  
monika.harant@itwm.fraunhofer.de

<sup>2</sup> Department of Mechanical Engineering  
Vrije Universiteit Brussel  
Pleinlaan 2, 1050 Brussels, Belgium  
matthias.basil.naf@vub.be

<sup>3</sup> CERC Human-Centred Robotics and Machine Intelligence  
University of Waterloo  
200 University Avenue West, N2L 3G1 Waterloo, Canada  
katja.mombaur@uwaterloo.ca

## EXTENDED ABSTRACT

### 1 Introduction

Exoskeletons are receiving increasing attention not only in the medical field as a rehabilitation tool, but also in industry to improve working conditions. Spinal exoskeletons are seen as a promising tool to assist workers with lifting tasks and reduce their muscle activity and thus their risk of low back pain. The development of wearable robots is challenging because they must be extensively tested on the human body. In [1], a method is presented to optimize the support of a lower body exoskeleton while it is worn by subjects. This method is difficult to apply to spinal exoskeletons because the subjects would have to lift objects repeatedly over a long period of time while the robot applies high forces on them. In this work, we illustrate an alternative approach by using multibody dynamics and optimal control to optimize the passive elements (PO) of an existing prototype [2] in simulation as well as evaluating a new design concept (DC) that incorporates motors at the hip joints. Both the human and the exoskeleton are simulated in an all-at-once approach that allows the calculation of forces applied by the exoskeleton and the muscle activity needed by the user to reproduce recorded lifting motions. Previous work applied this method successfully to a simple generic exoskeleton to analyze its influence on the dynamics of lifting motions using different cost functions [3].

### 2 Modeling the Human and Exoskeleton

The recorded lifting motions used in the optimization are symmetrical. This allows us to reduce the complexity of the system by modeling the human, exoskeleton, and box as symmetric rigid multibody systems in the sagittal plane. The human model consists of 11 degrees of freedom (DoF). Both arms and legs are lumped together. For the recorded persons, subject-specific models were created, based on anthropometric measurements. The human model is actuated by muscle torque generators (MTG) [4]. The exoskeleton model has 9 DoF and the dynamic parameters were derived from CAD models of an existing prototype. It generates torques at the lower back by 3 carbon fiber beams and at the hip joint by passive elements with a nonlinear torque-angle relationship. Mathematical models replicating the behavior of the passive elements are included in the optimization problem. For DC, a motor is attached to each hip joint to evaluate their effect on the support and contact forces between user and exoskeleton which affects their alignment. The weight of the pelvis module is increased by 3 kg to account for the additional actuators.

### 3 Optimal Control Problem Formulation

The lifting motion of the human model wearing the exoskeleton is set up as a 3-phase optimal control problem (OCP). In the first phase, the user stands in an upright position, bends down and makes contact with the box. In the second phase, the user generates enough force to lift the box. The last phase starts when the box leaves the ground and ends when the user holds the box in an upright position. The OCP is formulated as follows:

$$\min_{q, \dot{q}, z, \alpha, u, p} \Psi[q, \dot{q}, z, \alpha, u, p] := \sum_{i=1}^3 \left( \sum_{n=0}^{N_i} \|W_q(q(t_{i,n}) - q_{i,n}^{REF})\|^2 + \int_{t_i}^{t_{i+1}} \phi(q, \dot{q}, z, \alpha, u, p) dt \right) \quad (1)$$

$$s.t. \quad M(q)\ddot{q} + G_i(q)^T \lambda = \tau(q, \dot{q}, z, \alpha, u, p) - C(q, \dot{q}) \quad (2)$$

$$\dot{\alpha} = ((u_m - \alpha_m)/T_m)_{m=1, \dots, N_m} \quad (3)$$

$$f(q, z, p) = 0 \quad (4)$$

$$g_i(q, \dot{q}, z, \alpha, u, p) \geq 0, \quad i = 1, \dots, 3 \quad (5)$$

with  $q$ ,  $\dot{q}$ , and  $\ddot{q}$  the joint positions, velocities, and accelerations, respectively. The number of shooting nodes of phase  $i$  is denoted by  $N_i$ . The motion to be tracked is given for time  $t_{i,n}$  by the joint positions  $q_{i,n}^{REF}$  and the fitting accuracy is specified by a weighting matrix  $W_q$ . The algebraic states  $z$  and the system of equations (4) define the state of the beam. The parameters  $p$  describe the design of the passive elements of the exoskeleton. The controls  $u$  are the neural excitation of the MTG. Eq.(3) are the MTG activation dynamics with activation level  $\alpha$  and (de-)activation time constant  $T$ . In case of DC, the torque profile of the motors

is a control as well. The number of MTG is given by  $N_m$ . The equation of motion of the constrained multibody system is given by (2) with mass matrix  $M$ , constraint jacobian  $G_i$ , and unknown force variables  $\lambda$ . The function  $C$  contains the centrifugal, gravitational and Coriolis forces. The generalized forces are denoted by  $\tau$  consisting of the joint torques and forces generated by the MTG and the exoskeleton. The Constraints (5) include, among others, position constraints, constraints on hand-to-box, box-to-floor, and foot-to-floor contact forces, human/exoskeleton alignment regulations and limits on parameters, states and controls. The objective function (1) consists of a least squares term for tracking the recorded motion and a Lagrange term enforcing the reduction of human joint moments and pelvis contact moment. The OCP is discretized using direct multiple shooting and the resulting NLP is solved with SQP and active-set method.

## 4 Results

For the prototype optimization (PO), parameters describing the behavior of the beam and the passive elements were optimized. For DC, motor torque profiles were optimized as well. The results are compared to the original configuration (O) of the prototype. We present exemplary the results of one subject here. Many quantities were computed, Fig. 1 illustrates the most important ones. In both cases, the support of the exoskeleton was further improved (reduction of integr. lumbar moment: 16.5% (PO), 13.5%

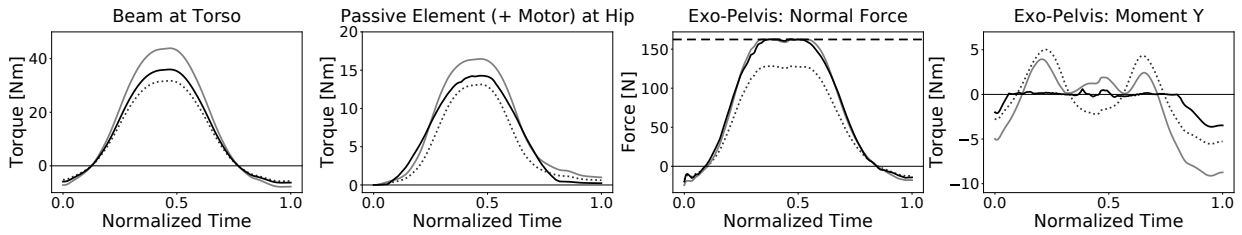


Figure 1: **Grey dotted line:** original configuration of the prototype; **Grey solid line:** optimized prototype; **Black line:** optimized new design concept. **From left to right:** Torque acting at the base of the 3 beams; torque produced by one passive element (and motor); Normal contact force acting at the pelvis with prescribed limit [5] (dashed line); Contact moment acting at the pelvis.

(DC), 11.8% (O); reduction of integr. hip moment: 14.1% (PO), 12.4% (DC), 10.1% (O); each value specifies the reduction with respect to results obtained by human-only simulation (without exoskeleton)). The support of DC is lower than PO because the limit on the pelvis normal force, the most restrictive constraint for the support, is reached at lower force/torque generation of the exoskeleton because of the increased pelvis module weight. As intended, adding the motor resulted in a high reduction of the moment acting at the pelvis contact, staying within [-3.6 Nm, 0.6 Nm] and yielding a very good alignment of exoskeleton and user. For PO, the contact moment decreased compared to O during the bent-down phase indicating a good balance between the force/torque generation of the beams and the passive hip elements, but became higher during standing.

## 5 Discussion

In this work, we present a method to optimize and evaluate design concepts for exoskeletons using an optimal control formulation. This setup can be used to optimize the design of passive elements described by multiple parameters and motor torque profiles that serve as guidelines for the next prototype. Note that these calculations can be done without having a real prototype. It also provides the analysis of contact forces between user and exoskeleton, the load reduction, and the actuation patterns of the user.

## Acknowledgments

This work was funded by the European Commissions within the H2020 project SPEXOR (GA 687662).

## References

- [1] J. Zhang, P. Fiers, K.A. Witte, R.W. Jackson, K.L. Poggensee, C.G. Atkeson, S.H. Collins. Human-in-the-loop optimization of exoskeleton assistance during walking. *Science*, 356(6344):1280-1284, 2017.
- [2] M.B. Näf, A.S. Koopman, S. Baltrusch, C. Rodriguez-Guerrero, B. Vanderborght, D. Lefeber. Passive Back Support Exoskeleton Improves Range of Motion Using Flexible Beams. *Frontiers in Robotics and AI*, 5:72, 2018.
- [3] M. Harant, M. Millard, N. Šarabon, K. Mombaur. Cost function evaluation for optimizing design and actuation of an active exoskeleton to ergonomically assist lifting motions. In *IEEE/RAS International Conference on Humanoid Robots (Humanoids)*, pages 186-193, 2019.
- [4] M. Millard, A. L. Emonds, M. Harant, and K. Mombaur. A reduced muscle model and planar musculoskeletal model fit for synthesis of whole body movements. *Journal of Biomechanics*, 89:11-20, 2019.
- [5] Ž. Kozinc, J. Babič, N. Šarabon. Human pressure tolerance and effects of different padding materials with implications for development of exoskeletons and similar devices. *Applied Ergonomics*, 93:103379, 2021.

# Towards Compliant Human-Exoskeleton Interactions Within Multibody Dynamics Simulations of Assisted Human Motor Control

Keaton A. Inkol, John McPhee

University of Waterloo, Canada  
kainkel@uwaterloo.ca

## EXTENDED ABSTRACT

### 1 Introduction

Often in the modelling and control of biomechanical assistive devices, it is assumed that the human and device are connected rigidly [1, 2]. For exoskeletons, this assumption ignores important phenomena like misalignment between device actuator and human joint axes of rotation [3]. Despite this, there are few investigations into human-exoskeleton compliance. Sánchez-Villamañán et al. [4] simulated a compliant human-exoskeleton interaction for the leg using an ideal spring; however, *only* the elasticity due to soft tissue deformation was considered. Therefore, the purpose of this research was to develop and assess (via simulation) the performance of an integrated human-exoskeleton model in which, via unilateral contact equations, the device cuffs and elastic straps (Velcro™) are responsible for the transfer of energy between subsystems.

### 2 Dynamic Model of Integrated Human-Exoskeleton

The human biomechanical and exoskeleton (Technaid® Exo-H3) mechatronic subsystem models were adopted from a whole-body integrated model we had designed prior [1] (Fig.1A). The passive human knee and ankle joints ( $\theta_{ha}, \theta_{hk}$ ) were modelled as muscle torque generators with no input activations [5]. Friction at the rotating exoskeleton joints ( $\theta_{ea}, \theta_{ek}$ ) involved both a Coulomb and viscous component [1]; a DC brushless motor (ideal actuator) applies torques to the knee. The unilateral contact forces that held the human shank within the Exo-H3 were assumed to arise from a combination of the following interactions: 1) movement of the posterior aspect of the shank relative to two synthetic cuffs attached to Exo-H3 link; 2) penetration of plantar heel/toe landmarks through the exoskeleton foot pad; 3) stretching of velcro straps (four total) which compress the human foot and leg against the Exo-H3 foot pad and cuffs respectively. For each contact element, an exoskeleton-fixed vector  $\hat{i}_n$  defined the direction along which penetration was evaluated and contact forces would act, e.g. applying a load to and stretching the lower leg strap results in a force on the exoskeleton along  $\hat{i}_{vl}$ . The foot pad and cuff elements were modelled using a linear spring-damper Elasto Gap function with arbitrarily high stiffness and damping values ( $k = 10^6$  N/m,  $d = 10^3$  N·s/m). The tension generated by any strap was modelled by a second-order polynomial function,  $T(\ell(t); k_\alpha, k_\beta, \ell_0) = k_\alpha(\ell(t) - \ell_0) + k_\beta(\ell(t) - \ell_0)^2 \quad \forall \ell(t) \geq \ell_0$  where  $\ell_0$  is a resting length parameter that affects tautness and  $\ell(t) \equiv \ell(\Theta(t))$  was the strap length that depends on the kinematic configuration given by  $\Theta \in \mathbb{R}^4$  where  $\Theta = [\theta_{ea}, \theta_{ek}, \theta_{ha}, \theta_{hk}]$  are the 4 degrees of freedom. No tension was developed when  $\ell(t) < \ell_0$ . The novel geometric derivation of  $\ell$  assumed the leg and foot could be comprised of linked cylinders with a known

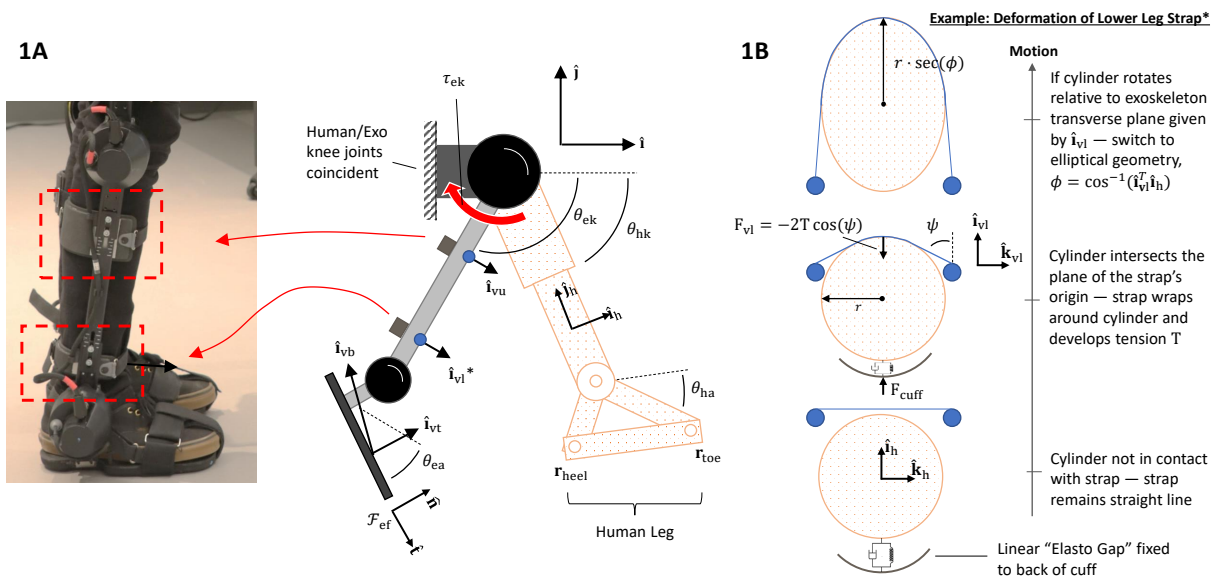


Figure 1: A) Schematic of the integrated human-exoskeleton model featuring compliant interactions. B) An overview of the approach to modelling elastic strap deformation, via cylindrical wrappings, and energy transfer through a stiff cuff component.

radius, around which a given strap can wrap (assuming deformation in the  $\hat{\mathbf{i}}_n$  direction; Fig. 1B). Since the cylinder could intersect the strap at an angle (e.g.  $\hat{\mathbf{i}}_v^T \hat{\mathbf{i}}_h \neq 0$  in Fig. 1), elliptical geometry had to be considered.

### 3 Simulation Experiment and Results

A simulation similar to the dynamometer setup in [1] was used herein to assess performance of the exoskeleton contact model. The exoskeleton knee motor (an ideal actuator) was responsible for driving the desired motion (knee extension ramp followed by knee flexion ramp at constant velocity of  $\pm 3.2$  m/s). Proportional-derivative (PD) control was used to manipulate the knee motor torque, which was capable of reaching the manufacturer-specified peak torque before saturating ( $\pm 152$  Nm). The data in Bader and Pearcy [6] was used to identify the elastic gains  $k_\alpha$  and  $k_\beta$ . Three different variations of Velcro® materials were tested: Standard ( $k_\alpha = 0$  N/m,  $k_\beta = 8.59 \cdot 10^4$  N/m<sup>2</sup>), “Kric Krac” ( $k_\alpha = 249$  N/m,  $k_\beta = 1.99 \cdot 10^4$  N/m<sup>2</sup>), and Elasticated ( $k_\alpha = 121$  N/m,  $k_\beta = 2.33 \cdot 10^3$  N/m<sup>2</sup>). Additionally, for each of the aforementioned types, a “Loose” and “Secured” condition was tested; the secured condition required the resting length of each velcro strap be reduced by 10-50 mm depending on location.

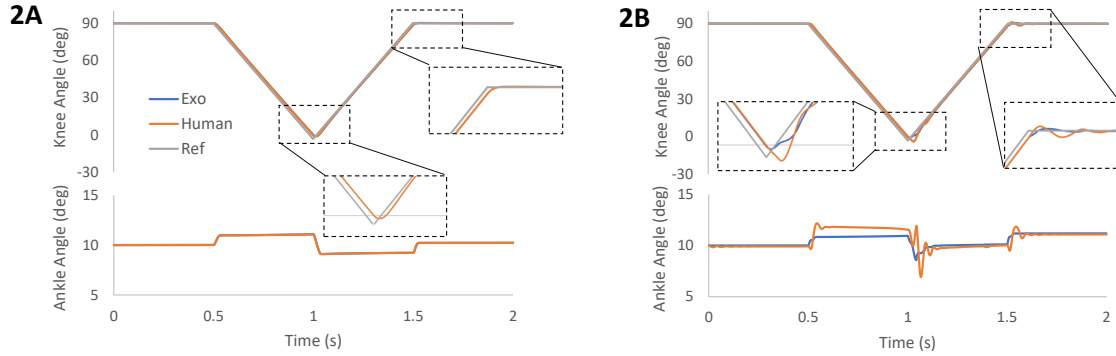


Figure 2: Representative data showing ankle (+’ve = plantarflexion) and knee (+’ve = flexion) trajectories for simulations using **A)** rigid connections and **B)** the compliant model presented herein (results presented for the secured Standard Velcro®).

Representative data for joint kinematics that follow from the use of rigid connections and Standard Velcro® (Secured) are shown in Fig. 2. Windows of interest in Fig. 2B have been highlighted, i.e. periods where phenomena unique to compliant connections like overshoot are captured. The average ankle joint misalignment (AJM), calculated using the Euclidean norm between human and exo ankle joint centre positions, showed a good response (lower AJM) to increases in strap tautness and baseline stiffness. Not surprisingly, the secured Standard Velcro was best at minimizing misalignments (AJM = 1.48 mm); making the strap loose substantially increased this error (AJM = 14.6 mm). The worst performance came from the Elasticated straps (loose AJM = 24.0 mm, secured AJM = 12.9 mm) followed by the Kric Krac straps (loose AJM = 16.9 mm, secured AJM = 2.51 mm).

### 4 Discussion

In general, the addition of multi-point unilateral contact equations to the integrated human-exoskeleton model allowed us to capture the transient phenomenon that are overlooked when assuming the interactions to be rigid. A notable component of our model is the ability to replicate design asymmetries in the exoskeleton, i.e. rigid cuff versus elastic strap on the posterior and anterior aspect of segments. This resulted in the overshoot of the human knee in Fig. 2B where the elastic strap was unable to halt momentum about the knee quickly, without being more taut.

### References

- [1] Inkol KA, McPhee J: Assessing Control of Fixed-Support Balance Recovery in Wearable Lower-Limb Exoskeletons Using Multibody Dynamic Modelling, 8th IEEE RAS/EMBS Conf Biomed Robotics Biomechatr (BioRob), 54-60, 2020.
- [2] Millard M, Sreenivasa M, Mombaur, K: Predicting the Motions and Forces of Wearable Robotics Systems Using Optimal Control, Front Robot AI, **4**(41):1-12, 2017.
- [3] Näf MB, Junius K, Rossini M, Rodriguez-Guerrero C, Vanderborght B, Lefeber D: Misalignment Compensation for Full Human-Exoskeleton Kinematic Compatibility: State of the Art and Evaluation, Appl Mech Rev, **70**(5):050802, 2018.
- [4] Sánchez-Villamañán MC, Torricelli D, Pons JL: Modeling Human-Exoskeleton Interaction: Preliminary Results, Wearable Robotics: Challenges and Trends, WeRob 2018. Biosyst Biorobotics, **22**:137-141, 2019.
- [5] Inkol KA, Brown C, McNally W, Jansen C, McPhee J: Muscle torque generators in multibody dynamic simulations of optimal sports performance, Multibody Syst Dyn **50**:435–452, 2020.
- [6] Bader DL, Pearcy MJ: Material properties of Velcro fastenings, Prosthet Orthot Int, **6**:93-96, 1982.

# Rehabilitation of Musculoskeletal Models Using Deep Reinforcement Learning

Queralt Madorell<sup>1</sup>, Albert Peiret<sup>1</sup>, Josep M. Font-Llagunes<sup>1</sup>

<sup>1</sup> Dept. of Mechanical Engineering and Biomedical Engineering Research Centre  
Universitat Politècnica de Catalunya, Diagonal 647, 08028, Barcelona, Spain  
email1@address

## EXTENDED ABSTRACT

### 1 Introduction

Neural rehabilitation is a long and complex process that patients undergo after suffering a nervous system injury, such as stroke. These kinds of injuries usually result in brain cells death and partial loss of mobility and coordination. During rehabilitation, the patient performs a series of movements and physical exercises that promote neural plasticity, the brain's mechanism to regenerate and make new pathways that substitute the damaged connections. Unfortunately, full recovery is almost impossible.

The rehabilitation process is tailored to the patient based on the physician's expertise, and it evolves with the patient's needs and recovery. However, few computational models for rehabilitation have been developed. For instance, Lee et al. [1] trained a musculoskeletal model of a healthy subject using deep reinforcement learning, and then a prosthetic leg was added to simulate an injury. Results showed how the artificial neural network that controlled muscle contraction was able to adapt and learn to move with the prosthetic leg.

Here we show how deep reinforcement learning can be used to control a musculoskeletal model. The algorithm is able to learn new and stable motions by maximizing the so-called reward function. The nervous system is modelled with an artificial neural network, and the deep deterministic policy gradient (DDPG) algorithm [2] is used to train the model in a simulated environment.

### 2 Methods

The musculoskeletal model is a multibody systems with bones represented by rigid bodies and joints actuated by muscles. Kinematic constraints represent the joints and muscle contraction dynamics is modelled with a Hill-type muscle model. The neural excitation of each muscle controls muscle fiber contraction, which results in a force being applied to the bones. Motion control of musculoskeletal models presents some challenges, such as muscle redundancy, which is why a nonlinear optimization is required to solve the control problem.

Continuous control in deep reinforcement learning can be achieved with the DDPG algorithm [2], which is an actor-critic method. The actor network learns the optimal policy, while the critic network learns the action-value function. The policy is the function that calculates the control input (i.e., muscle neural excitation) in terms of the system state (i.e., joint angles, velocities, and accelerations, as well as muscle activation). The action-value function assesses how well the actor network performs with the action taken at a given time.

The algorithm learns the actions that maximize the reward function, which is why selecting a meaningful and effective reward function is paramount in reinforcement learning. The reward can be seen as the reciprocal of the cost. In biomechanics, the metabolic cost associated with muscle contraction can be represented by muscle fiber activation. Here, the reward function is expressed as

$$r = - \sum_{\text{joints}} (\theta_i - \theta_i^*)^2 - \sum_{\text{muscles}} w_a a_i^2 \quad (1)$$

where  $\theta_i^*$  is the target value of the joint angle  $\theta_i$ , and  $w_a$  is a weight associated with the muscle activation  $a_i \in [0, 1]$ .

### 3 Results

A neural controller for a musculoskeletal model of the arm was trained using the DDPG algorithm to reach a target position with the hand. The 2-DoF model of the arm had 2 segments (upper-arm and forearm), and 8 muscles. The left side of Figure 1 shows the position of the model's hand on the sagittal plane as well as its joint angles used to shape the reward function. A total of 300.000 steps with random target positions of the ball were simulated to train the neural controller model using the DDPG algorithm. These steps were divided in episodes of 200 steps (0.01 seconds/step), which were the allotted time for the model to reach the ball. Once this termination condition was met, the ball's position was randomly reseted.

Once the model was trained, a scenario was designed to check the achieved results. The target configuration was set at  $54^\circ$  for  $\theta_1^*$  and at  $107^\circ$  for  $\theta_2^*$ , which was considered to require sufficient range of movement. The results are shown in the right side of Figure 1, where the absolute distance to the target point is shown.

These results show a little offset present in the X and Y coordinates, but overall the model has been successfully trained. It is able to reach the target in any position of its reach and it maintains the hand still in the target point for the entire duration of the episode.

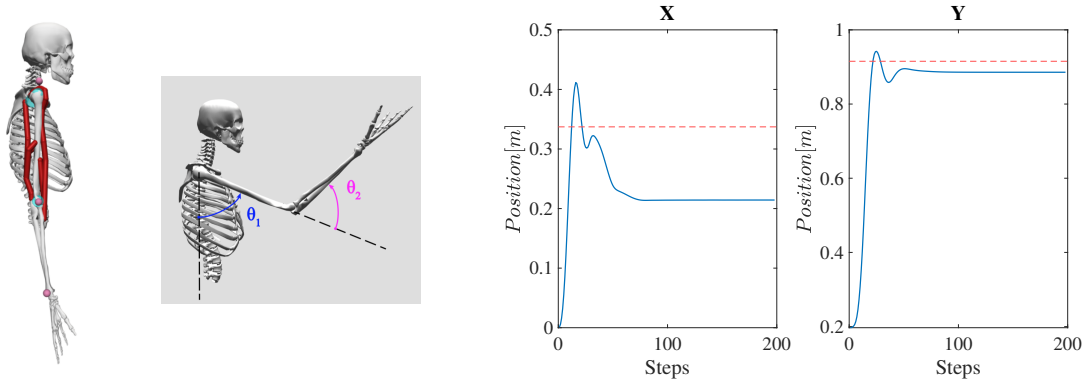


Figure 1: Motion generated using deep reinforcement using a target position of the hand.

#### 4 Conclusions

The present results are promising and show the potential that reinforcement learning has in finding generalized solutions to biomechanical problems. The subsequent line of work that is currently being considered is the use of this reinforcement learning-based framework as a basis for testing different rehabilitation devices. This could allow the modelling of neuromuscular conditions and the assessment of the most suitable rehabilitation devices a treatments for a given case.

#### References

- [1] Lee, S., Park, M., Lee, K. and Lee, J., 2019. "Scalable muscle-actuated human simulation and control," *ACM Transactions On Graphics (TOG)*, 38(4), pp.1-13.
- [2] Lillicrap, T.P., Hunt, J.J., Pritzel, A., Heess, N., Erez, T., Tassa, Y., Silver, D., Wierstra, D., 2016. "Continuous control with deep reinforcement learning," 4th International Conference on Learning Representations, *ICLR 2016 - Conference Track Proceedings*, 2016.

# Estimation of Intervertebral Efforts via an EMG-driven Multibody Model of the Sorensen Test

Simon Hinnekens<sup>1</sup>, Christine Detrembleur<sup>2</sup>, Philippe Mahaudens<sup>2</sup>, Paul Fiset<sup>1</sup>

<sup>1</sup> Institute of Mechanics, Materials and Civil Engineering  
Université catholique de Louvain  
Place du Levant 2, 1348 Louvain-la-Neuve, Belgium  
[simon.hinneken, paul.fisette]@uclouvain.be

<sup>2</sup> Institute of Experimental and Clinical Research  
Université catholique de Louvain  
Avenue Mounier 53, 1200 Bruxelles, Belgium  
[christine.detrembleur, philippe.mahaudens]@uclouvain.be

## EXTENDED ABSTRACT

### 1 Introduction

Spine is the central hinge of the human body. However, when correcting spinal surgery needs to be done, there is still a lack of objective information for its planning, such as intervertebral efforts. Indeed, intervertebral discs are the places where critical efforts occur in the spine. Spine geometry, kinematics and muscle forces are needed to compute these intervertebral efforts. If the first two are already tackled [1], assessing muscle forces is still challenging. For that purpose, both experimental and mathematical approaches can be used. Experimental methods consist in measuring directly or indirectly muscle forces through a well-targeted protocol. Electromyography (EMG) is commonly used although it is an indirect measurement. For these experimental methods, the number of participants is often limited. On the contrary, purely mathematical approaches allow to develop generic musculoskeletal models often based on the Hill muscle model and for which no experiment is performed. But parameters are numerous and difficult to estimate, all the more as these models deal with muscle redundancy.

The hybrid approach proposed in this research combines both experimental and mathematical approaches. It is based on an upfront experiment aiming at making the most of recorded EMG signals in order to develop musculoskeletal models. This approach was already presented previously for predefined static postures with encouraging results [2].

In this paper, the hybrid approach is used to assess trunk muscle efforts during the Sorensen test. Both static postures and dynamic motions are evaluated.

### 2 Materials and Methods

Nineteen healthy men (age:  $22.7 \pm 2.1$  years; mass:  $73.9 \pm 8.7$  kg; height:  $1.81 \pm 0.05$  m) with no back pathology participated in the experiment. The latter was divided into three parts: (i) three maximal voluntary contraction (MVC) tests, (ii) five loaded isometric contractions and (iii) six dynamic flexion/extension tasks. All the three parts were carried out in the Sorensen test posture as depicted on the left in Figure 1. MVC tests were used for normalization. Loaded isometric contractions consisted in holding the position for 15 sec with a mass from 0 to 8 kg with 2-kg steps applied randomly. Finally, dynamic tasks were carried out for two cycle durations (4 and 8 sec) and for three masses (0, 2 and 4 kg).

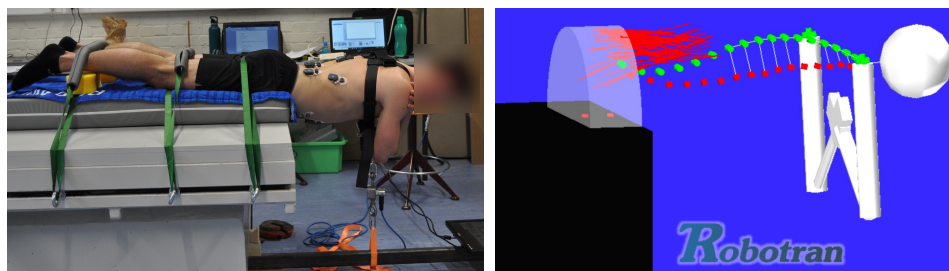


Figure 1: Sorensen test posture. Left: Experiment (UCLouvain 2020). Right: Multibody model in Robotran with muscles in red.

During the whole experiment, muscle activity of six bilateral trunk muscles was recorded using surface wireless EMG (BTS FREEEMG, 1000 Hz). Raw EMG signals were rectified, filtered using a 5th-order lowpass Butterworth filter with a cut-off frequency of 10 Hz, smoothed with a 150-ms window and normalized with respect to MVC contraction levels.

A musculoskeletal model of the trunk in the Sorensen test posture was developed using the multibody software Robotran [3] as illustrated on the right in Figure 1. It derived from a fully articulated thoracolumbar spine and rib cage model published previously [4]. It included fascicles of lumbar (LP) and dorsal (DP) paravertebral muscles and the quadratus lumborum (QL). It is worth mentioning that in the current hybrid approach, no optimization method was used for computing muscle forces. For isometric contractions, finding a unique mathematical solution was ensured with a deterministic muscle effort distribution. The idea was to use slopes from EMG linear regressions between activation levels (w.r.t. MVC) and lifted masses as indicators of the activation fraction for each muscle group (LP, DP and QL) for this precise effort situation. Then, inside each muscle group, the distribution between fascicles was based on their respective maximal isometric forces [4]. For dynamic tasks, muscle forces found in isometric contractions were used for calibration.



### 3 Results and Discussion

According to the previous process, muscle forces evaluation for isometric contractions was therefore equivalent to determine a unique ‘global muscle force’, the latter being distributed deterministically among all the fascicles. Normalized global muscle forces (global muscle forces divided by subject’s mass) are depicted on the left in Figure 2 for all masses and all subjects. The normalized muscle forces were obviously linear w.r.t. lifted masses due the linearity of equations of motion. However, it was comforting to observe — not showed here — a relatively good linear dependence between activation levels and lifted masses as reported previously [5]. More interestingly, it can be seen that subjects recruiting more their QL (vertical blue scale) developed greater muscle forces compared to subjects using more their paravertebral muscles. A physiological explanation is the orientation of muscle fascicles, i.e. QL fascicles are more oblique to the spine while LP and DP fascicles are more aligned. It impacts directly the lever arm and consequently the muscle force required to meet the gravity-induced torque.

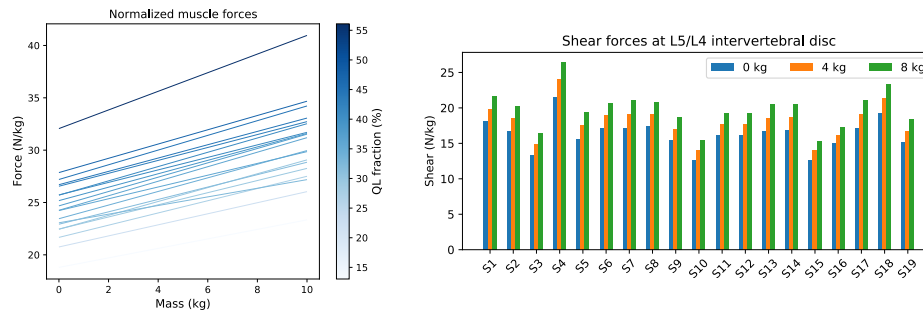


Figure 2: Loaded isometric contractions in the Sorensen test posture. Left: linear regressions between the normalized muscle forces and added masses. Right: normalized shear forces at L5/L4 intervertebral disc for three masses (0, 4 and 8 kg).

Intervertebral efforts — compressive, shear forces and bending moment — were also computed in order to evaluate the impact of individual strategies on them. Similarly to muscle forces, subjects using more their QL generated greater intervertebral efforts. This result was consistent with the greater global muscle force observed in those subjects and could also be explained by the orientation of QL fascicles. For illustration, shear forces for the L5/L4 intervertebral disc are showed on the right in Figure 2. Greater QL recruitment implied greater shear forces as in the subject S4. On the contrary, subjects 10 and 15 produced less shear forces as they used their paravertebral (LP and DP) muscles more. Shear forces had the greatest magnitude at the L5/L4 intervertebral disc compared to the other lumbar intervertebral discs. It must be reminded that shear forces in the Sorensen test posture are roughly aligned with gravity and are therefore particularly sollicitated. Compressive forces — not illustrated here — were also increased for higher QL recruitment and were greater for discs in the lower lumbar spine.

Experimental results and force computations for the dynamic tasks are currently under process and will be presented during the presentation.

### 4 Conclusion

Muscle forces associated to loaded isometric contractions in the Sorensen test posture were computed using an hybrid approach. This approach aimed at making the most of EMG signals from a well-designed experiment in order to develop the associated musculoskeletal model and the force computation in a deterministic way. Results highlighted the interest of considering individual motion strategies when evaluating muscle forces, particularly concerning the QL. Indeed, greater muscle forces and intervertebral efforts were obtained for subjects recruiting more their QL.

### References

- [1] G. Abedrabbo Ode. Quantification of intervertebral efforts using a multibody dynamics approach: application to scoliosis. PhD Thesis, Université catholique de Louvain, 2017.
- [2] S. Hinnekens, P. Mahaudens, C. Detrembleur, P. Fisette. EMG Measurements as inputs for a musculoskeletal model: quantification of abdominal and back muscle forces in static postures. *Computer Methods in Biomechanics and Biomedical Engineering*, 22(S1):147-149, 2019.
- [3] N. Docquier, A. Poncelet, P. Fisette. ROBOTRAN: a powerful symbolic generator of multibody models. *Mechanical Sciences*, 4:199–219, 2013.
- [4] A.G. Bruno, M.L. Bouxsein, D.E. Anderson. Development and Validation of a Musculoskeletal Model of the Fully Articulated Thoracolumbar Spine and Rib Cage. *Journal of Biomechanical Engineering*, 137(8):081003, 2015.
- [5] A.L. Hof. The relationship between electromyogram and muscle force. *Sportverletzung • Sportschaden*, 11(3):79-86, 1997.

**Section**

**CONTACT, IMPACT AND CONSTRAINTS**

CONTACT-1-2-3

# Model-based Co-simulation of Non-smooth Mechanical Systems

Ali Raoofian<sup>1</sup>, Albert Peiret<sup>2</sup>, József Kövecses<sup>1</sup>, Marek Teichmann<sup>3</sup>,

<sup>1</sup> Department of Mechanical Engineering,  
McGill University,

817 Sherbrooke St. West,

Montreal, QC H3A 0C3, Canada

ali.raoofian@mail.mcgill.ca, jozsef.kovecses@mcgill.ca

<sup>2</sup> Department of Mechanical Engineering,  
Polytechnic University of Catalonia,

Barcelona, Spain

albert.peiret@upc.edu

<sup>3</sup>CM Labs Simulations,  
645 Wellington,

Montreal, QC H3C 1T2, Canada

marek@cm-labs.com

## EXTENDED ABSTRACT

### 1 Introduction

Dynamic modelling and simulation of systems containing components with different physical domain and time-scale is a challenging task. In a *co-simulation* setting, the system is treated and modelled as a set of *sub-systems* which may require the use of different solvers and time scales suited to the particular physical behaviour of the subsystems. The subsystems only exchange a reduced set of coupling data at discrete-time communication points separated by time intervals termed *macro-steps*. However, the discrete-time communication between sub-systems, has discontinuities and time delays in the coupling variables, which can affect the stability and accuracy. The stability is impacted by the way data is exchanged between subsystems. Generally, iterative coupling schemes are more stable compared to their non-iterative counterparts [1]. However, since the available time to carry out the numerical integration is limited in most of real time applications, non-iterative methods are used. Keeping non-iterative co-simulation schemes stable is challenging. Using extrapolation and approximation of subsystem input variables is a common strategy to enhance the performance of non-iterative schemes between communication updates. However, using previous values of the coupling data to extrapolate inputs can give incorrect predictions specially in non-smooth systems where unilateral contacts are present.

In these problems, model-based prediction of the coupling variables at the *interface* between the sub-systems, can increase the accuracy and efficiency of the simulation. This interface modelling is developed based on a reduced model of the mechanical subsystem. Such a reduced interface model (RIM) is usually parameterized based on the degrees of freedom associated with the interface which can give a good insight about the behaviour of the mechanical subsystem. In this work, an enhanced RIM of non-smooth mechanical systems is introduced which accounts for contact attachments/detachments during the macro step which leads to more accurate results. In our previous work, the RIM was developed assuming that the state of the contacts will remain unchanged during the macro step [2]. That concept is extended here which also includes the complementarity conditions in the reduced model. Moreover, a parametric model is used to demonstrate the advantages of the proposed RIM over other methods.

### 2 Model-based co-simulation of mechanical systems

Consider a multibody system subjected to unilateral and bilateral constraints. Friction is neglected for now and the unilateral constraints are associated with normal contact directions. The multibody system is assumed to have  $n$  generalized velocities  $\mathbf{v}$  and set of  $n_q$  generalized coordinates  $\mathbf{q}$ , which are related by the transformation  $\dot{\mathbf{q}} = \mathbf{N}\mathbf{v}$ , where  $\mathbf{N}$  is  $n_q \times n$  transformation matrix. The dynamics equations can be written as

$$\mathbf{M}\dot{\mathbf{v}} = \mathbf{f} + \mathbf{A}^T \boldsymbol{\lambda}_c + \mathbf{B}^T \boldsymbol{\lambda}_i \quad (1)$$

where  $\mathbf{M}(\mathbf{q})$  is the  $n \times n$  the mass matrix,  $\mathbf{f}(\mathbf{q}, \mathbf{v})$  is  $n \times 1$  array of generalized applied forces (including the Coriolis and centrifugal terms) and  $\boldsymbol{\lambda}_c$  is the  $n_c \times 1$  array of constraint forces and moments. The interactions between the elements of the system are parameterized by  $n_c$  set of velocities  $\mathbf{w}_c = \mathbf{A}\mathbf{v}$ , where  $\mathbf{A}(\mathbf{q})$  is the  $n_c \times n$  constraint Jacobian matrix. Moreover, the  $n_i \times 1$  interface forces array  $\boldsymbol{\lambda}_i$  is containing force and moment components at the co-simulation interface. Depending on the kind of coupling, the interface force can be either an input or an output of the multibody system model in the co-simulation. The interface of the multibody systems with the other subsystems is parameterized by  $n_i$  set of interface velocities  $\mathbf{w}_i = \mathbf{B}\mathbf{v}$ , where  $\mathbf{B}(\mathbf{q})$  is the  $n_i \times n$  interface Jacobian matrix. We would like to obtain a reduced-order model of the multibody system that includes the interface velocities  $\mathbf{w}_i$  to estimate the system behaviour between communication points. This will allow us to determine the interface kinematics in terms of the interface forces  $\boldsymbol{\lambda}_i$ , and vice versa.

In order to obtain a reduced-order model of the system, first, a transformation should be performed to eliminate the degrees of freedom in  $\mathbf{v}$  that do not represent any interaction. The time derivative of the constraint velocities  $\mathbf{w}_c$  and the interface velocities  $\mathbf{w}_i$  can be written as

$$\begin{bmatrix} \dot{\mathbf{w}}_c \\ \dot{\mathbf{w}}_i \end{bmatrix} = \begin{bmatrix} \mathbf{A} \\ \mathbf{B} \end{bmatrix} \dot{\mathbf{v}} + \begin{bmatrix} \dot{\mathbf{A}} \\ \dot{\mathbf{B}} \end{bmatrix} \mathbf{v} \quad (2)$$

where  $\dot{\mathbf{A}}(\mathbf{q}, \mathbf{v})$  and  $\dot{\mathbf{B}}(\mathbf{q}, \mathbf{v})$  are the derivative of the constraint and interface Jacobian matrices, respectively. Then, the system acceleration  $\dot{\mathbf{v}}$  can be substituted from Eq. (1) into the Eq. (2), which yields

$$\begin{bmatrix} \dot{\mathbf{w}}_c \\ \dot{\mathbf{w}}_i \end{bmatrix} = \begin{bmatrix} \mathbf{A}\mathbf{M}^{-1}\mathbf{A}^T & \mathbf{A}\mathbf{M}^{-1}\mathbf{B}^T \\ \mathbf{B}\mathbf{M}^{-1}\mathbf{A}^T & \mathbf{B}\mathbf{M}^{-1}\mathbf{B}^T \end{bmatrix} \begin{bmatrix} \boldsymbol{\lambda}_c \\ \boldsymbol{\lambda}_i \end{bmatrix} + \begin{bmatrix} \mathbf{A}\mathbf{M}^{-1}\mathbf{f} + \dot{\mathbf{A}}\mathbf{v} \\ \mathbf{B}\mathbf{M}^{-1}\mathbf{f} + \dot{\mathbf{B}}\mathbf{v} \end{bmatrix} \quad (3)$$

In order to detect contact establishments and detachments between the communication points, the state of the contacts should be updated constantly at each micro step. Considering two different kinds of constraints (bilateral and unilateral), the set of constraint velocities in the system can be rearranged as  $\mathbf{w}_c = [\mathbf{w}_b^T \ \mathbf{w}_u^T]^T$ , where  $\mathbf{w}_b$  contains the bilateral constraint velocity components, and  $\mathbf{w}_u$  contains the normal contact velocity components associated with unilateral constraints. Now, Eq. (3) can be rearranged as

$$\begin{bmatrix} \dot{\mathbf{w}}_b \\ \dot{\mathbf{w}}_u \\ \dot{\mathbf{w}}_i \end{bmatrix} = \begin{bmatrix} \mathbf{H}_b & \mathbf{H}_{ub}^T & \mathbf{G}_b^T \\ \mathbf{H}_{ub} & \mathbf{H}_u & \mathbf{G}_u^T \\ \mathbf{G}_b & \mathbf{G}_u & \mathbf{H}_i \end{bmatrix} \begin{bmatrix} \boldsymbol{\lambda}_b \\ \boldsymbol{\lambda}_u \\ \boldsymbol{\lambda}_i \end{bmatrix} + \begin{bmatrix} \mathbf{b}_b \\ \mathbf{b}_u \\ \mathbf{b}_i \end{bmatrix} \quad (4)$$

Bilateral constraints can be defined by the equation as  $\mathbf{w}_b = \mathbf{0}$  which can be also be stated at the acceleration level as  $\dot{\mathbf{w}}_b = \mathbf{0}$ . On the other hand, unilateral constraints must be defined by inequalities to allow for possible contact detachment. A complementarity condition can be defined as  $\mathbf{0} \leq \boldsymbol{\lambda}_u \perp \dot{\mathbf{w}}_u \geq \mathbf{0}$ , where  $\perp$  denotes component-wise complementarity. The bilateral constraint forces  $\boldsymbol{\lambda}_b$  can be calculated from the first row of Eq. (4) as  $\boldsymbol{\lambda}_b = -\mathbf{H}_b^{-1} (\mathbf{H}_{ub}^T \boldsymbol{\lambda}_u + \mathbf{G}_b^T \boldsymbol{\lambda}_i + \mathbf{b}_b)$  and be substituted into the other two rows to obtain the reduced dynamic equations at the interface,

$$\begin{cases} \begin{bmatrix} \dot{\mathbf{w}}_u \\ \dot{\mathbf{w}}_i \end{bmatrix} = \begin{bmatrix} \tilde{\mathbf{H}}_u & \tilde{\mathbf{G}}^T \\ \tilde{\mathbf{G}} & \tilde{\mathbf{H}}_i \end{bmatrix} \begin{bmatrix} \boldsymbol{\lambda}_u \\ \boldsymbol{\lambda}_i \end{bmatrix} + \begin{bmatrix} \tilde{\mathbf{b}}_u \\ \tilde{\mathbf{b}}_i \end{bmatrix} \\ \mathbf{0} \leq \boldsymbol{\lambda}_u \perp \dot{\mathbf{w}}_u \geq \mathbf{0} \end{cases} \quad (5)$$

Depending on how the data is exchanged between the subsystems, either  $\boldsymbol{\lambda}_i$  or  $\dot{\mathbf{w}}_i$  can be a known value. For example if  $\boldsymbol{\lambda}_i$  is known, then the complementarity equation can be solved first by using the first row; and subsequently, the interface acceleration can be obtained from the second row and integrated with respect to time.

### 3 Example

A simple planar model of a hydraulically actuated box connected to a disc through a revolute joint was used to demonstrate the performance of the proposed RIM in a co-simulation setup. The hydraulic actuator is considered as the first subsystem and the box and the disc are regarded as the second subsystem. As shown in the Fig. 1(a), the box and disc are allowed to slide without friction. The manoeuvre consists in pushing the box from an initial position where the mechanical parts are at rest on the horizontal surface toward the ramp until the disc moves upward against the ramp. As shown in the Fig. 1(a), there is an instant where the disc is in contact with two surfaces. Using the *active constraint* method introduced in [2], the two contact points are treated as bilateral constraints during the macro step which makes the system redundant. However, by employing the proposed method, the contact detachment is taken into account in the reduced model. This can be illustrated in Fig. 1(b) where the hydraulic force is depicted. As a reference solution, the system is also simulated using *zero order hold* setup with macro step  $h = 0.2$  ms. Moreover, both model-based simulations are simulated with  $h = 10$  ms. According to Fig. 1(b), the hydraulic force obtained from the active constraint method is quite high due to the redundancy of the system at the configuration shown, while the results obtained using the proposed method is similar to the reference solution.

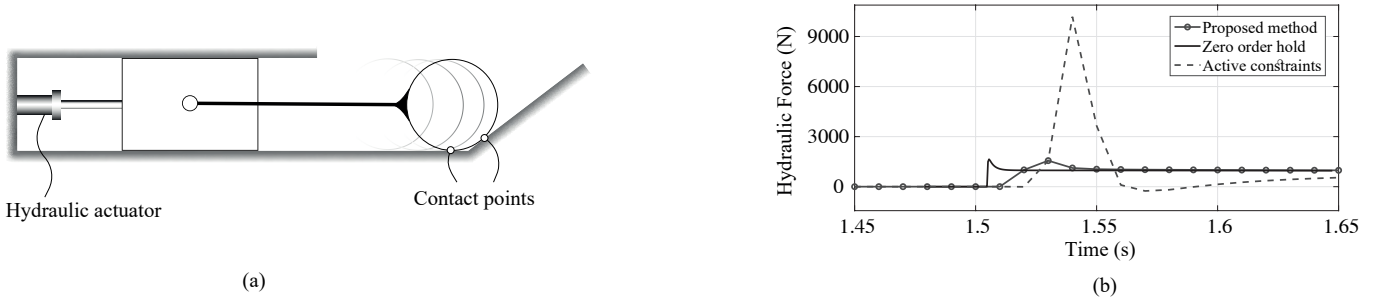


Figure 1: (a) Schematic of the planar case study (b) Forces obtained from hydraulic actuator using different approaches

### Acknowledgments

The reported work was supported by the Natural Sciences and Engineering Research Council Canada (NSERC), CM Labs Simulations, Inc. and the Fonds de Recherche du Québec – Nature et Technologies (FRQNT). The support is gratefully acknowledged.

### References

- [1] B. Schweizer, P. Li, D. Lu. Explicit and implicit cosimulation methods: Stability and convergence analysis for different solver coupling approaches. *Journal of Computational and Nonlinear Dynamics*, 10(5): paper 051007, 2015.
- [2] A. Peiret, F. González, J. Kövecses, M. Teichmann. Co-Simulation of Multibody Systems With Contact Using Reduced Interface Models. *ASME. J. Comput. Nonlinear Dyn.* 15(4): 041001, 2020.

# Further Investigation on LuGre Friction Force Model under Normal Load Variations

Filipe Marques<sup>1</sup>, Łukasz Woliński<sup>2</sup>, Marek Wojtyra<sup>2</sup>, Paulo Flores<sup>1</sup>, Hamid M. Lankarani<sup>3</sup>

<sup>1</sup>CMEMS-UMinho  
Department of Mechanical Engineering,  
University of Minho

Campus de Azurém, 4804-533 Guimarães, Portugal  
[fmarques, pflores]@dem.uminho.pt

<sup>2</sup>Warsaw University of Technology  
Institute of Aeronautics and  
Applied Mechanics

ul. Nowowiejska 24, 00-665 Warsaw, Poland  
[lwolinski, mwojtyra]@meil.pw.edu.pl

<sup>3</sup>Department of Mechanical Engineering  
Wichita State University  
Wichita, KS 67260-133, USA  
hamid.lankarani@wichita.edu

## EXTENDED ABSTRACT

### 1 Introduction

A large number of friction force models have been proposed in the literature to include the different friction attributes and to represent the frictional behavior with more detail [1, 2]. Generally, the friction models are divided into two groups, the “static” and “dynamic” models. The former group describes the steady-state behavior of friction force by enforcing a constant relationship between the relative tangential velocity and the corresponding friction force. The dynamic models are usually more complex since they consider an extra state variable, which describes the friction state, governed by a differential equation. Among the dynamic friction model, the LuGre model [3] has been gaining popularity and acceptance by the scientific community, since it presents a reasonable trade-off between easiness of implementation, range of modeled frictional phenomena, computational efficiency, and ability for parameters identification. These characteristics make LuGre model suitable for many applications in modeling of multibody mechanical systems. Despite its wide utilization, the LuGre model presents limitations under normal load variations, which resulted in its authors to present an amended version [4] to overcome some of those shortcomings. However, even the amended version has revealed some physical inconsistencies due to the occurrence of a drift during the sticking phase [5, 6]. In this work, a modification to the LuGre friction model is proposed to deal with normal load oscillations without the shortcomings of both the original and amended versions of the model.

### 2 LuGre Friction Force Models

The original LuGre model was proposed in 1995 [3] as an advancement of the Dahl friction model [7]. This model considers an analogy between the friction phenomena and a bristle deflection. An extra state variable used by the LuGre model,  $z$ , represents the average of bristle deflection and is governed by the following differential equation

$$\dot{z} = v - z \frac{\sigma_0 |v|}{G(v, N)}, \quad (1)$$

in which  $v$  denotes the relative tangential velocity,  $\sigma_0$  represents the bristle stiffness coefficient,  $N$  denotes the normal load magnitude, and  $G$  is a function that describes the friction force as velocity-dependent, represents the Stribeck effect, and incorporates static and kinetic friction force levels. In the original LuGre model, the friction force can be evaluated as

$$F = \sigma_0 z + \sigma_1 \dot{z} + \sigma_2 v, \quad (2)$$

where  $\sigma_1$  is the bristle damping coefficient which represents the micro-damping,  $\sigma_2$  denotes the viscous friction coefficient that corresponds to the macro-damping. This original version of the LuGre friction force model has been developed for constant normal force situations. Therefore, it cannot appropriately deal with cases in which the normal load varies, since load changes do not directly affect the result of Eq. (2).

Later, Canudas-de-Wit and Tsiotras [4] extended the original LuGre friction force model to overcome some of its limitations. In this amended version, the differential equation that governs the state variable is given as

$$\dot{z} = v - z \frac{\sigma_0^A |v|}{G^A(v)}, \quad (3)$$

where  $\sigma_0^A$  is a constant coefficient that represents the stiffness of bristle deflection per unit of normal load. In this amended model, the Stribeck function  $G^A$  is defined as a function of the static and kinetic friction coefficients, instead of the static and kinetic friction forces as in the original model. In the amended LuGre model, the friction force is calculated directly as a function of normal load, i.e.

$$F = (\sigma_0^A z + \sigma_1^A \dot{z} + \sigma_2^A v) N \quad (4)$$

where  $\sigma_1^A$  and  $\sigma_2^A$  are constant parameters that represent the bristle damping coefficient and viscous friction coefficient, respectively, per unit of normal load.

Both the original and the amended model exhibit limitations when the normal force varies during the contact interaction, as demonstrated in Section 3. The proposed modification to the LuGre friction model is intended to mitigate these limitations and

is similar to the amended model; however, the coefficients are defined differently, i.e.

$$\sigma_0^p = \sigma_0^a N, \quad \sigma_1^p = \sigma_1^a N, \quad \sigma_2^p = \sigma_2^a N, \quad (5)$$

and the friction force is given as

$$F = \sigma_0^p z + \sigma_1^p \dot{z} + \sigma_2^p v. \quad (6)$$

The most relevant feature of this modification is that it enforces a constant stiffness coefficient when the contact is in the sticking regime. In this way, it avoids the drift due to a variable stiffness, when the normal load varies.

### 3 Results and Discussion

In order to demonstrate the effectiveness of the proposed modification of the LuGre friction model, a simple block of mass moving on a horizontal surface is considered as an application with two examples. In these examples, the normal and pulling forces are prescribed to highlight the issues associated with each model.

Figure 1 shows the results of two examples considered. In the first case, a constant normal load is applied until 2 seconds of simulation and then it continuously decreases until the end of the simulation. As demonstrated in Figure 1a, the original LuGre model produces a ratio between the friction and normal forces that exceeds, in a significant manner, the static and kinetic friction coefficients. In the second case, a constant pulling force is applied well below the break-away force, and the normal force is subjected to continuous oscillations of about 10% of its average magnitude. The results of Figure 1b show that the amended model presents an unrealistic drift between the contacting surfaces, whereas the newly proposed model is free of this flaw.

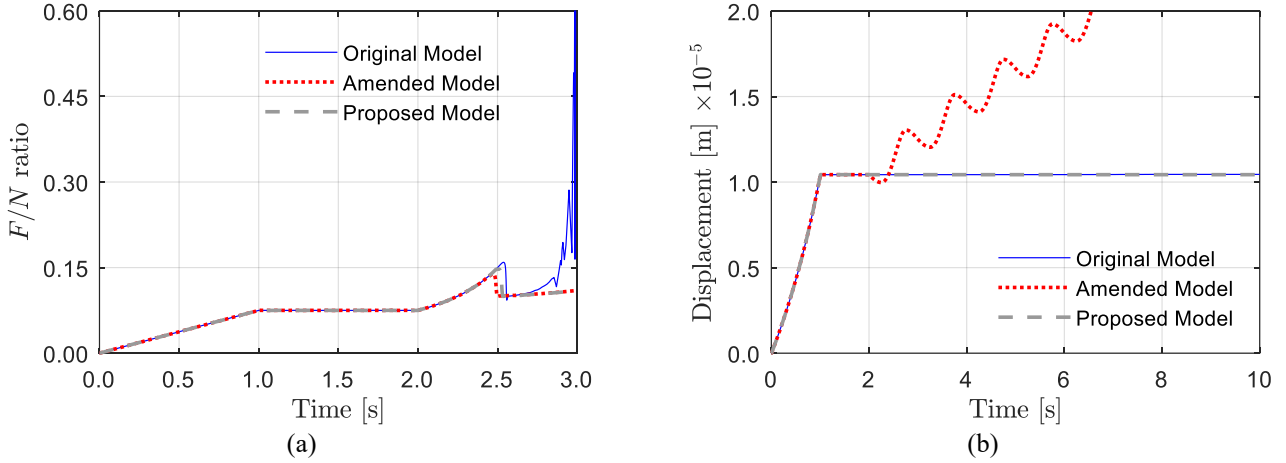


Figure 1: Results of (a) friction to normal force ratios in a case of normal force decreasing, and (b) displacement of the mass block in a case of normal load oscillation in the sticking regime

### Acknowledgments

This work has been supported by Portuguese Foundation for Science and Technology, under the national support to R&D units grant, with the reference project UIDB/04436/2020 and UIDP/04436/2020. This research has been supported by the National Science Centre (Poland) grant no. 2018/29/B/ST8/00374.

### References

- [1] E. Pennestrì, V. Rossi, P. Salvini, P. P. Valentini. Review and comparison of dry friction force models. *Nonlinear Dynamics*, 83(4):1785-1801, 2016.
- [2] F. Marques, P. Flores, J. C. Pimenta Claro, H. M. Lankarani. A survey and comparison of several friction force models for dynamic analysis of multibody mechanical systems. *Nonlinear Dynamics*, 86(3):1407-1443, 2016.
- [3] C. Canudas-de-Wit, H. Olsson, K. J. Åström, P. Lischinsky. A new model for control of systems with friction. *IEEE Transactions on Automatic Control*, 40:419-425, 1995.
- [4] C. Canudas-de-Wit, P. Tsiotras. Dynamic tire friction models for vehicle traction control. *Proceedings of the IEEE Conference on Decision and Control*, 4:3746-3751, 1999.
- [5] M. Wojtyra. Comparison of two versions of the LuGre model under conditions of varying normal force. *Proceedings of the 8th ECCOMAS Thematic Conference on Multibody Dynamics 2017, Prague 2017*, 335-344, 2017.
- [6] F. Marques, P. Flores, J. C. Pimenta Claro, H. M. Lankarani. Modeling and analysis of friction including rolling effects in multibody dynamics: a review. *Multibody System Dynamics*, 45(2):223-244, 2019.
- [7] P. R. Dahl. A solid friction model. Technical Report. The Aerospace Corporation, El Segundo, California, 1968.

# Multibody Fatigue Assessment in Industrial Mechanisms Considering Wear in Revolute Joints

Mario López-Lombardero<sup>1</sup>, Adrian Ramirez<sup>1</sup>, Mario Cabello<sup>1</sup>, Javier Cuadrado<sup>2</sup>

<sup>1</sup> Ikerlan Research Center  
Pº. J. M.<sup>a</sup> Arizmendiarieta, 2  
20500 Arrasate-Mondragón, Spain  
mlopez@ikerlan.es

<sup>2</sup> Lab. of Mechanical Engineering  
Univesity of La Coruña  
Mendizabal s/n, 15403 Ferrol, Spain  
javier.cuadrado@udc.es

## EXTENDED ABSTRACT

### 1. Introduction

In the design of mechanisms and dynamic machines, fatigue life should be considered as a fundamental factor to ensure the reliability of their components. However, the fatigue life prediction models currently used in mechanical design do not take into account the effect of relevant factors, as wear and the evolution of clearances it produces, which undoubtedly influences dynamic loads. These changes can vary the load ranges in some components of the machine during its life and, consequently, modify the stress levels on them. In the field of multibody system dynamics, there are studies focused on the modeling of clearances and wear in the rotating joints of mechanisms [1,2]. However, few studies relate the dynamic effects of these phenomena to the loads that must be born by the components of the mechanism. A paper has recently been published in which a methodology to evaluate the effect of the evolution of wear clearances on the fatigue life of components is proposed [3]. That work shows, in a single case study, the relevance that this effect may have on the fatigue life of a specific component of the machine.

In this work, the methodology developed in [3] was applied to two industrial use cases. Multibody dynamics (MBD) simulation was employed to consider the effect of the evolution of wear clearances present in rotating joints in the dynamic behavior of the machines over the time. In this way, a much more accurate description of the fatigue behavior of the machine components and estimation of the service life of the mechanism can be obtained than applying the classical machine design methods. In particular, the behaviors of a railway pantograph and an industrial press have been studied, and relevant design recommendations have been drawn from the study.

### 2. Metodology

The analysis of the industrial mechanisms studied in the present work was carried out by means of a MBD simulation procedure that allows to simulate the evolution of the clearances during the life of a machine. For this purpose, a wear model was implemented whose parameters were experimentally validated through an in-house developed test bench. The forward-dynamics simulation of the mechanism provides the reaction loads that are then used to evaluate the stresses in the components through finite element (FEM) models. In this way, the critical points can be identified and the stress histories at them can be calculated. This process enables to evaluate the evolution of fatigue damage with greater accuracy than classical machine design methods as it considers the variation along the time of dynamic loads due to clearances. Two representative case studies are presented below, for which the effects of considering the growth of clearances in the fatigue life of the mechanisms are opposite.

#### 2.1. Case study: industrial press

This case study considers the effect of a clearance in the rotating joint of an industrial press indicated in Figure 1a. The clearance does not grow uniformly, yet it grows more in the sector subject to the greatest efforts. As the size of the clearance increases along the time, the dynamic forces also increase, as illustrated in Figure 1b, which translates into a significant increase in stresses and, consequently, into a reduction of the fatigue life. Figure 2a shows the evolution of the clearance size along the work cycles of the machine, while Figure 2b plots the cumulative damage, which follows an exponential behavior. In fact, the model which takes into account the clearance effect predicts a premature break of the component.

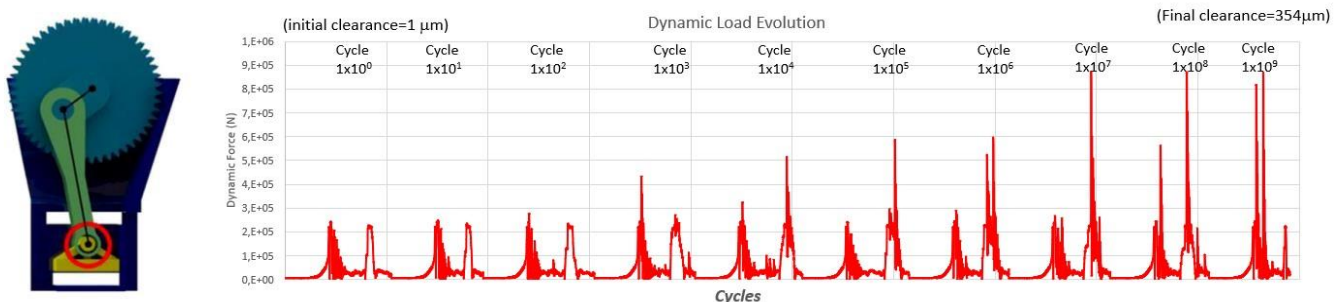


Figure 1: (a) Mechanism critical joint; (b) Dynamic load evolution due to the increase in the size of the clearance.



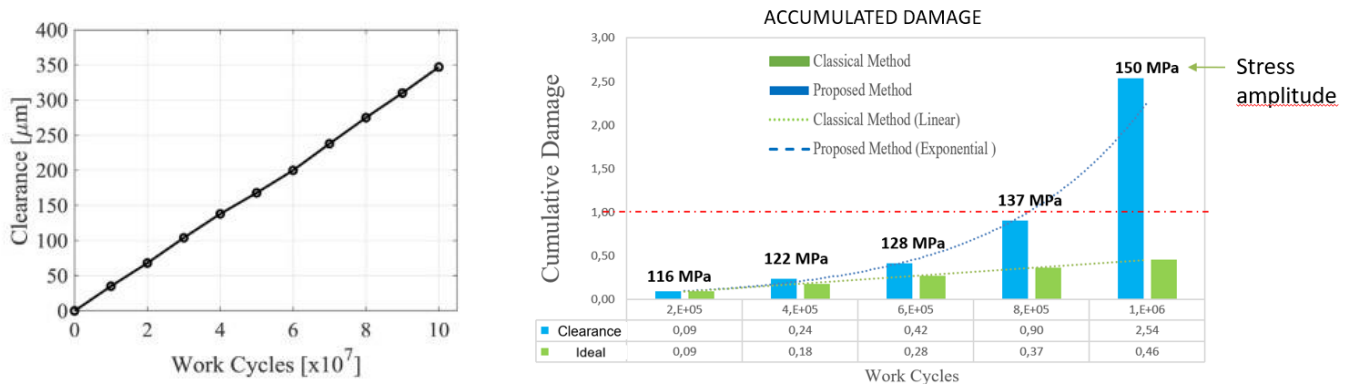


Figure 2: (a) Clearance Evolution. (b) Cumulative damage for the classical and the proposed approach

## 2.2. Case study: railway pantograph

This case study focuses on the mechanism of a railway pantograph. The mechanism is responsible for keeping the adequate contact force with the catenary cables that feed the towing vehicle. After applying the proposed fatigue life evaluation methodology, it turned out that the increase of clearances improved the fatigue resistance of the components, which would allow the use of tighter safety factors in the design. The results of this study are shown in Figure 3.

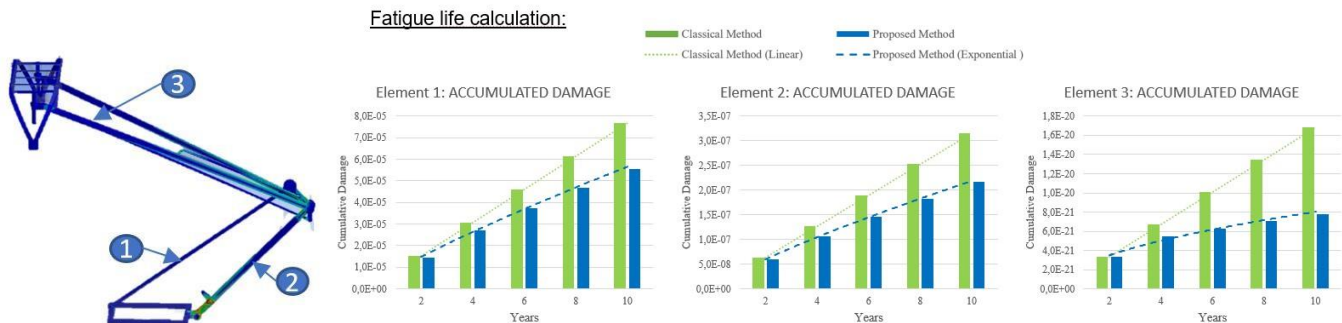


Figure 3: (a) Mechanism and components; (b) Cumulative damage in each component using the classical (green) and the proposed (blue) approaches.

## 3. Conclusion

The evolution of clearances due to wear has an important influence on the fatigue life of industrial machines and mechanisms. In addition, it is observed that this phenomenon may affect differently depending on the characteristics of the machine motion. The presence of clearances in cases with high dynamic forces involved causes these forces to increase, thus increasing the stresses, which in turn accelerate the accumulated damage, reducing the fatigue life. However, in certain mechanisms not subject to high dynamic loads, the clearances may slow down the accumulated damage due to the geometrical changes in the mechanism they cause, so that a less conservative safety factor could be applied in the design of the mechanism.

In order to improve machine design methods, we are currently working on a series of tools, based on MBD simulation, that seek to provide a better life prediction from the design stage. Furthermore, taking into account the force variations due to increased clearances allows the design of machines which can possess greater precision and greater structural and functional reliability. It is intended to develop design methodologies for joints that rely on predictions based on MBD simulation.

## References

- [1] Q. Tian, P. Flores, H.M. Lankarani, A comprehensive survey of the analytical, numerical and experimental methodologies for dynamics of multibody mechanical systems with clearance or imperfect joint, Mechanism and Machine Theory, vol. 122, pp. 1-57, 2018.
- [2] P. Flores, J. Ambrosio, Revolute joints with clearance in multibody systems, Computers and Structures, vol. 82, no. 17-19, pp. 1359-1369, 2004.
- [3] M. Ordiz, J. Cuadrado, M. Cabello, I. Retolaza, F. Martinez, D. Dopico, Prediction of fatigue life in multibody systems considering the increase of dynamic loads due to wear in clearances, Mechanisms and Machine Theory, vol. 160, art. 104293, 2021.

# The Tippedisk: A Minimal Model For Friction-Induced Inversion

Simon Sailer, Simon R. Eugster, Remco I. Leine

Institute for Nonlinear Mechanics  
University of Stuttgart  
Pfaffenwaldring 9, 70569, Germany  
[sailer, eugster, leine]@inm.uni-stuttgart.de

## EXTENDED ABSTRACT

*Summary.* The aim of this work is to introduce the tippedisk to the theoretical mechanics community as a new mechanical-mathematical archetype for friction-induced instability phenomena. The modeling, analysis and simulation of the tippedisk is discussed. Unlike the tippetop, the tippedisk has no rotational symmetry, which greatly complicates its analysis. Since the system can not be reduced to a planar one, one has to consider the full three-dimensional kinematics, being intrinsically nonlinear. The in-depth analysis leads to homoclinic connections and global bifurcations.

### 1 Introduction

Various gyroscopic systems which are interacting with a horizontal frictional support, such as Euler's disk [1], the rattleback [2] and the tippetop [3], form a scientific playground for research in theoretical mechanics. The tippetop [4, 5], as well as the related dynamics of spinning eggs [6], correspond to a subclass of gyroscopic systems which shows friction-induced instability phenomena. The tippetop is a rotationally symmetric top, consisting of a spherical body and a stem attached to it. The center of gravity (COG) does not coincide with the geometric center, such that the stem points upwards as the top rotates with non-inverted orientation. If the top is spun around its axis of symmetry, normal and friction forces are acting on the top, such that the top starts to invert its orientation and balances on its stem. Similar phenomena also occur for other axisymmetric bodies with rotational symmetry in inertia and geometry, for example spinning eggs [6]. But what happens if this symmetry does not exist? In this work we introduce the "tippedisk" as new archetype of a three-dimensional rigid body system with frictional contact. The tippedisk can be seen as a thin disk for which the COG does not coincide with the geometric center. If the tippedisk is spun around an in-plane axis, it can be observed that the COG rises until the disk remains in an inverted configuration. The inversion phenomenon is therefore not restricted to axisymmetric rigid bodies and also takes place for the tippedisk. We aim to conduct an in-depth stability analysis for the tippedisk. Moreover, the analytical study will be validated through various numerical models and the results will be compared to experimental data in future research.

### 2 Mechanical model

The mechanical system consists of a thin, rigid disk with mass  $m$ , radius  $r$ , eccentricity  $e$  and a frictional support. The simplest way to design such a disk, where the COG and the geometric center  $G$  do not coincide, is to take a homogeneous disk and to drill a hole (remove mass) at an arbitrary point, which does not coincide with the geometric center  $G$  of the disk.

In Figure 1 the mechanical model for the tippedisk is depicted. The right-handed body fixed  $B$ -system is attached to the disk, such that  $\mathbf{e}_z^B$  lies perpendicular to the surface of the disk. The  $\mathbf{e}_x^B$ -vector is defined as the normalized vector of  $\mathbf{r}_{GS}$ , which points from the geometric center  $G$  to the center of gravity  $S$ . The inertia tensor with respect to  $G$  expressed in the body fixed  $K$ -system is given as  ${}_B\Theta_G = \text{diag}(A, B, C)$ , where  $B < A < C$  holds. Since the disk is in contact with the support, we have to introduce a contact point  $C_1$  which is defined as the body fixed point with minimal height. Therefore, we introduce another coordinate system  $G$  in which  $\mathbf{r}_{GC_1} = -r\mathbf{e}_y^G$  holds. The gap between  $C_1$  and the flat support is measured as  $g_{N1}$ . We assume Signorini's law in normal direction and smooth Coulomb friction with friction coefficient  $\mu$  and smoothing parameter  $\varepsilon$ , see [7].

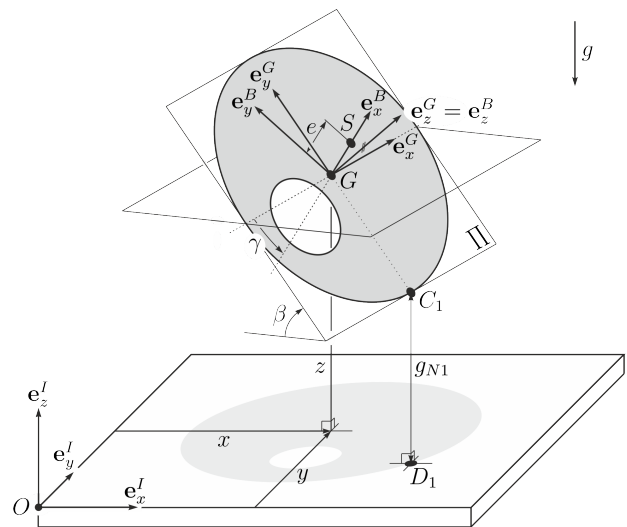


Figure 1: Mechanical model: tippedisk

For the following stability analysis it is convenient to parameterize the rotation matrix using Euler angles, such that the equations

of motion become ordinary differential equations. The angle  $\alpha$  describes the rotation around the  $\mathbf{e}_z^I$ -axis,  $\beta$  is the inclination angle around the  $\mathbf{e}_x^G$ -axis and  $\gamma$  the rotation angle around the  $\mathbf{e}_z^G$ -axis, corresponding to the Euler angles in common  $z$ - $x$ - $z$  convention.

### 3 Inversion Phenomenon

In a first step the local asymptotic stability of the stationary solutions is analyzed using an eigenvalue analysis. Hereto, the system is linearized around the non-inverted stationary solution ( $\beta = +\pi/2, \gamma = -\pi/2$ ) and the inverted one ( $\beta = +\pi/2, \gamma = +\pi/2$ ). As a result, it follows that the inverted stationary solution is locally asymptotically stable above a critical spinning velocity  $\Omega_{\text{crit}}$ , whereas the non-inverted one is always unstable. The application of perturbation techniques allows to determine a closed form expression of the critical spinning velocity  $\Omega_{\text{crit}}$ .

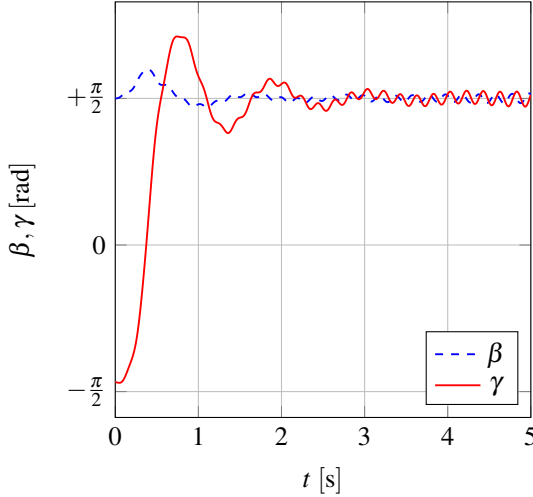


Figure 2: Evolution of the angles  $\beta$  (blue) and  $\gamma$  (red) during the process of inversion.

The evolution of the angles  $\beta$  (blue) and  $\gamma$  (red) are shown in Figure 2, obtained from time integration of a reduced system where the unilateral constraint is assumed to be bilateral. At time  $t = 0$ s, it holds

$$\begin{bmatrix} \beta_0 \\ \gamma_0 \end{bmatrix} = \begin{bmatrix} +\pi/2 \\ -\pi/2 - 0.1 \end{bmatrix}.$$

This initial configuration corresponds to a non-inverted disk perturbed in  $\gamma$ -direction. If the disk is spun around its in-plane axis of symmetry (i.e., in  $\mathbf{e}_x^B$ -direction) with supercritical angular spinning velocity  $\Omega_{x,0} = 40 \frac{\text{rad}}{\text{s}} > \Omega_{\text{crit}}$ , we observe that the angle  $\gamma$  changes sign and a damped oscillation near  $+\pi/2$  occurs. During the process of inversion, the angle  $\beta$  changes only slightly and converges asymptotically to  $\pi/2$ . Since  $\beta$  does not change significantly during the inversion, the inversion phenomenon is mainly characterized by the change of  $\gamma$ .

### 4 Conclusions

In this work the tippedisk has been introduced as a new toy to the playground of mechanical mathematical archetypes for gyroscopic systems under unilateral constraints and friction. The introduced mechanical model contains all relevant effects, such that it is able to describe the inversion phenomenon. Moreover, it can be used to validate numerically the results of the analytical analysis. The longterm goal of this project is a rigorous stability analysis and the qualitative approximation of the inversion process. In summary, it should be noted that the tippedisk can not be understood as a trivial generalization of the tippetop, since the dynamics are much more complex. In addition, the tippedisk serves as a link between analytical mechanics, theoretical mechanics and nonlinear dynamics.

### References

- [1] R. I. Leine. Experimental and theoretical investigation of the energy dissipation of a rolling disk during its final stage of motion. *Archive of applied mechanics*, 79(11):1063-1082, 2009.
- [2] A. V. Borisov, I. S. Mamaev. Strange attractors in rattleback dynamics. *Physics-Uspekhi*, 46(4):393, 2003.
- [3] N. M. Bou-Rabee, J. E. Marsden, L.A. Romero. Tippe Top inversion as a dissipation-induced instability. *SIAM Journal on Applied Dynamical Systems*, 3(3), 352-377, 2004
- [4] K. Magnus. Kreisel. Springer, Berlin; Heidelberg; New York, 1971.
- [5] R. J. Cohen. The tippe top revisited. *American Journal of Physics*, 45(1):12-17, 1977.
- [6] K. Moffatt, Y. Shimomura. Classical dynamics: Spinning eggs — a paradox resolved. *Nature*, 416(6879):385, 2002.
- [7] S. Sailer, S. R. Eugster, R. I. Leine. The Tippedisk: a Tippetop Without Rotational Symmetry. *Regular and Chaotic Dynamics*, 25(6):553-580, 2020.

# Do We Need to Impose Constraints at Acceleration Level in the Nonsmooth Generalized- $\alpha$ Method?

Alejandro Cosimo<sup>1,2</sup>, Federico Cavalieri<sup>2</sup>, Alberto Cardona<sup>2</sup>, Olivier Bruls<sup>1</sup>

<sup>1</sup> Department of Aerospace and Mechanical Engineering  
University of Liège  
Allée de la Découverte 9, 4000 Liège, Belgium  
acosimo@uliege.be, o.bruls@uliege.be

<sup>2</sup> Centro de Investigación de Métodos Computacionales (CIMEC)  
CONICET / UNL  
Colectora Ruta Nac Nro 168, Km 0, Paraje El Pozo, 3000 Santa Fe, Argentina  
fcavalieri@cimec.unl.edu.ar, acardona@cimec.unl.edu.ar

## EXTENDED ABSTRACT

### 1 Introduction

Nonsmooth techniques are particularly well-suited for the study of the dynamics of flexible multibody systems subject to contacts and impacts as shown in [1]. In that work, the nonsmooth generalized- $\alpha$  (NSGA) time integration scheme is presented. It is an event-capturing technique based on the splitting of the involved fields into a smooth and a (nonsmooth) impulsive contribution, where the former is integrated with second-order accuracy by means of the generalized- $\alpha$  scheme and the latter with first-order accuracy. The resulting scheme offers an effective control of the numerical dissipation and it does not present any drift of the bilateral and unilateral constraints at the position and velocity levels.

On the one hand, the robustness of the NSGA time integrator for problems involving nonlinear bilateral constraints and flexible elements was improved in [2]. The main difference with its predecessor is that the definition of the splitting is modified in order to ensure the decoupling of the smooth, the position correction and the velocity jump sub-problems. However, in that work no constraints at acceleration level were considered. On the other hand, the incorporation of contact constraints at acceleration level in the NSGA was studied in [3]. This paper showed that imposing acceleration constraints leads to the elimination of spurious oscillations of the constraints and Lagrange multipliers and to an improvement in terms of Newton iterations for problems characterized by contacts that remain closed in a persisting manner. However, the decoupling of the three sub-problems was not exploited and the study was limited to point-to-face unilateral contact conditions.

In this work, we investigate the incorporation of unilateral constraints at acceleration level in the context of the decoupled NSGA time integrator. The resulting scheme thus benefits both from the robustness of the decoupled version of the NSGA method and from the improved numerical properties brought by the acceleration constraints. Furthermore, the method is applied to a test-case involving contacts with curved surfaces and a performance and robustness analysis reveals the importance of imposing constraints at acceleration level when dealing with contacts between curved geometries.

### 2 Method

As it was already mentioned, the NSGA results from the splitting of the involved fields into a smooth and a nonsmooth impulsive contribution. There is some freedom for the definition of the problem governing the smooth prediction of the motion and, in the basic version of the algorithm, no contact information is exploited for this sub-problem. In contrast, in this work, the formulation of the smooth sub-problem takes into account contact information by imposing the bilateral and the unilateral constraints at acceleration level in the following manner:

$$-\ddot{\mathbf{g}}^{\overline{\mathcal{U}}}(\tilde{\mathbf{q}}, \tilde{\mathbf{v}}, t) = \mathbf{0} \quad (1a)$$

$$\text{if } g^j(\tilde{\mathbf{q}}, t) \leq 0 \text{ and } \dot{g}^j(\tilde{\mathbf{q}}, \tilde{\mathbf{v}}, t) \leq 0 \text{ then } 0 \leq \ddot{g}^j \perp \tilde{\lambda}^j \geq 0, \quad \forall j \in \mathcal{U} \quad (1b)$$

where  $g^j$ ,  $\dot{g}^j$  and  $\ddot{g}^j$  are the constraint  $j$  at position, velocity and acceleration levels,  $\mathcal{U}$  represents the set of unilateral constraints and  $\overline{\mathcal{U}}$  the set of bilateral constraints,  $\tilde{\mathbf{q}}$  and  $\tilde{\mathbf{v}}$  respectively denote the smooth contribution to the generalized coordinates and the velocity field, and  $\tilde{\lambda}^j$  denotes the smooth Lagrange multiplier. Equation (1) represents a frictionless contact problem, nevertheless, the method is also applicable to frictional contact problems. It should be observed that the definition of this problem depends only on the smooth contribution of the involved fields, and not on the total fields. Consequently, the smooth sub-problem can be solved independently of the other sub-problems, which represents a fundamental advantage. In the end, the resulting scheme will be characterized by the resolution of a sequence of three *decoupled* sub-problems.

### 3 Results

In this example, we compare the results obtained between the decoupled solver with and without constraints at acceleration level. The problem consists of one sphere of radius  $r_a = 1$  and mass  $m_a = 10$  orbiting around another fixed sphere of the same radius  $r_b = 1$  and mass  $m_b = 10$ . The two spheres are joined by means of a spring whose stiffness constant is 1000 and natural length is  $0.5(r_a + r_b)$ . The initial position of the fixed sphere is the origin and the moving sphere's center is at coordinates  $(0, r_a + r_b, 0)$ . The initial velocity for the moving sphere is given by  $\Omega_z = -\pi r_a$  and  $\mathbf{v}_y = -\pi$ . We solve for frictional contact by taking zero for every restitution coefficient and adopting a friction coefficient of  $\mu = 1.8$ . A total simulation time of 10 s is run with a time step of  $10^{-2}$  s.

The solutions obtained for this problem can be observed in Figure 1. A direct comparison of the results clearly states the need to impose constraints at acceleration level for problems of this kind. As it can be appreciated, no artificial increase of the kinetic energy is present when imposing constraints at acceleration level. This test clearly demonstrates that, unless the time step is decreased considerably, it is essential to impose acceleration constraints in the NSGA method in order to solve problems with persistent contact on curved surfaces.

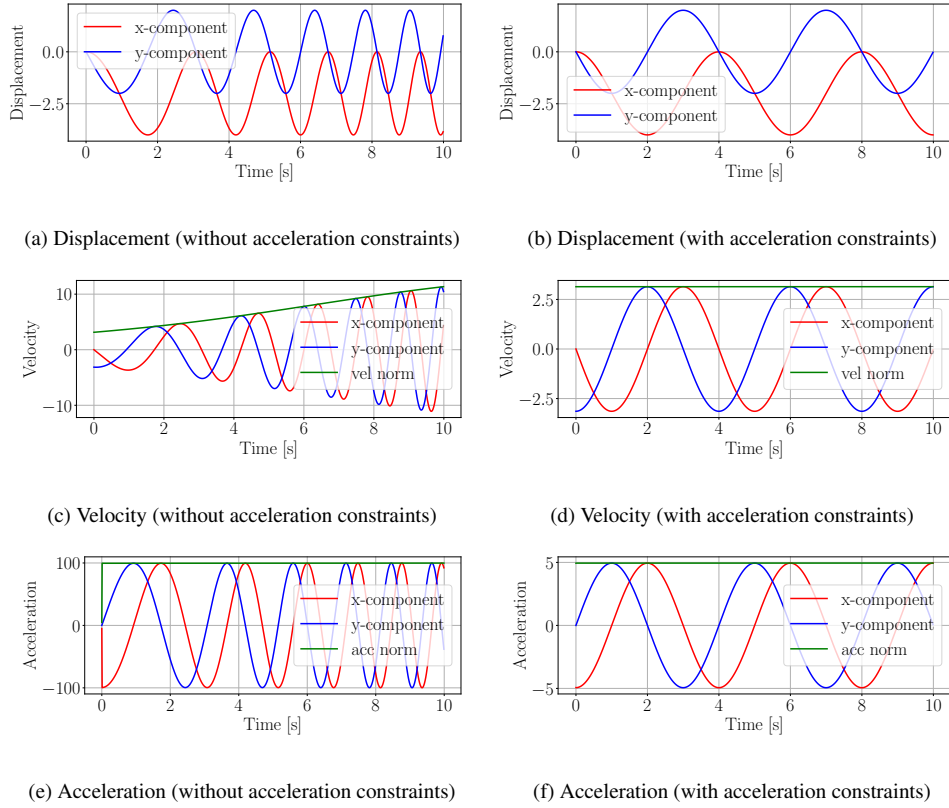


Figure 1: Comparison of the results obtained with and without imposing constraints at acceleration level. The results on the left are obtained without imposing acceleration constraints, whilst the ones on the right are obtained by imposing them.

## 4 Conclusion

This work proposes a variant of the NSGA in which constraints at acceleration level are taken into account in the smooth prediction sub-problem. This is done in such a way that the resulting integrator is characterized by a *decoupled* sequence of sub-problems. Through an example involving two spherical bodies, it is demonstrated that acceleration constraints help to solve contacts between curved surfaces, effectively eliminating the artificial increase of the kinetic energy that would appear otherwise.

## 5 Acknowledgements

This work received financial support from Consejo Nacional de Investigaciones Científicas y Técnicas (CONICET), Universidad Tecnológica Nacional PID-UTN AMECAFE0008102TC, and from the Robotix Academy project of the Greater Region.

## References

- [1] O. Brüls, V. Acary, and A. Cardona. Simultaneous enforcement of constraints at position and velocity levels in the nonsmooth generalized- $\alpha$  scheme. *Computer Methods in Applied Mechanics and Engineering*, 281:131–161, 2014.
- [2] A. Cosimo, J. Galvez, F.J. Cavalieri, A. Cardona, and O. Brüls. A robust nonsmooth generalized- $\alpha$  scheme for flexible systems with impacts. *Multibody System Dynamics*, 48:127–149, 2020.
- [3] O. Brüls, V. Acary, and A. Cardona. On the constraints formulation in the nonsmooth generalized- $\alpha$  method. In R.I. Leine, V. Acary, and O. Brüls, editors, *Advanced Topics in Nonsmooth Dynamics*, pages 335–374, Springer International Publishing, 2018.

# Planar Wrapping and Stretching of a Thick Strand on a Surface by Continuous Integration

Katharina Müller, Andres Kecskemethy

Chair for Mechanics and Robotics, University of Duisburg-Essen  
Lotharstr. 1, 47057 Duisburg, Germany  
katharina.mueller@uni-due.de, andres.kecskemethy@uni-due.de

## EXTENDED ABSTRACT

### 1 Introduction

In biomechanics, modeling strands like muscles or ligaments is required in many applications, notably in musculoskeletal systems. Here, it is standard practice to model muscles as thin massless lines and defining their path using via points or – more advanced – by defining surfaces as wrapping obstacles[1]. However, there are cases where the strand diameter is not negligible. Discrete methods, modeling the strand for example as a bead chain[2] provide a general and powerful workaround having the advantage of a fast derivation. The disadvantage is, however, that their implementation is mostly complex involving multiple contact detection and bookkeeping about it, which in turn can be associated with very high computation times. Also, in musculoskeletal simulation models, discrete approaches may lead to unrealistic forces when coupled to dynamic muscle models.

To overcome this shortness, in our previous work[3, 4], a novel approach was presented using continuous integration of smooth differential equations to frictionlessly wrap a thick strand with non constant conicity but constant length on a convex surface with non constant curvature. Compared to an implementation of the bead method for different levels of discretization fineness, the method was verified and high computational saving in the order of factors of 200–800 could be substantiated. The present contribution is an extension to cover elongation with compressible cross sections instead of the constant length condition. To simplify the problem and illustrate the idea of stretching compactly, one end of the muscle (end  $O$ ) is purposely held fixed.

### 2 Problem formulation

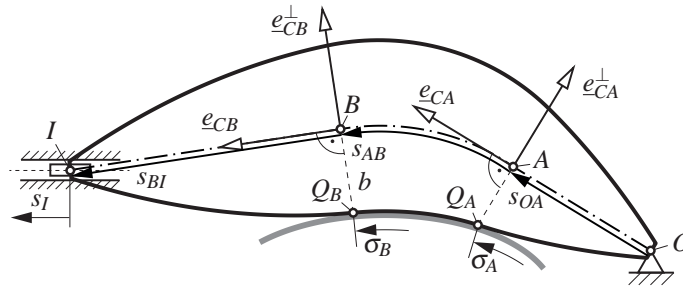


Figure 1: Thick strand with with free end  $O$  fixed and slidable free end  $I$  wraps on a surface between  $A$  and  $B$

As illustrated in Fig. 1, a curved strand with the half thickness  $b(s, \epsilon)$  defined with respect to the position  $s$  on the center line, and depending on the longitudinal strain  $\epsilon$ , is wrapped over a surface with its free end  $O$  fixed and its free end  $I$  slidable (joint variable  $s_I$ ). For the total center line length between  $O$  and  $I$ , it holds  $s_{OI} = \ell = \ell_0(1 + \epsilon)$  with the unstretched length  $\ell_0$  and the longitudinal strain  $\epsilon$ . For the cross contraction, the assumption  $\Delta V/V = (1 - 2\nu)\Delta\ell/\ell$  was used, with volume  $V$  and Poisson's ratio  $\nu$ . Between the contact points  $Q_A$  and  $Q_B$  the strand wraps around the surface with  $\sigma_A$  and  $\sigma_B$  being the surface variables, whereas  $A$  and  $B$  are the corresponding points on the center line of the strand marking the transition from the outer straight line segments  $s_{OA}$  and  $s_{BI}$  to the wrapped segment  $s_{AB}$  of the center line in the middle. At the cross sections at  $A$  and  $B$  a frame is introduced with the unit vector  $\underline{e}_C$  being normal to the cross section and  $\underline{e}_C^\perp$  being orthogonal to  $\underline{e}_C$ .

At both connection points  $A$  and  $B$ , the orthogonality condition applies that the end faces at  $A$  and  $B$  must be perpendicular to the free ends. In addition, the length conditions apply that the distance between  $O$  and  $A$  must correspond to the center line length  $s_{OA}$  and the distance between  $B$  and  $I$  must correspond to the total length  $\ell$  minus the length  $s_{OB}$  from  $O$  to  $B$ , namely  $s_{BI} = \ell - s_{OB}$ .

This leads to the position constraints at ends  $A$  and  $B$ :

$$\underline{g}_A = \begin{bmatrix} g_{1A} \\ g_{2A} \end{bmatrix} = \begin{bmatrix} s_{OA} - \Delta r_{OA}(\sigma_A, s_{OA}, \epsilon) \cdot \underline{e}_C(\sigma_A, s_{OA}, \epsilon) \\ \Delta r_{OA}(\sigma_A, s_{OA}, \epsilon) \cdot \underline{e}_C^\perp(\sigma_A, s_{OA}, \epsilon) \end{bmatrix} = 0 ; \quad \underline{z}_A = \begin{bmatrix} s_{OA} \\ \sigma_A \end{bmatrix} \quad (1)$$

$$\underline{g}_B = \begin{bmatrix} g_{1B} \\ g_{2B} \end{bmatrix} = \begin{bmatrix} \Delta r_{BI}(\sigma_B, s_{OB}, \epsilon) \cdot \underline{e}_C(\sigma_B, s_{OB}, \epsilon) + s_{OB} - \ell(\epsilon) \\ \Delta r_{BI}(\sigma_B, s_{OB}, \epsilon) \cdot \underline{e}_C^\perp(\sigma_B, s_{OB}, \epsilon) \end{bmatrix} = 0 ; \quad \underline{z}_B = \begin{bmatrix} s_I \\ \sigma_B \end{bmatrix} \quad (2)$$



and the corresponding velocity constraints

$$\dot{\underline{g}}_A = \mathbf{J}_A \dot{\underline{z}}_A + \frac{\partial \underline{g}_A}{\partial \underline{\varepsilon}} \dot{\underline{\varepsilon}} \stackrel{!}{=} 0 \quad \text{and} \quad \dot{\underline{g}}_B = \mathbf{J}_B \dot{\underline{z}}_B + \frac{\partial \underline{g}_B}{\partial \underline{\varepsilon}} \dot{\underline{\varepsilon}} \stackrel{!}{=} 0 . \quad (3)$$

where  $\Delta \underline{r}_{OA}$  and  $\Delta \underline{r}_{BI}$  are the vectors from  $O$  to  $A$  and from  $B$  to  $I$ , respectively,  $s_{OB} = s_{OA} + s_{AB}$  and  $\mathbf{J}_A = \partial \underline{g}_A / \partial \underline{z}_A$ ,  $\mathbf{J}_B = \partial \underline{g}_B / \partial \underline{z}_B$ .

### 3 Algorithm

The presented algorithm consists of two nested integrations. In the external integration, the constraint matching takes place, where the implicit velocity constraints at  $A$  and  $B$  are solved for derivatives of the state vectors with respect to time  $t$  as

$$\frac{d\underline{x}^{\text{constr}}}{dt} = \begin{bmatrix} \dot{\underline{z}}_A \\ \dot{\underline{z}}_B \end{bmatrix} = \begin{bmatrix} -\mathbf{J}_A^{-1} \frac{\partial \underline{g}_A}{\partial \underline{\varepsilon}} \\ -\mathbf{J}_B^{-1} \frac{\partial \underline{g}_B}{\partial \underline{\varepsilon}} \end{bmatrix} \dot{\underline{\varepsilon}} . \quad (4)$$

In  $\partial \underline{g}_B / \partial \underline{\varepsilon}$ , the derivative  $\partial s_{OB} / \partial \underline{\varepsilon} = \kappa_{AB}^{\underline{\varepsilon}}$  arises which describes how  $s_{OB}$  changes when  $\underline{\varepsilon}$  changes (longitudinal stretch, transversal shrink). This leads to a perturbation problem which can be solved for the interval  $[\sigma_A, \sigma_B]$  via the coupled ODEs (derivations are left out due to lack of space):

$$\frac{d\underline{x}^{\text{shoot}}}{d\sigma} = \frac{d}{d\sigma} \begin{bmatrix} s \\ \kappa_{AB}^{\underline{\varepsilon}} \end{bmatrix} = \begin{bmatrix} f(s, \sigma, \underline{\varepsilon}) \\ \left. \frac{\partial f}{\partial s} \right|_{\underline{\varepsilon}=\text{const}} \cdot \frac{\partial s}{\partial \underline{\varepsilon}} + \left. \frac{\partial f}{\partial \underline{\varepsilon}} \right|_{s=\text{const}} \end{bmatrix} . \quad (5)$$

A detailed derivation of the differential equation  $ds/d\sigma = f(s, \sigma)$  to compute the length of the wrapped center line was presented in [3] for a cone-shaped strand with constant aperture angle  $\alpha$  and in [4] for a convex curved strand, and it can be done analogously for the strand additionally dependent on the longitudinal strain  $\underline{\varepsilon}$ .

### 4 Results

The presented method was implemented in Matlab using the Runge-Kutta routine ode45 for integration of the velocity constraints in the range  $[\varepsilon_0, \varepsilon_E]$  and compared with iterations at position level using equidistant Newton steps (Table 1). The computations were performed on a processor Intel(R) Core(TM) i7-10850H CPU @ 2.70GHz. One can recognize that the integration method is more than twice as fast, with still excellent accuracy at the end of the integration.

Table 1: Computational results

Model and numeric parameters						Method	Computation time [s]	Accuracy
$\varepsilon_0$	$\varepsilon_E$	$\Delta \varepsilon$	tolNewton	tolODErel	tolODEabs	Integration	0.4726	3.0e-09
0.2	0.8	0.006	$10^{-8}$	$10^{-8}$	$10^{-8}$	Iteration	1.1097	-7.6e-11

### 5 Conclusion and Outlook

This contribution presents a continuous and fast method which allows for wrapping a thick strand with non constant aperture angle over a frictionless convex surface with non constant curvature now taking into account longitudinal elongation and lateral strain of the strand. Future work will include free end  $O$  freely movable, too, wrapping over multiple surfaces and the spatial contact surface case.

### References

- [1] A. Scholz, M. Sherman, I. Stavness, S. Delp, A. Kecskemethy. A fast multi-obstacle muscle wrapping method using natural geodesic variations. *Multibody Syst Dyn* 36, 195–219, 2016.
- [2] R. Franci and V. Parenti-Castelli. A new tool to investigate the interactions between elastic fibers and rigid bodies. *Proceedings of IFToMM 2007*, 2007.
- [3] K. Müller, A. Kecskemethy. A continuous and computationally efficient method for wrapping a “thick” strand over a surface – The planar single-surface case. In T. Uhl, editors, *Proceedings of the Advances in Mechanism and Machine Science. IFToMM WC 2019. Mechanisms and Machine Science*, vol 73. Springer, Cham, 2019.
- [4] K. Müller, A. Kecskemethy. A New Approach for Continuous Wrapping of a Thick Strand on a Surface – The Planar Case with Constant Length and Free Ends. In J. Lenarčič and B. Siciliano, editors, *Advances in Robot Kinematics 2020. ARK 2020. Springer Proceedings in Advanced Robotics*, vol 15. Springer, Cham, 2021.

# Train Bogie Dynamics Modeling With An Emphasis On Contact Mechanics In A Multibody Model

Martijn Vermaut<sup>1</sup>, Mohamed Bentefrit<sup>2</sup>, Frank Naets<sup>1</sup>, Wim Desmet<sup>1</sup>

<sup>1</sup>Department of Mechanical Eng.  
DMMS Lab, Flanders Make & LMSD, KU Leuven  
Celestijnenlaan 300, B-3001 Leuven, Belgium  
[martijn.vermaut, frank.naets, wim.desmet]@kuleuven.be

<sup>2</sup>Televic Rail  
Leo Bekaertlaan 1, B-8870 Izegem, Belgium  
m.bentefrit@televic.com

## EXTENDED ABSTRACT

### 1 Introduction

When it comes to train monitoring systems, and especially safety monitoring systems, the dynamics and stability of a bogie is an essential aspect. In order to gain more insight into the dynamics, a multibody model is constructed. The goal of creating a model of such a train bogie is to obtain a means to assess the stability of the train in a better and more cost-efficient manner. In order to do this the multibody model is scheduled to be integrated in a virtual sensing framework based on an extended Kalman Filter [1]. This allows a sensor set containing for instance only accelerometers and strain sensors to be used to virtually measure quantities that are otherwise hard to measure (e.g. strain in locations where it is difficult to place a strain sensor), or even impossible to measure (e.g. rail-wheel contact forces).

### 2 Model Construction

The multibody model of the train bogie is constructed with an in-house MultiBody Research Code (MBRC) [2]. This is a highly modular code written in Matlab which allows it to easily construct different multibody models with varying topology, but also to easily add component force models such as the contact model between the rail and the wheel. This contact model is a highly dedicated model that has been widely discussed in literature already [3]. But in order to use the multibody model in a state estimation feedback loop. The underlying equations need to be accessible [1]. In order to achieve this, a rolling contact model is implemented in the MBRC.

The contact model comprises of two stages: the geometric problem in which the contact points are sought, and the dynamic problem in which the force expressions are evaluated. These two stages are not completely decoupled as the choices in the latter may influence the requirements for the former. The contact model implemented in the MBRC assumes that the normal force expression is independent from the tangential force expression. Moreover the normal force expression is evaluated assuming Hertzian contact. The two most notable assumptions here are that the local deformations are much smaller than the overall component dimensions and that the contacting surfaces can be adequately locally approximated by quadratic surfaces which are not conformal. This allows the contacting surfaces to be assumed rigid such that the local flexibility should only be accounted for in the force expression but not in the contact search algorithm. It also allows the contact search algorithm to assume that only elliptical contact patches exist with in the middle a point where the surface are maximally penetrating.

In order to achieve smooth contacting surfaces, both the rail and the wheel surfaces are represented by Non-Uniform Rational B-Splines (NURBS) [4]. If the rail and wheel should be modeled as flexible, the NURBS parameters should be mapped onto the deformation patterns [5], but in a first modeling iteration this can be assumed to be unnecessary as the model is to be used in a state estimation feedback loop.

The contact search algorithm is split in two steps: the first step is the global search algorithm and the second stage is the local search algorithm. In the global search algorithm both surfaces are sampled and a Bounding Volume Hierarchy (BVH) is constructed [6]. It is very difficult to find contact between two general surfaces, but when both surfaces are convex the Separating Axis Theorem (SAT) can be used [6]. This theorem states that if two surfaces are convex and non-contacting, they can be projected onto an axis where they do not overlap. The BVH is then a binary (or higher) tree of nested convex primitives encompassing the full original geometry. If the global search algorithm using the BVH yields overlapping primitives, the corresponding sampled points of the underlying NURBS surfaces can be used as initial guess for the local search algorithm.

The local search algorithm uses a gradient-based solver (e.g. Newton-Raphson) to solve the contact conditions. These contact conditions define the point of maximal penetration for two contacting non-conformal surfaces as they are considered here: (1) the normals on both surfaces need to be colinear; (2) the penetration vector need to be colinear with these normal. As these conditions only impose constraints projected onto the tangent planes of the surfaces, no direct check on the penetration depth is performed. Therefore a sanity check is added imposing an upper and lower limit on the penetration depth to avoid infeasible contact locations to be found by the algorithm.

With the contact location(s) found, the force expressions can be evaluated. The normal force is computed via a standard Hertzian contact force expression. The tangential force expression can be evaluated with three different models: (1) a linear Kalker model; (2) a Polach model [7]; (3) a nonlinear Kalker model (based on FASTSIM2 [8]). These three models are given here in increasing order of modeling fidelity, but also in increasing order of computational complexity. In a multibody model a balance should be

found for the tangential force model that delivers enough complexity in the dynamics that can still be seen in the remainder of the mechanism without including effects that are barely visible other than in the contact patch itself. By having these three models available, this trade-off can be made on a case-per-case basis.

### 3 Multibody Considerations

In order to obtain fast convergence of the equations of motion, a tangent damping and stiffness matrix should be provided by the force expressions. For the two force expressions this can be done by applying the chain rule many times over until the required sensitivity information is obtained. For the contact location however this is more complicated. The contact location is implicitly defined by the contact conditions (i.e. the surface normals and penetration vector should be colinear). These implicit equations are a function of the generalized coordinates of each body that the surfaces are connected to, but also the two surface parameters of each surface where the contact is positioned. The sensitivity of the surface parameters at the contact location w.r.t. the generalized coordinates should thus be computed via implicit differentiation of the contact conditions.

The obtained tangent damping and stiffness matrices are validated using numerical derivatives for the case where the bodies are modeled in a Cartesian Coordinates formulation and in a Natural Coordinates formulation.

### 4 Results

In order to demonstrate the correct functionality of the bogie model a simulation is performed whereby the bogie is accelerating on a straight track, but as the track turns to the left the bogie keeps accelerating. The turn does not include banking of the track. In figure 1, the normal force on the left front wheel can be seen to be decreasing until a point where it loses contact and the bogie derails. The oscillations in the turn can be attributed to the dynamics of the inertia of the different components interacting through the suspension elements.

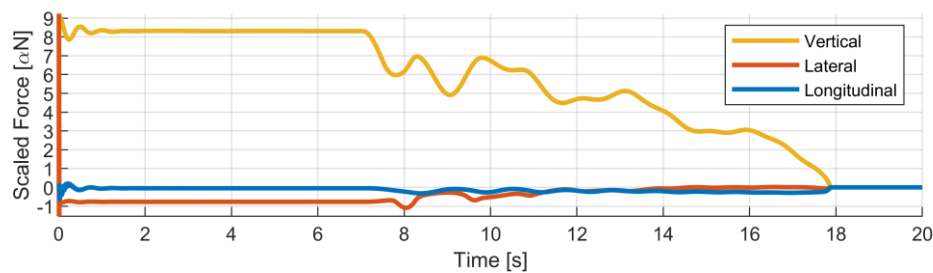


Figure 1: Contact forces in left front wheel

### 5 Future Work

The multibody model currently only contains rigid components to represent a.o. the bogie frame and lumped stiffness models to represent the primary and secondary suspension components. In a future update the bogie frame is to be replaced by an FE model. Another step to be taken is to include the model in a state estimation feedback loop in order to perform virtual sensing.

### Acknowledgements

Internal Funds KU Leuven are gratefully acknowledged for their support. This research was partially supported by Flanders Make, the strategic research center for the manufacturing industry.

### References

- [1] Adduci, R., Vermaut, M., Naets, F., Croes, J., & Desmet, W. (2021). A Discrete-Time Extended Kalman Filter Approach Tailored for Multibody Models: State-Input Estimation. *Sensors*, 21(13), 4495.
- [2] Vermaut, M., Tamarozzi, T., Naets, F., & Desmet, W. (2015). Development of a flexible multibody simulation package for in-house benchmarking. In *Proceedings of the ECCOMAS Thematic Conference on Multibody Dynamics International Center for Numerical Methods in Engineering (CIMNE)* (pp. 1560-1571).
- [3] Iwnicki, S. (Ed.). (2006). *Handbook of railway vehicle dynamics*. CRC/Taylor & Francis.
- [4] Piegl, L. A., & Tiller, W. (1997). *The NURBS book* (2nd ed). Springer.
- [5] Fiszer, J. (2017). *Advanced bearing modelling for the numerical analysis of system-level machine dynamics* [PhD Thesis]. KU Leuven.
- [6] Ericson, C. (n.d.). *Real-Time Collision Detection*. Elsevier.
- [7] Polach, O. (2005). Creep forces in simulations of traction vehicles running on adhesion limit. *Wear*, 258(7-8), 992-1000.
- [8] Vollebregt, E. A. H., & Wilders, P. (2011). FASTSIM2: a second-order accurate frictional rolling contact algorithm. *Computational Mechanics*, 47(1), 105-116.

# Efficient impact simulation using the flexible natural coordinate formulation and pinball model

Jari Peeters<sup>1,2</sup>, Luis Zapata<sup>1,2</sup>, Martijn Vermaut<sup>1,2</sup>, Frank Naets<sup>1,2</sup>

<sup>1</sup> DMMS lab  
Flanders Make

<sup>2</sup> Dept. of Mechanical Engineering  
KU Leuven  
Celestijnenlaan 300, 3001, Belgium  
frank.naets@kuleuven.be

## EXTENDED ABSTRACT

### 1 Introduction

Impact simulations are encountered in many engineering problems, for example in crashworthiness simulations [1]. Of particular interest is often the stress and strain distribution in the bodies to assess e.g. damage occurring due to the impacts. However, these problems have classically posed significant computational challenges due to the small timesteps required to resolve the impact conditions, and relatively expensive analysis of deformable components. In many cases full nonlinear finite-element simulations are performed. This leads to very high loads as both all nonlinear elements need to be evaluated together with the contact conditions. However, commonly the elastic deformation remains in the linear elastic range and the element nonlinearity is only required in order to enable large average component motion. In order to reduce this computational load, flexible multibody simulation can be employed. This allows to effectively reduce the computational load, as the average component motion can now be resolved on a component level with relative (small) flexible deformations described by a limited set of deformation modes. However, this reduced computational load on a component level, leads to a relative importance in the cost related to the contact conditions.

In order to obtain an effective framework for impact simulation, we propose a combination of the flexible natural coordinate formulation (FNCF) [3] with the classical pinball algorithm [2] for the contact description. The benefits of this approach are twofold. The FNCF approach allows a linear description of the absolute nodal coordinates as a function of the generalized multibody coordinates, which can be leveraged in the contact detection. The pinball algorithm is also very fast to evaluate if the center nodes are known and can be easily vectorized. This framework leads to an efficient approach which is validated numerically on an impact-drill example.

### 2 Flexible natural coordinate formulation with pinball contact

The flexible natural coordinate formulation employed in this work, features are redundant kinematic description where a set of local  $\mathbf{V}_l \in \mathbb{R}^{n \times m}$  and global  $\mathbf{V}_g \in \mathbb{R}^{n \times 9m}$  modes are present [3]. This allows to express the deformations with respect to the body-attached reference frame as:

$$\mathbf{u} = \mathbf{V}_l \mathbf{q}_l, \quad (1)$$

with  $\mathbf{q}_l \in \mathbb{R}^m$  the deformation participation factors. It also allows to express the absolute nodal coordinates as:

$$\mathbf{x} = \mathbf{V}_l \mathbf{q}_l + \mathbf{V}_r \mathbf{q}_r + \mathbf{V}_g \mathbf{q}_g \quad (2)$$

with  $\mathbf{q}_g \in \mathbb{R}^m$  the global participation factors,  $\mathbf{V}_l$  the translational modes with their amplitudes  $\mathbf{q}_l$ , and  $\mathbf{V}_r$  the rotational modes corresponding to the contributions in the rotation matrix  $\mathbf{q}_r$ . To ensure consistency in the rotation and between the deformations in the local and global frame, a set of (quadratic) constraint equations is added in the description  $\mathbf{c}(\mathbf{c}) = 0$ . This leads to a set of equations of motion of the form:

$$\mathbf{M}\ddot{\mathbf{q}} + \mathbf{K}\mathbf{q} - \frac{\partial \mathbf{c}^T}{\partial \mathbf{q}} \lambda = \mathbf{f}^{contact}(\mathbf{q}) \quad (3)$$

$$\mathbf{c}(\mathbf{q}) = 0 \quad (4)$$

The contact forces are expressed through the pinball algorithm [2]. In this approach, a sphere is hosted by a potential contact node and the contact forces are obtained through a penalty formulation. As the absolute nodal coordinates are readily obtained through the linear equation Eq. (2), this can be evaluated very efficiently.

### 3 Numerical validation

The numerical validation we consider is the *chuck* of an impact-drill. For the common operation, this component is repeatedly impacted by a *ram*. The model considered is shown in Fig. 1. The chuck is represented by a solid mesh with 43000 elements and 83000 nodes. For the ram, a single spherical body is employed. On the chuck body, 450 nodes host a pinball for the contact simulation, whereas only a single pinball is present for the ram. The flexible multibody model is constructed with a modal basis consisting of fifty free-free modes for the chuck body.

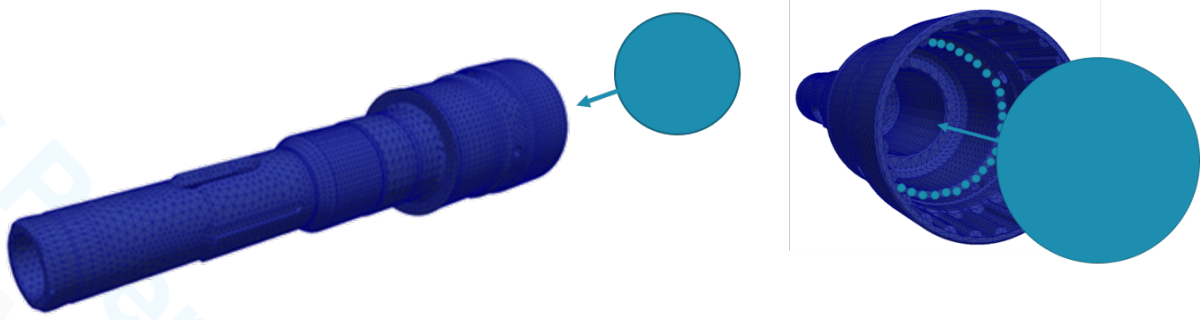


Figure 1: Chuck mesh with impacting ball

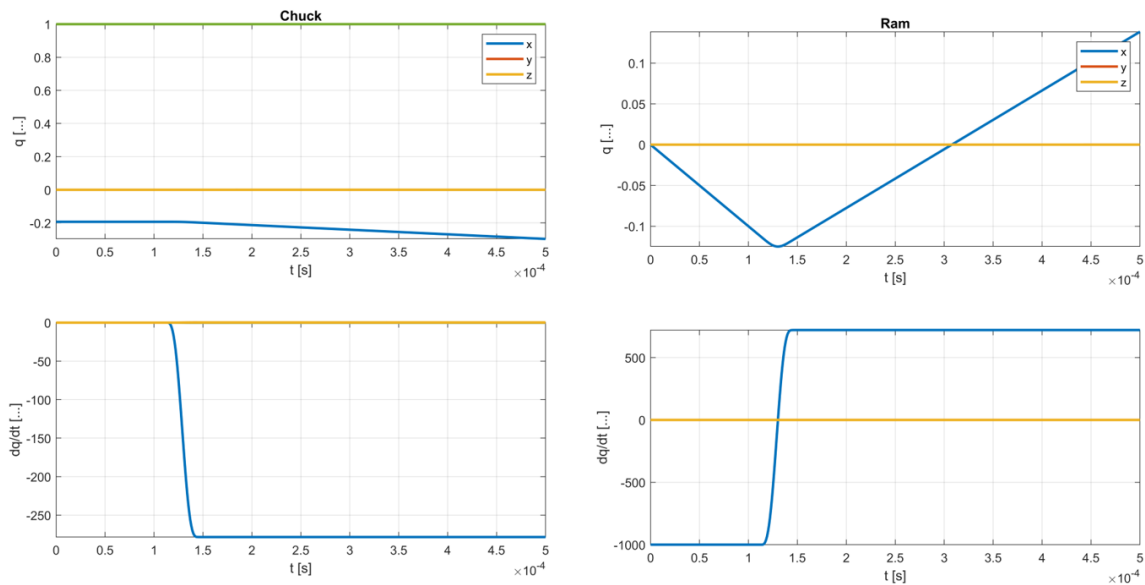


Figure 2: Response of chuck and ram, reference frame motion, during impact simulation (units omitted for confidentiality).

The simulation is performed and the resulting response of the overall translation for the chuck and the ram are shown in Fig. ?? . Moreover, the stress distribution and history are retrieved and correspond closely to those obtained from Abaqus simulations. The presented impact simulation using the proposed framework in Matlab takes around two minutes on a regular laptop, compared to several hours for the equivalent Abaqus simulation.

## Acknowledgments

The Internal Funds KU Leuven are gratefully acknowledged for their support. The Flanders Innovation & Entrepreneurship Agency, within the MODEMA project, is gratefully acknowledged for its support.

## References

- [1] R.J. Yang, N. Wang, C.H. Tho, J.P. Bobineau, B.P. Wang. Metamodeling Development for Vehicle Frontal Impact Simulation. *Journal of Mechanical Design*, 127 (5): 1014-1020, 2005
- [2] T. Belytschko, M.O. Neal. Contact-impact by the pinball algorithm with penalty and Lagrangian methods, *International Journal for Numerical Methods in Engineering*, 31:547-572, 1991
- [3] M. Vermaut, F. Naets, W. Desmet. A Flexible Natural Coordinates Formulation (FNCF) for the efficient simulation of small-deformation multibody systems. *International Journal for Numerical Methods in Engineering*, 115: 1353-370, 2018

# Long-term Rolling Motions of a Basketball on the Rim

Mate Antali<sup>1</sup>, Vince Havas<sup>1</sup>, Gabor Stepan<sup>1</sup>, S. John Hogan<sup>2</sup>

<sup>1</sup> Department of Applied Mechanics  
Budapest University of Technology and Economics  
Muegyetem rkp. 3., 1111, Budapest, Hungary  
antali@mm.bme.hu

<sup>2</sup> Department of Engineering Mathematics  
University of Bristol  
Mercant Venturers Bld., Woodland Rd, Bristol BS8 1UB, UK  
s.j.hogan@bristol.ac.uk

## EXTENDED ABSTRACT

### 1 Introduction

At a basketball match, it sometimes occur that the ball rolling around the rim for a very long time before falling inside or outside the rim. We want to understand this phenomenon by analysing the nonlinear dynamics of the ball on the rim. In the reduced phase space of the system, we can find a two-parametric family of equilibrium points (steady motions) which was first found by Liu et al [1] and the properties and role of these solutions were explored in details by the authors [2]. In the present analysis, we focus on the symmetries and the conserved quantities of the system to explore the behaviour of the ball around the steady motions, and determine the realizable long-term rolling solutions observed in practice.

### 2 Mechanical model

Let us model the ball and the rim by rigid bodies: The radius of the ball is  $r$ , its mass is  $m$ , and its mass moment of inertia  $jmr^2$  where  $j \approx 2/3$  is the dimensionless mass moment of inertia. The rim is modelled by a fixed rigid torus with a major radius  $R$  and the minor radius  $a$ , and we use a short-hand notation  $\rho = r + a$  (see Fig. 1).

By assuming pure rolling of the ball on the rim, the velocity state of the ball can be described by the components  $\omega_1$ ,  $\omega_2$  and  $\omega_3$  of the angular velocity vector, which are represented in a rotating coordinate system at the contact point  $C$  (see Fig. 2). The only external force on the ball comes from the gravity  $g$ , and we neglect all dissipation effects.

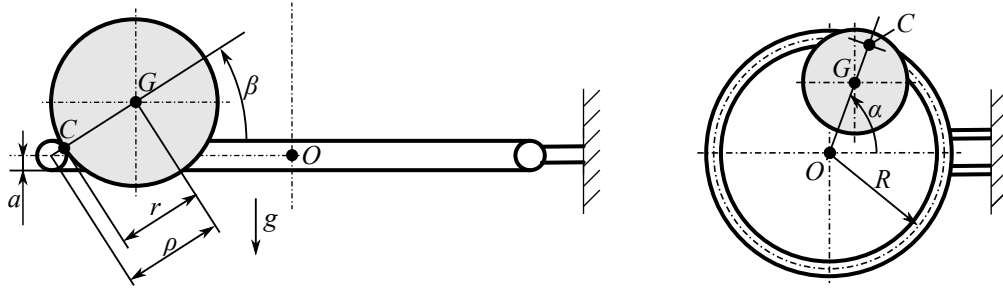


Figure 1: Sketch of the mechanical model. Left panel: side view of the ball on the rim. Right panel: top view of the ball on the rim. The position of the ball is determined by the angles  $\alpha$  and  $\beta$ . The geometric centre of the bodies are denoted  $G$  and  $O$ , and the contact point is denoted by  $C$ .

### 3 Equations of motion

By calculating the Newton-Euler equations of the ball, we get that the dynamics of the rolling basketball can be described in the reduced state space  $\mathbf{x} = (\beta, \omega_1, \omega_2, \omega_3)$ , and the evolution of these variables are given by the system

$$\dot{\beta} = \frac{r}{\rho} \omega_1, \quad (1)$$

$$\dot{\omega}_1 = \frac{(1+j)r\omega_3^2 \sin \beta - jr\omega_2\omega_3 \cos \beta}{(1+j)(R-\rho \cos \beta)} - \frac{g \cos \beta}{r(1+j)}, \quad (2)$$

$$\dot{\omega}_2 = \frac{rR\omega_1\omega_3}{\rho(R-\rho \cos \beta)}, \quad (3)$$

$$\dot{\omega}_3 = -\frac{r\omega_1\omega_3 \sin \beta}{R-\rho \cos \beta} - \frac{jr\omega_1\omega_2}{\rho(1+j)} \quad (4)$$



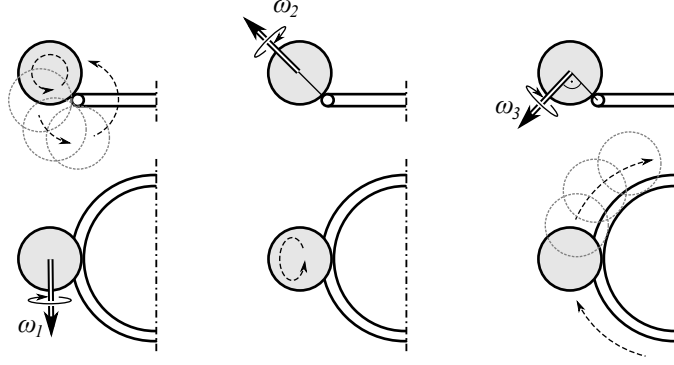


Figure 2: Description of the velocity state of the ball by angular velocity components. Left panel:  $\omega_1$  denotes the *transversal* angular velocity, which is coupled to the motion of the centre of the ball around the minor circle of the rim. Middle panel:  $\omega_2$  denoted the *orthogonal* angular velocity where the centre of the ball rests in place. Right panel:

of four nonlinear differential equations. This state space does not contain the angle  $\alpha$  and the orientation of the ball, which so-called *cyclic* quantities do not affect the dynamics of the other variables. Note, that the system (1)–(4) does not depend the mass  $m$  of the ball either.

#### 4 Steady motions

It can be checked that the system (1)–(4) possesses non-trivial equilibria in the form  $\mathbf{x} \equiv \mathbf{x}_0 = (\beta_0, 0, \omega_{20}, \omega_{30})$ , where the components satisfy

$$(1+j)r^2\omega_3^2\sin\beta - jr^2\omega_2\omega_3\cos\beta - g\cos\beta(R-\rho\cos\beta) = 0. \quad (5)$$

Thus, (5) determines a two-parametric family of equilibria, which form a two-surface in the four-dimensional state space. Each equilibrium point on this surface represents a *steady motion*, where the ball is rolling around the rim at a constant angle  $\beta$  while the angular velocity components in Fig. 2 remain unchanged. Linear stability analysis shows multiple non-hyperbolicity of these equilibria, and thus, a nonlinear global analysis of the system (1)–(4) is needed to explore the behaviour of the ball around these steady motions.

#### 5 Symmetries and conserved quantities

The system is conservative, and thus, the total energy is conserved. In addition, the system (1)–(4) has a symmetry under the reflection to the set  $\omega_2 = \omega_3 = 0$ , and it has also a time-reverse symmetry under the reflection to the hyperplane  $\omega_1 = 0$ . Moreover, by changing the independent variable from time  $t$  to  $\beta$ , (1)–(4) can be reduced to a system

$$\frac{d\omega_2}{d\beta} = \frac{R\omega_3}{R-\rho\cos\beta}, \quad \frac{d\omega_3}{d\beta} = -\frac{\rho\omega_3\sin\beta}{R-\rho\cos\beta} - \frac{j\omega_2}{1+j}. \quad (6)$$

By careful analysis of these properties and using the results in [3], we can discover important properties about the system. It can be shown that in addition to the total energy, there exist two further conserved quantities in the system. Moreover, it can be shown that the stable steady motions are surrounded by a region filled by *periodic solutions*, which mean oscillations in the angular velocity components and the angle  $\beta$ . This gives back the behaviour of the basketball which can be observed in several videos of basketball shots.

#### Acknowledgments

The research leading to these results has been supported by the Eotvos Lorand Research Network in the Premium Postdoctoral Fellowship Programme under the grant number PPD2018-014/2018.

#### References

- [1] C. Q. Liu, F. Li, R. L. Huston. Dynamics of a basketball rolling around the rim. *Journal of Dynamic Systems Measurement and Control*, 128:359–364, 2006.
- [2] M. Antali, V. Havas, S. J. Hogan, G. Stepan. Nonlinear dynamics of a basketball rolling around the rim. *Nonlinear Dynamics*, accepted, in publication.
- [3] O. M. O'Reilly. The dynamics of rolling disks and sliding disks. *Nonlinear Dynamics*, 10:287–305, 1996.

# Numerical Analysis of Contact-Impact Problems using Finite Element Method

Dániel Serfőző<sup>1</sup>, Balázs Pere<sup>2</sup>

<sup>1</sup> Department of Applied Mechanics  
Széchenyi István University  
Egyetem square 1., 9026 Győr, Hungary  
serfozo.daniel@ga.sze.hu

<sup>2</sup> Department of Applied Mechanics  
Széchenyi István University  
Egyetem square 1., 9026 Győr, Hungary  
pere.balazs@ga.sze.hu

## EXTENDED ABSTRACT

### 1 Introduction

There is a great interest towards the examination of dynamic contact and impact problems [1] due to their widespread applicability. The proper solution of these kinds of problems can be especially momentous in such fields like cogwheel drives and cutting metalwork. Contact and impact problems are hard to handle as a substantial nonlinearity occurs in the displacement field. The main problem is that due to the spatial discretization a spurious high frequency oscillation emerges in the resulting functions, which can easily cause divergence in the contact algorithm. Thus, in our study we focused on the best possible elimination of these oscillations by which the choice of the proper numerical method has a great importance.

### 2 Results and Discussion

When assessing the developed method, a simple one-dimensional problem is reviewed (see Fig. 1) which contains an elastic rod moving towards a rigid wall with a constant  $v_0$  velocity. In the literature, this 1D example is regarded as a standard test problem in which the exact solution have not been accurately reproduced yet using numerical methods. It emerges in many recent publications such as in the paper by Kim [2] showing that it is still actual to deal with this problem.

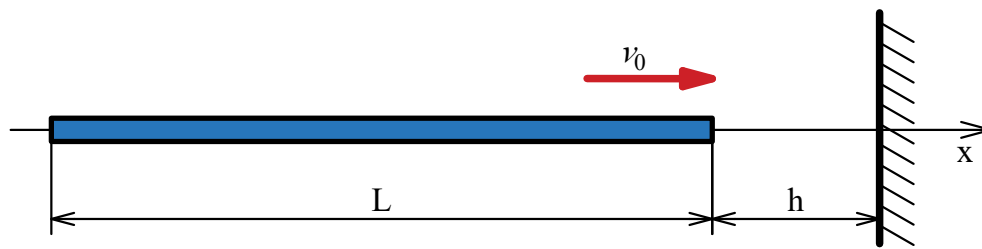


Figure 1: The mechanical model of the examined 1D problem

After the spatial discretization using the finite element method [3], the equation of motion can be written in the form of

$$\mathbf{M}\ddot{\mathbf{u}} + \mathbf{C}\dot{\mathbf{u}} + \mathbf{K}\mathbf{u} + \mathbf{G}^T\lambda = \mathbf{f} \quad (1)$$

$$\mathbf{G}(\mathbf{X} + \mathbf{u}) \geq \mathbf{0} \quad (2)$$

where  $\mathbf{M}$  is the mass matrix,  $\mathbf{C}$  is the damping matrix,  $\mathbf{K}$  is the stiffness matrix,  $\mathbf{G}$  is the contact constraint matrix,  $\mathbf{X}$  is the vector of nodal coordinates,  $\mathbf{f}$  is the load vector,  $\mathbf{u}$  is the nodal displacement vector and  $\lambda$  denotes the contact pressure. In the solution of the contact problem, the Lagrange multiplier technique was applied using the method published by Carpenter et al. [4]. The time integration of equations (1) and (2) was performed applying our newly developed forward increment method. In order to obtain the effectiveness of the proposed method, other solutions are also considered using well-known time integration methods like the backward Euler method, the Newmark method [5] and the HHT- $\alpha$  method [6] (see Fig. 2). In opposition to these schemes, the so called *bulk viscosity* method [7,8] provides a fundamentally different approach as a viscous damping (non-zero  $\mathbf{C}$ ) is combined with the central difference method. This special approach has a great potential as it is much faster than the reviewed time integration methods and can still assure the desired amount of damping. In our research we found this approach worthwhile to deal with, aiming to improve its effectiveness. Further details will be provided in the presentation.

### 3 Concluding Remarks

Compared to other widely used methods, our novel approach yields a significantly better solution for the examined model. The considered 1D contact problem is very simplistic, but the phenomena observed here have similar characteristics in higher dimension cases. Thereby, the proposed method must be applicable for more complex problems.

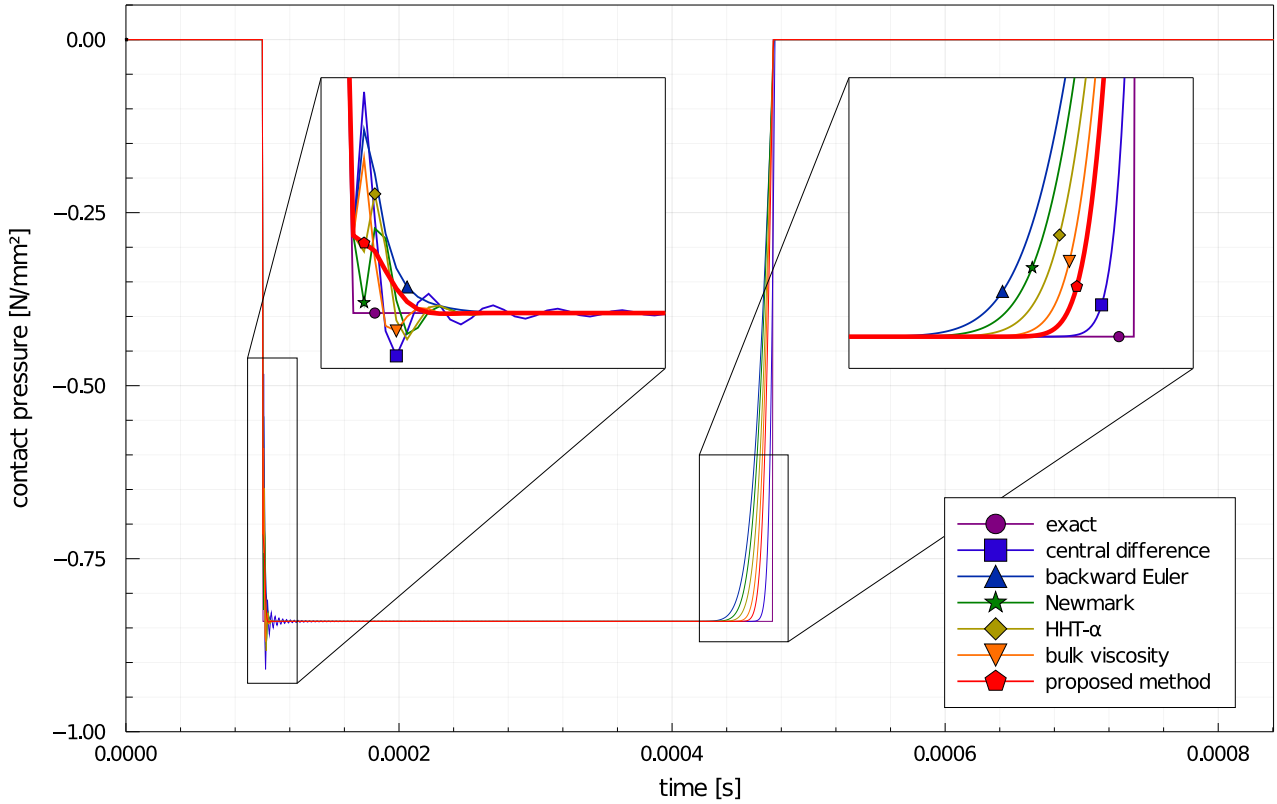


Figure 2: Time evolution of contact pressure

## Acknowledgments

The presentation and the research was funded by the project "HU-MATHS-IN – Intensification of the activities of the Hungarian Service Network of Mathematics for Industry and Innovations" (grant number EFOP-3.6.2.-16-2017-00015).

## References

- [1] P. Wriggers. Computational Mechanics. John Wiley Sons Ltd, 2002.
- [2] W. Kim. A new family of two-stage explicit time integration methods with dissipation control capability for structural dynamics. *Engineering Structures*, 195: 358-372, 2019.
- [3] K. J. Bathe. Finite element procedures. Klaus-Jurgen Bathe, 2006.
- [4] N. J. Carpenter; R. L. Taylor ; M. G. Katona. Lagrange constraints for transient finite element surface contact. *International journal for numerical methods in engineering*, 32.1: 103-128, 1991.
- [5] N. M. Newmark. A method of computation for structural dynamics. *Journal of the engineering mechanics division*, 85.3: 67-94, 1959.
- [6] H. M. Hilber. ; T. JR. Hughes ; R. L. Taylor. Improved numerical dissipation for time integration algorithms in structural dynamics. *Earthquake Engineering & Structural Dynamics*, 5.3: 283-292, 1977.
- [7] J. VonNeumann ; R. D. Richtmyer. A method for the numerical calculation of hydrodynamic shocks. *Journal of applied physics*, 21(3), 232-237, 1950.
- [8] L. Maheo ; V. Grolleau ; G. Rio. Numerical damping of spurious oscillations: a comparison between the bulk viscosity method and the explicit dissipative Tchamwa–Wielgosz scheme. *Computational Mechanics*, 51(1), 109-128, 2013.

# Port Crane Guidance Dynamics Analysed Via the Multibody Approach

Raül Acosta Suñé, Paul Fisette, Nicolas Docquier

Institute of Mechanics, Materials and Civil Engineering  
Université catholique de Louvain  
Place du Levant 2, 1348 Louvain-la-Neuve, Belgium  
[raul.acostasune, paul.fisette, nicolas.docquier]@uclouvain.be

## EXTENDED ABSTRACT

### 1 Context

During the last decade, major transformations in terms of cadence are taking place in ports, therefore the cranes that continually load and unload containers are also being impacted. These developments give rise to problems of a new nature: the behaviour of cranes was considered until now quasi-static or cyclical, but it is becoming progressively dynamic. These associated effects are causing significant damage to the cranes, the track and the foundations. This adversely affects the integrity of the rail guidance system leading to reduced operating performance, system downtime and costly repairs.

The goal of this research is to understand the dynamic effects of the parameters of a crane on track through a research project involving industrial partners. Dynamic effects present new challenges for crane manufacturers, track specialists and operators regarding the increasing loads and operational speeds, the goal is to model the whole system (crane, track, foundation) with an ad hoc multibody simulation, in order to capture the associated dynamic phenomena as precisely as possible, especially at the track level.

### 2 Model and methods

A complete crane model has been designed using the ROBOTRAN [1] symbolic multibody software. The outcome of this modelling work required gathering a series of data related to the crane's gantry, the rolling elements and the track, in order to feed a global multibody model with the following specific ingredients:

- A wheel/rail contact model definition taking high creepage and high forces into account. It is included in the form of vertical kinematic constraints (perfect wheels on a perfect rail) and tangent frictional forces based on the Kalker non-linear model [2]. To set the idea, the rail gauge, unlike to railway system, is 27,90 m. Moreover, the crane rail system must hold up to 40 tons per wheel.
- A rail alignment irregularities model which inevitably impact the crane's running quality. They are defined as sinusoids with amplitudes and wavelengths adapted to the norm ISO 12488-1.
- The modelling of side rollers (with vertical axes, Figure 1) in intermittent contact with the rail. It is treated, in this first model, as an unilateral spring/dumped system, whose lateral deflection mainly comes from that those of the rail (flexion and torsion) [3].
- Identification of the stiffnesses of the gantry (deflections in the 3 directions and eigen modes). The aim is to calibrate the multibody model on the finite element model (FEM) (continuous flexibilities) provided by the crane manufacturer.
- Motor control definition. Each wheel (see Figure 1) is controlled individually to correct the skewing phenomenon that represents a less than optimal behaviour in which wheel/rail creepages are high and induced undesired wear.

To validate the model, experiments are being carried out in the port via a strategic location of accelerometers and force sensors that are being installed on a test crane in Antwerp, Belgium (Europe). Various crane conditions are investigated: static configurations, lateral and longitudinal trajectories, etc.

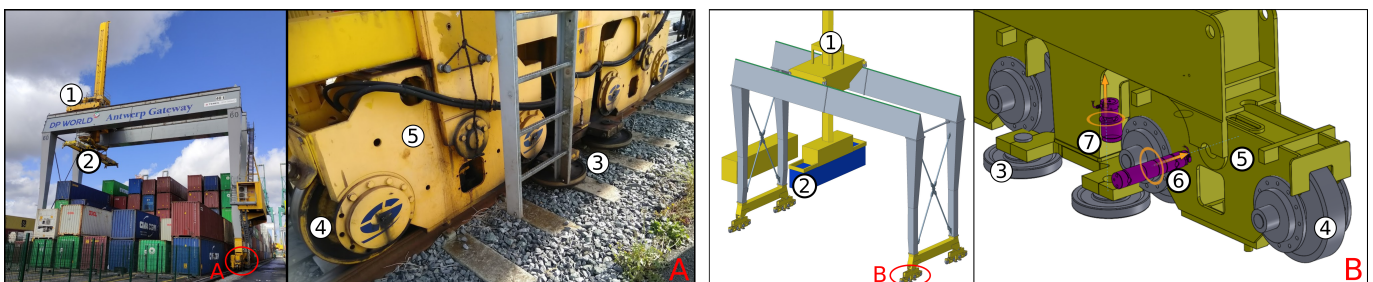


Figure 1: Real ASC model on the left and virtual 3D model on the right. Parts: trolley (1), container placement (2), side rollers (3), wheels (4), bogie (5), vertical force sensor (6) and lateral force sensor (7).

### 3 Results

Preliminary results from multibody simulations are already able to highlight the impact of several parameters on the crane dynamics. For instance, regarding vertical forces, force sensors are currently being installed in the axles of the bogies (Figure 1, the one on the right). The results on the left side of Figure 2 show that the trolley motion (Figure 1) has a significant effect on these vertical forces for a realistic trajectory of the crane, with a dynamic amplification that largely increases with the default and that is much higher than that currently recommended in the field.

In the port, to take track lateral irregularities into account, simulations with different roller-track plays (“gaps”) have been carried out. Significant differences (Figure 2, right) in the roller/rail lateral forces are revealed at the level of the rollers for different play values.

Other simulations show that the addition of irregularities in the rails affects the power dissipated at the level of the side rollers. This fact could be one of the main factors that explain the origin of the wear detected, thus future studies will delve into the analysis of these defects.

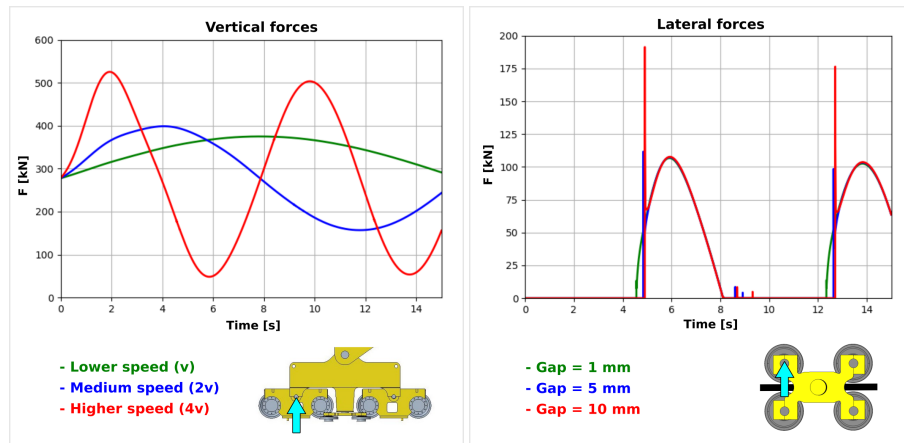


Figure 2: Resulting forces for a crane simulation in which the trolley (Figure 1), that manipulates a load of 40 t (container and holding elements included), moves laterally with a realistic sinusoidal speed. Its value is maximum in the middle of its trajectory and 0 at the ends. Left: the forces produced in the bogies axles are maximum when the trolley is on the same side and these peaks highly increase with the velocity. Right: example of lateral forces on side rollers for different gap roller-track values.

### 4 Conclusion and perspectives

Crane dynamics impacts operation and should be taken into account in the crane operation and track engineering, especially regarding the guidance issues. The current industrial problems which are generated by the rates highlight the need for a better comprehension of their behaviour. At this point, the multibody simulations of the model have shown to be able to study different realistic scenarios and to measure quantities forces, displacements or contact wear at its different levels (track, wheels, rollers, bogies). This model is being validated on the database obtained from field measurements and it is envisaged to be shown during the conference.

In terms of perspective, the multibody model of the crane will be coupled with the ballasted track conceived with the Discrete Element Method, as we previously did in a scientific paper [4], to finally have a complete model of the crane.

### Acknowledgments

The CRAMIC program ([www.gantrex.com/en/r-and-d](http://www.gantrex.com/en/r-and-d)) is a collaboration between Gantrex, SENSY, UCLouvain and BBRI supported by Wallonia and Mecatech Cluster. Each of the partners plays a key role throughout the program according to their specific areas of expertise, but nothing we have undertaken would have been possible without the help and active support of Konecranes (crane OEM) and DP World (Terminal operator) as external partners.

### References

- [1] N. Docquier, A. Poncelet, P. Fisette. ROBOTRAN: a powerful symbolic generator of multibody models. *Mechanical Sciences*, 4:199–219, 2013.
- [2] J.J. Kalker, *Three-Dimensional Elastic Bodies in Rolling contact*, 1990, Dordrecht, The Netherlands: Kluwer Academic Publishers.
- [3] Chen, Z., Andrawes, B. A mechanistic model of lateral rail head deflection based on fastening system parameters. *Proceedings of the Institution of Mechanical Engineers, Part F: Journal of Rail and Rapid Transit*, 231(9), 999–1014, 2016
- [4] N. Docquier, O. Lantsoght, F. Dubois, O. Brûls. Modelling and simulation of coupled multibody systems and granular media using the non-smooth contact dynamics approach. *Multibody System Dynamics*. 49, 181-202. 10.1007/s11044-019-09721-0, 2020.

# A Nonsmooth Dynamics Perspective on State Observer Design for Mechanical Systems with Unilateral Constraints

Pascal V. Preiswerk, Remco I. Leine

Institute for Nonlinear Mechanics  
University of Stuttgart  
Pfaffenwaldring 9, 70569 Stuttgart, Germany  
[preiswerk, leine]@inm.uni-stuttgart.de

## EXTENDED ABSTRACT

State observer designs for mechanical systems with impulsive motion, caused by unilateral constraints, typically assume that exact knowledge of the impact time instants is available through measurements. Only few attempts have been made to design a state observer that does not require contact time information. Furthermore, these types of observers use the measurement of the contact distance. We investigate the observer problem for linear mechanical systems with a single unilateral constraint, for which neither the impact time instant nor the contact distance is explicitly measured. A discretization based on a numerical scheme proposed by Paoli and Schatzman leads to a discrete linear complementarity system. From there, a dead-beat observer in the form of a linear complementarity problem can be deduced. In addition, a passivity-based, Luenberger-type state observer can be applied.

## 1 Introduction

In this work we investigate the state observer problem for mechanical systems with impulsive motion, i.e. systems with state jumps caused by unilateral constraints. As an example system, consider the oscillator depicted in Figure 1, consisting of two masses, connected by linear springs and viscous dampers. The oscillator is excited by an external force and the movement of the second mass is restricted by a motion limiting stop. An important aspect for the state observer design for such systems is whether or not the time instants where the state jumps occur are known or not. Most proposed observers assume that these jump or impact time instants can directly be extracted from measurements, for example by measuring all relevant positions in a system where the impact times are position dependent [1] or by directly measuring contact [2]. This allows for the design of a state observer that exhibits state jumps that occur at the same time instants as the observed system. Under a maximal monotone impact law, it is then possible to construct a Lyapunov function for the error dynamics (i.e. the time evolution of the difference between the estimated state and the actual state) which does not increase over impacts.

Only few attempts have been made to design state observers in the case of unknown impact time instants, such that the corresponding state jumps of the observed system and the state observer do not coincide. One of the main difficulties in such cases is the peaking phenomenon: even if the observer state nearly matches the real state, a slight mismatch in the impact time instants can lead to a large velocity error caused by velocity jumps. This makes it difficult to find a Lyapunov function to show the asymptotic stability of the error dynamics. One approach for such systems is to find a state transformation that transforms the original system into a new system without state jumps, for which conventional state observer techniques can be applied [3], [4]. However, such a transformation does not always exist and is in general difficult to find.

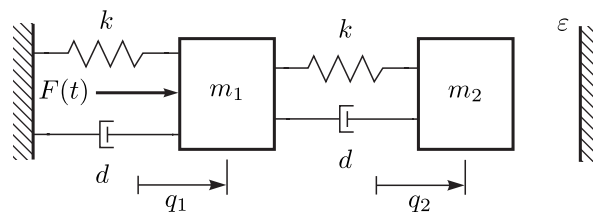


Figure 1: An example system with a single unilateral constraint.

## 2 Discrete state observer problem

Starting from the description of the dynamics in form of a measure differential inclusion, we make use of a time discretization which is based on the numerical scheme by Paoli and Schatzman [5]. In this scheme, the contact force laws are formulated on position level. Therefore, it is not required to keep track of an index set indicating whether or not a contact is open or closed, as in the case of contact force laws on velocity level. The resulting discretized dynamics has the following form of a linear



complementarity system (LCS)

$$\begin{aligned} \mathbf{x}_{k+1} &= \mathbf{A}\mathbf{x}_k + \mathbf{B}w_k + \mathbf{E}\mathbf{v}_k, \\ z_k &= \mathbf{C}\mathbf{x}_k + \mathbf{D}w_k + \mathbf{F}\mathbf{v}_k, \\ 0 &\leq z_k \perp w_k \geq 0, \\ \mathbf{y}_k &= \mathbf{G}\mathbf{x}_k, \end{aligned} \tag{1}$$

with the discrete state  $\mathbf{x}_k$  containing the generalized positions and velocities, the external input  $\mathbf{v}_k$  which is assumed to be known,  $w_k$  containing the contact force (or percussion), the contact distance  $z_k$  (here the gap between the colliding body and the limiting stop) as well as the measured output  $\mathbf{y}_k$ . The system matrices  $\mathbf{A}$  to  $\mathbf{F}$  in (1) are composed of the mass-, stiffness- and damping-matrix of the underlying linear mechanical system, as well as the generalized force directions and the step size  $\Delta t$  that has been used in the discretization process. The output matrix  $\mathbf{G}$  is assumed to be such that neither the contact distance nor the impact time instants can directly be extracted from the measurements. For the example oscillator in Figure 1 this could mean that we only measure the position  $q_1$  of the first mass.

For continuous linear complementarity systems, a passivity-based, Luenberger-type state observer has been proposed [6], which does not apply in the presence of impacts. However, the formulation (1) allows us to investigate to what extent this approach can be applied even if impacts occur. Analyzing the example system depicted in Figure 1 shows, that this Luenberger-type state observer is not applicable in its standard form, if only the position of the non-impacting mass is measured. However, an extended version of the observer that includes past and future measurements is applicable in such cases.

Furthermore, propagating equations (1) from an initial state  $\mathbf{x}_0$  and collecting all outputs, all constraint distances, all constraint forces and all inputs in

$$\mathbf{Y}_k = \begin{pmatrix} \mathbf{y}_0 \\ \mathbf{y}_1 \\ \vdots \\ \mathbf{y}_k \end{pmatrix}, \mathbf{Z}_k = \begin{pmatrix} z_0 \\ z_1 \\ \vdots \\ z_k \end{pmatrix}, \mathbf{W}_k = \begin{pmatrix} w_0 \\ w_1 \\ \vdots \\ w_k \end{pmatrix} \text{ and } \mathbf{V}_k = \begin{pmatrix} \mathbf{v}_0 \\ \mathbf{v}_1 \\ \vdots \\ \mathbf{v}_k \end{pmatrix}, \tag{2}$$

leads to a set of linear equations together with complementarity conditions of the form

$$\begin{aligned} \mathbf{Y}_k &= \mathbf{O}_k \mathbf{x}_0 + \mathbf{M}_k \mathbf{W}_k + \mathbf{N}_k \mathbf{V}_k, \\ \mathbf{Z}_k &= \bar{\mathbf{O}}_k \mathbf{x}_0 + \bar{\mathbf{M}}_k \mathbf{W}_k + \bar{\mathbf{N}}_k \mathbf{V}_k, \\ 0 &\leq \mathbf{Z}_k \perp \mathbf{W}_k \geq 0, \end{aligned} \tag{3}$$

which is known as a mixed linear complementarity problem (MLCP). If the number of measurements is equal to the number of states  $n$  (i.e. if  $k$  is equal to  $n-1$ ), then the matrix  $\mathbf{O} := \mathbf{O}_{n-1} = (\mathbf{G}; \mathbf{G}\mathbf{A}; \dots; \mathbf{G}\mathbf{A}^{n-1})$  is equal to the well known observability matrix of the non-impulsive motion. Therefore, assuming that the non-impulsive motion is observable,  $\mathbf{O}$  is invertible and the MLCP (3) can be written as a linear complementarity problem (LCP). The solution of this LCP for given measurements can serve as a dead-beat observer, i.e. a state observer that yields an exact state estimation in finite time (in this case after  $n$  measurements). In addition, the uniqueness of the LCP solution serves as a sufficient observability condition of the discretized system.

### 3 Conclusion

In this work, a numerical scheme was used to approximate the dynamics of mechanical systems with a single unilateral constraint. The formulation of the contact force law on position level leads to a discrete linear complementarity system. This allows for a simple dead-beat observer in the form of a linear complementarity problem. Furthermore, it allows the application of a passivity-based, Luenberger-type state observer, even in the case of unknown impact time instants.

### References

- [1] A. Tanwani, B. Brogliato, C. Prieur. Observer design for unilaterally constrained Lagrangian systems: A passivity-based approach. *IEEE Transactions on Automatic Control*, 61(9): 2386-2401, 2016.
- [2] M. Baumann, R.I. Leine. A synchronization-based state observer for impact oscillators using only collision time information. *Int. J. of Robust and Nonlinear Control*, 26(12): 2542-2563, 2016.
- [3] L. Menini, A. Tornambè. State immersion observers for mechanical systems with impacts. *55th IEEE Conference on Decision and Control (CDC)*, pp. 7117-7122, 2016.
- [4] J. Kim, H. Cho, A. Shamusarov, H. Shim., J.H. Seo. State estimation strategy without jump detection for hybrid systems using gluing function. *53rd IEEE Conference on Decision and Control*, pp. 139-144, 2014.
- [5] L. Paoli, M. Schatzman. A numerical scheme for impact problems I: the one-dimensional case. *SIAM J. on Num. Analysis*, 40(2): 702-733, 2002.
- [6] W.P.M.H. Heemels, M.K. Camlibel, J.M. Schumacher and B. Brogliato. Observer-based control of linear complementarity systems. *Int. J. of Robust and Nonlinear Control* 2011, 21(10): 1193-1218, 2011.

# Non-smooth numerical solution for Coulomb friction and rolling resistance

Eliaana Sánchez<sup>1</sup>, Alejandro Cosimo<sup>1,2</sup>, Alberto Cardona<sup>1</sup>, Olivier Brûls<sup>2</sup>, Federico J. Cavalieri<sup>1</sup>

<sup>2</sup> Centro de Investigación de Métodos Computacionales (CIMEC)  
Universidad Nacional del Litoral-CONICET  
Santa Fe, Argentina  
[esanchez, acardona, fcavalieri]@cimec.unl.edu.ar

<sup>1</sup>Department of Aerospace and Mechanical Engineering  
University of Liège  
Liège, Belgium  
[acosimo, o.bruls]@uliege.be

## EXTENDED ABSTRACT

### 1 Introduction

Friction and inertia loads play a relevant role in the operative performance of a mechanical system. For instance, in ball bearings, a correct formulation that properly describes the rolling dynamic motion requires to understand the influence of contact and frictional forces in order to accurately capture the slip, the rotation motion and the instant where the slip motion goes to pure rolling or viceversa. Friction effects in sphere bodies can be classified in three parts: i) *sliding friction*, where a set-valued force law with two degrees of freedom generates a resistive force to slide; ii) *rolling friction*, where two traslational degrees of freedom are required in the formulations; it is a set-valued force law that generates a resistive moment to rolling and iii) *drilling friction* or Coulomb-Contensou friction is a set-valued force law that generates a resistive moment to the normal relative spin of the bodies, thus only one rotational degree of freedom is required.

This work presents a new formulation to deal with the frictional impact of a spherical rigid body subject to friction in the field of non-smooth dynamics. In order to consider the mechanical and the geometrical properties of a sphere, a rigid body formulation with translational and rotational degrees of freedom is implemented which allows a complete general movement of the body. A node of the sphere situated in its center is linked with other node to a planar surface or either to a body considered flexible or rigid. The regularization of the variational frictional contact problem is performed with a mixed approach based on an augmented Lagrangian technique. The Coulomb friction's law leads to an implicit formulation that can be solved at every time step using a Newton semi-smooth algorithm [1]. The equations of motion are integrated with the recent decoupled version of the non-smooth generalized- $\alpha$  time integration scheme [2], where the constraints are imposed both at velocity and positions levels preventing any non-physical penetration. Additionally, the numerical results do not depend on the definition of any user-defined penalty parameter affecting the normal or tangential component of forces.

The nonlinear finite element method is adopted in this work to model the sphere element according to the methodology proposed by G radin and Cardona [4]. For the sphere element presented here, the generalized coordinate and velocity vectors are given by  $\mathbf{q} = [\mathbf{x}_A^T \ \boldsymbol{\Psi}_A^T]^T$  and  $\dot{\mathbf{q}} = [\dot{\mathbf{x}}_A^T \ \dot{\boldsymbol{\Psi}}_A^T]^T$ , respectively; where  $\mathbf{x}_A$  is the position of node A referred to the inertial frame  $\mathbf{X}$ ,  $\mathbf{Y}$  and  $\mathbf{Z}$  and  $\boldsymbol{\Psi}_A$  is the rotational vector of node A at the current configuration and where the dots denote time differentiation, see Fig. 1. Then, the general solution to the unilateral friction contact problem at position level is given by

$$(\mathbf{U}, \boldsymbol{\nu}) = \operatorname{arginf} [\Pi^{\text{int,ext}}(\mathbf{U}) + \Pi^c(\mathbf{U}, \boldsymbol{\nu})]$$

$$g_N \geq 0, \quad v_N \geq 0, \quad g_N v_N = 0; \quad \|\mathbf{g}_T\| \geq 0, \quad \|\boldsymbol{\nu}_T\| \leq \mu v_N, \quad \|\mathbf{g}_T\| (\|\boldsymbol{\nu}_T\| - \mu v_N) = 0; \quad \mathbf{g}_T = -\|\mathbf{g}_T\| \frac{\boldsymbol{\nu}_T}{\|\boldsymbol{\nu}_T\|} \quad (1)$$

where  $\mathbf{U}$  is the global displacement,  $\mu$  is the friction coefficient,  $\Pi^c$  is the contact potential and  $\Pi^{\text{int,ext}}$  represents the potential energy of the external and internal loads. Then,  $g_N$  is the normal gap and  $\mathbf{g}_T$  is the tangential relative displacement whereas  $v_N$  and  $\boldsymbol{\nu}_T$  are the normal and the tangential Lagrange multipliers at position level in the normal and tangential directions, respectively. The constrained optimization problem presented in Eq.(1) is reformulated according to the proposal of Alart and Curnier for quasi static problems in order to find the stationary values of an augmented Lagrangian function [1] which at position level is given by

$$\mathcal{L}^p(\mathbf{U}, \boldsymbol{\nu}) = -g_N k v_N + \frac{p}{2} g_N^2 - \frac{1}{2p} \operatorname{dist}^2 [k v_N - p g_N, \mathbf{R}^+] - k \mathbf{g}_T \cdot \boldsymbol{\nu}_T + \frac{p}{2} \|\mathbf{g}_T\|^2 - \frac{1}{2p} \operatorname{dist}^2 [k \boldsymbol{\nu}_T - p \mathbf{g}_T, C_{\xi_N}] \quad (2)$$

where  $p$  is a penalty parameter and  $k$  is a scale factor for the Lagrange multipliers. Both  $p$  and  $k$  are positive scalars which contribute to obtain an improvement of the convergence rate. Then,  $C_{\xi_N}$  is the extended friction Coulomb cone to the half line  $\mathbf{R}^-(\xi_N)$ , see [1]. Similarly, the augmented Lagrangian which regularizes the frictional contact problem at velocity level yields

$$\mathcal{L}^v(\mathbf{W}, \boldsymbol{\Lambda}) = -\dot{g}_N k \Lambda_N + \frac{p}{2} \dot{g}_N^2 - \frac{1}{2p} \operatorname{dist}^2 [k \Lambda_N - p \dot{g}_N, \mathbf{R}^+] - k \dot{\mathbf{g}}_T \cdot \boldsymbol{\Lambda}_T + \frac{p}{2} \|\dot{\mathbf{g}}_T\|^2 - \frac{1}{2p} \operatorname{dist}^2 [k \boldsymbol{\Lambda}_T - p \dot{\mathbf{g}}_T, C_{\sigma_N}] \quad (3)$$

where  $\mathbf{W}$  is the velocity jump and,  $\Lambda_N$  and  $\boldsymbol{\Lambda}_T$  are the Lagrange multipliers that represent the impulsive forces in the normal and in the tangential direction, respectively. Then,  $\dot{g}_{N,n+1}$  and  $\dot{\mathbf{g}}_{T,n+1}$  are the normal and tangential velocities, respectively. The contributions of the element to the discrete equations of motion and to the tangent operators are computed by the first and

second variations of Eqs.(2, 3), respectively. These equations are associated to the sliding friction as presented Cavalieri *et al* [3]. However, a real sphere is deformable and when rotates, an non-symmetric contact pressure distribution occurs. Then, the contact reaction  $v_N$  is displaced a distance  $\rho$  from the center of the mass of the sphere, see Fig.1. It produces an antagonist moment  $M = \rho v_N$  that generates a rolling resistance. This effect is more evident in elasto plastic or visco elastic materials, as for example in rubber composites of vehicle wheels. In a 3D movement, the moment  $M$  can be decomposed according to an orthonormal frame at node  $P$  of the contact plane given by the vectors  $N, T_1$  and  $T_2 \in \mathbb{R}^3$  referred to the inertial frame, see Fig.1. Thus, the moment can be written as  $M = M_N N + M_1 T_1 + M_2 T_2$ . As consequence of the rolling resistance, the displacement has to change the direction when the angular velocity changes sign and has to be zero if there is no rotation velocity. For this reason, the rolling friction model is a highly non-linear model and can be expressed as an inequality constraint. The rolling resistance produced by the moment  $M_T = M_1 T_1 + M_2 T_2$  is represented by the following constraints

$$\|M_T\| \leq \rho v_N \quad \|\omega_T\| (\|M_T\| - \rho v_N) = 0 \quad \omega_T = -\frac{\|\omega_T\| M_T}{\|M_T\|} \quad (4)$$

where  $\omega_T$  is the angular tangential velocity, see Fig.1. Finally, the normal component of the moment produces the *drilling* resistance where the equations can be also expressed as inequality constraints in analogous way as before

$$|M_N| \leq \gamma v_N \quad |\omega_N| (|M_N| - \gamma v_N) = 0 \quad \omega_N = -\frac{|\omega_N| M_N}{|M_N|} \quad (5)$$

where  $\omega_N$  is the angular normal velocity and  $\gamma$  is parameter equivalent to  $\rho$ . Finally, the Eqs.(4,5) have the same structure as the sliding friction model of Eq.(1) and thus they can be solved in a similar manner considering the tangential terms of the augmented Lagrangian given in Eqs.(2,3).

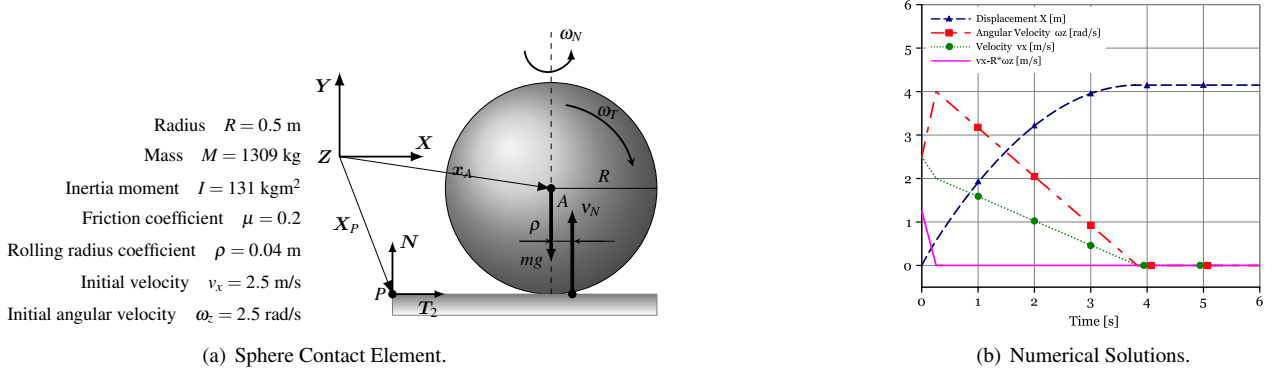


Figure 1: Numerical example of a sphere rolling on a plane.

The method presented in this work is validated from a simple test presented by Acary and Bourrier.[5] where a sphere is rolling on a planar surface. The initial conditions and mass properties are depicted in Fig.1-a. Figure 1-b shows that the sphere at beginning is in sliding process reaching a maximum angular velocity at 0.256 s. This behavior can be confirmed with the curve  $v_x - R\omega_z$  that is different to zero. Then, the velocities  $v_x$  and  $\omega_z$  decrease and the sphere goes in a pure rolling, it is  $v_x - R\omega_z = 0$ , until the movement stops completely as a consequence of the rolling resistance. Other more complex examples will be shown at the congress.

## Acknowledgments

This work has received financial support from Consejo Nacional de Investigaciones Científicas y Técnicas, the Robotix Academy project of the Greater Region, Universidad Tecnológica Nacional PID UTN AMECAFE0008102TC.

## References

- [1] P. Alart and A. Curnier. A mixed formulation for frictional contact problems prone to Newton like solution methods. *Computer Methods in Applied Mechanics and Engineering* 92:353-375, 1991.
- [2] A. Cosimo, G. Javier, F.J. Cavalieri, O. Bröls, A. Cardona. Robust nonsmooth generalized- $\alpha$  scheme for problems with flexible components, bilateral constraints and impacts. *Multibody System Dynamics*, 48(2), pp. 127-149, 2020.
- [3] F.J. Cavalieri, A. Cosimo, E. Sanchez, O. Bröls, A. Cardona. *Simulation of sliding friction of spherical rigid bodies subject to multiple impact collisions*. Mechanisms and Machine Science, Springer, 94, pp. 151-158, 2021.
- [4] G radin, M., Cardona, A.: Flexible Multibody Dynamics. Wiley, Hoboken, 2001.
- [5] V. Acary and F. Bourrier. Coulomb friction with rolling resistance as a cone complementarity problem. *European Journal of Mechanics - A/Solids*, 85:104046, 2021.

# On the Simulation of Freewheels Using the Methods of Non-Smooth Dynamics

Alessandro Tasora<sup>1</sup>, Dario Mangoni<sup>1</sup>, Nicolò Robuschi<sup>2</sup>

<sup>1</sup>Department of Engineering and Architecture  
University of Parma  
V.le delle Scienze, 121/a, Parma, Italy  
[alessandro.tasora, dario.mangoni]@unipr.it

<sup>2</sup>Manufacture d'Horlogerie Audemars Piguet SA,  
Chemin des dolines 7, CH-2400 Le Locle,  
Switzerland  
nicolo.robustchi@audemarspiguet.com

## EXTENDED ABSTRACT

### 1 Introduction

We propose an approach to the simulation of freewheels in the context of non-smooth dynamics, showing that a formulation based on complementarity constraints leads to a versatile and efficient time integration of this class of devices, even when embedded in complex multibody frameworks.

Freewheels, also known as overrunning clutches or one-way clutches, are unidirectional joints consisting of two rings, where the torque between the two rings can be transmitted in a single direction only, where they work as locked clutches. In the opposite direction, torque cannot be transmitted and they work as disengaged clutches [1]. Applications of this device are numerous in the field of mechanical engineering: for instance, they can be used for the automatic disengagement of motors when the output shaft is running faster, for safety or efficiency reasons such as in car automatic transmissions, in bicycles and in starter motors; otherwise, they can be used for generating intermitting unidirectional motion such as in dividers and conveyor belts. A remarkable application of freewheel mechanisms can be found self-winding watches, where the bidirectional oscillation of a small mass is used to store energy in the mainspring via unidirectional winding [2].

Different designs are available in literature: Fig.1 shows some common concepts. We note that most designs fall in two classes: on one hand we have freewheels that use *jamming* to lock the clutch simply using friction, such as the roller-type of Fig.1 a) and the sprag-clutch type of Fig.1 b), and on the other hand we have freewheels that use *ratcheting* where the reverse motion is counteracted by pawls that engage the teeth.

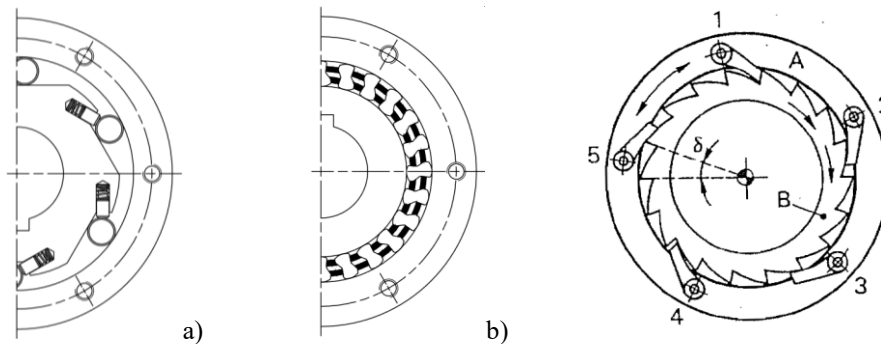


Figure 1: a) roller-type freewheel, b) sprag-clutch freewheel, c) ratchet freewheel. Drawings from [1,3]

In either case, conventional multibody tools already allow the modeling of these devices. However, in most instances one would need a complete 3D model including springs, sprags, rollers or pawls, each with complex 3D contact models, masses etc., hence leading to long computational times. In this work, similarly to [4] et al., we advocate the benefit of endorsing a custom model based on the mathematical framework of non-smooth dynamics. Such model expresses the behavior of both classes of freewheels with a single compact formulation, using complementarity constraints and set-valued force laws [5].

### 2 Formulation

If we assume that the *jamming* class of freewheels does not exhibit backlash or elastic deformation, its model corresponds immediately to a complementarity constraint of the type:

$$\lambda_i \geq 0 \perp \dot{\alpha}_i \geq 0 \quad (1)$$

where  $\lambda_i$  is the torque reaction within the  $i$ -th freewheel,  $\dot{\alpha}_i$  is the relative rotation speed of the two rings.

For the *ratcheting* class, one should consider the fact that the engagement of pawls happens only at steps with angular width  $\delta_{\alpha,i}$ , that is also a cause of backlash that can be in the  $[0, \delta_{\alpha,i}]$  range, depending on when the freewheel starts the inversion. For a ratchet with  $z$  teeth, one has  $\delta_{\alpha,i} = 2\pi/z$ , and if  $k$  pawls are unevenly spaced as in Fig.3.c), it is  $\delta_{\alpha,i} = 2\pi/(zk)$ . This too can

be expressed via a complementarity constraint:

$$\begin{cases} \alpha_i = n \delta_{\alpha,i} + \varphi_i: & \lambda_i \geq 0 \perp \dot{\alpha}_i \geq 0 \\ \alpha_i \neq n \delta_{\alpha,i} + \varphi_i: & \lambda_i = 0, \dot{\alpha}_i \in \mathbb{R} \end{cases} \quad \forall n \in \mathbb{Z} \quad (2)$$

where  $\varphi_i$  is an optional phase of the first teeth engagement. We remark that in a 1D powertrain model one has  $\dot{\alpha}_i = \dot{\beta}_k - \dot{\beta}_j$  where  $\beta$  is the rotation coordinate of some shaft, but more in general for a 3D multibody model one uses sparse jacobians  $D$  such that  $\dot{\alpha}_i = D_i^T \mathbf{v}$  where  $\mathbf{v}$  is the vector of the generalized velocities of the bodies.

We implemented the set-valued contact models above in a first order time stepper (discussed in [6]) that solves the non-smooth dynamics as a problem of Measure Differential Inclusions (MDI) over a time step  $h$ :

$$\begin{cases} \lambda \in Y \perp \mathbf{u}^{(l+1)} \in Y^* \\ M(\mathbf{v}^{(l+1)} - \mathbf{v}^{(l)}) = \mathbf{f}(\mathbf{q}^{(l)}, \mathbf{v}^{(l)}, t) + D^{(l)} \lambda \\ \mathbf{q}^{(l+1)} = \mathbf{q}^{(l)} + h \mathbf{v}^{(l+1)} \end{cases} \quad (3)$$

where we introduced a mass matrix  $M$ , system level forces  $\mathbf{f}$ , system level reactions  $\lambda$ , system level configuration  $\mathbf{q}$  and system level cone  $Y = (\times_i Y_{F,i}) \times (\times_j Y_{C,j}) \times (\times_k Y_{B,k})$ . This is built with second-order cones  $Y_{C,j}$  from the  $j$ -th frictional contact, with trivial cones  $Y_{B,k} = \mathbb{R}$  for the  $k$ -th bilateral constraint, and with  $Y_{B,k} = \mathbb{R}^+$  for the  $i$ -th freewheel. Also,  $Y^*$  is the dual cone of  $Y$ .

For the  $i$ -th *ratcheting* freewheel, the corresponding entry in the  $\mathbf{u}$  vector contains the  $\dot{\alpha}_i = D_i^T \mathbf{v}$  speed plus a stabilization term  $\frac{1}{h} \Phi_i$  that uses the floor operator  $[\cdot]$  and takes care of both sub cases of Eq.2 in discretized form:

$$\begin{aligned} \lambda_i \geq 0 \perp u_i \geq 0, \quad u_i &= D_i^T \mathbf{v} + \frac{1}{h} \Phi_i \\ \Phi_i &= \alpha_i - \left( \varphi_i + \delta_{\alpha,i} \left[ \frac{(\alpha_i - \varphi_i)}{\delta_{\alpha,i}} \right] \right). \end{aligned} \quad (4)$$

We also remark that, for  $\delta_{\alpha,i} = 0$  (null backlash) Eq.4 can be simplified by setting  $\Phi_i = 0$ , hence the same model can also reproduce the case of *jamming* freewheels as in Eq.1. The first part of Eq.3 is a Cone Complementarity Problem (CCP) and represents the most computationally intensive part of the time stepping scheme. We solve it using a projected spectral method or an accelerated Alternating Direction Method of Multipliers (ADMM) as described in [7].

## 4 Conclusion

We implemented the set-valued model of freewheels in our multibody simulation library, ProjectChrono, using C++ programming. The implementation is general in the sense that freewheels can coexist with rigid bodies, frictional contacts, actuators, clutches, brakes, finite elements etc. The freewheel can be used either in 1D powertrain models or interfaced to the rotational degree of freedom of revolute joints in 3D models. The model allows for backlash and arbitrary phasing of pawls.

We tested the approach with benchmarks that demonstrated the precision and efficiency of the method. As an application, we used the model in the analysis and optimization of a self-winding watch, where the proposed model provided a big speedup respect to the full model that contains all the 3D parts of the freewheel.

## References

- [1] P.L. Magnani, G. Ruggieri. Meccanismi per macchine automatiche. UTET, Turin, 2011.
- [2] C.A. Reymondin, G. Monnier, D. Jeanneret, U. Pelaratti. Théorie d'horlogerie. Fédération des écoles techniques, Switzerland, 1998.
- [3] C.T.S. catalog of freewheels, from <https://www.ctsitaly.it>, 2021.
- [4] M. Förg, Multi-Body Systems with Set-Valued Force Laws – Theory and Numerics. Düsseldorf, Lehrstuhl für Angewandte Mechanik, TU München, Diss., 2007.
- [5] C. Glocker, Set-Valued Force Laws, Springer-Verlag Berlin Heidelberg, 2001.
- [6] D. Negrut, R. Serban, A. Tasora, Posing Multibody Dynamics with Friction and Contact as a Differential Complementarity Problem, Journal of Computational and Nonlinear Dynamics, 13(1): 014503, 2018.
- [7] A. Tasora, D. Mangoni, S. Benatti, R. Garziera. Solving variational inequalities and cone complementarity problems in nonsmooth dynamics using the alternating direction method of multipliers, International Journal for Numerical Methods in Engineering; pp.1–21, 2021.

# Manufacturing Tolerance Optimization of Circuit Breaker Mechanism Using Multibody Dynamic Simulation

Narendra Akhadkar<sup>1</sup>, Gitesh Porwal<sup>2</sup>

<sup>1</sup>Schneider Electric Industries  
Grenoble, 38000, France  
narendra.akhadkar@se.com

<sup>2</sup>Altair Engineering  
Pune, 411004, India  
giteshp@altair.com

## EXTENDED ABSTRACT

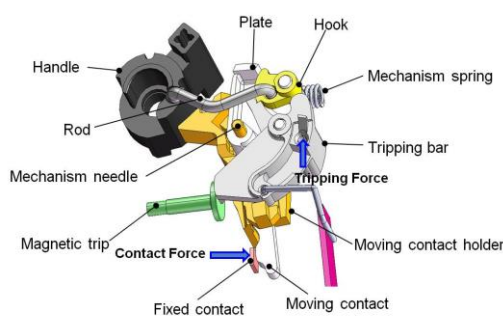
### 1 Introduction

A miniature circuit breaker is a device that switches and/or protects the lowest common distributed voltage in an electrical system. It is designed to protect conductors and insulation from damage due to overload and short circuit. Usually, the performance of these mechanisms is not as desired, due to the manufacturing tolerances on links, clearances in the joints and the assembly tolerances. The spatial revolute joint with clearance in both axial and radial direction adds five extra degrees of freedom into the system. Compared to planar mechanisms, spatial mechanisms can generate more complicated functions with the same number of links. Most of the previous work is focused on the radial clearance in the planar and spatial revolute joints [1-5]. However, more recently the influence of the axial clearance in the revolute joint has been studied in [4]. Most of the mechanisms in the Schneider Electric company use frictional contacts. There are various compliant models available to correctly model the multiple impacts and friction [2, 4].

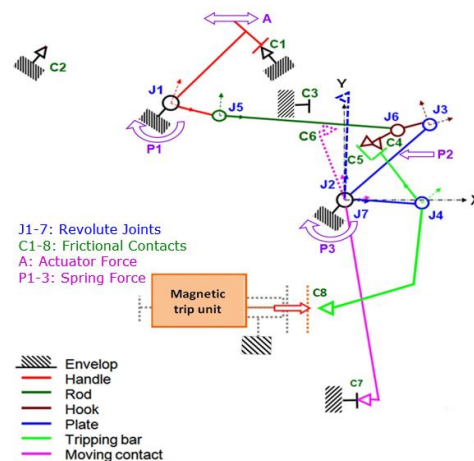
### 2 Miniature Circuit Breaker Mechanism

Miniature circuit breaker construction is simple, however very precise. In fact, a miniature circuit breaker has no replacement parts. It is not designed to be maintained. When a unit goes bad, it is simply replaced. A typical miniature circuit breaker mechanism is depicted in Figure 1(a).

All the mechanism parts are enclosed in between the case and cover parts. These parts are connected to each other through a revolute joint or frictional contact. In the following section we will see the detailed description of these joints and contacts. In the first step, the primary function of a mechanism is usually formulated in terms of kinematical quantities (link geometry, kinematic constraints, etc). Also, the various geometrical relations resulting from the kinematical analysis of the linkage mechanism are an essential ingredient for the dynamic analysis. The kinematical analysis of a miniature circuit breaker mechanism is of great importance. It consists of seven links, seven revolute joints with clearance in both radial and axial direction and four frictional contacts (see Figure 1(b)).



(a) 3D representation on C60 model.



(b) Kinematic representation

Figure 1: C-60 circuit breaker mechanism - ON position.

### 3 Newton-Euler Formulation of the Equation of Motion

In the Newton-Euler method the dynamics is written separately for each link/body. It includes the constraint forces acting on all bodies of the system and results in redundant equations with more equations than unknowns. These equations are evaluated in a numeric and a recursive way. However, by eliminating the reaction forces we can get the closed form of the dynamics.



The Newton-Euler equation of motion in matrix form is given as:

$$\begin{pmatrix} mI_{3 \times 3} & 0_{3 \times 3} \\ 0_{3 \times 3} & I_g \end{pmatrix} \begin{pmatrix} a_g \\ \alpha \end{pmatrix} + \begin{pmatrix} mS(\omega) \\ -S(I_g \omega) \end{pmatrix} \begin{pmatrix} v_g \\ \omega \end{pmatrix} = \begin{pmatrix} F_g \\ \tau_g \end{pmatrix} \quad (1)$$

where the subscript  $g$  denotes the center of gravity (CG),  $C_g \in \mathbb{R}^3$  is the coordinate of CG,  $m$  is mass of the body,  $a_g$  is the acceleration,  $F_g$  is the force acting at CG,  $\tau_g$  is the moment about CG,  $M = mI_{3 \times 3}$  is the mass matrix,  $I_g \in \mathbb{R}^{3 \times 3}$  is the inertia matrix about body's center of gravity,  $\omega$  is the angular velocity of the body relative to the inertial frame and expressed in body reference frame and  $S$  is the matrix cross product operator,  $a \times c := S(a)c$  and  $S = -S^T$  is a skew symmetric matrix.

#### 4 Sensitivity analysis and Experimental validation

We have performed the sensitivity analysis, in order to simulate the geometrical variations of the breaker mechanism to minimize the manufacturing cost and to ensure the assembly requirements. In case of the output variable of contact force, the statistical distribution is from [12:0; 15:1]N which is well within the limit defined by the USL (16:0N) and LSL (9:0N) (see Figure 2). However, the Gaussian distribution is not centered, the index of absolute centering is calculated as  $C_c = 0.3314$ , and the process capability index is  $C_{pk} = 1.631$ . The positive shift in the distribution ensures good contact pressure between the moving and fixed contact, which ultimately helps to reduce the arcing between the contacts. It will help to ensure the safety of the product even in the case of erosion between the contacts.

Simulation results are validated through the experimental tests (see Figure 3). The results of the experimental test are compared with the virtual test. In case of virtual test, the contact force at the static equilibrium is 14.96N. The percentage relative error in the contact force between the experiment and virtual test is 2.08%.

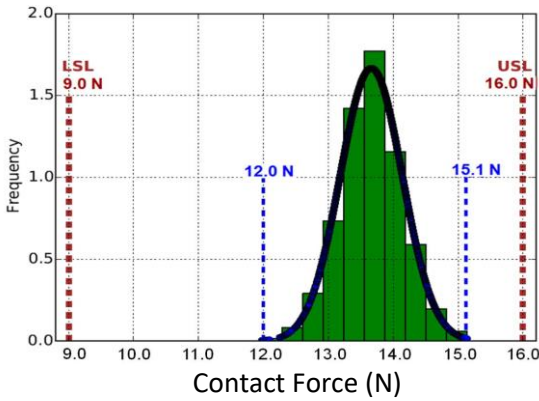


Figure 2: Variation of contact force - ON position.

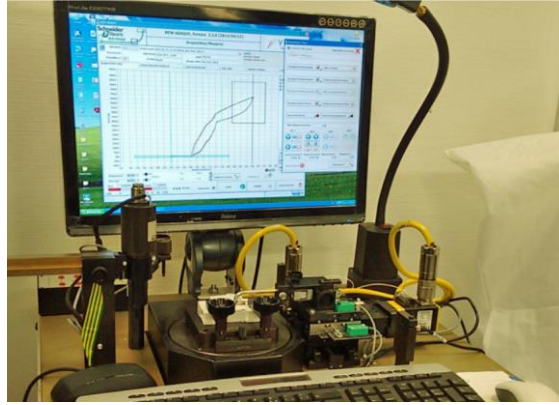


Figure 3: Experimental test bench for contact force measurement.

#### Conclusion

This paper is devoted to the numerical simulation of the C-60 circuit breaker built by Schneider Electric, using the so-called compliant method. It relies on the compliant models used to model impacts and friction. Emphasis is put on the modeling of three-dimensional revolute joints with axial and radial clearance. Moreover, detailed comparisons with experimental data obtained at the Schneider Electric laboratory, prove the very good prediction capabilities of the compliant approach, for this type of mechanisms.

#### References

- [1] Akhadkar, N., Acary, V. and Brogliato, B.: 3D revolute joint with clearance in multibody systems. In Computational Kinematics, pp. 11-18. Springer, Cham, 2018.
- [2] Flores, P.: A parametric study on the dynamic response of planar multibody systems with multiple clearance joints. Nonlinear Dyn. 61(4), 633–653 (2010).
- [3] Yan, S., Xiang, W., Zhang, L.: A comprehensive model for 3D revolute joints with clearances in mechanical systems. Nonlinear Dyn. 80(1), 309–328 (2015).
- [4] Brutti, C., Coglitore, G., Valentini, P.P.: Modeling 3D revolute joint with clearance and contact stiffness. Nonlinear Dyn. 66(4), 531–548 (2011).
- [5] Zhang, Z., Xu, L., Flores, P., Lankarani, H.M.: A Kriging Model for dynamics of mechanical systems with revolute joint clearances. J. Comput. Nonlinear Dyn. 9(3), 031013 (2014).

## 3D LuGre model for multibody systems involving contacts with stick-slip

Lorenzo Colantonio<sup>1</sup>, Pierre Dehombreux<sup>1</sup>, Michal Hajžman<sup>2</sup>, Olivier Verlinden<sup>1</sup>

<sup>1</sup> Faculty of Engineering

University of Mons

Place du Parc 20, B-7000 Mons, Belgium

[Lorenzo.Colantonio,Olivier.Verlinden,Pierre.Dehombreux]@umons.ac.be

<sup>2</sup> Faculty of Applied Sciences

University of West Bohemia

Univerzity 22, 306 14 Plzen, Czech Republic

mhajzman@kme.zcu.cz

### EXTENDED ABSTRACT

#### 1 Introduction

Friction is an extremely complex mechanism, which involves micro-interactions between the surfaces in contact. However, in multibody systems the general behaviour of friction at the macroscopic level is generally sufficient. Among the commonly used friction models [3], the LuGre one is very popular in multibody system and motion control as it is computationally efficient and able to reproduce most of phenomena observed in friction.

This paper presents an adaptation of the LuGre model, inspired namely from [5] for the management of the varying normal force and from [2] for the management of the direction of the slip velocity.

#### 2 Generalized 3D LuGre model

Let us consider a contact between a point A attached to body  $j$  with local position vector  $\vec{r}_A$  and a plane attached to body  $i$  (Figure 1) defined by the local position vector  $\vec{r}_P$  of a point P of the plane and its normal unit vector  $\vec{n}$ . A contact between a plane and a sphere could be managed in a similar manner. The inter-bodies penetration  $\delta$  and the penetration rate  $\dot{\delta}$  can be computed as:

$$\delta = (\vec{e}_P - \vec{e}_A) \cdot \vec{n} \quad \dot{\delta} = -\vec{V}_{rel} \cdot \vec{n} \quad (1)$$

$\vec{e}_P$  and  $\vec{e}_A$  being the respective position vectors with respect to the global reference coordinate system and  $\vec{V}_{rel}$  the relative velocity of body  $j$  with respect to body  $i$  (the plane) computed e.g. at the middle of the penetration zone (point M in Figure 1).

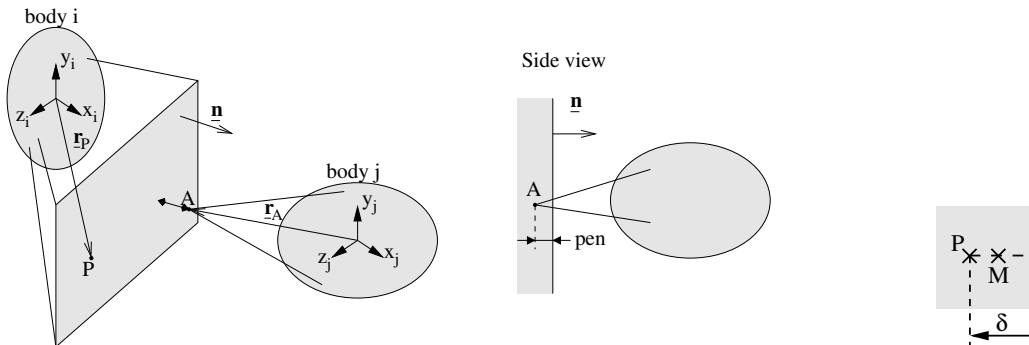


Figure 1: Contact between a plane and a point

The relative velocity is decomposed along the tangential ( $\vec{V}_t$ ) and normal ( $\vec{V}_n$ ) components

$$\vec{V}_n = (\vec{V}_{rel} \cdot \vec{n})\vec{n} \quad \vec{V}_t = \vec{n} \times (\vec{V}_{rel} \times \vec{n}) \quad (2)$$

The normal force ( $N$ ) is usually computed in terms of  $\delta$  e.g. according to the Hunt and Crossley formula

$$N = K_{contact} \delta^{p_K} + D_{contact} \delta^{p_D} \dot{\delta} \quad (3)$$

with  $K_{contact}$  the contact stiffness,  $D_{contact}$  the contact damping, and  $p_K$  and  $p_D$  fitting coefficients.

The friction force on the plane is computed according to a vector version of the LuGre equations. The bristle deformation is represented as a vector  $\vec{Z}$  possibly taking place in all directions, and driven by

$$\dot{\vec{Z}} = \vec{V}_t - \vec{Z} \frac{\sigma_0^M V_t}{G^M(V_t)} \quad \text{with} \quad G^M(V_t) = \mu_d + (\mu_s - \mu_d) e^{(-|V_t/V_{st}|)^\alpha} \quad (4)$$

with  $\mu_d$  and  $\mu_s$  the dynamic and static (or breakaway) friction coefficients respectively,  $G^M(V_t)$  the function describing the friction coefficient in terms of the magnitude  $V_t$  of the sliding velocity,  $V_{st}$  the Stribeck velocity and  $\alpha$  ranging from 0.5 to 2 [1]. Finally, the friction force on the plane is calculated from

$$\vec{F} = \left( \sigma_0^M \vec{Z} + \sigma_1^M \dot{\vec{Z}} + \sigma_2^M \vec{V}_t \right) N \quad (5)$$

with  $\sigma_0$  [ $\text{m}^{-1}$ ] the micro-stiffness,  $\sigma_1$  [ $\text{s/m}$ ] the micro damping, and  $\sigma_2$  [ $\text{s/m}$ ] the viscous effect, all of them per unit of normal force.

The previous vector expressions will lead to 3 scalar equations, corresponding to the projections along the X, Y, Z coordinates of a coordinate system, a priori arbitrary but usually attached to one of the contact surfaces.

With respect to the original LuGre model, the bristle deflection is 3D but, as it is driven by the tangential velocity vector, the friction force is naturally aligned with the latter. The same technique was used in [2] but in 2D only as the contact plane (the road) is known. Moreover, the normal force  $N$  is transferred from the expression of  $G_M$  to equation 5, as in [5]. This allows to manage more properly varying normal forces.

It can be demonstrated that under a constant sliding velocity  $\vec{V}_t$ , the steady-state friction force reads

$$\vec{F}_{ss} = \left( \left( \mu_d + (\mu_s - \mu_d) e^{(-|\frac{\vec{V}_t}{V_t}|^\alpha)} \right) \frac{\vec{V}_t}{V_t} + \sigma_2^M \vec{V}_t \right) N \quad (6)$$

which corresponds to the so-called GKF model [1].

### 3 Applications

The proposed model was first tested on a cube lying on the X-Y plane, subjected to gravity and a varying lateral force, the contact being implemented through 6 contact points regularly spaced on a circle. The example demonstrates the ability of the projected equations to be used in all directions, with multiple contact points and with varying normal force. The results perfectly agree with the ones presented in [5].

The second example is more complex and corresponds to the experimental setup investigated in [4] (Fig. 2). The setup is composed of 3 identical beams linked by a tie-boss, expected to represent turbine blades connected by friction elements. The purpose of the arrangement is to induce relative slip at the contacts to dissipate energy by friction when the blades are excited by frequencies close to resonance during speed up or slow down of the turbine. Out of resonance, the parts stick to each other and no dissipation, and consequently no wear, takes place. The right part of Figure 2 shows the time history of the sliding velocity exhibited by the LuGre model at some interface when the system is excited by a force of 0.5 N that follows a logarithmic swept sine from 30 Hz to 80 Hz. It can be observed that sliding takes place around resonance. Out of resonance, microslips take place, related to the bristle deformation, physically corresponding to deformation of the asperities in the contact. Comparison with the regularized GKF model will also be developed.

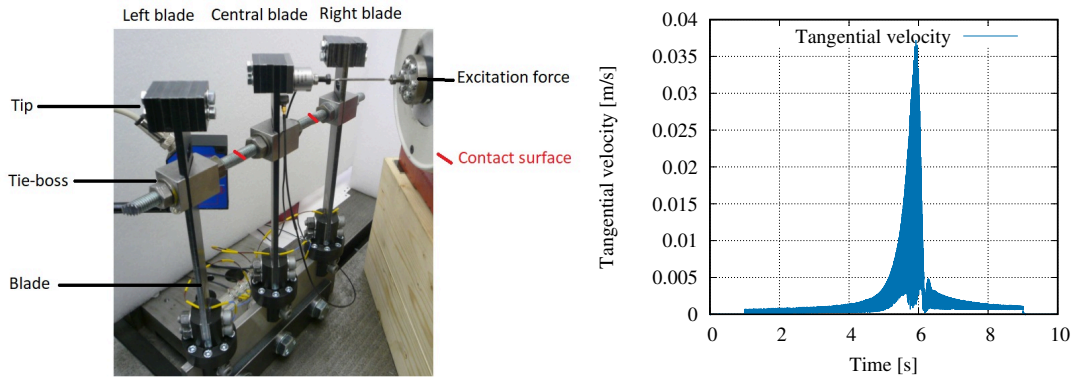


Figure 2: Experimental setup presented in [4] and example of simulation result

### References

- [1] Brian Armstrong-Helouvry, Pierre Dupont, and Carlos Canudas De Wit. A survey of models, analysis tools and compensation methods for the control of machines with friction. *Automatica*, 30(7):1083–1138, 1994.
- [2] Wei Liang, Jure Medanic, and Roland Ruhl. Analytical dynamic tire model. *Vehicle System Dynamics*, 46(3):197–227, 2008.
- [3] Ettore Pennestri, Valerio Rossi, Pietro Salvini, and Pier Paolo Valentini. Review and comparison of dry friction force models. *Nonlinear dynamics*, 83(4):1785–1801, 2016.
- [4] Ludek Pesek, Ladislav Pust, Vitezslav Bula, and Jan Cibulka. Numerical analysis of dry friction damping effect of tie-boss couplings on three blade bundle. In *ASME 2017 International Design Engineering Technical Conferences and Computers and Information in Engineering Conference*. American Society of Mechanical Engineers Digital Collection, 2017.
- [5] Marek Wojtyra. Comparison of two versions of the lugre model under conditions of varying normal force. *ECCOMAS Thematic conference on Multibody dynamics*, 19-22 june 2017, Prague.

# An Impact Model of Three-dimensional Rigid Rocking Blocks

Péter L. Várkonyi, Tamás Ther,

Department of Mechanics, Materials, and Structures  
Budapest University of Technology and Economics  
Muegyetem rkp. 3, H-1111 Budapest, Hungary  
{varkonyi.peter,ther.tamas}@epk.bme.hu

## EXTENDED ABSTRACT

### 1 Introduction

Rocking is a common behavior of rigid polyhedral blocks or stacks of multiple rigid blocks on a rigid base in response to dynamic excitation. From an engineering viewpoint, rocking structures such as masonry columns and arches show remarkable resilience under earthquake excitation [1]. At the same time, theoretical analysis of rocking systems is challenging due to the inherently non-smooth, hybrid and non-linear nature of motion caused by unilateral rigid contact and friction. Impact modeling is perhaps the most challenging aspect of the analysis.

Rigid impact models are typically formulated as instantaneous velocity jumps while the configuration of the system remains unchanged. This modeling approach is merely a phenomenological description of a complex, multi-scale (both in time and space) physical process and thus these models tend to involve empirically fitted model parameters (such as the classical coefficient of restitution) with somewhat limited potential to predict individual motion trajectories. Yet, rigid impact models remain popular due to their simplicity, which allows their integration into complex dynamic models.

Impacts often tend to be highly unpredictable if the impact process involves extended areas of contact. In those cases, the impact process is characterized by the competition between two microscopic quantities: small mechanical deformations, and small geometric imperfections of the contact surfaces. If the characteristic scale of deformations is significantly larger than that of geometric imperfections, then impacts are predictable and repeatable, whereas if it is significantly smaller than the scale of imperfections, then impacts become unpredictable. Importantly, the impacts of rocking structures always involve extended contact areas as impacts occur between two flat surfaces or between a straight edge and a surface.

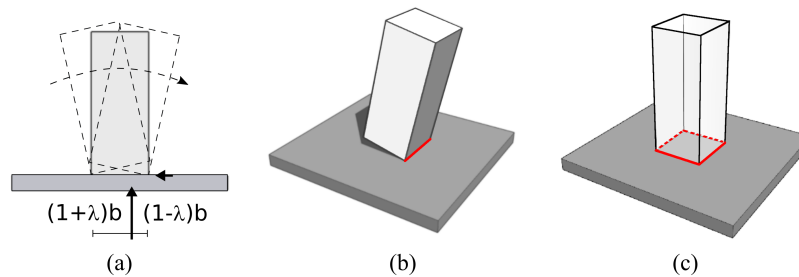


Figure 1: a: Impact in a planar model of rocking. Solid arrows represent the horizontal and vertical component of the net impact momentum. The position of the latter one is set by the dimensionless scalar parameter  $\lambda$ .  $b$  denotes the half-length of the base edge. b,c: edge and facet impacts in a three-dimensional model.

### 2 Models of rocking impacts

Rocking is often investigated using planar models. Many models of planar rocking impacts were inspired by the seminal work of Housner [2]. Typical assumptions of these models include lack of bouncing and slip, which are reasonable assumptions for slender blocks and arches. Under these assumptions, a one-parameter family of physically feasible impact maps emerges. Hence, planar rocking impact models involve one empirical parameter, which can be chosen in various ways. Popular dimensionless parametrizations of the impact map include the ratio of post-impact and pre-impact angular velocities or a parameter  $\lambda$  specifying the spatial position of the resultant impact momentum along the edge of contact [3], see Figure 1a. Experimental measurements reveal remarkable variability of the impact parameter value even for apparently identical setups and initial conditions. The variability is likely explained by sensitivity to geometric imperfections as highlighted above.

Works addressing three-dimensional rocking motion [4] have used a priori assumptions about impacts. A systematic investigation of rigid impact in 3D appears to be missing at this time. Here we develop a new model of three dimensional rigid rocking impact. Two types of impacts are considered (edge and facet impacts, see Figure 1b,c). By using methods similar to the literature concerning planar rocking, feasible outcomes of the impact map are parameterized by two (edge impacts) or three (facet impacts) scalars, representing the magnitude and position of the resultant impact momentum.

### 3 Empirical fitting and theoretical bounds of impact parameters

In the case of planar impact models, physical laws yield theoretical bounds of the impact parameter. In particular, the parameter  $\lambda$  in Figure 1a must be within the interval  $(0, 1)$  if one assumes that impacts involve unilateral contact interaction and they decrease the kinetic energy of the system. Empirical measurements of  $\lambda$  are mostly consistent with these findings, however values larger than 1 are found in some cases. The discrepancy between theoretical predictions and empirical results can be explained by unmodeled effects causing energy absorption between two impacts. Here, we identify similar parameter bounds for three-dimensional impacts.

In contrast to planar models, facet impact maps exhibit intriguing examples of solution non-existence and non-uniqueness. This new phenomenon originates in the fact that a block can rock around any of several vertices or edges immediately after an impact. The impact map involves all of these different scenarios, and the number of feasible scenarios may differ from one. In order to ensure solution uniqueness, we propose the elimination of one of the impact parameters, which results in a reduced model of facet impacts with 2 scalar parameters. The reduced model provably provides a unique solution.

The reduced model is tested by numerical simulation and impact parameters are tuned to achieve the best possible fit to free rocking experiments of cuboid blocks (Figure 2). We find that the reduced impact model matches experimental results well. On the other hand, optimal values of impact parameters are often beyond theoretical bounds. Some possible reasons of this discrepancy are briefly discussed.

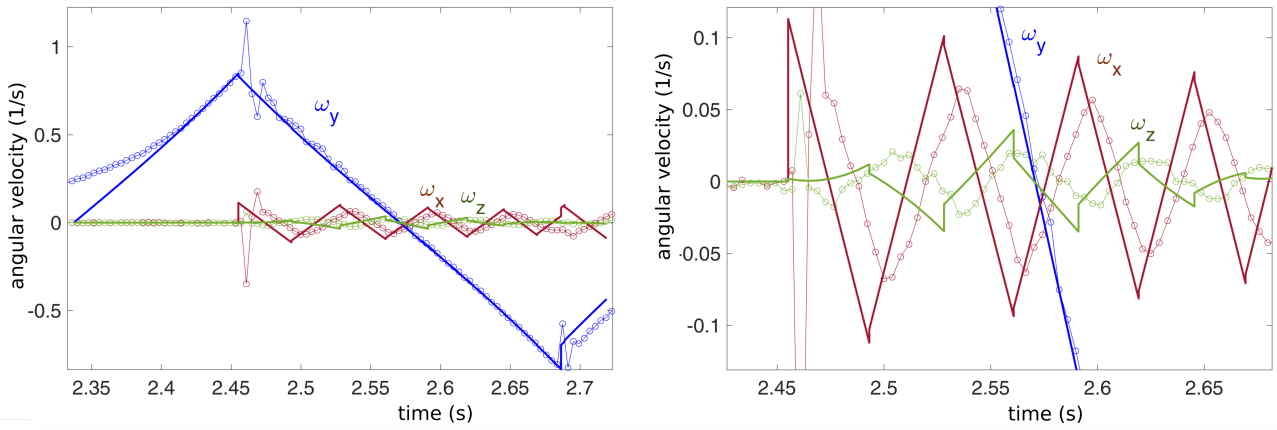


Figure 2: Left: comparison of experimental measured angular velocity functions (thin lines and circles) and numerical simulation with fitted initial conditions and impact parameter values (thick lines). Right: magnified detail of the same diagram.

### 4 Conclusions and future plans

We introduced a new 3D model of rocking impact, which is a natural extension of existing planar models. The new impact model allows investigation of the safety of rocking structures against overturning by numerical simulation. Our approach uncovers all feasible outcomes of an impact and thus it allows to assess the safety of rocking structures even if their behaviors are highly unpredictable. To achieve this goal we propose that rocking motion is simulated with various values of the impact parameters and the safety of the rocking structure is verified for each value.

### Acknowledgments

This work has been supported by the National Research, Development and Innovation Office under grant 124002.

### References

- [1] M.J. DeJong, L. De Lorenzis, S. Adams, J. A. Ochsendorf. Rocking stability of masonry arches in seismic regions. *Earthquake Spectra*, 24:847-865, 2008.
- [2] G.W. Housner. The behavior of inverted pendulum structures during earthquakes. *Bulletin of the seismological society of America*, 53:403-417, 1963.
- [3] M.N. Chatzis, M. Garcia Espinosa, and A.W. Smyth. Examining the energy loss in the inverted pendulum model for rocking bodies. *Journal of Engineering Mechanics*, 143(5):04017013, 2017.
- [4] D. Zulli, A. Contento, and A. Di Egidio. 3D model of rigid block with a rectangular base subject to pulse-type excitation. *International Journal of Non-Linear Mechanics*, 47:679-687, 2012.



## Synchronous Contact/Impact Events Modelling With A Smooth-Based Approach

Raúl Gismeros Moreno, Eduardo Corral Abad, Jesús Meneses Alonso, M.J. Gómez García and Cristina Castejón Sisamón

MAQLAB research group, Department of Mechanical Engineering, Universidad Carlos III de Madrid,  
Avenida de la Universidad 30, 28911 Leganés, Spain  
[rgismero, ecorral, meneses, mjggarci, castejon]@ing.uc3m.es

### EXTENDED ABSTRACT

There are two main ways of modelling a contact/impact event in the context of multibody dynamics: the non-smooth approach and the models based on contact forces. Each one has a distinct set of advantages and limitations [1]: non-smooth methods are known for considering bodies as rigid solids and their computational efficiency. However, some of these methods pose several issues when dealing with friction phenomena or multiple-simultaneous impact scenarios. On the other hand, models based on contact forces are continuous functions of the relative penetration (and its temporal derivative) of the contacting bodies, which are supposed to be deformable. Their main benefit is that there is no need to define unilateral restrictions. Nonetheless, the proper, accurate choice of the parameters of the definitions of the forces, as well as the right detection of the initial instant of contact [2], that makes the computing time to increase dramatically on certain occasions, are their most distinctive drawbacks.

This work focuses its scope on these second methods, proposing several models developed under this methodology and discussing the main issues that have arisen when designing, modeling, and verifying these models. The main purpose of this paper is to provide a reference to those researchers that work with smooth methods in the context of multibody dynamics of how to deal with them. Among the models presented, there are some engineering-focused ones, whereas the readers can also find some more practical, *day-to-day* examples.

The first model presented is a classical ball bearing, as shown in Figure 1. Two versions were developed. The first one, based on a sphere-sphere modelling of the contact between the elements, neglected axial loads. The latter, more advanced, considered axial loads and considered a sphere-cylinder contact interaction. The main problems faced with this model were related to the accuracy of the contact detection and the time step size. The proper choice of an ODE integrator from the Matlab library proved to be critical in the final results [3].

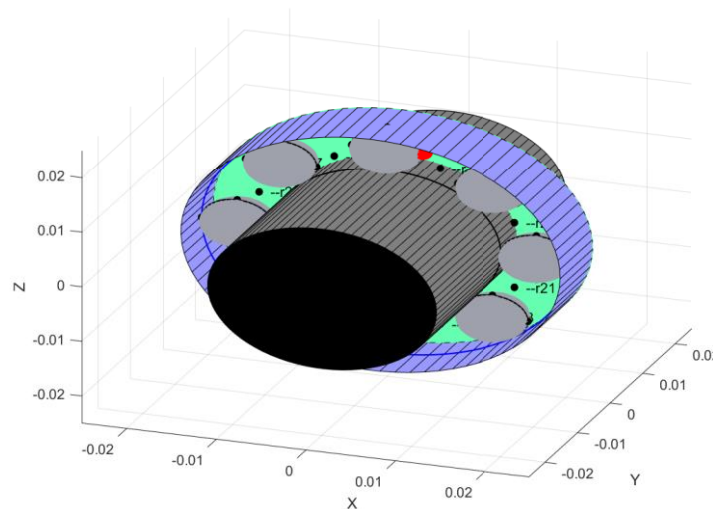


Figure 1: Matlab plot of the first model introduced: a ball bearing.

A model previously introduced and now further developed is a pool/billiard game [4] (see Figure 2). This time the pockets, as well as the cushions, have been modelled and implemented. In order to achieve this, some conditions have been defined to *de-activate* the sphere-plane interaction when a ball places over a pocket; and an innovative sphere-triangular prism contact interaction has been developed for the cushion-ball contact in the pocket areas. Some of the main issues arisen during the design and modelling phases were related to the effects of each contact interaction on the rest of contact relationships. For example, the initial distance between the balls of the rack (coloured balls in Figure 2) had an impact on the introduction of high frequencies in some of the balls, which led to unreasonable vertical displacements. This made necessary to rethink the physical characteristics of each interaction in order to obtain consistent results compared to the experimental values. Similar conclusions and some new ones regarding the elasticity of the impact were obtained from an additional model, a Newton's cradle, in which different contact force models and values of the coefficient of restitution, as well as sizes of the bodies, were considered.

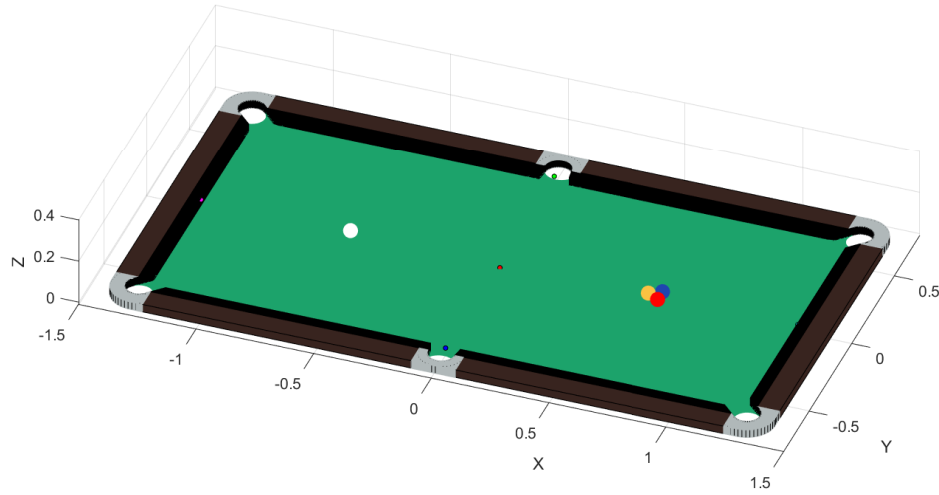


Figure 2: Matlab plot of the second model: a pool/billiard game.

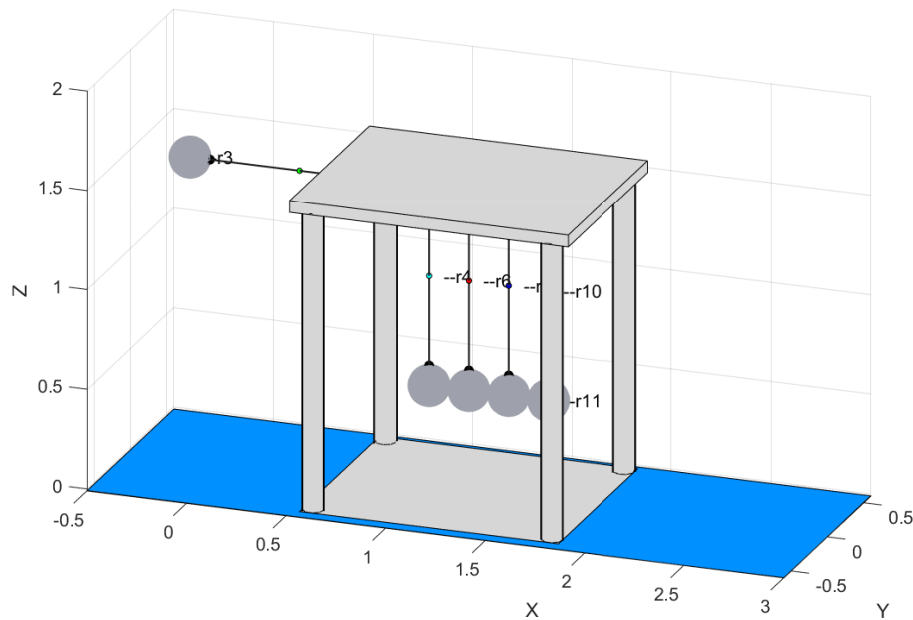


Figure 3: Matlab plot of the third model presented: Newton's cradle.

The third model proposed is a Newton's cradle, a device used with educational purposes to demonstrate the principles of conservation of momentum and conservation of energy with a set of swinging spheres (see Figure 3). In this case, two different situations were tested: a single ball was lifted and then released, and two balls were raised. Some issues arose related to the degree of elasticity of the impact and the contact detection between the static balls, as well as constraint violation phenomena.

## References

- [1] E. Corral, R. Gismeros Moreno, M. J. Gómez García, and C. Castejón, 'Nonlinear phenomena of contact in multibody systems dynamics: a review', *Nonlinear Dynamics*. Springer Science and Business Media B.V., pp. 1–27, Mar. 14, 2021, doi: 10.1007/s11071-021-06344-z.
- [2] P. Flores and J. Ambrósio, 'On the contact detection for contact-impact analysis in multibody systems', *Multibody Syst. Dyn.*, 2010, doi: 10.1007/s11044-010-9209-8.
- [3] L. F. Shampine and M. W. Reichelt, 'The MATLAB ode suite', *SIAM J. Sci. Comput.*, 1997, doi: 10.1137/S1064827594276424.
- [4] E. Corral, R. Gismeros, F. Marques, P. Flores, M. J. Gómez García, and C. Castejon, 'Dynamic Modeling and Analysis of Pool Balls Interaction', in *Computational Methods in Applied Sciences*, vol. 53, Springer, 2020, pp. 79–86.



**Section**

**EDUCATION, VALIDATION AND SOFTWARE DEVELOPMENT**

EDU

# Demystifying the Mechanical and Numerical Concepts Underlying Multibody System Dynamics: Development of an International MOOC

Paul Fisette<sup>1</sup>, Simon Hinnekens<sup>1</sup>, Emile Moreau<sup>1</sup>, Maxime Raison<sup>2</sup>

<sup>1</sup>Institute of Mechanics, Materials and Civil Engineering (IMMC)/MEED  
Université catholique de Louvain  
Place du Levant 2/L5.04.02  
1348 Louvain-la-Neuve, Belgium  
[\[paul.fisette, simon.hinneken, emile.moreau\]@uclouvain.be](mailto:paul.fisette,simon.hinneken,emile.moreau@uclouvain.be)

<sup>2</sup>Mechanical Engineering Department  
Polytechnique Montréal  
2500 Chemin de Polytechnique,  
H3T 1J4 Montreal QC, Canada  
[maxime.raison@polymtl.ca](mailto:maxime.raison@polymtl.ca)

## EXTENDED ABSTRACT

### 1 Introduction

Vehicles, bicycles, cranes, human bodies and robots are everyday examples of multibody systems (MBS). To compute their kinematic and dynamic characteristics, such as velocities, accelerations and forces, it is essential to learn how to model and simulate MBS. The problem is that this learning, which requires rigor and perseverance at any stage, can be off-putting in B.Eng. and sometimes demotivating, given the effort involved even for simple applications: one just has to redo the equations of a small cart in 2D to be convinced. The objective of this work is to demystify the mechanical and numerical concepts underlying MBS models, via the development of an international Massive Open Online Course (MOOC) - *Modeling and simulation of multibody systems* [1] - which takes advantage of the symbolic generation of the multibody equations.

### 2 Methods: symbolic approach in MBS

First, the general MBS approach in education places each student at the center of the learning: the students must “immerse themselves” in all aspects of MBS for all the more satisfaction at the end. This means that the students can manage everything: they have their own “code” to process any application. The MBS approach has already shown two educational benefits [2]:

1. It is well suited to the motivational learning of mechanics, by solving the MBS equations.
2. It enables to deal with concrete everyday mechanical applications, and to visualize abstract concepts of mechanics, mathematics, and numerical methods, e.g.: a singular Jacobian matrix due to kinematic singularity; a numerical integrator struggling because of numerical stiffness due to dry friction; etc. It also enables them to forge links between these domains.

Secondly, the symbolic approach of the ROBOTRAN software [3] particularly brings additional benefits. Overall, it is known to simplify equations [2]. But here, we will highlight three educational contributions of the symbolic approach:

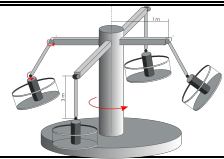
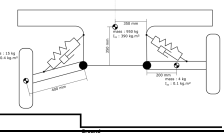
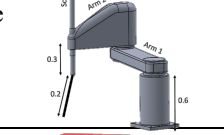
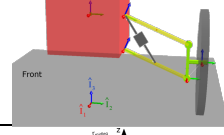
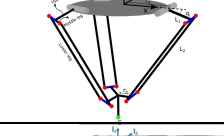
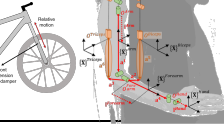
1. On the basis of a user-friendly graphical representation of any MBS, the software takes care of the necessary but tedious tasks (with great risk of human errors and of no real interest to the user), namely the generation of the MBS equations with formalisms such as the recursive Newton-Euler method or the virtual power principle, among others. ROBOTRAN does this whatever the complexity of the MBS (up to 300 degrees of freedom), such as the examples of Table 1 (third row).
2. The software allows therefore the student to focus on pedagogically interesting topics, i.e. understanding then programming e.g.: i. a tire/ground contact model, ii. a muscle model, iii. numerical concepts such as kinematic loop closure, equilibrium model-based convergence issues, integration model-based stiffness, etc. iv. the selection of results that are relevant to analyze for real and realistic applications, such as: the quasi-static equilibrium or the modal analysis of a vehicle, the inverse kinematics or dynamics of a parallel robot, the reaction forces inside mechanical transmissions, the sizing of actuators, or the net torques quantification in the human body.
3. As a practical asset, the symbolic equations can be generated remotely, which minimizes the local computer installation tasks, allowing any user to start quickly.

### 3 Result and discussion: a MOOC in « Modeling and simulation of multibody systems »

Our MOOC is based on prerequisites in Newtonian mechanics briefly reminded at the beginning of the course: linear algebra, vector theory and notation, basic numerical methods, and basic programming skills. The MOOC is general for any student wishing to learn modeling and simulation of MBS. To follow the course, the students can use the multibody software of their choice, e.g. from the list of software available at their institution or laboratory. However, to allow them to benefit from the symbolic approach, access to the ROBOTRAN software is also freely offered in the

context of the MOOC. The course was designed for a period of 14 weeks for students working 10–11 hours per week. The level is considered as intermediate (3–4<sup>th</sup> year of B.Eng.). The course type is instructor-led on a course schedule and is composed of 6 modules, detailed in Table 1.

Table 1: Current content of the MOOC in *Modeling and simulation of multibody systems*.

<i>Modules</i>	<i>Content</i>	<i>Examples to model and simulate</i>
1. Tree-like MBS	Bodies, joints, (Newton and Euler) equations of motion, modelling and simulation (motion computation by time integration, analysis of simple kinematic and dynamic performances)	Merry-go-round 
2: Forces and torques	Introducing forces and torques in an MBS, and dealing with these ones: 1. joint forces; 2. external forces; 3. point-to-point forces	Simplified vehicle suspension 
3. Driven motion	Driven motion, i.e. imposing the time evolution of specific generalized coordinates in MBS	SCARA-like pick-and-place robots 
4. Algebraic Constraints	Algebraic constraints (constrained MBS), DAE to ODE reduction and final equations of motion in minimal form	Quarter-car with parallel suspension 
5. Kinematic loops	MBS with kinematic loops, including cutting procedures and their numerical resolution, for three situations: 1. cut of a body, 2. cut of a ball joint, 3. cut and removal of connecting rod	Delta robot 
6. Numerical analysis	Direct kinematics, inverse kinematics, equilibrium, modal analysis, direct dynamics, inverse dynamics	Bicycle and human arm 

All along the MOOC, we present videos, examples, questions, and a rigorous writing of the fundamental concepts and equations. E.g: frames and vectors follow strict and systematic rules; there is no pseudo-centrifugal force; no oversimplification of problems to reduce the equations; we start from 3D systems as a general case, and 2D applications is a particular case, the reverse being a bit misleading in our opinion. To conclude, the MOOC allowed students to understand and program MBS faster, from a simple cart-pendulum to 3D Merry-go-round, vehicle suspensions, parallel robots and human body. Based on our experience with the first version of the MOOC, the current perspective is to divide it into 2 sub-courses: roughly, an intermediate one for unconstrained MBS from modules 1 to 3, and an advanced one for constrained MBS from modules 4 to 6.

## References

- [1] P. Fisette, M. Raison. Website of the MOOC in « Modeling and simulation of multibody systems ». <https://www.edx.org/course/modeling-and-simulation-of-multibody-systems> ; last visit: 11th June 2021.
- [2] P. Fisette, J.C. Samin. Engineering Education in Multibody Systems. Selected paper, In: Multibody Dynamics: Computational Methods and Applications, García Orden J.C., Goicolea, J.M. and Cuadrado J. ed(s), Vol. 4, pages 159-178. Dordrecht, The Netherlands, Springer, 2007.
- [3] P. Fisette et al. ROBOTRAN software, UCLouvain, Belgium. <https://www.robotran.be/> ; last visit: 11th June 2021.

# Validation of MBD-CFD Co-Simulation for Box Making Machine

Rohit Arora<sup>1</sup>, Atsushi Nakagawa<sup>2</sup>, Tomoshige Takata<sup>2</sup>, Tomohiro Akaki<sup>1</sup>, Hiroyuki Kanazawa<sup>1</sup>

<sup>1</sup> Machinery Research Department

Research & Innovation Center

Mitsubishi Heavy Industries, 676-0008 Takasago, Japan

rohit.arora.y8, tomohiro.akaki.2k, hiroyuki.kanazawa.57@mhi.com

<sup>2</sup> Fluid Dynamics Research Department

Research & Innovation Center

Mitsubishi Heavy Industries, 676-0008 Takasago, Japan

atsushi.nakagawa.qs, tomoshige.takata.pz@mhi.com

## EXTENDED ABSTRACT

### 1 Introduction

Cardboard boxes are the most familiar form of packaging and are a key part of the world's logistics and commodity distribution systems. Mitsubishi Heavy Industries, Ltd. (MHI) has been manufacturing box making machinery since 1955. In this paper, we will validate the co-simulation between multibody dynamics model simulating the motion of cardboard inside the counter-ejector portion of box making machine as shown in Figure 1, and fluid dynamics model simulating the fluid blown from the top duct over the cardboard sheet for robust stacking. Using validated model it will be possible to find operating condition that improves stability and reliability for transport and stacking of large cardboard sheet at high operating speed.

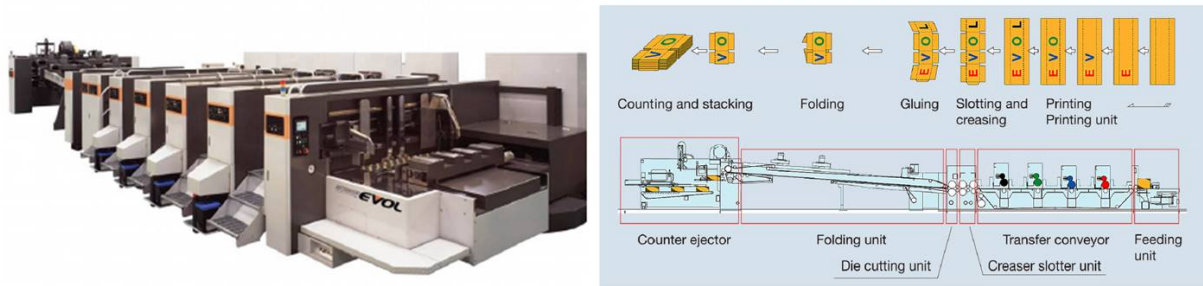


Figure 1: Basic configuration of a box making machine

### 2 Simulation of cardboard through counter ejector

Cardboard is modeled as a discrete beam model which is fed into counter ejector through rotating rollers as shown in Figure 2. As it passes, air blowing from duct pushes the cardboard down so that it gets stacked before the next cardboard enters the counter ejector section. Collision with front stoppers damps the kinetic energy of the cardboard. Co-simulation is done between multibody dynamics solver (MSC ADAMS) and fluid dynamics solver (ANSYS Fluent) through in-house coupling tool [1] which transfers force and deformation between different software.

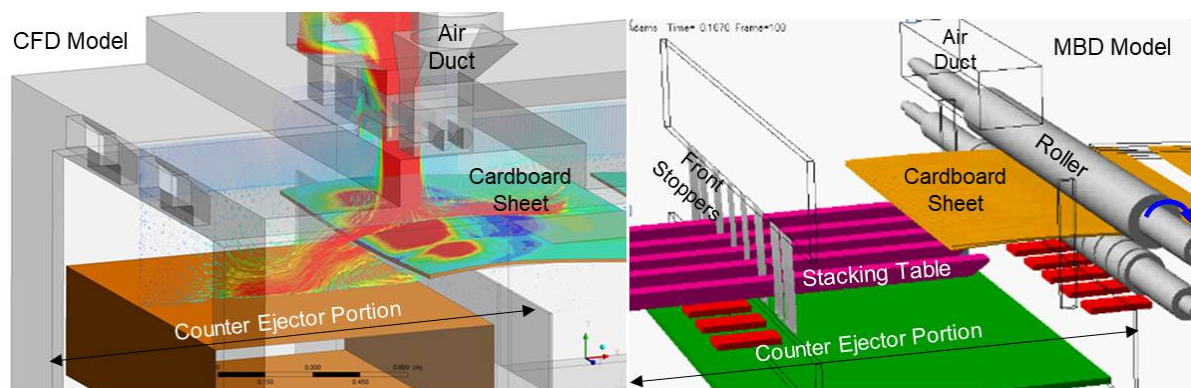


Figure 2: Representative CFD and MBD model of cardboard passing through counter ejector

### 3 Validation

Calibration of simulation model was done by measuring elemental stiffness and damping of cardboard sheet, pressure of airflow inside the counter ejector and various other contact parameters. After that trajectory of cardboard sheet was measured using laser

sensors and video imaging as shown in Figure 3 for different size of cardboard sheets with transport speed and gap between rollers as experimental parameter. We used the collected data for validating the model in order to confirm the prediction capability of co-simulation.

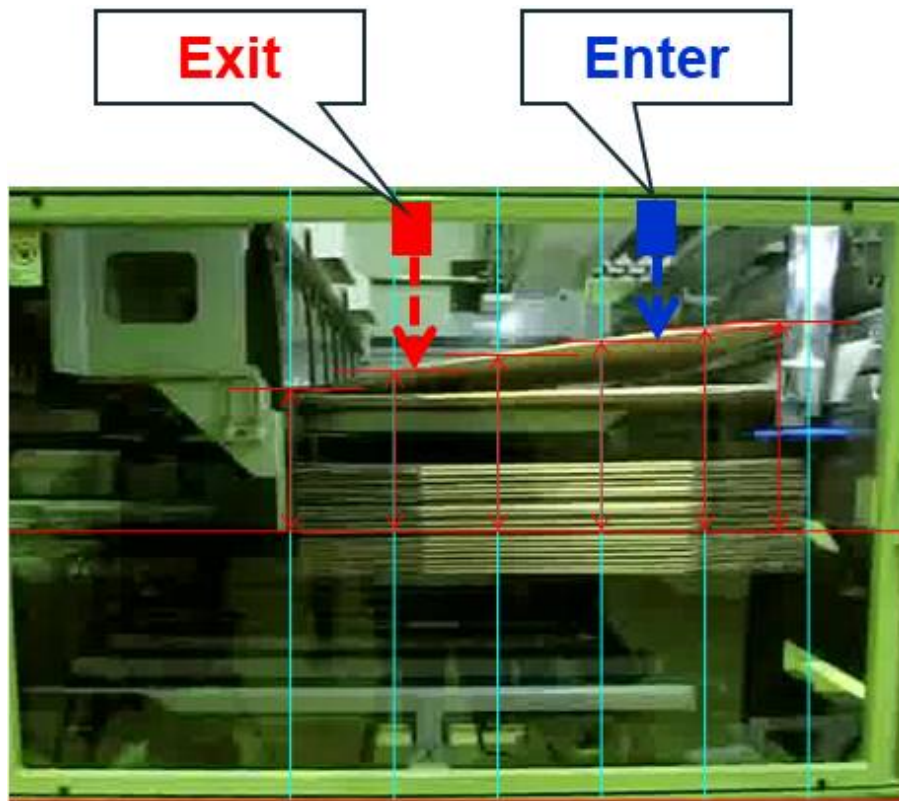


Figure 3: Deformation measurement through laser-sensor and video capture

## References

- [1] Arora, R.; Kanazawa, H.: Multibody, FEA and CFD simulation code coupling for fluid-solid interaction with large motion and non-linear deformation The 9th Asian Conference on Multibody Dynamics, 2018

# Development of a Cyber-Physical Test Bench for E-Powertrain Components

Borja Rodríguez<sup>1</sup>, A. J. Rodríguez<sup>1</sup>, D. Maceira<sup>1</sup>, F. Bottero<sup>1</sup>, E. Sanjurjo<sup>1</sup>,  
U. Lugrís<sup>1</sup>, M. Á. Naya<sup>1</sup>, F. González<sup>1</sup>, J. Cuadrado<sup>1</sup>

<sup>1</sup> Laboratorio de Ingeniería Mecánica  
University of A Coruña

Rúa Mendizábal s/n, 15403 Ferrol, Spain

{borja.rfrade, antonio.rodriguez.gonzalez, diego.maceira, francisco.bottero, emilio.sanjurjo,  
urbano.lugris, miguel.naya, f.gonzalez, javier.cuadrado}@udc.es

## EXTENDED ABSTRACT

### 1 Introduction

Electric Vehicles (EVs) are complex systems made up of components with different nature and dynamic response. As such, they can be considered multiphysics systems, in which mechanical, hydraulic, electric, electronic, and thermal effects, among others, play an important role during operation and interact with each other. For instance, the performance of electrical and mechanical components in EV powertrains is intertwined with their thermal state. This complexity must be considered during the product development cycle and the operation time of the vehicle, not only at system level, i.e., from the point of view of the overall behaviour of the whole car, but also at component level. Traditionally, new automotive components, technologies, and designs have been validated by means of experimental tests with full-vehicle prototypes. This paradigm hinders the early detection of defects and design flaws, which are often revealed only after field tests have started. The profound and rapid transformations currently undergone by the automotive industry require, however, modern and flexible tools to test and validate new designs as early as possible, before vehicle prototypes are ready.

Model-Based System Testing (MBST) is emerging as an enabling technology to allow the experimental testing of components and algorithms from the early stages of product development cycle. MBST relies on the combined use of computer simulation and physical experiments to streamline both component and system design and testing [1]. Cyber-physical test benches, in which a real-world component under test is interfaced to a computer simulation of the overall system and its environment, are an application example of MBST technology. Figure 1 shows the conceptual scheme and flow of information of such a bench, aimed at testing electric motors for vehicle powertrains.

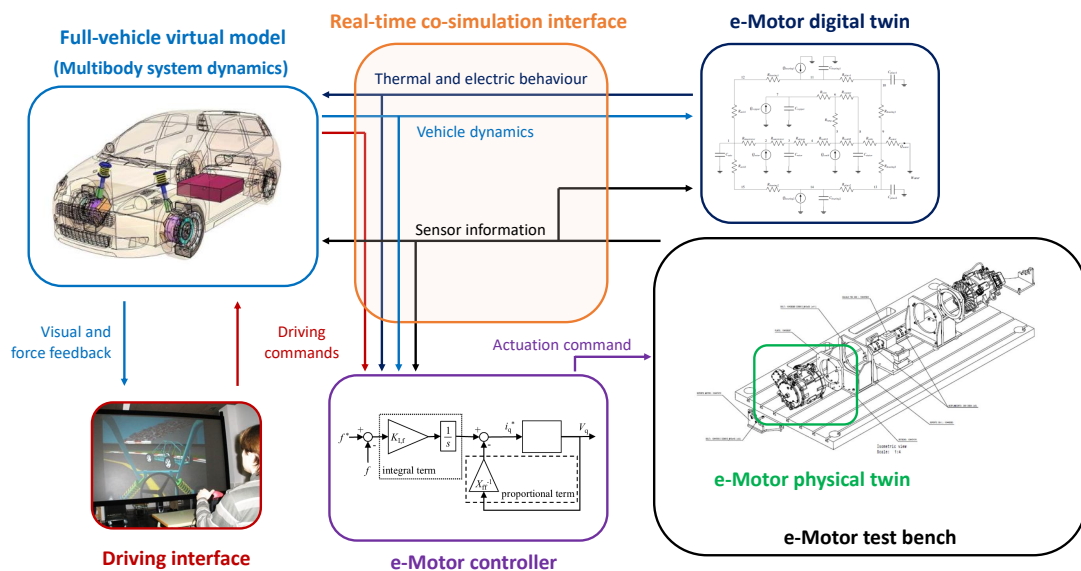


Figure 1: Elements of a cyber-physical test bench for e-powertrain motors.

In the test bench shown in Fig. 1, the motor under test is interfaced to a full-vehicle multibody system (MBS) dynamics simulation, which may reproduce a pre-defined manoeuvre or follow the commands of a human or virtual driver. The simulation determines the loads that the motor under test would have to bear during operation, and these are exerted by means of a second electric motor, in a back-to-back configuration [2]. Moreover, a digital twin (DT) of the motor is used to gain insight into the information provided by the sensors mounted on the system and monitor its behaviour beyond directly available measurements.



## 2 Research methodology

The operation of a cyber-physical test bench like the one described by Fig. 1 requires assembling together technologies from different engineering areas.

In the first place, real-time capable models, simulation methods, and implementations are a critical part in MBST setups. They must be detailed and accurate to guarantee reliable results, while complying with the predictability, compactness, and efficiency requirements of real-time applications. The proposed test bench requires this of the simulation of the MBS vehicle dynamics, and the electric behaviour and thermal effects within the motors [3].

The fidelity of computer simulations to the actual behaviour of the real-world systems that they represent needs to be ensured as well, so that the experimental results collected using the test bench correspond to the true performance of the components under test. The DT approach relies on a bi-directional exchange of information between the physical component and its virtual representation that enhances the accuracy of the latter, while enabling techniques like virtual sensing, which provide more information about the cyber-physical test bench than the one gathered by the system sensors alone or obtained from the simulation running on its own.

Finally, the physical-virtual interaction is orchestrated by means of a hybrid co-simulation environment, compatible with the Functional Mock-up Interface (FMI) standard.

## 3 Experimental setup

Our research team has designed and built two back-to-back cyber-physical test benches following the above-mentioned guidelines, as shown in figure 2.

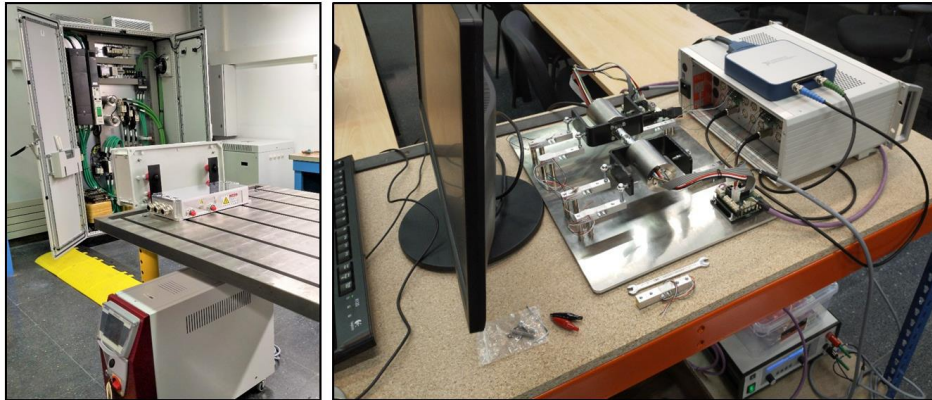


Figure 2: MBST cyber-physical test bench for e-powertrain motors, currently under construction (left) and fully operational scaled prototype (right).

A full-size testing facility for automotive-grade electric motors is currently under construction. The operation principles and implementation details are presently being tested in an already operational scaled prototype for low-power electric motors.

## Acknowledgments

The work reported here was supported by the HiPERFORM project, which has received funding from the ECSEL Joint Undertaking under grant agreement No. 783174, by AVL through the University Partnership Program, by the Ministry of Economy of Spain through project TRA2017-86488-R “Técnicas de co-simulación en tiempo real para bancos de ensayo en automoción” and the Ramón y Cajal program, contract No. RYC-2016-20222, and by the Galician Government under grant ED431B2016/031.

## References

- [1] F. Marques dos Santos, R. Pastorino, B. Peeters, C. Faria, W. Desmet, L. Goes, and H. Van der Auweraer. Model based system testing: Bringing testing and simulation close together. In: Wicks A., Niezrecki C. (eds) Structural Health Monitoring, Damage Detection & Mechatronics, 7:91-97, Springer, 2016.
- [2] E. V. Beyerleyn, P. V. Tyuteva. Energy Efficiency of Back-to-back Method for Induction Traction Motors Testing. 15th International Conference of Young Specialists on Micro/Nanotechnologies and Electron Devices (EDM), pages 359-361, Novosibirsk, Russia, 2014.
- [3] B. Rodríguez, F. González, M. Á. Naya, J. Cuadrado, Assessment of Methods for the Real-Time Simulation of Electronic and Thermal Circuits, *Energies*, 13(6):paper 1354, 2020.



**Section**

**FLEXIBLE MULTIBODY DYNAMICS**

**FLEX-1-2-3**

# An Improved Absolute Coordinate Formulation (ACF) for Flexible Multibody Dynamics

Andreas Zwölfer<sup>1</sup>, Johannes Gerstmayr<sup>2</sup>

<sup>1</sup> Technical University of Munich  
School of Engineering & Design  
Department of Mechanical Engineering  
Chair of Applied Mechanics  
Boltzmannstr. 15, 85748 Garching, Germany  
andreas.zwoelfer@tum.de

<sup>2</sup> University of Innsbruck  
Department of Mechatronics  
Technikerstr. 13, 6020 Innsbruck, Austria  
johannes.gerstmayr@uibk.ac.at

## EXTENDED ABSTRACT

### 1 Introduction

Flexible multibody (MB) dynamics refers to the computational strategies used to determine time histories of motion, deformation, strain, and stress of interconnected components undergoing large overall motion due to applied forces, constraints, contact, and initial conditions. Often linearly-elastic MB simulations, where the bodies flexibility is taken into account under the assumption of small deformations and strains, and a linear constitutive law, are sufficient for engineering systems. Linearly-elastic flexible MB formulations are usually based on a co-rotational / moving frame approach. The well-known representatives are the floating frame of reference formulation (FFRF) [1, 2] and the absolute coordinate formulation (ACF) [3, 4] (not to be mixed up with the absolute nodal coordinate formulation (ANCF)). Both formulations are based on a body-fixed coordinate system, which allows to use small strain measures, and may be employed to model arbitrary geometries discretized with solid finite elements (FEs). The advantage of the FFRF is that within the body-fixed floating frame the local flexible coordinates may be easily reduced using well-established modal reduction methods. Extensions are available to employ modal reduction also within the ACF framework, i.e., the so-called generalized component mode synthesis (GCMS) [5, 6] or extensions thereof [7], however, realized at the expense of a nine-fold increase of the flexible modal coordinates. Which is why, the FFRF prevailed in the MB community, despite the linear configuration space associated with the ACF, which yields a constant mass matrix. Nevertheless the ACF is popular within the FE community because it is a tailor-made FE formulation for the efficient high-fidelity simulation of systems undergoing large rigid body (RB) motions – the efficiency stems from the fact the Jacobi matrix may be pre-factorized once and for all times [3].

Looking at the equations of motion (EOMs) of the ACF [4], we have,

$$\bar{\mathbf{M}}\ddot{\mathbf{c}} + \mathbf{A}_{\text{bd}}\bar{\mathbf{K}}\mathbf{A}_{\text{bd}}^T\mathbf{c}_f + \mathbf{c}_f^T \frac{\partial \mathbf{A}_{\text{bd}}}{\partial \mathbf{c}^T} \bar{\mathbf{K}}\mathbf{A}_{\text{bd}}^T\mathbf{c}_f + \frac{\partial \mathbf{g}}{\partial \mathbf{c}^T} \boldsymbol{\lambda} = \mathbf{f}, \quad (1)$$

where  $\bar{\mathbf{M}}$  and  $\bar{\mathbf{K}}$  denote the constant mass and stiffness matrix from the underlying linear FE model, respectively,  $\mathbf{c}$  denotes the global nodal displacements,  $\mathbf{A}_{\text{bd}} = \text{diag}(\mathbf{A}, \dots, \mathbf{A})$  with rotation matrix  $\mathbf{A}$ ,  $\mathbf{c}_f$  is the flexible part of  $\mathbf{c}$ ,  $\mathbf{g}$  denotes the constraint equations with Lagrange multipliers  $\boldsymbol{\lambda}$ , and  $\mathbf{f}$  are the applied nodal forces. In comparison to the ACF, the FFRF EOMs read [2],

$$\mathbf{L}_F^T \bar{\mathbf{M}} \mathbf{L}_F \ddot{\mathbf{q}}_F + \mathbf{L}_F^T \bar{\mathbf{M}} \dot{\mathbf{L}}_F \dot{\mathbf{q}}_F + \text{diag}(\mathbf{0}, \mathbf{0}, \bar{\mathbf{K}}) \mathbf{q}_F + \mathbf{L}_F^T \frac{\partial \mathbf{g}}{\partial \mathbf{c}^T} \boldsymbol{\lambda} = \mathbf{L}_F^T \mathbf{f}, \quad (2)$$

where  $\mathbf{L}_F = \mathbf{L}_F(\mathbf{q}_F)$  is the coordinate Jacobi matrix between  $\mathbf{c}$  and the floating frame degrees of freedom (DOFs)  $\mathbf{q}_F$ . It is clear that we have highly non-linear stiffness terms but linear inertia forces when choosing  $\mathbf{c}$  as DOFs (1), or highly non-linear inertia terms but linear elastic forces when decomposing the DOFs into RB motion and local elastic deformation (2).

This contribution tries to combine RB DOFs with global elastic deformation DOFs to reduce the non-linearity of the conventional ACF (1). In doing so, the necessity to calculate the RB motion from the global nodal displacement field to obtain  $\mathbf{c}_f = \mathbf{c}_f(\mathbf{c})$  and  $\mathbf{A}_{\text{bd}} = \mathbf{A}_{\text{bd}}(\mathbf{c})$  becomes also obsolete. Hence, this paper drafts the idea of an improved ACF.

### 2 The method in a nutshell

Let us consider a representative FE-discretized body of a system with an attached floating frame  $\bar{\mathcal{F}}$ ; the origin of  $\bar{\mathcal{F}}$  is translated by  $\mathbf{q}_t$  with respect to (w.r.t.) the origin of the inertial frame  $\mathcal{F}$  and their orientations are related by the rotation matrix  $\mathbf{A}$ . Hence, the current position of the FE nodes is given by a RB translation, a RB rotation, and a flexible term [4, 2]

$$\mathbf{r} = \Phi_t \mathbf{q}_t + \mathbf{A}_{\text{bd}} \bar{\mathbf{x}} + \mathbf{c}_f, \quad (3)$$

with  $\Phi_t = [\mathbf{I} \ \dots \ \mathbf{I}]^T$ , where  $\mathbf{I}$  denotes the identity matrix, and  $\bar{\mathbf{x}}$  denoting the reference positions of the FE nodes in  $\bar{\mathcal{F}}$ . Eq. (3) reveals that the configuration of the flexible body is fully described by the translation of  $\bar{\mathcal{F}}$ , the rotation matrix, and the flexible deformation. Hence, these quantities are a suitable choice for the DOFs, i.e.,

$$\mathbf{q} = [\mathbf{q}_t^T \ \mathbf{a}^T \ \mathbf{c}_f^T]^T, \quad (4)$$

where  $\mathbf{a} = \text{vec}(\mathbf{A}^T)$ . This specific choice leads to a linear mapping between the nodal positions and the DOFs,

$$\mathbf{r} = [\Phi_t \quad (\bar{\mathbf{X}} \otimes \mathbf{I}) \mathbf{B} \quad \mathbf{I}_{\text{bd}}] \mathbf{q} = \mathbf{L} \mathbf{q}, \quad (5)$$

where  $\mathbf{L}$  is constant.  $\mathbf{B}$  is a constant Boolean matrix such that  $\text{vec}(\mathbf{A}) = \mathbf{B} \text{vec}(\mathbf{A}^T)$ ,  $\mathbf{I}_{\text{bd}} = \text{diag}(\mathbf{I}, \dots, \mathbf{I})$ ,  $\bar{\mathbf{X}}$  contains the reference nodal position of node  $i$  in row  $i$  in contrast to the stacked notation of  $\bar{\mathbf{x}}$ , and  $\otimes$  denotes Kronecker's product. Hence,

$$\dot{\mathbf{r}} = \mathbf{L} \dot{\mathbf{q}}, \quad (6)$$

which yields a constant mass matrix and no quadratic velocity vector, since  $\mathbf{L} = \text{const.} \Rightarrow \dot{\mathbf{L}} = \mathbf{0}$ , see the contrast in (2).

The EOMs may then be derived concisely (exploiting (5) and (6)) via Lagrange's equation for a general mechanical system, i.e.,

$$\underbrace{\frac{d}{dt} \left( \frac{\partial T}{\partial \dot{\mathbf{q}}^T} \right)}_{\text{inertia forces}} - \underbrace{\frac{\partial T}{\partial \mathbf{q}^T}}_{\text{elastic forces}} + \underbrace{\frac{\partial V}{\partial \mathbf{q}^T}}_{\text{constraint forces}} + \underbrace{\frac{\partial \mathbf{g}}{\partial \mathbf{q}^T} \boldsymbol{\lambda}}_{\text{applied forces}} = \underbrace{\frac{\partial \mathbf{r}}{\partial \mathbf{q}^T} \mathbf{f}}. \quad (7)$$

Note that linearly-elastic MB systems discretized via isoparametric FEs are fully described by [4, 2]

$$T = \frac{1}{2} \dot{\mathbf{r}}^T \bar{\mathbf{M}} \dot{\mathbf{r}}, \quad (8)$$

$$V = \frac{1}{2} \bar{\mathbf{c}}_f^T \bar{\mathbf{K}} \bar{\mathbf{c}}_f, \quad (9)$$

with the kinetic energy  $T$  and the strain energy  $V$ . Hence, the EOMs read

$$\begin{bmatrix} \Phi_t^T \bar{\mathbf{M}} \Phi_t & \Phi_t^T \bar{\mathbf{M}} (\bar{\mathbf{X}} \otimes \mathbf{I}) \mathbf{B} & \Phi_t^T \bar{\mathbf{M}} \\ \text{sym.} & \mathbf{B}^T (\bar{\mathbf{X}} \otimes \mathbf{I})^T \bar{\mathbf{M}} (\bar{\mathbf{X}} \otimes \mathbf{I}) \mathbf{B} & \mathbf{B}^T (\bar{\mathbf{X}} \otimes \mathbf{I})^T \bar{\mathbf{M}} \\ & & \bar{\mathbf{M}} \end{bmatrix} \begin{bmatrix} \dot{\mathbf{q}}_t \\ \dot{\mathbf{a}} \\ \dot{\mathbf{c}}_f \end{bmatrix} + \begin{bmatrix} \mathbf{0} & \mathbf{0} & \mathbf{0} \\ \text{sym.} & (\mathbf{C}_f \otimes \mathbf{I})^T \bar{\mathbf{K}} (\mathbf{C}_f \otimes \mathbf{I}) & \mathbf{0} \\ & & \mathbf{A}_{\text{bd}} \bar{\mathbf{K}} \mathbf{A}_{\text{bd}}^T \end{bmatrix} \begin{bmatrix} \mathbf{q}_t \\ \mathbf{a} \\ \mathbf{c}_f \end{bmatrix} + \frac{\partial \mathbf{g}}{\partial \mathbf{q}^T} \boldsymbol{\lambda} = \begin{bmatrix} \Phi_t^T \\ \mathbf{B}^T (\bar{\mathbf{X}} \otimes \mathbf{I})^T \\ \mathbf{I}_{\text{bd}} \end{bmatrix} \mathbf{f}, \quad (10)$$

where  $\mathbf{C}_f$  is the rearranged version of  $\mathbf{c}_f$  in analogy to  $\bar{\mathbf{X}}$  and  $\bar{\mathbf{x}}$ , as mentioned before.

### 3 Conclusion

This contribution drafts the idea of an improved ACF, which (i) reduces the non-linearity compared to the conventional ACF (1) and (ii) eliminates the necessity to calculate the RB motion from the global nodal displacement field to obtain  $\mathbf{c}_f = \mathbf{c}_f(\mathbf{c})$  and  $\mathbf{A}_{\text{bd}} = \mathbf{A}_{\text{bd}}(\mathbf{c})$  (1) via a clever choice of DOFs (4). This approach yields a constant mass matrix, a co-rotated stiffness matrix in the flexible part, and a “small” non-linear stiffness matrix in the RB rotation part (10).

Combining linearised Tisserand constraints with the orthogonality condition of the rotation matrix as reference conditions may eliminate coupling within the mass matrix, or other reference constraints may eliminate the non-linearity in the rotation part of the EOMs. The influence of the choice of the reference conditions and the applicability of, e.g., methods of snapshots to reduce the number of DOFs need to be investigated.

### References

- [1] A. A. Shabana. Dynamics of multibody systems, 4th edn. Cambridge University Press, Cambridge, 2013.
- [2] A. Zwölfer, J. Gerstmayr. The nodal-based floating frame of reference formulation with modal reduction. *Acta Mech.* **232**: 835–851, 2021.
- [3] J. Gerstmayr, J. Schöberl. A 3D finite element method for flexible multibody systems. *Multibody Syst. Dyn.* **15**(4): 305–320, 2006.
- [4] A. Zwölfer, J. Gerstmayr. Co-rotational formulations for 3D flexible multibody systems: A nodal-based approach. In: H. Altenbach et al., eds., *Contributions to Advanced Dynamics and Continuum Mechanics*, Springer, Cham, 2019.
- [5] A. Pechstein, D. Reischl, J. Gerstmayr. A generalized component mode synthesis approach for flexible multibody systems with a constant mass matrix. *ASME. J. Comput. Nonlinear Dynam.* **8**(1): 011019/1–011019/10, 2013.
- [6] A. Zwölfer, J. Gerstmayr. Preconditioning strategies for linear dependent generalized component modes in 3D flexible multibody dynamics. *Multibody Syst. Dyn.* **47**(1): 65–93, 2019.
- [7] M. Vermaut, F. Naets, W. Desmet. A flexible natural coordinates formulation (FNCF) for the efficient simulation of small-deformation multibody systems. *Int. J. Numer. Methods. Eng.* **115**(11): 1353–1370, 2018.

# Computation of Internal Forces in Beam Elements with Constrained Torsional Warping

Koen Dwarshuis, Ronald Aarts, Marcel Ellenbroek, Dannis Brouwer

Faculty of Engineering Technology  
University of Twente  
P.O. Box 217, 7500 AE Enschede, The Netherlands  
[k.s.dwarshuis, r.g.k.m.aarts, m.h.m.ellenbroek, d.m.brouwer]@utwente.nl

## EXTENDED ABSTRACT

### 1 Introduction

Modelling structures by beam-elements allows for very efficient computation of stress as result of (large) deformation. Beams can for example be used to model the leafsprings in flexure based mechanisms [1]. The stress computation can be divided in three steps, see Figure 1. 1) computation of the deformation and reaction forces in the mechanism. 2) computation of the internal forces and moments in each beam element on a finite number of points along the beam axis. 3) computation of the stress distributions over the cross sections based on the internal forces. The first purpose of this work is to show three methods to compute the internal forces (i.e. step 2). All methods give the same result if the deformation in each beam element is small. For larger deformations the results of the methods differ. The most accurate method is determined.

Torsion of a rectangular beam element causes warping of the cross section. This warping is constrained at clamped sides of leafsprings which causes significant extra stiffness and stress [2]. This effect can be included in a beam element by introducing two extra deformation modes, e.g. [3,4]. The total torsional moment is in this case composed of the Saint-Venant torsion and a contribution of the bimoment [2], (the bimoment is the internal force related to the warping). The second purpose of this work is to propose a method to accurately obtain the Saint-Venant torsion and bimoment, which are essential for computing the stress as a result of torsion.

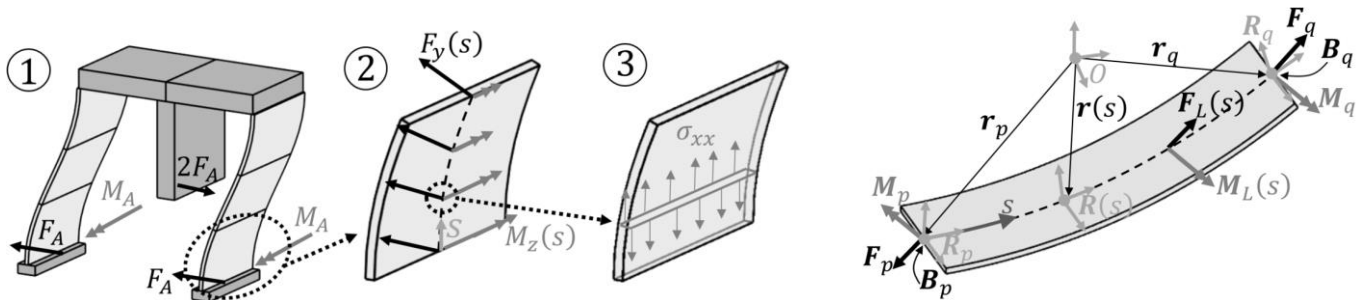


Figure 1: Left: three steps in the stress-computation, right: forces and positions of a beam element

### 2 Method

In step 1 the following is computed: at each node the forces ( $F_p = -F_q$ ), moments ( $M_p, M_q$ ), the bimoments ( $B_p, B_q$ ), its position ( $r_p, r_q$ ) and orientation ( $R_p, R_q$ ), see Figure 1. The internal positions,  $r(s)$ , and orientations,  $R(s)$ , can be obtained based on the deformation modes. Based on this information, three different method can be used to compute the internal forces:

1. Based on equilibrium:  $\{F_x, F_y, F_z\}^T = F_L(s) = R^T(s)F_q$ ,  $\{M_x, M_y, M_z\}^T = M_L(s) = R^T(s)(M_p + (r(s) - r_q) \times F_q)$
2. Based on the deformation modes. The mode shapes define the local displacement in the beam, which are related to the internal forces. For example the axial force is related to the axial displacement and the internal bending moments are related to the curvatures:  $F_x(s) = EAu'_x(s)$ ,  $M_z(s) = EI_z\phi'_z(s)$
3. Load interpolation functions: If a beam-formulation [4] is used that is based on the Hellinger-Reissner formulation, the load interpolation functions can be used to define internal forces.

In order to compute the stress as a result of torsion the Saint-Venant torsion,  $T_x$ , and the bimoment,  $B$ , have to be computed. Both are related to a derivative of the torsion angle and can therefore be obtained based on the mode-shapes:

$$B(s) = -EI_\omega \phi'_x(s), T_x(s) = GI_t \phi'_x(s). \quad (1)$$

The bimoment can optionally also be obtained by a linear interpolation between its values at the nodes ( $B_p, B_q$ ). However these methods are not very accurate. A better approximation can be obtained based on their relation with the total moment [2] which can be rewritten to a second order differential equation in  $T_x$  by using eq. (1):

$$M_x(s) = T_x(s) + B'(s) \Rightarrow M_x(s) = T_x(s) - EI_\omega/GI_t \cdot T_x''(s) \quad (2)$$

The boundary-conditions for this differential equation are that the Saint-Venant torsion at the both clamped sides of the leafspring equals zero. Based on this the differential-equation can be solved for  $T_x(s)$  based on which the bimoment  $B(s)$  can be obtained.

### 3 Results

The three methods are applied to a leafspring with properties: length:  $L = 100$  mm, width: 10 mm, thickness: 0.3 mm, material elasticity:  $E = 200$  GPa, Poisson ratio: 0.3. The left side of the beam is fixed to the ground and the right side is subjected to two different loading conditions.

- Bending: 50 mm displacement in the y-direction;
- Combined: 20 mm displacement in the y-direction, 20° torsion and zero rotation around the z-axis.

Figure 2 indicates that all three methods give the same result if many beam elements are used, and that the equilibrium-method gives in general the best results. Figure 3 shows results for the methods to obtain the bimoment and Saint-Venant torsion, indicating that the method based on the differential-equation gives very accurate results.

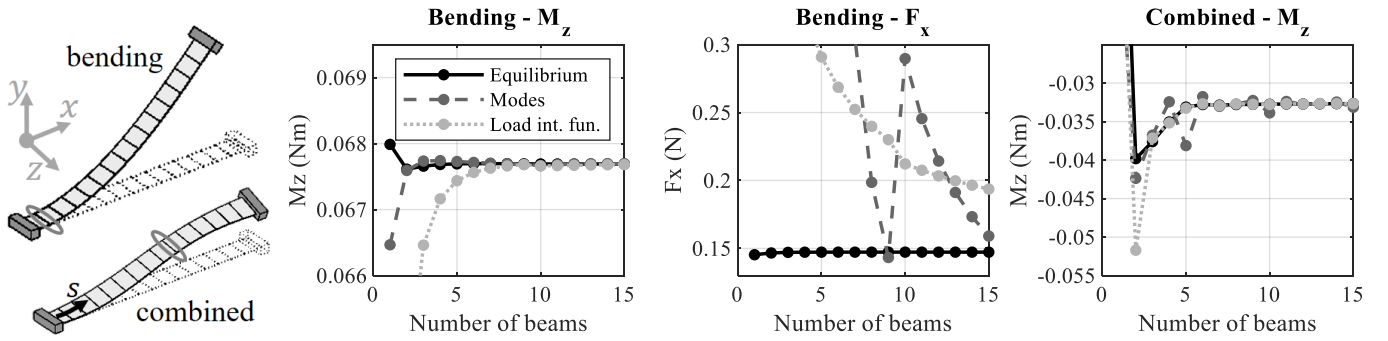


Figure 2: Two load-cases and the resulting internal forces evaluated at  $s = 0.1L$  for bending and  $s = 0.6L$  for combined.

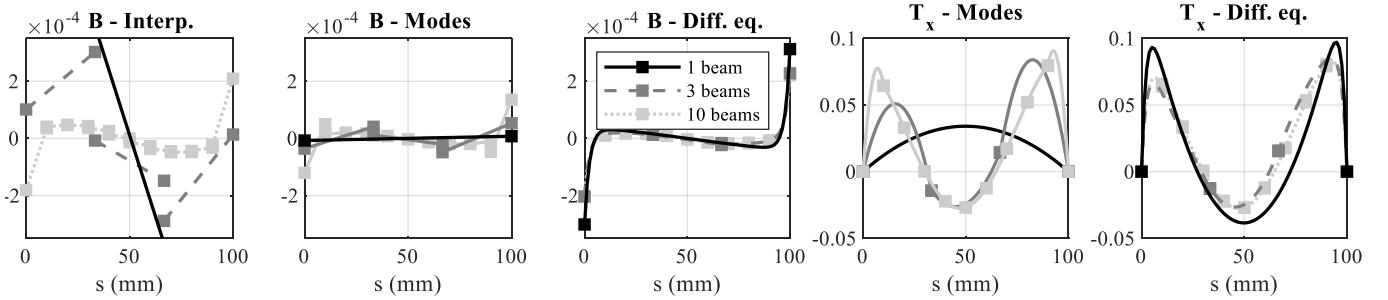


Figure 3: Bimoment and Saint-Venant torsion of the combined load-case for a leafspring modelled with 1, 3 and 10 beams.

### 4 Conclusions

This work shows three methods to obtain the internal forces in a beam element, which are essential to compute the stress. The most accurate method uses equilibrium to obtain internal forces. The bimoment and Saint-Venant torsion can accurately be obtained by an analytic solution of the differential equation that relates the total torsional moment to the Saint-Venant torsion.

### Acknowledgments

This work is part of the research programme HTSM 2017 with project number 16210, which is partly financed by the Netherlands Organisation for Scientific Research (NWO)

### References

- [1] S.E. Boer, R.G.K.M. Aarts, D.M. Brouwer and J.B. Jonker. Multibody modelling and optimization of a curved hinge flexure, in The 1st joint international conference on multibody system dynamics, Lappeenranta. 2010.
- [2] V.Z. Vlasov, Thin-walled elastic beams, Jerusalem: Israel program for scientific translations. 1961.
- [3] J.B. Jonker. Implementation of shear deformable thin-walled beam element for flexible multibody dynamics, in Proceedings of the 8th ECCOMAS thematic conference on multibody dynamics 2017, Prague, Czech Republic. 2017
- [4] M. Nijenhuis, J. Meijaard and D.M. Brouwer, A spatial closed-form nonlinear stiffness model for sheet flexures based on a mixed variational principle including third-order effects, Precision Engineering, 2020. **66**: p. 429-444.

# Modelling of Dielectric Elastomer Actuated Flexible Multibody Dynamics

Dengpeng Huang, Sigrid Leyendecker

Institute of Applied Dynamics  
Friedrich-Alexander-Universität Erlangen-Nürnberg  
Immerwahrstrasse 1, 91058 Erlangen, Germany  
dengpeng.huang@fau.de

## EXTENDED ABSTRACT

### 1 Introduction

Soft actuators are highly demanded for the actuation of soft robotics, micro robotics and biomedical devices. Because of their high efficiency in energy and flexibility in motion, the Dielectric Elastomer Actuators (DEAs) have served as artificial muscles for soft robotics, see e.g. [1, 2, 3] and [4]. The DEA cell is essentially made with the dielectric elastomer sandwiched between two electrodes. When the electrodes are charged, the electrostatic pressure will be induced in the dielectric elastomer leading to the deformation of the DEA cell. In real applications, the DEAs are usually composed by multiple stacked DEA cells to obtain large deformations. To efficiently predict and control the deformation of the DEAs, numerical modelling of the electromechanically coupled problem in dielectric elastomers is required.

The fundamental theory of nonlinear electroelasticity has been addressed by e.g. [5] and [6]. Constitutive models of dielectric elastomers have been investigated by e.g. [8] and [7]. In [9], a viscoelastic 3D finite element model is developed for the simulation of DEAs. This 3D finite element model is coupled with rigid bodies in [10]. Since a large number of degrees of freedom is required in the simulation of stacked DEAs by the 3D finite element method, the computation is very cost expensive for large systems. Additionally, some effort has to be made for the coupling between 3D finite element models and rigid bodies in multibody system. To cope with these challenges, the electromechanically coupled Cosserat beam model is developed for the simulation of DEAs recently in [11]. By applying proper electrical potentials on the electrodes, the developed beam model allows for multiple deformation modes, including contraction, bending, shear and torsion. It is also possible to combine different deformation modes in one beam to generate complex deformations.

To provide the actuation for robotic applications, the beam model for DEAs introduced above is extended to the multibody system dynamics in this work. The governing equations, the kinematic variables as well as the constitutive law for the beam DEA model will be introduced firstly. Then, the electromechanical coupling problem is solved within the variational time integration scheme with null space projection. The performance of the developed model will be demonstrated in the numerical examples.

### 2 DEA beam model

By treating the electric potential  $\phi_o$  at beam centroid and the incremental variables  $(\alpha, \beta)$  in the cross section as the electric degrees of freedom  $\boldsymbol{\phi} = [\phi_o \quad \alpha \quad \beta]^T$ , the configuration of the Cosserat beam model is extended to

$$\mathbf{q} = [\boldsymbol{\phi} \quad \mathbf{d}_1 \quad \mathbf{d}_2 \quad \mathbf{d}_3 \quad \boldsymbol{\phi}]^T \quad (1)$$

with  $\boldsymbol{\phi}$  the coordinate of beam centroid and  $\mathbf{d}_i (i = 1, 2, 3)$  the orthonormal triad. Corresponding to the electric potential, the electric field at  $(X^1, X^2, s)$  in the beam can be computed, see [11], as

$$\mathbf{E}^e = - \left[ \alpha(s, t) \mathbf{d}_1(s, 0) + \beta(s, t) \mathbf{d}_2(s, 0) + \left( \frac{\partial \phi_o(s, t)}{\partial s} + X^1 \frac{\partial \alpha(s, t)}{\partial s} + X^2 \frac{\partial \beta(s, t)}{\partial s} \right) \mathbf{d}_3(s, 0) \right]. \quad (2)$$

The extended Neo-Hookean model for the dielectric elastomer [9] is applied in the beam formulation by integrating the strain energy in the continuum over the beam cross section. The beam strain energy is given by

$$\Omega_b(\boldsymbol{\Gamma}, \mathbf{K}, \boldsymbol{\varepsilon}) = \int_{\Sigma} \Omega(\mathbf{C}, \mathbf{E}^e) dA, \quad (3)$$

where  $\boldsymbol{\Gamma}$  and  $\mathbf{K}$  are the beam stain measures,  $\boldsymbol{\varepsilon}$  is the strain-like variable conjugated with the electric displacement of the beam and  $\mathbf{C}$  is the right Cauchy Green tensor. The continuous Lagrangian is composed by the kinetic energy  $T(\dot{\mathbf{q}})$  and the internal potential energy  $V(\mathbf{q})$  with

$$L(\mathbf{q}, \dot{\mathbf{q}}) = T(\dot{\mathbf{q}}) - V(\mathbf{q}). \quad (4)$$

For the coupled hyperelastic material in a DEA, the internal potential energy is computed by an integration of the beam strain energy density  $\Omega_b$  in Eq. (3) over the line of centroids

$$V(\mathbf{q}) = \int_l \Omega_b(s) ds. \quad (5)$$

The system is semi-discretized with 1D finite elements. Then a temporal discretization, in particular the discrete EulerLagrange equations can be obtained by taking the variation of the discrete action and requiring stationarity. To eliminate the constraint forces from the system, the nodal reparametrisation  $\mathbf{q}_{n+1} = \mathbf{F}_d(\mathbf{u}_{n+1}, \mathbf{q}_n)$  and the discrete null space matrix  $\mathbf{P}_d$  are applied to the discrete EulerLagrange equations leading to

$$\mathbf{P}_d^T(\mathbf{q}_n) \left[ \frac{\partial L_d(\mathbf{q}_{n-1}, \mathbf{q}_n)}{\partial \mathbf{q}_n} + \frac{\partial L_d(\mathbf{q}_n, \mathbf{F}_d(\mathbf{u}_{n+1}, \mathbf{q}_n))}{\partial \mathbf{q}_n} + \mathbf{f}_n^{\text{ext}-} + \mathbf{f}_{n-1}^{\text{ext}+} \right] = \mathbf{0}, \quad (6)$$

where  $\mathbf{u}_{n+1}$  is the generalized configuration acting as the unknown variable,  $L_d$  is the discrete Lagrange, and  $\mathbf{f}_n^{\text{ext}-}$  and  $\mathbf{f}_{n-1}^{\text{ext}+}$  are the discrete generalized external forces.

### 3 Results

According to the specific application scenarios, several multibody systems actuated by DEAs will be developed in the numerical results. One of the examples is the robotic arm holding a package, where the flexible robotic arm is modeled by the beam and the package is treated as a rigid body. As shown in Fig. 1, by applying a nonuniform electric potential on the beam cross sections, the bending of the beam is induced and the package can be moved onto the desk.

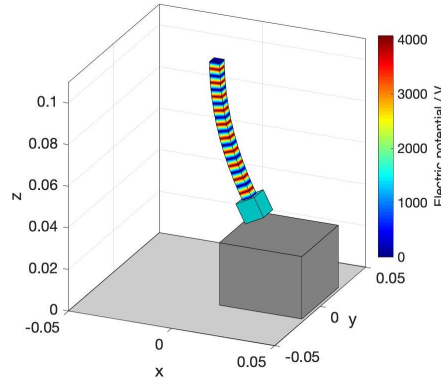


Figure 1: Robotic arm actuated by dielectric elastomer

### References

- [1] Yoseph Bar-Cohen. Electroactive polymers as artificial muscles: capabilities, potentials and challenges. In *Robotics 2000*, pages 188-196, 2000.
- [2] C Löwe, X Zhang, and G Kovacs. Dielectric elastomers in actuator technology. *Advanced Engineering Materials*, 7(5):361-367, 2005.
- [3] G Kovacs, L During, S Michel, and G Terrasi. Stacked dielectric elastomer actuator for tensile force transmission. *Sensors and actuators A: Physical*, 155(2):299-307, 2009.
- [4] Mihai Duduta, Ehsan Hajiesmaili, Huichan Zhao, Robert J Wood, and David R Clarke. Realizing the potential of dielectric elastomer artificial muscles. *Proceedings of the National Academy of Sciences*, 116(7):2476-2481, 2019.
- [5] DK Vu, P Steinmann, and G Possart. Numerical modelling of non-linear electroelasticity. *International Journal for Numerical Methods in Engineering*, 70(6):685-704, 2007.
- [6] A Dorfmann and RW Ogden. Nonlinear electroelasticity. *Acta Mechanica*, 174(3-4):167-183, 2005.
- [7] Zhigang Suo. Theory of dielectric elastomers. *Acta Mechanica Solida Sinica*, 23(6):549-578, 2010.
- [8] Xuanhe Zhao, Wei Hong, and Zhigang Suo. Electromechanical hysteresis and coexistent states in dielectric elastomers. *Physical review B*, 76(13):134113, 2007.
- [9] T Schlögl and S Leyendecker. Electrostatic-viscoelastic finite element model of dielectric actuators. *Computer Methods in Applied Mechanics and Engineering*, 299:421-439, 2016b.
- [10] T Schlögl and S Leyendecker. Dynamic simulation of dielectric elastomer actuated multibody systems. In *Smart Materials, Adaptive Structures and Intelligent Systems*, volume 50480, page V001T02A003. American Society of Mechanical Engineers, 2016a.
- [11] D Huang, and S Leyendecker. An electromechanically coupled beam model for dielectric elastomer actuators. *arXiv preprint arXiv:2103.06373*, 2021.



# Sloshing Dynamics Estimation for Liquid-filled Containers under 2-Dimensional Excitation

Roberto Di Leva<sup>1</sup>, Marco Carricato<sup>1</sup>, Hubert Gattringer<sup>2</sup>, Andreas Müller<sup>2</sup>

<sup>1</sup>Department of Industrial Engineering  
University of Bologna  
Viale del Risorgimento 2, 40136 Bologna, Italy  
[roberto.dileva, marco.carricato]@unibo.it

<sup>2</sup> Institute of Robotics  
Johannes Kepler University Linz  
Altenberger Straße 69, 4040 Linz, Austria  
[hubert.gattringer, a.mueller]@jku.at

## EXTENDED ABSTRACT

### 1 Introduction

The transport of containers filled with liquids finds application in several industrial cases, e.g. in food&beverage or pharmaceutical production and packaging lines. Typically, the manipulation of such containers is assigned to linear transport systems or to industrial serial robots, and the motion that is required to carry out the task is usually planar. The prediction of the liquid behavior inside the container (also known as liquid *sloshing*), under given motions of the container itself, is important to check whether the liquid would overflow, thus interrupting the industrial process. Additionally, a reliable sloshing prediction model can be exploited to limit the stirring of the liquid during task execution. This paper presents the validation of a model for estimation of the liquid maximum sloshing height (MSH), taking into account 2-dimensional planar motions of a cylindrical container.

### 2 State of the Art and Methods

The literature considers two main discrete approaches for the modelling of sloshing dynamics inside a container subject to 2-dimensional planar motion: a spherical pendulum [1] and a 2-dof mass-spring-damper system [2]. In both cases, the trajectories that are obtained from the resolution of the equivalent equations of motion (EOMs) are then employed to compute the MSH of the liquid. Among the several techniques that can be found in the literature, a novel method, proposed in [3] and based on the mass-spring-damper model, will here be used. This model was validated for rectilinear motions: the authors proposed the possible extension to planar motions, but no validation was provided to this case. The latter is the objective of this article.

### 3 Sloshing Model

We will consider a cylindrical container of radius  $R$ , filled with a liquid of height  $h$  and mass  $m_F$ . A simplified equivalent mechanical model can be used to reproduce the liquid sloshing dynamics. In particular, the mass-spring-damper model comprises a rigid mass  $m_0$  that moves rigidly with the container, and a series of masses  $m_n$ , with each of them representing the equivalent mass of each sloshing mode. Each modal mass  $m_n$  is restrained by a spring  $k_n$  and a damper  $c_n$ .

Table 1: Required conditions on a discrete mechanical model to be representative of the liquid sloshing dynamics.

The equivalent masses and moments of inertia must be preserved.	$m_F = m_0 + \sum_{n=1}^{\infty} m_n$ (1)
The height of the center of gravity must remain the same for small oscillations of the liquid.	$m_0 h_0 + \sum_{n=1}^{\infty} m_n h_n = 0$ (2)
The natural frequency associated with the $n$ -th mode must coincide with the one that can be obtained by the continuum model.	$\omega_n^2 = \frac{k_n}{m_n} = g \frac{\xi_{1n}}{R} \tanh(\xi_{1n} \frac{h}{R})$ (3)
The sloshing force acting on the container wall must be the same as the one calculated by the continuum model.	$m_n = m_F \frac{2R}{\xi_{1n} h (\xi_{1n}^2 - 1)} \tanh(\xi_{1n} \frac{h}{R})$ (4)

The model parameters can be determined by imposition of the equivalence conditions [4], which are shown in Table 1. In Equations (3) and (4),  $\xi_{1n}$  is the root of the derivative of the Bessel function of first kind with respect to the radial coordinate  $r$ , for the 1<sup>st</sup> circumferential mode and the  $n$ -th radial mode, while  $g$  is the gravity acceleration. The damping ratio  $\zeta_n$  can be determined by employing empirical formulas from the literature [4]. Depending on the assumption on the shape of the liquid free surface during motion, two mass-spring-damper models can be considered: the linear model (L model) and the nonlinear one (NL model).

### 4 Maximum Sloshing-Height Estimation

For a container under 2-dimensional planar motion on the horizontal  $xy$  plane, the excitation is provided by the container accelerations along the  $x$  and  $y$  directions, namely  $\ddot{\mathbf{S}}_0 = [\ddot{x}_0 \ \ddot{y}_0]^T$ . The L model considers two decoupled EOMs in the generalized coordinates  $\mathbf{s}_n = [x_n \ y_n]^T$  of the  $n$ -th mode:

$$\begin{cases} \ddot{x}_n + 2\zeta_n \omega_n \dot{x}_n + \omega_n^2 x_n = -\ddot{x}_0 \\ \ddot{y}_n + 2\zeta_n \omega_n \dot{y}_n + \omega_n^2 y_n = -\ddot{y}_0 \end{cases} \quad (5)$$

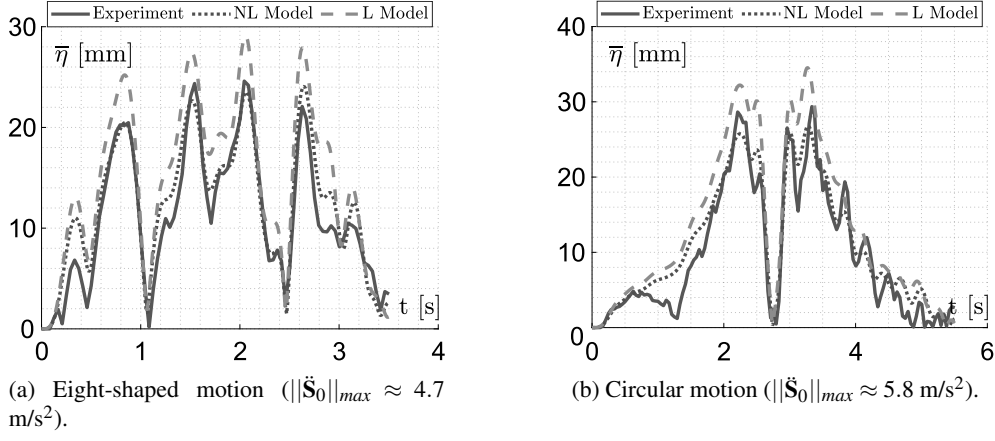


Figure 1: Comparison between the proposed models and the experimental results for an eight-shaped trajectory and a circular trajectory.

Under the assumption of a planar liquid free surface, the MSH of the  $n$ -th mode can be computed as:

$$\bar{\eta}_n = \frac{4hm_n}{m_F R} \sqrt{x_n^2 + y_n^2} \quad (6)$$

As far as the NL model is concerned, two coupled EOMs can be obtained:

$$\begin{cases} \ddot{x}_n + 2\omega_n \zeta_n [\dot{x}_n + C_n^2(\bar{x}_n^2 \dot{x}_n + \bar{y}_n \dot{y}_n \bar{x}_n)] + C_n^2(\bar{x}_n \dot{x}_n^2 + \bar{x}_n^2 \ddot{x}_n + \bar{x}_n \dot{y}_n^2 + \bar{x}_n \ddot{y}_n \bar{y}_n) + \omega_n^2 \bar{x}_n [1 + \alpha_n(\bar{x}_n^2 + \bar{y}_n^2)^{w-1}] + \frac{\ddot{x}_0}{R} = 0 \\ \ddot{y}_n + 2\omega_n \zeta_n [\dot{y}_n + C_n^2(\bar{y}_n^2 \dot{y}_n + \bar{x}_n \dot{x}_n \bar{y}_n)] + C_n^2(\bar{y}_n \dot{y}_n^2 + \bar{y}_n^2 \ddot{y}_n + \bar{y}_n \dot{x}_n^2 + \bar{y}_n \ddot{x}_n \bar{x}_n) + \omega_n^2 \bar{y}_n [1 + \alpha_n(\bar{x}_n^2 + \bar{y}_n^2)^{w-1}] + \frac{\ddot{y}_0}{R} = 0 \end{cases} \quad (7)$$

where  $\bar{x}_n = x_n/R$ ,  $\bar{y}_n = y_n/R$ . The NL model requires a nonlinear spring, with exponent  $w$  and coefficient  $\alpha_n \in [1/2, 2/3]$ . The liquid free surface is nonplanar and its shape can be described by means of a Bessel function. Analogously to the L-model case, the estimation of the  $n$ -th mode MSH can be computed as:

$$\bar{\eta}_n = \frac{\xi_{1n}^2 hm_n}{m_F R} \sqrt{x_n^2 + y_n^2} \quad (8)$$

The total MSH is the sum of the MSHs  $\bar{\eta}_n$  for all modes.

## 5 Experimental Results

The experimental setup considered a cylindrical container with radius  $R = 50$  mm and liquid static height  $h = 70$  mm. The employed liquid is water, which was coloured by adding dark brown powder, in order to obtain a better contrast for the image processing analysis. The motions were performed by an industrial robot (Stäubli RX130L) and recorded by a GoPro Hero3 camera. The trajectories were planned so that the robot followed three paths, each of them with different motion profiles: a back-and-forth linear path (indicated as *l-motion*); an eight-shaped path (*e-motion*); and a circular path, performed twice in succession (*c-motion*). For the sake of brevity, only the results of two 2-dimensional planar motions are reported in Figure 1. It has to be noticed that, while the NL model exhibits a better tracking of the liquid's real MSH, the assumption of planar free surface of the L model overestimates the MSH, hence providing a more conservative evaluation.

## 6 Conclusions

A novel technique for the MSH estimation of liquid inside a container subject to 2-dimensional planar motions was proposed, extending what was presented in [3]. Results of the experiments were provided, to prove the effectiveness of the estimation.

## References

- [1] W. Aribowo, T. Yamashita and K. Terashima. "Integrated Trajectory Planning and Sloshing Suppression for Three-dimensional Motion of Liquid Container Transfer Robot Arm". *Journal of Robotics*, vol. 2015, pp. 1-15, 2015.
- [2] H. Bauer. "Nonlinear Mechanical Model for the Description of Propellant Sloshing". *AIAA Journal*, vol. 4, no. 9, pp. 1662-1668, 1966.
- [3] L. Guagliumi, A. Berti, E. Monti and M. Carricato. "A Simple Model-based Method for Sloshing Estimation in Liquid Transfer in Automatic Machines". *IEEE Access*, 2021, doi:10.1109/ACCESS.2021.3113956.
- [4] R. A. Ibrahim. "Liquid Sloshing Dynamics: Theory and Applications". Cambridge University Press, 2005.

# Eigenfrequency Assignment to Flexible-link Multibody Systems Using Taylor Expansion of a Parametric Modal Model

Roberto Belotti<sup>1</sup>, Ilaria Palomba<sup>2</sup>, Erich Wehrle<sup>1</sup>, Renato Vidoni<sup>1</sup>

<sup>1</sup>Faculty of Science and Technology  
Free University of Bozen-Bolzano  
Piazza Università 5, 39100 Bolzano, Italy  
[roberto.belotti,erich.wehrle,renato.vidoni]@unibz.it

<sup>2</sup>Department of Industrial Engineering  
University of Padova  
Via Venezia 1, 35121 Padova, Italy  
ilaria.palomba@unipd.it

## EXTENDED ABSTRACT

The design optimization of vibrating mechanical systems properly designs the dynamic behavior in terms of eigenfrequencies and/or eigenvectors through modification of physical parameters. Design variables can include e.g. geometrical and material properties that have consequence on inertial, stiffness and damping terms. Diverse methods have been developed to address the assignment of desired eigenfrequencies, eigenvectors, or both for linear vibrating systems [1]. Conversely, the assignment of a desired dynamic behavior to mechanical systems characterized by nonlinear dynamic models, such as flexible-link multibody systems (FLMS), is still an open issue. This paper proposes a method based on an approximated parametric modal model to assign desired eigenfrequencies to FLMSs moving along a given path.

FLMSs are modelled using the Equivalent Rigid-Link System (ERLS) approach [2]. The motion of the system is expressed through a coupled dynamic formulation that takes into account both the rigid-body dynamics and the elastic deformations of the links, modeled through finite element methods.

Let  $\mathbf{x} \in \mathbb{R}^{n_x}$  be the vector of model parameters, comprised of the ERLS generalized coordinates  $\mathbf{q} \in \mathbb{R}^{n_q}$  and the design parameters  $\mathbf{y} \in \mathbb{R}^{n_y}$  that can be modified, i.e.,  $\mathbf{x} = \{\mathbf{q}^T \ \mathbf{y}^T\}^T$ . The eigenvalue problem, neglecting damping and considering a slowly varying motion (i.e., negligible velocity-dependent terms), is

$$\mathbf{K}(\mathbf{x})\phi_i(\mathbf{x}) = \lambda_i(\mathbf{x})\mathbf{M}(\mathbf{x})\phi_i(\mathbf{x}), \quad (1)$$

where  $\mathbf{M}$  and  $\mathbf{K}$  are the mass and stiffness matrix, respectively,  $\lambda_i$  is the  $i^{\text{th}}$  eigenvalue and  $\phi_i$  is the  $i^{\text{th}}$  eigenvector. The Taylor expansions of order  $p$  of  $\mathbf{M}(\mathbf{x})$  and  $\mathbf{K}(\mathbf{x})$  in a neighborhood of  $\mathbf{x}_0$  are

$$\mathbf{M}(\mathbf{x}_0 + \delta\mathbf{x}) \approx \sum_{|\alpha|=0}^p \frac{\partial^\alpha \mathbf{M}(\mathbf{x}_0)}{\alpha!} \delta\mathbf{x}^\alpha, \quad \mathbf{K}(\mathbf{x}_0 + \delta\mathbf{x}) \approx \sum_{|\alpha|=0}^p \frac{\partial^\alpha \mathbf{K}(\mathbf{x}_0)}{\alpha!} \delta\mathbf{x}^\alpha, \quad (2)$$

where the multi-index notation for partial derivatives has been used, i.e.,  $\alpha$  is a  $n$ -tuple of nonnegative integers. Analogously, the Taylor expansions of order  $p$  of  $\lambda_i$  and  $\phi_i$  are

$$\lambda_i(\mathbf{x}_0 + \delta\mathbf{x}) \approx \sum_{|\alpha|=0}^p \frac{\partial^\alpha \lambda_i(\mathbf{x}_0)}{\alpha!} \delta\mathbf{x}^\alpha, \quad \phi_i(\mathbf{x}_0 + \delta\mathbf{x}) \approx \sum_{|\alpha|=0}^p \frac{\partial^\alpha \phi_i(\mathbf{x}_0)}{\alpha!} \delta\mathbf{x}^\alpha. \quad (3)$$

The coefficients of the Taylor expansion of the eigenvalues and the eigenvectors in (3) are computed iteratively [2,3] starting from the first up to the desired Taylor's order  $p$ : by substituting the functions in (2) and (3), evaluated at  $\mathbf{x} = \mathbf{x}_0$ , in (1) and solving for the derivatives of  $\lambda_i$  and  $\phi_i$  of order  $p$ , the following is obtained:

$$\begin{Bmatrix} \partial^p \phi_i \\ \partial^p \lambda_i \end{Bmatrix} = \begin{bmatrix} \partial^0 \mathbf{M} \partial^0 \lambda_i - \partial^0 \mathbf{K} & \partial^0 \mathbf{M} \partial^0 \phi_i \end{bmatrix}^\dagger \left\{ \sum_{\substack{|\beta|=1 \\ \beta_2 \neq |\beta|}}^p \partial^{\beta_1} \mathbf{K} \partial^{\beta_2} \phi_i - \sum_{\substack{|\gamma|=1 \\ \gamma_2 \neq |\gamma| \\ \gamma_3 \neq |\gamma|}}^p \partial^{\gamma_1} \mathbf{M} \partial^{\gamma_2} \lambda_i \partial^{\gamma_3} \phi_i \right\}, \quad (4)$$

where  $\dagger$  denotes the pseudoinverse matrix and  $\beta = (\beta_1, \beta_2)$  and  $\gamma = (\gamma_1, \gamma_2, \gamma_3)$  are two multi-indexes.

Let us denote the Taylor expansion of order  $p$  of the  $i^{\text{th}}$  eigenvalue by  $\lambda_i^p(\mathbf{x})$ . In this work, it is proposed to further simplify  $\lambda_i^p(\mathbf{x})$  by neglecting the terms in which variables  $\mathbf{y}$  have degree higher than 1. The obtained polynomial, which is henceforth denoted by  $\hat{\lambda}_i^p(\mathbf{x})$ , is linear in the variables  $\mathbf{y}$ . The rationale behind this logic is that this approximation is beneficial from the point of view of numerical tractability of the eigenfrequency assignment problem, whereas the loss of accuracy is not problematic, since eigenfrequency assignment is often carried out despite having an incomplete or uncertain knowledge of the system eigenfrequencies [4].

For any trajectory  $t \mapsto \mathbf{q}(t)$ ,  $t \in [0, T]$ , it is possible to define the cost function  $f(\mathbf{y}) = \int_0^T [\hat{\lambda}_i^p(\mathbf{q}(t), \mathbf{y}) - \lambda_{i,d}(t)]^2 dt$ , where  $\lambda_{i,d}(t)$  is a function that encompasses all the desired eigenvalues at any time instant. The optimal values of the design parameters can be computed solving the optimization problem

$$\min_{\mathbf{y} \in \Gamma} f(\mathbf{y}). \quad (5)$$

It must be noted that  $f(\mathbf{y})$  is a quadratic function, and if the constraint set  $\Gamma$  can be defined by linear equalities and inequalities, the optimization problem (5) is quadratic.

In order to validate the proposed method, the two-degree- of-freedom (dofs) flexible-link planar manipulator in Figure 1.a is considered and the lowest eigenfrequency is to be designed to a desired value. The links of the mechanism are modeled by means of Euler-Bernoulli beam elements. The resulting model has 23 dofs, with two rigid dofs of the ERLS, i.e.  $\mathbf{q} = \{q_1 \ q_2\}^T$ , and 21 elastic dofs.

The desired eigenfrequency is assigned by the addition of two point-masses: one placed at the elbow joint, and one placed at the end of the second link. Let  $m_1$  and  $m_2$  be the masses to be determined. Hence,  $\mathbf{y} = \{m_1 \ m_2\}^T$ . It is supposed that the maximum allowable value for both  $m_1$  and  $m_2$  is 0.250 kg.

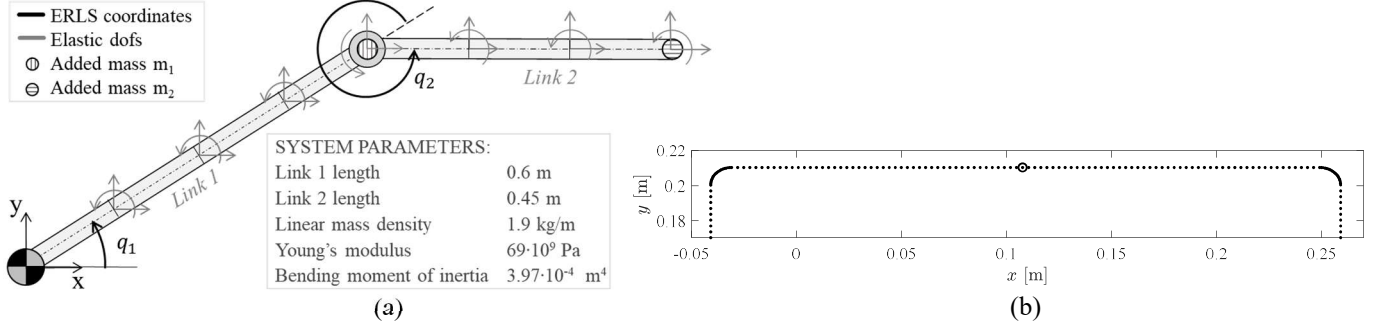


Figure 1: Finite element model of the flexible-link manipulator (a). End-effector trajectory (b).

The trajectory in Figure 1.b is traced by the end-effector. The trajectory has been discretized with 152 samples at constant time rate. Each point in the figure represents a sample. The same discretization will be used throughout the present example.

The Taylor expansion of order 4 of the lowest eigenfrequency has been computed, in a neighborhood of  $\mathbf{x}_0 = \{1.817 \text{ rad} \ 5.312 \text{ rad} \ 0.125 \text{ kg} \ 0.125 \text{ kg}\}^T$ . The position at the expansion point is the one indicated by the circle in Figure 1.b, i.e., the middle of the trajectory, and the mass is halfway between zero and the maximum allowable value.

The maximum relative error of  $\hat{\lambda}_1^4$  is 0.09%. If the nonlinear, higher order terms of  $\mathbf{y}$  are discarded, the approximation is obviously deteriorated, but still acceptable. The maximum relative error of  $\hat{\lambda}_1^4$  is 1.6%.

The optimization problem (5) is solved using an interior-point algorithm with the objective of designing the lowest eigenfrequency  $\lambda_{1,d}(t) \equiv 190$  Hz. The coefficients of function  $f$  have been computed by quadrature, using the trapezoidal method. The obtained optimal modifications are  $m_1 = 0.225$  kg and  $m_2 = 0.000$  kg. The numerical solution of problem (5) can be computed efficiently, as the algorithms for quadratic optimization require few iterations to converge. The eigenfrequencies of the original and modified systems are shown for comparison in Figure 2.

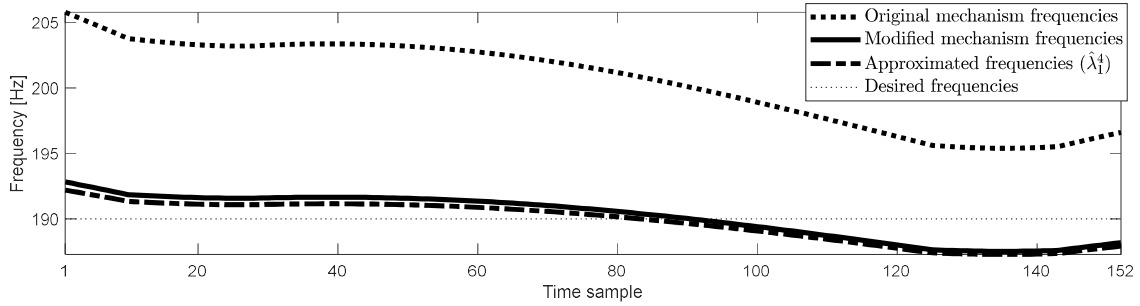


Figure 2: Eigenfrequency comparison.

The results indicate that, if the mechanism is modified according to the proposed method, the obtained first eigenfrequency of the mechanism falls within  $\pm 3$  Hz of the desired frequency for this example.

## Acknowledgments

This work was partially supported by the Free University of Bozen-Bolzano funds within the project TN200Y: “COVI: COnfinement of Vibrations by passive modifications in flexible multibody systems”.

## References

- [1] G. M. Gladwell. Inverse problems in vibration. Springer, Dordrecht, 1986.
- [2] I. Palomba, R. Vidoni. Flexible-link multibody system eigenvalue analysis parameterized with respect to rigid-body motion. Applied Sciences, 9.23:5156, 2019.
- [3] P. Wittmuess, B. Henke, C. Tarin and O. Sawodny, Parametric modal analysis of mechanical systems with an application to a ball screw model. In Proceedings of the 2015 IEEE Conference on Control Applications, pages 441–446. Sydney, 2015.
- [4] L. J. Adamson, S. Fichera, and J. E. Mottershead. Receptance-based robust eigenstructure assignment. Mechanical Systems and Signal Processing, 140:106697, 2020.

# Satisfying floating frame constraints in an absolute interface coordinates floating frame formulation

Jurnan Schilder, Marcel Ellenbroek

Faculty of Engineering Technology  
University of Twente  
P.O. Box 217, 7500AE Enschede, The Netherlands  
j.p.schilder@utwente.nl  
m.h.m.ellenbroek@utwente.nl

## EXTENDED ABSTRACT

In the field of flexible multibody dynamics, many applications consists of systems of which individual components are subjected to large rigid body motions and small elastic deformations. Under these circumstances, the floating frame of reference formulation, or simply the floating frame formulation, is a very suitable formulation to describe the system's dynamics. In this formulation, the generalized coordinates of a single flexible body consist of the absolute coordinates of the body's floating frame relative to the inertial frame and a set of coordinates that describe the body's elastic behavior locally, relative to the floating frame.

For general purposes, the local elastic coordinates can be interpreted as the generalized coordinates corresponding to the reduction basis with which linear finite element models of induvial bodies are reduced, using well-developed model order reduction techniques. For the sake of simplicity and without loss of generality, suppose that the elastic behavior is described by Craig-Bampton boundary modes only. In this case, the generalized coordinates consist of the absolute floating frame coordinates and local interface coordinates. This is shown schematically in figure 1.

The different bodies of the multibody system are connected to each other at the interface points. The corresponding kinematic constraints are enforced using Lagrange multipliers. The resulting equations of motion form a set of differential-algebraic equations. In order to solve for the system's motion, it is essential that the generalized coordinates describe each body's configuration uniquely. This means that any combination of the local elastic coordinates may not result in rigid body motions, as these are already described by the absolute floating frame coordinates.

Assuming that the set of (possibly unreduced) local elastic coordinates could still describe rigid body motions, a set of six constraint equations can be imposed on the local position and orientation of the floating frame. These constraint equations will be referred to as the floating frame constraints. In literature various choices for the floating frame constraints are reported. Most commonly encountered methods attach the floating frame to an interface point, attach the floating frame to the body's center of mass, compute the floating frame coordinates as the (weighted) average of interface coordinates or compute the floating frame coordinates by minimizing a body's elastic energy.

In the standard floating frame formulation, the constrained equations of motion are solved numerically. At each time step, the constrained equations of motion are solved for the generalized accelerations and Lagrange multipliers. Only the independent generalized accelerations are integrated in time twice, to obtain the independent generalized coordinates at the new time step. The dependent generalized coordinates at the new time step are determined such that the kinematic constraint equations are satisfied on the position level. To this end, a Newton-Raphson procedure is used, in which the newly obtained independent generalized coordinates are accepted and only the dependent generalized coordinates are updated. Once the constraints are satisfied with sufficient accuracy, the constrained equations of motion are formulated on the new time step and the process is repeated to advance in time further.

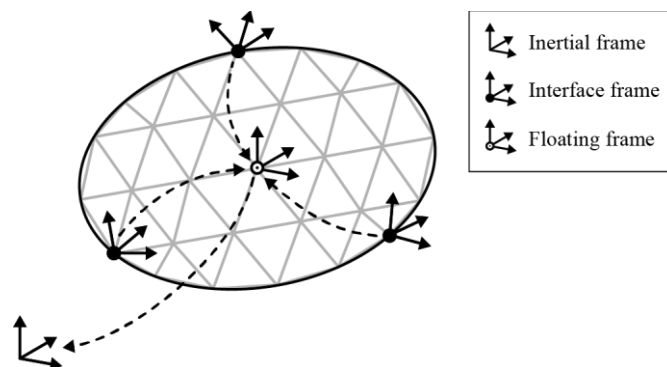


Figure 1: Generalized coordinates in the standard floating frame formulation.

Consider a body with  $N$  interface points. Let the floating frame be attached to point  $P_j$  of which the absolute coordinates with respect to inertial frame  $O$  are denoted by  $\mathbf{q}_j^{O,O}$ . The local interface coordinates are denoted by  $\mathbf{q}^{j,j}$ . The absolute interface coordinates are denoted by  $\mathbf{q}^{O,O}$ . In earlier work, the authors presented a method that defines the floating frame constraints by demanding zero elastic displacement and rotation in a material point to which the floating frame is attached [1]. This can be formulated as:

$$[\Phi_{CB}]\mathbf{q}^{j,j} = \mathbf{0} \quad (1)$$

in which  $[\Phi_{CB}]$  is the  $6 \times 6N$  constant matrix of Craig-Bampton boundary modes evaluated at the location of the floating frame  $P_j$ . The floating frame constraints (1) can be used to establish unique kinematic relations that express variations in the absolute floating frame coordinates and variations in the local interface coordinates in terms of variations in the absolute interface coordinates. This can be expressed in the following general form:

$$\delta \mathbf{q}_j^{O,O} = [\mathbf{A}_1(\mathbf{q}_j^{O,O}, \mathbf{q}^{j,j})]\delta \mathbf{q}^{O,O}, \quad \delta \mathbf{q}^{j,j} = [\mathbf{A}_2(\mathbf{q}_j^{O,O}, \mathbf{q}^{j,j})]\delta \mathbf{q}^{O,O} \quad (2)$$

in which  $[\mathbf{A}_1]$  and  $[\mathbf{A}_2]$  are transformation matrices that still depend on the absolute floating frame coordinates and local interface coordinates. The main advantage of this method is that it (I) removes the rigid body motions from the elastic coordinates and (II) simultaneously enables the multibody system's constrained equations of motion to be reformulated in terms of absolute interface coordinates. In these coordinates, kinematic constraints can be enforced directly, eliminating the Lagrange multipliers from the problem. The resulting equations of motion in this new formulation form a set of more convenient differential equations in terms of the absolute interface coordinates, which are considered to be independent coordinates. The absolute floating frame coordinates and local interface coordinates are now considered to be dependent coordinates.

Solving the transformed equations of motion numerically in time can be done using standard techniques. At each time step, absolute acceleration of the interface coordinates  $\ddot{\mathbf{q}}^{O,O}$  is solved from the system's equation of motion. By numerical time integration, the incremental change in the absolute interface coordinates  $\Delta \mathbf{q}^{O,O}$  is obtained and the absolute interface coordinates at the next time step can be computed.

However, the system's global mass matrix and elastic forces depend in general on the orientation of the floating frame and the local elastic deformation, i.e. on the dependent coordinates. In order to compute these accurately, it is found to be essential to determine the global position and orientation of the floating frame on the new time step accurately.

The problem can be formulated as follows: Given the absolute interface coordinates on the new time step, how to determine the absolute floating frame coordinates such that the floating frame constraints are satisfied on the new time step?

Substituting the incremental change in independent coordinates  $\Delta \mathbf{q}^{O,O}$  in equations (2) results in an incremental change in the floating frame coordinates  $\Delta \mathbf{q}_j^{O,O}$  and local interface coordinates  $\Delta \mathbf{q}^{j,j}$ . These coordinates can be updated by:

$$\mathbf{q}_{n+1} = \mathbf{q}_n + \Delta \mathbf{q}_n \quad (3)$$

in which  $n$  denotes the number of the incremental update and  $\mathbf{q}$  refers to either set of coordinates. Due to the integration error, the new local interface coordinates  $(\mathbf{q}^{j,j})_{n+1}$  will in general not satisfy the floating frame constraints (1). To solve this, the updated dependent coordinates can be used to update the transformation matrices to  $[\mathbf{A}_1]_{n+1}$  and  $[\mathbf{A}_2]_{n+1}$ . With this, equations (2) are used to obtain improved increments  $\Delta \mathbf{q}_{n+1}$  in the dependent coordinates, and (3) is used to obtain improved coordinates. This process is repeated until the floating frame constraints (1) are satisfied with sufficient accuracy. Note that throughout the above incremental updates, the change in the absolute interface coordinates  $\Delta \mathbf{q}^{O,O}$  is kept fixed: It is determined from the numerical time integration and accepted.

In the full paper and corresponding presentation, all details relevant for a successful numerical implementation of the above formulation that is kinematically consistent are presented. It is explained that in practice only very few iterations are required to satisfy the floating frame constraints, as time steps will be generally small. Moreover, it is explained that these iterations are computationally cheap and do not result in a significant increase of the overall simulation time, because the iterations are performed on the body level and not on system level. Relevant numerical examples are used to explain why updating the absolute floating frame coordinates could be of importance for obtaining realistic simulation results.

## References

- [1] M.H.M. Ellenbroek, J.P. Schilder. On the use of absolute interface coordinates in the floating frame of reference formulation for flexible multibody dynamics. *Multibody System Dynamics*, 43 (3), 193-208, 2018.

# Flexible Multibody Dynamics and Sensitivity Analysis in the Design of a Morphing Leading Edge for High-Performance Sailplanes

Veit Gufler<sup>1</sup>, Erich Wehrle<sup>1</sup>, Johannes Achleitner<sup>1,2</sup>, Renato Vidoni<sup>1</sup>

<sup>1</sup> Faculty of Science and Technology  
Free University of Bozen-Bolzano  
Universitätsplatz 1, 39100 Bozen, South Tyrol, Italy  
{Veit.Gufler, Erich.Wehrle, Renato.Vidoni}@unibz.it

<sup>2</sup> Institute of Aircraft Design  
Technical University of Munich  
Boltzmannstr. 15, 85748 Garching, Germany  
Johannes.Achleitner@tum.de

## EXTENDED ABSTRACT

### 1 Introduction

High-performance sailplanes have a large envelope of operating speeds. Fixed-geometry aircraft are designed to be a compromise for this wide speed range. Form-variable – or morphing – wings have shown to increase performance particularly when the leading edge of the wing is morphed in combination with a conventional trailing-edge flap [1, 2, 3]. Morphing leading edges have been modeled with traditional “hinged” mechanisms [2, 4] and with compliant mechanisms [3, 5]. Here, flexible multibody dynamics including rigid and flexible bodies is applied to a hinged mechanism, see fig. 1. Flexible multibody simulation is a valuable tool to simulate and optimize flexible deformations and large displacements and rotations that are desired in this behavior. An in-house flexible multibody simulation code SiMULi is extended here to accommodate simulation and sensitivity analysis for the design optimization of a morphing leading edge for sailplanes.

The developed methodology includes efficient sensitivity analysis for use in gradient-based design optimization of flexible mechanisms. In the following, this is developed for the simulation of a morphing leading edge concept using a flexible wing structure and a mechanism with rigid bodies driving the deformation from the high-speed profile configuration to the low-speed profile configuration.

### 2 Flexible multibody dynamics

The simulation of flexible multibody dynamics is categorized in three subcomponents as described in [6]: governing equation, time integration and nonlinear solver. The simulation is referred as primal analysis to differentiate from the sensitivity analysis. The governing equations are given by index-1 differential–algebraic equations for the motion of flexible multibody systems and the constraint equations of kinematic joints,

$$\underline{R} = \begin{bmatrix} \underline{m} & \underline{J}_{\Phi}^T \\ \underline{J}_{\Phi} & \underline{0} \end{bmatrix} \begin{bmatrix} \underline{\ddot{q}} \\ \underline{\dot{\lambda}} \end{bmatrix} - \begin{bmatrix} \underline{F}_{\text{ext}} + \underline{F}_v - \underline{d}\underline{\dot{q}} - \underline{k}\underline{q} \\ \underline{F}_c \end{bmatrix} = \underline{0}, \quad (1)$$

where  $\underline{R}$  is the residual,  $\underline{q}$  is the generalized position,  $\underline{\lambda}$  are Lagrangian multipliers of the kinematic constraints,  $\underline{m}$  is the mass,  $\underline{d}$  is the damping,  $\underline{k}$  is the stiffness,  $\Phi$  are kinematic constraints,  $\underline{J}$  is the Jacobian (i.e. the partial derivative with respect to position),  $\underline{F}_{\text{ext}}$  is the external force,  $\underline{F}_c$  is the right hand side of acceleration constraints,  $\underline{F}_v$  is the quadratic velocity force and overdots represent the first  $\dot{\phantom{x}}$  and second  $\ddot{\phantom{x}}$  differentiation with respect to time. Single underlined symbols  $\underline{x}$  represent vectors, double underlined symbols  $\underline{\underline{x}}$  are two-dimensional matrices and those without underlines are scalars.

The floating frame of reference formulation (FFRF) is used to represent flexibility [7]. The generalized positions of a flexible body with FFRF is given by the position and orientation of the reference frame and flexible deformations of the FE nodes. In this implementation of FFRF, a linear-elastic material model is used, which leads to a linear stiffness matrix, while the mass matrix is highly nonlinear. Numerical time integration is implemented with generalized- $\alpha$  method as a predictor–corrector scheme. To consider the nonlinearities of the system, Newton–Raphson iterations are used.

### 3 Design sensitivity analysis

The sensitivities of the system responses with respect to certain parameters are useful in design optimization, uncertainty analysis as well as the direct use of the sensitivities. Design sensitivity analysis is carried out here with a semi-analytical approach using

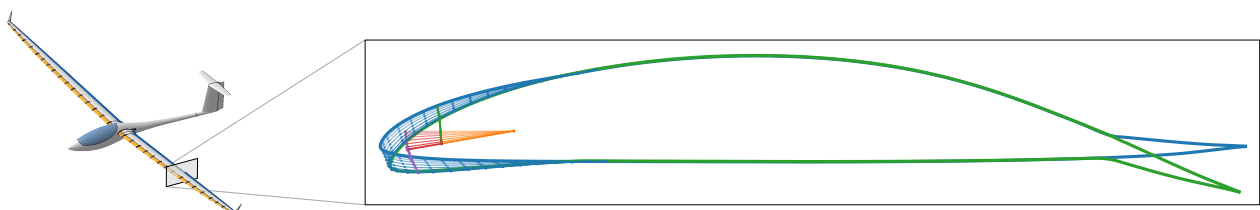


Figure 1: Morphing wing with mechanism for — high-speed and — low-speed airfoil configurations.



direct differentiation. The differentiation must be carried through all three steps of the calculation routine: governing equation, sensitivity analysis and nonlinear solver.

The direct differentiation of the primal equations results in the governing equations for the sensitivity analysis,

$$\underline{\underline{\nabla R}} = \begin{bmatrix} \underline{\underline{m}} & \underline{\underline{J}}_{\Phi}^T \\ \underline{\underline{J}}_{\Phi} & \underline{\underline{0}} \end{bmatrix} \begin{bmatrix} \underline{\underline{\nabla \dot{q}}} \\ \underline{\underline{\nabla \lambda}} \end{bmatrix} - \underline{\underline{\nabla F}}_{\text{pseudo}}, \quad (2)$$

where the pseudo load  $\underline{\underline{\nabla F}}_{\text{pseudo}}$  contains the partial derivatives of the system parameters,

$$\underline{\underline{\nabla F}}_{\text{pseudo}} = \begin{bmatrix} \underline{\underline{\nabla F}}_{\text{ext}} + \underline{\underline{\nabla F}}_v - \underline{\underline{\nabla m}}\ddot{q} - \underline{\underline{\nabla d}}\dot{q} - \underline{\underline{d}}\underline{\underline{\nabla \dot{q}}} - \underline{\underline{\nabla k}}q - \underline{\underline{k}}\underline{\underline{\nabla q}} - \underline{\underline{\nabla J}}_{\Phi}^T \underline{\underline{\lambda}} \\ \underline{\underline{\nabla F}}_c - \underline{\underline{\nabla J}}_{\Phi} \underline{\underline{\lambda}} \end{bmatrix}. \quad (3)$$

To limit the implementation effort in the simulation code, the partial derivatives are evaluated with numerical forward differences, thus resulting in a semi-analytical approach. The Jacobian of the sensitivity analysis is that of the primary analysis [6], allowing for an efficient calculation method of the gradients. This is the key to efficient sensitivity analysis of multibody dynamics. Without this simplification, the Jacobian of the sensitivity analysis is four-dimensional, requiring excessive memory usage.

#### 4 Morphing wing model

The design of the target geometry of the morphing wing sailplane in undeformed and morphed configuration is presented in [1] and shown in fig. 1. A significant performance advantage over conventional sailplanes with a camber changing flap is calculated. In earlier work [5], the morphing actuation is intended to be achieved using compliant mechanisms.

In this work, a conventional “hinged” mechanism is investigated for actuation. Flexible multibody dynamics with FFRF is applied to the planar model of the mechanism, consisting of the flexible outer shell modeled with Euler–Bernoulli beams and four rigid bodies for the actuation, that are connected by five revolute and one rigid joints. Here, we are especially interested that the wing profile in morphed configuration approximates the target shape as closely as possible, while complying with the material limits.

To understand how these are effected by the design variables, a sensitivity analysis of the deviation of the morphed configuration from the target shape described by the root mean square error and the maximum stress is performed with respect to design variables that include geometric properties, material properties and the position and torque of the actuator. Fig. 2a shows the stress distribution during the motion of the mechanism and fig. 2b shows the sensitivity with respect to the Young’s modulus (see full paper for full set of results). The results of the sensitivity analysis show how the design parameters can be changed in order to improve the design and can be used in uncertainty analysis or in gradient-based design optimization to find the optimum design of the actuation mechanism.

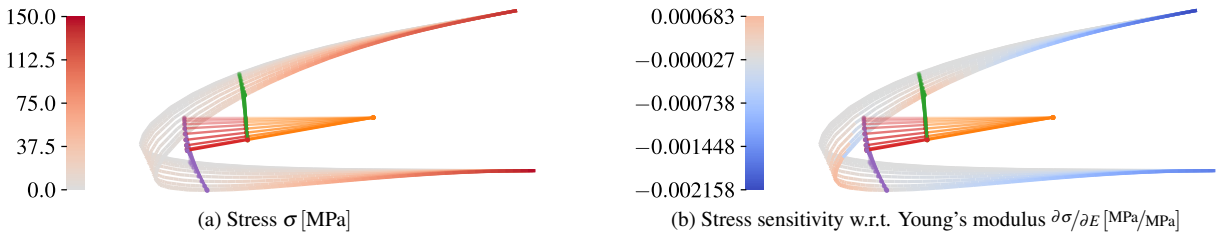


Figure 2: Analysis results for the morphing wing via flexible multibody dynamics in SIMuLi

#### References

- [1] Achleitner, J., Rohde-Brandenburger, K., Rogalla von Bieberstein, P., Sturm, F., Hornung, M.: Aerodynamic design of a morphing wing sailplane. In: AIAA Aviation 2019 Forum, Reston, Virginia, AIAA (2019)
- [2] Sinapius, M., Monner, H.P., Kintscher, M., Riemenschneider, J.: DLR’s morphing wing activities within the European network. *Procedia IUTAM* **10** (2014) 416–426
- [3] Sturm, F., Achleitner, J., Jocham, K., Hornung, M.: Studies of anisotropic wing shell concepts for a sailplane with a morphing forward wing section. In: AIAA Aviation 2019 Forum, Reston, Virginia, AIAA (2019)
- [4] Rudenko, A., Hannig, A., Monner, H.P., Horst, P.: Extremely deformable morphing leading edge: Optimization, design and structural testing. *Journal of Intelligent Material Systems and Structures* **29**(5) (2017) 764–773
- [5] Reinisch, J., Wehrle, E., Achleitner, J.: Multiresolution topology optimization of large-deformation path-generation compliant mechanisms with stress constraints. *Applied Sciences* **11**(6)(2479) (2021)
- [6] Wehrle, E., Gufler, V.: Lightweight engineering design of nonlinear dynamic systems with gradient-based structural design optimization. In: *Proceedings of the Munich Symposium on Lightweight Design*. Springer Berlin Heidelberg (2021) 44–57
- [7] Shabana, A.A.: *Dynamics of multibody systems*. 5 edn. Cambridge University Press (2020)

# Simultaneous Space-Time Discretization for Controlling the Motion of Rigid Bodies Actuated Through Elastic Ropes

Timo Ströhle and Peter Betsch

Institute of Mechanics, Karlsruhe Institute of Technology, 76131 Karlsruhe, Germany  
timo.stroehle@kit.edu, peter.betsch@kit.edu

## EXTENDED ABSTRACT

### 1 INTRODUCTION

The inverse dynamics of flexible mechanical systems is concerned with searching forces acting on the system such that a finite number of selected points of the system follow a prescribed motion. One subclass of such systems are elastic strings for large deformations which can be seen as a one-dimensional continuum. Here the aim is to find a force which acts at one end of the string, such that the other end follows a prescribed trajectory (see Fig. 1). In this connection, the end of the string might be attached to a mass point or connected to a rigid body (see below).

In the first part of this contribution two methods are presented which enable this class of problems to be solved. More precisely, a space-time finite element method and an approach based on the method of characteristics are established. Both methods are based on a simultaneous space-time discretization of the problem at hand (see [3]). In the second part of this contribution a strategy to solve a cooperative control problem consisting of a rigid body controlled through several elastic ropes undergoing large deformations is presented (see Fig.2). For that purpose, the rigid body can be described as a Cosserat point subjected to geometric constraints.

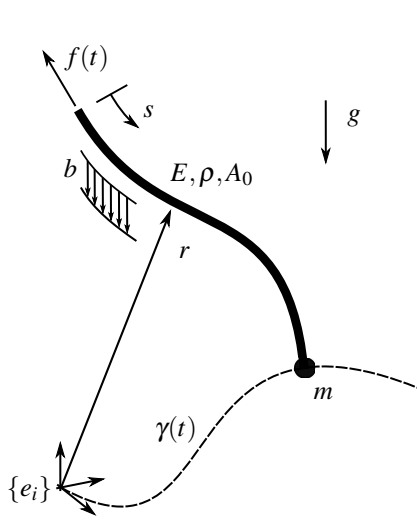


Figure 1: Illustration of the elastic rope for large deformations only actuated by  $f(t)$  at  $s = 0$  such that the rope at  $s = 1$  follows the prescribed trajectory  $\gamma(t)$

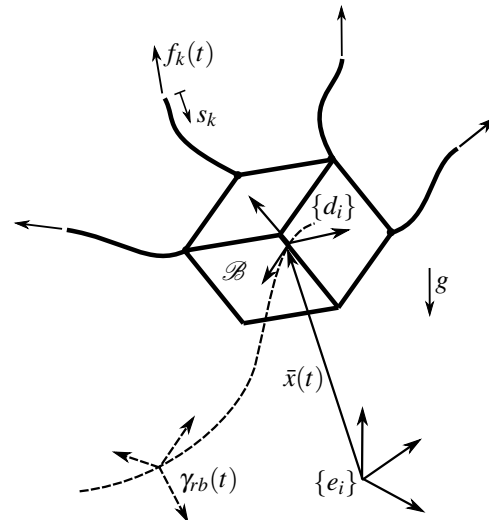


Figure 2: Cooperative transport of a rigid body through  $k \in \mathbb{N}$  elastic ropes only actuated by  $f_k(t)$  at  $s_k = 0$  such that the prescribed motion of the rigid body is realized

### 2 ELASTIC ROPES

The motion of elastic ropes (see Fig. 1) undergoing large deformations can be described in terms of the normed arc-length  $s \in S = [0, 1] \subset \mathbb{R}$  in the reference configuration by quasi-linear hyperbolic partial differential equations (see [1] for more details) of the form

$$A(r, s, t) \partial_t^2 r(s, t) - \partial_s (B(r, s, t) \partial_s r(s, t)) = C(r, s, t) \quad \forall \quad (s, t) \in \Omega \quad (1)$$

Note, that due to the quasi-linearity of the problem at hand, the coefficients  $A \in \mathbb{R}$ ,  $B \in \mathbb{R}$  and  $C \in \mathbb{R}$  may depend on the space and time variables as well as on the solution  $r(s, t) : S \times T = \Omega \subset \mathbb{R}^2 \mapsto \mathbb{R}^3$  for time  $t \in T = [0, \infty)$ . To solve the PDE at hand uniquely the following initial

$$r(s, 0) = r_0(s), \quad \partial_t r(s, 0) = v_0(s) \quad \forall \quad s \in S \quad (2)$$

and boundary conditions

$$B \partial_s r(0, t) = f(t), \quad B \partial_s r(1, t) = n(t), \quad r(1, t) = \gamma(t) \quad \forall \quad t \in T \quad (3)$$

need to be defined. Herein  $f(t) : T \mapsto \mathbb{R}^3$  is the searched actuating force at  $s = 0$  and  $n(t) : T \mapsto \mathbb{R}^3$  is the contact force at  $s = 1$ . If a mass point is attached to the rope at  $s = 1$ , the contact force can be directly computed from the prescribed trajectory of the rope at  $s = 1$  and hence the trajectory of the mass point via

$$n(t) = m(\partial_t^2 \gamma(t) + g) \quad (4)$$

Now, the initial boundary value problem constituting the control problem at hand can be solved by applying the newly proposed numerical method based on a simultaneous space-time discretization.

### 3 RIGID BODY

When considering general rigid bodies, in principle the same strategy as for the attached mass point can be applied. The actuating forces needed to achieve the desired motion of the rigid body can be calculated directly from the governing equations of motion. These forces can then be inserted into the Neumann boundary condition of the control problem (3). In this contribution a Cosserat point subjected to geometric constraints is used to describe the motion of a rigid body with density  $\rho_0 : \mathcal{B}_0 \mapsto \mathbb{R}$  and total mass  $M = \int_{\mathcal{B}_0} \rho_0 \, dV$  (see [2] for more details).

$$M \partial_t^2 \bar{x} - f_{ext} = 0 \quad (5)$$

$$E_{ij} \partial_t^2 d_j - f_{ext}^i + \Lambda_{ij} d_j = 0 \quad (6)$$

$$g_c(d_i) = d_i \cdot d_j - \delta_{ij} = 0 \quad (7)$$

Herein  $E_{ij}$  are the components of the referential Euler tensor which is closely related to the classical inertia tensor of rigid body dynamics. Furthermore,  $f_{ext}$  is the resultant external force and  $f_{ext}^i$  are the external director forces. The geometric constraints (7) are enforced by the Lagrange multipliers  $\Lambda_{ij}$ . To force the rigid body at hand to follow a prescribed motion  $\gamma_{rb}(t) = [\gamma_{\bar{x}} \quad \gamma_{d_i}]^T$  additionally to the holonomic constraints (7), the following control constraints

$$g_s = q - \gamma_{rb}(t) = 0 \quad (8)$$

are introduced. In (8) the motion of the rigid body, which is fully described by the directors  $d_i : T \mapsto \mathbb{R}^3$  and the position of the centre of gravity  $\bar{x} : T \mapsto \mathbb{R}^3$  is contained in  $q = [\bar{x} \quad d_i]^T$ . The servo-constraints (8) of course must not violate the holonomic constraints (7). The differential part of the DAE at hand, consisting of (5) and (6), together with the control constraint (8) yield an algebraic equation for the actuating force  $\bar{f}(t) = [f_{ext} \quad f_{ext}^i]^T$  conjugate to  $q$  given by

$$\bar{f}(t) = D \partial_t^2 \gamma_{rb}(t) + F \gamma_{rb}(t) - \bar{G} \quad (9)$$

with

$$D = \begin{bmatrix} M & 0 \\ 0 & E_{ij} \end{bmatrix}, \quad F = \begin{bmatrix} 0 & 0 \\ 0 & \Lambda_{ij} \end{bmatrix}, \quad \bar{G} = \begin{bmatrix} G \\ 0 \end{bmatrix} \quad (10)$$

where  $G$  is the gravitational force. Note that the actuating forces depend on the Lagrange multipliers and hence a unique solution for the actuation of the rigid body requires the Lagrange multipliers to be partly specified. In essence, this amounts to partly specifying the stresses within the rigid body.

After  $\bar{f}(t) = [f_{ext} \quad f_{ext}^i]^T$  is computed, the  $k \in \mathbb{N}$  contact forces  $n_k(t)$  for the  $k$  ropes at  $s_k = 1$  can be easily computed by knowing the position of the contact point of the rope at the rigid body through the following linear relation:

$$n(t) = H^{-1} \bar{f}(t) \quad (11)$$

Herein the invertible matrix  $H$  depends on the contact points of the  $k$  ropes and the rigid body. Once the forces  $n_k$  have been calculated, each rope can be solved separately by inserting the forces into the corresponding boundary condition of the quasi-linear hyperbolic partial differential equation established in the first part of this contribution. The applicability of this cascade-like approach is underpinned by numerical investigations.

### References

- [1] S. S. Antman. Nonlinear Problems of Elasticity. Springer, 2005.
- [2] P. Betsch. Energy-Momentum Integrators for Elastic Cosserat Points, Rigid Bodies and Multibody Systems. In P. Betsch, editor, Structure-preserving Integrators in Nonlinear Structural Dynamics and Flexible Multibody Dynamics, pages 31-89. CISM International Centre for Mechanical Sciences 565, Udine, 2016.
- [3] T. Ströhle and P. Betsch. Controlling Nonlinear Elastic Systems in Structural Dynamics. In Proceedings of the 14th World Congress on Computational Mechanics (WCCM) and ECCOMAS Congress, Virtual Congress, 11-15 January, 2021.

# Multipoint Constraints for Interface Reduction in Flexible Multibody Systems

Alessandro Cammarata<sup>1</sup>, Rosario Sinatra<sup>2</sup>, Pietro Davide Maddio<sup>3</sup>

University of Catania, DICAR  
Via S. Sofia 64, 95125, Italy

<sup>1</sup> alessandro.cammarata@unict.it, <sup>2</sup> rosario.sinatra@unict.it, <sup>3</sup> pietro.maddio@unict.it

## EXTENDED ABSTRACT

### 1 Introduction

Interface reduction is a recurring problem in substructuring and model reduction theory [1]. In structural dynamics, some of these interface reductions perform reduction at system-level considering the assembled system while others perform reduction at component-level by considering the uncoupled substructures [2, 3].

In flexible multibody dynamics, the interfaces are primitive geometric features, i.e. points, lines, and surfaces, employed to define mechanical joints, and their deformation is strongly coupled to the internal dynamics of a component, and can therefore not be reduced to a small number of nodes. Therefore, a double problem arises: reducing the dofs associated with the interface nodes in order to have an efficient reduced model, linking the interfaces of two bodies in a correct way to form a joint. The presence of a joint between two bodies means that there cannot be a common reduction of the interfaces, or at least that it must be updated over time as the configuration of the bodies changes. In practice, what is done is to individually reduce each interface to a single virtual node, usually a not collocated node outside the volume of the body. This reduction occurs through two types of multipoint constraints (MPCs): the rigid multipoint constraint, usually referred to as the RBE2 element, and the interpolation multipoint constraint, usually referred to as the RBE3 element [4]. Subsequently, the virtual nodes of the two interfaces are linked through kinematic constraints necessary to define a type of joint.

In [5] the authors raised the problem of the scarce use of RBE3 in multibody simulations and identified the disappearance of the dependent coordinates, operated by FE software after the process of eliminating the multipoint constraints, as one of the possible causes. The method proposed in [5] has practical implications to be used in commercial FE software but neglects important aspects related to the presence of MPCs and generic reference conditions (RCs) within the Finite Element Floating Frame of Reference Formulation (FE-FFRF). Here, a different approach is presented that is perfectly integrated inside the FE-FFRF working with every RCs.

### 2 Methodology

Given a component discretized into FE, let  $\mathcal{B}$ ,  $\mathcal{I}$ , and  $\mathcal{V}$ , be the sets of boundary, internal, and virtual nodes, respectively. All interface nodes belong to  $\mathcal{B}$ , while  $\mathcal{V}$  contains the virtual nodes necessary to create an MPC; the remaining nodes belong to  $\mathcal{I}$ . The virtual nodes are necessary to create an MPC and can be collocated, that is physical nodes of the mesh or non-collocated nodes, i.e. nodes not belonging to the body's volume. Then, the RBE2 and RBE3 elements can be described in terms of the mentioned sets:

$$\mathbf{F} : \mathcal{B} \rightarrow \mathcal{V} \Rightarrow \mathbf{q}_B = \mathbf{F}\mathbf{q}_V, \quad (\text{RBE2}) \quad (1a)$$

$$\mathbf{G} : \mathcal{V} \rightarrow \mathcal{B} \Rightarrow \mathbf{q}_V = \mathbf{G}\mathbf{q}_B, \quad (\text{RBE3}) \quad (1b)$$

where  $\mathbf{F}$  and  $\mathbf{G}$  are linear functions of the independent nodes whose expressions are reported in [4, 5]. The vectors  $\mathbf{q}_B$  and  $\mathbf{q}_V$  contain the displacements of nodes belonging to  $\mathcal{B}$  and  $\mathcal{V}$ , respectively. Usually,  $\dim(\mathcal{V}) < \dim(\mathcal{B})$  and this explains the limited use of RBE3 in multibody applications. While imposing the RCs on the virtual nodes of the RBE2 elements is often immediate, doing the same with the RBE3 element needs some tricks.

Suppose to apply the RCs on the virtual nodes of  $\mathcal{V}$  and that the RCs can be expressed through the following linear constraint equations

$$\mathbf{D}\mathbf{q}_V = \mathbf{0} \quad (2)$$

where  $\mathbf{D}$  is a matrix containing the coefficients of these equations.

#### 2.1 RBE2 element

By introducing Eq.(1b) into Eq.(2), we derive

$$\mathbf{D}\mathbf{F}^\top \mathbf{F}\mathbf{q}_V = \mathbf{0} \Rightarrow \mathbf{D}\mathbf{F}^\top \mathbf{q}_B = \mathbf{0} \Rightarrow \mathbf{B}_2 = \text{null}(\mathbf{D}\mathbf{F}^\top) \quad (3)$$

where  $\mathbf{F}^\dagger$  is the generalized inverse of  $\mathbf{F}$  and  $\mathbf{B}_2$  is the matrix of the RCs such that  $\mathbf{q}_B = \mathbf{B}_2 \boldsymbol{\eta}$  being  $\boldsymbol{\eta}$  a reduced set of independent elastic parameters. Usually, this procedure is not needed as  $\mathbf{B}_2$  can be directly found removing the constrained *dof* from  $\mathbf{q}_V$ , i.e.

$$\mathbf{q}_V = \mathbf{B}_2 \mathbf{q}_V^* \quad (4)$$

where  $\mathbf{q}_V^*$  is the reduced set of independent elastic coordinates. Exploiting Eq.(4), it is derived that

$$\mathbf{q}_B = \mathbf{F} \mathbf{B}_2 \mathbf{q}_V^* \Rightarrow \mathbf{T} = \mathbf{F} \mathbf{B}_2 \quad (5)$$

in which  $\mathbf{T}$  is the transformation matrix that contains both the RBE2 and RCs.

## 2.2 RBE3 element

By introducing Eq.(1b) into Eq.(2), we have

$$\mathbf{D} \mathbf{G} \mathbf{q}_B = \mathbf{0} \Rightarrow \mathbf{q}_B = \mathbf{B}_2 \boldsymbol{\eta}, \quad \mathbf{B}_2 = \text{null}(\mathbf{D} \mathbf{G}) \quad (6)$$

By substituting into Eq.(1b) we obtain  $\mathbf{q}_V = \mathbf{G} \mathbf{B}_2 \boldsymbol{\eta}$ . In this case, the direct substitution carried out in the RBE2 element is not possible and the final transformation matrix  $\mathbf{T} \equiv \mathbf{G} \mathbf{B}_2$  maps a reduced set of independent elastic parameters into the virtual node displacement vector  $\mathbf{q}_V$ .

## 3 Numerical simulation

To demonstrate the applicability of the method the normal modes of a connecting rod with simply-supported RCs have been derived. Fig. 1 confirms that the RBE2s stiffen the component preventing deformation of the interfaces.

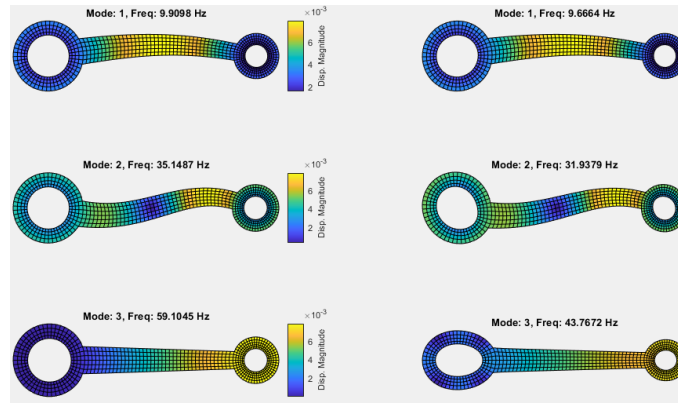


Figure 1: Normal modes of a simply-supported connecting-rod: (left) the first three flexible modes and natural frequencies considering two RBE2 elements; (right) the first three flexible modes and natural frequencies considering two RBE3 elements.

## 4 Conclusions

A novel formulation to introduce MPCs within FFRF-base multibody codes has been proposed. The final transformation matrices mapping the set of independent parameters/coordinates into the virtual node displacements are compatible with the reference conditions necessary for a correct application of the FE-FFRF.

## References

- [1] M. S. Allen, D. Rixen, M. Van der Seijs, P. Tiso, T. Abrahamsson, R. L. Mayes, Substructuring in engineering dynamics, Springer, 2020.
- [2] D. Krattiger, L. Wu, M. Zacharczuk, M. Buck, R. J. Kuether, M. S. Allen, P. Tiso, M. R. Brake, Interface reduction for hurty/craig-bampton substructured models: Review and improvements, Mechanical Systems and Signal Processing 114 (2019) 579–603.
- [3] P. Holzwarth, P. Eberhard, Interface reduction for cms methods and alternative model order reduction, IFAC-PapersOnLine 48 (1) (2015) 254–259.
- [4] M. Nastran, Basic dynamic analysis user's guide, MSC. Software Corporation. USA 546.
- [5] G. H. Heirman, W. Desmet, Interface reduction of flexible bodies for efficient modeling of body flexibility in multibody dynamics, Multibody System Dynamics 24 (2) (2010) 219–234.

# Influence of the Flexibility of the Railway Locomotive Bogies Components on its Dynamics

João Pagaimo, Pedro Millan, João Costa, Jorge Ambrósio<sup>1</sup>

<sup>1</sup>IDMEC, Instituto Superior Técnico  
University of Lisbon  
Address, 1044-001 Lisbon, Portugal  
{joao.pagaimo, pedro.millan, joao.n.costa,  
jorge.ambrosio}@tecnico.ulisboa.pt

## EXTENDED ABSTRACT

### 1 Introduction

The use of flexible multibody models of vehicles is of major importance in aerospace, mostly due to their flexible appendages but not only, and for ‘light’ road vehicles. It is not common the use of flexible bodies in the modelling of heavy railway vehicles such as freight locomotives, as the flexibility of the vehicle mechanical components is not expected to play a role in their dynamics. However, when the purpose of the study of these vehicles is not only to understand how the degradation of some of their structural components affects their performance but also how their level of degradation can be sensed in order to deploy maintenance action, the dynamic response of particular mechanical components may be of importance. A flexible multibody methodology based on body referential and mode component synthesis is applied here [1,2]. The reference conditions and the use of virtual bodies [3] are overviewed and advanced in order to accommodate the practical finite element models of the flexible components. The dynamics of the railway locomotive with flexible bogie chassis and wheelsets is simulated in realistic operating conditions in a mountainous railway track, being the results discussed with the emphasis on their use to support the equipment sensing for maintenance planning purposes.

### 2 Flexible Multibody Methods

The flexible multibody formulation used in this work assumes that the structural deformations of the flexible bodies are elastic and small. The finite element method is used to describe the body structure about a body fixed frame, with no restrictions on the type of finite elements used for the body representation, as shown in Fig.1(a) [2]. The reference conditions used in this work to ensure that the rigid body motion is unique are selected among the fixed node, mean axis and principal axis conditions. It is shown that for general flexible bodies the use of mean axis or principal axis conditions is preferred to the use of fixed node conditions because these ensure that the location of the body fixed frame and the orientation of its axis are consistent with the assumption that the first moments of area are null and that the inertia products of the inertia tensor are null. Furthermore, being the finite elements used in the construction of the flexible body models unrestricted it can happen that solid elements, with 3 degrees of freedom (dof) and beam or shell elements with six dof per node are used in the model. This has no consequences when using the mean axis or the principal axis conditions, but it is problematic when using a fixed node condition.

The mode component synthesis is used to reduce the number of generalized coordinates required to represent the flexible body. To the set of vibration modes associated to the lower natural frequencies of the bodies a set of static correction modes is added to ensure the correct representation of local deformations [4].

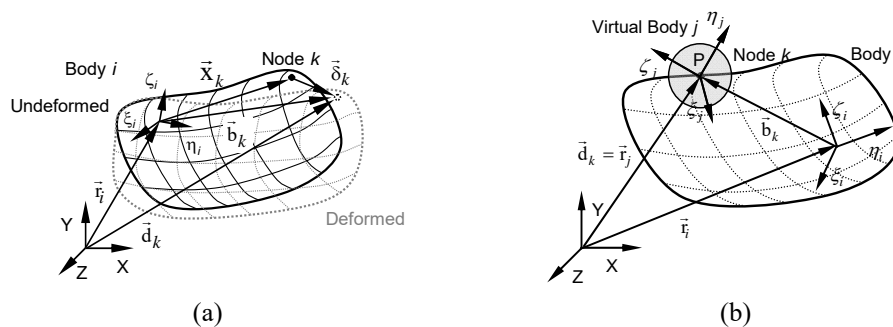


Figure 1: General representation of a flexible multibody highlighting the use of virtual bodies to setup kinematic joints.

The use of the complete library of kinematic joints, already developed for use rigid multibody systems, is available to the modeler by using virtual rigid bodies, as depicted in Fig. 1(b). These virtual bodies are massless and rigidly attached to particular points of the flexible body, generally nodes. The issue addressed in this work is that when the nodes of the finite element model only have 3-translation dof, at least three nodes are required to define the kinematic constraints with a virtual massless body. By using these enhanced formulation the flexible multibody methodology used here is able to handle any finite element model generated with the use of any commercial, or homemade, finite element code, turning the task of developing the multibody model and the finite element models of the flexible bodies into independent tasks.

### 3 Vehicle Model with Flexible Components

The complete model of the freight locomotive is similar to that presented in a companion paper [4], it is not further detailed here. The bogies of the locomotive consider that the chassis and the wheelsets are flexible as shown in Fig. 2, i.e., they allow for structural deformations. Although no consequences in terms of vehicle dynamics are expected, the dynamic response of the flexible components can be used for structural health monitoring. The main objective is that by using healthy and damaged models of the selected structural elements it is possible to relate structural performance with damage condition. In this form, a maintenance program for the locomotive bogies can be envisaged based on sensor data.

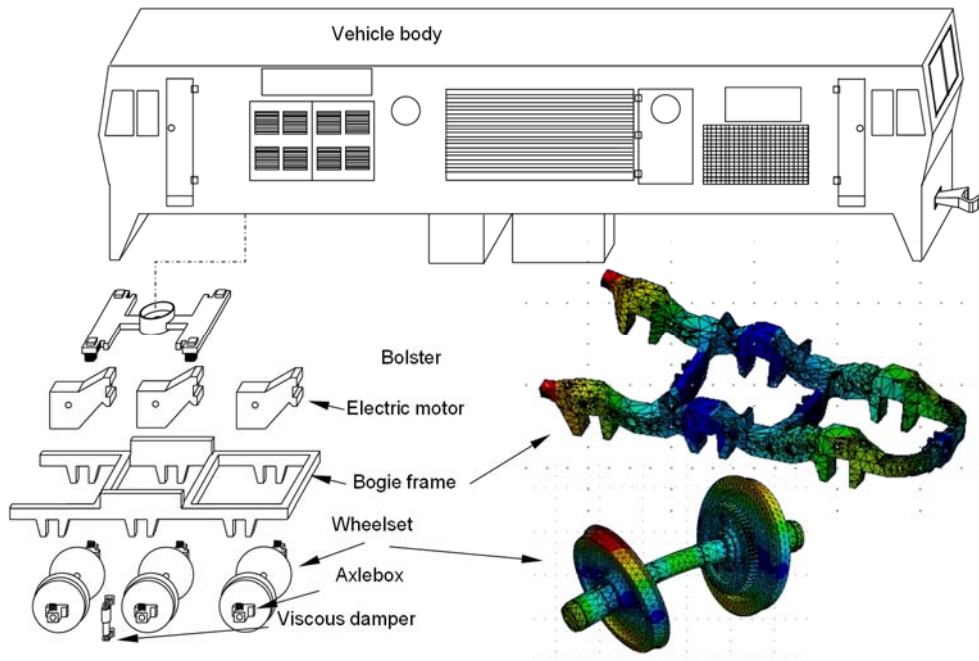


Figure 2: Exploded view of the railway locomotive model highlighting the flexible bodies of the motor bogies.

### 4 Preliminary Conclusions

In the process of applying a well-known flexible multibody methodology to the study of a realistic railway vehicle several shortcomings of the original methodology are addressed and solved. The consequences of separating the multibody and flexible bodies modelling tasks implies that no restrictions exist for the selection of finite elements. Due to the existence of finite elements with six and with three dof per node, the application of reference conditions and of virtual bodies has limitations that have to be overcome. This work not only shows how to generalize the use of reference conditions and virtual bodies, independently of the number of dof per finite element node, but also show, in a practical application to a freight railway vehicle, the use of flexible multibody models for structural degradation and maintenance planning.

### Acknowledgments

The work reported in this paper has a fundamental input from the Shift2Rail JU under the project LOCATE (Locomotive bOgie Condition mAinTEnance) with the grant n°881805. This work was supported by FCT, through IDMEC, under LAETA project number UIDB/50022/2020.

### References

- [1] J. Ambrósio, J. Gonçalves, Complex Flexible Multibody Systems with Application to Vehicle Dynamics, Multibody System Dynamics, DOI: 10.1023/A:1017522623008, 6(2), 163-182, 2001.
- [2] J. Ambrósio, M. A. Neto and R. Leal, Optimization of a complex flexible multibody systems with composite materials, Multibody Systems Dynamics, 18(2), 117-144, 2007.
- [3] J. Gonçalves, J. Ambrósio, Advanced Modeling of Flexible Multibody Dynamics Using Virtual Bodies, Computer Assisted Mechanics and Engineering Sciences, 9 (3), 373-390, 2002.
- [4] P. Millan, J. Pagaimo, J. Ambrósio, H. Magalhães, P. Antunes, Influence of the Friction Model on the Dynamics of Railway Freight Vehicle, ECCOMAS Thematic Conference on Multibody Dynamics, Budapest, Hungary, December 12-15, 2021.



# Flexible Multibody Impact Simulations of Hierarchically Refined Isogeometric Models

Tobias Rückwald, Alexander Held, Robert Seifried

Institute of Mechanics and Ocean Engineering  
Hamburg University of Technology  
Eißendorfer Straße 42, 21073 Hamburg, Germany  
{tobias.rueckwald, alexander.held, robert.seifried}@tuhh.de

## EXTENDED ABSTRACT

### 1 Introduction

The objective of this work is a detailed simulation of impacts in flexible multibody systems. Thereby the floating frame of reference formulation is used [1], which requires global shape functions of the flexible body. A finite element model consisting of isoparametric elements is often used to determine the global shape functions. A disadvantage of isoparametric elements is that the geometry is discretized. Impact simulations however, depend on an accurate representation of the geometry. As an alternative approach, isogeometric elements can be used where there is no error in the representation of the geometry. For this reason, the isogeometric analysis (IGA) will be employed in this work to determine the global shape functions. Furthermore, the isogeometric finite element model will be refined using two different approaches. The differences between the most commonly used refinement, the global refinement, and a local refinement using a hierarchical approach will be compared in an impact simulation.

### 2 The IGA in a Flexible Multibody Impact Simulation

The main advantage of the IGA is the exact representation of the geometry. This is achieved by the use of basis-splines (B-splines) as the local shape functions of the isogeometric elements. These splines are defined in the so-called parameter space which can be seen in Fig. 1. The figure also shows the knots which span the elements. In order to visualize the geometry, the parameter space is transformed into the physical space. This transformation is accomplished with the non-uniform rational B-splines (NURBS). For a more detailed introduction to the IGA, see, for instance, [2].

In the context of a flexible multibody simulation, the finite element model is then reduced. To capture precise deformations and stresses in the area of contact, a large number of eigenmodes would be required. Instead, here a combination of eigenmodes and static shape functions are used to describe the flexible body. Low frequency eigenmodes represent the global deformation, and the high eigenfrequency static shape functions capture the local deformation in the contact area. Here, another feature of the IGA is advantageous. Compared to isoparametric elements, isogeometric elements can approximate high modes more accurately [2]. Besides an efficient approximation of the flexible body through global shape functions, an efficient refinement of the flexible body in the contact area is necessary in advance.

### 3 Hierarchical Refinement

In impact simulations, particularly high forces and stresses occur in the contact area. Therefore, many elements and degrees of freedom in the contact area are necessary for an accurate simulation. The basic approach to refine the IGA model consists of a combination of two global refinement approaches. On the one hand, the order of the B-splines can be increased, and on the other hand, additional knots can be inserted. These refinements do not affect the geometry but more elements are created and the

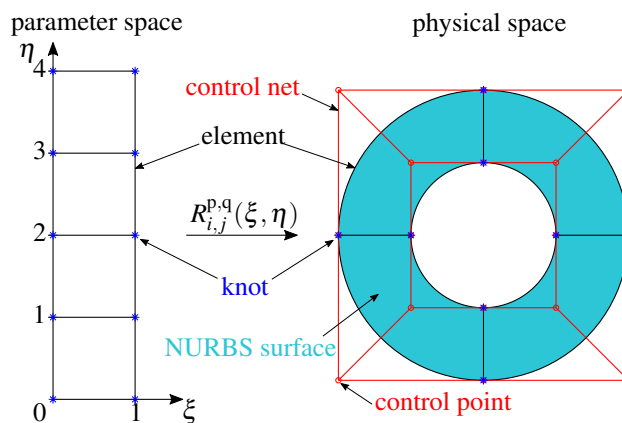


Figure 1: Parameter space and physical space in the IGA.

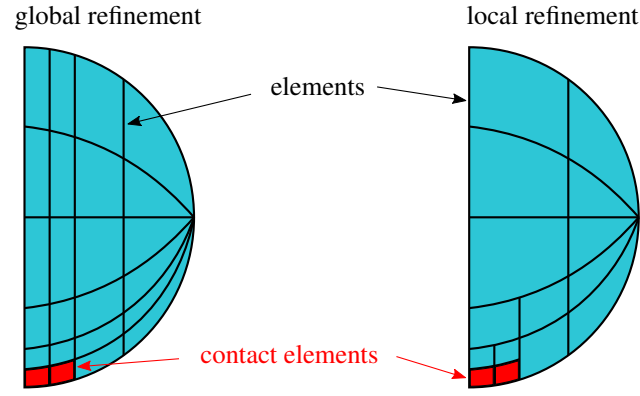


Figure 2: Differences between global and hierarchical (local) refinement for an axisymmetric sphere.

number of degrees of freedom is increased. The disadvantage of inserting knots is shown on the left-hand side of Fig. 2. The accumulation of elements in the contact area influences the element distribution in the whole body. Local refinement strategies are required to address this issue. One method for a local refinement involves a hierarchical approach which can be seen on the right-hand side of Fig. 2. The concept of the hierarchical refinement is the property of B-splines to be represented by a linear combination of finer B-splines defined on smaller knot-intervals, see Fig. 3. A detailed introduction to the hierarchical refinement in the IGA can be found in [3]. The locally refined and reduced isogeometric model is then incorporated in a flexible multibody simulation as described in Section 2.

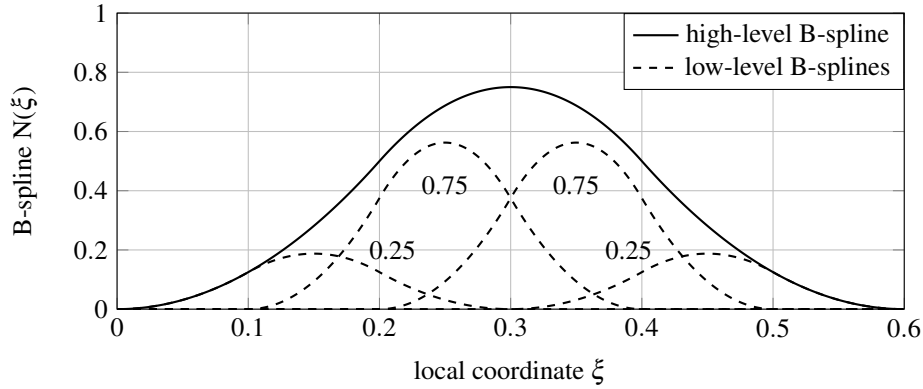


Figure 3: Concept of the hierarchical refinement in the IGA.

#### 4 Application Examples

Two application examples are presented in this work. In the first application example, the impact of two flexible spheres is modeled. The spheres are represented by an axisymmetric semicircle, as depicted in Fig. 2. The impact is simulated by a penalty method and is limited to a frictionless normal contact. The analytical solution of Hertz [4] and a full nonlinear isoparametric finite element model in ANSYS are used as references. Additionally, the focus will be on comparing a globally and locally refined IGA model. Both models have an identical element density in the contact area. The models are then compared in terms of accuracy and computational speed. The second application example involves a wave propagation setup in which elastodynamic effects are represented in a long flexible rod. Further application examples include large rigid body rotations.

#### References

- [1] R. Schwertassek and O. Wallrapp. *Dynamik flexibler Mehrkörpersysteme (in German)*. Teubner B.G. GmbH, 2014.
- [2] J.A. Cottrell, T.J.R. Hughes, and Y. Bazilevs. *Isogeometric Analysis*. John Wiley & Sons, Ltd, 2009.
- [3] D. Schillinger, L. Dedè, M.A. Scott, J.A. Evans, M. J. Borden, E. Rank, and T.J.R. Hughes. An isogeometric design-through-analysis methodology based on adaptive hierarchical refinement of NURBS, immersed boundary methods, and t-spline CAD surfaces. *Computer Methods in Applied Mechanics and Engineering*, 249-252:116–150, 2012.
- [4] K. L. Johnson. *Contact Mechanics*. Cambridge University Press, 2004.

## A toolkit of componets to design a soft gripper

Malte Grube<sup>1</sup>, Hristiana Velichkova<sup>2</sup>, Jan Christian Wieck<sup>1</sup>, Bodo Fiedler<sup>2</sup>, Robert Seifried<sup>1</sup>

<sup>1</sup> Institute of Mechanics and Ocean Engineering  
Hamburg University of Technology  
Eissendorfer Strasse 42, 21073 Hamburg, Germany  
[malte.grube, robert.seifried]@tuhh.de

<sup>2</sup> Institute of Polymer and Composites  
Hamburg University of Technology  
Denickestraße 15, 21073 Hamburg, Germany  
[hristiana.velichkova, fiedler]@tuhh.de

### EXTENDED ABSTRACT

Soft material robots are an emerging and fast-growing field of research with potential application in various technical fields. These applications include, but are not limited to medical applications and all sorts of human-machine-interaction. Due to the soft structure, conventional components and design methodologies are not applicable. Therefore, new actuators, sensors and control concepts are currently developed.

Soft robots are particularly suitable for gripping applications. Their flexible design allows them to grip differently shaped objects with little control effort while their softness protects even sensitive objects from damage. For reliable control of the gripping process of various objects accurate knowledge about the position, orientation and deformation of the gripper is essential. Many soft robots use the bending deformation of long slender rods to generate the necessary motion. For example, the fingers of a flexible hand can be considered as such a deformable rod. Therefore, especially bending sensors are of interest for soft robots. However, conventional sensors cannot be used for estimation of the robot's curvature, since they would destroy the robot's softness. Other conventional sensors with an already flexible structure, such as strain gauges, cannot be used due to the large strains that occur in soft robots. Therefore, various, mostly resistive, capacitive, magnetic or optical, sensors are currently being developed for soft robots.

Conventional actuators cannot be integrated into soft material robots, since they are rigid components. They would counteract the soft structure. Additionally, conventional actuators are designed for rigid robots with a very limited number of degrees of freedom. As soft robots typically have an unlimited number of degrees of freedom conventional actuators are often not suitable for the actuation of soft robots. Therefore, alternative concepts, such as cable-driven actuators, shape memory alloys (SMA) or electroactive polymers (EAP) as actuators are necessary for soft robots.

Furthermore, for simulation and control of soft robots accurate modeling of soft robots is required. Modeling rod-like structures with large deformations is especially important for soft robots. In contrast to rigid robots and flexible link robots, large elastic deformations occur in soft robots. Therefore, established modeling methods in traditional robotics, such as modeling with rigid multibody systems or flexible multibody systems using the floating frame of reference approach, are unsuitable for soft robots. For soft robots methods such as ANCF, the geometrically exact rod theory or piecewise constant curvature approaches are necessary.

In this contribution a toolkit is presented, which has been developed for the design of new soft robots. It contains concepts for the sensing, actuation and modeling of soft robots. In fig. 1 an overview of the components in this toolkit is given. Some of these components will then be used in this contribution to build a gripper with three fingers. It is based on the structure of a human hand and is constructed from three simple soft robot segments.

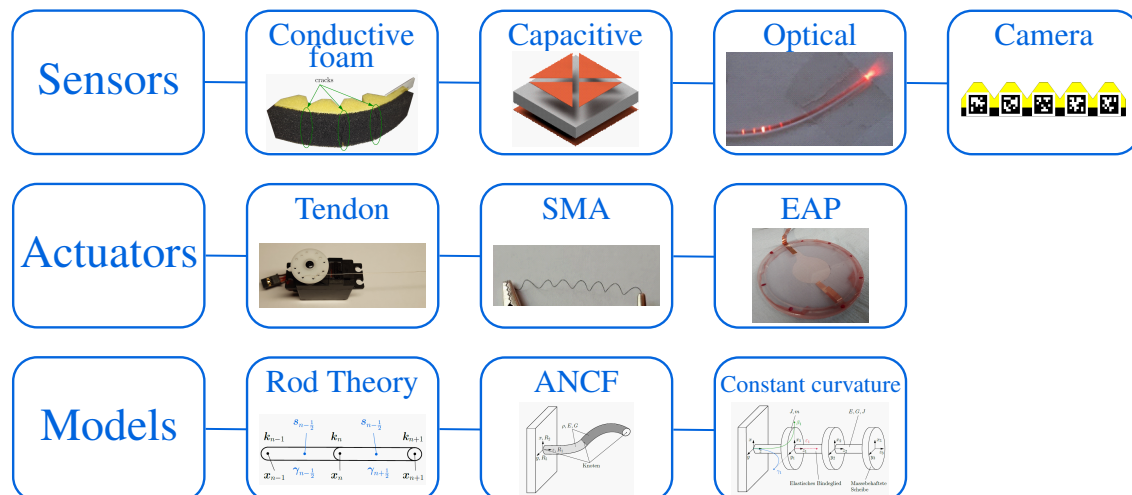


Figure 1: Overview of the Toolbox.

One of these segments is shown in fig. 2. The soft robot segment is made of foam and is actuated by a tendon. In addition, a resistive bending sensor made of electrically conductive foam is integrated. The resistive curvature sensor is based on electrically conductive foam attached to the robot. Deformations of the foam lead to a change in electrical resistance which can be measured and used to determine the curvature of the soft robot. For the conductive foam a high conductivity and a sufficient mechanical robustness to prevent fatigue and the formation of cracks is of importance. The resistance of the foam can be measured with a simple voltage divider. Since the sensor behavior is nonlinear and hysteretic, a neural network is used to determine the curvature of the soft robot from the measured foam resistances. In fig. 3 the total bending angle of the soft robot segment, measured with the electrically conductive foam, is shown for a sinusoidal variation of the bending angle. From the measured curvature of all three fingers of the gripper the shape of the gripped object shall be determined.

The soft robot segment is actuated by a servo via a tendon. This allows a simple design, easy control and comparatively high actuation forces. For the simulation of the gripping process the geometrically exact rod theory is used. The three fingers of the gripper are modeled as separate rods. This model can represent bending, torsion, axial deformations and shear deformations. However, due to the design of the gripper the dominating deformation is bending.

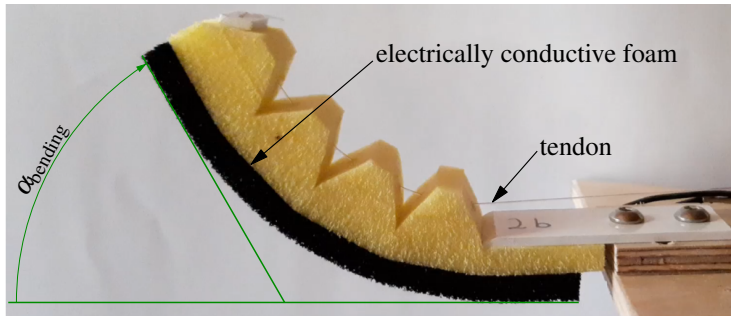


Figure 2: Soft robot segment.

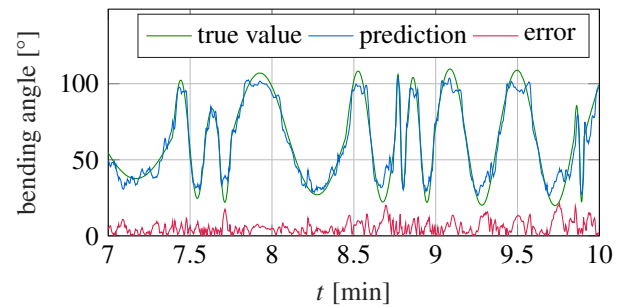


Figure 3: Measured and true bending angle.

# Adjoint optimisation of worm-like body locomotion

Jose J. Muñoz<sup>1,2,3</sup>, Ashutosh Bijalwan<sup>1,2</sup>,

<sup>1</sup> Laboratori de Càlcul Numèric  
Universitat Politècnica de Catalunya  
08034, Barcelona, Spain

j.munoz@upc.edu, ashutoshbijalwan48@gmail.com

<sup>2</sup> Centre Internacional de Mètodes Numèrics en Enginyeria  
Gran Capità s/n  
08034 Barcelona, Spain

<sup>3</sup> Institut de Matemàtiques de la UPC - BarcelonaTech  
c/ Pau Gargallo 14  
08028 Barcelona, Spain

## EXTENDED ABSTRACT

### 1 Continuous optimisation problem

This work aims at computing the optimal sequence of body motion that maximises the displacement of the centre of mass of soft worm-like body. The body has been discretised in space, and its kinematics is given by a vector  $\mathbf{x}(t) = \{\mathbf{x}^0(t), \mathbf{x}^1(t), \dots, \mathbf{x}^m(t)\}$  that represents the body coordinates at each one of the  $M$  nodes  $\mathbf{x}_i(t)$ . The dynamical equilibrium is given by a second order ODE that for each point  $\mathbf{x}_i$  reads,

$$\mathbf{g}^i(\ddot{\mathbf{x}}, \dot{\mathbf{x}}, \mathbf{x}, \mathbf{u}) \equiv \rho \ddot{\mathbf{x}}^i + \boldsymbol{\eta} \dot{\mathbf{x}}^i + \nabla_{\mathbf{x}^i} U - \mathbf{m}^i(t) = \mathbf{0}, i = 1, \dots, M \quad (1)$$

with  $\mathbf{m}^i(t)$  an input function,  $U(\mathbf{x})$  an elastic potential, and  $\boldsymbol{\eta}$  a frictional coefficient matrix. The optimisation of the locomotion is considered by minimising the following cost function:

$$J(T) = \frac{1}{2} \int_0^T (\mathbf{x}(t) - \mathbf{x}_d)^T \mathbf{R} (\mathbf{x}(t) - \mathbf{x}_d)^T dt + \frac{\alpha}{2} \int_0^T \|\mathbf{m}(t)\|^2 dt$$

with  $\mathbf{x}_d$  a constant target position,  $\mathbf{R}$  a weighting matrix, and  $[0, T]$  the interval of interest. Parameter  $\alpha$  represents the cost of the active bending of the worm. In summary, we aim at solving the following continuous optimisation problem:

$$\min_{\mathbf{m}} J(T) \quad (2)$$

$$s.t. \mathbf{g}^i(\ddot{\mathbf{x}}, \dot{\mathbf{x}}, \mathbf{x}, \mathbf{m}) = \mathbf{0} \quad (3)$$

$$\ddot{\mathbf{x}}(0) = \ddot{\mathbf{x}}_0, \dot{\mathbf{x}}(0) = \dot{\mathbf{v}}_0 \quad (4)$$

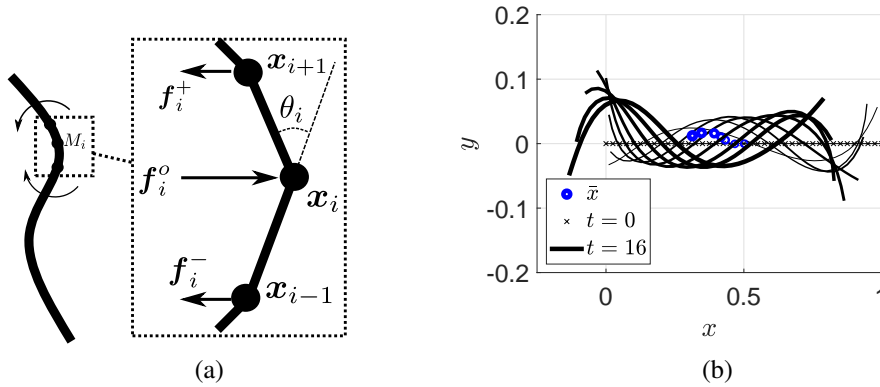


Figure 1: (a) Schematic of worm model with set of forces that form an active moment  $M_i$ , and (b) Illustrative motion for a given sequence of active moments, with center of mass  $\bar{\mathbf{x}}$ .

### 2 Optimality equations of discretised problem

We follow the approach discretise-then-differentiate in order to solve numerically the optimisation problem [1]. In the following we replace the superscript  $i$  indicating the node for simplicity. The cost function  $J(T)$  is discretised in time with a series of time point  $t_n, n = 0, \dots, N$  and replaced by

$$J = \frac{1}{2} \sum (\mathbf{x}_n - \mathbf{x}_d)^T \mathbf{R} (\mathbf{x}_n - \mathbf{x}_d) + \frac{\alpha}{2} \sum_{n=1}^N \|\mathbf{m}_n\|^2$$

and the set of ODEs in (1) are replaced by the following set of equations at each time  $t_{n+1}$ :

$$\begin{aligned}\mathbf{g}_{n+1} &\equiv \rho \frac{\Delta v}{\Delta t} + \nabla_x U + \boldsymbol{\eta} \mathbf{v}_{n+1} + \mathbf{m}_{n+1} = \mathbf{0} \\ \mathbf{h}_{n+1} &\equiv \mathbf{v}_{n+1} - \frac{\Delta \mathbf{x}}{\Delta t} = \mathbf{0}\end{aligned}$$

In order to write the optimality conditions we build the Lagrangian function [4, ?]:

$$L = J + \sum_{n=1}^N \boldsymbol{\lambda}_n \mathbf{g}_n + \sum_{n=1}^N \boldsymbol{\mu}_n \mathbf{h}_n \quad (5)$$

The optimality conditions then read:

$$\begin{aligned}\frac{\partial L}{\partial \mathbf{x}_n} = \mathbf{0} : & \quad \mathbf{R}(\mathbf{x}_n - \mathbf{x}_d) + \left( \frac{\partial \mathbf{g}_n}{\partial \mathbf{x}_n} \right)^T \boldsymbol{\lambda}_n + \left( \frac{\partial \mathbf{g}_{n+1}}{\partial \mathbf{x}_n} \right)^T \boldsymbol{\lambda}_{n+1} + \left( \frac{\partial \mathbf{h}_n}{\partial \mathbf{x}_n} \right)^T \boldsymbol{\mu}_n + \left( \frac{\partial \mathbf{h}_{n+1}}{\partial \mathbf{x}_n} \right)^T \boldsymbol{\mu}_{n+1} = \mathbf{0} \\ \frac{\partial L}{\partial \mathbf{v}_n} = \mathbf{0} : & \quad \left( \frac{\partial \mathbf{g}_n}{\partial \mathbf{v}_n} \right)^T \boldsymbol{\lambda}_n + \left( \frac{\partial \mathbf{g}_{n+1}}{\partial \mathbf{v}_n} \right)^T \boldsymbol{\lambda}_{n+1} + \left( \frac{\partial \mathbf{h}_n}{\partial \mathbf{v}_n} \right)^T \boldsymbol{\mu}_n + \left( \frac{\partial \mathbf{h}_{n+1}}{\partial \mathbf{v}_n} \right)^T \boldsymbol{\mu}_{n+1} = \mathbf{0} \\ \frac{\partial L}{\partial \mathbf{m}_n} = \mathbf{0} : & \quad \alpha \mathbf{m}_n + \left( \frac{\partial \mathbf{g}_n}{\partial \mathbf{m}_n} \right)^T \boldsymbol{\lambda}_n + \left( \frac{\partial \mathbf{g}_{n+1}}{\partial \mathbf{m}_n} \right)^T \boldsymbol{\lambda}_{n+1} + \left( \frac{\partial \mathbf{h}_n}{\partial \mathbf{m}_n} \right)^T \boldsymbol{\mu}_n + \left( \frac{\partial \mathbf{h}_{n+1}}{\partial \mathbf{m}_n} \right)^T \boldsymbol{\mu}_{n+1} = \mathbf{0} \\ \frac{\partial L}{\partial \boldsymbol{\lambda}_n} = \mathbf{0} : & \quad \mathbf{g}_n = \mathbf{0} \\ \frac{\partial L}{\partial \boldsymbol{\mu}_n} = \mathbf{0} : & \quad \mathbf{h}_n = \mathbf{0}\end{aligned}$$

Note that these correspond to the time-discretisation of the adjoint equations associated to the continuous optimisation problem in (2) [2].

### 3 Numerical Solution

The non-linear equations form a banded but coupled systems with unknowns  $\mathbf{z}_n = \{\mathbf{x}_n, \mathbf{v}_n, \mathbf{m}_n, \boldsymbol{\lambda}_n, \boldsymbol{\mu}_n\}$ ,  $n = 1, \dots, N$ . The solution strongly depends on the initial iterates  $\mathbf{z}^0$ , which can be estimated by solving successive uncoupled systems where only  $\mathbf{z}^n$  is unknown, but all other variables up to time  $t_{n-1}$  fixed. We present solutions with full Newton-Raphson and also resorting using adapted conjugate gradient strategies [3] based on finding optimal directionn for  $\mathbf{m}_n$  from the error in the third optimallity condition. For linear systems, where all the terms in parenthesis in the optimality conditions are constant, a closed solution may be found in terms of initial  $\mathbf{z}_1$  and last unknowns  $\mathbf{z}_N$ .

### Acknowledgements

This work has been financially supported by the Spanish Ministry of Science and Innovation through grants DPI2016-74929-R and CEX2018-000797-S, and the local government Generalitat de Catalunya with grant 2017 SGR 1278.

### References

- [1] J.T. Betts. *Practical Methods for Optimal Control and Estimation Using Nonlinear Programming*. Society for Industrial and Applied Mathematics (SIAM), Philadelphia, USA, 2nd edition, 2010.
- [2] A.E. Bryson and Y.C. Ho. *Applied Optimal Control. Optimization, Estimation and Control*. Taylor & Francis, New York, U.S.A., 1975.
- [3] L.S. Lasdon, S.K. Mitter, and A.D. Waren. The conjugate gradient method for optimal control problems. 12(2):132–138, 1967.
- [4] R.F. Stengel. *Optimal control and estimation*. Dover, New York, USA, 1994.
- [5] David G. Hull. *Optimal control theory for applications*. Mechanical Engineering Series. Springer, New York, 2003.

# Topology Optimization for Eigenfrequencies of a Flexible Multibody System

Jialiang Sun<sup>1</sup>, Qiang Tian<sup>2</sup>, Haiyan Hu<sup>1,2</sup>

<sup>1</sup>State Key Laboratory of Mechanics and  
Control of Mechanical Structures  
Nanjing University of Aeronautics and  
Astronautics  
Nanjing 210016, China  
sunjialiang@nuaa.edu.cn  
hhyae@nuaa.edu.cn

<sup>2</sup>MOE Key Laboratory of Dynamics  
and Control of Flight Vehicle  
School of Aerospace Engineering  
Beijing Institute of Technology  
Beijing 100081, China  
tianqiang\_hust@aliyun.com

## EXTENDED ABSTRACT

### 1 Introduction

Topology optimization has the ability to improve the dynamic performance of a flexible multibody system (FMBS) while reducing its weight. Recent years have witnessed the fast development of the dynamic topology optimization of a FMBS. However, previous works [1] mainly focused on the dynamic response topology optimization of a FMBS, that is, reducing the deformations, vibrations, and stresses of a FMBS. Some works [2] also tried to take the dynamic characteristics of a FMBS into consideration when doing the topology optimization, but only considered one flexible structure instead of a FMBS. Hence, in this work, dynamic characteristics topology optimization of a FMBS is studied by considering the eigenfrequency objectives or constraints.

### 2 Dynamic model of a FMBS

In order to obtain a convincing topology optimization result, an accurate dynamic model of the FMBS to be optimized should be established first. In this work, the absolute nodal coordinate formulation (ANCF) is used to describe the large deformation and large overall motion of a FMBS. As a non-incremental finite element method, ANCF has many merits such as constant mass matrix, simple (mostly linear) kinematic constraints, direct link to topology optimization models which also requires finite element discretization, and so on.

The dynamic equations of a general FMBS described via ANCF can be expressed as

$$\begin{cases} \mathbf{M}\ddot{\mathbf{q}} + \mathbf{F}(\mathbf{q}) + \Phi_q^T \boldsymbol{\lambda} = \mathbf{Q}(\mathbf{q}, \dot{\mathbf{q}}) \\ \Phi(\mathbf{q}, t) = \mathbf{0} \end{cases} \quad (1)$$

where  $\mathbf{M}$  is the constant mass matrix of the system,  $\mathbf{q}$  is the vector of generalized coordinates,  $\boldsymbol{\lambda}$  is the Lagrange multiplier vector,  $\mathbf{F}$  is the nonlinear elastic force vector, and  $\mathbf{Q}$  is the generalized external force vector. The second equation in Eq. (1) represents the kinematic constraints including driving constraints, and  $\Phi_q$  denotes the partial derivative matrix of constraint equation with respect to the generalized coordinate vector.

By linearizing Eq. (1) about the equilibrium state  $(\mathbf{q}_0, \boldsymbol{\lambda}_0, t_0)$ , one gets

$$\hat{\mathbf{M}}\delta\ddot{\mathbf{y}} + \hat{\mathbf{C}}\delta\dot{\mathbf{y}} + \hat{\mathbf{K}}\delta\mathbf{y} = \mathbf{0} \quad (2)$$

where  $\hat{\mathbf{M}} = \begin{bmatrix} \mathbf{M} & \mathbf{0} \\ \mathbf{0} & \mathbf{0} \end{bmatrix}$ ,  $\hat{\mathbf{C}} = \begin{bmatrix} \mathbf{C} & \mathbf{0} \\ \mathbf{0} & \mathbf{0} \end{bmatrix}$ ,  $\hat{\mathbf{K}} = \begin{bmatrix} \mathbf{K} & \Phi_q^T \\ \Phi_q & \mathbf{0} \end{bmatrix}$ ,  $\mathbf{C} = \partial\mathbf{Q}/\partial\dot{\mathbf{q}}$ ,  $\mathbf{K} = \partial(\mathbf{F} + \Phi_q^T \boldsymbol{\lambda} - \mathbf{Q})/\partial\mathbf{q}$ ,  $\delta\mathbf{y} = [\delta\mathbf{q}^T \ \delta\boldsymbol{\lambda}^T]^T$ . By

substituting the solution  $\delta\mathbf{y} = e^{\gamma t}\mathbf{Z}$  into Eq. (2), the eigenvalue problem of a FMBS can be obtained as follows [3]

$$(\gamma^2 \hat{\mathbf{M}} + \gamma \hat{\mathbf{C}} + \hat{\mathbf{K}})\mathbf{Z} = \mathbf{0} \quad (3)$$

where  $\gamma$  is the eigenvalue whose imaginary part represents eigenfrequency and  $\mathbf{Z}$  is the corresponding eigenvector.

### 3 Topology optimization for eigenfrequencies of a FMBS

Topology optimization aims at placing given material within a prescribed design domain to achieve optimized performances. It can change the mass and stiffness matrices by optimizing the distribution of the material so as to control the eigenfrequencies of a FMBS as desired. For example, if one wants to maximize the first-order eigenfrequency of a FMBS, the topology optimization formulation can be mathematically expressed as follows



$$\begin{aligned}
& \underset{\boldsymbol{\rho} \in \mathbb{R}^{N_\rho}}{\text{maximize}} && \omega_1 \\
& \text{subject to} && \left( \gamma_n^2 \hat{\mathbf{M}} + \gamma_n \hat{\mathbf{C}} + \hat{\mathbf{K}} \right) \mathbf{Z}_n = \mathbf{0}, \quad (n = 1, 2, \dots, N_d) \\
& && V(\boldsymbol{\rho}) - V_{\text{spec}} = 0 \\
& && 0 < \rho_{\min} \leq \rho_e \leq 1, \quad (e = 1, 2, \dots, N_\rho)
\end{aligned} \tag{4}$$

where the objective function  $\omega_1$  is the first-order eigenfrequency of a FMBS. Among the constraints, the first one is the complex eigenvalue problem with  $N_d$  denoting the number of degrees of freedom for the system. The second constraint is the equality volume constraint, where  $V(\boldsymbol{\rho})$  is the volume ratio of the flexible multibody system and  $V_{\text{spec}}$  is a specified volume fraction.  $\rho_e$  is the design variable [4], i.e., the density of the  $e$ -th finite element,  $\rho_{\min}$  is a small positive number and usually  $\rho_{\min} = 10^{-9}$ .

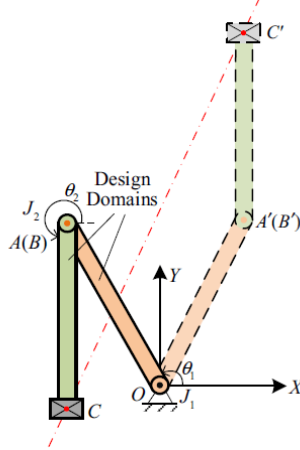


Figure 1: A two-link flexible manipulator

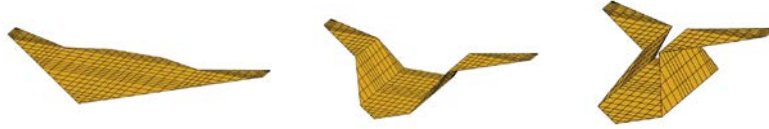


Figure 2: A flexible folding-wing aircraft

#### 4 Case studies

As shown in Figures 1 and 2, some numerical examples are presented to validate the accuracy of the dynamic model for modal analysis of a FMBS and to show the effectiveness of the topology optimization methodology for eigenfrequencies of a FMBS.

#### Acknowledgments

This work was supported in part by the National Natural Science Foundation of China under Grants 12002153, 11832005 and the Natural Science Foundation of Jiangsu Province under Grants BK20200434.

#### References

- [1] E Tromme, A Held, P Duysinx, O Brls. System-based approaches for structural optimization of flexible mechanisms. Archives of Computational Methods in Engineering, 25(3): 817-844, 2018.
- [2] J Sun, Q Tian, H Hu, N. L. Pedersen. Topology optimization for eigenfrequencies of a rotating thin plate via moving morphable components. Journal of Sound and Vibration, 448: 83-107, 2019.
- [3] C Yang, D Cao, Z Zhao, Z Zhang, G Ren. A direct eigenanalysis of multibody system in equilibrium. Journal of Applied Mathematics, 2012: 1-12, 2012.
- [4] E Andreassen, A Clausen, M Schevenels, B. S. Lazarov, O Sigmund. Efficient topology optimization in MATLAB using 88 lines of code. Structural and Multidisciplinary Optimization, 43(1): 1-16, 2011.

Wallyson Thomas<sup>1</sup>, Rouben Rostamian<sup>2</sup>, Attila Szilagyi<sup>3</sup>

<sup>1</sup>Faculty of Mechanical Engineering and Informatics  
University of Miskolc  
Miskolc, 3515, Hungary  
szmwally@uni-miskolc.hu

<sup>2</sup>Department of Mathematics and Statistics  
University of Maryland  
Baltimore County  
Baltimore, MD 21250, USA  
rostamian@umbc.edu

<sup>3</sup> Faculty of Mechanical Engineering and Informatics  
University of Miskolc  
Miskolc, 3515, Hungary  
szilagyi.attila@uni-miskolc.hu

## DYNAMIC ANALYSIS OF AN INTERNAL TURNING TOOL WITH ELASTIC FOUNDATION (WINKLER MODEL)

### 1 Introduction

A problem of the internal turning process is the appropriate fixation of the boring bar at the lathe's tool holder. Conventional fixation generally does not guarantee a satisfactory static stiffness to this fixture and this is a factor of increased vibration. The results showed by [1] that if the Easy Fix bushing is used, it is possible to machine holes almost 30% longer than using a conventional bushing, due to its smaller mass, better distribution of the clamping force and geometry of the Easy Fix bushing as we can see in Figure 1.

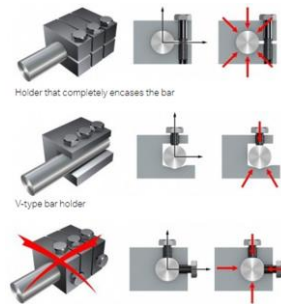


Figure 1: Clamping conditions to internal turning tool

This paper focuses on the clamping properties influence on the dynamic properties of clamped boring bars. The boring bar is modeled as a cantilever Euler–Bernoulli beam and a three span configuration in a Winkler foundation, in this way, this theory is applied to derive the transcendental equation for a general case applicable to the system with span beam at an arbitrary location. Eigenvalue plots of the first five modes are presented along with their respective mode shapes. The corresponding natural frequency equations are given and obtained by numerical calculation. The theoretical calculations are validated and discussed. These results confirm that within reason, the theory matches the literature and have relatively approach with the experimental values.

### 2 Materials and methods

For the internal turning tests of this work, the tool holder was set at a CNC Romi Galaxy 10, Fanuc 21iT command, 7 CV of main power and maximum spindle speed of 6000 rpm. The vibration signal of the internal turning bar was captured with one piezoelectric accelerometer connected to a data acquisition board developed by Bruel & Kjaer with RT Pro Dynamic Signal Analysis software. The FRF's (Frequency Response Function) were obtained by impact tests (test tap). For this, an impact hammer and accelerometer were used. The frequency range of the vibration signals was from 0 to 10000 Hz, 1Hz interval with the smallest possible resolution in the system used. The experiments evaluated overhangs higher than  $L/D = 3$ , since smaller ratios do not get relevant results for this research, as has also been stated by [2].

The tool holder had a diameter of 16 mm and a total length (L) of 270 mm where L1 indicates the tool overhang, L2 the fixture length and L3 the tail of the tool which the corresponding ISO code of A16R SCLCR 09-R - Sandvik. The Easy Fix bushing made by steel had ISO code is: 132L-4016105-B – Sandvik.

The clamp housing was analyzed with different overhangs (L/D) as follow: 3; 3.25; 3.5; 3.75; 4; 4.25; 4.5; 4.75 and 5. The manufacturer's catalogues recommended a maximum L/D ratio for a conventional alloy steel cutting tool, equal to 4 [3]. However, it is an underestimation of the critical L/D ratio, as the dynamics of machine tool and clamping or the selection of cutting conditions and workpiece material also partly contribute to the dynamics of cutting process. Therefore, it was chosen a limit overhang of 5.

Assuming a constant cross-section along the boring bar, neglecting the head, the dimensions from Figure 3 result in a cross-sectional area (A) equal to  $1.922 \cdot 10^{-4} \text{ m}^2$ , moment of inertia (I) equal to  $2.750 \cdot 10^{-9} \text{ m}^4$  and Young Modulus (E) equal to 200 GPa.

As reported in Figure 2, impact tests were executed by hammering the tool tip in transverse direction (perpendicular to the insert

rake angle), since it is mostly responsible for the regenerative effect causing chatter during the cutting process. After that, the accelerometer transfers the signal to the computer (with the modal analysis software RT photon - Brüel & Kjær) and this signal is captured by the data acquisition module. Owing to geometrical dimensions in Table 1 of the clamping-boring bar structure with the corresponding cross sections, just transverse direction was measured during the impact test in different overhang configurations, also confirming the hypotheses outlined by [4].

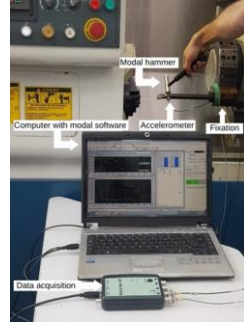


Figure 2. Setup for Modal Analysis experiment

### 3 Results and discussion

The beam, in Figure 3, occupies the interval  $0 < x < (L1+L2+L3)$ . The part  $L2$  is embedded in Winkler foundation of a uniform stiffness  $k$ . The rest of the beam moves freely. At  $x = 0$  and  $x = (L1+L2+L3)$  the second and third derivatives of the displacement are zero, that is, we are dealing with free-free boundary conditions. The equation (1) represents the equation of motion of the beam:

$$EI \frac{\partial^4 y}{\partial x^4} + \rho A \frac{\partial^2 y}{\partial t^2} + K(x)y = 0 \quad (1)$$

where  $y = y(x, t)$  is the transverse displacement at the point  $x$  at time  $t$ . The coefficient  $K(x)$  is the stiffness of the foundation (at  $x$ ) measured as force per unit length per unit displacement.  $K(x)$  may vary with  $x$  in an arbitrary way in general but in our calculations we are specifically interested in the cases where  $K(x)$  is piecewise constant.

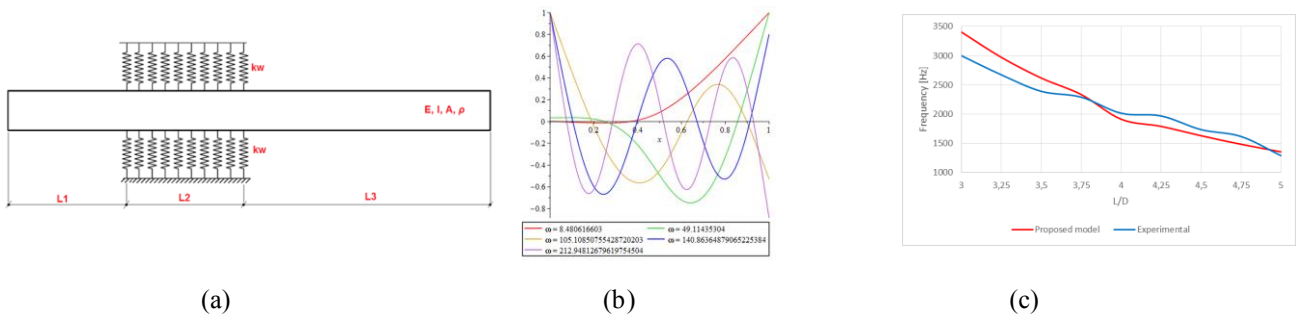


Figure 3: (a) Proposed model for a beam partially supported on a Winkler foundation (mid-support), (b) mode shapes of the proposed model and (c) comparison between the numerical values and the experimental results of the internal turning tool with Easy Fix tool-holder.

### 4 Conclusion

It was possible to model a fixation of the tooling system by applying Euler Bernoulli beam model with Winkler Foundation. Furthermore, costly and time-consuming experiments could be replaced by even analytical modelling with manual calculations, which enables us to judge the influence of the geometrical dimensions, the material properties, the possible overhangs and the fixation dimensions of the tool-holder system.

### References

- [1] Thomas, Wallyson; Diniz, Anselmo Eduardo; Suyama, D. I.; Magri, A. comparação entre a fixação convencional e a bucha easy fix para torneamento interno de aço endurecido com longos balanços da ferramenta, (IX Cobef), Brazil, 2017.
- [2] HOSHI, T. Vibration analysis of mechanical cutting. Kogyo Chasakai Publishing Co. Ltd 1990.
- [3] SANDVIK. Silent tool for turning: overcome vibrations in internal turning. 2016. < [http://www.sandvik.coromant.com/en-us/products/silent\\_tools\\_turning](http://www.sandvik.coromant.com/en-us/products/silent_tools_turning)>. Acess 2021.
- [4] Lazoglu, Ismail, Fuat Atabey, and Yusuf Altintas. "Dynamics of boring processes: Part III-time domain modeling." International journal of machine tools and manufacture 42, no. 14 (2002): 1567-1576.

# Non-Linear Beam Formulation with NURBS Interpolation for the Simulation of Sliding Contacts

Paul Wasmer, Peter Betsch

Institute of Mechanics, Karlsruhe Institute of Technology, 76131 Karlsruhe, Germany  
paul.wasmer@kit.edu, peter.betsch@kit.edu

## EXTENDED ABSTRACT

### 1 Introduction

Beam elements play an important role in the simulation of many engineering problems, for example in the simulation of sliding contacts such as aerial runways. One of the most important models in the non-linear analysis is the geometrically exact beam formulation [1, 2]. The geometrically exact beam formulation allows arbitrarily large deformations with finite strains, while the cross-section of the beam remains planar.

The orientation of the beam's cross-section is mostly described using rotational variables. However, without additional effort, the discretization of the rotations with finite elements is not frame-indifferent [3]. Thus, we use a formulation based on directors, three orthonormal vectors, to describe the orientation of the beam's cross-section [4, 5, 6, 7]. As shown by Simo [8] structure-preserving time integrators are of great advantage as non-preserving integrators may not be stable. Therefore, an energy-momentum conserving time integrator is used.

For the simulation of sliding contact problems a smooth representation of the geometry over element boundaries is necessary to achieve a structure-preserving model [9]. For this purpose the isogeometric analysis using non-uniform rational B-Splines (NURBS) is well suited as NURBS of order higher than one are at least  $C^1$  continues over element boundaries.

We, therefore, implement NURBS into the director-based geometrically exact beam formulation [4]. This beam formulation is then used for the simulation of an energy-conserving sliding contact of two beams. The contact condition is implemented using a structure-preserving null-space matrix approach [9].

### 2 Constrained Geometrically Exact Beam Formulation

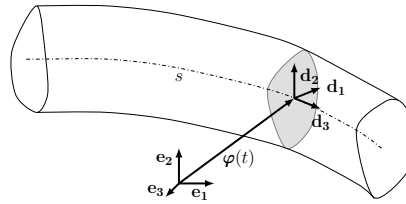


Figure 1: Configuration of a beam

The configuration of a beam is shown in Fig. 1. The position of any point of the beam can be described by

$$\mathbf{x}(s, t, \theta^1, \theta^2) = \boldsymbol{\varphi}(s, t) + \theta^\alpha \mathbf{d}_\alpha(s, t), \quad (1)$$

where  $s \in [s_1, s_2]$  ( $s_1, s_2 \in \mathbb{R}$ ) is referred to as the arc-length,  $\boldsymbol{\varphi} \in \mathbb{R}^3$  describes the reference curve of the beam and  $\theta^\alpha \in \mathbb{R}$  are convective coordinates. In this connection,  $\boldsymbol{\varphi}$  points to the centerline of the beam and  $\theta^\alpha$  gives the position on the cross-section. Three directors  $\mathbf{d}_i \in \mathbb{R}^3$  are used, where  $\mathbf{d}_1$  and  $\mathbf{d}_2$  span the cross-sectional area of the beam and  $\mathbf{d}_3$  is defined by

$$\mathbf{d}_3(s, t) = \mathbf{d}_1(s, t) \times \mathbf{d}_2(s, t). \quad (2)$$

The directors are mutually orthonormal for all  $t \in \mathbb{R}$ . That is,

$$\mathbf{d}_i(t) \cdot \mathbf{d}_j(t) = \delta_{ij}, \quad (3)$$

where  $\delta_{ij}$  denotes the Kronecker delta. To enforce the orthonormality of the directors constraints are used

$$\boldsymbol{\lambda} : [\mathbf{d}_i \otimes \mathbf{d}_i - \mathbf{I}] = \boldsymbol{\lambda} : \boldsymbol{\Phi} = 0, \quad (4)$$

where the constraints  $\boldsymbol{\Phi}$  are given by

$$\boldsymbol{\Phi} = \mathbf{d}_i \otimes \mathbf{d}_i - \mathbf{I}. \quad (5)$$

In case of Lagrange shape function the constraints are usually strongly enforced at the nodes [4, 6]. However, as the shape functions are not interpolatory in case of discretization with NURBS the constraints must be enforced in a weak sense, leading to the corresponding contribution to the weak form

$$G^{\text{con}}(\mathbf{d}_i, \boldsymbol{\lambda}, \delta \mathbf{d}_i, \delta \boldsymbol{\lambda}) = \int_0^L \boldsymbol{\lambda} : \text{Grad}(\boldsymbol{\Phi}) \cdot \delta \mathbf{d}_i + \delta \boldsymbol{\lambda} : \boldsymbol{\Phi} ds. \quad (6)$$

### 3 Sliding Contact

A sketch of the sliding of a beam  $\mathcal{A}$  along a beam  $\mathcal{B}$  is shown in Fig. 1. The contact condition can be modeled using a penalty

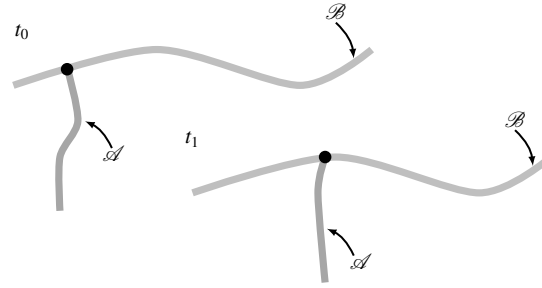


Figure 2: Sliding contact of two beams at times  $t_0$  and  $t_1$

approach, Lagrange multipliers, or the combination of both, an augmented Lagrangian approach. However, these methods have significant disadvantages, as they are either unstable or increase the complexity and size of the numerical system [10]. Hence, here the null space matrix approach, also reported as the master-slave approach, is applied. The null space matrix relates the coordinates of both beams without additional variables and does not increase the complexity of the underlying DAE. Additionally to the smooth interpolation with NURBS, we use a mid-point evaluation of the contact constraints in combination with an energy-momentum conserving time integration scheme resulting in an energy-conserving contact algorithm.

### References

- [1] J. C. Simo. A finite strain beam formulation. The three-dimensional dynamic problem. Part I., *Computer Methods in Applied Mechanics and Engineering*, 49 (1): 55-70, 1985.
- [2] J. C. Simo, L. Vu-Quoc. On the dynamics of flexible beams under large overall motions-the plane case: Part I, *Journal of Applied Mechanics*, 53 (4): 849-854, 1986.
- [3] M. Crisfield, G. Jelenić. Objectivity of strain measures in the geometrically exact three-dimensional beam theory and its finite-element implementation, *Proceedings of the Royal Society A Mathematical, Physical and Engineering Science*, 455: 1125-1147, 1998.
- [4] P. Betsch, P. Steinmann. Frame-indifferent beam finite elements based upon the geometrically exact beam theory, *International Journal for Numerical Methods in Engineering*, 54 (12): 1175-1788, 2002.
- [5] P. Betsch, P. Steinmann. Constrained dynamics of geometrically exact beams, *Computational Mechanics*, 31: 49-59, 2003.
- [6] I. Romero, F. Armero. An objective finite element approximation of the kinematics of geometrically exact rods and its use in the formulation of an energy-momentum conserving scheme in dynamics, *International Journal for Numerical Methods in Engineering*, 54 (12): 1683-1716, 2002
- [7] J. Harsch, G. Capobianco, S. Eugster. Finite element formulations for constrained spatial nonlinear beam theories, *Mathematics and Mechanics of Solids*, 0: 1-26, 2021.
- [8] J. C. Simo, N. Tarnow, M. Doblare. Non-linear dynamics of three-dimensional rods: Exact energy and momentum conserving algorithms, *International Journal for Numerical Methods in Engineering*, 38 (9), 1431-1473, 1995
- [9] A. Sibilieau, J. Muñoz. Conserving time-integration of beams under contact constraints using B-Spline interpolation, *MULTIBODY DYNAMICS 2011, ECCOMAS Thematic Conference*, Brussels, Belgium, 2011 (July 2011)
- [10] G. Jelenić, M. Crisfield. Dynamic analysis of 3D beams with joints in presence of large rotations, *Computer methods in applied mechanics and engineering*, 190: 4195-4230, 2011

# Coupled Multibody Model Of Industrial Robot With Milling Simulator For Trajectory Compensation

Valentin Dambly<sup>1</sup>, Hoai Nam Huynh<sup>2</sup>, Olivier Verlinden<sup>1</sup>, Édouard Rivière-Lorphèvre<sup>1</sup>

<sup>1</sup> Faculty of Engineering  
University of Mons

Place du parc 20, 7000 Mons, Belgium

[valentin.dambly, olivier.verlinden, edouard.rivierelorphèvre]@umons.ac.be

<sup>2</sup> Department of Mechanical Engineering  
University of British Columbia

BC V6T 1Z4, Vancouver, Canada

hoainam.huynh@ubc.ca

## EXTENDED ABSTRACT

### 1 Introduction

Robotic machining is a fast-growing technology in the field of mechanical manufacturing. Indeed, it is generally accepted that for the same working space, a fully equipped robotic machining cell can cost 30 to 50% less than a conventional machine tool. Furthermore, robotic machining enables an interesting agility in the cutter motion to deal with complex workpieces geometry. However, inaccuracies resulting either from vibrations or deflections occur while the robot is subjected to cutting forces. As an order of magnitude, the tool-tip deviation in 6060 Aluminium is typically 200  $\mu\text{m}$  and can rise up to 300  $\mu\text{m}$ .

The causes of these issues are numerous and have been identified then classified according to their nature [1]. Among the deviations sources, a major contribution appears to be the flexibility of the robot. It has been investigated and appears to be caused by the robot articulations in a proportion of 80% while the remaining flexibility issues from the structural elasticity of the links [2].

In order to improve the accuracy of robotic machining operations, several approaches have been carried out such as the study of stable cutting conditions and the online/offline compensation of the tool trajectory [1]. Within the frame of industry 4.0 and the concept of virtual twin, offline models can be developed in order to predict instabilities and compensate deviations. However, for the offline compensation, it is necessary to model both aspects of the operation, on the one hand the model of the cutting machine, being an industrial robot in robotic machining, and on the other hand, the machining model including the resulting geometry of the workpiece.

The articular flexibility is introduced in the multibody model by adding rotational degrees of freedom at the articulations (along transmission and orthogonal directions). Several approaches are developed in the literature depending on the parameters chosen for the flexibility modelling [1]. These approaches propose to determine an equivalent torsional stiffness value at the articulation and to use this value to calculate the corresponding deflection of the tool centre point [4, 5]. It has been shown that the articular flexibility modelling is improved by adding a damping contribution [2]. An illustration of the articular flexibility is given in the figure 1a. With the introduction of damping, the direct compensation of the position is no longer sufficient.

A robot performing a machining operation can be considered as a multibody chain with perturbation forces applied on the tool centre point (TCP). In order to be able to simulate 5-axis operations, it is necessary to couple a machining force module that can compute these forces for such TCP motion. Concerning the modelling of machining operation, several approaches exist depending on the motive of the simulation [3]. The most appropriate candidates for time-based simulation where the cutting forces are needed at each time-step are the voxel and the dixel approaches [3]. Models coupled with voxel method have been developed for model-based compensation [5]. However, the complexity of voxel model is  $O(n^3)$  against  $O(n^2)$  for dixel. The proposed machining force module is then based on dixel representation technique.

### 2 Applied Methods

A coupled model is proposed with the multibody model of the robot subjected to machining forces, computed by an in-house 3D dixel-based machining module. The latter must then be computed at each time step along the tool path. The multibody model includes the flexibility induced by the structure and the articulations [2].

The multibody system including the additional degrees of freedom consists of an under-actuated system subjected to perturbation forces. Instead of acting in the control variables space, the compensation will focus on the operational space variables. In order to compensate the deviations, a solution is proposed where the trajectory in the operational space is discretized in nodes with a compensation applied on them. The algorithm given in figure 1b aims to detect and add nodes at critical locations of the path and reposition them to reduce the deviation.

The replacement of the trajectory nodes is improved with an optimisation layer. The design variables are the positions and velocities of successive nodes. The optimisation problem is given in the following equation:

$$\min_{p_{n_i}, v_{n_i}, p_{n_{i+1}}, v_{n_{i+1}}} \sum_{k=0}^N \|p_{TCP} - p_t\| \cdot \gamma_k \quad (1)$$

where the parameters are successive nodes  $(n_i, n_{i+1})$  positions and velocities,  $p_{TCP}$  is the tool centre point position,  $p_t$  the ideal path and  $\gamma_k$  is a weighting factor equal to 1 while machining and 0 else where. As a proof of concept, the node replacement

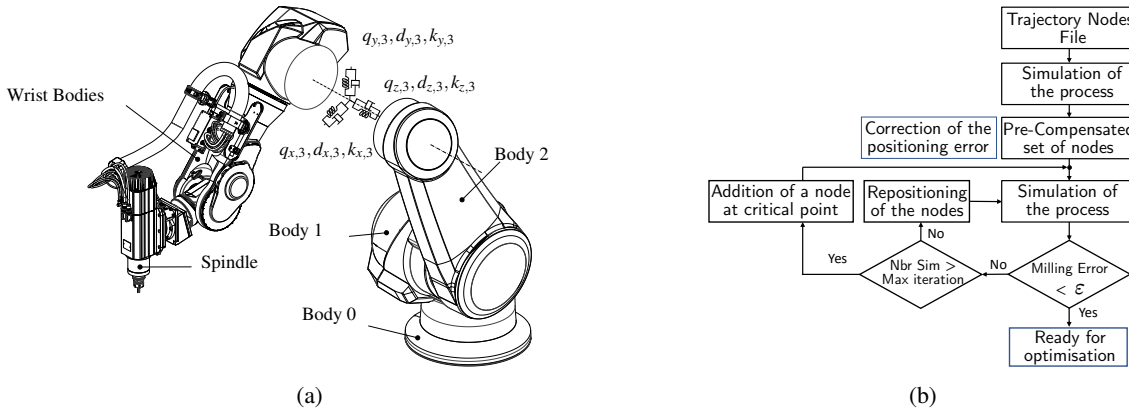


Figure 1: (a) : Representation of the multibody modelling of a Stäubli TX200 robot dedicated to machining. For readability reasons, the articular flexibility is only explicitly shown for the third joint. (b) : Node placement algorithm for trajectory compensation in the operational space.

with optimisation layer in the operation has been carried out for the simplified model represented in figure 2a. The results of this approach are given in figure 2b, where the TCP deviation is cancelled following the repositioning performed by the algorithm and the optimisation layer focused on the entrance deviation compensation.

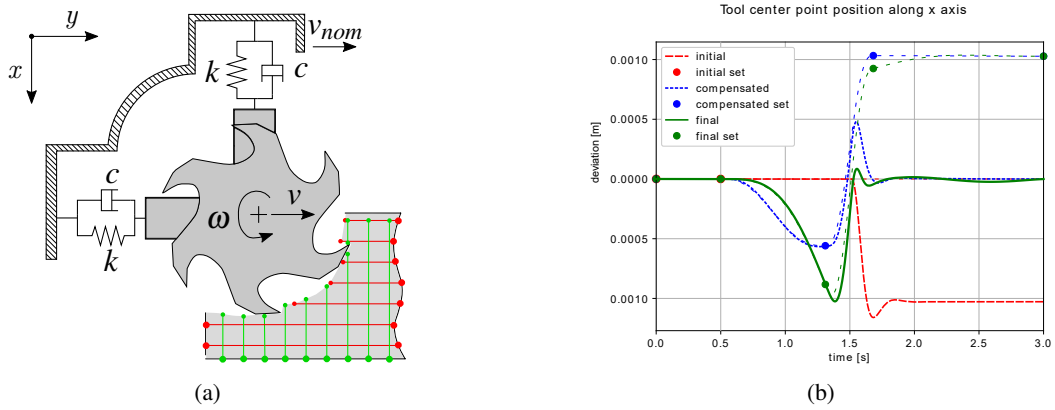


Figure 2: (a) : Simplified system, consisting of tool attached, through spring-damper pairs, to a body moving along y and coupled with the dixel modelled workpiece. (b) : Comparison of deviations in the normal directions at the entrance of the workpiece depending on the input trajectories. Three trajectories are represented : the initial (unmodified) one, the one resulting from the node replacement algorithm 1b and the one after optimisation process.

## Acknowledgments

The authors would like to acknowledge the Belgian National Fund for Scientific Research (FNRS-FRS) for the grant allotted to V. Dambly.

## References

- [1] A. Verl, A. Valente, S. Melkote, C. Brecher, E. Ozturk, T. Tunc. Robots in machining, Elsevier Ltd., CIRP Annals, vol.68, pages 799-822, 2019.
- [2] H. N. Huynh, H. Assadi, V. Dambly, E. Rivière-Lorphèvre, O. Verlinden. Direct method for updating flexible multibody systems applied to a milling robot. Elsevier Ltd., Robotics and Computer-Integrated Manufacturing, vol. 68, 2021.
- [3] Y. Altintas, P. Kersting, D. Biermann, E. Budak, B. Denkena, I. Lazoglu. Virtual process systems for part machining operations. CIRP Annals - Manufacturing Technology, vol. 63, pages 585-605, 2014.
- [4] A. Klimchik, D. Bondarenko, A. Pashkevich, S. Briot, B. Furet. Compliance Error Compensation in Robotic-Based Milling, Informatics in Control, Automation and Robotics, Springer, vol. 283, pages 197-216, 2014.
- [5] M.F. Zaeh, F. Schnoes, B. Obst, D. Hartmann. Combined offline simulation and online adaptation approach for the accuracy improvement of milling robots. Elsevier Ltd., CIRP Annals, vol.69, pages 337-340, 2020.



**Section**

**FORMALISMS AND NUMERICAL METHODS**

FORM-1-2-3

# Tensorial Deformation Measures for the Floating Frame of Reference Formulation

Valentin Sonneville<sup>1</sup>, Michel Géradin<sup>2</sup>

<sup>1</sup> Department of Mechanical Engineering, Chair of Applied Mechanics  
Technical University of Munich,  
Boltzmannstr. 15, 85748 Garching, Germany  
valentin.sonneville@tum.de

<sup>2</sup> Institute for Advanced Study  
Technical University of Munich  
Lichtenbergstr. 2a, 85748 Garching, Germany  
mgeradin@gmail.com

## EXTENDED ABSTRACT

For the geometrically linear behavior of an elastic body, the finite element method defines a discretized energy of deformation

$$\mathcal{V} = \frac{1}{2} \underline{u}^T \underline{K} \underline{u} \quad (1)$$

where  $\underline{K}$  is the constant stiffness matrix and  $\underline{u}$  is an array of small nodal translations and rotations with respect to a global, inertial frame. For geometrically non-linear problems, like those encountered in flexible multibody systems [1, 2], the treatment of large amplitude motions implies that the nodal variables of a finite element model are finite motions, namely finite translations  $\underline{x}(t) \in \mathbb{R}^3$  and finite rotations  $\underline{R}(t) \in SO(3)$ , both expressed with respect to a global, inertial frame. A common strategy in flexible multibody systems is to extend eq. (1) to large amplitude motions by arguing that, when expressed with respect to an appropriate frame, displacements remain small. To that end, the discretized energy of deformation must be expressible as

$$\mathcal{V} = \frac{1}{2} \underline{E}^T \underline{K} \underline{E}$$

where  $\underline{K}$  is the stiffness matrix of the linear case in eq. (1) and  $\underline{E}$  is now an array of appropriate 6-dimensional deformation measures, whose definition involves essentially two steps [3, 4]:

1. The definition, from the nodal motions, of relative motions that are *objective*, i.e. that are not affected by rigid-body motions.
2. The extraction, from the objective relative motions, of deformation measures that are *tensorial*, i.e. that leave the energy of deformation unaffected under a change of reference.

In the floating frame of reference formulation, the definition of nodal deformation measures is classically done by stacking the translational part of the relative motion and rotation parameters of the rotational part:

$$\underline{F}_{e,i} = \begin{bmatrix} \underline{x}_{e,i} \\ p(\underline{R}_{e,i}) \end{bmatrix} = \begin{bmatrix} \underline{R}_{r,i}^T \underline{R}_F^T (\underline{x}_i - \underline{x}_F) - \underline{R}_{r,i}^T \underline{x}_{r,i} \\ p(\underline{R}_{r,i}^T \underline{R}_F^T \underline{R}_i) \end{bmatrix}, \quad \text{for each node } i, \quad (2)$$

where  $p$  is a parameterization of rotation and

- $(\underline{x}_i(t), \underline{R}_i(t))$  are the nodal coordinates in the current configuration resolved in the global, inertial frame,
- $(\underline{x}_F(t), \underline{R}_F(t))$  are the coordinates of the floating frame of reference resolved in the global, inertial frame,
- $(\underline{x}_{r,i}, \underline{R}_{r,i})$  are the nodal coordinates of the undeformed configuration resolved in the floating frame,
- $(\underline{x}_{e,i}(t), \underline{R}_{e,i}(t))$  are the nodal coordinates of a relative motion resolved in the floating reference configuration.

While being objective, the classical deformation measures in eq. (2) are not tensorial. Their lack of tensoriality is essentially due to the fact that they do not include the available information of the change in the orientation of the local material fibers when evaluating the translational part of the deformation. Indeed, this information suggests that translational deformation is partly due to the change in orientation rather than due to a pure effect of translation. In this work, we show that

$$\underline{E}_i = \begin{bmatrix} \underline{\varepsilon}_i \\ \underline{\kappa}_i \end{bmatrix} = \begin{bmatrix} \underline{T}_p^{-T}(\underline{\kappa}_i) \underline{x}_{e,i} \\ p(\underline{R}_{e,i}) \end{bmatrix} = \begin{bmatrix} \underline{T}_p^{-T}(\underline{\kappa}_i) & \underline{0} \\ \underline{0} & \underline{I} \end{bmatrix} \underline{F}_{e,i}, \quad \text{for each node } i, \quad (3)$$

are objective, tensorial deformation measures, where  $\underline{T}_p$  is the tangent operator associated with parametrization  $p$ . They exhibit a localized, non-linear coupling between the translational and rotation parts. While such deformation measures appear naturally from the algebraic manipulations when kinematics is treated in terms of motions [5], namely coupled translations and rotations,

they can be constructed geometrically as the parameters of a fictitious constant-deformation path between the floating reference configuration and the current configuration.

In numerical applications, we show that these deformation measures are able to capture accurately complex effects of deformation that are usually claimed to be outside of the scope of the floating frame of reference formulation. For instance, the centrifugal stiffening effect that characterizes the dynamic problem described by Wu and Haug [6] can be captured accurately by the tensorial deformation measures, whereas the classical deformation measures exhibit a response that is too soft, see Fig. 1

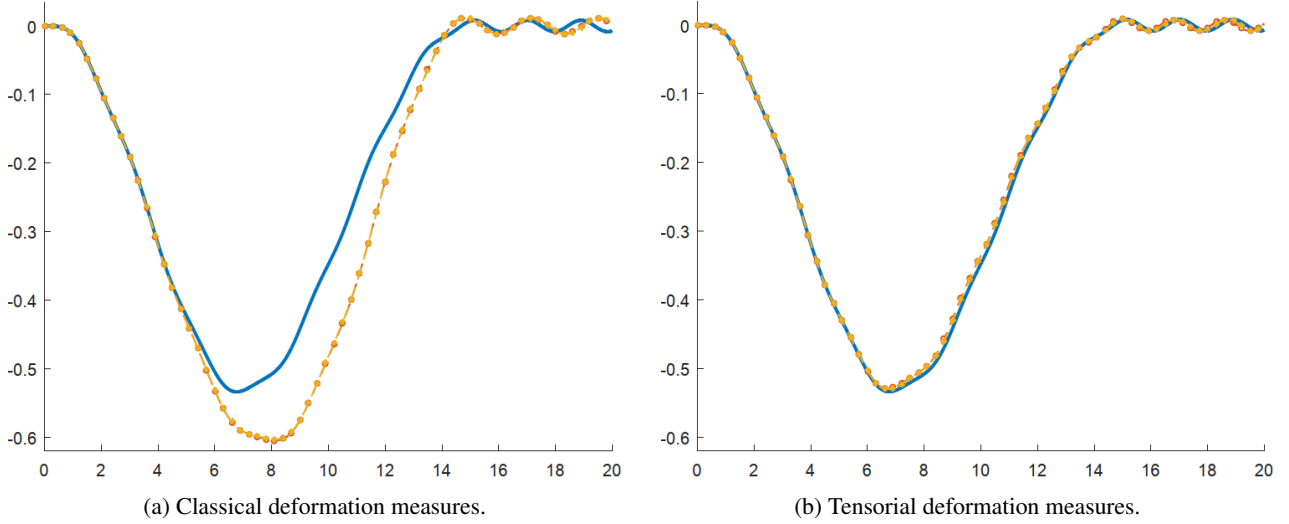


Figure 1: Time history of the transverse tip displacement for the rotating beam example by Wu and Haug [6]. Reference solution from a non-linear finite element analysis [5] (—), floating frame of reference solution (\*—).

The simplicity of relationship between the classical deformation measures and the proposed tensorial deformation measures in eq. (3) suggests that existing implementations could be modified easily.

## References

- [1] M. Géradin and A. Cardona. *Flexible Multibody System: A Finite Element Approach*. John Wiley & Sons, New York, 2001.
- [2] O.A. Bauchau. *Flexible Multibody Dynamics*. Springer, Dordrecht, Heidelberg, London, New-York, 2011.
- [3] P. Masarati and M. Morandini. Intrinsic deformable joints. *Multibody System Dynamics*, 23(4):361–386, 2010.
- [4] O.A. Bauchau, L.H. Li, P. Masarati, and M. Morandini. Tensorial deformation measures for flexible joints. *Journal of Computational and Nonlinear Dynamics*, 6(3):031002 1–8, 2011.
- [5] V. Sonnevile, M. Scapolan, M. Shan, and O. A. Bauchau. Modal reduction procedures for flexible multibody dynamics. *Multibody System Dynamics*, 51:377–418, 2020.
- [6] E.J. Wu, S. Haug. Geometric non-linear substructuring for dynamics of flexible mechanical elements. *International Journal for Numerical Methods in Engineering*, 26:2211–2226, 1988.

# Direct Sensitivity Analysis of Spatial Multibody Systems with Friction using Penalty Formulation

Adwait Verulkar<sup>1</sup>, Corina Sandu<sup>1</sup>, Daniel Dopico<sup>2</sup>, Adrian Sandu<sup>3</sup>

<sup>1</sup> Terramechanics, Multibody and  
Vehicle Systems Laboratory  
Dept. of Mechanical Engineering  
Virginia Tech  
Blacksburg, Virginia 24061  
[adwaitverulkar, csandu]@vt.edu

<sup>2</sup> Laboratorio de Ingeniería Mecánica  
Dept. of Naval and Industrial Engineering  
University of A Coruña  
A Coruña, Spain 15001  
ddopico@udc.es

<sup>3</sup> Computational Science Laboratory  
Dept. of Computer Science  
Virginia Tech  
Blacksburg, Virginia 24061  
sandu@vt.edu

## EXTENDED ABSTRACT

### 1 Introduction

From the onset of the 21<sup>st</sup> century, the focus of the research in multibody dynamics has shifted to modeling of *real* systems. Such systems are typically characterized by non-linear phenomenon like friction, imperfections in the joints including lubrication and clearances, and systems with discontinuous velocity trajectories, or in other words, hybrid-dynamical systems. Joint friction occurs in all mechanical systems and can possibly have a substantial impact on the dynamics, optimal control, wear, and consequently the operational life of the system. Optimization of such systems is a novel area of research and the methodologies of direct and adjoint sensitivity analysis are the most prominent gradient-based optimization techniques employed for this purpose. Time-based sensitivities are relatively cheaper to compute through direct and adjoint methods as compared to other numerical techniques like finite differences for the same accuracy [1]. Before any of these studies can be conducted, a proper choice of the multibody formulation is necessary. Although Lagrangian formulations are comparatively simple, they contain redundant states (Lagrange multipliers) and require DAE integrators for computation of dynamics and sensitivities. Moreover, Lagrangian formulations are not well suited to handle redundant constraints and singularities. Both of these limitations can be addressed by using the modified Lagrangian formulation, also known as the penalty formulation, which was introduced by Bayo et al. in 1988 [2].

The contribution of this article is in the development of the equations of motion and the methodology of direct sensitivity analysis of multibody systems with joint friction using the penalty formulation. Friction in the system has been represented using the Brown and McPhee friction model [3]. A case study has been conducted on a spatial mechanism and the results of dynamics and sensitivity analysis have been presented. Results of the penalty formulation have also been compared with those obtained through the index-1 Lagrangian formulation.

### 2 Penalty formulation for multibody systems with joint friction

Bayo et al. [2] modified the Lagrangian formulation based on the Hamiltonian description of dynamics, but instead of appending the constraints  $\Phi$  to the formulation, the authors incorporated them in the formulation itself using a penalty matrix  $\alpha$ . This approach leads to a system of  $n$  ordinary differential equations (ODEs) as opposed to the  $n + m$  differential algebraic equations (DAEs) of the classical Lagrangian formulations. The equations of motion can be expressed in a compact ODE form as follows

$$\bar{M}\ddot{q} = \bar{Q} \quad (1)$$

where

$$\bar{M} = M + \Phi_q^T \alpha \Phi_q \quad (2)$$

$$\bar{Q} = Q + Q^{Af*} - \Phi_q^T \alpha (\dot{\Phi}_q \dot{q} + \dot{\Phi}_t + 2\xi \omega \dot{\Phi} + \omega^2 \Phi) \quad (3)$$

In penalty formulation, the Lagrange multipliers are approximated with the following term

$$\lambda^* = \alpha (\ddot{\Phi} + 2\xi \omega \dot{\Phi} + \omega^2 \Phi) \quad (4)$$

Since, the exact Lagrange multipliers do not exist in penalty formulation, the friction force vector  $Q^{Af*}$  is calculated based on the approximate Lagrange multipliers given in Equation (4). The term that depends on the Lagrange multipliers in  $Q^{Af*}$  is actually the magnitude of the joint reaction force  $F_n^*$ . Based on Haug (2018) [4], the equation for the joint reaction force in the joint-fixed reference frame for a body  $i$  using approximate Lagrange multipliers can be written as

$$F_n^* = \left| \mathbf{F}_i^{rk} \right| = \left| -\mathbf{C}_i^{kT} \mathbf{A}_i^T \Phi_{\mathbf{r}_i}^{kT} \lambda^{*k} \right| \quad (5)$$

In penalty formulation, neither of the constraint equations nor their derivatives are exactly satisfied, however, reasonable accuracy can be achieved through a right choice of penalty factors, natural frequency and damping ratio. In this analysis, we have considered  $\alpha = 1000$ ,  $\xi = 1$  and  $\omega = 10$  rad/s.

### 3 Direct sensitivity analysis for multibody systems with joint friction

The direct differentiation method for the sensitivity analysis using the penalty formulation was first presented by Pagalday (1997) [5]. To obtain the expression for the model sensitivities, Equation (1) is differentiated with respect to the model parameters.

$$\frac{d\bar{\mathbf{M}}}{d\rho_k}\ddot{\mathbf{q}} + \bar{\mathbf{M}}\frac{d\ddot{\mathbf{q}}}{d\rho_k} = \frac{d\bar{\mathbf{Q}}}{d\rho_k}, \quad k = 1, 2, \dots, p \quad (6)$$

The derivatives can be expanded and rearranged into  $p$  Tangent Linear Models (TLMs) as follows

$$\bar{\mathbf{M}}\ddot{\mathbf{q}}_\rho + \bar{\mathbf{C}}\dot{\mathbf{q}}_\rho + (\bar{\mathbf{K}} + \bar{\mathbf{M}}_q\ddot{\mathbf{q}})\mathbf{q}_\rho + \mathbf{L}^{Af*}\boldsymbol{\lambda}_\rho^* = \bar{\mathbf{Q}}_\rho - \bar{\mathbf{M}}_\rho\ddot{\mathbf{q}} \quad (7)$$

The term  $\boldsymbol{\lambda}_\rho^*$  represents the sensitivities of the approximate Lagrange multipliers with respect to the design parameters  $\boldsymbol{\rho}$ . These can be expressed in terms of the sensitivities of the generalized coordinates and their derivatives. This substitution yields the final form of the Tangent Linear Model as shown below

$$(\bar{\mathbf{M}} + \alpha\mathbf{L}^{Af*}\boldsymbol{\Phi}_q)\ddot{\mathbf{q}}_\rho + (\bar{\mathbf{C}} + \alpha\mathbf{L}^{Af*}(\ddot{\boldsymbol{\Phi}}_q + 2\xi\omega\dot{\boldsymbol{\Phi}}_q))\dot{\mathbf{q}}_\rho + (\bar{\mathbf{K}} + \bar{\mathbf{M}}_q\ddot{\mathbf{q}} + \alpha\mathbf{L}^{Af*}(\ddot{\boldsymbol{\Phi}}_q + 2\xi\omega\dot{\boldsymbol{\Phi}}_q + \omega^2\boldsymbol{\Phi}_q))\mathbf{q}_\rho = \bar{\mathbf{Q}}_\rho - \bar{\mathbf{M}}_\rho\ddot{\mathbf{q}} - \alpha\mathbf{L}^{Af*}(\ddot{\boldsymbol{\Phi}}_\rho + 2\xi\omega\dot{\boldsymbol{\Phi}}_\rho + \omega^2\boldsymbol{\Phi}_\rho) \quad (8)$$

### 4 Results and conclusion

A case study was conducted on a spatial slider crank mechanism with joint friction to validate the proposed methodology. This mechanism was adapted from Haug (1989) [6] and the schematic of this system is shown in Figure 1(a). For comparison, the dynamics and sensitivities of the connecting rod with respect to the crank length have been plotted in Figures 1(b) and 1(c) respectively using the index-1 Lagrangian and penalty formulations. The computation using the penalty formulation was found to be 26% faster than the index-1 formulation with the maximum RMSE error in sensitivities of 0.5% for a simulation time of 1 second.

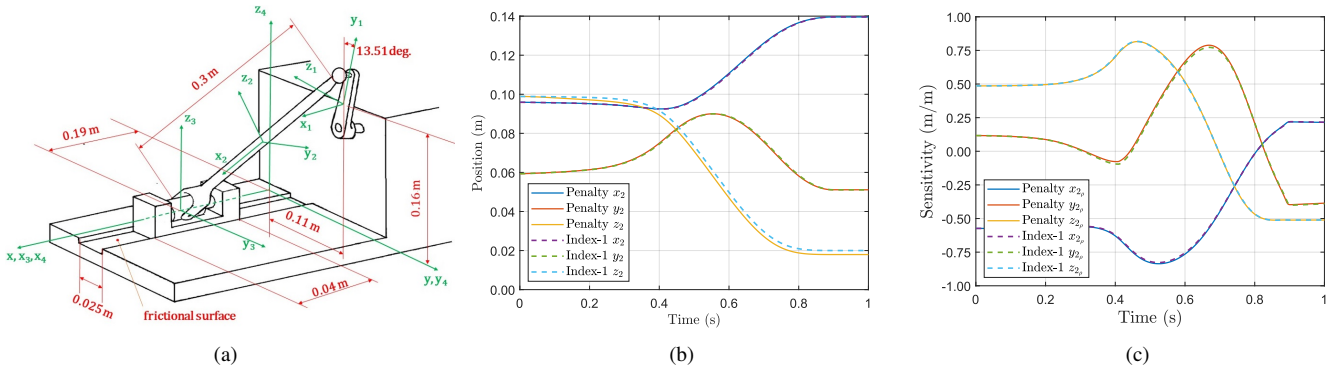


Figure 1: (a) Mechanism schematic. (b) Connecting rod position history. (c) Sensitivity of rod position to crank length.

### Acknowledgments

The work has been supported in part by the Robert E. Hord Jr. Professorship and by the Terramechanics, Multibody, and Vehicle Systems Laboratory at Virginia Tech.

### References

- [1] Y. Zhu, C. Sandu, D. Dopico, and A. Sandu, "Benchmarking of adjoint sensitivity-based optimization techniques using a vehicle ride case study," *Mechanics Based Design of Structures and Machines*, vol. 46, no. 2, pp. 254–266, 2018.
- [2] E. Bayo, J. García de Jalón, and M. A. Serna, "A modified lagrangian formulation for the dynamic analysis of constrained mechanical systems," *Computer Methods in Applied Mechanics and Engineering*, vol. 71, no. 2, pp. 183–195, 1988.
- [3] P. Brown and J. McPhee, "A Continuous Velocity-Based Friction Model for Dynamics and Control with Physically Meaningful Parameters," *Journal of Computational and Nonlinear Dynamics*, vol. 11, no. 5, pp. 1–6, 2016.
- [4] E. J. Haug, "Simulation of spatial multibody systems with friction," *Mechanics Based Design of Structures and Machines*, vol. 46, no. 3, pp. 347–375, 2018. [Online]. Available: <https://doi.org/10.1080/15397734.2017.1377086>
- [5] J. M. Pagalday and A. Avello, "Optimization of multibody dynamics using object oriented programming and a mixed numerical-symbolic penalty formulation," *Mechanism and Machine Theory*, vol. 32, no. 2, pp. 161–174, Feb 1997. [Online]. Available: <https://www.sciencedirect.com/science/article/pii/S0094114X96000377>
- [6] E. J. Haug, *Computer aided kinematics and dynamics of mechanical systems, volume 1: Basic methods*, Massachusetts, 1989.

# An Iterative Procedure For Dynamic Integrity Assessment

Giuseppe Habib

Department of Applied Mechanics  
Faculty of Mechanical Engineering  
Budapest University of Technology and Economics  
Műegyetem rkp. 5., 1111 Budapest, Hungary  
habib@mm.bme.hu

## EXTENDED ABSTRACT

### 1 Introduction

Local stability is one of the most critical properties of a dynamical state. Engineers heavily exploit this concept. Nevertheless, scientists dealing with dynamical systems are aware that, despite its local stability, a system might diverge from its state if subject to a perturbation sufficient to make it cross the boundary of its basin of attraction (BOA). However, the computation of a system's BOAs is computationally very demanding. A few methods for the identification of BOAs of dynamical systems exist [1]. Analytical methods are generally based on Lyapunov functions. However, they are not a feasible option for the majority of real applications. The cell mapping method is probably the most efficient numerical technique for BOA estimation [2]. Experimental methods are almost inexistent, except for a few exceptions [3].

The objective of this study is to develop an algorithm for the robustness assessment of equilibrium points. The procedure reduces the computational cost for global stability analysis by identifying the local integrity measure (LIM) [1] only, overlooking fractal and intermingled portions of the BOA, which are hard to identify and practically less relevant.

### 2 Methodology

The algorithm is based on a simple framework. Considering a predefined region of the phase space, initially, the maximal value of the LIM is calculated, being equal to the minimal distance between the equilibrium point of interest and the boundary of the region of the phase space considered. Then, a trajectory of the system in the phase space is computed. If the trajectory does not converge to the desired solution, the LIM is estimated as the minimal distance between the equilibrium point of interest and any point of the non-convergent trajectory. The new estimated value of the LIM (an overestimate of the real LIM value) defines a hypersphere in the phase space denominated hypersphere of convergence, limiting the region of interest. If a simulation converges to the desired solution, then the LIM is not reduced in that iteration. Initial conditions of each simulation are chosen as the farthest point from any other already tracked point within the hypersphere of convergence.

In order to automatically classify the computed trajectories, the phase space is divided into cells. A trajectory is classified as converging or non-converging to the desired solution by analyzing the cells in which points of the trajectory lie. To reduce computational time, if a trajectory reaches a cell already tracked by a previous trajectory, the simulation is interrupted; all cells containing points of the trajectory are classified according to the reached and already tracked cell. A graphical explanation of the classification procedure adopted is illustrated in Fig. 1.

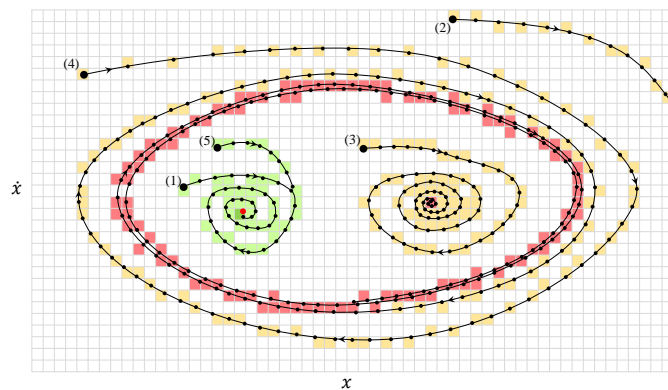


Figure 1: Illustrative examples of trajectory classification. (1) Converging to a known equilibrium; (2) leaving the considered phase space region; (3) converging to an unknown equilibrium; (4) converging to an unknown periodic solution; (5) converging to an already tracked cell.

### 3 Results

We implemented the algorithm on systems of various dimensions (up to dimension 8); the analysis illustrated that the algorithm could rapidly and efficiently estimate the LIM value in all cases studied. In particular, the first few iterations already provided a relatively accurate estimate of the real LIM value. The majority of the subsequent simulations converged to the equilibrium of interest, except few ones, which improved the initial estimate of the LIM. Figure 2a represents the trend of the LIM estimate for the case of a Duffing-van der Pol oscillator with an attached tuned mass damper (4-dimensional system). The black line in Fig. 2a follows the described path. Light blue lines represent the LIM trend for other repetitions of the algorithm. All curves have a similar tendency. The system under study presents a stable equilibrium point (red cross in Fig. 2b) coexisting with a stable periodic solution (black line in Fig. 2b) for the considered parameter values. We remark that, in Fig. 2b, tracked points are projected on a section of the phase space, which makes it appear that red dots are within the hypersphere of convergence (green dashed line) while they are not.

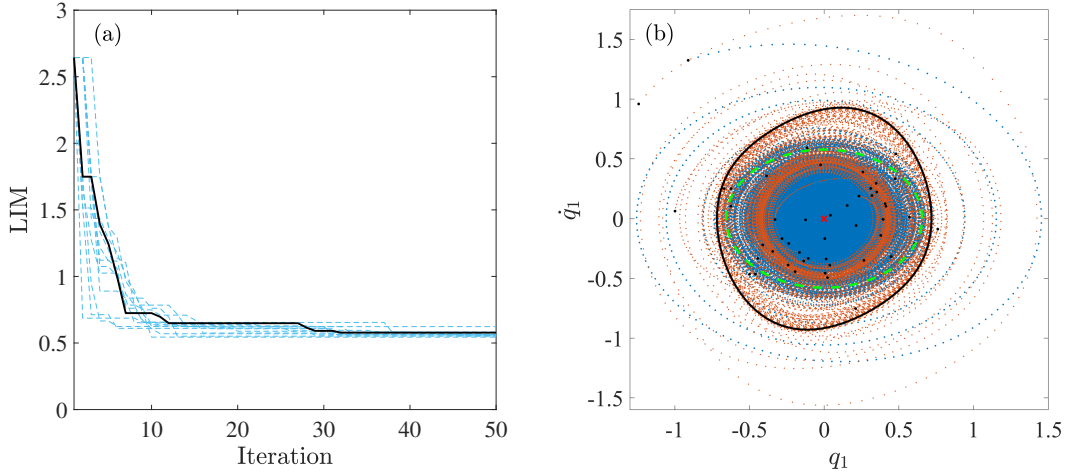


Figure 2: (a) LIM estimated value; (b) projection of the points tracked during the computation; blue and red points: converging and non-converging points, respectively, dashed green line: section of the hypersphere of convergence.

### 4 Conclusions

In this study, a new algorithm for estimating the robustness of a stable equilibrium was developed. The algorithm utilizes an approach different from existing numerical methods for global analysis. It does not aim at studying the whole basin of attraction of a solution; instead, it directly tries to estimate the local integrity measure (LIM). From an engineering point of view, this quantity has obvious relevance for the safety of a dynamical system. The obtained results suggest that the proposed algorithm is a viable option for the robustness assessment of an equilibrium point. In particular, thanks to its quickness, it has the potentiality to be utilized in industrial environments, where rapid solutions are generally pursued. Future research developments should aim to make the algorithm utilizable for the robustness estimation of other kinds of solutions, such as periodic motions.

### Acknowledgments

The Hungarian National Science Foundation financially supported this research under grant number OTKA 134496.

### References

- [1] S. Lenci, G. Rega. Global nonlinear dynamics for engineering design and system safety. Springer, 2019.
- [2] C. S. Hsu. A theory of cell-to-cell mapping dynamical systems. Journal of Applied Mechanics, 47(4):931-939, 1980.
- [3] L. N. Virgin. Introduction to experimental nonlinear dynamics: a case study in mechanical vibration. Cambridge University Press, 2000.



# Hamiltonian-based Optimal Control of Multibody Systems in the Presence of Artificial Discontinuities

Maciej Pikuliński, Paweł Malczyk

Institute of Aeronautics and Applied Mechanics  
Faculty of Power and Aeronautical Engineering  
Warsaw University of Technology  
Nowowiejska str. 24, 00-665 Warsaw, Poland  
[mpikulinski, pmalczyk]@meil.pw.edu.pl

## EXTENDED ABSTRACT

### 1 Introduction

Optimization of multibody or robotic systems always poses challenging problems. Methods in this broad field might concern finding an optimal finite set of time-independent design variables or whole time-domain functions in optimal control tasks. The difficulty stems from the fact that the minimized cost function is implicitly interconnected with the dynamics model. When a gradient-based optimization method is used, the model, in most cases, being a differential-algebraic equation (DAE), makes the gradient computation a cumbersome task.

A great variety of methods is utilized to overcome the problem, e.g., direct differentiation methods or adjoint methods [1]. Our research concentrates on implementing the adjoint method for optimal control of multibody systems in the Hamiltonian setting as we recognize the advantages of using such a set of tools [2]. To be precise, a multibody system is modelled by index-1 DAE in the form

$$\begin{cases} \dot{\mathbf{p}} = \mathbf{M}(\mathbf{q})\dot{\mathbf{q}} - [\Phi_{\mathbf{q}}(\mathbf{q})]^T \boldsymbol{\sigma} & (1a) \\ \dot{\mathbf{p}} = \mathbf{f}(\mathbf{q}, \dot{\mathbf{q}}, \mathbf{u}) - [\dot{\Phi}_{\mathbf{q}}(\mathbf{q}, \dot{\mathbf{q}})]^T \boldsymbol{\sigma} & (1b) \\ \Phi(\mathbf{q})\dot{\mathbf{q}} = \mathbf{0} & (1c) \\ \mathbf{q}(0) = \mathbf{q}_0, \mathbf{p}(0) = \mathbf{p}_0, & (1d) \end{cases}$$

where  $\mathbf{q}, \mathbf{p} \in \mathbb{R}^n$  are dependent coordinates and articulated momenta, respectively, and  $\boldsymbol{\sigma} \in \mathbb{R}^m$  is a Lagrange multiplier, which might be interpreted as constraint force impulse since  $\boldsymbol{\lambda} = \dot{\boldsymbol{\sigma}}$ , where  $\boldsymbol{\lambda}$  is a constraint force. Moreover,  $\mathbf{u}(t)$  is the control function,  $\mathbf{M}(\mathbf{q})$  is the mass matrix and  $\mathbf{f}(\mathbf{q}, \dot{\mathbf{q}}, \mathbf{u})$  represents forces acting on the system. The model incorporates position constraints  $\Phi(\mathbf{q}) = \mathbf{0} \in \mathbb{R}^m$  differentiated to the velocity constraints level.

Considering  $\boldsymbol{\sigma}$  variable, we conclude that some of the vector's elements might become excessively large as the simulation proceeds. Essentially, that is the case for constraint forces whose sign remains unchanged, and  $\boldsymbol{\sigma}$ , being an integral of the  $\boldsymbol{\lambda}$ , continually grows. Consequently, after some time, changes of other elements become insignificant, and the direction of the  $\boldsymbol{\sigma}$  vector might be imprecise. This inaccuracy propagates through the dynamic model as well as the adjoint equations. The issue has a significant impact on finding  $\dot{\mathbf{p}}$  from (1b) because the summand  $[\dot{\Phi}_{\mathbf{q}}(\mathbf{q}, \dot{\mathbf{q}})]^T \boldsymbol{\sigma}$  might eventually overweight forces  $\mathbf{f}(\mathbf{q}, \dot{\mathbf{q}}, \mathbf{u})$  due to the discussed integral growth.

Herein, we propose an approach to limit the values of the  $\boldsymbol{\sigma}$  elements by resetting them at certain events without changing the physics of the phenomena. Unfortunately, this act of resetting introduces discontinuities in the model and renders the task more demanding. As these discontinuity events depend primarily on the implementation, we call the discontinuities artificial in contrast to these of other origins, e.g., impacts or unilateral constraints.

In this work, we follow the framework proposed in [3] to cope with discontinuities both in the forward dynamic task and the solution of the adjoint equations, which alone are an active research area [3, 4]. We simplify the optimal control task by parametrizing the control function  $\mathbf{u}(\mathbf{b}, t)$ , where  $\mathbf{b} \in \mathbb{R}^k$  is a vector of time-independent parameters. Thanks to this assumption, a finite set of variables must be optimized instead of a time function. Ultimately, the optimization methods require a gradient of the cost function  $J(\mathbf{b})$ , which we model as follows

$$J(\mathbf{b}) = \int_0^T h(\mathbf{q}, \dot{\mathbf{q}}, \mathbf{u}, t) dt + S(\mathbf{q}, \dot{\mathbf{q}})|_T, \quad (2)$$

where the integrand  $h(\mathbf{q}, \dot{\mathbf{q}}, \mathbf{u}, t)$  and the end-time cost function  $S(\mathbf{q}, \dot{\mathbf{q}})$  are designed so as to fulfill requirements imposed on the control signal.

### 2 Resetting the $\boldsymbol{\sigma}$ and discontinuities in the model

The so-called transition condition

$$g(\dot{\mathbf{q}}^-, \mathbf{p}^-, \mathbf{q}^-, \mathbf{p}^-, \boldsymbol{\sigma}^-, \mathbf{u}, t_i) = 0 \quad (3)$$

defines time  $t_i$  at which the resetting event takes place. At time  $t_i$ , the system transforms from  $\mathbf{S}_{i-1}^i$  mode to  $\mathbf{S}_i^{i+1}$ , which is

described by the transition function  $\mathbf{T}(\cdot)$ . This function relates values  $\mathbf{a}^-$  just before the event with their counterparts  $\mathbf{a}^+$  in the new mode. If we change  $\boldsymbol{\sigma}$  by  $\Delta\boldsymbol{\sigma}$  to lower its value, the jump conditions, under the assumption of coordinates  $\mathbf{q}$  and forces  $\mathbf{Q} = \mathbf{M}(\mathbf{q})\ddot{\mathbf{q}} + \dot{\mathbf{M}}(\mathbf{q})\dot{\mathbf{q}} - [\Phi_{\mathbf{q}}(\mathbf{q})]^T \boldsymbol{\lambda}$  to be invariant, are as follows

$$\mathbf{T}(\dot{\mathbf{q}}^+, \dot{\mathbf{p}}^+, \mathbf{q}^+, \mathbf{p}^+, \boldsymbol{\sigma}^+, \dot{\mathbf{q}}^-, \dot{\mathbf{p}}^-, \mathbf{q}^-, \mathbf{p}^-, \boldsymbol{\sigma}^-, \mathbf{u}, t_i) = \mathbf{0} \leftrightarrow \begin{cases} \mathbf{q}^+ - \mathbf{q}^- = \mathbf{0}, & \dot{\mathbf{q}}^+ - \dot{\mathbf{q}}^- = \mathbf{0}, \\ \dot{\mathbf{p}}^+ - \dot{\mathbf{p}}^- - \Phi_{\mathbf{q}}^T \Delta\boldsymbol{\sigma} = \mathbf{0}, & \dot{\mathbf{p}}^+ - \dot{\mathbf{p}}^- - \dot{\Phi}_{\mathbf{q}}^T \Delta\boldsymbol{\sigma} = \mathbf{0}, \\ \boldsymbol{\sigma}^+ - \boldsymbol{\sigma}^- - \Delta\boldsymbol{\sigma} = \mathbf{0}. \end{cases} \quad (4)$$

Analogously, we argue in the full paper that the jump conditions might be derived for the adjoint variables.

The introduced approach is applied to optimal control of dual-arm manipulation. The resulting motion of the robotic arms (shown in Fig. 1) produces significant differences in values of summands (1b). In Fig. 2, a comparison of solutions with and without the  $\boldsymbol{\sigma}$ -resetting procedure is presented. In this test case, the  $\boldsymbol{\sigma}$ -resetting routine dimmed the  $[\Phi_{\mathbf{q}}(\mathbf{q}, \dot{\mathbf{q}})]^T \boldsymbol{\sigma}$  by the order of magnitude.

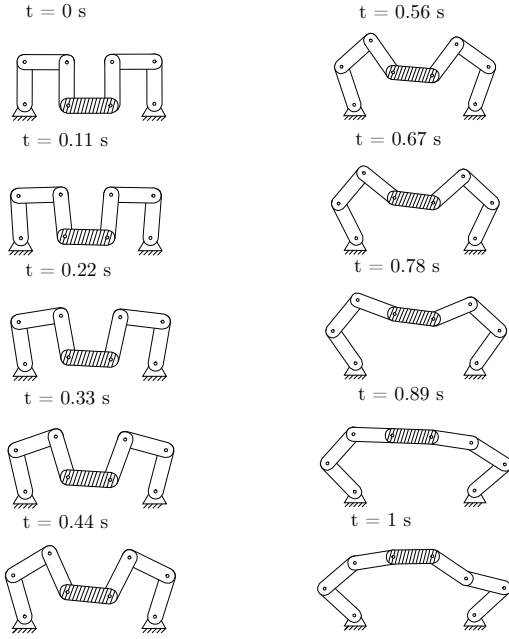


Figure 1: Motion of the bi-manual task.

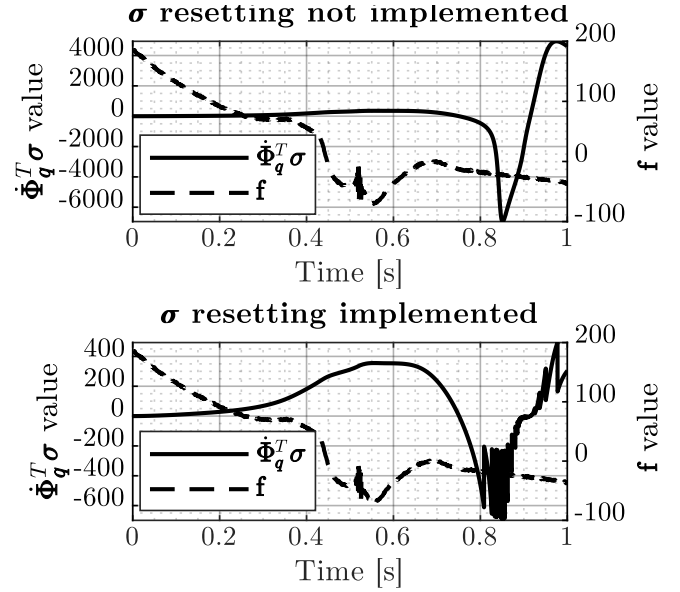


Figure 2: Results of  $\boldsymbol{\sigma}$  resetting introduction.

### 3 Conclusions

This paper presents a method to overcome the problem of the unexpected growth in the values of  $\boldsymbol{\sigma}$  vector, which may deteriorate the quality of the forward dynamics solutions and may adversely influence the results produced by the adjoint method. The proposed approach extends the framework shown in [1, 2] by devising the adjoint method, which is adapted to deal with artificial discontinuities.

We consider this paper as an intermediate step in deriving a more general method, which would directly operate on a time function and support discontinuities stemming from various physical effects, e.g. joint friction forces or impacts. These two features are of current interest for the authors.

**Acknowledgments.** This work has been supported by National Science Center under grant No. 2018/29/B/ST8/00374.

### References

- [1] P. Maciąg, P. Malczyk, and J. Frączek. “Hamiltonian direct differentiation and adjoint approaches for multibody system sensitivity analysis”. In: *International Journal for Numerical Methods in Engineering* 121.22 (2020), pp. 5082–5100. DOI: 10.1002/nme.6512.
- [2] M. Pikuliński and P. Malczyk. “Adjoint method for optimal control of multibody systems in the Hamiltonian setting”. In: *Mechanism and Machine Theory* 166 (2021), p. 104473. ISSN: 0094-114X. DOI: 10/gvgv.
- [3] R. Serban and A. Recuero. “Sensitivity Analysis for Hybrid Systems and Systems With Memory”. In: *Journal of Computational and Nonlinear Dynamics* 14.9 (2019). 091006. ISSN: 1555-1415. DOI: 10.1115/1.4044028.
- [4] S. Corner, A. Sandu, and C. Sandu. “Adjoint sensitivity analysis of hybrid multibody dynamical systems”. In: *Multibody System Dynamics* 49.4 (2020), pp. 395–420. ISSN: 1573-272X. DOI: 10.1007/s11044-020-09726-0.

# A system identification procedure for multibody system dynamics

Ehsan Askari<sup>1</sup>, Guillaume Crevecoeur<sup>2</sup>

<sup>1</sup> Department of Electromechanical, Systems and Metal Engineering, Ghent University, B-9052 Zwijnaarde, Belgium,  
[ehsanaskary@gmail.com](mailto:ehsanaskary@gmail.com)

<sup>2</sup> Department of Electromechanical, Systems and Metal Engineering, Ghent University, B-9052 Zwijnaarde, Belgium,  
[Guillaume.Crevecoeur@ugent.be](mailto:Guillaume.Crevecoeur@ugent.be)

## 1 Introduction

In classic mechanics, governing equations of a system are derived on the basis of, for example, the mass and momentum conservation laws, and principle laws in thermodynamics. Developing such constitutive models to show mechanisms in real-life scenarios requires a good knowledge of the system and its environment. The complexity of machines and multi-physics phenomena involved, environmental conditions, and the lack of information on how system parameters vary over time hinder the accurate construction of efficient physics-based models. In data science, there is a great possibility to integrate statistical learning concepts with classical approaches in applied mechanics and mathematics to discover sophisticated and accurate models of complex dynamical systems directly from data [1]. Such data-driven based models have been obtained using Pareto front, sparsity, time-series (TS) data, equation-free modelling, nonlinear regression, empirical dynamic modelling, modelling emergent behavior, and automated inference of dynamics [1-3]. Data-based model discovery approaches have demonstrated a great capability in fluid mechanics, material science, and dynamical systems to generate parsimonious models [4]. On top of that, the value of system parameters used in the theoretical models of multibody systems plays a very important role in accurately predicting the response of a physical system [5]. Knowing the dynamic equations of a system, linear regression methods are employed to estimate such system parameters. However, in the case that the developed physics-based model does not take into account either the physics of the problem fully or the environment of a given system due to the lack of knowledge, the system parameters estimated from such biased mathematical models can not represent the system accurately. Moreover, in the era of the fourth industrial revolution (Industry 4.0) that is the industry trend and activity towards automation and data exchange in the industry [6], huge amounts of data are available due to the affordable cost of sensors and the universal industrial trend towards smart machines, factories and systems. Thus, the present study aims at developing a data-driven method to identify multibody systems. The governing equations of multibody system dynamics are discovered directly from TS datasets of a given mechanism using an evolutionary symbolic sparse regression approach without prior knowledge of the respective machine. For the discovery of physical models, a dictionary of basis functions is used. To reduce the risk that this dictionary is not covering all functionality required to unravel hidden physical laws, an exploration-exploitation strategy is followed to evolutionarily build and validate the function dictionaries. A symbolic ridge regression method based on genetic programming is used to conduct this process. Illustrative examples are finally considered to demonstrate the capability of the presented approach.

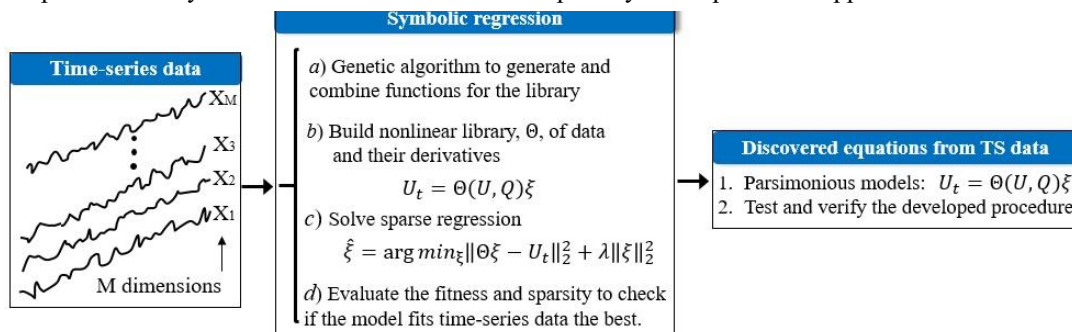


Fig. 1. The workflow of the system identification (SI) approach.

## 2 Mathematical modeling

The ridge regression approach is employed to discover physics-based models directly from TS data while a general form of nonlinear and linear governing equations is considered and there are no restrictions on the functional form of candidate terms, e.g. trigonometric functions, polynomial nonlinearities, etc. In order to avoid overfitting symbolic regression methods, parsimonious models are selected that balance the model's accuracy and complexity [2]. For the discovery of physical models, a dictionary of basis functions is constructed by setting up multiple dictionaries and comparing their ability to discover physical laws. This strategy is embedded in an exploration-exploitation algorithm to evolutionarily build and validate the dictionaries, in which a symbolic genetic algorithm programming is developed to generate symbolic functions randomly and evolutionarily promote mathematical terms that represents the data relatively better than others available in the population. Both genetic algorithm mutation and crossover are employed while the fitness is defined according to the mean square error calculated based on data obtained from each candidate of the governing equations in the population at each generation and the input data. On top of that, after a few generations, a term promoting the model sparsity is multiplied by the previous fitness function as well. The workflow of the model developed in this study is represented in Fig. 1. Three illustrative examples are also considered and the respective discovered models are compared to reference theoretical formulations for validation purposes. The sensitivity of the developed identification system is assessed and errors associated with each case study are reported.

## 3 Results and discussion

The models distilled by the suggested method, corresponding to the TS data obtained theoretically from the mechanisms listed in Table 1, are listed while the associated error percentage is reported by comparing each theoretical reference and its respective discovered model. The evolutionary symbolic regression method used in this study works subjected to the properties listed in

Table 2. The constant  $c$  in the terminal set can get a random value in the range of  $[-10, 10]$  that is adjustable. The results show that the suggested algorithm gives the possibility to reveal both the structure of constitutive equations and the parameter magnitudes of multibody systems. The developed methodology automatically builds the proper library using genetic programming. However, one has to manually add functions that are likely to appear in the system's governing equation once using just regression methods, which requires human involvement with prior knowledge of a given system. Moreover, the robustness of the approach is evaluated by adding Gaussian white noise with zero mean to the TS data associated with the case study (ii) with different levels of signal-to-noise ratio (SNR), i.e. 20 and 30 db. It is observed that the maximum increase of the error percentage is by 8.23 % and occurs when the noisy data with SNR =20 db is used.

Table 1. Demonstrative examples considered in this study to show the efficiency of the presented SI algorithm.

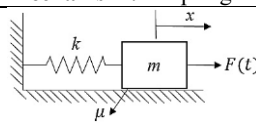
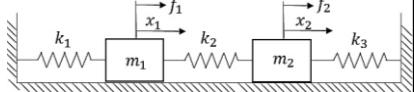
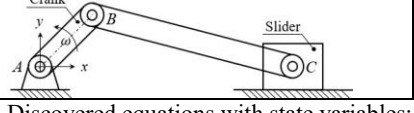
<b>Mechanism i:</b> A spring-mass system with Stribeck friction		
	<p>Stribeck friction model: <math>\mu(\dot{x}) = \begin{cases} (c_d + (c_f - c_d) \exp(-\xi( \dot{x}  - v_0))) \text{sgn}(\dot{x}) &amp;  \dot{x}  &gt; v_0 \\ (c_f - \frac{c_f}{v_0^2} ( \dot{x}  - v_0)^2) \text{sgn}(\dot{x}) &amp;  \dot{x}  \leq v_0 \end{cases}</math></p> <p>Characteristics: <math>m = 10 \text{ kg}</math>, <math>k = 2000 \text{ Nm}^{-1}</math>, <math>F(t) = 200 \sin(2t) \text{ N}</math>, <math>c_f = 0.15</math>, <math>c_d = 0.065</math>, <math>g = 9.81 \text{ m/s}^2</math>, <math>v_0 = 0.1 \text{ m/s}</math>, <math>\xi = -3</math>. Initial values: <math>z _{t=0} = 0</math></p>	
Discovered equations using the state-space representation with state variables: $\mathbf{z}^T = (x \quad \dot{x}) = (z_1 \quad z_2)$		Error (%)
$\dot{\mathbf{z}} = \begin{cases} \begin{pmatrix} 1.0000z_2 \\ 19.9983 \sin(t) - 199.9831z_1 - 0.6389 \text{sgn}(z_2) - 1.1241 \text{sgn}(z_2) \exp(-3.0010 z_2 ) \end{pmatrix} &  z_2  > v_0 \\ \begin{pmatrix} 1.0000z_2 \\ 19.9925 \sin(2.0000t) - 199.9253z_1 + 146.7341z_2^2 \text{sgn}(z_2) - 29.3915z_2 \end{pmatrix} &  z_2  \leq v_0 \end{cases}$		0.45
<b>Mechanism ii:</b> A two-degree-of-freedom spring-mass system		
	<p>Characteristics: <math>m_1 = 10 \text{ kg}</math>, <math>m_2 = 5 \text{ kg}</math>, <math>k_1 = 200 \text{ Nm}^{-1}</math>, <math>k_2 = 300 \text{ Nm}^{-1}</math>, <math>k_3 = 200 \text{ Nm}^{-1}</math>, <math>\omega_1 = 2 \text{ rad/s}</math>, <math>\omega_2 = 5 \text{ rad/s}</math>, <math>f_1(t) = 200 \sin \omega_1 t \text{ N}</math>, <math>f_2(t) = 100 \sin(\omega_2 t + \alpha_1) \text{ N}</math>, <math>\alpha_1 = \frac{\pi}{3} \text{ rad}</math>. Initial values: <math>z _{t=0} = 0</math></p>	
Discovered equations using the state-space representation with state variables: $\mathbf{z}^T = (x_1 \quad x_2 \quad \dot{x}_1 \quad \dot{x}_2) = (z_1 \quad z_2 \quad z_3 \quad z_4)$		Error (%)
$\dot{\mathbf{z}} = \begin{pmatrix} 1.0000z_3 \\ 1.0000z_4 \\ -20.0002 \sin(-2.0003t) + 30.0308z_2 - 49.9949z_1 \\ -19.9945 \sin(-5.0074t - 1.0361) + 59.3456z_1 - 99.9539z_2 \end{pmatrix}$		2.46
<b>Mechanism iii:</b> Crank-slider mechanism		
	<p>Characteristics: <math>\ \overline{AB}\  = 0.1 \text{ m}</math>, <math>\ \overline{BC}\  = 0.5 \text{ m}</math>, <math>\omega = 2 \text{ rad/s}</math>. Initial value: <math>z _{t=0} = \ \overline{AB}\  + \ \overline{BC}\ </math></p>	
Discovered equations with state variables: $\dot{z}_1 = \dot{x}$		Error (%)
$\dot{z}_1 = -0.2000 \sin(2.0000t) - 0.2004 \frac{\sin(2.0021t) \sin(1.9904t + 1.5609)}{\sqrt{24.8584 + \sin(-2.0049t) \sin(2.0001t)}} \quad *24.8584 = 5.0013 \times 4.9704$		2.03

Table 2. Evolutionary parameters used for discovering system equations

Parameter	Value
Population size	(i) 600, (ii) 600, and (iii) 800
Crossover and mutation rates	0.8 and 0.2, respectively
Number of generations	(i) 19, (ii) 50, and (iii) 73
Function and terminal sets	$\{+, \times, \div, \sin, \sqrt{\quad},   \quad  , \exp, \text{sgn}\}, \{t, z_1, z_2, z_3, z_4, c, 1\}$

#### 4 Conclusion

An evolutionary symbolic regression method was presented for the system identification of multibody system dynamics. The function candidates were constructed randomly based on a function set and terminal set defined in the genetic programming in the first place and the governing equations were obtained using the ridge regression approach. The fitness in genetic programming was evaluated based on mean square error and the equation complexity. The procedure was used to investigate three case studies, which subsequently demonstrated a good efficiency and capability to identify not only the system parameters but also the governing equations of multibody systems. Being an ongoing research study, the future direction of this study can be to extend the procedure to discover parsimonious equations of a system from experimentally acquired data.

#### Acknowledgments

The first author acknowledges Marie Skłodowska-Curie Actions - Seal of Excellence of the FWO with Project No. 12ZZ521N.

#### References

- [1] J.P. Crutchfield, B.S. McNamara. Equations of motion from a data series. *Complex Syst* 1(3):417-452, 1987.
- [2] M. Schmidt, H. Lipson. Distilling free-form natural laws from experimental data. *Science* 324(5923):81-85, 2009.
- [3] S.L. Brunton et al., Discovering governing equations from data by sparse identification of nonlinear dynamical systems. *PNAS* 113(15):3932-3937, 2016.
- [4] S.L. Brunton, et al. Machine Learning for Fluid Mechanics. *Annual Review of Fluid Mechanics* 52(1):1-31, 2020.
- [5] T. Uchida, C.P. Vyasarayani, M. Smart, J. McPhee. Parameter identification for multibody systems expressed in differential-algebraic form. *Multibody Syst Dyn* 31:393-403, 2014.
- [6] H. Lasi, et al. Industry 4.0. *Business & Information Systems Engineering* 4(6):239-242, 2014.

# Sparse Identification Of Open-loop Multibody System Dynamics

Paweł Małczyk, Janusz Frączek

Institute of Aeronautics and Applied Mechanics  
Faculty of Power and Aeronautical Engineering  
Warsaw University of Technology  
Nowowiejska str. 24, 00-665 Warsaw, Poland  
pmałczyk@meil.pw.edu.pl, jfraczek@meil.pw.edu.pl

## EXTENDED ABSTRACT

### 1 Background and problem statement

Identification of unknown multibody system dynamics from given experimental or numerical data is of paramount importance for accurate future state predictions or application of advanced model-based control strategies. Traditionally, robot dynamics models are identified by exploiting the fact that the equations of motion might be rewritten to a form which is linearly dependent on the standard set of unknown parameters [1]. Subsequently, the least-squares (regression) approach is used to find the values by minimizing the error between the predicted and measured output vector. On the other hand, much advancements have been done in the field of sparse identification of nonlinear system dynamics [2],[3]. The authors use there sparse regression to discover equations of motion and create parsimonious models with the fewest terms out of the candidates from the predefined library of functions. The approach tends to prevent overfitting. The sparsity is achieved by using the least-squares regression with  $L^1$  regularization term that penalizes sparsity of the generated model and exploits usually LASSO to find the solutions. An interesting alternative to the LASSO framework seems to be the SINDy method [2], which iteratively executes the least-squares algorithm and then threshold all coefficients that are smaller than some user-defined regularization term. The SINDy (sparse identification of nonlinear dynamical systems) approach has been successfully extended in a number of ways to include e.g.: inputs and control, incorporate physical constraints or discover dynamics expressed in terms of partial differential equations.

Unfortunately, sparse identification of implicit ordinary differential equations written in terms of rational functions, which are usually formulated for open-loop multibody systems, seems to be still a challenging issue. The problem is resolved by generating the null space to the matrix involving the function candidates. Nevertheless, this approach is known to be susceptible to measurement noise [3]. The other method to deal with rational nonlinearities exploits partial knowledge of the identified model to transform the procedure into a sequence of multiple executions of the SINDy framework. Although this method might be parallelized, it is also computationally expensive [3]. The objective of this paper is to present the application of the sparse identification procedure for fully actuated, open-loop multi-rigid-body systems, which partially alleviate the above-mentioned flaws. The proposed reformulation avoids the need to compute the problematic null space matrices and poses the least-squares problem in a standard setting in which a multibody system trajectory and the corresponding velocities, accelerations in combination with control forces/torques are measured and delivered to the identification procedure.

### 2 Joint-coordinate formulation and sparse identification

The joint-coordinate formulation is used in this paper to generate the equations of motion for an open-loop multibody system. The procedure ultimately gives a system of ordinary differential equations for the unknown joint positions, velocities, and accelerations. For an open-chain system containing  $n_b$  bodies and  $n$  degrees of freedom, joint coordinates are defined by the following vector  $\mathbf{q} \in \mathcal{R}^n$ . It can be shown [4] that the equations of motion for a multi-rigid-body system can be written as

$$\underbrace{(\mathbf{H}^T \mathbf{M} \mathbf{H})}_{\mathcal{M}} \ddot{\mathbf{q}} - \underbrace{\mathbf{H}^T (\mathbf{Q} - \mathbf{M} \dot{\mathbf{H}} \dot{\mathbf{q}})}_{\mathcal{F}} = \mathbf{u} \quad \rightarrow \quad \mathcal{M}(\mathbf{q}) \ddot{\mathbf{q}} - \mathcal{F}(\mathbf{q}, \dot{\mathbf{q}}) = \mathbf{u}, \quad (1)$$

where  $\mathbf{M} \in \mathcal{R}^{n_b \times n_b}$  is the mass matrix,  $\mathbf{Q} \in \mathcal{R}^{n_b}$  is a vector of applied forces,  $\mathbf{H} = \mathbf{H}(\mathbf{q}) \in \mathcal{R}^{n_b \times n}$  represents the joint's motion subspace matrix, which relates the absolute and relative velocities ( $\mathbf{V} = \mathbf{H} \dot{\mathbf{q}}$  and  $\mathbf{V} \in \mathcal{R}^{n_b}$  is a vector of absolute velocities). To evaluate  $\mathbf{H}$  one needs to consider the type of joints in the chain and the topology of the system. The quantity  $\mathbf{u} \in \mathcal{R}^n$  is a vector of applied control forces/torques at joints that are measured together with the joint-space trajectories  $\mathbf{q}$  and their time derivatives  $\dot{\mathbf{q}}$ ,  $\ddot{\mathbf{q}}$  to be passed onto the identification procedure described next.

The sparse identification concept [2] is exploited in this paper to identify the nonlinear dynamics of open-chain multibody systems from simulated data. It is assumed that the dynamics of a system can be represented by the linear combination of columns from a feature library  $\Theta = \Theta(\mathbf{q}, \dot{\mathbf{q}}, \ddot{\mathbf{q}}) \in \mathcal{R}^{n \times p}$  that consists of predefined basis functions multiplied by entries of the unknown vector of coefficients  $\xi \in \mathcal{R}^p$  such that

$$\mathcal{M}(\mathbf{q}) \ddot{\mathbf{q}} - \mathcal{F}(\mathbf{q}, \dot{\mathbf{q}}) = \Theta(\mathbf{q}, \dot{\mathbf{q}}, \ddot{\mathbf{q}}) \xi = \mathbf{u} + \epsilon, \quad (2)$$

where  $\epsilon \in \mathcal{R}^n$  is the residual error vector to be minimized. Eq. (2) can be regarded as a measurement in one time instant. In reality, the values in the formula (2) should be evaluated at a sufficient number of points in time along appropriately defined

trajectories [1]. There is a vast number of identification procedures to estimate  $\xi$  from the overdetermined system of linear equations (2). Those based on the standard least-squares approach would usually give a solution in which every term from the predefined library is active in the model. In consequence, the identified model would be prone to overfitting. However, if sparsity of  $\xi$  is induced by the regularization term, then most of the entries in  $\xi$  are zero and the generated model tends to prevent from such phenomenon to appear. Formally, the problem might be written as regularized regression:

$$\xi^* = \underset{\xi}{\operatorname{argmin}} \|\Theta\xi - \mathbf{u}\|_2 + \alpha\|\xi\|_1, \quad (3)$$

where the parameter  $\alpha$  corresponds to a regularization coefficient. The approach proposed in the paper generates sparse nonlinear multibody models from data by bypassing the need to evaluate the null space matrix of the  $\Theta$  matrix.

### 3 Preliminary results and summary

To demonstrate the validity of the proposed approach, a sample planar two-body system shown in Fig. 1 is simulated for 5 sec. The trajectory  $\mathbf{q}, \dot{\mathbf{q}}, \ddot{\mathbf{q}}$  ( $\mathbf{q} = [q_1 \ q_2]^T$ ) resulted from predefined control signals  $\mathbf{u} = [u_1 \ u_2]^T$  is recorded every 0.01 sec.. Then, sparse identification is performed to evaluate the active terms in the feature library that consists of e.g. harmonic functions, products of squared velocities by harmonic functions, products of harmonic functions times the accelerations. The penalty factor is set experimentally to  $\alpha = 0.001$ . The algorithm correctly identifies the sample planar system. The model is subsequently used in the inverse dynamics control (IDC) that should realize the trapezoidal velocity trajectory at translational and revolute joint. The results are comparatively set with the pure PD controller and shown in Fig. 2. The IDC method with the model performs better than the simple PD approach, which partially verifies the identified equations for the open-loop system.

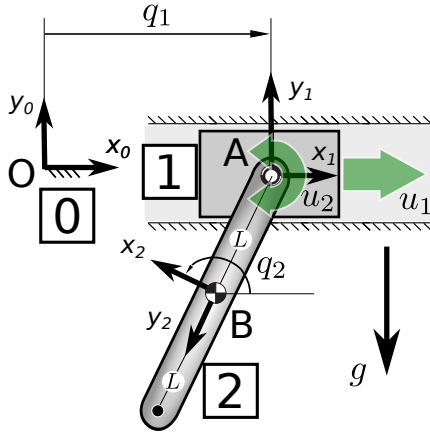


Figure 1: Multibody system ( $L = 0.25 \text{ m}$ ,  $m_1 = 0.5 \text{ kg}$ ,  $m_2 = 0.2 \text{ kg}$ ,  $J_1 = J_2 = 0.005 \text{ kgm}^2$ ,  $g = 9.81 \frac{\text{m}}{\text{s}^2}$ ,  $q_1(0) = 0 \text{ m}$ ,  $q_2(0) = -\frac{3\pi}{4} \text{ rad}$ ). The following control signals ( $u_1 = \sin(0.01t)$ ,  $u_2 = -0.01 \sin(2t)$ ) are used in the identification phase

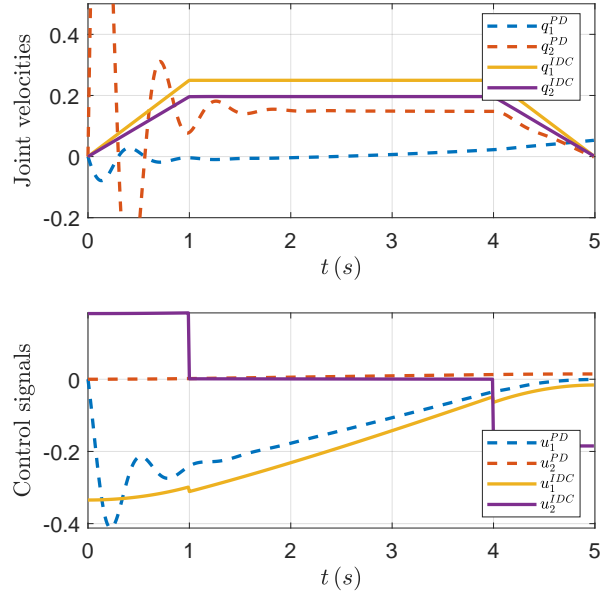


Figure 2: The top plot shows joint velocities for ideal PD controller set against inverse dynamics control (IDC) that exploits the identified model. The bottom plot presents the corresponding control signals that force the system to move from  $\mathbf{q}_{init} = [0 \ \frac{3}{4}\pi]^T$  to  $\mathbf{q}_{final} = [1 \ \pi]^T$

**Acknowledgments.** This work has been supported by Excellence Initiative, Research University in the field of Artificial Intelligence and Robotics under grant no. 1820/25/Z01/POB2/2021.

### References

- [1] J. Hollerbach, W. Khalil, M. Gautier. Model Identification, Springer Handbook of Robotics, chapter 14, 321–344, 2008.
- [2] S. Brunton, J. Proctor, J. Kutz. Discovering governing equations from data by sparse identification of nonlinear dynamical systems. Proc. Natl Acad. Sci. USA 113, 3932–3937, 2016.
- [3] K. Kaheman, J. Kutz, S. Brunton. SINDy-PI: a robust algorithm identification of nonlinear dynamics. Proc. of the Royal Society A 476. 1–25, 2020.
- [4] R. Featherstone. Rigid Body Dynamics Algorithms. Springer, 2008.

# Cutting the Knot: Critical Features of Centrifugal Vibration Absorbers Modeling

Mattia Cera<sup>1</sup>, Marco Cirelli<sup>2</sup>, Ettore Pennestri<sup>1</sup>, Pier Paolo Valentini<sup>1</sup>

<sup>1</sup> Department of Enterprise Engineering  
University of Rome Tor Vergata  
via del Politecnico, 1, 00133 Rome, Italy  
mattia.cera@uniroma2.it  
pennestri@mec.uniroma2.it  
valentini@ing.uniroma2.it

<sup>2</sup> University Niccolò Cusano  
Via Don Carlo Gnocchi, 3, 00166 Rome, Italy  
marco.cirelli@unicusano.it

## EXTENDED ABSTRACT

### 1 Introduction

The centrifugal pendulum vibration absorber (CPVA) is a widely adopted order-tuned device, aimed to isolate torsional vibrations in rotating and reciprocating machinery. The absorbers counteract torque disturbance at a given harmonic order through their oscillation along a prescribed path. The dynamic behavior and damping performance heavily depend on a geometric feature, namely the absorber COM trajectory.

Early investigations on this topic are due to Salomon [1], Sarazin [2], Den Hartog [3] and Newland [4]. Their design solutions were based on linear approximation, absorber small oscillation and circular paths. The first design architecture, the Salomon's one, is constituted by a series of rollers, which act as absorbers, whereas the most common architecture now is the bifilar one, as shown in Figure 1. According to the slots orientation, the relative absorber motion can be a translation or a rotation. The corresponding pendula are denoted as parallel and trapezoidal bifilar dampers, respectively.

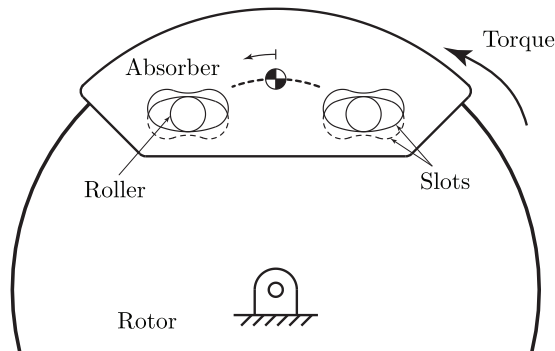


Figure 1: Parallel bifilar pendulum

For large oscillation, nonlinear behavior is observed. Madden [5] and Denman [6] were the first to investigate the advantages of tautochronism for vibration isolation improvement. The critical feature of tautochrone dampers, based on epicycloidal paths, is a quasi-linear behavior, even for large oscillation. Significant theoretical groundwork is also due to Shaw and coworkers (e.g. [7, 8, 9]). Recent developments in this area are portrayed by Cera *et al.* [10, 11, 12], Mayet & Ulbrich [13, 14] and Gomez *et al.* [15].

### 2 Problem description and modeling

Most of the previously cited contributions share simplifying hypotheses that neglect important physical phenomena. Although such hypotheses are required for the settings of design equations, as well as the casting of analytical models, these may heavily affect the expected CPVA performance. To shed some light in this intricate topic, the present investigation is an attempt to fill this apparent gap through an holistic modeling of these devices. With its capability to embrace and handle complex physical features, multibody dynamics undoubtedly offers an effective framework.

For our purposes, a CPVA multibody dynamics model with the following relevant characteristics has been developed:

- parallel bifilar architecture;
- quasi-tautochrone behavior;
- thirteen rigid bodies: four absorbers, one rotor, two rollers for each absorber;
- each roller is caged and meshes with slots carved both on the absorbers and on the rotor, its shape is such to enforce quasi-tautochrone dynamic behavior;



- for smoothing impacts observed during transients, each absorber includes two stop dampers at the edges.

Particular care was dedicated to the contact modeling of kinematic elements of the caged roller joints [16] and of the stop dampers.

### 3 Simulation analysis and conclusions

The effects herein analyzed in the multibody dynamics simulation are due to the following issues:

- rotor start and stop, sharp acceleration and deceleration transients;
- synchronous response of the absorbers;
- friction coefficient required to establish pure rolling condition between roller and slots;
- multi harmonic content of the disturbing torque;

The first results confirm the need of a multibody dynamics of these important devices. In fact, a procedure where multibody dynamics simulation is included in the design iteration, allows solutions with more effective vibration attenuation.

### References

- [1] F. Salomon, Device apted to eliminate oscillations, US Patent 2,103,643.
- [2] R. Sarazin, Means adapted to reduce the torsional oscillations of crankshafts, US Patent 2,079,226.
- [3] J. P. D. Hartog, Mechanical vibrations, fourth edition, The Journal of the Royal Aeronautical Society 61 (554).
- [4] D. E. Newland, Nonlinear aspects of the performance of centrifugal pendulum vibration absorbers, ASME Journal of Engineering for Industry 86 (3) (1964) 257–263.
- [5] J. Madden, Constant frequency bifilar vibration absorber (1980).
- [6] H. H. Denman, Tautochronic bifilar pendulum torsion absorbers for reciprocating engines, Journal of Sound and Vibration 159 (2) (1992) 251–277.
- [7] C. P. Chao, S. W. Shaw, C. T. Lee, Stability of the unison response for a rotating system with multiple tautochronic pendulum vibration absorbers, Journal of Applied Mechanics 64 (1) (1997) 149–156.
- [8] A. Alsuwaiyan, S. Shaw, Performance and dynamic stability of general-path centrifugal pendulum vibration absorbers, Journal of Sound and Vibration 252 (5) (2002) 791–815.
- [9] S. W. Shaw, B. Geist, Tuning for performance and stability in systems of nearly tautochronic torsional vibration absorbers, Journal of Vibration and Acoustics 132 (4).
- [10] M. Cirelli, J. Gregori, P. Valentini, E. Pennestrì, A design chart approach for the tuning of parallel and trapezoidal bifilar centrifugal pendulum, Mechanism and Machine Theory 140 (2019) 711–729.
- [11] M. Cirelli, M. Cera, E. Pennestrì, P. P. Valentini, Nonlinear design analysis of centrifugal pendulum vibration absorbers: an intrinsic geometry-based framework, Nonlinear Dynamics 102 (3) (2020) 1297–1318.
- [12] M. Cera, M. Cirelli, E. Pennestrì, P. P. Valentini, Design analysis of torsichrone centrifugal pendulum vibration absorbers, Nonlinear Dynamics 104 (2) (2021) 1023–1041.
- [13] J. Mayet, H. Ulbrich, Tautochronic centrifugal pendulum vibration absorbers general design and analysis, Journal of Sound and Vibration 333 (2014) 711–729.
- [14] J. Mayet, H. Ulbrich, First-order optimal linear and non linear detuning of centrifugal pendulum vibration absorbers, Journal of Sound and Vibration 335 (2015) 34–54.
- [15] E. R. Gomez, I. L. Arteaga, L. Kari, Normal-force dependant friction in centrifugal pendulum vibration absorbers: Simulation and experimental investigations, Journal of Sound and Vibration 492 (2021) 115815.
- [16] M. Cera, M. Cirelli, E. Pennestrì, P. Valentini, The kinematics of curved profiles mating with a caged idle roller - higher-path curvature analysis, Mechanism and Machine Theory 164 (2021) 104414.

# GENERIC-Based Integration of Constrained Dissipative Mechanical Systems

Vanessa Valdes y Beck, Peter Betsch

Institute of Mechanics, Karlsruhe Institute of Technology, 76131 Karlsruhe, Germany  
vanessa.beck@kit.edu, peter.betsch@kit.edu

## EXTENDED ABSTRACT

### 1 Introduction

GENERIC is an acronym for “General Equation for Equilibrium Reversible Irreversible Coupling” [1] and facilitates the thermodynamically consistent formulation of general thermoelastic dissipative material behavior [2]. In particular, GENERIC can be viewed as extension of the Hamiltonian framework of dynamics to dissipative systems [3]. Correspondingly, GENERIC has been used as starting point for the development of Energy-Momentum-Entropy schemes [4, 5, 6] which can be viewed as extension of Energy-Momentum schemes for Hamiltonian systems with symmetry.

In the present work we aim at the inclusion of constraints into GENERIC along with structure-preserving time-stepping schemes for constrained dissipative mechanical systems.

### 2 Representative model problem

To introduce the main building blocks of GENERIC for dissipative systems, we consider the discrete model problem of a thermo-viscoelastic double pendulum [7] depicted in Figure 1.

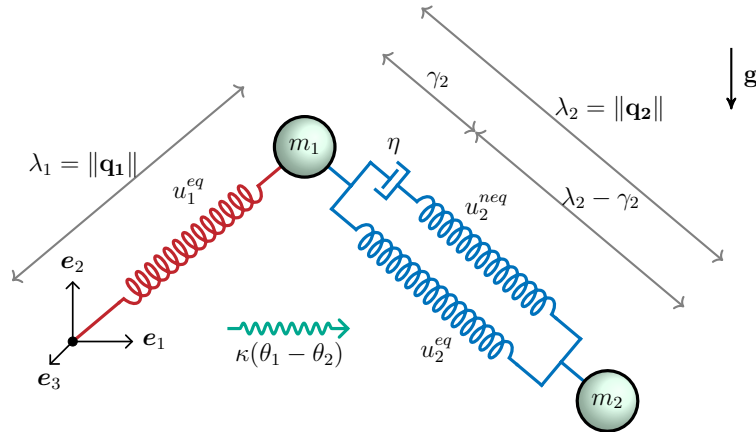


Figure 1: The thermo-viscoelastic double pendulum

The system’s dynamic evolution is characterized by the time derivative of the vector of the state variables

$$\mathbf{z} = [\mathbf{q}_1^T, \mathbf{q}_2^T, \mathbf{p}_1^T, \mathbf{p}_2^T, \tau_1, \tau_2, \gamma_2]^T. \quad (1)$$

The corresponding state space  $\mathcal{S}$  is given by

$$\mathcal{S} = \{\mathbf{z} \in (\mathbb{R}^{n_{\text{dim}}} \times \mathbb{R}^{n_{\text{dim}}} \times \mathbb{R}^{n_{\text{dim}}} \times \mathbb{R}^{n_{\text{dim}}} \times \mathbb{R} \times \mathbb{R} \times \mathbb{R}), \mathbf{q}_1 \neq 0, \mathbf{q}_2 \neq 0\} \quad (2)$$

with  $n_{\text{dim}} \in \{2, 3\}$ , being the spatial dimension.

In (1),  $\mathbf{q}_\alpha, \mathbf{p}_\alpha, \tau_\alpha, \gamma_\alpha$  ( $\alpha = 1, 2$ ) are the thermo-element’s respective generalized positions, conjugate momenta, thermodynamic and internal variables. Each element’s material response is determined by a temperature-dependent free Helmholtz energy function  $\psi_\alpha$ . Legendre transformation enables the computation of the entropy and internal energy. Thus, a generalized thermodynamic variable  $\tau_\alpha \in \{s_\alpha, \theta_\alpha, u_\alpha\}$  can be introduced, allowing for the choice of the entropy, the temperature or internal energy. A law for the heat flux and an evolution equation for  $\gamma_\alpha$  complete the description of the thermodynamic problem.

The model problem at hand is thermally insulated and represents a closed system. Thus the total energy is conserved. Due to heat conduction and viscous deformations the system is dissipative leading to a non-decreasing total entropy. In addition to that, the system is invariant with respect to rotations about base vector  $\mathbf{e}_2$ , so that the corresponding component of the total angular momentum is a conserved quantity.

### 3 GENERIC-based formulation

GENERIC casts a system's evolution equations in a matrix-vector formulation

$$\dot{\mathbf{z}} = \dot{\mathbf{z}}_{\text{rev}} + \dot{\mathbf{z}}_{\text{irr}} = \mathbf{L}(\mathbf{z})\nabla E(\mathbf{z}) + \mathbf{M}(\mathbf{z})\nabla S(\mathbf{z}) \quad (3)$$

by separating the contributions to the reversible and irreversible dynamics. The reversible time evolution is controlled by the product of the Poisson matrix  $\mathbf{L} : \mathcal{S} \rightarrow \mathbb{R}^{\dim(\mathbf{z}) \times \dim(\mathbf{z})}$  and the gradient of the total energy  $E : \mathcal{S} \rightarrow \mathbb{R}$ . The dissipative matrix  $\mathbf{M} : \mathcal{S} \rightarrow \mathbb{R}^{\dim(\mathbf{z}) \times \dim(\mathbf{z})}$  acts on the gradient of the total entropy  $S : \mathcal{S} \rightarrow \mathbb{R}$  and yields the system's irreversible dynamics.

GENERIC imposes the following degeneracy conditions

$$\begin{aligned} \mathbf{L}\nabla S &= \mathbf{0} \\ \mathbf{M}\nabla E &= \mathbf{0} \end{aligned} \quad (4)$$

besides restrictions on the Poisson and dissipative matrices for reasons of thermodynamic consistency.

### 4 ENERGY-MOMENTUM-ENTROPY time-stepping scheme

We apply a structure-preserving variant of the implicit mid-point rule to numerically integrate the evolution equation (3). The Energy-Momentum-Entropy time-stepping scheme can be written in the form

$$\frac{\mathbf{z}_{n+1} - \mathbf{z}_n}{\Delta t} = \mathbf{L}(\mathbf{z}_{n+1}, \mathbf{z}_n) \mathbf{D}E(\mathbf{z}_{n+1}, \mathbf{z}_n) + \mathbf{M}(\mathbf{z}_{n+1}, \mathbf{z}_n) \mathbf{D}S(\mathbf{z}_{n+1}, \mathbf{z}_n) . \quad (5)$$

Herein,  $\mathbf{D}(\bullet)(\mathbf{z}_{n+1}, \mathbf{z}_n)$  denotes a discrete derivative in the sense of Gonzalez [8]. The resulting scheme is capable to exactly reproduce the fundamental structure properties of the model problem mentioned at the end of Section 2. This implies (i) conservation of total energy, (ii) non-decreasing total entropy, and (iii) conservation of the 2-component of the total angular momentum.

### 5 Constrained dissipative mechanical systems

The aim of the present work is to extend GENERIC to dissipative systems subjected to constraints. In particular, the inclusion of ideal constraints needs to preserve the thermodynamically consistent framework of GENERIC. The thus extended formulation will provide the ideal starting point for the design of structure-preserving schemes for constrained dissipative mechanical systems.

### References

- [1] H. C. Öttinger. Beyond Equilibrium Thermodynamics. John Wiley & Sons Inc., New Jersey, 2005.
- [2] M. Mielke. Formulation of thermoelastic dissipative material behavior using GENERIC. *Continuum Mechanics and Thermodynamics*, 23:233-256, 2011.
- [3] I. Romero. A Characterization of Conserved Quantities in Non-Equilibrium Thermodynamics. *Entropy*, 15(12):5580-5596, 2013.
- [4] S. Conde Martín, P. Betsch and J. C. García Orden. A temperature-based thermodynamically consistent integration scheme for discrete thermo-elastodynamics. *Communications in Nonlinear Science and Numerical Simulation*, 32:63-80, 2016.
- [5] P. Betsch and M. Schiebl. Energy-momentum-entropy consistent numerical methods for large-strain thermoelasticity relying on the GENERIC formalism. *International Journal for Numerical Methods in Engineering*, 119(12):1216-1244, 2019.
- [6] M. Schiebl and P. Betsch. Structure-preserving space-time discretization of large-strain thermo-viscoelasticity in the framework of GENERIC. *International Journal for Numerical Methods in Engineering*, 122(14):3448-3488, 2021.
- [7] V. S. Valdes y Beck, M. Schiebl and P. Betsch. Structure-Preserving Discretization in the Framework of a Discrete Model Problem for Large-Strain Thermo-Viscoelasticity. In *WCCM-ECCOMAS2020, Proceedings of the 14th World Congress on Computational Mechanics (WCCM) and ECCOMAS Congress. Virtual Congress*, 2021.
- [8] O. Gonzalez. Time Integration and Discrete Hamiltonian Systems. *Journal of Nonlinear Science*, 6:449-467, 1996.

# On Modeling Joint Friction Forces in the Constrained Hamiltonian Formulation

Paweł Malczyk, Marek Wojtyra

Institute of Aeronautics and Applied Mechanics  
Faculty of Power and Aeronautical Engineering  
Warsaw University of Technology  
Nowowiejska str. 24, 00-665 Warsaw, Poland  
pmalczyk@meil.pw.edu.pl, mwojtyra@meil.pw.edu.pl

## EXTENDED ABSTRACT

### 1 Background and problem statement

Modeling friction is a challenging problem that has been investigated for a while in multibody system dynamics simulations. The tribological models that represent friction phenomena are too complex to be broadly used in multibody simulations due to the fact that the required computational expense is excessively large. The friction models used in multibody simulations result from a compromise which takes into account the range of captured frictional effects (e.g., Stribeck effect, stick-slip motion, viscous damping, microslips, external force rate dependency, hysteresis, frictional memory, etc.), the expected fidelity, the possibilities for identification of parameters, the mathematical complexity, the effectiveness of numerical calculations and perhaps other factors. It is quite often the case that relatively simple, lumped models of frictional contact are used in multibody calculations, especially when they are intended for control purposes [1]. In this approach, the micro-scale contact phenomena are not directly represented in their full complexity. As a result, these models are computationally effective and a reasonably small number of parameters needs to be identified, while they are still capable to capture the essence of the complicated friction phenomena.

When choosing the friction model, numerical issues are not to be underestimated. The strong nonlinearity in the vicinity of zero relative velocity (which has the form of discontinuity in the classical Coulomb and Amontons model) results in numerically stiff, and therefore computationally cumbersome, system dynamics, especially when redundant constraints are imposed on the system [2]. The efficiency of multibody system simulations is strongly affected by taking friction effects into account. The time step of numerical integration must be severely decreased to capture the essential effects. Moreover, whenever friction force is a nonlinear function of normal reactions, an iterative process (most often fixed-point iterations) must be employed – at each time step – to find the Lagrange multipliers which represent magnitudes of normal reaction forces. The objective of this research is to adapt the classical Coulomb friction model to the constrained Hamiltonian formulation in which positions and momenta play the primary role. It is interesting to note that the impulses of joint loads are readily available in the Hamiltonian framework employed here. Therefore, by taking the time derivatives of the impulses, one might find the approximations of both constraint reaction forces as well as friction forces. In contrast to the classical, acceleration-based formulation, the proposed approach approximates the friction effects without the need to employ an iterative process, which forms a novelty stemming from the paper.

### 2 Friction forces in the Hamiltonian formulation

The translational and angular position of rigid bodies in a multibody system in a global reference frame are described by a vector of  $n$  dependent coordinates  $\mathbf{q} \in \mathcal{R}^n$ . If the number of coordinates is greater than the number of the system's degrees of freedom, the algebraic constraints are introduced to express the relations between coordinates in a multibody system. Usually, these relationships express the fact that bodies are connected by joints. Let us assume that  $m$  independent holonomic constraint equations are imposed on the system that let one yield the kinematic velocity equations as well.

$$\Phi(\mathbf{q}, t) = \mathbf{0} \quad \rightarrow \quad \dot{\Phi}(\mathbf{q}, \dot{\mathbf{q}}, t) = \Phi_{\mathbf{q}} \dot{\mathbf{q}} + \Phi_t = \mathbf{0}, \quad (1)$$

where  $\Phi_{\mathbf{q}} \in \mathcal{R}^{m \times n}$  is the constraint Jacobian matrix and  $\dot{\mathbf{q}} \in \mathcal{R}^n$  is a vector of translational and angular velocities. The constrained Hamiltonian equations of motion that enforce velocity level constraints can be written in the form [3, 4]

$$\begin{bmatrix} \mathbf{M} & \Phi_{\mathbf{q}}^T \\ \Phi_{\mathbf{q}} & \mathbf{0} \end{bmatrix} \begin{bmatrix} \dot{\mathbf{q}} \\ \boldsymbol{\sigma} \end{bmatrix} = \begin{bmatrix} \mathbf{P}^* \\ -\Phi_t \end{bmatrix}, \quad (2)$$

$$\dot{\mathbf{P}}^* = \mathbf{Q}(\mathbf{q}, \dot{\mathbf{q}}, t) + \mathbf{Q}_f(\mathbf{q}, \dot{\mathbf{q}}, \boldsymbol{\lambda}) + \dot{\Phi}_{\mathbf{q}}^T \boldsymbol{\sigma}, \quad (3)$$

where  $\mathbf{M}$  is the inertia matrix for all bodies in the system,  $\boldsymbol{\sigma}$  represents a vector of  $m$  additional Lagrange multipliers associated with the velocity level constraint equations,  $\mathbf{P}^*$  is a vector of modified momenta,  $\mathbf{Q}$  contains position- and velocity-dependent forces and torques, and  $\mathbf{Q}_f$  is a vector of generalized Coulomb friction forces/torques, which are nonlinear functions of positions  $\mathbf{q}$ , velocities  $\dot{\mathbf{q}}$ , and the Lagrange multipliers  $\boldsymbol{\lambda}$ . The authors argue in the paper that the unknown multipliers  $\boldsymbol{\lambda}$  might be computed from the relation  $\boldsymbol{\lambda} = \dot{\boldsymbol{\sigma}}$ , which follows after the completion of the first step in Eq. (2).

### 3 Preliminary results and summary

To demonstrate the validity of the proposed approach, a sample four-bar mechanism shown in Fig. 1 is simulated. The masses, inertias, and link lengths are given in the caption of the figure. Three sources of loads are modeled in the system. The gravity forces act on all bodies in the system. The external force  $F_{ex}(t)$  defined in Fig. 1 (green arrow) acts on body two only. Joint friction torques denoted by red symbols in the figure are expressed by discontinuous Coulomb friction model

$$T_i = -a\mu F_N(\mathbf{q}, \boldsymbol{\lambda}) \text{sign}(\omega_i^{rel}), \quad (4)$$

where  $F_N$  is the absolute value of normal reaction force due to contact,  $\omega_i^{rel}$  is a joint relative velocity, and  $a\mu$  is a product of the radius of a shaft and the coefficient of friction.

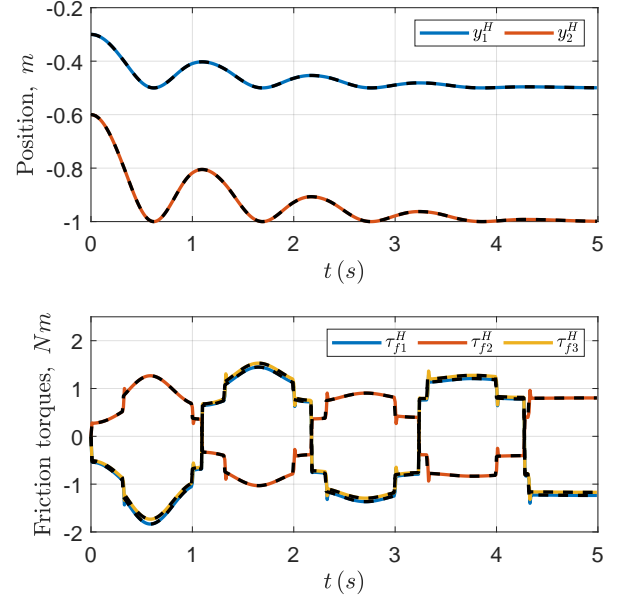
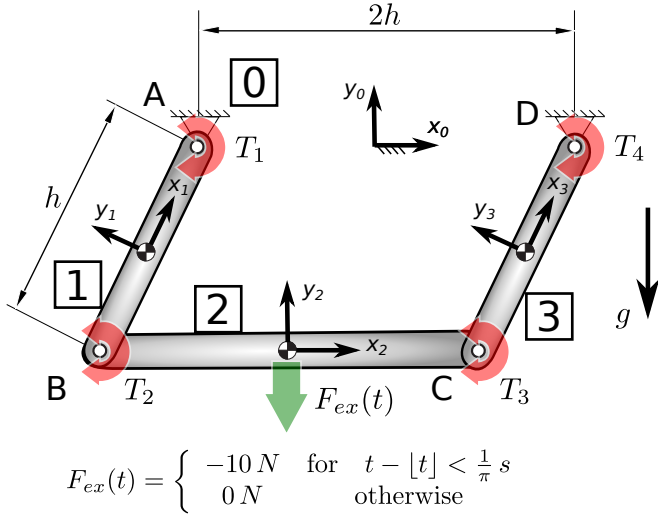


Figure 1: Planar four-bar mechanism ( $h = 1 \text{ m}$ ,  $m_1 = m_3 = 1 \text{ kg}$ ,  $m_2 = 2 \text{ kg}$ ,  $J_1 = J_3 = \frac{1}{12} \text{ kgm}^2$ ,  $J_2 = \frac{2}{3} \text{ kgm}^2$ ,  $g = 10 \frac{\text{m}}{\text{s}^2}$ ,  $a\mu = 0.04$ )

Figure 2: Vertical position of body 1 and 2, and Coulomb friction torques for the Hamiltonian (H, coloured lines) and acceleration-based formulation (dotted lines)

The motion of the system is investigated by using Hamilton's equations of motion (2), (3) proposed in the paper and integrated with the 4<sup>th</sup>-order Runge-Kutta fixed-step routine with the time-step  $\Delta t = 0.01 \text{ s}$ . The Lagrange multipliers  $\boldsymbol{\lambda}$  are found from the relation  $\boldsymbol{\lambda} = \dot{\boldsymbol{\sigma}}$  by using the second-order backward finite difference. Other methods to compute numerical derivatives might be exploited here in order to increase the accuracy of the approximation. The upper plot in Fig. 2 shows vertical positions of the first and second body of the four-bar. The graph at the bottom demonstrates the time histories of the generalized friction torques acting on the bodies vs. time. The results show that the four-bar system responds in a discontinuous manner when it comes to friction torques. Essentially, identical solutions are obtained with a more classical, acceleration-based approach that seems to be computationally more demanding than the proposed method due to the fixed-point iterations employed at each time step. Further research is possible to model friction in the Hamiltonian framework including the issue of computing numerical derivatives and its subtle interplay with the integrator on top of the quality of the results and computational efficiency of the procedure.

**Acknowledgments.** This work has been supported by National Science Center under grant No. 2018/29/B/ST8/00374.

### References

- [1] F. Marques, P. Flores, J. C. Pimenta Claro, H. M. Lankarani. A survey and comparison of several friction force models for dynamic analysis of multibody mechanical systems, *Nonlinear Dyn.*, 86(3), 1407–1443, 2016.
- [2] J. Frączek, M. Wojtyra. On the unique solvability of a direct dynamics problem for mechanisms with redundant constraints and Coulomb friction in joints. *Mechanism and Machine Theory*, 46, 312–334, 2011.
- [3] K. Chada, P. Malczyk, J. Frączek. A parallel Hamiltonian formulation for forward dynamics of closed-loop multibody systems. *Multibody System Dynamics*, 39(1), 51–77, 2017.
- [4] P. Maciag, P. Malczyk, J. Frączek. Hamiltonian direct differentiation and adjoint approaches for multibody system sensitivity analysis. *International Journal for Numerical Methods in Engineering*, 121(22), 5082–5100, 2020.

# Efficient Earthquake Simulation Of Stiff And High DOF Bridge Expansion Joint Models With Python

Michael Tahedl<sup>1</sup>, Fredrik Borchsenius<sup>2</sup>, Andreas Taras<sup>3</sup>

<sup>1</sup> MAURER Engineering GmbH  
Frankfurter Ring 193, 80807 Munich  
Germany  
m.tahedl@maurer.eu

<sup>2</sup> Faculty of Mechanical Engineering  
OTH Regensburg  
Prüfening Str. 58, 93049 Regensburg  
Germany  
fredrik.borchsenius@oth-regensburg.de

<sup>3</sup>Dept. of Civil, Environmental  
and Geomatic Engineering  
ETH Zürich  
Stefano-Franscini-Platz 5, 8093 Zürich  
Switzerland  
taras@ibk.baug.ethz.ch

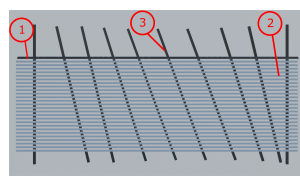
## EXTENDED ABSTRACT

### 1 Introduction

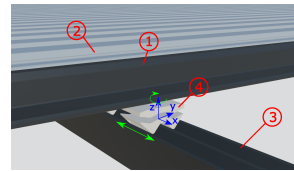
Earthquakes are one of the most dangerous hazards to our civilization. Protecting buildings is of special interest in earthquake engineering to save life during an earthquake as well as to maintain critical infrastructure for rescue operations after such an event. In this work, special attention is given to the bridge expansion joints, which connects the bridge with the abutment. Other works like [1] investigated the seismic response of bridges with models which represent the pounding on finger expansion joints. In this work however, a multibody dynamics model of more complex modular expansion joints will be built with which the effect on seismic events on bridges will be investigated. The mechanical control mechanism of modular expansion joints can, depending on the bridge size, consist of several hundred bodies and therefore around thousand degrees of freedom (DOF).

### 2 Modeling

The investigated expansion joint type is a so called swivel joist expansion joint as displayed in figure 1. The edge beam is connected to the bridge structure and defines the moving side of the expansion joint. The rubber bearings, which are connected to the edge and center beams with a bushing to represent their flexibility, can rotate about the local z-axis. They can also slide along the corresponding joist and can be therefore seen as prismatic joint pair. The bearings are preloaded with 25kN which produces friction forces of 1-3kN, depending on the used sliding material. The joist endings on the opposite side of the edge beam are fixed to the environment in all translational directions.



(a) Top view



(b) 1: Edge Beam, 2: Center Beam, 3: Joist, 4: Bearing

Figure 1: Expansion joint model with 307 rigid bodies, 270 bushings, 270 friction force elements and 270 prismatic sliding joints

The model can be built as a 3D or 2D model. A rigid body in the 3D model is described by three cartesian coordinates and four Euler parameters. To reduce the DOF, a 2D model with 921 DOF is implemented for the displayed expansion joint in figure 1, where a rigid body has DOF in translational x- and y-direction as well as a rotational DOF around the z-axis. The friction between the bearings and the corresponding joists is described by the regularized Coulomb friction model as described in [2].

The kinematic differential equations of each 2D body, the constraint equations arising from the prismatic joints and the forces of the connecting bushings leading to the well known differential algebraic equation (DAE) system of index 3. Reducing the index to 1 and applying the stabilization of Gear, Gupta and Leimkuhler [3], the DAE can be rewritten as a ordinary differential equation (ODE) of the form

$$\begin{aligned} \dot{y} &= z + J_g^T - \underbrace{(J_g J_g^T)^{-1}}_{\mu} J_g z \\ M \dot{z} &= F^e + J_g^T - \underbrace{(J_g M^{-1} J_g^T)^{-1}}_{\lambda} (J_g z + J_g M^{-1} F^e) \end{aligned} \quad (1)$$

where  $y$  are the position coordinates,  $z$  are the velocities,  $M$  is the mass matrix,  $F^e$  are the external forces,  $J_g$  is the jacobian matrix  $\partial g(y)/\partial y$  of the constraint equations  $g(y)$  and  $\lambda$  as well as  $\mu$  are the Lagrange multipliers. The calculation of  $F^e$ ,  $J_g$  and the Lagrange multipliers is performed by functions implemented in Python. Those functions are using the fast and well known *numpy* library for dot products and solving linear equation systems.

### 3 Optimization

Even though the implementation in Python is mostly done with *numpy* arrays and methods, which are programmed in C to achieve better performance, some functions with pure Python code are called very often and can therefore benefit from code optimization. One possibility is to compile the already programmed Python code with *numba*, which is a just in time compiler for Python with *numpy*. A compilation of functions, which are called up to  $5 \times 10^5$  times per time step like the computation of the bushing forces, reduces the time needed for a function call of  $\dot{q} = f(t, q)$  from 0.25s to 0.02s on a machine with 16 Intel Core i7 CPU's at 3.8GHz.

Hairer and Wanner [4] suggest implicit methods for stiff ODE. Those methods need to solve a nonlinear equations system for every time step. In order to solve this equation system, the Jacobian Matrix  $\partial f / \partial q$  is needed. The determination of this matrix is the most time consuming part at large models because many function evaluations of  $f(t, q)$  are needed. Using the sparsity pattern of the Jacobian as described by Curtis, Powell and Reid [5], only non-zero entries of the Jacobian need to be calculated which reduces the overall computation time from 120s with a dense Jacobian by finite differences to 50s. This functionality is already implemented within *scipy.integrate*, only the sparsity pattern must be calculated in advance which could be done by finite differences. A very promising alternative to the sparsity pattern of the Jacobian is a parallelization of the column-wise computation. Therefore, a wrapper function for the calculation of the independent columns of the Jacobian is implemented which spawns processes with the Python *multiprocessing* module, which is highly effective for those CPU bound tasks. With this parallelization, the Jacobian can be evaluated in less than 15s and might be even more efficient on machines with a higher core count.

### 4 Results

With the aforementioned optimization the model displayed in figure 1 could be simulated in less than 8 hours. The edge beam is connected to a single DOF mass which represents the bridge. This mass is connected to the environment by a bushing with the stiffness and damping properties of the corresponding bridge. The environment itself executes a ground motion caused by an earthquake. The following graph shows the acceleration of the bridge with and without the expansion joint.

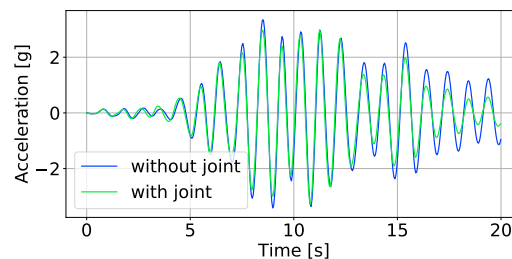


Figure 2: Acceleration of the theoretical bridge model during an earthquake event with and without the expansion joint

### 5 Conclusion

The optimization steps made it possible to achieve a simulation result for high DOF expansion joint models with many stiff force elements in a few hours instead of several days. The result gives a first impression how an expansion joint performs during an earthquake event. The peak acceleration of the theoretical bridge decreased significantly which indicates that expansion joints could be further developed to act as a seismic protection device.

### References

- [1] G. Quan, K. Kawashima. Effect of finger expansion joints on seismic response of bridges. Structural Eng./Earthquake Eng. JSCE Vol. 27, 2010.
- [2] J. T. Oden, J. A. C. Martins. Models and computational methods for dynamic friction phenomena, Computer methods in applied mechanics and engineering 52, p. 527-634, 1985.
- [3] C.W. Gear, G.K. Gupta, B. Leimkuhler. Automatic integration of Euler-Lagrange equations with constraints. Journal of Computational and Applied Mathematics Vol. 12-13, pp. 77-90, 1985.
- [4] E. Hairer, G. Wanner. Solving Ordinary Differential Equations II: Stiff and Differential-Algebraic Problems, Springer, Berlin Heidelberg, 2010.
- [5] A. Curtis, M. J. D. Powell, J. Reid. On the estimation of sparse Jacobian matrices. Journal of the Institute of Mathematics and its Applications, Vol. 13, pp. 117-120, 1974.



# Projection Continuation for Minimal Coordinate Set Dynamics of Constrained Systems

Ping Zhou<sup>1</sup>, Andrea Zanoni<sup>2</sup>, Pierangelo Masarati<sup>2</sup>

<sup>1</sup> School of Astronautics  
Harbin Institute of Technology  
Harbin, China  
ping.zhou@polimi.it

<sup>2</sup> Department of Aerospace Science and Technology  
Politecnico di Milano  
via La Masa 34, 20156, Milano, Italy  
{andrea.zanoni,pierangelo.masarati}@polimi.it

## EXTENDED ABSTRACT

### 1 Problem Description

A generic constrained system dynamics problem is formulated by adding  $m$  (holonomic, in the present case, and ideal) kinematic constraints, in form of the set of algebraic equations

$$\mathbf{c}(\mathbf{x}, t) = \mathbf{0} \quad (1)$$

to a set of  $n$  ordinary differential equations ( $n > m$ ) that express the dynamics of an unconstrained system of  $n$  coordinates  $\mathbf{x}$ ,

$$\mathbf{M}\ddot{\mathbf{x}} = \mathbf{f} \quad (2)$$

equations that are modified by the addition of the constraint reactions  $\mathbf{f}_c = -\mathbf{c}_x^T \lambda$  as

$$\mathbf{M}\ddot{\mathbf{x}} + \mathbf{c}_x^T \lambda = \mathbf{f} \quad (3)$$

where  $\mathbf{c}_x = \mathbf{A}$  is the partial derivative of the constraint equations  $\mathbf{c}$  with respect to the coordinates  $\mathbf{x}$ , namely the constraint Jacobian matrix, and  $\lambda$  are the corresponding Lagrange multipliers.

The Minimal Coordinate Set approach consists in defining a suitable subspace  $\mathbf{T}$  of the space spanned by the coordinates  $\mathbf{x}$  which is tangent to the constraint manifold, namely  $\mathbf{T}^T \mathbf{A}^T \equiv \mathbf{0}$ , such that

$$\dot{\mathbf{x}} = \mathbf{T}\dot{\mathbf{q}} + \beta' \quad (4a)$$

$$\ddot{\mathbf{x}} = \mathbf{T}\ddot{\mathbf{q}} + \beta'' \quad (4b)$$

where  $\mathbf{q}$  are local, truly independent coordinates, with  $\beta'$  non-zero only in case of rheonomous constraints, and  $\beta''$  defined accordingly. The constrained dynamics problem, projected in such subspace, yields

$$\mathbf{T}^T \mathbf{M} \mathbf{T} \ddot{\mathbf{q}} + \mathbf{T}^T \mathbf{A}^T \lambda = \mathbf{T}^T \mathbf{f} - \mathbf{T}^T \mathbf{M} \beta'' \quad (5)$$

Among the several approaches proposed in the literature [1], a suitable choice for  $\mathbf{T}$  is obtained through the QR decomposition of the transpose of the constraint Jacobian matrix,

$$\mathbf{A}^T = \mathbf{Q}\mathbf{R} = \begin{bmatrix} \mathbf{Q}_1 & \mathbf{Q}_2 \end{bmatrix} \begin{bmatrix} \mathbf{R}_1 \\ \mathbf{0} \end{bmatrix} = \mathbf{Q}_1 \mathbf{R}_1 \quad (6)$$

where matrix  $\mathbf{Q}$  is orthogonal and submatrix  $\mathbf{R}_1$  is upper triangular. Submatrix  $\mathbf{Q}_2$  represents an optimal choice for  $\mathbf{T}$ .

Submatrices  $\mathbf{Q}_1$  and  $\mathbf{R}_1$  are uniquely determined, once  $\mathbf{A}$  is known. Submatrix  $\mathbf{Q}_2$ , instead, is only subjected to matrix  $\mathbf{Q}$ 's constraint of being orthogonal, namely  $\mathbf{Q}_2^T \mathbf{Q}_2 \equiv \mathbf{I}$  and  $\mathbf{Q}_2^T \mathbf{Q}_1 \equiv \mathbf{0}$ , but otherwise undefined.

In fact, the QR decomposition produces a “local” representation of the constraint Jacobian matrix; as such, the generalized coordinates associated with the subspace  $\mathbf{T} = \mathbf{Q}_2$ , which do not have any specific physical meaning, represent a local reparameterization of the subspace of the coordinates that is tangent to the constraint manifold. When the QR decomposition is computed at different time steps  $t_k$ , if  $n - m > 1$  the columns of the resulting  $\mathbf{Q}_{2k}$  are completely unrelated, their resulting value being dictated by the internal intricacies of the QR decomposition algorithm.

The aim of the present work is to propose a simple and intuitive algorithm that tracks the evolution of the subspace spanned by  $\mathbf{Q}_2$  using some sort of “continuation,” to somewhat preserve the continuity of the generalized coordinates, by minimizing the amount of deviation of the subspace that is intrinsically required to maintain  $\mathbf{Q}_2$  tangent to the constraint manifold.

Consider the time derivative of the transpose of the constraint Jacobian matrix,

$$\dot{\mathbf{A}}^T = \dot{\mathbf{Q}}\mathbf{R} + \mathbf{Q}\dot{\mathbf{R}} \quad (7)$$

<sup>1</sup>Ping Zhou is currently a visiting PhD student at Politecnico di Milano.

The derivative of matrix  $\mathbf{Q}$  may be expressed as  $\dot{\mathbf{Q}} = \mathbf{Q}\mathbf{\Omega}$ , where the skew-symmetric nature of matrix  $\mathbf{\Omega}$  descends from the orthogonality of matrix  $\mathbf{Q}$ .

When the problem is integrated numerically, the solution from time step  $t_k$  to time step  $t_{k+1}$  is computed. The QR decomposition at time  $t_k$  yields submatrices  $\mathbf{Q}_{1k}$  and  $\mathbf{R}_{1k}$ . The generalized velocities at time  $t_k$  are computed with reference to the subspace spanned by  $\mathbf{Q}_{2k}$ . After computing the solution at the new time step, the Jacobian matrix at time  $t_{k+1}$  is known. As such, through the economy QR decomposition of its transpose, submatrices  $\mathbf{Q}_{1k+1}$  and  $\mathbf{R}_{1k+1}$  are determined. Instead of computing also submatrix  $\mathbf{Q}_{2k+1}$  through the full QR decomposition, the proposed continuation algorithm is used as illustrated in the following. Consider

$$\mathbf{Q}_1^T \dot{\mathbf{A}}^T \mathbf{R}_1^{-1} = \mathbf{Q}_1^T \dot{\mathbf{Q}}_1 + \dot{\mathbf{R}}_1 \mathbf{R}_1^{-1} \quad (8)$$

Matrix  $\dot{\mathbf{R}}_1 \mathbf{R}_1^{-1}$  is the product of two upper triangular matrices, thus it is itself an upper triangular matrix. Matrix  $\mathbf{Q}_1^T \dot{\mathbf{Q}}_1 = \mathbf{\Omega}_1$  is skew-symmetric by construction; it can be seen as  $\mathbf{\Omega}_1 = \mathbf{\Omega}_{1L} - \mathbf{\Omega}_{1L}^T$ , where  $\mathbf{\Omega}_{1L} = \text{stril}(\mathbf{\Omega}_1)$  is the strictly lower triangular part of matrix  $\mathbf{\Omega}_1$ . Thus one can write

$$\text{stril}(\mathbf{Q}_1^T \dot{\mathbf{A}}^T \mathbf{R}_1^{-1}) = \mathbf{\Omega}_{1L} \quad (9)$$

since  $\text{stril}(\dot{\mathbf{R}}_1 \mathbf{R}_1^{-1}) \equiv \mathbf{0}$  by construction. One can show that the derivative of matrix  $\mathbf{Q}$ ,

$$\dot{\mathbf{Q}} = \begin{bmatrix} \dot{\mathbf{Q}}_1 & \dot{\mathbf{Q}}_2 \end{bmatrix} = \begin{bmatrix} \mathbf{Q}_1 & \mathbf{Q}_2 \end{bmatrix} \begin{bmatrix} \mathbf{\Omega}_1 & -\mathbf{R}_1^{-T} \dot{\mathbf{A}} \mathbf{Q}_2 \\ \mathbf{Q}_2^T \dot{\mathbf{A}}^T \mathbf{R}_1^{-1} & \cancel{\mathbf{\Omega}_2} \end{bmatrix} = \begin{bmatrix} \mathbf{Q}_1 & \mathbf{Q}_2 \end{bmatrix} \begin{bmatrix} \mathbf{\Omega}_1 & -\mathbf{\Omega}_{21}^T \\ \mathbf{\Omega}_{21} & \mathbf{0} \end{bmatrix} = \mathbf{Q}\mathbf{\Omega} \quad (10)$$

is entirely known, where the bottom right block should contain an arbitrary contribution  $\mathbf{\Omega}_2$ , that is set to zero to modify as little as possible the subspace  $\mathbf{Q}_2$ ; specifically,

$$\dot{\mathbf{Q}}_2 = -\mathbf{Q}_1 \mathbf{\Omega}_{21}^T = -\mathbf{A}^+ \dot{\mathbf{A}} \mathbf{Q}_2 \quad (11)$$

Thus, the subspace  $\mathbf{Q}_2$  can be integrated, taking appropriate measures (e.g. using Munthe-Kaas' method [2]) to guarantee that the resulting matrix  $\mathbf{Q}$  preserves orthogonality, and submatrix  $\mathbf{Q}_1$  matches that resulting from the decomposition of the transpose of the constraint Jacobian matrix. For example, for  $\mathbf{\Omega}$  constant across a time step of duration  $t_{k+1} - t_k = h$ ,

$$\mathbf{Q}_{k+1} = \mathbf{Q}_k e^{\mathbf{\Omega}h} \quad (12)$$

or

$$\mathbf{Q}_{2k+1} = e^{-\mathbf{A}^+ \dot{\mathbf{A}} h} \mathbf{Q}_{2k} \quad (13)$$

the latter being only a first-order approximation of the former, since the intrinsic skew-symmetric structure of the exponent matrix  $\mathbf{\Omega}$  is lost.

Submatrix  $\mathbf{Q}_{2k+1}$  resulting from the proposed integration may need to be corrected to guarantee orthogonality with respect to submatrix  $\mathbf{Q}_{1k+1}$  obtained from the economy QR decomposition of  $\mathbf{A}_{k+1}^T$ .

## 2 Results

The full paper will present numerical results that illustrate the proposed formulation.

## Acknowledgments

The first author acknowledges support from the China Scholarship Council.

## References

- [1] L. Mariti, N. P. Belfiore, E. Pennestrì, and P. P. Valentini. Comparison of solution strategies for multibody dynamics equations. *Intl. J. Num. Meth. Engng.*, 2011. doi:10.1002/nme.3190.
- [2] Hans Munthe-Kaas. High order Runge-Kutta methods on manifolds. *Applied Numerical Mathematics*, 29(1):115–127, 1999. doi:10.1016/S0168-9274(98)00030-0.

# The GGL Variational Principle for Constrained Mechanical Systems

Philipp L. Kinon, Peter Betsch

Institute of Mechanics, Karlsruhe Institute of Technology, 76131 Karlsruhe, Germany  
philipp.kinon@student.kit.edu, peter.betsch@kit.edu

## EXTENDED ABSTRACT

### 1 Introduction

We present an extension of the Livens variational principle (sometimes also referred to as Hamilton-Pontryagin principle) to mechanical systems subject to holonomic constraints. The newly proposed principle embodies an index reduction in the spirit of the often-applied GGL stabilization and thus may be termed “GGL principle”. The Euler-Lagrange equations of the GGL principle assume the form of differential-algebraic equations (DAEs) with differentiation index two. In contrast to the original GGL-DAEs, the present formulation fits into the Hamiltonian framework of mechanics. Therefore, the GGL principle facilitates the design of symplectic integrators. In particular, it offers the possibility to construct variational integrators. Due to the close relationship of the GGL principle to optimal control, previously developed direct methods based on the philosophy “first discretize then optimize” can be used to obtain variational integrators for constrained mechanical systems. These integrators are symplectic by design. Furthermore, slight modifications can be applied to obtain energy-momentum consistent integrators which represent another important class of structure-preserving time-stepping schemes.

### 2 The original Livens principle

Consider a dynamical system with  $d$  degrees of freedom with positions  $\mathbf{q} \in \mathbb{R}^d$ . From Hamilton’s principle of least action one can proceed by allowing the velocities to be independent variables  $\mathbf{v} \in \mathbb{R}^d$ . Thus, the kinematic relation  $\dot{\mathbf{q}} = \mathbf{v}$  has to be enforced by means of a Lagrange multiplier  $\mathbf{p} \in \mathbb{R}^d$ . The corresponding augmented functional reads

$$\tilde{S}(\mathbf{q}, \mathbf{v}, \mathbf{p}) = \int_0^T [L(\mathbf{q}, \mathbf{v}) + \mathbf{p} \cdot (\dot{\mathbf{q}} - \mathbf{v})] dt, \quad (1)$$

where  $L(\mathbf{q}, \mathbf{v})$  is the Lagrangian. The functional (1) was firstly termed *Livens principle* (cf. Sec. 26.2 in Pars [1]) after G.H. Livens who proposed this functional for the first time (cf. Livens [2]). More recently, Marsden and co-workers [3, 4] coined the name *Hamilton-Pontryagin principle* for this functional due to its close relation to the classical *Pontryagin principle* from the field of optimal control. Due to its mixed character with three independent fields  $(\mathbf{q}, \mathbf{v}, \mathbf{p})$ , it resembles the *Hu-Washizu principle* from the area of elasticity theory.

Livens principle unifies both Lagrangian and Hamiltonian viewpoints on mechanics and automatically accounts for the Legendre transformation. By stating the stationarity condition  $\delta \tilde{S}(\mathbf{q}, \mathbf{v}, \mathbf{p}) = 0$  and executing the variations with respect to every independent variable, one obtains the three equations of motion

$$\dot{\mathbf{q}} = \mathbf{v}, \quad (2a)$$

$$\dot{\mathbf{p}} = D_1 L(\mathbf{q}, \mathbf{v}), \quad (2b)$$

$$\mathbf{p} = D_2 L(\mathbf{q}, \mathbf{v}). \quad (2c)$$

With regard to (2c) the multiplier  $\mathbf{p}$  can be identified as the conjugate momentum, which thus directly emanates from the principle. Within the framework of Hamiltonian dynamics momentum variables have to be defined a priori or emerge from the Legendre transformation as a fiber derivative of  $L(\mathbf{q}, \dot{\mathbf{q}})$ . Note that after reinserting (2c) into (2b) and making use of (2a), Livens principle traces back to the Lagrangian equations of the second kind.

For natural mechanical systems the Lagrangian takes the form  $L(\mathbf{q}, \mathbf{v}) = \frac{1}{2} \mathbf{v} \cdot \mathbf{M} \mathbf{v} - V(\mathbf{q})$ , where  $\mathbf{M}$  is the mass matrix and  $V(\mathbf{q})$  is a potential function. Now (2c) yields  $\mathbf{p} = \mathbf{M} \mathbf{v}$ , so that (2a) and (2b) can be rewritten as

$$\dot{\mathbf{q}} = \mathbf{M}^{-1} \mathbf{p}, \quad \dot{\mathbf{p}} = -D V(\mathbf{q}). \quad (3)$$

These equations correspond to the Hamiltonian form of the equations of motion.

### 3 The GGL method for constrained mechanical systems

Assume that the coordinates  $\mathbf{q}$  are redundant due to the presence of  $m$  independent scleronomic, holonomic constraints  $g_k : \mathbb{R}^d \rightarrow \mathbb{R}$  ( $k = 1, \dots, m$ ). The constraints can be comprised in a column vector  $\mathbf{g} \in \mathbb{R}^m$ , such that

$$\mathbf{g}(\mathbf{q}) = \mathbf{0}. \quad (4)$$

Since all constraint functions shall be independent, the constraint Jacobian  $\mathbf{G}(\mathbf{q}) = \mathbf{D}\mathbf{g}(\mathbf{q})$  is of rank  $m$ . As (4) is true for any point in time, the time derivative has to vanish accordingly (*consistency condition*). Thus, the constraints *on velocity level* or *secondary constraints*

$$\frac{d}{dt}\mathbf{g}(\mathbf{q}) = \mathbf{G}(\mathbf{q})\dot{\mathbf{q}} = \mathbf{0} \quad (5)$$

are induced. It is well-known that the motion of the constrained mechanical systems under consideration is governed by differential-algebraic equations (DAEs) which have differentiation index  $\nu = 3$ . These equations of motion can be derived with a variational approach, which augments Livens principle (1). Accordingly, introducing  $\hat{S}(\mathbf{q}, \mathbf{v}, \mathbf{p}, \boldsymbol{\lambda}) = \tilde{S}(\mathbf{q}, \mathbf{v}, \mathbf{p}) + \int_0^T \boldsymbol{\lambda} \cdot \mathbf{g}(\mathbf{q}) dt$ , stating the stationary condition  $\delta \hat{S}(\mathbf{q}, \mathbf{v}, \mathbf{p}, \boldsymbol{\lambda}) = 0$  and eliminating the velocities as above leads to an extension of the Hamiltonian equations (3) for constrained systems, such that the index-3 DAEs are obtained as

$$\dot{\mathbf{q}} = \mathbf{M}^{-1}\mathbf{p}, \quad \dot{\mathbf{p}} = -\mathbf{D}V(\mathbf{q}) - \mathbf{G}(\mathbf{q})^T \boldsymbol{\lambda}, \quad \mathbf{g}(\mathbf{q}) = \mathbf{0}. \quad (6)$$

The classical GGL stabilization, which traces back to Gear et al. [5], represents an index reduction technique by minimal extension (see, for example, Kunkel and Mehrmann [6]). The main idea of the GGL stabilization is to couple the secondary constraints into the dynamics by making use of additional variables  $\boldsymbol{\gamma} \in \mathbb{R}^m$ , such that the system of equations of motion is extended and the differentiation index drops to  $\nu = 2$ . Correspondingly, the numerical ill-conditioning of index-3 DAEs are alleviated without having the drawback of drift phenomena. The resulting index-2 DAEs can be written in the form

$$\dot{\mathbf{q}} = \mathbf{M}^{-1}\mathbf{p} + \mathbf{G}(\mathbf{q})^T \boldsymbol{\gamma}, \quad (7a)$$

$$\dot{\mathbf{p}} = -\mathbf{D}V(\mathbf{q}) - \mathbf{G}(\mathbf{q})^T \boldsymbol{\lambda}, \quad (7b)$$

$$\mathbf{0} = \mathbf{g}(\mathbf{q}), \quad (7c)$$

$$\mathbf{0} = \mathbf{G}(\mathbf{q})\mathbf{M}^{-1}\mathbf{p}. \quad (7d)$$

Ever since, the GGL stabilization has been widely used and is thus of great importance. Numerical methods can be constructed directly by discretizing the DAEs (7). Note however that due to the GGL modification of the kinematic equation (7a), the system (7) loses its Hamiltonian structure. For the time-continuous case, some algebra leads to  $\boldsymbol{\gamma} = \mathbf{0}$ . Consequently, the GGL-DAEs boil down to the standard formulation (6).

#### 4 The GGL principle

The newly proposed GGL principle relies on the generalization of Livens principle (1) by considering Lagrange multipliers  $\boldsymbol{\lambda}, \boldsymbol{\gamma} \in \mathbb{R}^m$  to enforce the primary constraints (4) and secondary constraints (5), respectively. Imposing stationarity on a corresponding augmented action integral

$$\delta S_{\text{GGL}}(\mathbf{q}, \mathbf{v}, \mathbf{p}, \boldsymbol{\lambda}, \boldsymbol{\gamma}) = 0 \quad (8)$$

yields Euler-Lagrange equations with a kinematic relation similar to (7a). Thus equations in the fashion of (7) are obtained with an additional term in the momentum equation. By discretizing the action integral of the GGL principle variational integrators for the simulation of constrained dynamical systems can be achieved, which are by design symplectic.

Similar to the classical GGL stabilization one obtains  $\boldsymbol{\gamma} = \mathbf{0}$  for the time-continuous case. The equations of motion derived by means of the GGL principle however do not require  $\boldsymbol{\gamma} = \mathbf{0}$  to conserve the Hamiltonian  $H$  or the symplectic structure. The equations of motion induced by the GGL principle have Hamiltonian structure with a corresponding augmented Hamiltonian

$$H_{\text{GGL}}(\mathbf{q}, \mathbf{p}, \boldsymbol{\lambda}, \boldsymbol{\gamma}) = \frac{1}{2}\mathbf{p} \cdot \mathbf{M}^{-1}\mathbf{p} + V(\mathbf{q}) + \boldsymbol{\lambda} \cdot \mathbf{g}(\mathbf{q}) + \boldsymbol{\gamma} \cdot \mathbf{G}(\mathbf{q})\mathbf{M}^{-1}\mathbf{p}. \quad (9)$$

The novel framework thus also allows for an energy-momentum consistent discretization.

#### References

- [1] L. A. Pars. A treatise on analytical dynamics. The Mathematical Gazette, 50(372): 226-227, 1966.
- [2] G. H. Livens. On Hamilton's principle and the modified function in analytical dynamics. Proceedings of the Royal Society Edinburgh, 39(IX): 113-119, 1919.
- [3] N. Bou-Rabee and J. E. Marsden. Hamilton–Pontryagin Integrators on Lie Groups Part I: Introduction and Structure-Preserving Properties. Foundations of Computational Mathematics, 9(2): 197-219, 2009.
- [4] H. Yoshimura and J. E. Marsden. Dirac structures in Lagrangian mechanics Part II: Variational structures. Journal of Geometry and Physics, 57(1): 209–250, 2006.
- [5] C. W. Gear, B. Leimkuhler and G. K. Gupta. Automatic integration of Euler-Lagrange equations with constraints. Journal of Computational and Applied Mathematics, 12-13: 77-90, 1985.
- [6] P. Kunkel and V. Mehrmann. Differential-Algebraic Equations. European Mathematical Society, Zürich, 2006.

# Combined Inverse Dynamics and Constraint Force Analysis of Parallel Kinematic Machines

Daniel Gnad, Hubert Gattringer, Andreas Müller

Institute of Robotics  
Johannes Kepler University Linz  
Altenbergerstraße 69, 4040 Linz, Austria  
[daniel.gnad, hubert.gattringer, a.mueller]@jku.at

## EXTENDED ABSTRACT

### 1 Introduction

Compared to serial robotic systems, parallel kinematic machines (PKMs) [4] offer benefits like superior agility, high acceleration and payload. This leads to increased wear and fatigue of individual components, in particular joints. That has to be considered and taken into account for time optimal motion planning in order to reduce and limit the joint reaction forces  $\lambda$ . Moreover, limiting the joint reaction forces allows to reduce wear of the linkages and avoid damage of the mechanism in advance. However it is common practice to only consider the actuator torques  $\tau$  as limitations. The classical approach is to obtain the actuator torques using inverse dynamics and calculate the constraint forces separately if needed. In this paper a formulation is presented that obtains both in one step for a given motion trajectory  $\mathbf{q}(t)$  of the actuated joints. To this end, the system is completely constrained to have DOF zero. An important advantage is that the mass matrix  $\mathbf{M}$  of the absolute coordinate formulation need not be inverted. The presented approach is a completely general one, although the  $\delta = 4$  DOF Delta robot is considered as an example throughout this paper.

### 2 Forward Kinematics

The rigid multibody system comprised of  $N$  bodies is modeled using absolute coordinates with the vector  $\mathbf{z}_i^T = [\boldsymbol{\varphi}_i^T \ \mathbf{r}_i^T]$ . The orientation  $\boldsymbol{\varphi}_i$  is described using e. g. Euler parameter or quaternions and  $\mathbf{r}_i$  denotes the position of the center of gravity (COG) of each body  $i$  resolved in the inertial frame  $\mathcal{F}_I$ . The velocities are summarized by the twist  $\mathbf{V}_i^T = [{}_R\boldsymbol{\omega}_i^T \ \mathbf{v}_i^T]$  in a mixed representation, where the angular velocity  ${}_R\boldsymbol{\omega}_i$  of each body  $i$  is resolved in a body fixed reference frame  $\mathcal{F}_R$ , whereas the velocity  $\mathbf{v}_i$  is again resolved in the inertial frame.

The task of the forward kinematics of the mechanism is to express the system twist  $\mathbf{V}^T = [\mathbf{V}_1^T \ \dots \ \mathbf{V}_N^T]$  as a function of the generalized coordinates  $\mathbf{q} \in \mathbb{V}^\delta$  and velocities  $\dot{\mathbf{q}}$ . In case of the Delta robot,  $\mathbf{q}$  corresponds to the arm angles of the upper part of each limb and the rotation angle of the telescope bar. As a starting point to analytically express the system twist  $\mathbf{V}$  the velocity constraints

$$\mathbf{0} = \mathbf{G}(\mathbf{z})\mathbf{V}, \quad (1)$$

arising from the joints, are taken into account and directly solved with the orthogonal complement to obtain

$$\mathbf{V} = \mathbf{P} \begin{bmatrix} -\tilde{\mathbf{G}}_1^{-1} \tilde{\mathbf{G}}_2 \\ \mathbf{I} \end{bmatrix} \dot{\mathbf{q}} = \mathbf{F} \dot{\mathbf{q}}, \quad (2)$$

where  $\mathbf{I}$  denotes an identity matrix of dimension  $\delta$  and  $\mathbf{z}$  the orientation and position of all bodies. A permutation matrix  $\mathbf{P}$  to sort the elements of the twist  $\mathbf{V} = \mathbf{P}\tilde{\mathbf{V}}$ , such that the  $\delta$  independent entries are the last ones of  $\tilde{\mathbf{V}}$ , is introduced to yield a partitioned velocity constraint matrix  $\tilde{\mathbf{G}} = [\tilde{\mathbf{G}}_1 \ \tilde{\mathbf{G}}_2] = \mathbf{G}\mathbf{P}$ . To solve the forward kinematics for a PKM on position level in general iterative methods or numerical integration should be used, whereas for the Delta robot a closed solution  $\mathbf{z} = \mathbf{f}(\mathbf{q})$  can be found.

### 3 Dynamics

The equations of motion (EOM) for a single body  $\mathbf{M}_i \ddot{\mathbf{V}}_i + \mathbf{C}_i \mathbf{M}_i \mathbf{V}_i = \mathbf{W}_i^{\text{act}} + \mathbf{W}_i^{\text{grav}}$ , where  $\mathbf{M}_i = \text{diag}(\boldsymbol{\Theta}_i, \mathbf{I}m_i)$  denotes the mass matrix,  $\mathbf{C}_i = \text{diag}({}_R\tilde{\boldsymbol{\omega}}_i, \mathbf{0})$  and  $\mathbf{W}_i^{\text{act}}, \mathbf{W}_i^{\text{grav},T} = [\mathbf{0}^T \ m_i \mathbf{g}^T]$  the wrenches regarding actuation and gravitation are summarized to obtain the EOM of the assembled system

$$\mathbf{M}\dot{\mathbf{V}} + \mathbf{G}^T \boldsymbol{\lambda} = -\mathbf{C}\mathbf{M}\mathbf{V} + \mathbf{W}^{\text{act}} + \mathbf{W}^{\text{grav}}. \quad (3)$$

The Lagrange multipliers  $\boldsymbol{\lambda}$  are in particular the joint reaction wrenches due to the velocity constraints (1) of the joints. With the time derivative  $\dot{\mathbf{G}}(\mathbf{z}, \mathbf{V})\mathbf{V} + \mathbf{G}(\mathbf{z})\dot{\mathbf{V}} = \mathbf{0}$  of the velocity constraints (1) the well known equation system

$$\begin{bmatrix} \mathbf{M} & \mathbf{G}^T \\ \mathbf{G} & \mathbf{0} \end{bmatrix} \begin{bmatrix} \dot{\mathbf{V}} \\ \boldsymbol{\lambda} \end{bmatrix} = \begin{bmatrix} -\mathbf{C}\mathbf{M}\mathbf{V} + \mathbf{W}^{\text{act}} + \mathbf{W}^{\text{grav}} \\ -\dot{\mathbf{G}}\mathbf{V} \end{bmatrix} \quad (4)$$

has to be solved for the unknowns  $\dot{\mathbf{V}}$  and  $\boldsymbol{\lambda}$ , as shown in [1], [3].

#### 4 Inverse Dynamics combined with Constraint Force Analysis

To additionally obtain the required motor torques  $\boldsymbol{\tau}$  besides the joint reaction forces  $\boldsymbol{\lambda}$  within the same calculation step *servo constraints* [2] are added to the velocity constraints (1) to obtain a general, affine Pfaffian form

$$\mathbf{G}_{\text{ext}} \mathbf{V} = \dot{\mathbf{q}} \quad \text{with} \quad \mathbf{G}_{\text{ext}} := \begin{bmatrix} \mathbf{G} \\ \mathbf{G}_q \end{bmatrix}, \quad \dot{\mathbf{q}} := \begin{bmatrix} \mathbf{0} \\ \dot{\mathbf{q}} \end{bmatrix}. \quad (5)$$

In case of the Delta robot, the corresponding entry of the angular velocity of the upper body of each limb is constrained to be equal to the given motion  $\dot{q}$  and analogously for the motor of the telescope bar. A combination of the EOM (3) with the time derivative of the extended velocity constraint matrix (5) yields

$$\begin{bmatrix} \mathbf{M} & \mathbf{G}_{\text{ext}}^T \\ \mathbf{G}_{\text{ext}} & \mathbf{0} \end{bmatrix} \begin{bmatrix} \dot{\mathbf{V}} \\ \boldsymbol{\lambda}_{\text{ext}} \end{bmatrix} = \begin{bmatrix} -\mathbf{CMV} + \mathbf{W}^{\text{grav}} \\ -\dot{\mathbf{G}}_{\text{ext}} \mathbf{V} + \ddot{\mathbf{q}} \end{bmatrix} \quad \text{with} \quad \mathbf{G}_{\text{ext}}^T \boldsymbol{\lambda}_{\text{ext}} = \mathbf{G}^T \boldsymbol{\lambda} + \mathbf{G}_q^T \boldsymbol{\tau}, \quad (6)$$

where the extended Lagrange multipliers  $\boldsymbol{\lambda}_{\text{ext}}^T = [\boldsymbol{\lambda}^T \quad \boldsymbol{\tau}^T]$  include the necessary actuator torques  $\boldsymbol{\tau}$  for the given motion  $\mathbf{q}$ . A comparison between (4) and (6) reveals that  $\mathbf{W}^{\text{act}} = -\mathbf{G}_q^T \boldsymbol{\tau}$  holds.

Additionally the extended velocity constraint matrix  $\mathbf{G}_{\text{ext}}$  is a regular, quadratic, full rank matrix and hence invertible, whereas  $\mathbf{G}$  is not quadratic. A numerical advantage is the sparsity of the extended velocity constraint matrix  $\mathbf{G}_{\text{ext}}$ , which can be exploited to efficiently solve the two equations within (6) separately. At first the forward kinematics problem

$$\mathbf{G}_{\text{ext}} \dot{\mathbf{V}} = -\dot{\mathbf{G}}_{\text{ext}} \mathbf{V} + \ddot{\mathbf{q}}. \quad (7)$$

is solved for  $\dot{\mathbf{V}}$  with given  $\ddot{\mathbf{q}}$ . Then the extended Lagrange multipliers  $\boldsymbol{\lambda}_{\text{ext}}$  are obtained by solving

$$\mathbf{G}_{\text{ext}}^T \boldsymbol{\lambda}_{\text{ext}} = -\mathbf{M} \dot{\mathbf{V}} - \mathbf{CMV} + \mathbf{W}^{\text{grav}}. \quad (8)$$

A combination of (7) and (8) yields the analytic solution

$$\boldsymbol{\lambda} = \mathbf{G}_{\text{ext}}^{-T} [\mathbf{M} \mathbf{G}_{\text{ext}}^{-1} (\dot{\mathbf{G}}_{\text{ext}}(\mathbf{z}, \mathbf{V}) \mathbf{V} - \ddot{\mathbf{q}}) - \mathbf{CMV} + \mathbf{W}^{\text{grav}}]. \quad (9)$$

However it is computationally more efficient to subsequently solve (7) and (8) using (sparse) linear algebra solver instead of computing the numerical inverse.

#### 5 Conclusion, Example and Outlook

A main advantage of this absolute coordinate formulation is that allows to deal with zero entries of the mass matrix  $\mathbf{M}$ , whereas this inverse matrix notably appears two times within the classical solution  $\boldsymbol{\lambda} = (\mathbf{GM}^{-1}\mathbf{G}^T)^{-1}[\dot{\mathbf{G}}\mathbf{V} + \mathbf{GM}^{-1}(-\mathbf{CMV} + \mathbf{W})]$  as derived from (4) in [1]. Due to the mixed formulation the mass matrix  $\mathbf{M}$  is additionally purely diagonal with constant entries. While the classical solution presumes a regular mass matrix, formulation (9) allows to have zero entries of  $\mathbf{M}$  and this is in particular important when model data is not available or cannot be obtained from any identification procedure. As an example regarding the Delta robot, the presented method enables to set the moment of inertia along the longitudinal axis of the upper body of each limb to zero. This still yields the exact results of the dynamics model. Furthermore the inertia along the longitudinal axis of the rods of each limb can be set to zero, if their effect on the dynamics model shall be neglected, resulting in a simplified model that consequently differs from the original model. In general the user can set any desired inertia entry to any value.

One benefit of the presented methods is that it boils down to solving the uniquely determined equation systems (7) and (8). A further numerical advantage is the sparsity of the coefficient matrix  $\mathbf{G}_{\text{ext}}$ , which allows to use tailored sparse linear algebra methods for large systems while the numerical inverse is computationally quite expensive. Hence a massive improvement regarding computation time of the sparse equation systems over the dense ones in C++ and Matlab is supposed. A comparison of the behavior of the different solvers for dense and sparse equation systems of the "Eigen" package in C++ will be presented to verify the numerical advantage.

#### Acknowledgments

This work has been supported by the "LCM – K2 Center for Symbiotic Mechatronics" within the framework of the Austrian COMET-K2 program.

#### References

- [1] Nikravesh, P. E.: Computer-aided analysis of mechanical systems, Prentice Hall (1988)
- [2] Blajer, W. and Seifried, R. and Kołodziejczyk, K.: Servo-constraint realization for underactuated mechanical systems, Springer: Archive of Applied Mechanics, vol. 8, nr. 9, pp 1191–1207, 2015
- [3] Bremer, H.: Elastic Multibody Dynamics: A Direct Ritz Approach. Springer-Verlag, Heidelberg, 2008
- [4] Merlet, J.P.: Parallel robots, Vol. 128, Springer Science & Business Media, 2005

# Kane's Equations for Nonholonomic Systems in Bond-Graph-Compatible Velocity and Momentum Forms

James Phillips<sup>1</sup>, Farid Amirouche<sup>2</sup>

<sup>1</sup> Senior Applications Engineer  
Applied Dynamics International  
Ann Arbor, MI, USA  
phillips@adi.com

<sup>2</sup> Department of Orthopaedic Surgery  
University of Illinois at Chicago  
Chicago, IL, USA  
amirouch@uic.edu

## EXTENDED ABSTRACT

### 1 Introduction

Bond graphs are a widely used graphical formalism for representing dynamic systems, which may encompass multiple energy domains, in a uniform fashion, using a small set of ideal elements [1]. Prior to the appearance of our 2018 paper [2], the most advanced methods for representing multibody systems in a concise bond-graph form were based on generalized momentum, using the so-called IC bond-graph element, and these were limited to holonomic systems. In [2] we introduced a bond-graph-compatible momentum method for nonholonomic systems, based on Kane's equations [3], but it was limited to scleronomic systems. In this paper we extend our momentum method to incorporate systems with external time-varying constraints, and we find that this momentum method is partially Hamiltonian (to be defined below). We also introduce a velocity-based method that is partially Lagrangian (also to be defined below). Finally, we introduce a generalization of the IC bond-graph element, the nonholonomic or NIC bond-graph element, and exhibit bond graphs for our nonholonomic methods.

Kane's formulation is used in the development, because it can provide concise, matrix-based descriptions of multibody systems [4]. The methodology here differs from [4] however, in that it makes no assumptions about the kinematic formulation, other than that a set of partial velocity vectors describing the system is available. For the greatest generality, we begin with particle systems, and then specialize the results to systems of rigid bodies.

### 2 Assumptions and Formulation

We consider a simple nonholonomic system in an inertial frame, with all rheonomic constraints initially relaxed, making it scleronomic. Therefore assume  $R$  generalized coordinates  $q_r$  completely determine the positions of all particles in the frame, and  $S$  generalized velocities  $f_s$  completely determine the coordinate derivatives  $\dot{q}_r$ .  $S$  is the number of scleronomic degrees of freedom for the system, and the number of nonholonomic constraints is  $R - S$ . The coordinate derivatives and generalized velocities are related through the matrix equation

$$\dot{\mathbf{q}} = \mathbf{Q}\mathbf{f}, \quad (1)$$

where  $\mathbf{q}$  and  $\dot{\mathbf{q}}$  are length  $R$  column matrices of coordinates and coordinate derivatives,  $\mathbf{f}$  is a length  $S$  column matrix of generalized velocities, and  $\mathbf{Q}$  is an  $R \times S$  matrix of rank  $S$ , a function only of the generalized coordinates  $\mathbf{q}$ . After finding equations of motion for the scleronomic degrees of freedom  $\mathbf{f}$ , we will then apply  $S_c$  rheonomic constraints, leaving  $S - S_c$  degrees of freedom.

Initially we regard the system as a constrained collection of particles. The inertial velocity  $\mathbf{v}$  of every particle in the system can be expressed as

$$\mathbf{v} = \left( \frac{\partial \mathbf{v}}{\partial \mathbf{f}^T} \right) \mathbf{f}, \quad (2)$$

where  $\partial \mathbf{v} / \partial \mathbf{f}^T$  is a row matrix of partial velocity derivatives, each of which is a function only of the generalized coordinates  $\mathbf{q}$ . These are nonholonomic partial velocities, in Kane's terminology. Each particle has a differential mass  $dm$ , and a differential linear momentum  $d\mathbf{p}$ , defined as

$$d\mathbf{p} = \mathbf{v} dm. \quad (3)$$

### 3 Results Obtained for General Particle Systems

For the sake of space in this abstract, we will concentrate on the results for scleronomic particle systems. The full paper will give additional results for rheonomic systems and for rigid body systems. Initially we find the traditional velocity form of Kane's equations as

$$\mathbf{A}\dot{\mathbf{f}} + \bar{\mathbf{D}}\mathbf{f} = \mathbf{e}, \quad (4)$$

where  $\mathbf{A}$  is the system mass matrix given by (using Stieltjes integration over differential mass elements in space)

$$\mathbf{A} \equiv \int \left( \frac{\partial \mathbf{v}}{\partial \mathbf{f}} \right) \cdot \left( \frac{\partial \mathbf{v}}{\partial \mathbf{f}^T} \right) dm, \quad (5)$$



$\bar{\mathbf{D}}$  is the system gyrator matrix given by

$$\bar{\mathbf{D}} \equiv \int \left( \frac{\partial \mathbf{v}}{\partial \mathbf{f}} \right) \cdot \frac{d}{dt} \left( \frac{\partial \mathbf{v}}{\partial \mathbf{f}^T} \right) dm, \quad (6)$$

and  $\mathbf{e}$  represents the total generalized impressed forces,  $\mathbf{e} \equiv \int (\partial \mathbf{v} / \partial \mathbf{f}) \cdot d\mathbf{F}$ , where  $d\mathbf{F}$  is the per-particle impressed force vector. By differentiation of the equation for  $\mathbf{A}$ , it is obvious that

$$\dot{\mathbf{A}} = \bar{\mathbf{D}} + \bar{\mathbf{D}}^T. \quad (7)$$

Defining the generalized momentum column matrix  $\mathbf{p}$  as  $\mathbf{p} \equiv \mathbf{A}\mathbf{f}$ , we then find the momentum form of Kane's equations as a pair of two equations:

$$\dot{\mathbf{p}} = \mathbf{e} + \bar{\mathbf{D}}^T \mathbf{f}, \quad (8)$$

$$\mathbf{f} = \mathbf{A}^{-1} \mathbf{p}. \quad (9)$$

Using the kinetic energy function  $T$ , defined as

$$T(\mathbf{q}, \mathbf{p}) \equiv (1/2) \mathbf{p}^T \mathbf{A}^{-1}(\mathbf{q}) \mathbf{p}, \quad (10)$$

the second equation of the pair can be written as

$$\mathbf{f} = \frac{\partial T}{\partial \mathbf{p}}; \quad (11)$$

this is what we call the partial Hamiltonian property. Using also the definition of  $\bar{\mathbf{D}}$  from (6), we find

$$\hat{\mathbf{e}} \equiv \bar{\mathbf{D}}^T \mathbf{f} = \int \frac{d}{dt} \left( \frac{\partial \mathbf{v}}{\partial \mathbf{f}} \right) \cdot d\mathbf{p}, \quad (12)$$

which has a straightforward per-particle interpretation. Although  $\bar{\mathbf{D}}$  is uniquely defined, any matrix  $\mathbf{D}$  that satisfies (7) and for which  $\mathbf{D}\mathbf{f} = \bar{\mathbf{D}}\mathbf{f}$  will serve for  $\bar{\mathbf{D}}$  in Eqs. (4), (8).

Finally we find a modified velocity form of Kane's equations as

$$\mathbf{A}\dot{\mathbf{f}} + \left( \frac{\partial \hat{\mathbf{p}}}{\partial \mathbf{q}^T} \right) \dot{\mathbf{q}} = \mathbf{e} + \hat{\mathbf{e}}. \quad (13)$$

where  $\hat{\mathbf{p}}$  is generalized momentum as a function of  $\mathbf{q}$  and  $\mathbf{f}$ :

$$\hat{\mathbf{p}}(\mathbf{q}, \mathbf{f}) \equiv \mathbf{A}(\mathbf{q})\mathbf{f}. \quad (14)$$

The left side of (13) can also be written as  $\dot{\hat{\mathbf{p}}} = d(\partial T^* / \partial \mathbf{f}) / dt$ , where  $T^*$  is the kinetic co-energy function

$$T^*(\mathbf{q}, \mathbf{f}) \equiv (1/2) \mathbf{f}^T \mathbf{A}(\mathbf{q}) \mathbf{f}. \quad (15)$$

This leads us to describe this form as partially Lagrangian. Equation (13) is believed to be a new result for nonholonomic systems.

## 4 Conclusions

The  $\mathbf{Q}$ ,  $\mathbf{A}$ ,  $\bar{\mathbf{D}}$  and  $\mathbf{D}$  matrices defined above provide a complete set of matrix parameters for nonholonomic multibody systems, applying both to general particle and to rigid-body systems. They are the parameters that characterize the NIC bond-graph element, allowing concise bond graphs for nonholonomic systems to be constructed, as illustrated in Fig. 1.

## References

- [1] Karnopp, D., Margolis, D., Rosenberg, R.: System Dynamics. Third edn. Wiley (2000)
- [2] Phillips, J.R., Amirouche, F.: A momentum form of Kane's equations for scleronomic systems. Mathematical and Computer Modelling of Dynamical Systems **24**(2) (2018) 143–169
- [3] Kane, T.R., Levinson, D.A.: Dynamics: Theory and Applications. McGraw-Hill (1985)
- [4] Amirouche, F.: Fundamentals of multibody dynamics: theory and applications. Springer Science & Business Media (2007)

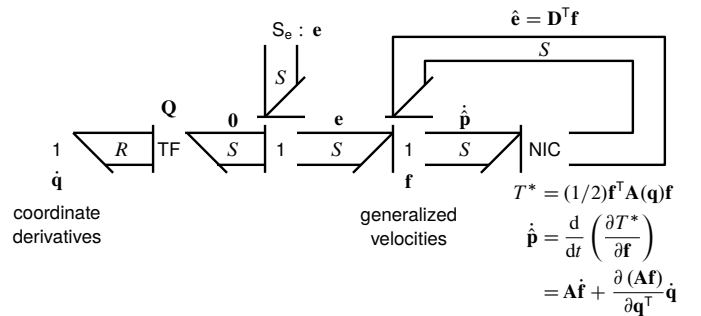


Figure 1: Multibond graph of partially Lagrangian form

# Cable-Actuated Soft Finger Modeling Using an ALE Approach

Olivier Devigne<sup>1</sup>, Alejandro Cosimo<sup>1,2</sup>, Olivier Bruls<sup>1</sup>

<sup>1</sup> Department of Aerospace and Mechanical Engineering  
University of Liège  
Allée de la Découverte 9, 4000 Liège, Belgium  
{o.devigne, acosimo, o.bruls}@uliege.be

<sup>2</sup> Centro de Investigación de Métodos Computacionales (CIMEC)  
Universidad Nacional del Litoral - CONICET  
Colectora Ruta Nac 168, 3000 Santa Fe, Argentina

## EXTENDED ABSTRACT

### 1 Motivation

Soft robots, such as soft grippers, are a relatively new class of robots made of soft materials, namely silicon or plastic. They exhibit various advantages. Indeed, their manufacturing processes, often relying on 3D printing, are inexpensive. Soft grippers, which enter in the scope of the industry 4.0 development, grant flexibility to the tasks to be accomplished. For instance, the same programming sequence making use of adequate force and torque sensors can be used for the grasping of objects of different sizes and consistencies, as it can be the case in the food industry [1, 2]. The consequence is that almost no damage is done to the manipulated parts. Moreover, in the context of human-robot collaboration, soft robots are safer to the user because of their deformable nature and their lighter design.

The actuation of soft robots may rely on 3 different techniques. The first and most natural one is to make use of a linear actuator on one or several points of the deformable structure to induce a motion. The second one relies on pressure and vacuum by inflating or deflating deformable chambers inside the robot, enabling bending, for example. The third technique is to use a cable going through the structure and attached to one or several key points, pulling the deformable robot in the desired direction. Considering more specifically the case of a soft finger composed of phalanges, attaching a cable to the upper phalange and pulling it produces the bending of the finger. The objective of this work is to develop numerical methods for the simulation of such cable-actuated robots, as illustrated in Figure 1a. It implies several numerical challenges. For instance, an accurate cable model, accounting for its extension and capturing the contact and friction phenomena inside the finger, must be developed. In order to numerically approach the simulation of such flexible systems, a nonlinear finite element method (FEM) is often followed thanks to its versatility. In this context, the cable is discretized into several elements, enabling the precise description of these contact phenomena.

Nevertheless, it should be noted that, often, the need to discretize the cable into small elements is only needed in some key regions which interact with the structure. This situation is comparable to the case of reeving systems, where small elements are needed around the pulley, but larger elements could be used anywhere else. However, because the cable is moving around the pulley with time, one is thus often constrained to work with smaller elements than needed along the whole cable in order to accurately represent contact and friction happening between the pulley and the cable. In order to circumvent this difficulty, a popular option is to work with an arbitrary Lagrangian-Eulerian (ALE) formulation [3, 4, 5].

### 2 Method

In an ALE formulation, the positions of some nodes of the finite element discretization remain fixed during the simulation, while the cable is flowing through these nodes, inducing a mass flow, as it would be the case in an Eulerian formulation. However, it also enables mesh motion, which is an advantage in the modeling of a cable-actuated finger. Indeed, the contact and friction locations occurring due to the change of direction of the phalanges under the cable action are known *a priori*, as shown in Figure 1b, while the rest of the cable is contact-free. From a mesh point of view, these points are modeled using nodes of the cable which are constrained to the finger where a flow of material occurs. The other nodes of the cable can follow the material particles, as shown in Figure 1c.

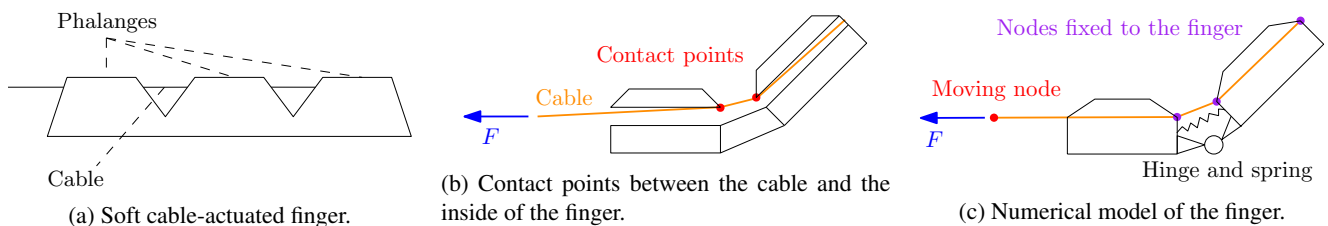


Figure 1: Soft finger, occurrence of contact due to the cable actuation and associated numerical model.

In this work, an ALE formulation for a simple cable element is presented. Based on [6], it gives a continuous formulation embedded in a consistent variational framework starting from the Dirichlet principle, which can be later discretized. The novelty

consists in the addition of constraints to recover the equations of motion in a multibody set-up expressed in a Lie group formalism [7, 8]. The global idea is to write the equations of motion in terms of a reference configuration that does not necessarily match neither with the material nor the spatial configurations. In the resulting equations of motion two sets can be identified. The first one represents the spatial motion problem, where the spatial location of material particles is tracked, whereas the second set represents the material motion problem, where this time the material particle corresponding to a specific spatial location is tracked. These two sets of equations give interesting features in a discretized context. For the spatial motion problem, a residual force is nothing else than a classical body force commonly met in Lagrangian FEM. However, a residual material force, emanating from the other set, can be understood as a force arising, noticeably, from a non-optimal mesh placement, meaning that a vanishing material force represents an optimal material placement of the node. In other words, in this formulation, nodes which are not materially nor spatially constrained will move to reach a global minimum of the potential energy.

### 3 Results

This ALE cable formulation is applied to a soft finger model. The problem consists in a finger where phalanges are assimilated to rigid bodies linked by joints and torsion springs. The cable is attached to the last phalange and pulled from the other end, in a similar fashion as in Figure 1c. In addition, the contact between the phalanges is modeled. This leads to obtain nonsmooth equations of motion which are integrated using the nonsmooth generalized- $\alpha$  method [9, 10]. It must be emphasized that, in this case, the cable is considered massless and that no friction develops between the cable and the phalanges. The modeling of these effects will be subject of a future work.

It is shown that contact between the cable and the finger is captured by the introduction of a bilateral constraint and the points at which contact occurs see a flow of mass of the cable, as expected. Moreover, contact between the phalanges is precisely accounted for. This model is a promising first step towards a multibody representation of a soft finger.

### 4 Conclusion

As a conclusion, the ALE formulation proposed in this work can be successfully applied to cable modeling, noticeably in a soft robot actuation context. Compared to [3, 4, 5], the procedure starts directly from the variational principle and leads to the equations of motion in a systematic manner. The method also builds on the work from [6] by the addition of constraints and the inclusion of this formulation within a multibody framework in a Lie group formalism.

### Acknowledgements

This work is funded by the Robotix Academy project of the Greater Region.

### References

- [1] Z. Wang and S. Hirai, "A 3D printed soft gripper integrated with curvature sensor for studying soft grasping," in *2016 IEEE/SICE International Symposium on System Integration (SII)*, pp. 629–633, IEEE, 2016.
- [2] Y. Wei, Y. Chen, T. Ren, Q. Chen, C. Yan, Y. Yang, and Y. Li, "A novel, variable stiffness robotic gripper based on integrated soft actuating and particle jamming," *Soft Robotics*, vol. 3, no. 3, pp. 134–143, 2016.
- [3] J. L. Escalona, "An arbitrary Lagrangian–Eulerian discretization method for modeling and simulation of reeving systems in multibody dynamics," *Mechanism and Machine Theory*, vol. 112, pp. 1–21, 2017.
- [4] J.-P. Liu, Z.-B. Cheng, and G.-X. Ren, "An arbitrary Lagrangian–Eulerian formulation of a geometrically exact Timoshenko beam running through a tube," *Acta Mechanica*, vol. 229, no. 8, pp. 3161–3188, 2018.
- [5] Y. Peng, Y. Wei, and M. Zhou, "Efficient modeling of cable-pulley system with friction based on arbitrary-Lagrangian-Eulerian approach," *Applied Mathematics and Mechanics*, vol. 38, no. 12, pp. 1785–1802, 2017.
- [6] E. Kuhl, H. Askes, and P. Steinmann, "An ALE formulation based on spatial and material settings of continuum mechanics. part 1: Generic hyperelastic formulation," *Computer Methods in Applied Mechanics and Engineering*, vol. 193, no. 39-41, pp. 4207–4222, 2004.
- [7] O. Brüls, A. Cardona, and M. Arnold, "Lie group generalized- $\alpha$  time integration of constrained flexible multibody systems," *Mechanism and Machine Theory*, vol. 48, pp. 121–137, 2012.
- [8] V. Sonnevile, *A geometric local frame approach for flexible multibody systems*. PhD thesis, Université de Liège, Liège, Belgique, 2015.
- [9] A. Cosimo, J. Galvez, F. J. Cavalieri, A. Cardona, and O. Brüls, "A robust nonsmooth generalized- $\alpha$  scheme for flexible systems with impacts," *Multibody System Dynamics*, vol. 48, no. 2, pp. 127–149, 2020.
- [10] O. Devigne, A. Cosimo, and O. Brüls, "Soft finger modeling using a nonsmooth contact approach," in *Proceedings of the 4th Robotix-Academy Conference for Industrial Robotics*, 2020.

# Rotational Component and Translational Component in a Measured Velocity Data

Wan Suk Yoo<sup>1</sup>, Jae Yeon Kim<sup>2</sup>, Soo Jin Kim<sup>3</sup>

<sup>1</sup>Faculty of Mechanical Engineering  
Pusan National University  
Busan, 46288, South Korea  
wsyoo@pusan.ac.kr

<sup>2</sup>Digital Appliance Company  
LG Electronics,  
Changwon, 51533, South Korea  
jaeyeon1.kim@lge.com

<sup>3</sup>Digital Appliance Company  
LG Electronics,  
Changwon, 51533, South Korea  
soojin1004.kim@lge.com

## EXTENDED ABSTRACT

### 1 Introduction

To verify the motion of a system, velocities are frequently measured with a measurement device. In the measured velocity data, rotational component and translational component is combined together. To calculate the angular component in a planar motion, just measured data at two points P and Q is enough to determine the angular velocity. In a three-dimensional case, in which the angular velocity is a  $3 \times 1$  vector, velocity data at three points P, Q, and R is required to determine the angular velocity. Moreover, the accuracy of calculated angular velocity depends on the selection of three points. In this paper, the selection scheme for three measuring points is reviewed.

### 2 Measured Data in a Washing Machine

As shown in Figure 1, several points are selected and velocities are measured at these points, in which the measured velocity is combined both rotational component and translational component.

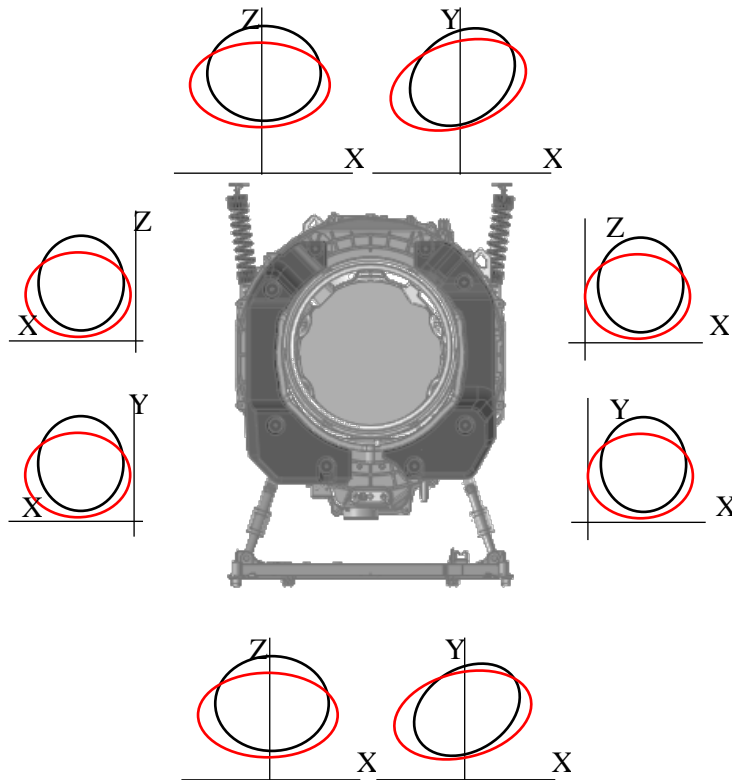


Figure 1: Measured data in a washing machine

### 3 Rotational Component and Translational Component in the Measured Data

When three velocities at three points (P, Q, and R) are measured as shown in Figure 2, the relation between two points P and R can be written as Equation (1). Since the coefficient matrix in Equation (1) is singular, it is required one more equation to

determine angular velocity uniquely. One more equation can be obtained from the velocity relation between P and R, as shown in Equation (2).

If we choose the first and the second equation from Equation (1) and the third equation from Equation (2), then the equation for angular velocity become equation (3). Then, what will be the best choice for three points P, Q, and R? If three points are selected on a straight line, then the coefficient matrix in Equation (3) becomes singular, which is the worst case and should be avoided. When two lines PQ and PR are almost perpendicular, it'll be the best choice to ensure the coefficient matrix to be nonsingular.

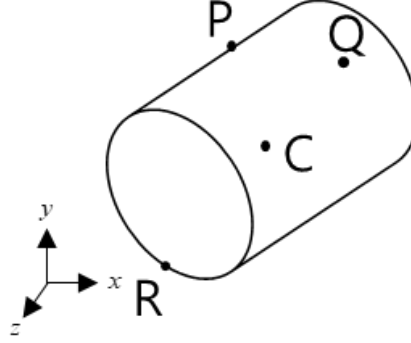


Figure 2: Three points P, Q and R in a space

$$V_Q = V_P + \omega \times r_{Q/P}, \quad V_Q - V_P = \omega \times r_{Q/P}$$

$$\begin{pmatrix} V_{xQ/P} \\ V_{yQ/P} \\ V_{zQ/P} \end{pmatrix} = \begin{bmatrix} 0 & z_{Q/P} & -y_{Q/P} \\ -z_{Q/P} & 0 & x_{Q/P} \\ y_{Q/P} & -x_{Q/P} & 0 \end{bmatrix} \begin{bmatrix} \omega_x \\ \omega_y \\ \omega_z \end{bmatrix} \quad (1)$$

$$V_R = V_P + \omega \times r_{R/P}, \quad V_R - V_P = \omega \times r_{R/P}$$

$$\begin{pmatrix} V_{xR/P} \\ V_{yR/P} \\ V_{zR/P} \end{pmatrix} = \begin{bmatrix} 0 & z_{R/P} & -y_{R/P} \\ -z_{R/P} & 0 & x_{R/P} \\ y_{R/P} & -x_{R/P} & 0 \end{bmatrix} \begin{bmatrix} \omega_x \\ \omega_y \\ \omega_z \end{bmatrix} \quad (2)$$

$$\begin{pmatrix} V_{yQ/P} \\ V_{zQ/P} \\ V_{xR/P} \end{pmatrix} = \begin{bmatrix} -z_{Q/P} & 0 & x_{Q/P} \\ y_{Q/P} & -x_{Q/P} & 0 \\ 0 & z_{R/P} & -y_{R/P} \end{bmatrix} \begin{bmatrix} \omega_x \\ \omega_y \\ \omega_z \end{bmatrix} \quad (3)$$

## Acknowledgments

This research is supported by the Digital Appliance Company, LG Electronics.

## References

- [1] G. Pittner and R. Barczewski, Numerical and experimental vibration analysis of domestic washing machine drum, *Int. J. Appl. Mech. Eng.*, no. May 2012, 2014.
- [2] S. Son, S. Lee, and D. Choi, Experiment-Based Design Optimization of a Washing Machine Liquid Balancer for Vibration Reduction, *Int. J. Precis. Eng. Manuf.*, vol. 13, no. 8, pp. 1433–1438, 2012.

# An Efficient Algorithm for Solving Time Optimal Control Problems in Multibody Dynamics

Philipp Eichmeir, Wolfgang Steiner<sup>1</sup>

<sup>1</sup> University of Applied Sciences Upper Austria  
Stelzhamerstrasse 23, 4600 Wels, Austria  
Institute of Mechanics and Mechatronics, TU Wien  
Getreidemarkt 9, 1060 Vienna, Austria  
wolfgang.steiner@fh-wels.at

## EXTENDED ABSTRACT

In the last few years, engineers have been increasingly faced with the challenge of solving formidable optimization and control tasks for more and more complex simulation models. For this reason, there is a growing demand in both research and industry to develop efficient and reliable algorithms to cope with these tasks and to design optimal processes. In this contribution we propose an iterative algorithm, based on the adjoint gradient computation in [1], for solving time optimal control problems in multibody dynamics.

The dynamics of constrained multibody systems is commonly described by a set of differential-algebraic equations of the form

$$\begin{aligned} \mathbf{M}(\mathbf{q}(t))\ddot{\mathbf{q}}(t) + \mathbf{C}_q^T(\mathbf{q}(t))\boldsymbol{\lambda}(t) &= \mathbf{f}(\mathbf{q}(t), \dot{\mathbf{q}}(t), \mathbf{u}(t)) \\ \mathbf{C}(\mathbf{q}(t)) &= \mathbf{0}, \end{aligned} \quad (1)$$

where  $\mathbf{q}(t) \in \mathbb{R}^n$  denotes the vector of generalized coordinates,  $\mathbf{u}(t) \in \mathbb{R}^m$  the vector of control inputs and  $\boldsymbol{\lambda}(t) \in \mathbb{R}^l$  the vector of Lagrange multipliers.  $\mathbf{M}(\mathbf{q}(t))$  is the mass matrix of the system and  $\mathbf{f}(\mathbf{q}(t), \dot{\mathbf{q}}(t), \mathbf{u}(t))$  is the vector of applied and gyroscopic forces. The constraint equations are collected in  $\mathbf{C}(\mathbf{q}(t))$  and  $\mathbf{C}_q(\mathbf{q}(t)) = \partial \mathbf{C} / \partial \mathbf{q}$  denotes the associated constraint Jacobian. For given initial conditions  $\mathbf{q}(t_0) = \mathbf{q}_0$  and  $\dot{\mathbf{q}}(t_0) = \mathbf{v}(t_0) = \mathbf{v}_0$  the equations of motion in Eq. (1) can be solved numerically for  $\mathbf{q}(t)$ ,  $\mathbf{v}(t)$  and  $\boldsymbol{\lambda}(t)$  by applying a DAE-solver for index three equations. Now we are looking for control inputs  $\mathbf{u}(t)$ , which minimize the cost functional

$$J = \int_{t_0}^{t_f} [1 + \Pi(\mathbf{q}(t), \mathbf{v}(t), \mathbf{u}(t))] dt. \quad (2)$$

Here  $\Pi(\mathbf{q}(t), \mathbf{v}(t), \mathbf{u}(t))$  denotes a penalty function in order to introduce constraints on  $\mathbf{q}(t)$ ,  $\mathbf{v}(t)$  and  $\mathbf{u}(t)$ . The final time  $t_f$  is considered free, and we claim the system to satisfy a set of final conditions of the form

$$\boldsymbol{\phi}(\mathbf{q}(t_f), \mathbf{v}(t_f), t_f) = \mathbf{0}, \quad \boldsymbol{\phi} : \mathbb{R}^n \times \mathbb{R} \rightarrow \mathbb{R}^r. \quad (3)$$

In order to circumvent the solution of a two-point boundary value problem, which can be derived from Eq. (1), Eq. (2) and Eq. (3) by using Pontryagin's minimum principle, we apply an iterative solution strategy by computing the gradient of the cost functional with respect to the control inputs. As a first step to compute an update of the final time and the control history, we solve the adjoint system:

$$\begin{aligned} \dot{\mathbf{w}}(t) &= -\Pi_q^T - \mathbf{G}\mathbf{p}(t) - \mathbf{C}_q^T\boldsymbol{\mu}(t) - (\mathbf{C}_q\mathbf{v})_q^T\boldsymbol{\sigma}(t) & \mathbf{C}_q\mathbf{p}(t) &= \mathbf{0} \\ \frac{d}{dt}(\mathbf{M}\mathbf{p}(t)) &= -\Pi_v^T - \mathbf{w}(t) - \mathbf{f}_v^T\mathbf{p}(t) - \mathbf{C}_q^T\boldsymbol{\sigma}(t) & \mathbf{C}_q\mathbf{w}(t) &= \mathbf{0}, \end{aligned} \quad (4)$$

in which we introduced the adjoint variables  $\mathbf{p}(t), \mathbf{w}(t) \in \mathbb{R}^n$ ,  $\boldsymbol{\mu}(t), \boldsymbol{\sigma}(t) \in \mathbb{R}^l$  and the abbreviation  $\mathbf{G}(t) = \mathbf{f}_q^T - (\mathbf{C}_q^T\boldsymbol{\lambda})_q^T - (\mathbf{M}\dot{\mathbf{v}})_q^T$ . The matrices  $\Pi_q(t) = \partial \Pi / \partial \mathbf{q}$ ,  $\Pi_v(t) = \partial \Pi / \partial \mathbf{v}$ ,  $\mathbf{f}_q(t) = \partial \mathbf{f} / \partial \mathbf{q}$ ,  $\mathbf{f}_v(t) = \partial \mathbf{f} / \partial \mathbf{v}$  must be computed from a forward solution of Eq. (1). With the right boundary conditions  $\mathbf{w}(t_f) = \mathbf{0}$  and  $\mathbf{p}(t_f) = \mathbf{0}$ , Eq. (4) can be solved backwards in time. Beside Eq. (4), we introduce a second adjoint system to relate the control variations with the final conditions in Eq. (3):

$$\begin{aligned} \dot{\mathbf{W}}(t) &= -\mathbf{G}\mathbf{P}(t) - \mathbf{C}_q^T\boldsymbol{\mathcal{M}}(t) - (\mathbf{C}_q^T\mathbf{v})_q^T\boldsymbol{\mathcal{S}}(t) & \mathbf{C}_q\mathbf{P}(t) &= \mathbf{0} \\ \frac{d}{dt}(\mathbf{M}\mathbf{P}(t)) &= -\mathbf{W}(t) - \mathbf{f}_v^T\mathbf{P}(t) - \mathbf{C}_q^T\boldsymbol{\mathcal{S}}(t) & \mathbf{C}_q\mathbf{W}(t) &= \mathbf{0}, \end{aligned} \quad (5)$$

where we have introduced some more set of adjoint variables  $\mathbf{P}(t), \mathbf{W}(t) \in \mathbb{R}^{n \times r}$  and  $\boldsymbol{\mathcal{M}}(t), \boldsymbol{\mathcal{S}}(t) \in \mathbb{R}^{l \times r}$ . The final values can be computed from:

$$\left( \boldsymbol{\phi}_q^T - \mathbf{W} \right) \Big|_{t_f} = \mathbf{0} \quad \text{and} \quad \left( \boldsymbol{\phi}_v^T - \mathbf{M}\mathbf{P} \right) \Big|_{t_f} = \mathbf{0}. \quad (6)$$

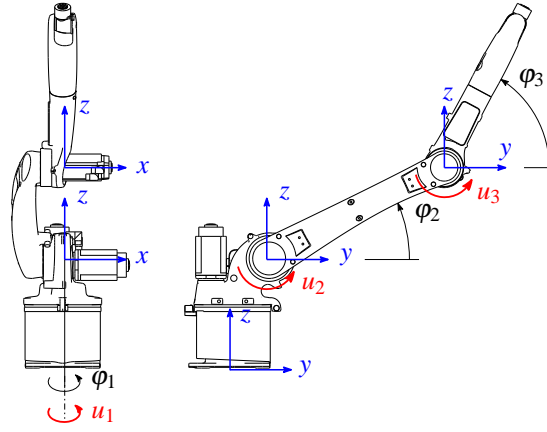


Figure 1: Sample figure representing a guided motion

The updates of the final time  $t_f$  and of the control history  $\mathbf{u}(t)$  are then given by

$$\delta t_f = -\kappa \alpha \left( 1 + \Pi(\mathbf{q}(t_f), \mathbf{v}(t_f), \mathbf{u}(t_f)) + \boldsymbol{\xi}^T \boldsymbol{\phi}(\mathbf{q}(t_f), \mathbf{v}(t_f), t_f) \right), \quad \text{and} \quad \delta \mathbf{u}(t) = -\kappa \left( \Pi_{\mathbf{u}}^T + \mathbf{f}_{\mathbf{u}}^T \mathbf{p}(t) + \mathbf{f}_{\mathbf{u}}^T \mathbf{P}(t) \boldsymbol{\xi} \right). \quad (7)$$

Herein, the parameter  $\alpha$  serves for scaling and the number  $\kappa$  denotes the step size of the updates.  $\boldsymbol{\xi} \in \mathbb{R}^r$  is a vector of multipliers in order to combine both adjoint systems in Eq. (4) and Eq. (6) and to reduce the cost functional in Eq. (2) and the error in Eq. (3) within each iteration simultaneously.

As an example, we consider a robot, shown in Fig. 1, consisting of three robot arms and a particle mass at the end of the kinematic chain. We describe the system by 14 redundant generalized coordinates. We are interested to control the torques  $u_1$ ,  $u_2$  and  $u_3$  in the joints that minimize the end time. The results are summarized in Fig. 2.

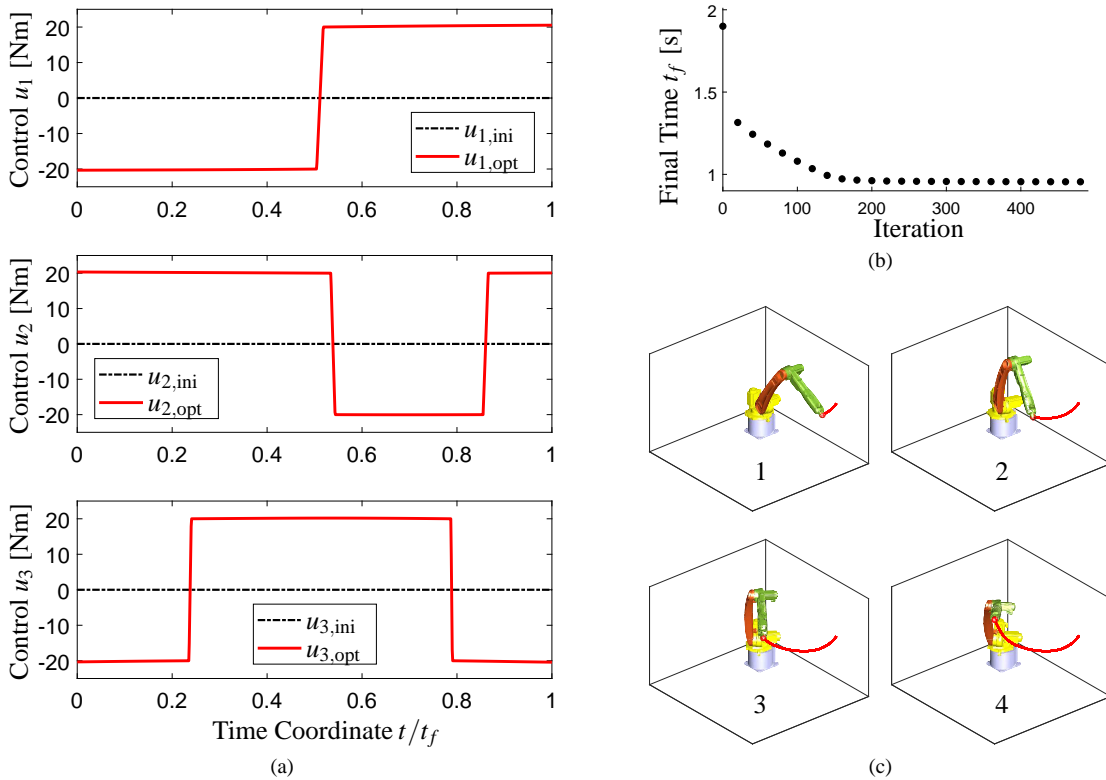


Figure 2: Results: (a) Initial and Optimal Control (b) Convergence (c) Trajectory

## References

- [1] P. Eichmeir, K. Nachbagauer, K. Sherif, T. Lauß, W. Steiner. Time-Optimal Control of Dynamic Systems Regarding Final Constraints. Journal of Computational and Nonlinear Dynamics, 2021.



**Section**  
**MULTIBODY KINEMATICS**

KIN

# A Set of Generalized Coordinates and Their Influence on System Dynamics

Altay Zhakatayev<sup>1</sup>, Yuriy Rogovchenko<sup>2</sup>, Matthias Pätzold<sup>3</sup>

<sup>1</sup> Dept. of Mathematics  
University of Agder  
Kristiansand, 4604, Norway  
altay.zhakatayev@uia.no

<sup>2</sup> Dept. of Mathematics  
University of Agder  
Kristiansand, 4604, Norway  
yuriy.rogovchenko@uia.no

<sup>3</sup>Dept. of ICT  
University of Agder  
Grimstad, 4604, Norway  
matthias.paetzold@uia.no

## EXTENDED ABSTRACT

### 1 Introduction

The Lagrangian and Hamiltonian mechanics utilize *generalized coordinates* (GCs), which can be any set of variables suitable to fully describe the configuration of a mechanical system. A set of GCs is not unique: there are infinitely many sets of GCs, which are equally valid for describing the system's dynamics from the theoretical point of view. However, from a numerical or computational point of view, there can be differences. For simple systems with a few degrees-of-freedom (DOF), it is expected that there will be no discernible differences in the choice of a set of GCs. For such systems, the computational efficiency is also not an issue. However, for complex multi-body systems with a large number of DOF, the efficiency and computational time required to perform the analysis can vary greatly depending on the selected set of GCs.

Efficient formulation of dynamic equations was recently discussed in [1, 2]. However these papers did not address the effect of different sets of GCs on the solution of dynamic equations. In addition, there is a gap in the literature dedicated to finding optimal sets of GCs that lead to the numerical solution of differential equations with minimal error within the shortest simulation time. To the best of the authors' knowledge, there are no general qualitative rules for selecting the optimal set of GCs. It is possible that there is a procedure, yet to be discovered, which helps to identify the optimal set of GCs for each system. As a result, there is a need in modern engineering for deeper investigations of the apparent freedom of choice of GCs for system description. In this work, our main motivation is to investigate the influence of a choice of GCs on the numerical solution of dynamic equations. The main objective and novelty of this paper is to find a pattern for the dependence of simulation error and time on the selected set of GCs. Another objective is to find the optimal set of GCs for a single-link spherical pendulum (considered as a test system).

### 2 Kinematics of the Spherical Pendulum

As our test system, we consider a single-link spherical pendulum which is symmetrical with respect to the rotation about its axis, Fig. 1a. We specifically chose the spherical pendulum because its motion is three-dimensional. Due to rotational symmetry around its own symmetry axis, only two angles are required to fully specify the configuration (orientation) of the pendulum in our model. The Euler angles were generalized to rotations with respect to non-orthogonal axes in [3]. The generalized Euler angles are also called Davenport angles [4]. In this work, two Davenport angles will be denoted as  $q_1$  and  $q_2$  and will be used as GCs. In the following, we will consider two cases for the set of GCs. In the first case (Case I), we assume that the axis of the first GC  $q_1$  is aligned along the global axis  $X$ , while the axis of the second GC has an arbitrary initial direction with respect to the global axes, Fig. 1b. In the second case (Case II), it is assumed that the axis of the first GC  $q_1$  has an arbitrary initial direction with respect to the global axes, while the second GC  $q_2$  has its initial direction aligned with respect to the global axis  $Y$ , as shown in Fig. 1c. In both cases, intrinsic rotations are assumed, so that the axis of  $q_2$  is influenced by the rotation  $q_1$ . Also, in both cases, kinematics depends on two angular parameters:  $\eta$  and  $\varepsilon$ , Fig. 1. Different sets of GCs, with the corresponding differential equations of motion, are obtained by varying these two parameters.

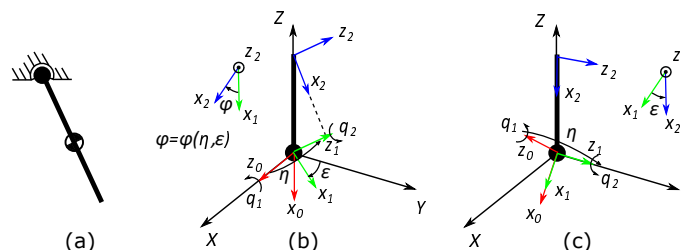


Figure 1: Schematic diagrams of the spherical pendulum (a), its kinematics with coordinate frames, angular parameters, and GCs for the Case I (b) and Case II (c).  $\varphi$  is the angular parameter which depends on  $\eta$  and  $\varepsilon$ .

### 3 Simulations

Simulations were performed to investigate the influence of a set of GCs on the dynamic behavior. By using the Lagrangian formalism and the Symbolic Math Toolbox™ of MATLAB, a system of two coupled second-order differential equations was automatically generated for the link motion in terms of the GCs  $q_1$  and  $q_2$ . These equations contain the parameters  $\eta$  and  $\varepsilon$ . By specifying the number of intervals  $N \in \mathbb{N}$  and the angular step size  $\Delta = \pi/N$ , the range of variation for  $\eta$  is chosen as  $\eta = i\Delta$ ,  $i = 1, 2, \dots, N-1 \in \mathbb{N}$ . Similarly, the range for  $\varepsilon$  is  $\varepsilon = i\Delta$ ,  $i = -N, -N+1, \dots, N-1 \in \mathbb{Z}$ . The number of steps used to vary the

parameters was chosen to be  $N = 20$ . The analytical solution of a mass-point spherical pendulum oscillation, expressed in the spherical coordinate frame, was also obtained as a baseline case. For each set of GCs, the root-mean-square error (RMSE)  $Er$  with respect to a baseline case was computed. Simulation time  $\tau$  was also recorded. Two different initial conditions (ICs) were considered. The first IC (denoted by IC1) corresponds to the situation where the initial values of GCs are nonzero, i.e.,  $q_1 \neq 0$ ,  $q_2 \neq 0$ , while the initial values of the generalized velocities (GVs) are zero, i.e.,  $\dot{q}_1 = \dot{q}_2 = 0$ . The second IC (denoted by IC2), assumes that the initial values of the GCs are zero  $q_1 = q_2 = 0$ , while the initial values of the GVs are nonzero.

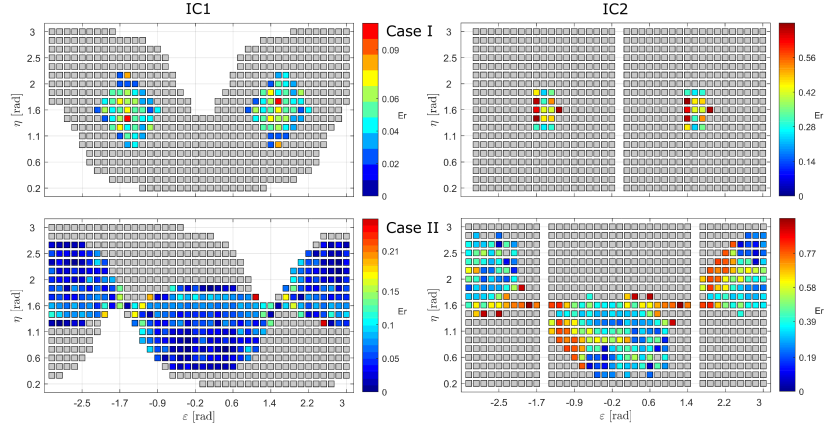


Figure 2: The RMSE  $Er$  for the Cases I-II with two different ICs. Note that the scaling of color bars is different.

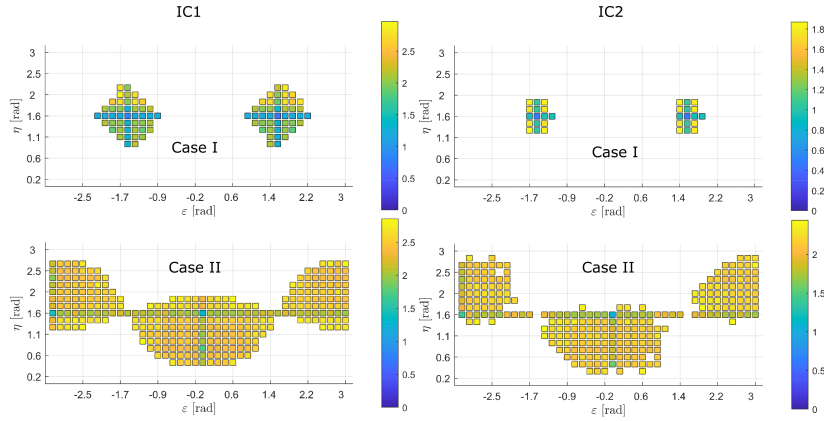


Figure 3: Simulation time ( $\log_{10}(\tau/\tau_r)$ ) for the Cases I-II with two different ICs. Note that the scaling of color bars is different.

#### 4 Results and Conclusions

The RMSE  $Er$  of the simulations for the Cases I-II and the two different ICs are shown in Fig. 2. Each sub-figure displays  $Er$  as a function of the parameters  $\eta$  and  $\varepsilon$ . An orthogonal set of GCs do not necessarily result in the smallest  $Er$ . This might be explained by the different degrees of coupling and interplay of simulation errors in the dynamic equations of motion. The results for the simulation times  $\tau$  are shown in Fig. 3, where  $\tau_r$  is the simulation time of the baseline case. Here we can clearly see that the orthogonal set of GCs ( $\eta = \pi/2$  and  $\varepsilon = \pm\pi/2$  for Case I,  $\eta = \pi/2$  and  $\varepsilon = 0$  (or  $\varepsilon = \pi$ ) for Case II) leads to a faster simulation. These observations are valid for two cases and for both ICs.

Different sets of GCs (generalized Euler angles) have been considered from the accuracy point of view and the computation time. It has been shown that a set of orthogonal GCs (Davenport angles) allows a fast integration of the equations of motion. However, the choice of orthogonal Davenport angles do not necessarily result in the minimum gross simulation error. In summary, a set of GCs affects the system scope, simulation error and simulation time. The optimal set of GCs that minimizes the RMSE does not simultaneously minimize the simulation time and vice versa.

#### Acknowledgments

This work has been carried out within the scope of the CareWell project funded by the Research Council of Norway (300638/O70).

#### References

- [1] González, F., Dopico, D., Pastorino, R., Cuadrado, J.: Behaviour of augmented Lagrangian and Hamiltonian methods for multibody dynamics in the proximity of singular configurations. *Nonlinear Dynamics* **85**(3), 1491–1508 (2016)
- [2] Yang, L., Yao, W., Li, Z.: UK method for solving multi-body system dynamics with singular problems. *Advances in Mechanical Engineering* **10**(4), 1–13 (2018)
- [3] Davenport, P.B.: Rotations about nonorthogonal axes. *AIAA Journal* **11**(6), 853–857 (1973)
- [4] Shuster, M.D., Markley, F.L.: Generalization of the Euler angles. *J. Astronaut. Sci.* **51**(2), 123–132 (2003)

# Effects for Reduction of Computational Effort in Multibody Dynamic Models – A Case Study

Chiyu Sun<sup>1,2</sup>, Huiping Shen<sup>2</sup>, Andr s Kecskem thy<sup>1</sup>

<sup>1</sup> Chair of Mechanics and Robotics  
University of Duisburg-Essen  
Lotharstr. 1, 47057 Duisburg, Germany  
chiyu.sun@uni-due.de  
andres.kecskemethy@uni-due.de

<sup>2</sup> Faculty of Mechanical Engineering  
Nanjing University of Science and Technology  
Xiaolingwei Street 200, 210094 Nanjing, China  
shp65@126.com

## EXTENDED ABSTRACT

### 1 Introduction

Nowadays, multibody codes are ubiquitous and can solve very general problems. A common way to reduce computational effort is to reduce symbolic terms [1]. However, due to their generic formulation, often they do not consider special properties of the system or of its target accuracy requirements, thus leading to many unneeded terms which unnecessarily slow-down computational efficiency. When developing fast codes, e.g., for microprocessor controls, users hence often develop task-specific formulations, seeking to remove terms which are deemed not to be relevant, but without a systematic procedure for their identification. While symbolical code generation can catch a large number of unnecessary computations, there are some additional effects which lead to substantial effort reduction which are not "seen" by symbolical code processors. These effects are (1) single bodies or subsystems move in sub-groups of SE(3), (2) inertia tensors feature special properties such as symmetry or negligible moments of inertia, and (3) some terms do not contribute substantially to precision as their respective mass effects are negligible compared to neighbor terms. This paper analyses the effects of such simplifications for a sample mechanism – the 3R1T parallel structure – featuring all characteristics listed above. The investigation shows that all three types of effects lead to reduction of computational effort, with diminishing impact. While the analysis is based only on a single case study, it can be assumed to be generally applicable and thus to shed some light onto where efficiency increases can be achieved. A fully automated procedure would have to be able to identify all these three effects and is not developed here.

### 2 Case Study: The 3T1R parallel platform

The topology and mass properties of the regarded case-study 3T1R mechanism are shown in Figure 1. The system is a 4 degree-of-freedom "lower-mobility" mechanism with 4 branches and four driving pair at the base as revolute joints.

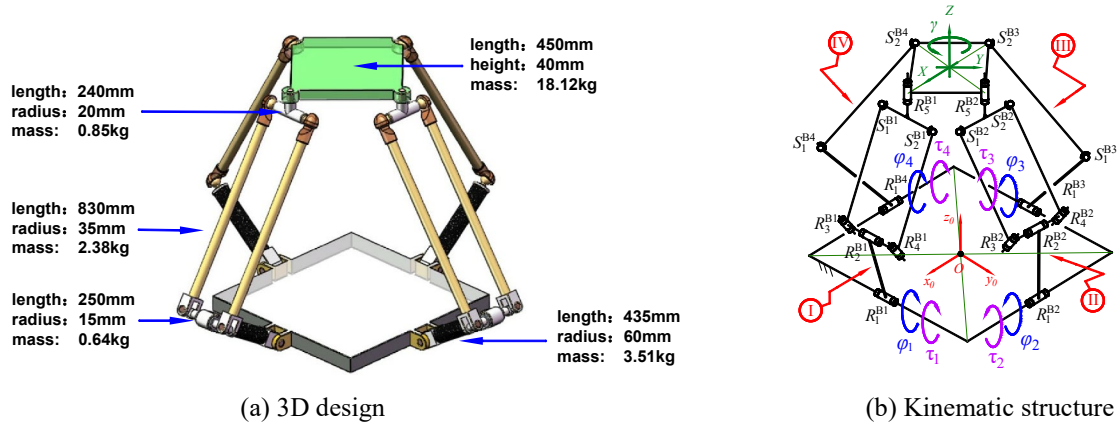


Figure 1: Kinematic structure and mass properties of the multibody system for the case study (3T1R mechanism)

### 3 Stages for reduction of computational effort

Due to its special design, the moving platform moves as 3D translation ( $X, Y, Z$ ) and a rotation ( $\gamma$ ) about the global  $Z$  axis and distal transversal links of the parallelogram undergo only pure 3D translation. The equations of motion [2] for the platform are:

$$\text{Inverse dynamics: } \underline{\tau} = \mathbf{B}^{-1} \left[ \mathbf{M} \ddot{\underline{q}} + \underline{b}(\underline{q}, \dot{\underline{q}}) - \underline{Q}^{(e)} \right]; \quad \underline{\tau} \in \mathbb{R}^4, \quad \mathbf{B} \in \mathbb{R}^{4 \times 4}, \quad \mathbf{M} \in \mathbb{R}^{4 \times 4}, \quad \underline{b} \in \mathbb{R}^4, \quad \underline{Q}^{(e)} \in \mathbb{R}^4. \quad (1)$$

$$\text{Direct dynamics: } \mathbf{M} \ddot{\underline{q}} + \underline{b}(\underline{q}, \dot{\underline{q}}) = \underline{Q}(\underline{q}, \dot{\underline{q}}); \quad \underline{Q} \in \mathbb{R}^4, \quad \underline{q} = [X, Y, Z, \gamma]^T \in \mathbb{R}^4. \quad (2)$$

Where  $\underline{q}$ ,  $\mathbf{M}$ ,  $\underline{b}$ ,  $\underline{Q}$ ,  $\underline{Q}^{(e)}$  are the generalized coordinates, mass matrix, centrifugal and Coriolis forces, applied forces, and applied forces without actuator torques  $\underline{\tau}$ , respectively, and  $\mathbf{B}$  is the Jacobian mapping actuator rates to generalized velocities.

Reduction of computational effort involves three stages:

Stage 1: Recognizing bodies moving within sub-groups of SE(3) and cancelling corresponding not-needed terms.

Stage 2: Recognizing special inertial effects (symmetry, negligible moments of inertia).

Stage 3: Recognizing terms which are negligible due to small-mass or small-motion effects; this can only be done for sample motions that are assumed to be representative.

The special sub-motion properties in this case are: (a) special motion 3T1R of the platform, (b) pure translation of distal transversal links of the parallelograms, and (c) pure rotation of the driving cranks. The special inertial effects are the slim nature and approximate symmetry of the coupler bars of the parallelogram with respect to rotations about axes normal to the bars.

For the third stage, an empirical algorithm to neglect terms was developed consisting of the following steps: (1) sample the simulation at  $n$  time points (here  $n=100000$ ); (2) at each time point, sort terms according to the size of their numerical value; (3) cut-off terms whose contribution is below the target accuracy, counting the number of time points where each term is neglected; (4) sort neglected terms over all  $n$  time points according to the number of neglections at time points; (5) start globally removing neglected terms in the order from highest to lowest number of time-point neglections and check for each such overall neglection the accuracy of the whole simulation. Continue until overall accuracy is trespassed. This computation takes several hours, but is only a preprocessing done once for a given mechanism, while the resulting equations then run at optimal CPU time while maintaining the target accuracy.

The method can be also applied to redundant coordinates if the subspace motion properties are known. Due to lack of space, only the main ideas can be described; the co derivations are being prepared for a paper form.

## 4 Results

Table (c) in Figure 2 shows the achievable reduction of computational effort and incurred error with respect to an ADAMS simulation for a sample motion as represented in Figure 2 (a) and (b) (input and output, respectively). Error is measured as the maximal absolute difference between the actuator torque  $\tau_1$  computed in the reduced model and computed in ADAMS throughout the whole simulation. Stage 0 is the reference including all terms in a full 3D model without expression reductions (such as in a general multibody code). One can see that sub-group motion reduction (Stage 1) contributes to approx. 30% of total reduction (without generating errors), while special inertia effects (Stage 2) contribute to another 11% (with only a slight error of 0.42%). Allowing for errors in the final computations renders in this case reductions of computational efforts of another 1%-7%.

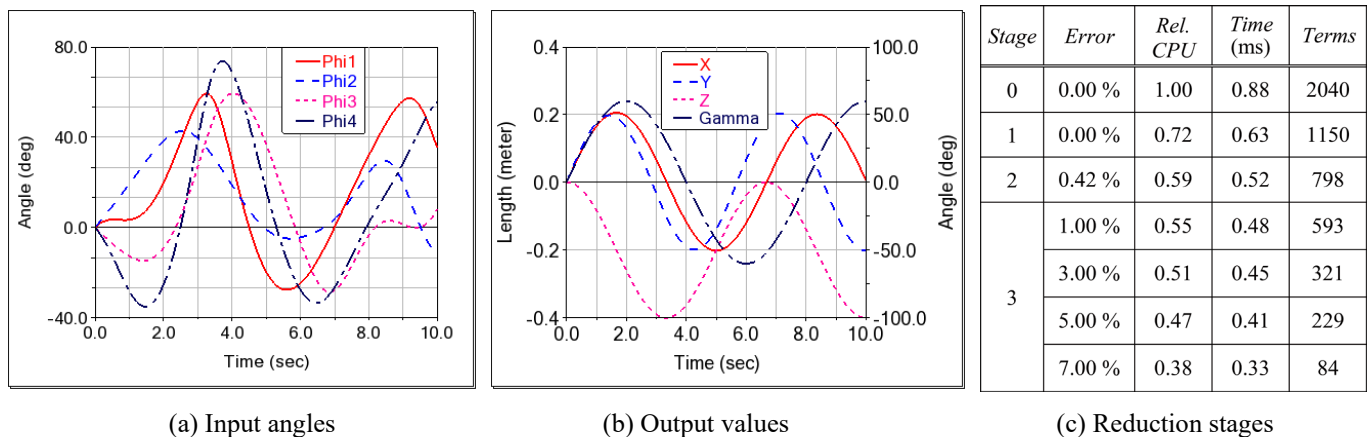


Figure 2: Simulation and reduction information of 3T1R mechanism

## 5 Conclusion, Outlook, Acknowledgements

While the present analysis was performed only for a single case-study, it is believed that the sources of effort reduction may be comparable for other mechanisms with similar simplification effects. An important component for the automatic simplification is the automatic detection of SE(3) sub-group motion for individual bodies or substructures embedded in a general spatial mechanism, as well as the generation of representative trajectories of a sample application. This is planned for future research. This work was partially funded by Zentrales Innovationsprogramm Mittelstand (ZIM) under project number ZF4047825RP9.

## References

- [1] X. Ge, W. Zhao. Symbolic Linearization of Differential/Algebraic Equations Based on Cartesian Coordinates. Technische Mechanik, 25: 230-240, 2005.
- [2] M. Hiller, A. Kecskemethy. Equations of motion of complex multibody systems using kinematical differentials. Transactions of the Canadian Society for Mechanical Engineering, 13: 113-121, 1989.

# Optimal Design Of Multibody Systems Using Independent Adjoint Variables

Paweł Maciąg, Paweł Malczyk, Janusz Frączek

Institute of Aeronautics and Applied Mechanics  
Faculty of Power and Aeronautical Engineering  
Warsaw University of Technology  
Nowowiejska str. 24, 00-665 Warsaw, Poland  
[pmaciag, pmalczyk, jfraczek]@meil.pw.edu.pl

## EXTENDED ABSTRACT

### 1 Background and contribution

In the design and development of many complex multibody systems researchers have to consider trade-off between various system attributes such as sizing, performance, comfort or cost. Computational optimization methods are almost always required for most design tasks and the gradient information of an objective function is heavily exploited in the generation of sensitivities. One of the most accurate and computationally efficient methods of calculating derivatives of performance measure and state variables with respect to design variables are based on the mathematical models of multibody system (MBS) stated as a system of ordinary differential equations (ODEs) or differential-algebraic equations (DAEs). In optimal design of MBS, an implicit dependency exists between state and design variables. One major model-based technique is the adjoint variable method. The approach tends to generate a system of adjoint DAEs, which is usually difficult to solve backward in time [1, 2, 3].

An abundance of well established methods for the efficient solution of equations of motion (EOM) is available in the literature. Some of them, expressed in joint coordinates, give rise to fast sequential or highly-parallelizable algorithms, e.g. [4], [5]. On the other hand, a rather weak link exists between the mentioned efficient formulations and their full exploitation in the adjoint variable method. This paper aims at formulating a method for systematic reduction of the adjoint DAE system corresponding to the constrained Hamilton's EOM to a system of ODEs by introducing a minimal set of adjoint variables. In consequence, a backward adjoint problem might be solved by a standard ODE integration routine, in which the intermediate quantities taken from the joint-based forward dynamics formulation are heavily reused.

### 2 Problem statement

Let us consider a set of constrained Hamilton's canonical EOM, where the algebraic constraints imposed on the MBS have the form  $\Phi(\mathbf{q}) = \mathbf{0}$ , and  $\mathbf{q}$  denotes a vector of generalized coordinates. The time derivative of constraint equations is equal to:  $\dot{\Phi} = \mathbf{C}\mathbf{V} = \mathbf{0}$ , where  $\mathbf{C}$  stands for the constraints Jacobian matrix and  $\mathbf{V}$  refers to the spatial velocity vector. Moreover, absolute velocities for all bodies in a system can be expressed as a stacked vector, which is a product of *allowable motion subspace*  $\mathbf{H}$  and a vector of *joint velocities*  $\boldsymbol{\beta}$ , i.e.:  $\mathbf{V} = \mathbf{H}\boldsymbol{\beta}$  [5]. This is an implicit representation of the constraints  $\dot{\Phi} = \mathbf{0}$ . Since  $\boldsymbol{\beta}$  is a vector of unconstrained variables for open-chain systems, the following relation also holds:  $\mathbf{C}\mathbf{H} = \mathbf{0}$ . The equations of motion in absolute- and joint-based formulation have the following form:

$$\mathbf{M}\mathbf{V} + \mathbf{C}^T \boldsymbol{\sigma} = \mathbf{P}^*, \quad \mathbf{C}\mathbf{V} = \mathbf{0} \quad (1) \quad \hat{\mathbf{p}} = \mathbf{H}^T \mathbf{M}\mathbf{H}\boldsymbol{\beta} = \hat{\mathbf{M}}\boldsymbol{\beta} \quad (3)$$

$$\dot{\mathbf{P}}^* = \mathbf{Q} + \dot{\mathbf{C}}^T \boldsymbol{\sigma}. \quad (2) \quad \dot{\hat{\mathbf{p}}} = \mathbf{H}^T \mathbf{Q} + \dot{\mathbf{H}}^T \mathbf{M}\mathbf{H}\boldsymbol{\beta} \quad (4)$$

The symbols  $\mathbf{M}$  and  $\hat{\mathbf{M}}$  denote a mass matrix, formulated in absolute and joint coordinates, respectively. The quantity  $\boldsymbol{\sigma}$  can be interpreted as a constraint force impulse. This means that the following condition is fulfilled  $\dot{\boldsymbol{\sigma}} = \boldsymbol{\lambda}$ , where  $\boldsymbol{\lambda}$  is a vector of constraint loads at each joint. Moreover,  $\mathbf{P}^*$  and  $\mathbf{Q}$  denote augmented momenta and spatial force vectors, respectively. Subsequently, the quantity  $\hat{\mathbf{p}}$  is the projection of  $\mathbf{P}^*$  onto the subspace  $\mathbf{H}$ , which can be interpreted as a joint-space momentum. A prevalent task arising in the field of optimal design or control of MBS is to minimize the following performance index:

$$J = \int_0^{t_f} h(t, \mathbf{q}, \mathbf{V}, \mathbf{b}) dt + S(\mathbf{q}, \mathbf{V}), \quad (5)$$

where  $\mathbf{b}$  denotes a vector of design parameters or a set of discretized input functions. The second term in eq. (5) is a terminal cost, suitable for prescribing a particular state of the system at the terminal time  $t_f$ .

### 3 Formulation of the adjoint method using independent costates

The first step in deriving the adjoint method is to augment the performance measure by appending eq. (5) with underlying system of equations premultiplied by arbitrary Lagrange multipliers:

$$\bar{J} = \int_0^{t_f} \left[ h + \boldsymbol{\eta}^T (\mathbf{P}^* - \mathbf{M}\mathbf{V} - \mathbf{C}\boldsymbol{\sigma}) + \boldsymbol{\xi}^T (\dot{\mathbf{P}}^* - \mathbf{Q} - \dot{\mathbf{C}}\boldsymbol{\sigma}) - \boldsymbol{\mu}^T \dot{\Phi} \right] dt + S. \quad (6)$$



The multipliers  $\boldsymbol{\eta}, \boldsymbol{\xi}, \boldsymbol{\mu}$  are often referred to as *adjoint* or *costate* variables. By taking a total variation of the extended performance measure (6) and requesting necessary conditions for the extremum of a functional yields an adjoint system of DAEs [1]:

$$\dot{\boldsymbol{\xi}} = \boldsymbol{\eta}, \quad \mathbf{M}\dot{\boldsymbol{\eta}} + \mathbf{C}^T \dot{\boldsymbol{\mu}} = \mathbf{R}_A, \quad \mathbf{C}\dot{\boldsymbol{\eta}} = -2\dot{\mathbf{C}}\boldsymbol{\eta} - \dot{\mathbf{C}}\boldsymbol{\xi} \quad (7)$$

supplied with boundary conditions for  $\boldsymbol{\xi}^{(0)}, \boldsymbol{\eta}^{(0)}, \boldsymbol{\mu}^{(0)}$ . A closer look at eqs. (1) and (7) reveals numerous analogies, which we aim at exploiting. First, let us establish spatial relations between absolute–coordinate adjoint variables. In the paper, we argue that the following relations hold:  $\boldsymbol{\xi} = \mathbf{H}\mathbf{c}$  and  $\boldsymbol{\eta} = \mathbf{H}\mathbf{e} + \dot{\mathbf{H}}\mathbf{c}$ , where  $\mathbf{c}$  and  $\mathbf{e}$  denote vectors of *independent costate* variables. The derivative of the latter relation yields a crucial transformation, which can be interpreted as an implicit representation of the constraints imposed on the system (7). It can be exploited to project a system of DAE (7) onto the subspace  $\mathbf{H}$  yielding the costate (adjoint) system in independent coordinates:

$$\dot{\mathbf{c}} = \mathbf{e}, \quad (\mathbf{H}^T \mathbf{M} \mathbf{H}) \dot{\mathbf{e}} = \mathbf{H}^T (\mathbf{R}_A - 2\mathbf{M}\dot{\mathbf{H}}\mathbf{e} - \mathbf{M}\dot{\mathbf{H}}\mathbf{c}) \Rightarrow \hat{\mathbf{M}}\dot{\mathbf{e}} = \mathbf{R}_A^*. \quad (8)$$

Equation (8) may be solved backwards in time for the unknown variables  $\mathbf{c}$  and  $\mathbf{e}$ . The integration is initialized with the values evaluated from their absolute–coordinate counterparts  $\boldsymbol{\xi}^{(0)}, \boldsymbol{\eta}^{(0)}$ . Once the costate variables are computed, the variables can be utilized to efficiently and reliably compute the gradient of the performance measure (5).

#### 4 Preliminary results and conclusions

This paper extends the scope of our previous work [1] by deriving spatial relations between adjoint variables linked with Hamilton’s canonical EOM. Consequently, by reframing explicit constraints imposed on the adjoint system into their implicit counterparts, we introduced the so-called joint–space costate variables. As a result, the DAE describing the adjoint system was transformed into an unconstrained first–order system of differential equations. ODEs are usually much simpler and more convenient to handle, while integrating joint variables and do not raise constraint violations. We present preliminary results for a simple test case where a pendulum moves in a gravitational field with two torsional springs attached to its fixture (c.f. fig. 1). The goal is to find a static equilibrium conditions by selecting suitable neutral lengths of the springs. This can be stated as an optimal design problem, and fig. 2 displays the values of the adjoint variables at the initial step of the procedure. The independent costate variables remain consistent with their absolute–coordinate counterparts derived in ref. [1].

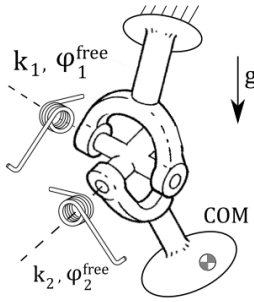


Figure 1: The layout of the pendulum with torsional springs attached to a Hooke joint.

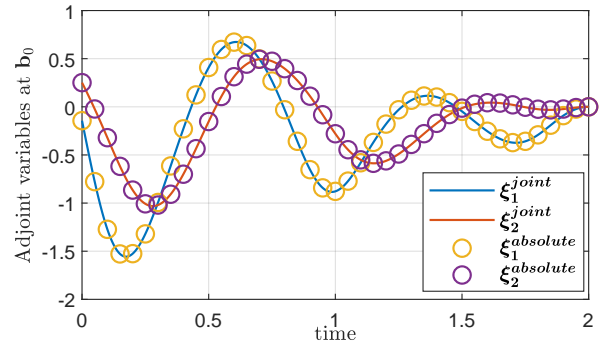


Figure 2: The adjoint variables recreated from the joint costate variables (solid lines) compared with their absolute–coordinate counterparts [1] (dots).

**Acknowledgments.** This work has been supported by National Science Center under grant No. 2018/29/B/ST/8/00374.

#### References

- [1] P. Maciąg, P. Malczyk, and J. Frączek. “Hamiltonian direct differentiation and adjoint approaches for multibody system sensitivity analysis”. In: *International Journal for Numerical Methods in Engineering* 121.22 (Aug. 2020), pp. 5082–5100. DOI: 10.1002/nme.6512.
- [2] D. Dopico, A. Sandu, and C. Sandu. “Adjoint sensitivity index-3 augmented Lagrangian formulation with projections”. In: *Mechanics Based Design of Structures and Machines* (2021), pp. 1–31. DOI: 10.1080/15397734.2021.1890614.
- [3] K. Nachbagauer, S. Oberpeilsteiner, K. Sherif, and W. Steiner. “The Use of the Adjoint Method for Solving Typical Optimization Problems in Multibody Dynamics”. In: *Journal of Computational and Nonlinear Dynamics* 10.6 (2015). DOI: 10.1115/1.4028417.
- [4] R. Featherstone. *Rigid Body Dynamics Algorithms*. Springer US, 2008. DOI: 10.1007/978-1-4899-7560-7.
- [5] K. Chadaj, P. Malczyk, and J. Frączek. “A parallel Hamiltonian formulation for forward dynamics of closed-loop multibody systems”. In: *Multibody System Dynamics* 39.1 (2017), pp. 51–77. DOI: 10.1007/s11044-016-9531-x.



# Quaternion Spline Interpolation for Suspension Kinematics and Dynamics

Václav Houdek<sup>1,2</sup>, Michal Hajžman<sup>1</sup>, Olivier Verlinden<sup>2</sup>

<sup>1</sup> Faculty of Applied Sciences  
University of West Bohemia  
Technická 8, 301 00 Pilsen  
Czech Republic

{vaclavh,mhajzman}@kme.zcu.cz

<sup>2</sup> Faculty of Engineering  
University of Mons  
Place du Parc 20, 7000 Mons  
Belgium

olivier.verlinden@umons.ac.be

## EXTENDED ABSTRACT

### 1 Introduction

Problems of kinematics are, in many cases, characterized by a set of nonlinear algebraic equations that have to be constructed and solved at each time step. The procedure can be computationally time consuming so that it is interesting to develop suitable methods to improve the simulation efficiency. Moreover, parametrization of finite rotations is an essential issue in multibody kinematics and dynamics. Among the available options, the concept of quaternions shows some interesting properties to describe body rotations, especially when dealing with interpolation.

The main idea is to solve in a preliminary step the kinematics of specific subsystems, i.e. to pre-compute the position and the orientation of important bodies of the subsystem, in terms of a set of independent parameters whose number corresponds to the number of degrees of freedom of the subsystem. The pre-computation leads to a look-up table from which the situation of each body, i.e. its X, Y, Z coordinates and the quaternions describing its orientation, can be computed by interpolation. The size of the table and the distribution of the pre-computed points are also addressed in this study: with an optimal distribution, the required accuracy can be obtained with a minimal size of the table, and consequently with lower memory requirements. The main motivation of the work is the efficient representation of suspension kinematics (see Figure 1) for the purpose of vehicle dynamics problems. It is particularly relevant for suspensions, whose up and down motion can be interpolated from only one parameter. For example, authors of [1] use two dimensional analytical functions to express suspension kinematics and then solve problems of vehicle dynamics.

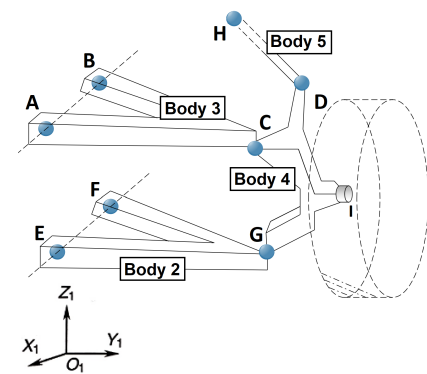


Figure 1: Scheme of a double wishbone suspension

### 2 Spline, B-spline and quaternion spline interpolation

Generally, *spline interpolation* is a form of interpolation where the interpolant is a special type of piecewise low degree polynomial called a spline. Spline interpolation provides lower interpolation error [3] and also avoids the problem of Runge's phenomenon, in which oscillation can occur when interpolating using high degree polynomials. B-spline as another spline function is a piecewise polynomial function. However, B-spline function is defined as a linear combination of control points  $p_i$  and basis functions, which is also the origin of its name – **B**-spline. The function has several useful properties such as local support property; changing  $p_i$  affect the curve in the parameter range  $x_i < x < x_{i+n}$  [4].

The base functions  $B_i^k(t)$ 's are defined by the following recurrence relation [5]:

$$B_i^k(t) = \frac{t - t_i}{t_{i+k-1} - t_i} B_i^{k-1}(t) + \frac{t_{i+k} - t}{t_{i+k} - t_{i+1}} B_{i+1}^{k-1}(t), \quad \text{where} \quad B_i^1(t) = \begin{cases} 1 & t_i \leq t \leq t_{i+1} \\ 0 & \text{otherwise.} \end{cases} \quad (1)$$

The B-spline quaternion curve with a cumulative basis form is formulated as [5]

$$\hat{Q}(t) = \hat{q}_0^{\tilde{B}_0^k(t)} \prod_{i=0}^{n+1} (\hat{q}_{i-1}^{-1} \hat{q}_i)^{\tilde{B}_i^k(t)}, \quad \text{where} \quad \tilde{B}_i^k(t) = \sum_{j=i}^{n+1} B_j^k(t). \quad (2)$$

where the control points  $\hat{q}_i$  are precomputed so as to reproduce a given sequence of data quaternions  $\hat{Q}_i$  ( $i = 0, 1, \dots, n$ ). We assume  $k = 4$ , so  $C^2$  continuity is achieved [5].

### 3 Obtained results and their discussion

Every rotation in a three-dimensional Euclidean space can be parametrized by two quantities: a unit vector  $\mathbf{e}$  indicating the direction of an axis of rotation, and the angle  $\theta$  describing the magnitude of the rotation about the axis. Assuming 3 body

configurations  $i$ ,  $i+1$  and  $i+2$ , we get 2 relative angles ( $\theta_{i,i+1}$  and  $\theta_{i+1,i+2}$ ), 2 rotation axes ( $\mathbf{e}_{i-1,i}$  and  $\mathbf{e}_{i,i+1}$ ), and 1 so-called axis difference  $\phi_i$  defined as the angle between  $\mathbf{e}_{i-1,i}$  and  $\mathbf{e}_{i,i+1}$ . Both,  $\theta$  and  $\phi$  measure the variation between successive body configurations and play an important role in the precision of the interpolation.

The interpolation methodology was studied on a double wishbone car suspension (Figure 1) whose kinematic solution was obtained from a solver based on the Cartesian coordinates approach. The precision of the interpolation was measured by angle error  $\theta_{ex,in}$ , which is defined as an angle between exact and interpolated orientation.

Different input data for the interpolation were generated and it turned out that the precision is not determined only by the values of  $\theta$  and/or  $\phi$ , but also by their smoothness. To demonstrate this phenomena the look-up table data generation was performed and a threshold was imposed in the same time for  $\theta$  and  $\phi$ . The kinematics had to be recomputed to fulfil desired  $\theta_{0.2}$  and  $\theta_{0.01}$ , which are angle distances obtained by converting  $\theta$  to a smoothing spline with a tuning (or smoothing) parameter 0.2 and 0.01 [6]. Figure 2 shows  $\theta$ ,  $\theta_{0.2}$  and  $\theta_{0.01}$ , and Figure 3 shows the achieved angle errors of the interpolation while using look-up tables corresponding to  $\theta$ ,  $\theta_{0.2}$  and  $\theta_{0.01}$ , respectively.

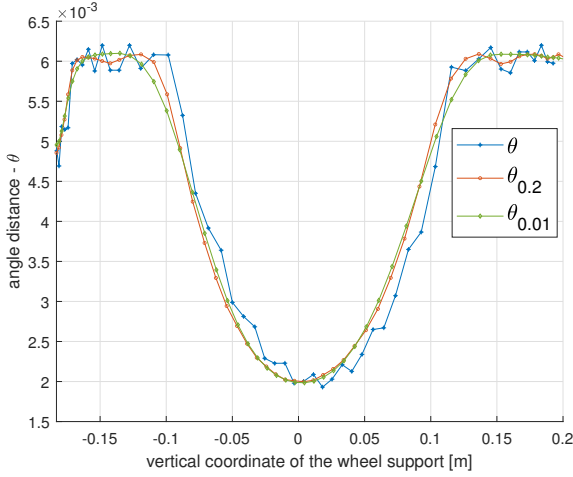


Figure 2: Angle distance  $\theta$

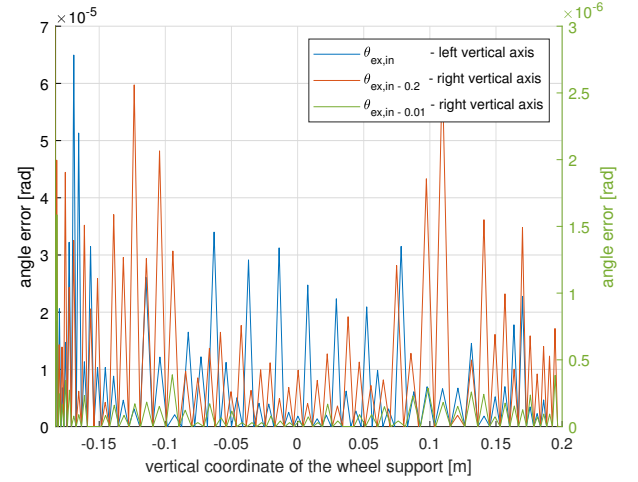


Figure 3: Angle error

## 4 Conclusion

This paper deals with the usage of quaternion interpolation in the multibody kinematics, which allows to reduce the computational costs for more complex dynamic analyses. The parametric study showed the importance of the continuity of input data. The smoother the input data are the lower the angle error is achieved. However, look-up table size remains the same. This proves the importance of the right choice of input data. Presented methodology is further implemented in EasyDyn for a testing simple vehicle (Figure 4). It is further planned to use the introduced approach for fast dynamical simulations during optimization processes needed in the Formula SAE development.

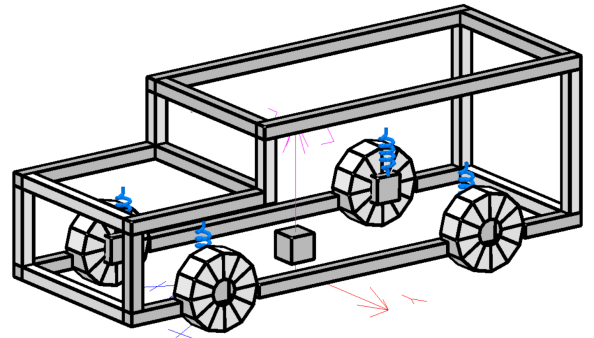


Figure 4: Illustration of vehicle dynamic model in EasyDyn

## References

- [1] G. Rill, A. Arrieta Castro. A Novel Approach for Parametrization of Suspension Kinematics. In M. Klomp et al., editors, Advances in Dynamics of Vehicles on Roads and Tracks, IAVSD 2019, pages 1848–1857. Springer, Cham, 2020.
- [2] T. Mercy, R. Van Parys, G. Pipeleers. Spline-Based Motion Planning for Autonomous Guided Vehicles in a Dynamic Environment. IEEE Transactions on Control Systems Technology, 26: 2182–2189, 2018.
- [3] J. H. Ahlberg, E. N. Nilson, J. L. Walsh. The theory of Splines and Their Applications. Academic Press, New York and London, 1967.
- [4] G. D. Knott. Interpolating Cubic Splines Birkhäuser, Boston, 2000.
- [5] M. J. Kim, M. S. Kim, and S. Y. Shin. A C2-continuous B-spline quaternion curve interpolating a given sequence of solid orientations. Proceedings of Computer Animation, pages 72–81. IEEE, Geneva, 1995.
- [6] T. C. M. Lee. Smoothing parameter selection for smoothing splines: a simulation study. Computational Statistics & Data Analysis, 42: 139 – 148, 2003.

# Design Optimization of Quality Inspection Robots for Particle Accelerator Components

Hannes Gamper<sup>1,2</sup>, Adrien Luthi<sup>1</sup>, Hubert Gattringer<sup>2</sup>, Andreas Mueller<sup>2</sup>, Mario Di Castro<sup>1</sup>

<sup>1</sup> BE-CEM-MRO

CERN - European Organization for Nuclear Research  
Espl. des Particules 1, 1211 Meyrin, Switzerland  
{hannes.gamper, adrien.luthi, mario.di.castro}@cern.ch

<sup>2</sup>Institute of Robotics

Johannes Kepler University, Linz  
Altenbergerstraße 69, 4040 Linz, Austria  
{a.mueller, hubert.gattringer}@jku.at

## EXTENDED ABSTRACT

### 1 Introduction

Power plants and big industrial or science facilities like the European Organization for Nuclear Research (CERN), are often confronted with very specialized automation problems in complex environments for their laboratories, experiments or test rigs. These frequently lead to specific requirements that do not allow the usage of standard industrial robots. Thus, a design problem with almost no restrictions on the actual robot topology, but very hard requirements concerning other parameters like workspace, allowed robot space, and accuracy has to be solved.

This paper presents an approach to this problem by setting up a non-linear optimization algorithm. The optimization departs from a tentative serial robot topology with consecutive rotational joints with parallel rotation axes. The tentative topology should have a higher degree of freedom than the expected optimal solution. Then, the algorithm will optimize the degree of freedom, the position accuracy or error propagation and the joint torques, while reaching the desired end-effector position, avoiding self collisions and collisions with its surrounding. The algorithm will be demonstrated by optimizing the design of a surface inspection robot for Radio Frequency Cavities as used in the Large Hardron Collider (LHC), the Linear Accelerator (LINAC) or the Future Circular Collider (FCC), see figure 1.

### 2 Requirements for a Cavity Inspection Systems

Radio Frequency Cavities are performing the linear acceleration of charged particles in straight sections of accelerator machines and thus make up one of the key elements in a collider complex. The cavities structure and geometry define their specific radio-frequency at which the strong electromagnetic field, created inside the tubes, oscillates to accelerate each particle passing through. The inner surface quality of the cavities is critical to withstand the high energy densities, since every scratch or crack would lead to higher local resistance, thus a rapid increase in temperature during operation and in the end to failure of the system. Therefore, some kind of automated, mechanical structure has to follow the complex cavity geometry and take record of the surface quality after full assembly of the cavities. Finding the optimal topology of such a mechanical structure with respect to certain constraints like collision avoidance for the three different cavity types and minimal error propagation in direction perpendicular to the cavity surface, is a perfect example for the generic problem described in section 1. Previously developed cavity inspection systems, like [1] were extensively tested at CERN, but did not satisfy the specific requirements concerning the level of automation, accuracy, repeatability and how much of the inner cavity surface could be inspected and mapped.

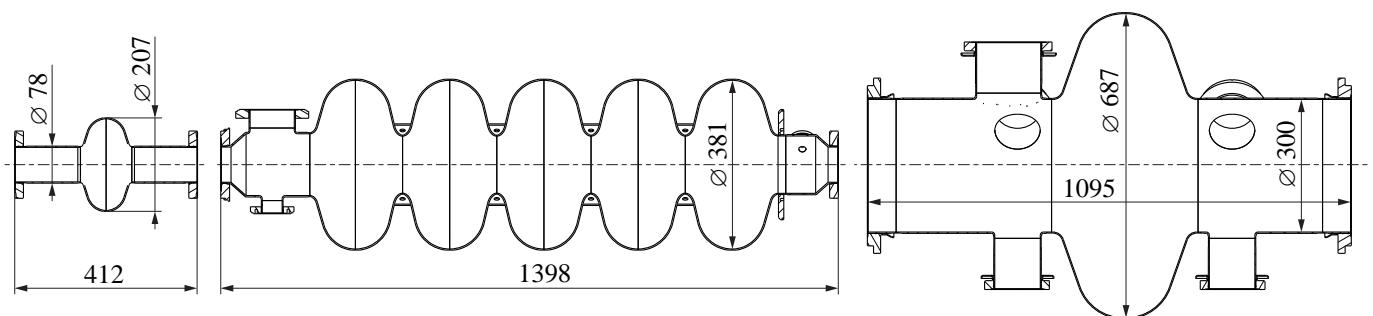


Figure 1: Cavity Types for FCC, LINAC and LHC (left to right, all units in mm)

The main challenge for a robotic system is the complex workspace and especially the difference in diameter of the entrance of the smallest cavity (FCC) and the point with maximum diameter of the biggest cavity (LHC). Furthermore, the system has to detect surface anomalies of only 10 $\mu$ m. A 18MP camera with liquid lens, allowing it to focus between 20 to 25mm, will be used. In order to provide one full image of the inner surface, the pictures will be stitched together after the inspection. Thus, accuracy error of the end-effector position tangential to cavity surface should be not more than 1.2mm to obtain only 10% of overlapping error and not more than 1mm in direction perpendicular to the cavity surface, which would change the contained surface area in the image.

### 3 Design Optimization

The start of the presented design optimization algorithm is a parametrized kinematic and dynamic robot model with a tentative Degree of Freedom (DoF), which is at least equal or higher than the one of the expected optimal solution, in the form

$$\mathbf{z} = \mathbf{f}(\mathbf{q}, \mathbf{p}) \quad \text{and} \quad \mathbf{M}(\mathbf{q}, \mathbf{p})\ddot{\mathbf{q}} + \mathbf{g}(\mathbf{q}, \dot{\mathbf{q}}, \mathbf{p}) = \mathbf{Q}, \quad (1)$$

with the geometric parameters  $\mathbf{p}$ , generalized joint coordinates  $\mathbf{q}$ , the cartesian coordinates  $\mathbf{z}$ , direct kinematics  $\mathbf{f}(\mathbf{q}, \mathbf{p})$ , mass matrix  $\mathbf{M}(\mathbf{q}, \mathbf{p})$ , the nonlinear term  $\mathbf{g}(\mathbf{q}, \dot{\mathbf{q}}, \mathbf{p})$  and the vector  $\mathbf{Q}$  representing the motor torques. While reaching all desired locations  $\mathbf{z}_{des}$  the  $n_R$  serial link robot has to avoid  $c_{RR} = \frac{1}{2} \frac{n_R!}{(n_R-2)!}$  possible self collisions and  $c_{RE} = n_R n_E$  collisions with the environment. The aim of this algorithm is to determine a set of geometric parameters  $\mathbf{p}$ , such that the necessary input torque, the robot link lengths, the degree of freedom  $nDoF$  of the robotic system and the error propagation will be optimized and the impact of these objectives can be tuned independently. This is expressed as linear combination of the multiple objectives

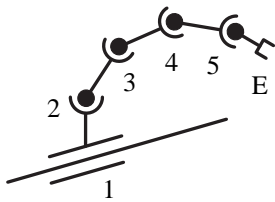
$$J(\mathbf{x}, \mathbf{p}) = \underbrace{\mathbf{Q}^T(\mathbf{x}, \mathbf{p})\mathbf{K}_Q\mathbf{Q}(\mathbf{x}, \mathbf{p})}_{J_1} + \underbrace{\mathbf{k}_p^T \arctan(\mathbf{p})}_{J_2} + \underbrace{\mathbf{k}_w^T \mathbf{w}(\mathbf{x}, \mathbf{p})}_{J_3}, \quad (2)$$

with the diagonal weighting matrix  $\mathbf{K}_Q = \text{diag}(\mathbf{k}_Q)$  and weighting vectors  $\mathbf{k}_p$  and  $\mathbf{k}_w$ .  $\mathbf{w}(\mathbf{x}, \mathbf{p})$  denoting the directional kinematic manipulability  $w_j = \sum_{i=1}^3 |\mathbf{n}_j^T \mathbf{u}_{j,i} \sigma_{j,i}|$ , according to [2], but written in vector form for all  $j = 1 \dots n_p$  positions of interest. Using the unit vector of direction  $\mathbf{n}$  and the major and minor axes of the manipulability ellipses  $\sigma_i \mathbf{u}_i$  from the singular value decomposition of the geometric Jacobian  $\mathbf{J}(\mathbf{q}, \mathbf{p}) = \left[ \left( \frac{\partial \mathbf{v}_E}{\partial \dot{\mathbf{q}}} \right)^T \left( \frac{\partial \boldsymbol{\omega}_E}{\partial \dot{\mathbf{q}}} \right)^T \right]^T$  with the linear and angular velocities  $\mathbf{v}_E$  and  $\boldsymbol{\omega}_E$ , respectively. The term  $J_1$  represents the torque,  $J_2$  represents the length of the robot links and at the same time the degree of freedom of the system, and term  $J_3$  represents the error propagation along the mechanical structure in the direction of interest. Thus the optimization problem can be set up as a non-linear global optimization with non-linear equality and in-equality constraints

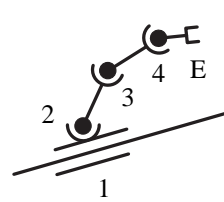
$$\begin{aligned} \min_{\mathbf{q}, \mathbf{p}} \quad & J(\mathbf{Q}, \mathbf{p}) \\ \text{s.t.} \quad & \mathbf{f}(\mathbf{q}, \mathbf{p}) - \mathbf{z}_{des} = \mathbf{0} \\ & -\mathbf{c}(\mathbf{q}, \mathbf{p}) \leq \mathbf{0} \\ & \mathbf{ub}(\mathbf{q}, \mathbf{p}) \leq \mathbf{0} \\ & \mathbf{lb}(\mathbf{q}, \mathbf{p}) \leq \mathbf{0}, \end{aligned} \quad (3)$$

with the distance to the desired cartesian position and orientation  $\mathbf{f}(\mathbf{q}, \mathbf{p}) - \mathbf{z}_{des}$ , vector  $\mathbf{c}(\mathbf{q}, \mathbf{p}) \in \mathbb{R}^{(c_{RR}+c_{RE}) \times 1}$  containing the minimal distances between possible collision objects and vectors  $\mathbf{ub}(\mathbf{q}, \mathbf{p})$ ,  $\mathbf{lb}(\mathbf{q}, \mathbf{p}) \in \mathbb{R}^{nDoF^2 \times 1}$  limiting the link lengths and joint ranges.

Here, the described design optimization algorithm is applied to the cavity inspection system. Since all the rotational joint axes are parallel to the gravity vector, the term  $J_1$  in equation 2 can be neglected. Similar work as been studied in [3], but did not optimize the DoF of the system. In figure 2 and table 1 a tentative initial topology and geometry and the output of the optimization is shown in figure 3 and table 2. The variable  $l_{A,B}$  in tables 1 and 2 describe the distance from joint A to joint B.



length	[mm]
$l_{1,2}$	30
$l_{2,3}$	30
$l_{3,4}$	30
$l_{4,5}$	20
$l_{5,E}$	20



length	[mm]
$l_{2,3}$	0
$l_{3,4}$	221
$l_{4,5}$	51
$l_{5,E}$	50

Figure 2: Initial Topology

Table 1: Initial Geometry

Figure 3: Optimized Topology

Table 2: Optimized Geometry

Thus, the presented method provides a convenient way to find an optimal topology with respect to all above mentioned objectives, as opposed to a manual design choice which would be a very tedious process even with only 5 DoF. A prototype for the Cavity Inspection System is currently under construction at CERN.

### References

- [1] Iwashita Yoshihisa, Tajima Yujiro, Hayano Hitoshi, Development of High Resolution Camera for Observations of Superconducting Cavities, 2008, The American Physical Society.
- [2] Khair Nait-Chabane, Philippe Hoppenot, Etienne Colle, Directional Manipulability For Motion Coordination of an Assistive Mobile Arm, 2007, ICINCO.
- [3] E.J. Van Henten, D.A. Van't Slot, C.W.J. Hol, L.G. Van Willigenburg, Optimal manipulator design for a cucumber harvesting robot, 2009, Computers and Electronics in Agriculture.

# Analytical Port Inversion For A Flexible Beam Model In The Two-Input Two-Output Port Approach

Antonio Fiozzi<sup>1</sup>, Daniel Alazard<sup>1</sup>, Francesco Sanfedino<sup>1</sup>

<sup>1</sup> Institut Supérieur de l'Aéronautique et de l'Espace (ISAE-SUPAERO)  
Université de Toulouse  
31055 Toulouse, FRANCE  
antonio.fiozzi@student.isae-supaero.fr, [daniel.alazard, francesco.sanfedino]@isae-supaero.fr

## EXTENDED ABSTRACT

In the past decades, structural and control co-design has attracted a lot of attention due to its ability of merging multiple multi-disciplinary requirements in a single design flow. Moreover, the increasing use of large structures, appendages and mechanisms for space applications has rendered flexible modal analysis mandatory for the design of proper spacecraft control laws.

In order to tackle the non-trivial modeling and analysis of these large and complex space systems, a sub-structuring technique using a multi-body approach is often considered to conceptually simplify the model. Seeing the overall structure as an assembly of multiple simpler sub-systems with increasing complexity has also the advantage of handling different types of boundary conditions at block assemblage level and easy sub-system validation. The wide use of this approach for space applications has raised a significant interest in the development of proper modeling techniques that can prove to be versatile enough to account for multiple multi-body configurations, ranging from open-loop chains to closed-loops mechanisms.

Many sub-structuring techniques can be found in literature. A common approach is linked to the Finite Element Method (FEM) or the Assumed Modes Method (AMM) [1]. However, these methods are heavily influenced by the set of predetermined boundary conditions assigned to the model, which may drastically vary in time. The Transfer Matrix (TMM) [2] and Finite Element-Transfer Matrix (FE-TMM) Methods link the state vectors of two extremities of the flexible body using a transfer function. These approaches, well suited for serially connected bodies, have inversion problems due to possible non-square systems and are not viable for mechanism design. Methods based on effective mass/inertia of the appendages [3] are viable options for multi-body tree-like structures, but they lose the complete vibrational description, as they only deliver the dynamic relation at the appendage root point using a simplified model of the body.

The Two-Input-Two-Output Port (TITOP) Model, a direct dynamic approach initially proposed in [4] for the in-plane bending of a uniform beam and later extended to the complete three-dimensional behaviour in [5], overcomes these issues. The structure is conceived as a minimal state-space transfer between the accelerations and wrenches at the extremity points of the appendage and embeds both the direct and inverse dynamics: the IN/OUT channels are easily numerically invertible to account for multiple boundary conditions. Moreover, as seen in [5], this approach in a block-diagram model permits the design of closed-chain multi-body systems for any boundary conditions by creating feedback loops and inverting IN/OUT channels.

The TITOP model for a generic flexible appendage  $\mathcal{L}_i$ , schematized in Fig.1 as  $D_{PC}^{\mathcal{L}_i}(s)$ , has as inputs the wrench  $\mathbf{W}_{\mathcal{L}_{i+1}/\mathcal{L}_i, C}$  (forces and torques) exerted by the body  $\mathcal{L}_i$  at point  $C$  and the accelerations  $\ddot{\mathbf{u}}_P$  (linear and angular) imposed by the body  $\mathcal{L}_{i-1}$  at point  $P$ . If the input is an acceleration then the output is a wrench and vice versa. These models, already implemented in a toolbox developed at ISAE-Supaero - the Satellite Dynamics Toolbox (SDT) [6]- represent the basis of this research.

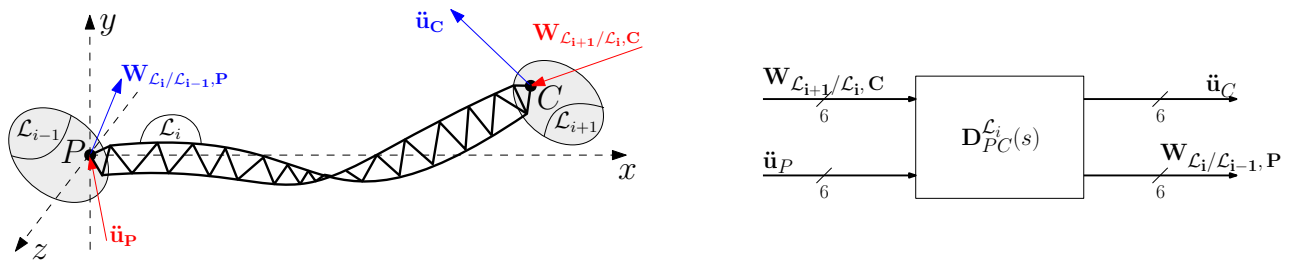


Figure 1: TITOP scheme and nomenclature for a generic flexible appendage  $\mathcal{L}_i$

Nevertheless, the application of the numerically inverted TITOP model seen in [5] showed some critical aspects, specifically in obtaining the *clamped-clamped* boundary conditions (inversion of the first six channels). In particular, this structural model fundamental for the creation of closed-loop kinematics is prone to computational errors. Most notably, it is supposed to have twelve modes at exactly zero frequency but, due to numerical issues, they present a quasi-null finite value instead. This issue, which may seem trivial at single beam level, can have a huge impact in the context of sub-structuring models: it may introduce numerical issues due to block repetitions as well as adding the need of major model reduction at global structure level.

This research therefore proposes a new approach to obtain a TITOP *clamped-clamped* model, introducing a novel analytical procedure to invert the TITOP channels to obtain a model which does not need to be reduced and does not present the previously discussed numerical issues. This was achieved by relying on a modal transformation of the state variables, distinguishing from flexible and junction modes, as introduced in [3] and later on applied by [7].



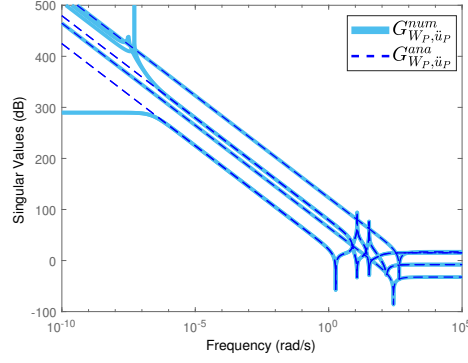


Figure 2: Singular values for the analytically  $\mathbf{G}_{\mathbf{W}_P, \ddot{\mathbf{u}}_P}^{ana}(s)$  and numerically  $\mathbf{G}_{\mathbf{W}_P, \ddot{\mathbf{u}}_P}^{num}(s)$  inverted models

To obtain the desired result, the modal representation found in [7] is used, with  $\boldsymbol{\eta}_k$  as modal coordinates and  $\boldsymbol{\Phi}_{Ck}$  as the flexible eigenvector matrix. A change of variables is applied to the system, introducing vector  $\boldsymbol{\epsilon}_k$ , composed by two sub-arrays:  $\boldsymbol{\epsilon}_{k_1}$  and  $\boldsymbol{\epsilon}_{k_2}$ . The first one, of size  $\{6 \times 1\}$ , corresponds to the 12 poles at zero of the system. The second vector has size  $\{4 \times 1\}$  and determines the internal vibrational response of the system.

$$\boldsymbol{\eta}_k = \mathbf{F}\boldsymbol{\epsilon}_k = \begin{bmatrix} \boldsymbol{\Phi}_{Ck}^+ & null(\boldsymbol{\Phi}_{Ck}) \end{bmatrix} \begin{bmatrix} \boldsymbol{\epsilon}_{k_1} \\ \boldsymbol{\epsilon}_{k_2} \end{bmatrix} \quad (1)$$

The  $(\cdot)^+$  operator denotes the generalized inverse (or pseudo-inverse) of the non-square matrix and  $null(\cdot)$  the null space operator (or kernel). The use of this last operator, when the equation is inverted, allows the creation of a model whose modes corresponding to  $\boldsymbol{\epsilon}_{k_1}$  are set intrinsically to zero, while the modes associated with  $\boldsymbol{\epsilon}_{k_2}$  will not be simplified.

Given a beam of length  $l$ , section  $s$ , density  $\rho$ , Young modulus  $E$ , Poisson's ratio  $\nu$ , second moments of area along y and z axes  $I_y$ ,  $I_z$  and damping coefficient  $\xi$ , the following parameters were used as a case study to obtain the singular value plots seen in Fig.2 :  $l = 20\text{ m}$ ,  $s = 0.0004\text{ m}^2$ ,  $\rho = 2700\text{ kg/m}^3$ ,  $E = 70\text{ GPa}$ ,  $\nu = 0.35$ ,  $I_y = 6.7e-7\text{ m}^4$ ,  $I_z = 6.7e-7\text{ m}^4$ ,  $\xi = 0.001$ .

The  $\mathbf{G}_{\mathbf{W}_P, \ddot{\mathbf{u}}_P}(s)$  transfer between  $\ddot{\mathbf{u}}_P$  and  $\mathbf{W}_{\mathcal{L}_i/\mathcal{L}_{i-1}, P}$  is showed in Fig.2 in form of singular value plots. The analytically inverted TITOP beam model  $\mathbf{G}_{\mathbf{W}_P, \ddot{\mathbf{u}}_P}^{ana}(s)$  is compared to the numerically inverted TITOP model  $\mathbf{G}_{\mathbf{W}_P, \ddot{\mathbf{u}}_P}^{num}(s)$ . The two responses match exactly except for near-to-zero frequency values: in this range the numerical inversion produces artificial behaviours like non-physical zeros and poles. The proposed analytical system overcomes these issues, granting an infinite gain at zero frequency with a correct  $1/s^2$  dynamic at the low frequency range. This is in fact the expected behaviour of the system, where the imposition of non-compatible accelerations at the two extremities of the rigid beam produces infinite efforts.

In conclusion, the introduction of an analytical *clamped-clamped* TITOP beam model has allowed the creation of a new important tool for the structural modeling of large space structures. This will allow for the creation of more complex closed-loop chain structural components without having issues related to numerical inversion or having the need to perform model reduction. In the context of a multi-body modeling approach, the creation of this model will allow for better results throughout all phases of design as it will be widely present and vastly used to create large space multi-body systems.

## References

- [1] R. J. Theodore and A. Ghosal, "Comparison of the assumed modes and finite element models for flexible multilink manipulators," *The International journal of robotics research*, vol. 14, no. 2, pp. 91–111, 1995.
- [2] F. Leckie and E. Pestel, "Transfer-matrix fundamentals," *International Journal of Mechanical Sciences*, vol. 2, no. 3, pp. 137 – 167, 1960. [Online]. Available: <http://www.sciencedirect.com/science/article/pii/0020740360900011>
- [3] A. Girard and N. Roy, *Structural dynamics in industry*. John Wiley & Sons, 2010, vol. 7.
- [4] H. H. S. Murali, D. Alazard, L. Massotti, F. Ankersen, and C. Toglia, "Mechanical-attitude controller co-design of large flexible space structures," in *Advances in Aerospace Guidance, Navigation and Control*. Cham: Springer International Publishing, 2015, pp. 659–678.
- [5] J. Chebbi, V. Dubanchet, J. A. P. Gonzalez, and D. Alazard, "Linear dynamics of flexible multibody systems," *Multibody System Dynamics*, vol. 41, no. 1, pp. 75–100, 2017.
- [6] D. Alazard and C. Cumer, *Satellite Dynamics Toolbox*, 2021. [Online]. Available: <https://personnel.isae-supaero.fr/daniel-alazard/matlab-packages/satellite-dynamics-toolbox.html>
- [7] F. Sanfedino, D. Alazard, V. Pommier-Budinger, A. Falcoz, and F. Boquet, "Finite element based n-port model for preliminary design of multibody systems," *Journal of Sound and Vibration*, vol. 415, pp. 128–146, 2018.

**Section**

**MECHATRONICS, ROBOTICS AND CONTROL**

**MECHATR-1-2-3**



# A Compliant and Redundantly Actuated 2-DOF 3RRR PKM: Less is More

Dustin Berendsen, Aditya Sridhar, Ronald Aarts

Faculty of Engineering Technology, Applied Mechanics & Data Analysis,  
University of Twente, P.O. Box 217, 7500 AE Enschede, The Netherlands  
berendsendustin@gmail.com, adityaganesh1994@gmail.com, r.g.k.m.aarts@utwente.nl

## EXTENDED ABSTRACT

### 1 Introduction

In [1] a compliant and redundantly actuated 2-DOF 3RRR parallel kinematic manipulator (PKM) has been introduced as “best of both worlds” for precision applications. Being a compliant mechanism, or more precisely a flexure-based mechanism, deterministic behaviour can be realised because of the low level of friction, hysteresis and backlash. Being also a redundantly actuated PKM, it combines the advantages of PKM, i.e. the high stiffness, low inertia and large accelerations, with an improved handling of singularities and optimised actuator loading made possible by the redundancy. Simulations indeed demonstrated advantages of combining both concepts. The flexure hinges in compliant manipulators inherently show a reduced support stiffness for large joint angles. In a PKM with a redundant link this reduction can be limited. Furthermore, the redundant actuation offers a possibility to combine load balancing techniques with preloading of the compliant joints to balance the actuator efforts needed to keep the end effector (EE) stationary at any position different from the equilibrium position [1].

A PKM with “classical” joints can be operated throughout the complete kinematically admissible range [2]. Mimicking this behaviour with flexure joints is a challenge as the required joint angles are quite large even for advanced joint concepts that emerged in recent years. Hence we investigate in this paper how a similar performance can be obtained throughout the same or larger workspace area as before (“more”) when the joint angles are limited (“less”). This can be accomplished by using longer links, which come with the drawback of an increased mass, but can still be beneficial if this is compensated by an increased support stiffness due to less required joint rotations. The optimisation of this trade-off is presented in this paper as well the experimental validation with an outlook to the implementation of a control scheme.

### 2 Design Optimisation

The three arms of the 3RRR PKM are assumed to be similar and the actuators are located at the corners of an equilateral triangle, see Figure 1(a). At first a simplified kinematic model is used to determine the reachable workspace and the required joint rotations. The rigid links are connected with ideal rotational joints. Two important geometrical parameters are the total length  $L$  of each arm and the distance  $R$  of each actuator to the centre of the triangle. The workspace reachable by the EE is bounded by three circular arcs with radii  $L$  of which an example is shown in red and labelled “Def<sup>n</sup> 1” in Figure 1 (b). This is the workspace that has been considered in [1]. The worst case dynamic performance is found in the corners of this area where two arms are fully stretched. In these locations the support stiffness will be lowest as several joints are at or close to their extreme rotation angles.

The blue curves, labelled “Def<sup>n</sup> 2”, in Figure 1 (b) present a first alternative workspace definition. Instead of trying to move to all reachable locations, the corners are cut off e.g. by limiting the workspace to the enclosed circle. It can be shown that using longer arms a larger workspace area can now be reached with the same ratio between mass and support stiffness as before. Although this is an improvement, it appeared that for controlled EE motion still difficulties arose from singular behaviour near the three locations on the enclosed circle where one of the arms is fully stretched.

Hence a third definition of the workspace is presented with the green curves, labelled “Def<sup>n</sup> 3”, in Figure 1 (b). This workspace is a circle which is taken some fixed offset smaller than the maximum enclosed circle such that the (near) singularities are avoided. This results in a reduced range of the motions for the joints as presented in Figure 1 (c). The joint angles in this figure are computed for a manipulator where the total arm length  $L$  is split into equal halves for the upper and lower arm respectively. The

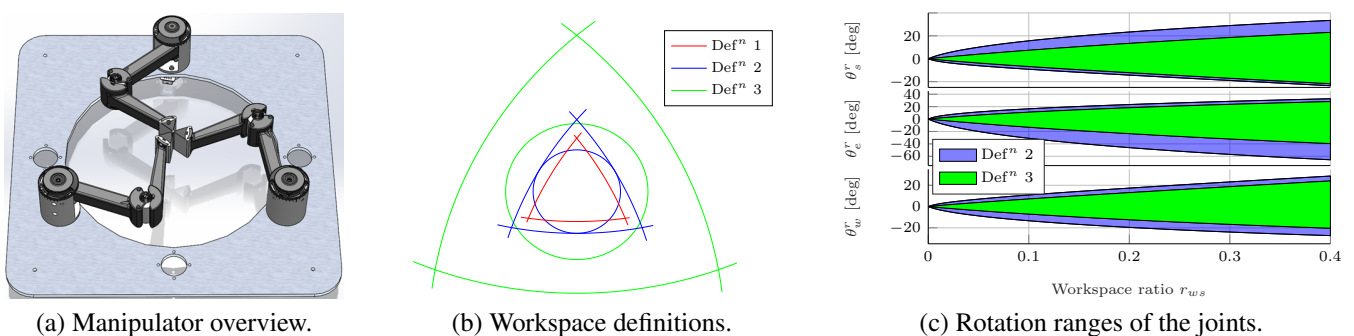


Figure 1: Design of the planar 2-DOF 3RRR PKM with compliant joints.

required rotational range is presented as a function of the so-called (linear) workspace ratio, which is defined as  $r_{ws} = \sqrt{A_{ws}/A_{fp}}$ , where  $A_{ws}$  is the workspace area and  $A_{fp}$  is the triangular area of the manipulator's footprint. It can be seen that the third definition of the workspace requires smaller joint angles to reach the same area. A drawback is that the arm length increases even more which could result in less support stiffness as will be examined next in a dynamic analysis.

In this analysis a dynamic model of the manipulator is used to obtain an optimal design of the system to be manufactured with 3D printing. It involves the following ingredients:

- A more detailed flexible multibody model of the manipulator. The shoulder and elbow joint are butterfly joints. In the wrist three links are connected with a tri-cartwheel joint. All leaf springs are modelled with non-linear flexible beam elements in the SPACAR software package.
- The manipulator model depends on a few geometric parameters like the arm length  $L$ , dimensions of the leaf springs in the flexure joints, orientation of the joints relative to the links, pre-tension of the elbow and shoulder joints. The locations of the actuators and shoulder joints are fixed.
- The required actuator torques are computed that are needed to position the EE at any location in the workspace. The actuator redundancy can be exploited to minimise either the 2-norm or  $\infty$ -norm of the torques.
- The system's natural frequencies are computed in the neutral configuration as well as in two critical EE locations on the border of the workspace. Furthermore the maximum occurring stress is simulated.

The design is optimized for a maximum workspace ratio  $r_{ws}$  where parasitic resonance frequencies are always above 45 Hz as in previous designs, stresses are below material limits and driving torques satisfy actuator limits.

### 3 Numerical and experimental results

The design optimisation resulted in a further increase of the workspace area while the first simulated parasitic natural frequency is kept above 45 Hz. More specifically, the workspace ratios as shown in Figure 1(a) are respectively  $r_{ws} = 0.1922$  in the original “Def<sup>n</sup> 1” (red) [1],  $r_{ws} = 0.2167$  for “Def<sup>n</sup> 2” (blue), but can now be increased to  $r_{ws} = 0.3532$  (green).

The dynamic behaviour of the actual manipulator has been characterized with system identification where a multi-sine excitation is used to estimate the frequency response of Figure 2(a). The redundant actuation and the sensing are transformed to two degrees of freedom being both in-plane translations of the EE. The first higher order natural frequency is sufficiently high.

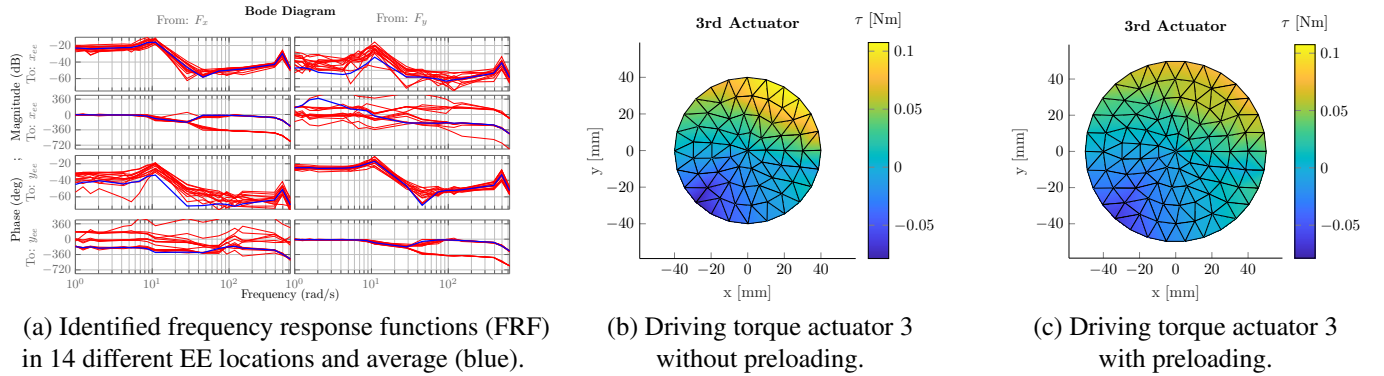


Figure 2: Experimental results of the planar 2-DOF 3RRR PKM with compliant joints.

The balancing of the actuator torques is investigated by positioning the EE throughout the workspace with and without preloading of elbow and shoulder joints. Figure 2(c) shows that with preloading the maximum torque of actuator 3 stays well within the imposed limit. The torques for the other actuators show similar behaviour, rotated  $\pm 120^\circ$ . Without this preloading it can be seen in Figure 2(b) that the torque limits are already exceeded before the edges of the workspace are reached. More details and closed-loop motion control will be outlined in the full paper.

### 4 Conclusion

This paper shows a new design of a planar 2-DOF 3RRR parallel manipulator with redundant actuation and compliant joints. It was found that a combination of longer link lengths and restricted ranges for the joints rotation results in a manipulator that can reach a larger workspace area with similar performance as before [1].

### References

- [1] R. Cornelissen, A. Müller, and R. Aarts. A Compliant and Redundantly Actuated 2-DOF 3RRR PKM: Best of Both Worlds? In A. Kecskeméthy and F. Geu Flores, editors, *Multibody Dynamics 2019*, pages 163–171, Springer, 2020.
- [2] K. Krajoski, A. Müller, H. Gattringer, M. Jörgl. Design, modeling and control of an experimental redundantly actuated parallel platform. In K. Niel and P.M. Roth, editors, *Proceedings of the OAGM&ARW Joint Workshop 2016 “Computer Vision and Robotics”*, pages 209–216. University of Applied Sciences Upper Austria, Wels Campus, 2016.

# Simulation of the Dynamics of the 3-CRS Parallel Robot with a Bond Graph Approach

Benjamin Boudon<sup>1</sup>, Pierre Malafosse<sup>1</sup>, Louis Guigon<sup>1</sup>, Rebecca Margetts<sup>2</sup>, Chedli Bouzgarrou<sup>1</sup>,  
Thu Thuy Dang<sup>1</sup>, Nicolas Bouton<sup>1</sup>,

<sup>1</sup> Université Clermont Auvergne, CNRS

SIGMA Clermont, Institut Pascal

F-63000 Clermont-Ferrand, France

[benjamin.boudon, pierre.malafosse, louis.guigon,

chedli.bouzgarrou, thu-thuy.dang, nicolas.bouton]@sigma-clermont.fr

<sup>2</sup> Nottingham Trent University

Digital Innovation Research Group, Department of Engineering

Clifton, Nottingham. NG11 8NS. UK

rebecca.margetts@ntu.ac.uk

## EXTENDED ABSTRACT

### 1 Context

For many applications in robotics, it is crucial to take into account all the physical phenomena: of course mechanics but also electrical and thermal. To do so, a mechatronic approach is needed so as to gather, in the same model, different physics. The Bond Graph (BG) offers this multi-physics approach in the modeling, the control and analysis of parallel robots. Computer science and software dedicated to BGs have considerably progressed the last two decades and give new insights on older research works made in multibody modeling with Bond Graphs [1, 2].

The first studies in this frame have been conducted on 3-CRS: a parallel reconfigurable robot [3, 4]. The 3-CRS robot is an original parallel mechanism having 6 degrees of freedom (DOFs) with only 3 limbs (Figure 1). This mechanism uses two motorized joints per limb: the prismatic joint and the following revolute joint. This new paradigm of actuation opens up research fields on new families of robots, which should particularly interest the parallel robotics community. According to its dimensional synthesis, this mechanism can have remarkable kinematic properties such as a large orientation workspace or reconfiguration capabilities.

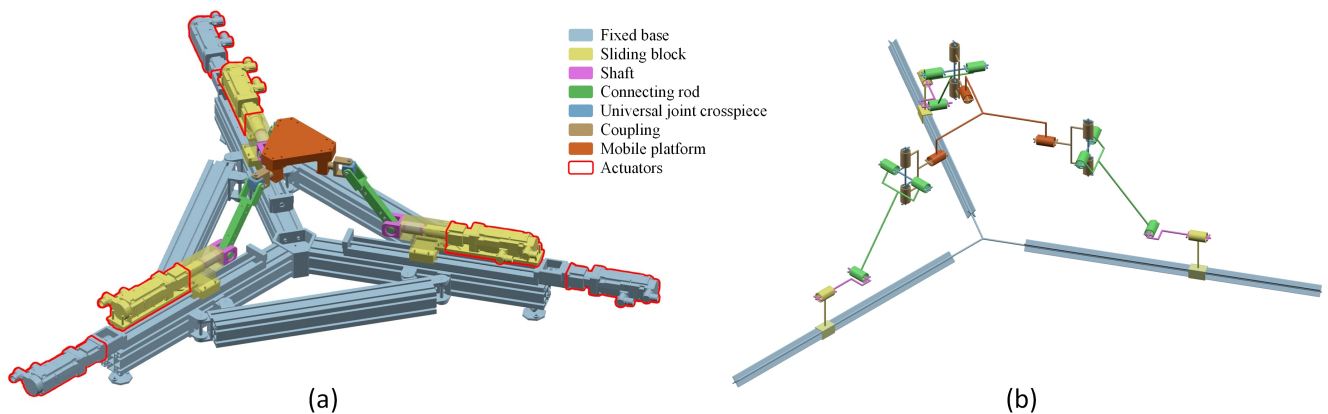


Figure 1: CAD visualization (a) and kinematics scheme (b) of the 3-CRS robot

### 2 Problem description

What can be the benefits of a BG approach be in the modeling, simulation and control of parallel robots, as opposed to a classic approach? Different lines of work can be considered: a modular modeling approach thanks to its structural and object oriented features, the possibility of model inversion-based control with the bi-causal Bond Graph, or the model reduction features and the energetic analysis due to its intrinsic properties. At this stage of the project, the focus is on the modeling of parallel robots (the application with the 3-CRS robot is shown in this paper) with a modular and mechatronic approach using Bond Graph.

### 3 Methodology

The Tierneho and Bos [5] method has been selected for modelling the robot with BG, because this method allows a modular approach. This method – which has been already used to model complex multibody systems [6, 7] – enables a multibody system to be built as an assembly of rigid bodies models and joints models. The modular approach has been improved here by the creation of a model library and the implementation properties of 20-sim objects, which allows different variants of an object to be represented. The theoretical foundations of this method are based on the use of absolute coordinate systems and Newton–Euler equations. The dynamic equations of a rigid body therefore depend on its mass/inertia properties and on geometric parameters for the body under consideration. The kinematic joints constrain the effort and flow vectors in the assembly of two bodies, so that the desired relative motion can be achieved. Consequently, the dynamic equations of the complete system consist of the dynamic equations of each body and the constraint equations at the velocity level of each joint. The equations obtained

are differential algebraic equations (DAE's) whose numerical resolution requires specific numerical integration methods such as Backward Differential Formula (BDF).

The model of the electromechanical actuators (brushed DC motors + reduction gears) has been incorporated so as to obtain a complete mechatronic model. A complete controller (Figure 2) has been designed with:

- a trajectory generation block to define different types of geometric trajectories and time scaling
- an inverse geometric model to transform the task coordinates into joint coordinates
- and a PID controller to define the axis control for each actuator

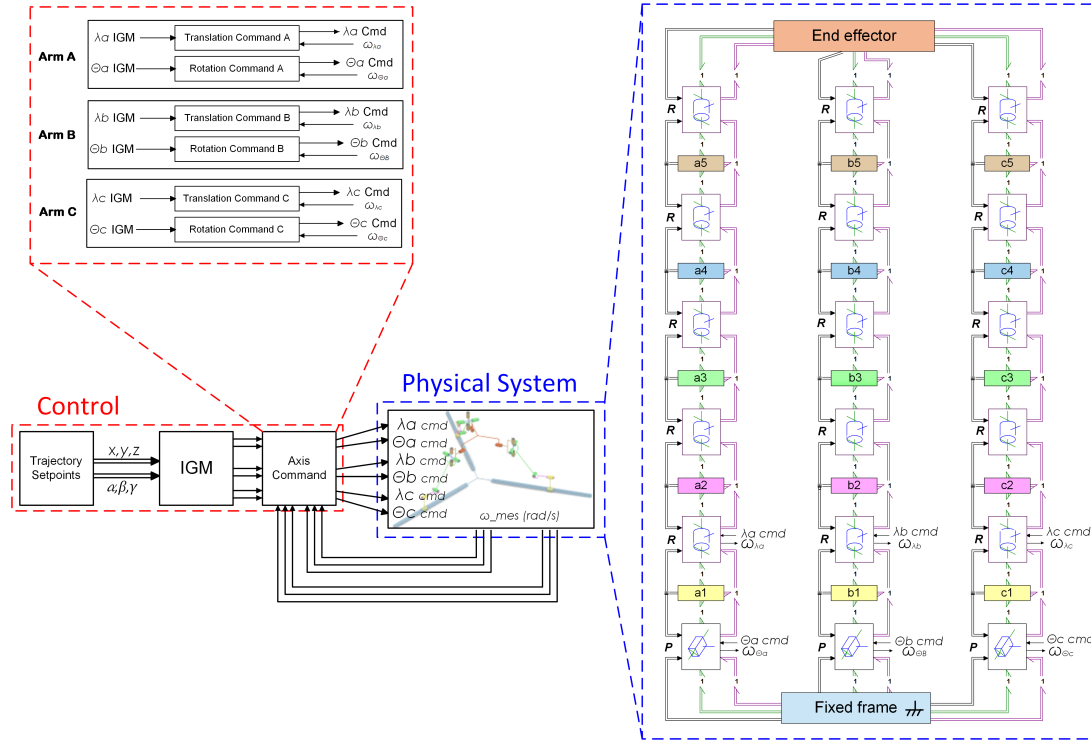


Figure 2: Bond graph model (20-sim) of the 3-CRS robot

#### 4 First results

Simulations have been conducted in 20-sim software for different geometric trajectories and time scaling of the end effector in the work space. The results have been verified with the 3D mechanics of 20-sim, a commercial multi-body dynamics software. Validation using a prototype already built in the lab is planned.

#### References

- [1] A. Zeid and J. L. Overholt. Singularly perturbed formulation : explicit modeling of multibody systems. *Journal of The Franklin Institute*, 332(1):21–45, 1995.
- [2] Wilfrid Marquis-Favre and Serge Scavarda. Bond graph representation of multibody systems with kinematic loops. *Journal of the Franklin Institute*, 335B(4):643–660, 1998.
- [3] Anh Vu Nguyen, Belhassen Chedli Bouzgarrou, Karine Charlet, and Alexis Béakou. Static and dynamic characterization of the 6-dofs parallel robot 3crs. *Mechanism and machine theory*, 93:65–82, 2015.
- [4] Chedli Bouzgarrou, Adrien Koessler, and Nicolas Bouton. Singularity analysis and reconfiguration mode of the 3-crs parallel manipulator. In *2020 IEEE International Conference on Robotics and Automation (ICRA)*, pages 10384–10390. IEEE, 2020.
- [5] A.M. BOS. *Multibody Systems in Terms of Multibond Graphs with Application to a Motorcycle Multibody system*. Phd thesis, 1986.
- [6] Benjamin Boudon, François Malburet, and Jean-Claude Carmona. Simulation of a helicopter's main gearbox semiactive suspension with bond graphs. *Multibody System Dynamics*, 40(4):375–405, 2017.
- [7] Benjamin Boudon, Thu Thuy Dang, Rebecca Margetts, Wolfgang Borutzky, and François Malburet. Simulation methods of rigid holonomic multibody systems with bond graphs. *Advances in Mechanical Engineering*, 11(3):1687814019834153, 2019.

# Motion Control of a Crane-like Manipulator Relying on the HTC Vive - Precision and Accuracy of the Pose Estimation

Roland R. Zana<sup>1</sup>, Ambrus Zelei<sup>2</sup>,

<sup>1</sup> Department of Applied Mechanics  
Budapest University of Technology and Economics  
Muegyetem rkp 3., 1111 Budapest, Hungary  
zana\_r@mm.bme.hu

<sup>2</sup> MTA-BME Research Group on Dynamics of  
Machines and Vehicles  
Muegyetem rkp 3, 1111 Budapest, Hungary  
zelei@mm.bme.hu

## EXTENDED ABSTRACT

### 1 Introduction

Spatial pose-estimation devices for mobile and cable-suspended robots have been rapidly developed. The pose estimation sensor unit of the HTC virtual reality system, which operates with swept laser beams, has aroused many researchers' interest. We present experiments with a double pendulum robot: the ACROBOTER equipped with the HTC Vive Tracker. The tracking of pre-defined end-effector trajectories of various speeds was ensured by linear feedback controller. The pose feedback of the controller was provided by the HTC Vive. As a reference, the realized trajectory was measured by the OptiTrack motion capture system. The accuracy of the HTC Vive sensor was assessed focusing on the trajectory speed, acceleration and jerk.

### 2 Methods

The ACROBOTER [1] is an under actuated crane-like indoor domestic robot prototype, see mechanical model in Fig. 1 left. From mechanical point of view, it is a spatial double pendulum. The main cable, and three secondary cables are connecting the Climbing Unit with the Cable Connector and the Swinging Unit. The 12 DoF robot is equipped with winches and fan actuators, which sums up to 7 independent control inputs. It is a good experimental tool for testing underactuated control algorithms [2, 3].

The mechanical model of the system is described by using redundant coordinate set  $\mathbf{q}$ . For simulation purposes, the equation of motion is formulated in the following general form, together with the geometric constraints - represented in the acceleration level with Baumgarte stabilization: ( $\mathbf{M}$  is the mass matrix,  $\mathbf{C}$  is the vector of velocity-related inertial forces and gravitational forces,  $\boldsymbol{\varphi}_q$  is the constraint Jacobian,  $\boldsymbol{\lambda}$  is the vector of Lagrange-multipliers,  $\mathbf{H}$  is the control input matrix,  $\boldsymbol{\tau}$  is the vector of independent control inputs,  $\alpha$  and  $\beta$  are the Baumgarte parameters):

$$\begin{bmatrix} \mathbf{M} & \boldsymbol{\varphi}_q^T \\ \boldsymbol{\varphi}_q & \mathbf{0} \end{bmatrix} \begin{bmatrix} \ddot{\mathbf{q}} \\ \boldsymbol{\lambda} \end{bmatrix} = \begin{bmatrix} \mathbf{H}\boldsymbol{\tau} - \mathbf{C} \\ -\boldsymbol{\varphi}_q\dot{\mathbf{q}} - 2\alpha\boldsymbol{\varphi}_q\dot{\mathbf{q}} - \beta^2\boldsymbol{\varphi} \end{bmatrix}. \quad (1)$$

The control input - for the simulation and for the measurements as well - was obtained by using the following formula:

$$\mathbf{u} = -\mathbf{K}_P\mathbf{e} - \mathbf{K}_D\dot{\mathbf{e}} + \mathbf{u}^*, \quad (2)$$

where the gain matrices  $\mathbf{K}_P, \mathbf{K}_D$  are constant diagonal matrices, and  $\mathbf{u}^*$  is the estimation of the input forces that compensate the gravitational effects furthermore the error vector  $\mathbf{e}$  is composed of the real SC winch angles  $\vartheta_i$ , the desired winch angle  $\vartheta^d$ , the real SU position coordinates  $x_{SU}, y_{SU}$ , the desired SU position coordinates  $x_{SU}^d, y_{SU}^d$ , the measured yaw angle  $\psi_{SU}$  of the SU and the desired yaw angle  $\psi_{SU}^d$  of the SU:

$$\mathbf{e} = [\vartheta_1 - \vartheta^d, \vartheta_2 - \vartheta^d, \vartheta_3 - \vartheta^d, x_{SU} - x_{SU}^d, y_{SU} - y_{SU}^d, \psi_{SU} - \psi_{SU}^d]^T \quad (3)$$

The Tracker Unit was placed on the SU and four trajectories with different speed were defined (average speed: 0.031 m/s, 0.041 m/s, 0.063 m/s, 0.12 m/s), in order to gain information about the dynamic effects on the accuracy and the precision.

### 3 Results and conclusion

Although, the prototype of the ACROBOTER manipulator was already able to operate in 2009 [4], the details of the trajectory tracking performance have never been published and the achieved trajectory speed was very low. The improved prototype of the ACROBOTER achieved stable pose control (Fig. 1 right) even for 0.55 m/s max. trajectory speed. The HTC Vive Tracker pose measurement unit was proved to be satisfactory for a feedback control loop if 5 mm position error is acceptable. Within our statistical analysis, we expressed the position and angular error as the function of the trajectory speed which can be useful in further researches and applications. It was also proved that the pose error correlates to the acceleration and the jerk, see Fig. 2. As an additional result, we observed that the OptiTrack operation was not affected at all by the Vive Lighthouses. However, the OptiTrack infrared light sources, spoiled the operation of the Vive Tracker by disturbing its sensors. After switching off the



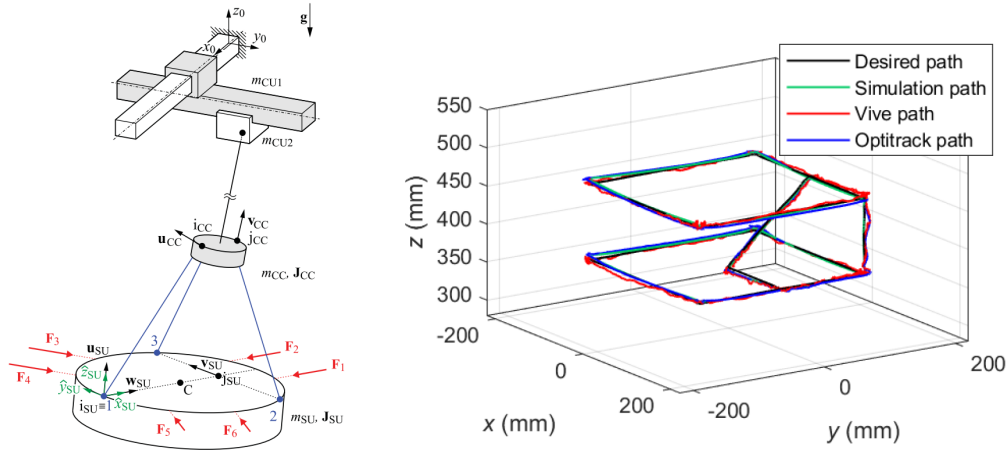


Figure 1: Left: Dynamic model of the double pendulum robot, Right: Trajectory tracking performance

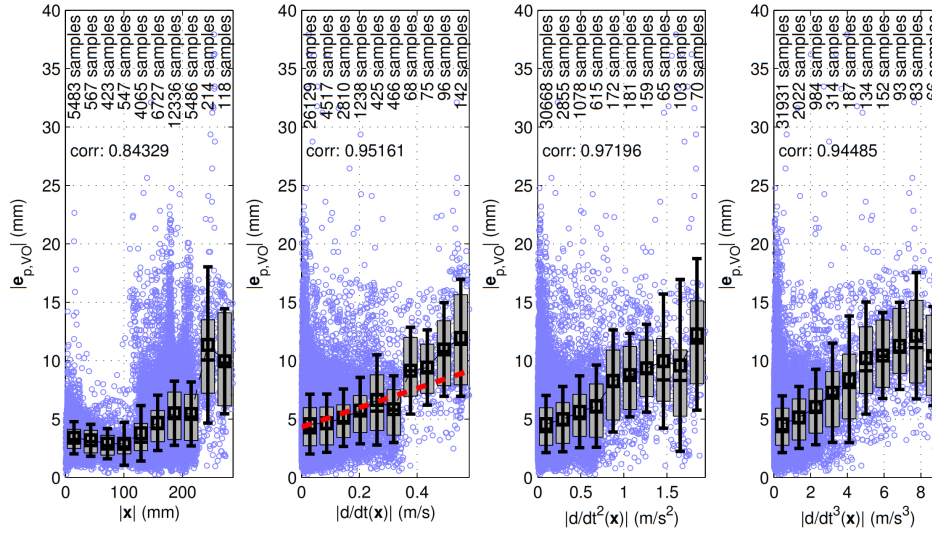


Figure 2: The influence of the distance of the actual position from the origin, the trajectory speed, acceleration and jerk on the VO (Vive – OptiTrack) position measurement error. The black squares show the mean value, the standard deviation is shown by the vertical black lines, the IQR is visualized by the light grey area, in which the horizontal line shows the median. The regression line is shown by red dashed line in the second panel.

OptiTrack infrared light sources and placing active markers on the robot, the OptiTrack and Vive worked together well. We also report that the performance of the HTC Vive highly depends on its vibration isolation from the object on which it is attached.

## Acknowledgments

The research reported in this paper and carried out at BME has been supported by the NRDI Fund (TKP2020 IES, Grant No. BME-IE-BIO and TKP2020 NC, Grant No. BME-NC) based on the charter of bolster issued by the NRDI Office under the auspices of the Ministry for Innovation and Technology and by the Hungarian National Research, Development and Innovation Office (Grant no. NKFI-FK18 128636).

## References

- [1] R.R. Zana, A. Zelei: Feedback motion control of a spatial double pendulum manipulator relying on swept laser based pose estimation. *International Journal of Optomechatronics*, 15(1): 32-60, 2021.
- [2] M.W. Spong: Partial Feedback Linearization of Underactuated Mechanical Systems. In: *Proc. of IEEE/RSJ International Conference on Intelligent Robots and Systems (IROS'94)*. Munich, Germany, 1994.
- [3] O. Svenja, R. Seifried: Real-time trajectory control of an overhead crane using servo-constraints. *Multibody System Dynamics*, 42(1):1-17, 2017.
- [4] G. Stépán, Et Al.: ACROBOTER: A ceiling based crawling, hoisting and swinging service robot platform. In *Beyond Gray Droids: Domestic Robot Design for the 21st Century, Workshop at Human Computer Interaction*, Cambridge, UK; pp. 1-4, 2009

# State Estimation of a Hydraulically Driven Multibody System Using the Unscented Kalman Filter

Qasim Khadim, Yashar Shabbouei Hagh, Suraj Jaiswal, Marko K. Matikainen, Aki Mikkola, Heikki Handroos,

Department of Mechanical Engineering  
LUT University of Technology  
Yliopistonkatu 34, 53850 Lappeenranta, Finland  
[qasim.khadim, yashar.shabbouei.hagh, suraj.jaiswal, marko.matikainen, aki.mikkola, heikki.handroos]@lut.fi

## EXTENDED ABSTRACT

### 1 Introduction

To estimate states of a mechanical system, the independent coordinate method was introduced in [1] by using the independent positions and velocities of the multibody models as the states of a Kalman filter. Using this method, a system of full coordinates can be estimated in terms of independent coordinates in both open- and closed-loop multibody models. The independent coordinate method is further extended to hydraulically actuated systems [2] in an application of state estimation using an indirect extended Kalman filter (EKF). Being one of the state estimation method based on Kalman filter, EKF has been applied to different applications for nonlinear systems [3]. However, due to several reported performance degradation which are mostly related to the linearization procedure of the EKF, an alternative solution named as the unscented Kalman filter (UKF) is proposed based on the unscented transformation (UT) method [4]. This study proposes the state estimation of hydraulically driven systems using the UKF. The implementation of state estimation algorithm is explained using the simulation models of mechanism which are named as real system, simulation model and state estimator. The sensor measurements are taken from the real system. White Gaussian noise is added to the sensor measurements to replicate the actual sensors. The modelling errors are introduced in the force model of the simulation model and state estimator. As an example, the proposed state estimation algorithm is applied to a hydraulically actuated four-bar mechanism. The application of UKF is explained through the working cycle of a hydraulic actuator in the state estimator and the results are compared to real system.

### 2 Hydraulically actuated multibody model

In this study, the double-step semi-recursive formulation is used to model the closed-loop multibody model. The equations of motion using this formulation can be written as [5]

$$\mathbf{R}_z^T \mathbf{R}_d^T \mathbf{T}^T \overline{\mathbf{M}} \mathbf{T} \mathbf{R}_d \mathbf{R}_z \ddot{\mathbf{z}}^i = \mathbf{R}_z^T \mathbf{R}_d^T (\mathbf{T}^T \overline{\mathbf{Q}} - \mathbf{T}^T \overline{\mathbf{M}} \mathbf{D}), \quad (1)$$

where  $\mathbf{R}_z$  is the velocity transformation matrix,  $\mathbf{R}_d$  is the block-diagonal matrix,  $\mathbf{T}$  is the constant path matrix,  $\overline{\mathbf{M}}$  is the composite mass matrix of the system,  $\ddot{\mathbf{z}}^i$  is the vector of independent relative joint accelerations,  $\overline{\mathbf{Q}}$  is vector of the composite forces and  $\mathbf{D} = \mathbf{T} \mathbf{R}_d \begin{bmatrix} -(\Phi_z^d)^{-1} (\Phi_z \dot{\mathbf{z}}) \\ 0 \end{bmatrix} + \mathbf{T} \mathbf{R}_d \dot{\mathbf{z}}$  represent the absolute accelerations, when the vector of relative joint accelerations  $\ddot{\mathbf{z}}$  is zero. Here,  $\Phi_z^d$  is the jacobian matrix of constraint equations with respect to the vector of dependent relative joint positions,  $\Phi_z$  is the first time derivative of the jacobian matrix of constraint equations with respect to the vector of relative joint positions  $\mathbf{z}$  and  $\dot{\mathbf{z}}$  is the vector of relative joint velocity. The lumped fluid theory is used to model the hydraulic actuators. The second order differential equations, Eq. (1), is converted into the first order differential equations as

$$\begin{bmatrix} \dot{\mathbf{z}}^i \\ \ddot{\mathbf{z}}^i \end{bmatrix} = \begin{bmatrix} \dot{\mathbf{z}}^i \\ (\mathbf{M}'^\Sigma)^{-1} \mathbf{Q}'^\Sigma \end{bmatrix} \equiv \mathbf{f}(\mathbf{x}), \quad (2)$$

where  $\mathbf{x} = [\mathbf{z}^i \quad \dot{\mathbf{z}}^i]^T$ ,  $\mathbf{M}'^\Sigma = \mathbf{R}_z^T \mathbf{R}_d^T \mathbf{T}^T \overline{\mathbf{M}} \mathbf{T} \mathbf{R}_d \mathbf{R}_z$  and  $\mathbf{Q}'^\Sigma = \mathbf{R}_z^T \mathbf{R}_d^T (\mathbf{T}^T \overline{\mathbf{Q}} - \mathbf{T}^T \overline{\mathbf{M}} \mathbf{D})$  represent the accumulated mass matrix and accumulated force vector, respectively. Here,  $\mathbf{z}^i$  and  $\dot{\mathbf{z}}^i$  represent the respective vectors of the independent relative joint positions and velocities.

### 3 Unscented Kalman filter methodology

At prediction stage, UKF is initiated by an initial covariance matrix  $\mathbf{P}_{k-1}^+$  and an independent state vector  $\hat{\mathbf{x}}_{k-1}^+$ . Through unscented transformation [4], a set of  $2L+1$  sigma points  $\chi_k$  is generated in which  $L$  represents the length of independent state vector  $\hat{\mathbf{x}}_{k-1}^+$ . With the equation (2), the mean independent state vector  $\hat{\mathbf{x}}_k^-$  is computed. The covariance matrix  $\mathbf{P}_k^-$  is calculated using the weights and a white Gaussian process noise  $\mathbf{w}$ , as mentioned in [4]. Further, using sensor measurements  $\mathbf{h}_k$  and a white Gaussian measurement noise  $\mathbf{v}$ , the independent state vector and the associated covariance matrix is corrected for the next time step as

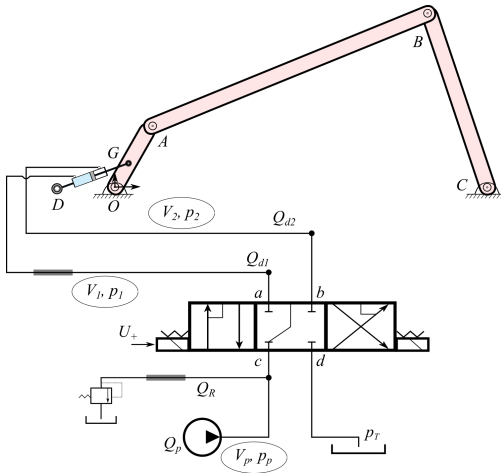
$$\begin{cases} \mathbf{K}_k = \mathbf{P}_{x_k y_k} \mathbf{P}_{y_k}^{-1} \\ \hat{\mathbf{x}}_k^+ = \hat{\mathbf{x}}_k^- + \mathbf{K}_k (\mathbf{h}_k - \mathbf{y}_k^-) \\ \mathbf{P}_k^+ = \mathbf{P}_k^- - \mathbf{K}_k \mathbf{P}_{y_k} \mathbf{K}_k^T \end{cases}, \quad (3)$$



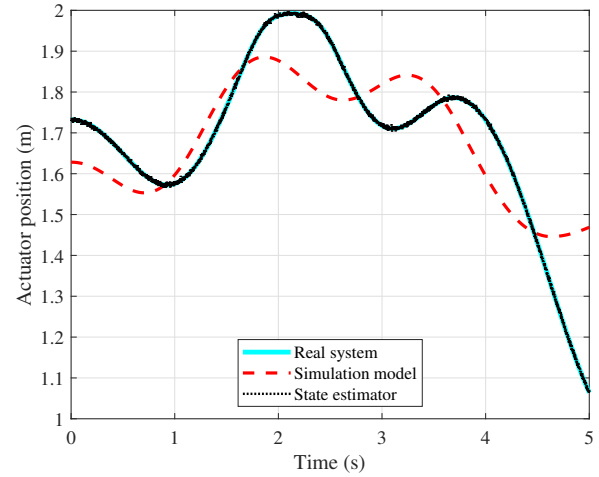
where  $\mathbf{K}_k$  is the Kalman gain,  $\mathbf{P}_{x_k y_k}$  and  $\mathbf{P}_{y_k}$  are the covariances in UKF [4] and  $\mathbf{y}_k^{'-}$  is the approximated weighted mean.

#### 4 Results and Conclusion

The detailed modeling of the hydraulically driven four-bar mechanism, as shown in Figure 1a, using the double-step semi-recursive formulation and the lumped fluid theory in a monolithic coupling can be found in [6]. From the real system, measurements of the actuator position  $s$ , pump pressure  $p_p$ , and pressure on the piston side  $p_1$  are considered. In the state estimator, the state vector  $\mathbf{x} = [s \ \dot{s} \ p_p \ p_1 \ p_2]^T$  is used for the presented case example in the UKF. Here,  $\dot{s}$  is the actuator velocity and  $p_2$  is the pressure on the piston-rod side. The results of state estimation UKF algorithm are presented in Figure 1 in terms of the estimation of working cycle of the hydraulic actuator. As can be seen, despite the modelling errors, the actuator position of state estimator is precisely following the real system. However, in case of simulation model, the actuator position is different than the real system due to modelling errors. Further, the root mean square error associated to the working cycle of state estimator with respect to the real system is 0.02 % which demonstrates the accuracy of state estimation UKF algorithm. The state estimation using hydraulically actuated multibody model and UKF can find applications in the digital twin of heavy machinery.



(a) Hydraulically driven four-bar mechanism.



(b) The working cycle of mechanism is explained in terms of the hydraulic actuator position.

Figure 1: Implementation of UKF state estimation in the hydraulically driven four-bar mechanism and working cycle. In Figure 1a, A, B, C, D, G, O are the points on mechanism. a, b, c and d are the ports of directional control valve.  $Q_{d1}$ ,  $Q_{d2}$ ,  $Q_R$  and  $Q_p$  are the flow rates.  $V_p$ ,  $V_1$  and  $V_2$  represent the hydraulic control volumes.  $p_T$  is the constant pressure tank.

#### References

- [1] E. Sanjurjo, M. A. Naya, J. L. Blanco-Claraco, et al. Accuracy and efficiency comparison of various nonlinear Kalman filters applied to multibody models. *Nonlinear Dynamics*, 88:1935–1951, 2017.
- [2] S. Jaiswal, E. Sanjurjo, J. Sapanen, et al. State estimator based on an indirect extended Kalman filter for a hydraulically actuated multibody system. *Multibody System Dynamics*, Under Review, 2021.
- [3] A. R. Ghiasi, A. A. Ghavifekr, Y. Shabbouei Hagh, et al. Designing adaptive robust extended Kalman filter based on Lyapunov-based controller for robotics manipulators. In *proceedings of the IEEE 2015 6th International Conference on Modeling, Simulation, and Applied Optimization (ICMSAO)*, pages 1–6, 2015.
- [4] E. A. Wan and R. Van Der Merwe. The unscented Kalman filter for nonlinear estimation. In *Proceedings of the IEEE 2000 Adaptive Systems for Signal Processing, Communications, and Control Symposium (Cat. No. 00EX373)*, pages 153–158, 2000.
- [5] J. Rodríguez, J. M. Jiménez, F. J. Funes, et al. Recursive and residual algorithms for the efficient numerical integration of multi-body systems. *Multibody System Dynamics*, 11:295–320, 2004.
- [6] Q. Khadim, M. Kiani-Oshtorjani, S. Jaiswal, et al. The estimation of characteristic curve of directional control valve in a combined multibody and hydraulic system using augmented discrete extended Kalman filter. *Sensors*, Under Review, 2021.

# Synthesis of Trajectory of Underactuated Multibody System

Michael Valasek<sup>1</sup>

<sup>1</sup>Faculty of Mechanical Engineering  
Czech Technical University in Prague  
Technická 4, 16600 Praha 6,  
Czech Republic  
Michael.Valasek@fs.cvut.cz

## EXTENDED ABSTRACT

### 1 Introduction

The control of underactuated multibody systems is a challenge. If the admissible trajectory is known then the control can be carried out by piecewise linearization and linear control around such trajectory. The key problem is the synthesis of admissible trajectory. This paper is devoted to an iterative method of admissible trajectory synthesis.

### 2 Problem statement

The underactuated multibody system is transformed into state space description

$$\frac{d}{dt} x = f(x) + g(x)u \quad (1)$$

with state  $x$ , the control  $u$  and system vectors  $f(x)$  and  $g(x)$ . The initial and final states  $x_0$  and  $x_f$  are equilibrium states of the system (1). It is supposed that the system (1) remains controllable after linearization at the initial and final states.

The system (1) is decomposed by the decomposition used for Nonlinear Quadratic Regulator (NQR) [1] (named also State Dependent Riccati Equation (SDRE)).

$$\frac{d}{dt} x = A(x)x + g(x)u \quad (2)$$

### 3 Admissible Trajectory Iteration

The influence of system properties during the motion given by the matrix  $A(x)$  is unknown. Therefore this influence is approximated by some  $i$ -th trajectory

$$x^{(i)} = x^{(i)}(t) \quad (3)$$

Suitable initial trajectory might be just the connection between initial and final states in each DOF.

This trajectory is substituted into dynamics (2)

$$A^{(i)} = A(x^{(i)}(t)) = A^{(i)}(t) \quad (4)$$

$$g^{(i)} = g(x^{(i)}(t)) = g^{(i)}(t) \quad .$$

that leads to linear time varying system approximating the investigated system (2)

$$\frac{d}{dt} x = A^{(i)}(t)x + g^{(i)}(t)u \quad (5)$$

This linear time varying system (5) is used for computation of intermediate trajectory  $x^{(i*)}$

$$\frac{d}{dt} x^{(i*)} = A^{(i)}(t)x^{(i*)} + g^{(i)}(t)u^{(i*)} \quad (6)$$

from the initial into the final states. Then another intermediate trajectory is constructed as the convex combination of previous ones by a constant  $\alpha_i$

$$x^{(i**)} = (1-\alpha_i)x^{(i)} + \alpha_i x^{(i*)} \quad (7)$$

This intermediate trajectory is used for another approximation of the dynamics

$$A^{(i*)} = A(x^{(i**)}(t)) = A^{(i*)}(t) \quad (8)$$

$$g^{(i*)} = g(x^{(i**)}(t)) = g^{(i*)}(t) \quad .$$

and finally the next trajectory iteration is computed

$$d/dt x^{((i+1)e)} = A^{(i*)}(t)x^{((i+1)e)} + g^{(i*)}(t)u^{((i+1)e)} \quad (9)$$

The constant  $\alpha_i$  is chosen by halving  $\alpha = \alpha/2$  from 1 in such way that the deviation between subsequent trajectory iterations is decreased. The trajectory deviation is introduced

$$D^{(i)} = \int_{t_0}^T (x^{(i)}(t) - x^{((i-1)*)}(t))^2 dt + (u^{(i)}(t) - u^{((i-1)*)}(t))^2 dt \quad (10)$$

And the decrease  $D^{((i+1)e)} < D^{(i)}$  is required

$$\begin{aligned} \text{If } D^{((i+1)e)} < D^{(i)} \text{ then } x^{(i+1)} &= x^{((i+1)e)}, D^{(i+1)} = D^{((i+1)e)} \\ \text{else } \alpha &= \alpha/2 \text{ and return to } x^{(i*)} = (1-\alpha)x^{(i)} + \alpha x^{(i*)} \text{ and continue to new } D^{((i+1)e)} \end{aligned} \quad (11)$$

#### 4 Proof of iteration convergence

The above described procedure and the proof are based on such choice of constant  $\alpha_i$  that the subsequent trajectories are mutually close (vicinity of previous iteration) in such a way that the linearization of dynamics is for them valid. The idea is based on the procedure of optimal trajectory synthesis [2]. The change of trajectories within one iteration is

$$\begin{aligned} x^{(i+1)} &= x^{(i*)} + \delta x_{i+1} \\ u^{(i+1)} &= u^{(i*)} + \delta u_{i+1} \end{aligned} \quad (12)$$

So the values  $\delta x_{i+1}$  and  $\delta u_{i+1}$  are small and their dynamics can be described

$$d/dt \delta x_{i+1} = A(x^{(i)}(t)) \delta x_{i+1} + g(x^{(i)}(t)) \delta u_{i+1} + \delta A(x^{(i)}(t)) \alpha_i (x^{(i*)} - x^{(i)}) x^{((i+1))} + \delta g(x^{(i)}(t)) \alpha_i (x^{(i*)} - x^{(i)}) u^{((i+1))} \quad (13)$$

If  $\alpha_i=0$  then  $d/dt \delta x_{i+1} = A(x^{(i)}(t)) \delta x_{i+1} + g(x^{(i)}(t)) \delta u_{i+1}$  and  $\delta x_{i+1}(t) = 0$ ,  $\delta u_{i+1}(t) = 0$  and  $D(i+1) = 0$

For increasing  $\alpha_i$  the value of  $D(i+1)$  increases because the dynamics of  $d/dt \delta x_{i+1}$  is excited by the nonzero terms  $\delta A(x^{(i)}(t)) \alpha_i (x^{(i*)} - x^{(i)}) x^{((i+1))} + \delta g(x^{(i)}(t)) \alpha_i (x^{(i*)} - x^{(i)}) u^{((i+1))}$

These terms are nonzero exactly when  $x^{(i*)} \neq x^{(i)}$  and  $D(i+1) \neq 0$  for  $\alpha_i > 0$ .

It ensures the validity of used Taylor series for  $A(x)$ . It is ensured by appropriate small value of  $\alpha_i > 0$ . The modifications of trajectories  $x_{i+1}$  must be done step by step.

The value of  $\alpha_i$  is increased until it is reached  $D(i+1) = \kappa D(i)$  where  $\kappa < 1-\beta$  and  $\beta$  is firmly fixed positive value, for example  $\beta=0.1, 0.2, \dots, 0.5$ . Then maximum value of  $\kappa$  is 0.9, 0.8, ..., 0.5.

By the choice of  $\alpha_i$  and  $\kappa$  it is ensured that the sequence of  $D(i+1)$  is convergent

Thus the sequence of  $D(i+1)$  is decreasing below some geometric sequence. Therefore  $D(i+1)$  converges to 0 but being sequence with nonzero values.  $D(i+1) \rightarrow 0$  q.e.d.

#### 5 Conclusion

The approximation of dynamics through its decomposition and trajectory iteration enables by subsequent modification from initial trajectory step by step within the vicinity of previous ones into the finally admissible trajectory.

#### References

- [1] Valášek, M., Steinbauer, P.: Nonlinear Control of Multibody Systems. In: "Euromech Colloquium 404, Advances in Computational Multibody Dynamics", Lisboa: Instituto Technico Superior, Av. Rovisco Pais, 1999, p. 437–444
- [2] Valášek, M.: Synthesis of optimal trajectory of industrial robots, Kybernetika, Vol. 22 (1986), No. 5, 409–424

# Extending the Admissible Control-Loop Delay for the Inverted Pendulum Subject to PDA Feedback by Detuning the Delays

Tamas Balogh, Balazs Varszegi, Tamas Insperger

Department of Applied Mechanics  
Budapest University of Technology and Economics and  
MTA-BME Lendület Human Balancing Research Group  
Budapest, Hungary  
[tamas.balogh,varszegi,insperger]@mm.bme.hu

## EXTENDED ABSTRACT

### 1 Introduction

In this study, we analyze proportional-derivative-acceleration (PDA) feedback of a second-order unstable plant governed by

$$\ddot{\varphi}(t) - a_0\varphi(t) = -k_p\dot{\varphi}(t - \tau_p) - k_d\ddot{\varphi}(t - \tau_d) - k_a\ddot{\varphi}(t - \tau_a), \quad (1)$$

where  $a_0$  is fixed, and  $a_0 > 0$ ,  $\tau_p > 0$ ,  $\tau_d > 0$ ,  $\tau_a > 0$ .

Following [1] one can also think of (1) as a control system with a single control-loop latency  $\tau$  with some additional delays (or delay detunings)  $\delta_p$ ,  $\delta_d$  and  $\delta_a$  in all the three terms, i.e.  $\tau_p = \tau + \delta_p$ ,  $\tau_d = \tau + \delta_d$ ,  $\tau_a = \tau + \delta_a$  and  $\delta_p \geq 0$ ,  $\delta_d \geq 0$ ,  $\delta_a \geq 0$ . These additional delays are introduced in hopes of improving the stabilizability of the original system with a single delay  $\tau$ . Hence, (1) can be considered as a detuned PDA feedback.

Special cases of (1) involve delayed PD feedback ( $k_a = 0$ ,  $\tau_p = \tau_d$ ), detuned PD feedback ( $k_a = 0$ ) and delayed PDA feedback ( $\tau_p = \tau_d = \tau_a$ ). The critical delay for delayed PD feedback was derived by Schürer [2], while for detuned PD and delayed PDA feedback it was given by Sieber and Krauskopf [1]. The goal of this study is to determine the critical delay  $\tau_{\text{crit}}$  of the detuned PDA feedback, which can be defined as the maximum of  $\min\{\tau_p, \tau_d, \tau_a\}$  such that the system is still stabilizable.

### 2 Critical point ( $m_0 = 5, k_a = -1$ )

The characteristic function of (1) reads

$$D(s) = s^2 - a_0 + k_p e^{-s\tau_p} + k_d s e^{-s\tau_d} + k_a s^2 e^{-s\tau_a}. \quad (2)$$

Equation (1) is a neutral delay-differential equation (NDDE), therefore strong stability requires that  $|k_a| < 1$ .

In order to find the critical parameters corresponding to the critical delay, first, we investigate the maximal multiplicity of the characteristic root  $s = 0$ . This idea is motivated by the multiplicity-induced-dominancy (MID) property [3]. It can be shown that the root  $s = 0$  of the quasipolynomial (2) cannot have a multiplicity greater than or equal to 6 if  $|k_a| < 1$ . Similarly, multiplicity 5 of  $s = 0$  cannot occur if  $0 \leq k_a \leq 1$ . However, if  $-1 \leq k_a < 0$  then multiplicity 5 can be reached, and the minimum of the delays is maximal for  $k_a = -1$  (see the solid black line and the black point in Fig. 1). Therefore, we focus on the case  $k_a = -1$ . In this case, the control parameters and the delays satisfy the conditions  $D^{(i)}(0) = 0$ ,  $i = 0, 1, \dots, 4$  and  $k_a = -1$ . This system of equations gives a unique solution satisfying  $\tau_p, \tau_d, \tau_a > 0$ :

$$k_p = a_0, \quad k_d = 2\sqrt{6a_0}, \quad k_a = -1, \quad \tau_p = 2\sqrt{\frac{6}{a_0}}, \quad \tau_d = \sqrt{\frac{6}{a_0}}, \quad \tau_a = 2\sqrt{\frac{6}{a_0}}. \quad (3)$$

With parameters (3) and  $z = \sqrt{6s}/\sqrt{a_0}$  the quasipolynomial (2) has an equivalent form

$$\tilde{D}(z) = \left( \frac{z^2}{6} - 1 \right) \sinh z + z. \quad (4)$$

It can be shown that (4) has only purely imaginary roots.

### 3 Stabilization for $\tau_d < \sqrt{6/a_0}$ ( $m_{s_0} = 5$ )

In order to stabilize (2), we choose the control parameters in a way that a real root  $s_0$  has multiplicity 5, i.e.  $D^{(i)}(s_0) = 0$ ,  $i = 0, 1, \dots, 4$ . The first three equations ( $D^{(i)}(s_0) = 0$ ,  $i = 0, 1, 2$ ) are linear in  $k_p$ ,  $k_d$  and  $k_a$ , and the gains can be given as explicit functions of  $s_0$ ,  $\tau_p$ ,  $\tau_d$  and  $\tau_a$ . Substitution into the remaining two equations ( $D^{(i)}(s_0) = 0$ ,  $i = 3, 4$ ) gives two polynomial equations for  $s_0$ ,  $\tau_p$ ,  $\tau_d$  and  $\tau_a$ . For a fixed pair  $(\tau_d, \tau_a)$  one can find  $s_0$  and  $\tau_p$  numerically. Among the possible solutions only the ones should be considered where  $s_0 < 0$  and  $\tau_p > 0$ . Then one can check the stability of (2) by the condition  $|k_a| < 1$  and by calculating the number of unstable roots according to the numerical method [4]. The results are shown in Fig. 1.

Figure 1 shows that we can use a detuned PDA controller to stabilize the unstable open-loop system  $P(s) = s^2 - a_0$  if the control-loop latency  $\tau$  is smaller than  $\sqrt{6/a_0}$ . That is, for every  $0 < \tau_d = \tau < \sqrt{6/a_0}$  we can find  $\tau_p, \tau_a > \tau$  for which (2) is stabilizable.

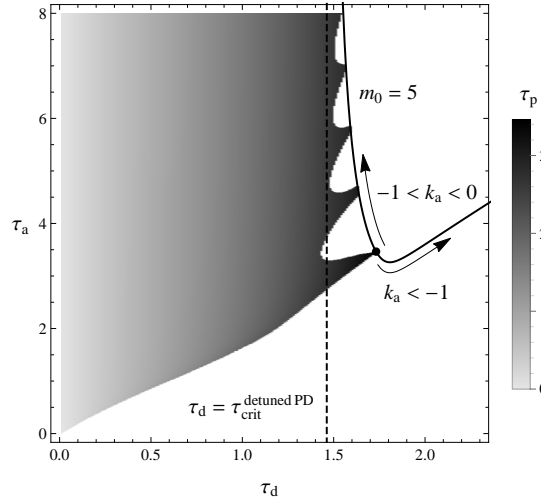


Figure 1: The region of feedback delays that can be stabilized by a real root  $s_0$  with multiplicity  $m_{s_0} = 5$  if  $a_0 = 2$

#### 4 Conclusions

The critical delay and the corresponding critical parameters (feedback delays  $\tau_p$ ,  $\tau_d$ ,  $\tau_a$  and control gains  $k_p$ ,  $k_d$ ,  $k_a$ ) are summarized in Table 1 for PD, detuned PD, PDA and detuned PDA feedbacks. Detuning the feedback terms in PD feedback increases the achievable feedback delay by 47% [1]. Adding acceleration feedback increases the critical delay by 41% (by a factor of  $\sqrt{2}$ ) [1]. Here, we have shown that the critical delay can further be increased, up to 73% (by a factor of  $\sqrt{3}$ ) via employing detuned PDA feedback. This improved stabilizability can be exploited by assigning a negative real root with multiplicity 5. That is, this way we can always construct a stabilizing controller for any feedback delay smaller than the critical delay.

Table 1: Critical parameters for  $a_0 = 2$

	PD	detuned PD	PDA	detuned PDA
$\tau_p$	$\sqrt{\frac{2}{a_0}} = 1$	$\sqrt{6 + 4\sqrt{3}} \sqrt{\frac{1}{a_0}} = 2.54$	$\frac{2}{\sqrt{a_0}} = 1.41$	$2\sqrt{\frac{6}{a_0}} = 3.46$
$\tau_d$	$\sqrt{\frac{2}{a_0}} = 1$	$\sqrt{\frac{6+4\sqrt{3}}{3}} \sqrt{\frac{1}{a_0}} = 1.47$	$\frac{2}{\sqrt{a_0}} = 1.41$	$\sqrt{\frac{6}{a_0}} = 1.73$
$\tau_a$	-	-	$\frac{2}{\sqrt{a_0}} = 1.41$	$2\sqrt{\frac{6}{a_0}} = 3.46$
$k_p$	$a_0 = 2$	$a_0 = 2$	$a_0 = 2$	$a_0 = 2$
$k_d$	$\sqrt{2a_0} = 2$	$\sqrt{6 + 4\sqrt{3}} \sqrt{a_0} = 5.08$	$2\sqrt{a_0} = 2.83$	$2\sqrt{6a_0} = 6.93$
$k_a$	-	-	1	-1
$\tau_{crit}$	$\sqrt{\frac{2}{a_0}} = 1$	$\sqrt{\frac{6+4\sqrt{3}}{3}} \sqrt{\frac{1}{a_0}} = 1.47$	$\frac{2}{\sqrt{a_0}} = 1.41$	$\sqrt{\frac{6}{a_0}} = 1.73$

#### Acknowledgments

The research reported in this study and carried out at BME has been supported by the NRDI Fund (TKP2020 IES, Grant No. BME-IE-BIO and TKP2020 NC, Grant No. BME-NC) based on the charter of bolster issued by the NRDI Office under the auspices of the Ministry for Innovation and Technology and by the Hungarian-Chinese Bilateral Scientific and Technological Cooperation Fund under Grant no. 2018-2.1.14-TÉT-CN-2018-00008.

#### References

- [1] J. Sieber and B. Krauskopf. Extending the permissible control loop latency for the controlled inverted pendulum. *Dynamical Systems*, 20(2): 189–199, 2005.
- [2] F. Schürer. Zur Theorie des Balancierens. *Mathematische Nachrichten*, 1(5): 295–331, 1948.
- [3] I. Boussaada, H.U. Ünal and S-I. Niculescu. Multiplicity and stable varieties of time-delay systems: A missing link. In *Proceeding of the 22nd International Symposium on Mathematical Theory of Networks and Systems*, pages 1–6, 2016.
- [4] Q. Xu and Z. Wang. Exact stability test of neutral delay differential equations via a rough estimation of the testing integral. *International Journal of Dynamics and Control*, 2(2): 154–163, 2014.

# Robust motion planning for underactuated multibody systems through a variational approach

Paolo Boscariol, Dario Richiede

Dipartimento di Tecnica e Gestione dei Sistemi Industriali  
Università degli Studi di Padova  
Stradella S. Nicola 3, 36100 Vicenza, Italy  
paolo.boscariol@unipd.it  
dario.richiede@unipd.it

## EXTENDED ABSTRACT

### 1 Introduction

A method for robust trajectory planning in underactuated multibody systems, aimed at reducing the effects of the uncertainty on the main parameters, is here presented. The method is based on an indirect variational formulation, which is translated into a Two-Point Boundary Value Problem (TPBVP) and solved numerically. By exploiting the mathematical frame proposed in [1] for inverse dynamics, and then extended in [2] for trajectory planning, robustness is obtained by including the sensitivity functions within the problem, together with boundary constraints on the trajectory. A formulation aimed at reducing both the residual and the transient oscillations, while keeping small and smooth the control effort, is proposed and numerically validated.

### 2 System model formulation

The model of a  $n$ -dimensional underactuated multibody system, with  $\mathbf{q}$  the vector of the independent coordinates, can be partitioned by defining the vector of  $m < n$  actuated generalized coordinates, and the vector  $\mathbf{q}_u$  of the  $n - m$  unactuated ones:

$$\begin{bmatrix} \mathbf{M}_{aa} & \mathbf{M}_{au} \\ \mathbf{M}_{au}^T & \mathbf{M}_{uu} \end{bmatrix} \begin{bmatrix} \ddot{\mathbf{q}}_a \\ \ddot{\mathbf{q}}_u \end{bmatrix} = \begin{bmatrix} \mathbf{K}_a(\mathbf{q}) \\ \mathbf{K}_u(\mathbf{q}) \end{bmatrix} + \begin{bmatrix} \mathbf{G}_a(\mathbf{q}, \dot{\mathbf{q}}) \\ \mathbf{G}_u(\mathbf{q}, \dot{\mathbf{q}}) \end{bmatrix} + \begin{bmatrix} \mathbf{B}_a \\ 0 \end{bmatrix} \mathbf{F} \quad (1)$$

The equation of the internal dynamics,  $\ddot{\mathbf{q}}_u = \mathbf{M}_{uu}^{-1}(\mathbf{K}_u + \mathbf{G}_u) - \mathbf{M}_{uu}^{-1}\mathbf{M}_{au}^T\ddot{\mathbf{q}}_a$ , highlights that the motion of the unactuated coordinates is excited by the motion of the actuated ones. By assuming that the actuated DOFs are not disturbed by the motion of the unactuated ones (e.g because of effective control or small inertia ratio), the problem of optimal motion planning for load vibration control can just rely on the internal dynamics. To get a more accurate representation, in this work a simplified model of the actuators dynamics is included as well in the model adopted for motion planning, to account for their finite bandwidths and to obtain a smooth trajectory; and effective choice is, for example, a first-order linear model. The actual acceleration of the actuated coordinates is therefore written as a function of the reference acceleration  $\ddot{\mathbf{q}}_a^{ref}(t)$ ,  $\ddot{\mathbf{q}}_a(t) = -\frac{1}{\tau}\ddot{\mathbf{q}}_a(t) + \frac{1}{\tau}\ddot{\mathbf{q}}_a^{ref}(t)$ , and this equation is accounted together with the internal dynamics in the control synthesis. This model is then cast as a set of first-order ODEs,  $\dot{\mathbf{x}} = \mathbf{f}(\mathbf{x}, t, \mathbf{u})$ , as required for solving the trajectory optimization problem, with  $\mathbf{u} = \ddot{\mathbf{q}}_a^{ref}$  the control vector and  $\mathbf{x} = [\dot{\mathbf{q}}_u, \ddot{\mathbf{q}}_a, \dot{\mathbf{q}}_a, \mathbf{q}_u, \mathbf{q}_a]^T$  the state vector.

### 3 Variational formulation of robust trajectory planning

The robust trajectory planning problem is formulated as a TPBVP by augmenting the state with the sensitivity function  $\mathbf{S}(t) = \frac{\partial \mathbf{x}(t)}{\partial \mu}$  ( $\mu$  is a critical uncertain scalar parameter),  $\mathbf{x}^r(t) := \begin{bmatrix} \mathbf{x}(t) \\ \mathbf{S}(t) \end{bmatrix}$ , and by solving the following problem, where the scalar function  $g^r$  is chosen to fulfill the required goals of the trajectory design:

$$\left\{ \begin{array}{l} \min J^r(\mathbf{x}^r, t, \mathbf{u}) = \min \int_{t_0}^{t_f} g^r(\mathbf{x}^r, t, \mathbf{u}, \mu) dt \\ \text{subject to :} \\ \mathbf{x}(t_0) = \mathbf{x}_0; \quad \mathbf{x}(t_f) = \mathbf{x}_f; \\ \mathbf{S}(t_0) = 0; \quad \mathbf{S}(t_f) = 0; \\ \dot{\mathbf{x}}(t) = \mathbf{f}(\mathbf{x}(t), t, \mathbf{u}, \mu); \quad \dot{\mathbf{S}}(t) = \frac{\partial \mathbf{f}(\mathbf{x}(t), t, \mathbf{u})}{\partial \mu}; \end{array} \right. \quad (2)$$

### 4 Application example

The numerical test case consists of a double-pendulum crane ( $m_1 = 0.192$  kg,  $m_2 = 0.201$  kg,  $L_1 = 0.470$  m,  $L_2 = 0.391$  m). The trolley motion is a rest-to-rest displacement with 0.3 m amplitude to be completed in 3 s. The uncertain parameter is  $L_1$ . Two

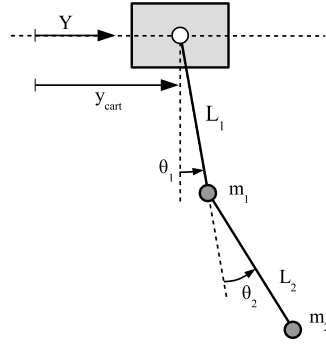


Figure 1: Scheme and kinematic model of the double-pendulum crane

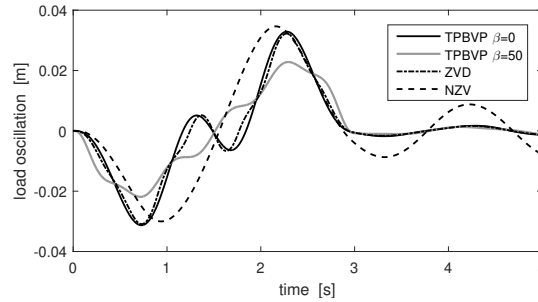


Figure 2: Load oscillation with perturbed plant ( $\Delta L_1 = +20\%$ )

Table 1: Performance measurements: motion profile and load oscillation

Test	$\ddot{y}_{max}$ [m/s <sup>2</sup> ]	$\ddot{y}_{RMS}$ [m/s <sup>2</sup> ]	$\ddot{y}_{max}$ [m/s <sup>3</sup> ]	$\ddot{y}_{RMS}$ [m/s <sup>3</sup> ]	transient peak [mm]	transient RMS [mm]	residual peak [mm]	residual peak, $\Delta L_1 = 20\%$ [mm]
NZV	0.2141	0.1299	1.6982	0.7381	27.347	17.037	0.169	8.850
ZVD	0.7067	0.3727	20.5333	6.0468	28.807	14.917	0.042	1.622
TPBVP, $\beta = 20$	0.5571	0.2283	19.2325	3.6195	21.984	12.943	0.001	1.470
TPBVP, $\beta = 50$	0.7030	0.2835	25.5660	4.2066	19.646	12.374	0.001	1.465

benchmark input shaping methods are adopted: the Negative Zero Vibration (NZV) and the Zero Vibration Derivative (ZVD) shapers [3] with fifth-degree polynomials. The goal of motion planning is to design a robust profile with negligible residual and transient oscillations of the end-effector (mass  $m_2$ ). To meet the last requirement, the cost function has been defined as  $g = \frac{1}{2}u^2 + \beta \exp\left((\gamma(L_1 \sin(\theta_1) + L_2 \sin(\theta_1 + \theta_2)))^2\right)$ . Two values of  $\beta$  ( $\beta = 0$  and  $\beta = 50$ ) have been chosen to show how it affects the load oscillation ( $\gamma$  is set to 50 for all the tests). The features of the commanded trolley profile are summarized in the left part of Table 1 through the peak and RMS values of acceleration and jerk. The load response, in term of peak and RMS oscillations, are reported in the right part of Table 1 in the case of unperturbed and perturbed plants. The comparison shows that the proposed method has better robustness than the widely adopted ZVD shaper, while requiring lower actuator effort and bandwidth. The comparison with the NZV shows that a slightly higher trolley acceleration is required by the proposed method, while jerk increases remarkably. On the other hand, a great improvement of the transient and steady-state load response is ensured both in the ideal situation and in the presence of model mismatch. These results and the possibility to trade off between reducing transient and residual oscillations and keeping small the control effort by means of a suitable definition of the cost function, corroborate the effectiveness of the proposed approach for solving trajectory planning in underactuated multibody systems.

## References

- [1] P. Boscariol and A. Gasparetto. Robust model-based trajectory planning for nonlinear systems. *Journal of Vibration and Control*, 22(18):3904–3915, 2016.
- [2] P. Boscariol and D. Richiedei. Robust point-to-point trajectory planning for nonlinear underactuated systems: Theory and experimental assessment. *Robotics and Computer-Integrated Manufacturing*, 50:256–265, 2018.
- [3] W. Singhose. Command shaping for flexible systems: A review of the first 50 years. *International Journal of Precision Engineering and Manufacturing*, 10(4):153–168, 2009.



# Uni-frequency 6 DOF Active Dynamic Absorber for Spatial Mechanisms

Zbyněk Šika<sup>1</sup>, Jan Krivošej<sup>1</sup>, Tomáš Vyhřídál<sup>1,2</sup>

<sup>1</sup>Faculty of Mechanical Engineering  
Czech Technical University in Prague  
Technická 4, Praha 6, 16000  
Czech republic  
Zbynek.Sika@fs.cvut.cz

<sup>2</sup>Czech Institute of Informatics Robotics and Cybernetics  
Czech Technical University in Prague  
Jugoslávských partyzánů 3, Praha 6, 16000  
Czech republic  
Tomas.Vyhridal@fs.cvut.cz

## EXTENDED ABSTRACT

### 1 Introduction

Vibration plays a negative role in many engineering applications and often needs to be eliminated. Let us, for example, mention the impact of machine tool vibration to workpiece surface quality and fatigue in compliant structures, adverse effect of base vibration in precise instruments such as electron microscopes, deep space telescopes, particle detectors, etc. Vibration compensation is a big task also in control of robotic machines, considering classical industrial robots, micromanipulation assembly lines (e.g., in microchip production), or high precision surgery robots. The idea of the passive vibration absorber connected to the primary mechanical structure to suppress its vibrations is known and patented for approximately one hundred years. The main benefit of this passive approach is that no (or minimal) energy needs to be exerted to damp the oscillations. The active versions of vibration absorption concept (Figure 1) however significantly improve its efficiency. There is a lot of ways of control algorithm design. The interesting alternative is a Delayed Resonator (DR) approach [1], [2], [3] – an active vibration absorber with delayed feedback from the position, velocity or acceleration measurements. Piezoactuators or voice-coil actuators can be typically used as active elements. The concept of active dynamic absorbers for use planar serial robot has been introduced and formulated in [4]. Reducing the vibrations of the robots by means of active absorbers has the advantage that it can only be realized with the help of local sensors, for example with built-in encoders or a few extra accelerometers. In addition, the active absorbers allow the adaptation to the highly variable modal properties of the robot during motion in the workspace. The presented research extends the results of [4] for spatial mechanisms and replaces the LQR method with an observer [4] by simpler and more specific concept of uni-frequency 6 DOF absorbers.

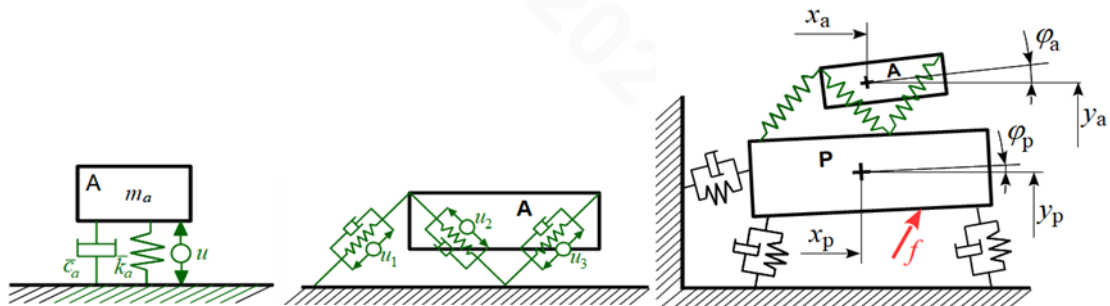


Figure 1: a) 1 DOF active absorber b) 3 DOF active planar absorber c) 3 DOF absorber on primary platform [5]

### 2 Uni-frequency 6 DOF active dynamic absorber

For many types of machines, such as serial robots, the first eigenfrequency and the corresponding eigenmode are the most critical for unwanted excitation. The respective eigenmode often has a complex spatial shape and, for example, in the case of serial robots, it is considerably different for different end-effector positions in the workspace. Planar delayed resonator for entire vibration absorption (Figure 1 b), c)) has been proposed and analyzed in [5]. The basis for the implementation of an active absorber is a mechanical structure with properties as close as possible to an uni-frequency absorber with one multiple natural frequency and the smallest possible mechanical dissipation during the motion. The situation with a spatial absorber is more complicated than with a planar variant and requires detailed analysis.

The uni-frequency absorber configuration with one triple natural frequency can be achieved with a tuned planar absorber (Figure 1 b)) with 3 degrees of freedom and three 3 springs [5]. On the other hand, in an analogous spatial absorber with 6 degrees of freedom, a uni-frequency configuration cannot be achieved, either by distributing the mass, nor by placing 6 springs and/or by tuning their stiffness. Many parametric and topological variants were analyzed. As an example, eigenfrequencies of a set of regular absorbers with a different platform height, including cubic and octahedron architectures (Figure 2 b)) are given on Figure 3. The octahedron architecture (Figure 2 b) - lower) has one triple, one double and one single eigenfrequency. The cubic architecture (Figure 2 b) - upper) is closest to the uni-frequency ideal. Five of six eigenfrequencies are identical and only one is different (Figure 3), namely the eigenfrequency corresponding to the twisting/torsional mode around triangular platform axis

(Figure 2 c)). However, even here, the active forces (Figure 2 c) - lower) from the voice-coil actuators (Figure 2 c) - upper) must have one additional component compared to the planar variant [5], correcting the resulting passive twisting/torsional stiffness around the platform axis so that the absorber is change to uni-frequency. Subsequently, applying delayed position feedbacks from voice-coil length encoder sensors, the 3D-6 DOF absorber is turned to the ideal absorber at the given frequency similarly as for the planar variant [5]. Multiple pole of the 3D-DR is assigned at the frequency to be compensated. In addition, the active absorbers allow the adaptation to the highly variable modal properties of the serial robot during motion in the robot workspace similarly to [4].

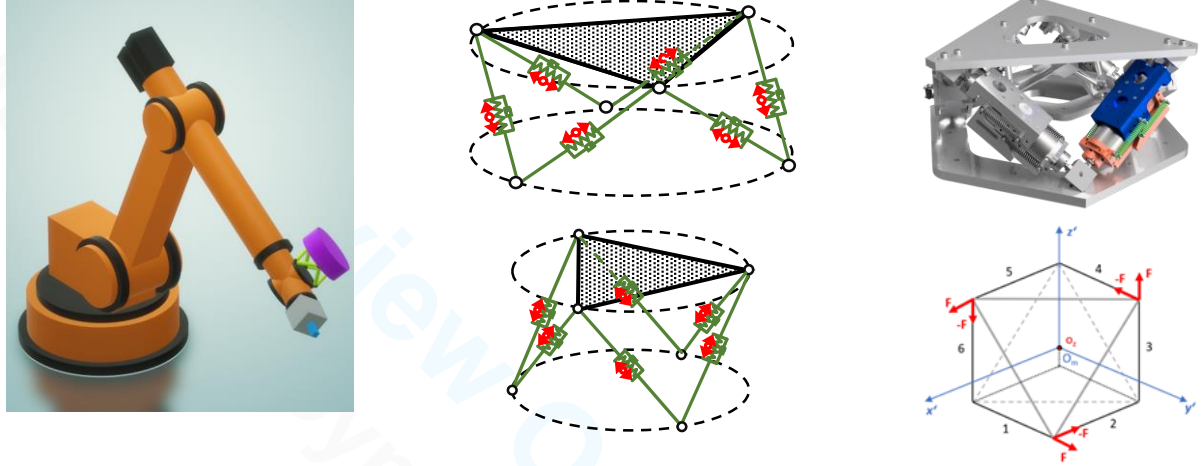


Figure 2: a) 6 DOF active absorber on robot b) Cubic and octahedron configurations c) Design concept and actuators forces

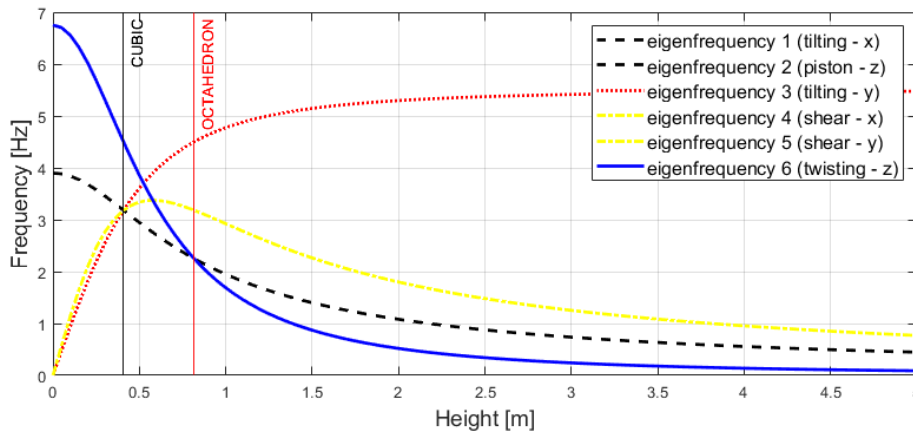


Figure 3: Height dependency of eigenfrequencies of regular 6 DOF absorbers, including cubic and octahedron configurations

## Acknowledgments

The work has been supported by the Czech Science Foundation project GA21-00871S “Active non-collocated vibration absorption for robots and mechanical structures”.

## References

- [1] N. Olgac, B. Holm-Hansen. A novel active vibration absorption technique: delayed resonator. *Journal of Sound and Vibration*, 176: 93–104, 1994.
- [2] M. Valášek, N. Olgac, Z. Neusser. Real-time tunable single-degree of freedom, multiple-frequency vibration absorber, *Mech. Syst. Signal Process*, 133, 106244, 2019.
- [3] T. Vyhlídal, M. Anderle, J. Bušek, S. Niculescu. Time-delay algorithms for damping oscillations of suspended payload by adjusting the cable length, *IEEE/ASME Trans. Mechatron.* 22 (5): 2319–2329, 2017.
- [4] K. Kraus, Z. Šika, P. Beneš, J. Krivošej, T. Vyhlídal. Mechatronic robot arm with active vibration absorbers. *Journal of Vibration and Control*, 26 (13-14): 1145-1156, 2020.
- [5] Z. Šika, T. Vyhlídal, Z. Neusser. Two-Dimensional Delayed Resonator for Entire Vibration Absorption. *Journal of Sound and Vibration*, 500, 116010, 2021.

# Synthesis of an Extended Kalman Filter for Cable-Driven Parallel Robots

Giovanni Boschetti<sup>1</sup>, Francisco González<sup>2</sup>, Giulio Piva<sup>1</sup>, Dario Richiedei<sup>1</sup>, Borja Rodríguez Frade<sup>2</sup>, Alberto Trevisani<sup>1</sup>

<sup>1</sup>Department of Management and Engineering

University of Padua

Stradella S. Nicola 3, 36100,

Vicenza, Italy

[giovanni.boschetti, dario.richiedei, alberto.trevisani]@unipd.it,

giulio.piva@phd.unipd.it

<sup>2</sup>Laboratorio de Ingeniería Mecánica

University of A Coruña

Rúa Mendizábal s/n, 15403,

Ferrol, Spain

[f.gonzalez, borja.rfrade]@udc.es

## EXTENDED ABSTRACT

### 1 Introduction

Cable-driven parallel robots (CDPRs) are light-weight multibody systems where rigid links are replaced by cables to move an end-effector either in very large workspaces or with extremely high dynamics. A critical issue in the operation of CDPRs is ensuring tensile cable forces through proper motion planning and control [1], thus requiring advanced algorithms such as model-based control schemes using state feedback. Since the direct measurement of the whole state is often not feasible, especially of the end-effector state variables, the development of state observers is of primary interest [2]. In this work, a nonlinear state observer based on an Extended Kalman Filter is developed and validated numerically. Some preliminary results are shown too.

### 2 Dynamic modelling of a cable-suspended parallel robot

The studied CDPR is sketched in Figure 1. It is a cable-suspended parallel robot in the sense that a three-DOF suspended end-effector (modelled as a point mass  $m$ ) is driven by four cables winding on drums actuated by motors (whose equivalent moments of inertia are  $J_{m,1}, J_{m,2}, J_{m,3}, J_{m,4}$ ). The system is therefore overactuated, as often happens in CDPRs to increase the static

equilibrium workspace [1]. The vector of dependent coordinates  $\mathbf{q} = [\mathbf{P}^T \quad \boldsymbol{\theta}^T]^T$  includes the absolute Cartesian position of the end-effector  $\mathbf{P} = [x_p \quad y_p \quad z_p]^T$  and the angular positions of the motors  $\boldsymbol{\theta} = [\theta_1 \quad \theta_2 \quad \theta_3 \quad \theta_4]^T$ . Under the assumption that cables are perfectly stiff and hence behave as holonomic ideal kinematic constraints, the  $i^{th}$  constraint ( $i=1, \dots, 4$ ) that relates the end-effector coordinates and the angular positions of the motors is  $\mathbf{l}_i = \mathbf{p} - \mathbf{a}_i$  (with  $\mathbf{a}_i$  the absolute position of the exit-point of cable  $i$ ), where  $\|\mathbf{l}_i\| = l_{0,i} + r_i\theta_i$  is the cable length ( $l_{0,i}$  is the cable length corresponding to  $\theta_i=0$  and  $r$  is the drum radius). The

dynamic model in dependent coordinates is therefore represented through the following set of DAEs,  $\begin{cases} \mathbf{M}\ddot{\mathbf{q}} + \mathbf{J}^T\boldsymbol{\lambda} = \mathbf{f} \\ \boldsymbol{\Phi}(\mathbf{q}) = \mathbf{0} \end{cases}$ , where  $\mathbf{J}$  is the Jacobian of the position constraints  $\boldsymbol{\Phi}$ ,  $\mathbf{M} = \text{diag}(m, m, m, J_{m,1}, J_{m,2}, J_{m,3}, J_{m,4})$  is the mass matrix of the system,  $\boldsymbol{\lambda}$  is the vector of the Lagrange's multipliers and  $\mathbf{f}$  contains the external forces (gravity forces, motor torques, friction torques).

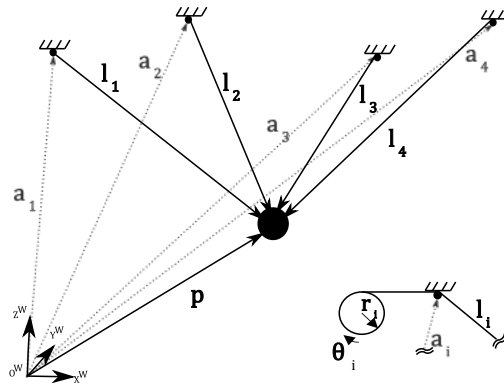


Figure 1: CSPR driven by four cables and detail of the drum and the exit point of the  $i$ -th cable.

### 3 Development of the Extended Kalman Filter (EKF)

An EKF provides optimal estimates  $\hat{\mathbf{x}}(k)$  of the actual state  $\mathbf{x}(k) = [\dot{\mathbf{q}}^T \quad \mathbf{q}^T]^T$  of a first-order system representation, by merging the prediction of a nominal, discrete-time model  $\mathbf{x}(k+1) = f(\mathbf{x}(k), \mathbf{f}(k))$  with the measurements retrieved from a proper set of

sensors  $\mathbf{y}(k) = g(\mathbf{x}(k), \mathbf{f}(k))$ . The resulting closed-loop estimation is based on a prediction-correction scheme,  $\hat{\mathbf{x}}(k+1) = f(\mathbf{x}(k), \mathbf{f}(k)) + \mathbf{K}(\mathbf{y}(k) - \hat{\mathbf{y}}(k))$ , where  $\mathbf{K}$  is the filter gain and  $\mathbf{y}(k) - \hat{\mathbf{y}}(k)$  is the output-estimation error ( $\hat{\mathbf{y}}(k)$  is the estimated output).  $\mathbf{K}$  is updated at each time step  $k$  through the model Jacobian matrices and the covariance matrices of the model and the measurement noises; the latter ones are, in practice, tuning parameters [2].

In the test case, observability is ensured by including into  $\mathbf{y}$  the measures provided by 3 motor encoders with 150 pulses (in 4x operation). Assessment of the results is done by comparing  $\hat{\mathbf{x}}(k)$  with  $\mathbf{x}(k)$  inferred from the model assumed as “the real system” and with no quantization, and with the state estimated through the forward kinematics and the noisy measurements (filtered numerical derivatives have been adopted, with a 15-Hz bandwidth, first-order, low-pass filter). The model used by the state observer has been converted into ODEs with dependent coordinates through different formulations (such as penalty formulation, Udwadia-Kalaba formulation), to retain all the variables in the estimation and handle redundancy. The “real system” has been instead modelled through independent coordinates, obtained through the projection matrix method, to see the impact of different multibody formulations in the estimation. A sample result is provided in Figure 2, where the penalty formulation [3] has been adopted; details on the estimation errors are shown in Figure 3. It is evident that the EKF gets rid of the quantization effectively by providing estimates with small errors and negligible delays; in contrast the speed estimates obtained through forward kinematics are not acceptable. Sensitivity analysis, by assuming random bounded perturbations of  $\mathbf{M}$ , corroborates the EKF effectiveness. For example, a +10% perturbation of all the entries of  $\mathbf{M}$  increases the RMS errors less than 0.1%.

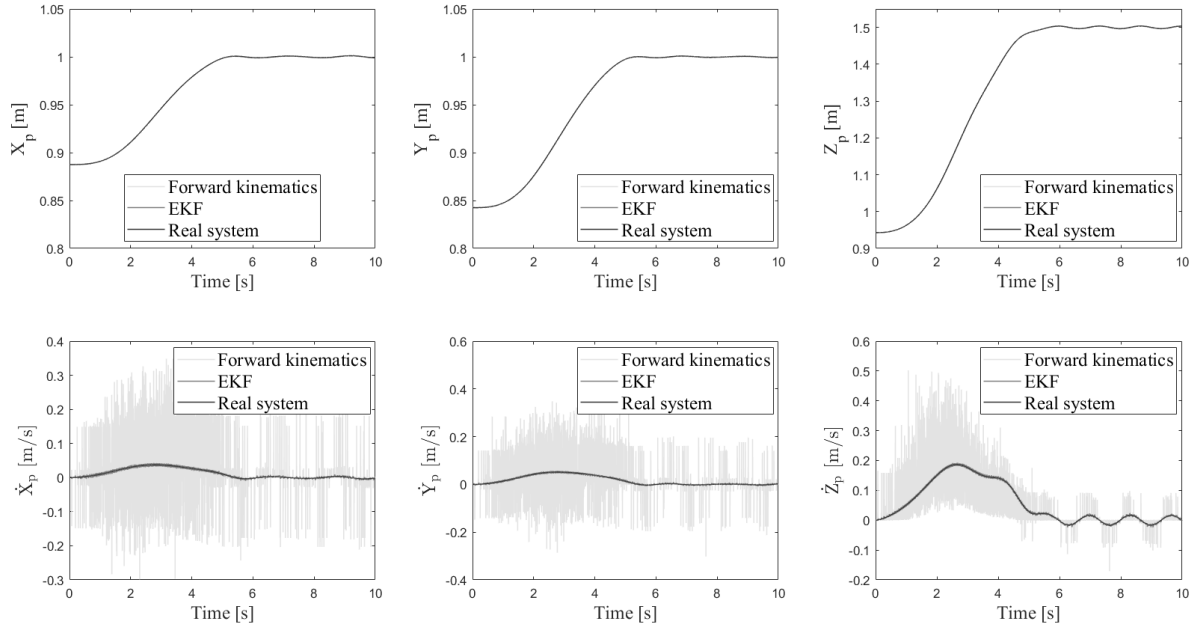


Figure 2: Comparison of actual and estimated  $\mathbf{P}$  and  $\dot{\mathbf{P}}$ .

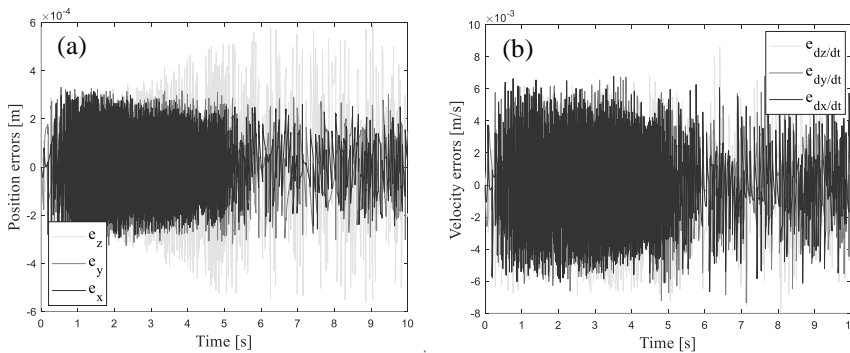


Figure 3: Time-history of position and velocity estimation errors of the EKF (a,b), and table with the comparisons

	EKF	Forward kinematics
$e_x^{RMS}$ [m]	1.13e-4	1.20e-4
$e_y^{RMS}$ [m]	1.32e-4	1.26e-4
$e_z^{RMS}$ [m]	2.04e-4	2.43e-4
$e_{dx/dt}^{RMS}$ [m/s]	2.13e-3	0.064
$e_{dy/dt}^{RMS}$ [m/s]	2.24e-3	0.059
$e_{dz/dt}^{RMS}$ [m/s]	2.53e-3	0.055

## References

- [1] A. Trevisani. Planning of dynamically feasible trajectories for translational, planar, and underconstrained cable-driven robots. *Journal of System Science and Complexity*, vol. 26, no. 5, pages 695–717, 2013.
- [2] R. Pastorino, D. Richiedei, J. Cuadrado, and A. Trevisani. State estimation using multibody models and non-linear Kalman filters. *International Journal of Non-Linear Mechanics*, vol. 53, pages 83–90, 2013.
- [3] F. González and J. Kövecses. Use of penalty formulations in dynamic simulation and analysis of redundantly constrained multibody systems. *Multibody System Dynamics*, vol. 29, no. 1, pages 57–76, 2013.

# Path Tracking in Cable Suspended Parallel Robots through Position-Dependent Model Predictive Control with Embedded Integrator

Jason Bettega<sup>1</sup>, Dario Richiedei<sup>2</sup>, Alberto Trevisani<sup>3</sup>

<sup>1</sup>Department of Management  
and Engineering  
Università degli Studi di Padova  
Stradella S. Nicola 3, 36100 Vicenza,  
Italy  
jason.bettega@phd.unipd.it

<sup>2</sup>Department of Management  
and Engineering  
Università degli Studi di Padova  
Stradella S. Nicola 3, 36100 Vicenza,  
Italy  
dario.richiedei@unipd.it

<sup>3</sup>Department of Management  
and Engineering  
Università degli Studi di Padova  
Stradella S. Nicola 3, 36100 Vicenza,  
Italy  
alberto.trevisani@unipd.it

## EXTENDED ABSTRACT

### 1 Introduction

Precise path tracking control in Cable Suspended Parallel Robots (CSPRs) is a challenging topic in the field of control of multibody systems, due to the positivity constraints on cable tensions. Trajectory planning strategies have been suggested to a-priori ensure positive and bounded cable tensions along given paths (e.g. [1]). Conversely, standard controllers, such as PID, usually only adopt a-posteriori verification and control saturation. More conveniently, in this paper precise path tracking trajectory control in a CSPR is solved by exploiting and extending the concept of Model Predictive Control (MPC). Indeed, one of MPC promising features is the ability of including constraints in the optimal solution, by solving a constrained optimization problem [2]. In this paper the preliminary results on a novel architecture of MPC, tailored for CSPRs, are anticipated. First, since the dynamic model is non-linear, the proposed scheme is based on a two-step strategy which splits the system into two subsystems and uses them in a sequential approach to simplify control implementation. Then, MPC with embedded integrator (MPC-EI) is adopted to ensure precise path tracking.

### 2 System model

The studied system is depicted in Figure 1. It consists of a lumped mass ( $m$ ) suspended by 3 cables and driven by 3 motors. Let  $\mathbf{q} = [\mathbf{p}^T \ \boldsymbol{\theta}^T]^T$  be a set of 6 dependent coordinates containing the absolute cartesian position of the end-effector  $\mathbf{p} = [x_p \ y_p \ z_p]^T$  and the absolute motor rotations  $\boldsymbol{\theta} = [\theta_1 \ \theta_2 \ \theta_3]^T$ . Cables are assumed perfectly stiff and hence behave as holonomic ideal constraints: the kinematic constraint equation relating  $\theta_i$  ( $i = 1, 2, 3$ ) to the length of the  $i^{\text{th}}$  cable is therefore  $\rho_i = \rho_{i0} - r_i \theta_i$ , where  $\rho_i$  is the  $i^{\text{th}}$  cable length ( $\rho_i = \|\mathbf{p} - \mathbf{A}_i\|$  with  $\mathbf{A}_i$  the absolute position of the  $i^{\text{th}}$  exit point),  $r_i$  is the  $i^{\text{th}}$  drum radius and  $\rho_{i0}$  is the cable length when  $\theta_i = 0$ . The resulting dynamic model, in terms of non-minimal coordinates, is  $\mathbf{M}\ddot{\mathbf{q}} + \mathbf{J}^T \boldsymbol{\lambda} = \mathbf{Q}$ , where  $\mathbf{M} = \text{diag}\{J_1, J_2, J_3, m, m, m\}$ ,  $\mathbf{J}$  is the Jacobian of the position constraints,  $\boldsymbol{\lambda}$  is the vector of the Lagrange multipliers and  $\mathbf{Q}$  contains the external forces (gravity forces, friction, motor torques). To meet the formalism of control theory, the set of DAEs obtained is converted into a minimal set of ODEs. By exploiting a matrix  $\mathbf{R}$  such that  $\dot{\mathbf{q}} = \mathbf{R}\dot{\mathbf{p}}$ , the usual form of a multibody system dynamic model is obtained:  $(\mathbf{R}^T \mathbf{M} \mathbf{R})\ddot{\mathbf{p}} + (\mathbf{R}^T \mathbf{M} \dot{\mathbf{R}})\dot{\mathbf{p}} = \mathbf{R}^T \mathbf{Q}$ . Such a model has been implemented to simulate the real system in a Matlab-Simulink environment, also including simplified models of the sensors and the actuators.

### 3 Design of the two-stage control scheme

In the first step of control design, the subsystem made by the suspended load is considered, and MPC is applied to compute the required cable tensions  $T_i$  collected in vector  $\mathbf{T}$ . The dynamic model adopted is the following one, where  $\mathbf{g} = [0 \ 0 \ -9.81]^T$ :

$$m\ddot{\mathbf{p}} = m\mathbf{g} + \sum_{i=1}^3 \left( -T_i \frac{\mathbf{p} - \mathbf{A}_i}{\|\mathbf{p} - \mathbf{A}_i\|} \right) \quad (1)$$

To provide effective path tracking, MPC with embedded integrator is adopted. By introducing the difference variables  $\Delta \boldsymbol{\chi}_d(k) = \boldsymbol{\chi}_d(k) - \boldsymbol{\chi}_d(k-1)$  ( $\boldsymbol{\chi}_d(k) \in \mathbb{R}^6$  is the state vector of the first-order representation of (1)), and  $\Delta \mathbf{T}(k) = \mathbf{T}(k) - \mathbf{T}(k-1)$ , then the following discrete-time augmented state-space model is formulated for the MPC design:

$$\boldsymbol{\chi}(k+1) = \begin{bmatrix} \mathbf{A}_d & \mathbf{0}_{6 \times 3} \\ \mathbf{C}_d \mathbf{A}_d & \mathbf{I}_3 \end{bmatrix} \boldsymbol{\chi}(k) + \begin{bmatrix} \mathbf{B}_d(\mathbf{p}) \\ \mathbf{C}_d \mathbf{B}_d(\mathbf{p}) \end{bmatrix} \Delta \mathbf{T}(k), \quad \mathbf{y}(k) = [\mathbf{0}_{3 \times 6} \ \mathbf{I}_3] \boldsymbol{\chi}(k) \quad (2)$$

$\mathbf{A}_d \in \mathbb{R}^{6 \times 6}$  is the constant dynamic matrix,  $\mathbf{B}_d(\mathbf{p}) \in \mathbb{R}^{6 \times 3}$  is the pose-dependent input matrix,  $\mathbf{y}(k) \in \mathbb{R}^3$  is the output (equals to the end-effector pose),  $\mathbf{C}_d \in \mathbb{R}^{3 \times 6}$  is the output matrix and  $\boldsymbol{\chi}(k) = [\boldsymbol{\Lambda} \mathbf{x}_d(k) \quad \mathbf{y}_d(k)]^T$  is the augmented state vector. The cost function  $J = (\mathbf{Y}^{\text{des}} - \mathbf{Y})^T \mathbf{R}_Y (\mathbf{Y}^{\text{des}} - \mathbf{Y}) + \Delta \mathbf{T}^T \mathbf{R}_{\Delta T} \Delta \mathbf{T}$  is defined and minimized in the presence of bounds on the allowable tensions ( $T_{\min}, T_{\max}$ ), where  $\mathbf{R}_Y$  and  $\mathbf{R}_{\Delta T}$  are weighting matrices,  $\mathbf{Y}$  and  $\mathbf{Y}^{\text{des}}$  are the predicted and the reference output over the prediction horizon. Finally, optimal cable tensions  $T_i^{\text{MPC}}$  are achieved at each time step through the receding horizon principle.

The second stage computes the optimal motor torques  $C_{m,i}$  through a feedforward approach, by exploiting the inverse-dynamic model of each actuator and the desired acceleration  $\ddot{\theta}_i^{\text{ref}}$  and speed  $\dot{\theta}_i^{\text{ref}}$ , computed through inverse kinematics of the load reference,  $C_{m,i}(k) = J_i \ddot{\theta}_i^{\text{ref}}(k) + f_{v,i} \dot{\theta}_i^{\text{ref}}(k) + r_i T_i^{\text{MPC}}(k)$ .

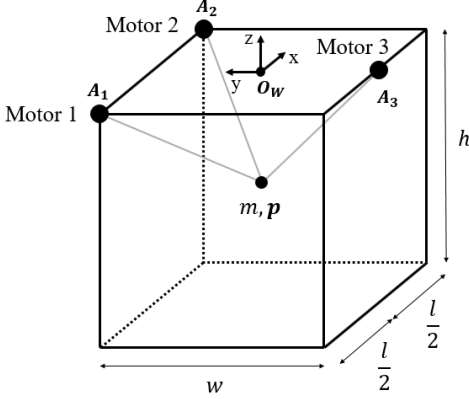


Figure 1: Scheme of the CSPR under investigation

Table 1: System parameters

$J_1, J_2, J_3$	Motor moments of inertia	$2.6e^{-5} [kgm^2]$
$f_{v,1}, f_{v,2}, f_{v,3}$	Motor viscous friction coefficients	$5e^{-3} [Nms/rad]$
$r_1, r_2, r_3$	Radius of the pulleys	$0.036 [m]$
$m$	Mass of the suspended load	$2.94 [kg]$
$T_{\min}; T_{\max}$	Minimum and maximum tensions	$5; 100 [N]$
$T_s$	Sampling time	$2e^{-3} [s]$
$N_c; N_p$	Control and prediction horizons	$1; 60$
$\mathbf{R}_Y; \mathbf{R}_{\Delta T}$	Weighting matrices	$\mathbf{I}_{180}; 1e^{-3} \mathbf{I}_3$

#### 4 Numerical results

The system parameters are stated in Table 1. A planar circular path has been assumed and a 5<sup>th</sup>-degree polynomial has been chosen as the trajectory. The spatial tracking is shown in Figure 2 and corroborates the control effectiveness: the actual and reference paths are almost overlapped, and the RMS value of the contour error is just  $8.3 \times 10^{-4} [m]$ . A classical MPC without embedded integrator is also tested for comparison, it provides an RMS contour error equal to  $10.1 \times 10^{-3} [m]$ . The same figure also shows the optimal cable tensions commanded by the MPC-EI, showing that cable constraints are satisfied. More details on the results, together with other path references, will be proposed in the full paper and in the conference presentation.

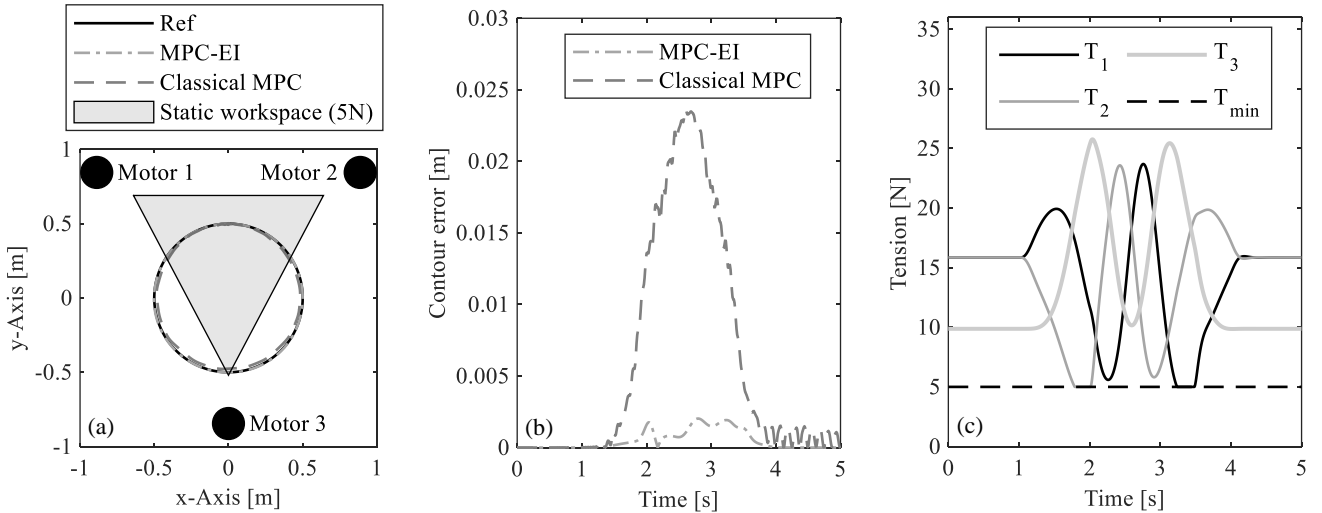


Figure 2: Comparison between MPC formulation with (MPC-EI) and without ("Classical MPC") embedded integrator, in terms of path tracking (a) and contour error (b). Cable tensions for MPC-EI (c).

#### References

- [1] A. Trevisani. Underconstrained planar cable-direct-driven robots: A trajectory planning method ensuring positive and bounded cable tensions. *Mechatronics* 20: 113–127, 2010
- [2] P. Boscariol, A. Gasparetto, V. Zanotto. Active position and vibration control of a flexible links mechanism using model-based predictive control. *Journal of dynamic systems, measurement, and control* 132(1), 2010



# A Heuristic Sequencing Method for Time Optimal Tracking of Open and Closed Paths

Christian Zauner<sup>1</sup>, Hubert Gatringer<sup>1</sup>, Andreas Müller<sup>1</sup>, Matthias Jörgl<sup>2</sup>

<sup>1</sup> Institute of Robotics, Johannes Kepler University Linz  
Altenbergerstraße 69, 4040 Linz, Austria  
{christian.zauner, hubert.gatringer, a.mueller}@jku.at

<sup>2</sup> Trotec Laser GmbH  
Freilingstraße 99, 4614 Marchtrenk, Austria  
matthias.joergl@troteclaser.com

## EXTENDED ABSTRACT

### 1 Introduction

Tracking sequences of predefined open and closed paths is of crucial interest for applications like laser cutting and similar production processes. Since these paths are often not connected the question arises, how these paths should be sorted in order to minimize overall process time. Although a more general approach would be conceivable, this work focuses on paths on the 2D plane and gantry like robotic systems as shown in figure 1. These systems are subject to restrictions like maximum velocity, acceleration and jerk for each axis respectively. Furthermore there are process specific constraints. In case of the laser cutting process the maximum velocity tangentially to the path depends on the material which has to be cut and in order to ensure a clean cut the velocity at the beginning and at the end of each path has to be zero. Subject to these constraints a time optimal path tracking solution for each path can be found and the optimal partial solutions can be connected by time optimal trajectories along straight lines as shown in figure 2. But with an increasing number of paths to track the impact of the non-productive traversing time introduced by these links on the overall process time is getting dominant if the sequencing is not handled properly.

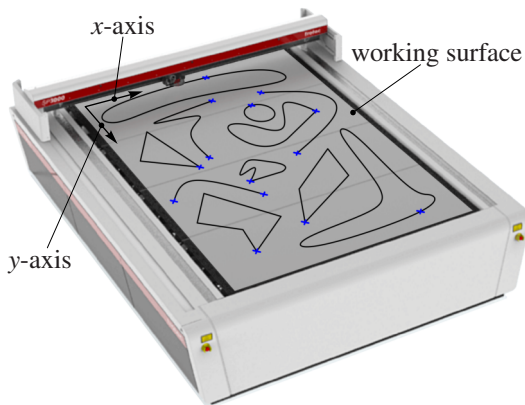


Figure 1: Gantry laser cutting machine

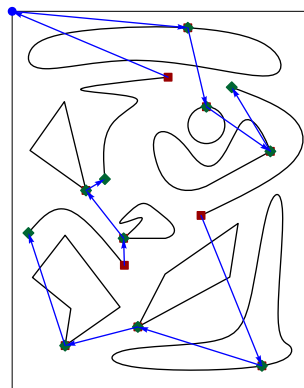


Figure 2: Time optimal tour

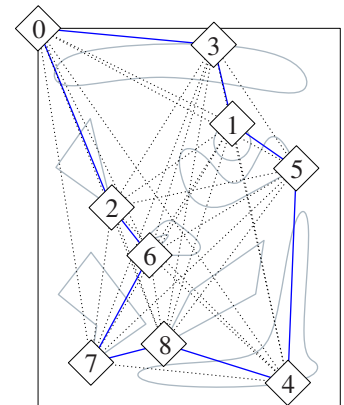


Figure 3: Graph of closed paths

Considering a sequence of solely closed paths the start and end points coincide and since the tracking of the defined path in between is assumed to be known and time optimal the resulting problem boils down to a traveling salesman problem where the coordinates of the start/end points are the nodes and the connecting trajectories are the edges of a fully connected graph as depicted in figure 3. The traveling salesman problem is a very well known NP-hard combinatorial problem, which is assumed to be not solvable in polynomial time. Although there exist many exact algorithms to solve a traveling salesman problem like branch-and-cut or branch-and-bound, an exact solution is getting more and more impractical with an increasing number of nodes respectively paths, since the calculation time also contributes to the overall process time. Actually for most applications a good approximation of the exact solution would suffice. This can be achieved efficiently by heuristic algorithms. In this work two different heuristics are examined and compared with respect to their applicability to problems where also open paths occur.

### 2 Edge Weights defined by Minimum Traversing Time

In order to compute the edge weights of the fully connected graph a special metric is introduced. Since the overall goal is to achieve a time optimal solution all the considered links connecting two points on the 2D plane have to be time optimal on their own. Therefore the distance between two arbitrary points can be expressed by the minimum time needed to traverse a straight line between these two points satisfying the constraints of the robotic system. On gantry systems with perpendicular axis the minimum path time is the maximum time needed by one of the axis. The resulting distance measure satisfies the triangle inequality as well as the remaining requirements of a metric.

### 3 Christofides Algorithm

The Christofides algorithm [1] is a construction heuristic based on the minimum spanning tree of the graph. The main steps of the algorithm are: perfect matching of the vertices of the minimum spanning tree with an odd degree, combining the edges from



the perfect matching with the minimum spanning tree, forming an Eulerian circuit on the result, converting the Eulerian circuit into a Hamiltonian circuit by skipping repeating vertices. The total sum of the edge weights (tour length) of the so gained tour over all nodes of the graph is guaranteed to be within 1 and 1.5 times the length of the optimal tour, if the edge weights satisfy the triangle inequality.

As shown in [2] this algorithm can also be used to obtain a near optimal solution for problems with open paths. Therefore the start and end points of open paths are treated as separate nodes. In order to guarantee that the open paths are traversed, the edge weights between these nodes are set to a value less than the smallest edge weight resulting from any connecting trajectory. But as stated in [2] this leads to the downside that the triangle inequality is no longer satisfied and the major benefit, which is the upper bound of 150 % of the optimal tour length, does no longer apply.

#### 4 Application of Lin-Kernighan-Helsgaun Algorithm to Time Optimal Sequencing of Open and Closed Paths

In contrast to the Christofides algorithm, which terminates once a feasible solution is found, the Lin-Kernighan algorithm modified by Helsgaun (LKH) [3] is an iteratively improving heuristic. After a preprocessing phase, essentially based on an extended minimum spanning tree, a suboptimal initial solution is generated with any suitable and fast construction heuristic. This initial solution is then improved by so called  $k$ -opt exchanges, which means that in every iteration step  $k$  edges of the current tour are replaced by  $k$  other edges in order to improve the tour. Special heuristic rules are applied to decide which edges should be removed and which edges should be used instead. This drastically reduces the according search spaces and consequently also the calculation time. To decrease the calculation time even further the  $k$ -opt exchanges are constructed sequentially from  $k = 2$  to  $k = 5$ . Once an improvement is found the exchange is applied immediately and the algorithm proceeds with the next iteration step. The algorithm terminates when no further improvement of the tour length with respect to  $k \leq 5$  and the applied heuristic rules can be found. This algorithm can be applied straight forward to a problem with solely closed paths. In order to use this algorithm with open and closed paths some modifications in the problem setup and the algorithm are necessary.

In the preprocessing phase and for the heuristic rule evaluation the start and end points of an open path are represented by one node of the graph. Whenever a distance measure related to a node representing an open path is needed all combinations of end points are considered and the edge with the minimum weight is chosen as depicted in figure 4.

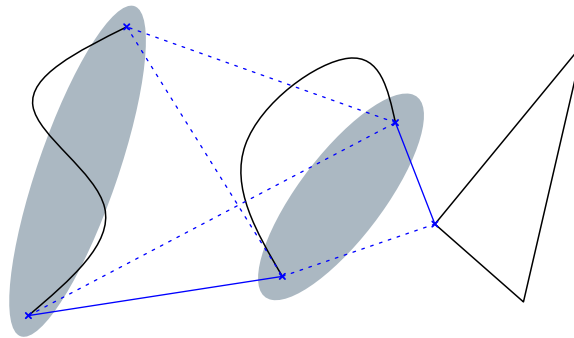


Figure 4: Definition of edges in case of open paths

However in the construction and improvement phase it has to be ensured, that exactly one edge is leading to/from either end point of an open path. Additionally on every iteration step, whenever an edge containing a node representing an open path is considered to be added to the current tour, a local subproblem has to be solved. This subproblem checks whether flipping the sequential order of the two end points of the affected open path may improve the solution.

A detailed description of the full algorithm as well as the results of comparing these two heuristic approaches with the exact solution regarding calculation time and solution quality will be presented in the full paper.

#### Acknowledgments

Supported by the "LCM - K2 Center for Symbiotic Mechatronics" within the framework of the Austrian COMET-K2 program.

#### References

- [1] N. Christofides, "Worst-case analysis of a new heuristic for the travelling salesman problem," tech. rep., Carnegie-Mellon Univ Pittsburgh Pa Management Sciences Research Group, 1976.
- [2] M. Jörgl, H. Gatringer, and A. Müller, "An Almost Time Optimal Route Planning Method for Complex Manufacturing Topologies," in *Computer Aided Systems Theory – EUROCAST 2015*, pp. 673–680, Springer International Publishing, 2015.
- [3] K. Helsgaun, "An effective implementation of the Lin–Kernighan traveling salesman heuristic," *European Journal of Operational Research*, vol. 126, no. 1, pp. 106–130, 2000.

# Delayed control of an unstable chain of integrator: An interesting relation between the system parameter and the admissible time lag.

Balazs A. Kovacs, Tamas Insperger

Department of Applied Mechanics  
Budapest University of Technology and Economics  
Muegyetem rkp. 3, 1111 Bp., Hungary  
balazs.kovacs@mm.bme.hu

MTA Lendulet Human Balancing Research Group  
Budapest University of Technology and Economics  
Muegyetem rkp. 3, 1111 Bp., Hungary  
insperger@mm.bme.hu

## EXTENDED ABSTRACT

### 1 Introduction

In this study, a benchmark problem was taken under investigation, namely a cascade of simple integrator as a plant and controlled via delayed state feedback. One crucial property of this plant, that it has an unstable positive feedback, which requires control in order to maintain the desired set point. A simple example could be constructed with one integrator  $n = 1$ , such as the model of exponential growth. Another example for a double integrator  $n = 2$ , one can think of this as a simple pendulum turned upside-down, where the pinpoint is under the rod. In both cases, the main system parameter defines the stability of the equilibrium.

It should be noted that the problem was extensively studied by many [1, 2, 3, 4], from many aspects, such as controllability, detectability and stabilizability. Various conditions were already identified regarding stability and stabilizability of linear time invariant systems, but generally for stable plants or without delay dependent conditions. It was shown that, for a stable chain of integrator arbitrarily large  $\tau \geq 0$  is admissible in order to achieve asymptotic stability [3, 4]. On the other hand, an unstable system must be controlled to achieve the requirements, which raises the question of stabilizability and a bound for maximal delay. This phenomena is usually inevitable, due to the finite speed of information propagation in any medium (solid, fluid, networks, etc.).

### 2 Problem statement

Generally in control theory, the object is focused on stable or marginally stable system. The stabilizability of these systems is closely related to controllability but should not be mixed. Open loop plants can be stabilized by state feedback by choosing the correct gains. However, time delay in the input of the closed loop system can cause unstable behavior beyond a certain point. This can be simply explained by the fact, that the open loop system depart the equilibrium state determined by its time constant and the controller is not able to react fast enough due to the time delay. This suggest, along with other researches [5], that there is a connection between maximal admissible delay ( $\tau_{crit}$ ) and the time constant of an unstable integrator. Time constant in this sense is different than the one used in control theory (generally defined for stable plants), but has the same role. Now, consider the following simple ( $n = 1$ ) unstable integrator with a delayed input

$$\dot{y}_1(t) = by_1(t) + u(t - \tau), \quad (1)$$

where  $b > 0$  is the system parameter or time constant. Introducing a chain of integrator on top of that will result in a more complex behavior, while the stability properties and the dominant root is placed similarly on the complex plane. Eq. (1) can be generalized for a chain of integrator ( $n \geq 2$ ), such as

$$\begin{aligned} \dot{y}_i(t) &= y_{i+1}(t), \quad i = 1, \dots, n-1 \\ \dot{y}_n(t) &= by_1(t) + u(t - \tau). \end{aligned} \quad (2)$$

In order to stabilize the open loop system a suitable controller has to be designed. State feedback is proven to be effective in pole placement, when the eigenvalues of the system are controllable. The control input is formulated as,

$$u(t) = - \sum_{j=0}^{n-1} a_j y_{j+1}(t) - a_n \dot{y}_n(t), \quad (3)$$

where  $a_j$ ,  $j = 1, \dots, n$  are the feedback gains. The term  $a_n \dot{y}_n(t)$  is not necessary for stabilization, but can improve the performance of the controller. Due to this, the governing system is a neutral functional differential system of equations. Ultimately, the goal is to determine the relation between the system parameter  $b$  and the critical time delay. Furthermore, the concept could reflect or even give insight on the stabilizability of unstable system with time delay involved in the control loop.

### 3 Results

In case when there is no delay  $\tau = 0$ , a  $n^{\text{th}}$  order polynomial has to be investigated. This was done already by many and conditions are readily available for determining stability. An important observation is that, for asymptotic stability, the necessary number of

control inputs (control gains) cannot be less than the order of the system. This can be explained by the fact, that the number of poles are the same as the order of regular polynomials, therefore it needs at least  $n$  control variable. Assuming the delayed state feedback, the characteristic equation of (2) can be written in a general form as,

$$\lambda^n - b + e^{-\lambda\tau} \sum_{j=0}^n a_j \lambda^j = 0. \quad (4)$$

Here  $n$  represents the number of integrator in the chain or the order of the system in other words. Eq. (4) is called a quasi-polynomial due to the delay term, i.e., infinitely many roots appear on the complex plane. The stability of neutral delay differential equations depends greatly on the coefficient of the neutral term [6]. Therefore, a necessary condition for stabilizability is  $|a_n| \leq 1$ . Several methods exist in practice to determine the stability properties of delayed system, but usually a combination of them has to be used to get a full picture about stabilizability. The system is, by nature, has infinitely many poles on the closed left half of the complex plane. By rigorous analysis, one can observe that such a delayed system loses its stability in a multiplicity induced manner [7]. At the margin of stability the system has zero roots with multiplicity of  $n + 1$ . This property can be used in order to determine the control gains as well as the critical delay. A closed formula, generalized for  $n$  integrator can be deduced as

$$\tau_{\text{crit}} = \sqrt[n]{\frac{n!(a_n + 1)}{b}}. \quad (5)$$

Another necessary condition for stabilizability corresponds to the delay of the input signal with regular state feedback. It is inevitable for the controller to act faster than a critical time limit  $\tau \leq \tau_{\text{crit}}$ , in order to achieve stability. Interestingly, the critical delay for a system described here is inversely proportional to  $n^{\text{th}}$  root of the system parameter  $b$ .

#### 4 Discussion

The study was focusing on a chain of integrators with an unstable open loop plant and controlled via a delayed state feedback. The stabilizability of the system was investigated with special focus on the admissible delay. It was observed, that the maximal delay allowed in the closed loop system depends on the system parameter of the chain as well as, on the order of the system. Along this observation, it can be stated that the critical delay has a close connection to the rightmost root of the unstable system. The results presented here, are specific to the model discussed. On the other hand, it can reflect on the control of higher order system or multi-body systems. This might be straightforward, but further investigation is necessary for the generalization of the results.

#### Acknowledgments

The research reported in this paper and carried out at BME has been supported by the NRD Fund (TKP2020 IES, Grant No. BME-IE-BIO and TKP2020 NC, Grant No. BME-NC) based on the charter of bolster issued by the NRD Office under the auspices of the Ministry for Innovation and Technology.

#### References

- [1] E. D. Sontag. Mathematical control theory: Deterministic finite dimensional systems. Springer-Verlag, New York, 1998.
- [2] F. Mazenc, S. Mondie, S.-I. Niculescu. Global asymptotic stabilization for chains of integrators with a delay input. IEEE Trans. Autom. Control, vol. 48/1, pp 57-63, 2003.
- [3] S.-I. Niculescu, W. Michiels. Stabilizing a Chain of Integrators Using Multiple Delays. IEEE Trans. Autom. Control, vol. 49/5, pp 802-807, 2004.
- [4] Z. Lin, H. Fang. On asymptotic stabilizability of linear systems with delayed input. IEEE Trans. Autom. Control, vol. 52/6, pp 998-1013, 2007.
- [5] G. Stepan, L. Kollar. Balancing with reflex delay. Mathematical and Computer Modeling, vol. 31, pp 199-205, 2000.
- [6] W. Michiels, S.-I. Niculescu. Stability and stabilization of time-delay systems: an eigenvalue-based approach. Soc. for Industrial and Applied Mathematics, 2007.
- [7] I. Boussaada, S.-I. Niculescu. Characterizing the codimension of zero singularities for time-delay systems. Acta Applicandae Mathematicae, vol.145, pp 47-88, 2016.

# Reinforcement Learning Assisted Robotic Contact Tasks

Siamak Arbatani<sup>1</sup>, József Kövecses<sup>1</sup>, Marek Teichmann<sup>2</sup>

<sup>1</sup> Department of Mechanical Engineering and  
Centre for Intelligent Machines  
McGill University  
817 Sherbrooke St. West  
Montréal, Québec H3A 0C3, Canada  
[siamak.arbatani, jozsef.kovecses]@mcgill.ca

<sup>2</sup> CMLabs Simulations  
645 Wellington  
Montréal, Québec H3C 1T2, Canada  
marek@cm-labs.com

## EXTENDED ABSTRACT

### 1 Introduction

Conventional feedback control of robotic insertion tasks is challenging due to the presence of the contact forces. A small misalignment between the insertion tool and socket can lead to jamming during the insertion as a result of contact forces. Reinforcement learning (RL) has shown strong potential for learning of the control policies in challenging robot control scenarios. In this work, we examine a potential augmentation of the conventional control with RL to avoid jamming during robotic insertion tasks.

### 2 Modelling of jamming during robotic contact

Establishment of contacts between tool and socket is inevitable and slightest misalignment between the tool and socket would lead to increasing the contact forces and eventually the tool would jam in the socket. Appropriate contact modelling methods are needed to represent jamming in an insertion task [1] schematically shown in Fig. 1. In this work, the jamming phenomena is modelled using the Vortex simulation environment [1]. A 3D model of the robotic arm is constructed in Vortex. Each link of the arm is modelled as a 6 DOF rigid body and actuated joints are defined between the links to construct the arm mechanism.

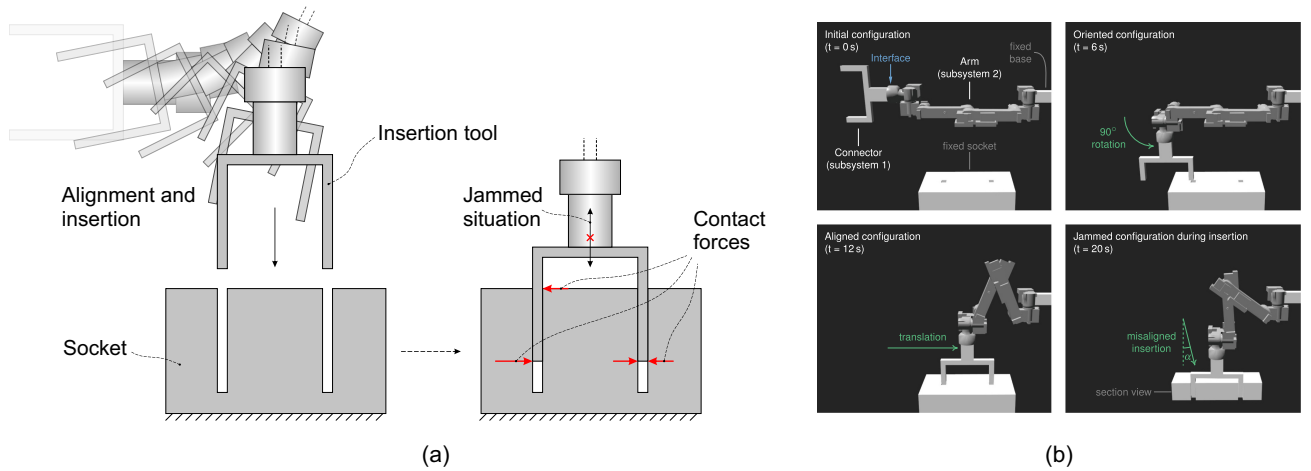


Figure 1: (a) Jamming of a robot tool during the insertion task, (b) Model of a robotic arm performing a contact task with misaligned socket, which leads to jamming of the connector in the socket [1].

### 3 Training of an RL agent for the insertion task

An RL training environment is constructed from the insertion model outlined in the previous section. The observation space in this environment is defined as the contact interaction force and torque components between the tool and the end effector, the joint angles and absolute position of the end effector. On the other hand, a continuous action space is defined as added components to the joint velocities. Based on the inverse kinematics (IK) formulation of the modelled robotic arm, angular velocities of the three active joints during the insertion step are computed as follows:

$$\begin{aligned} v_S &= V_S \\ v_E &= V_E - V_S \\ v_W &= -V_E \end{aligned} \tag{1}$$

where  $v_S$ ,  $v_E$  and  $v_W$  are angular velocities of shoulder, elbow and wrist joints (shown in Fig. 2), and  $V_S$  and  $V_E$  are angular velocity components computed in terms of the insertion velocity and the insertion angle.

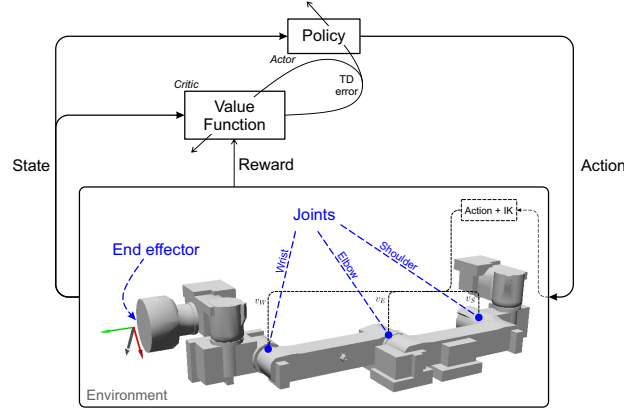


Figure 2: DDPG agent and robotic arm environment.

The deep deterministic policy gradient (DDPG) algorithm is used in this work on the grounds that the continuous action space is needed for this training environment (Fig. 2). A DDPG agent is an actor-critic RL agent which searches for an optimal policy with maximum cumulative long-term reward [2]. Actions of the DDPG agent,  $\mathbf{a} = [a_0 \ a_1]^T$ , are augmented with the joint velocities as:

$$\begin{aligned} v_S &= V_S + a_0 \\ v_E &= V_E - V_S + (a_1 - a_0) \\ v_W &= -V_E - a_1 \end{aligned} \quad (2)$$

The reward function is designed so use the absolute values of the force and torque components sensed at the end effector (interaction force and torque between the tool and end effector) and receive reward when the end effector advances in the predefined motion path for the insertion. Four layers of 32 units with ReLU activation functions are used for each of the actor and critic networks and the agent is trained with Adam optimizer for 500 episodes. Keras-rl2 [3] with TensorFlow 2 backend is used for the DDPG agent implementation and training. Contact force and torque components are plotted in Fig. 3 for both the IK and RL assisted cases. It can be seen that the RL agent tends to induce low amplitude vibration at the end effector which seems to ease the insertion action. The jamming spikes at step = 240 are smaller and short-lived in the RL assisted scenario, in contrast to the purely IK control scenario.

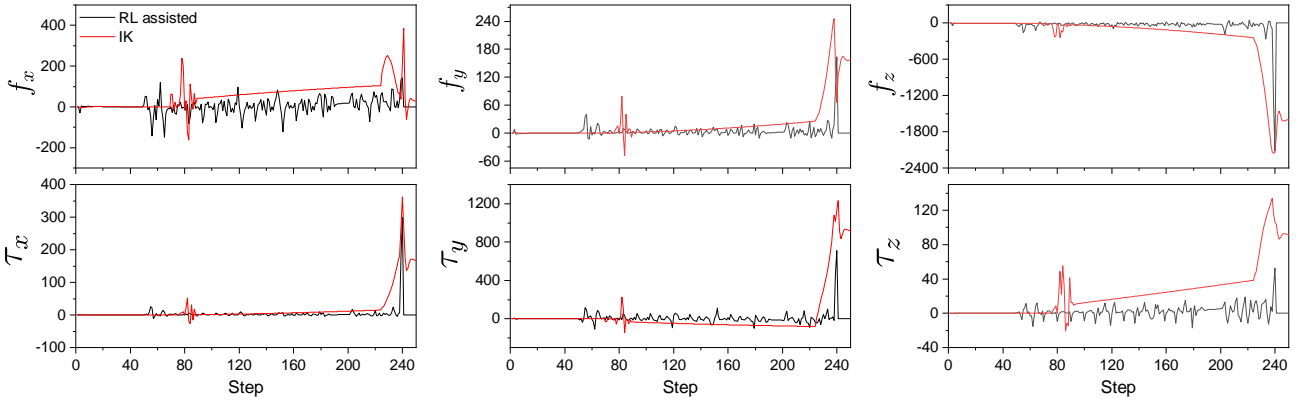


Figure 3: Constraint force and torque for IK and RL assisted control of the insertion task.

## References

- [1] A. Peiret., F. González, J. Kövecses, M. Teichmann, A. Enzenhoefer. Model-Based Coupling for Co-Simulation of Robotic Contact Tasks. IEEE Robotics and Automation Letters, 5(4):5756-5763, 2020.
- [2] Timothy P. Lillicrap and Jonathan J. Hunt and Alexander Pritzel and Nicolas Heess and Tom Erez and Yuval Tassa and David Silver and Daan Wierstra. Continuous control with deep reinforcement learning. International Conference on Learning Representations (ICLR), 2016.
- [3] T. McNally. keras-rl2. GitHub, <https://github.com/wau/keras-rl2>, 2019.

# Motion Capture Based Model Identification of the Humanoid Robot REEM-C using Static Poses

Felix Aller<sup>1</sup>, Monika Harant<sup>2</sup>, and Katja Mombaur<sup>3</sup>

<sup>1</sup> Institute of Computer Engineering  
Heidelberg University  
Berliner Str. 45, 69120 Heidelberg, Germany  
felix.aller@ziti.uni-heidelberg.de

<sup>2</sup> Department of Mathematics for the Digital Factory  
Fraunhofer Institute for Industrial Mathematics  
Fraunhofer-Platz 1, 67663 Kaiserslautern, Germany  
monika.harant@itwm.fraunhofer.de

<sup>3</sup> CERC Human-Centred Robotics and Machine Intelligence  
University of Waterloo  
200 University Avenue West, Waterloo, Canada, N2L 3G1  
katja.mombaur@uwaterloo.ca

## EXTENDED ABSTRACT

### 1 Introduction

The development of dynamic whole-body motions on complex multibody systems such as humanoid robots is a challenging task and requires knowledge of the exact dynamic properties of the mechanical system. Consequently, much attention is paid to model identification using multibody dynamics, initially for manipulators in the 1980s [1]. This method was extended to be applicable to humanoid robots [2]. Subsequent work further extends this by also including joint torque information of the actuated joints [3]. Each method requires a set of trajectories with the aim to excite all the dynamics of the system in order to consequently minimize the error in the joint torque estimation using inverse dynamics [4]. Both methods have already been compared by applying them to a state-of-the-art humanoid [5]. A disadvantage of dynamic model identification lies in the fact that acceleration data is approximated, which can lead to errors in parameter estimation. Furthermore, most robots, such as the one used in this work, are not equipped with sensors to measure joint torques. It has also not yet been investigated to what extent the simultaneous optimization of all dynamic parameters can lead to redundancies in the optimization problem. In this work we carry out a model identification procedure on the humanoid robot REEM-C by PAL Robotics. We focus on identifying the static parameters and update center-of-mass (COM) locations and masses so that the model best fits the experimental data, which consists of a variety of static poses. This approach of splitting the identification of dynamic and static parameters and the use of static poses allows for a more precise approximation of the latter. The level of model improvement is evaluated by means of a dynamic reference motion.

### 2 Applied Method for Model Identification

Static poses offer the advantage of taking a measurement at a stage when the robot is almost at rest and the measurements are nearly free of noise. One disadvantage, however, is that a large amount of poses are required. Therefore, a set of 172 static poses of the humanoid robot REEM-C was recorded using a state-of-the-art motion capture system and external force plates. A combination of systematic and randomly generated poses was used. We distinguish 6 categories of poses: Double-legged: feet 2 cm apart on one force plate, focus on right arm (1), feet 2 cm apart on one force plate, focus on torso joints (2), feet 2 cm apart on one force plate crouching (3), feet 20 cm apart with both feet on one force plate, and on one force plate each (4) (Fig. 1(a, c)). Single-legged: standing on the right leg, focus on left leg (5), standing on the left leg, focus on right leg (6) (Fig. 1(b)).

For each configuration, the individual degrees of freedom were systematically set to less than 10% and more than 90% of their minimum and maximum joint range. In addition, at least 10 random poses were generated for the categories on both feet.

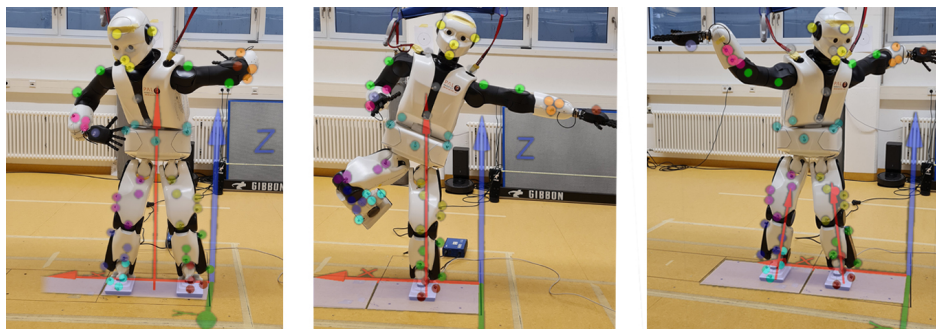


Figure 1: Three different types of static poses of the humanoid REEM-C with applied marker set on force plates with indicated force vector: (a) standing on both feet on one force plate, (b) standing on one foot, (c) standing on both feet on two force plates.

The recorded marker data are fitted to the model using inverse kinematics. Initial experiments indicated a global position error due to gear backlash, which propagates through the entire system when a joint configuration required the ground-projected COM

(GCOM) to be close to the edge of the support polygon. Therefore, by fitting marker data, more accurate joint configurations are calculated than if the internal sensor data were used. For each static pose, the GCOM obtained by the dynamic properties of the model is compared to the GCOM obtained through force plate measurements. Their deviation is minimized by solving a least squares problem by updating a set of static model parameters  $p_s$ :

$$\min_{p_s} \sum_{m=1}^{N_m} \|g_{GCOM}(q_m, p_s) - GCOM_m^{REF}\|^2 \quad (1)$$

$$s.t. \quad g_{mass}(p_s) = M \quad (2)$$

with  $N_m$  the number of poses considered and  $GCOM_m^{REF}$  the recorded GCOM of pose  $m$ . The functions  $g_{GCOM}$  and  $g_{mass}$  calculate the GCOM of pose  $m$  specified by the recorded joint positions  $q$  and the total mass of the robot model based on the current static parameter values  $p_s$ . The measured total mass of the robot is denoted by  $M$ . The parameters consist of the mass and COM location of the main segments of the robot: shank, thigh, pelvis, trunk, upper arm, forearm and hand. Segments consisting of only a motor and a cover could not be considered during the optimization and were fixed at the values given in the original model, as the change in the measured GCOM would be too small and lead to redundancies in the problem formulation. The same applies to the head and foot segments. The optimization problem is solved with the SQP method using Gauss-Newton Hessian and a Levenberg-Marquardt regularization term.

### 3 Improvement of the Original Model

During the optimization the deviation between recorded and model GCOM was reduced from (avg. 9.2 mm, std. 2.3 mm) to (avg. 0.6 mm, std. 0.4 mm). For reference, the actual support polygon of REEM-C when standing on one leg is estimated to be 15.5 cm  $\times$  10.6 cm, with an actual foot size of 21.0 cm  $\times$  14.0 cm. To validate the model identification a dynamic reference motion similar to a human squat exercise was recorded and all the torques were calculated using inverse dynamics. To assess the quality of the model we evaluated the joint torques and forces acting in the base link (residual forces), which should be 0 since these degrees of freedom are not actuated.

Table 1: Avg. [std] residual torques and forces of the base link obtained by inverse dynamics of the squat-motion.

<i>Model</i>	$T_x$ [Nm]	$T_y$ [Nm]	$T_z$ [Nm]	$F_x$ [N]	$F_y$ [N]	$F_z$ [N]
Original Model	5.66 [0.98]	5.98 [4.07]	0.68 [0.48]	1.86 [1.66]	2.28 [1.72]	103.02 [4.03]
Optimized Model	0.87 [0.69]	1.35 [1.01]	0.41 [0.30]	1.86 [1.66]	2.29 [1.73]	2.68 [3.04]

Our results show a significant improvement of the model by updating the segment masses and COM locations. The unaccounted mass of  $\sim 10.5$  kg was distributed to the respective segments thus reducing the vertical force  $F_z$  acting in the base link from 103.02 N to 2.68 N (Tab. 1). The proper distribution of masses is reflected under the concurrent substantial decrease of the residual torques along all axes ( $T_x - T_z$ ). The remaining error is most likely related to the unidentified moments of inertia, which will be improved in future work on basis of the updated parameters.

### Acknowledgments

This work was supported by the project EUROBENCH (European Robotic Framework for Bipedal Locomotion Benchmarking, [www.eurobench2020.eu](http://www.eurobench2020.eu)) funded by H2020 Topic ICT 27-2017 under grant agreement number 779963.

### References

- [1] Atkeson, Christopher G., Chae H. An, and John M. Hollerbach. "Estimation of inertial parameters of manipulator loads and links." *The International Journal of Robotics Research* 5.3 (1986): 101-119.
- [2] Ayusawa, Ko, Gentiane Venture, and Yoshihiko Nakamura. "Identification of the inertial parameters of a humanoid robot using unactuated dynamics of the base link." *Humanoids 2008-8th IEEE-RAS International Conference on Humanoid Robots*. IEEE, 2008.
- [3] Mistry, Michael, Stefan Schaal, and Katsu Yamane. "Inertial parameter estimation of floating base humanoid systems using partial force sensing." *2009 9th IEEE-RAS International Conference on Humanoid Robots*. IEEE, 2009.
- [4] Gautier, Maxime, and Wisama Khalil. "Exciting trajectories for the identification of base inertial parameters of robots." *The International journal of robotics research* 11.4 (1992): 362-375.
- [5] Ogawa, Yusuke, Gentiane Venture, and Christian Ott. "Dynamic parameters identification of a humanoid robot using joint torque sensors and/or contact forces." *2014 IEEE-RAS International Conference on Humanoid Robots*. IEEE, 2014.



# High-Speed Trajectory Tracking on Robotic Arm by Learning the Dynamic Response of the PID Controller with a Neural Network

Baptiste Toussaint<sup>1</sup>, Maxime Raison<sup>1</sup>

<sup>1</sup>Department of mechanical engineering  
Polytechnique Montreal  
Montréal, Canada  
[baptiste.toussaint, maxime.raison]@polymtl.ca

## EXTENDED ABSTRACT

### 1 Context

The transfer of robotics into everyday life is currently accelerating, with 20 million robots expected to be in use worldwide by 2030 [1]. However, today, there are still main obstacles for a mass transfer of robots to society, namely the limitations of dexterity, velocity, and accuracy [2]. Especially, high-speed robots involve significant accelerations, and usually large movements. Successfully performing high-speed trajectories requires either an accurate robot model or an aggressive tracking with high-gain feedback when the model parameters, such as frictions, inertias, masses, etc., cannot be easily computed. As stated in [3]: *“learning to track such trajectories in a safe and reliable way, when accurate models of the arm are not available, is an open problem”*. Even if the traditional PID is known to be stable for position control [4] and relatively easy to use, this one is not effective for aggressive tracking, due to the motor response times. Therefore, more complex methods have been developed for trajectory tracking, mainly the *iterative learning control*, which can be combined with movement primitives, and/or neural network (NN) to learn parameters and variables of the dynamic model (e.g. [3]). But two main practical problems with these complex methods are: 1. generalizing to many trajectories without reducing the accuracy; 2. stabilizing the torque control in robots due to joint friction.

The objective of this study is to propose a control method for high-speed trajectory tracking of a robotic arm, by combining both a PID – stable and easy to implement – and learning the dynamic response of the PID with a NN – to predict and correct its errors. The effectiveness of this method has been tested with a 3D-printed 5 degrees of freedom serial collaborative robotic arm (or “co-bot”) developed in our laboratory.

### 2 Methods

The problem of control was defined as follows:

- 1. Build a dataset of various trajectories of the robotic arm** by using a PID controller for each joint. Building the dataset required an effective feedback of the motors to get accurate data to feed the NN. All data were composed of five variables for each of the five motors: the angle,  $q_i$ , and the angular velocity,  $\dot{q}_i$  of a motor  $i$  at two consecutive instants  $t$  and  $t+\delta$ , i.e.  $q_i(t)$ ,  $q_i(t+\delta)$ ,  $\dot{q}_i(t)$ ,  $\dot{q}_i(t+\delta)$ , and the command,  $u_i(t)$ , sent to this motor during these two instants.
- 2. Train a NN for each joint to learn the dynamic model through the response of the PID controller.** As shown in Figure 1, four variables were used as input features for the NN: the motor angle  $q_i(t)$  and velocity  $\dot{q}_i(t)$  at a given instant  $t$ , and the position  $q_i(t+\delta)$  and velocity  $\dot{q}_i(t+\delta)$  at the next instant  $t+\delta$ . The output variable, or target, from the NN was the positional command  $u_i(t)$  given to the motor during these two instants. By giving several trajectory data to the NN, this one will learn which command to send to each motor to go from a state  $[q_i(t), \dot{q}_i(t)]$  to the next one,  $[q_i(t+\delta), \dot{q}_i(t+\delta)]$ . In an implicit way, this enables to learn the dynamic model of the robotic arm.
- 3. Generate a new set of commands for the motors** that consider the response time of the controller to send the required series of command to each motor, so that these ones execute the desired trajectory. To generate the corrected series of command, we provide the desired  $q_i(t)$ ,  $q_i(t+\delta)$ ,  $\dot{q}_i(t)$ ,  $\dot{q}_i(t+\delta)$  as input to the trained NN. Then, the NN returned the command  $u_i(t)$  to the motor between the two instants  $t$  and  $t+\delta$ .

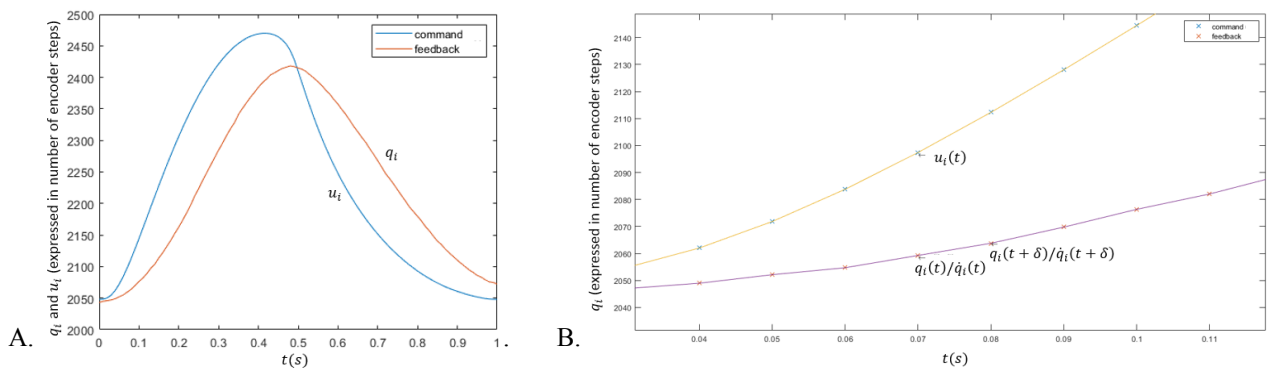


Figure 1. For a given motor  $i$ : A. The given command  $u_i(t)$  along a trajectory, and the corresponding feedback  $q_i(t)$ . B. Zoom in on these curves: feedback motor angles  $q_i(t)$  and  $q_i(t+\delta)$  as feedback features for the NN at all instants  $t$ , and the corresponding position command  $u_i(t)$  as output variable/target from the NN.

### 3 Results

For a given motor  $i$ , Figure 2A presents the error along a tracked trajectory, according to final desired positions and velocities, by comparing these errors between a standard PID and the proposed method combining a PID with dynamics learning by a NN. Figure 2B presents the time evolution of the motor angles  $q_i(t)$  and command  $u_i(t)$  in a PID, and the corresponding corrected  $q_i(t)$  and command  $u_i(t)$  with the proposed method combining PID and NN.

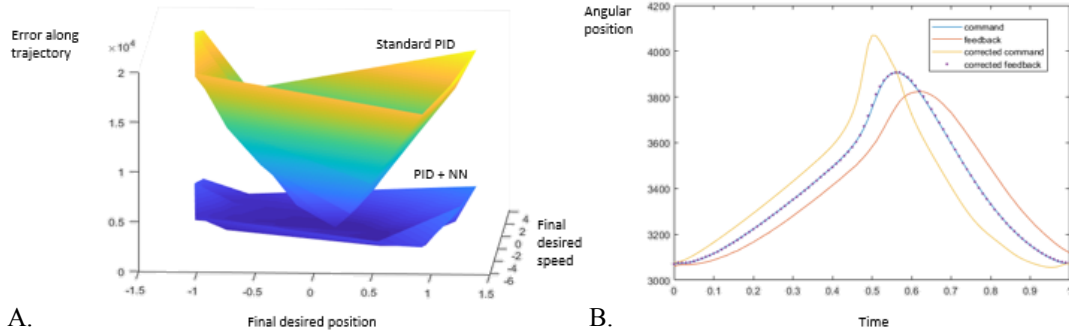


Figure 2. For a given motor  $i$ : A. Error along a tracked trajectory, according to final desired positions and velocities: comparison between a standard PID and the proposed method combining a PID and NN. B. Feedback motor angles  $q_i(t)$  and command  $u_i(t)$  in a PID, and the corresponding corrected feedback  $q_i(t)$  and command  $u_i(t)$  with the proposed method combining PID and NN.

A variety of high-speed trajectory tracking tests with our complete serial co-bot will be presented at the conference.

### 4 Discussion and conclusion

Globally, Figure 2 illustrates the interest of adding a NN to learn the dynamic response of the motor to correct the command so as the motor tracks exactly a desired trajectory. Especially, Figure 2A shows that the error with the proposed method combining PID and NN is relatively stable compared to the simple PID, and significantly lower for large movements and/or high velocities. Figure 2A also shows that the NN minimizes the tracking errors, even when the motors are not powerful enough to track exactly the desired trajectory. In fact, the figure shows that with a classic PID, the more speed and movement are done, the greater the error. Figure 2B shows that using the NN, the error is nearly zero when the motors are powerful enough. The error along the trajectory just starts increase when the limits are reached (on the edge of the figure). These observations could contribute to allow a high-speed position control and to reduce the complexity of the required controller to effectively track an aggressive trajectory. The use of a position control is also more intuitive than a torque control. Another advantage of the proposed method is that it can be transposed to several robots without modification. Indeed, no dynamic model must be given to the NN: this one only requires an accurate feedback of various trajectories. The perspectives of this study are to make easier the command of robotic arms while guaranteeing solid performances, even for aggressive trajectories or robots for which a complete dynamic model is hard to obtain.

### References

- [1] C. Taylor. Robots could take over 20 million jobs by 2030, study claims. <https://www.cnbc.com/2019/06/26/robots-could-take-over-20-million-jobs-by-2030-study-claims.html>; last visit: 24th June 2021.
- [2] A. Billard, K. Danica. Trends and challenges in robot manipulation. *Science* 364.6446, 2019.
- [3] O. Koç, G.J. Maeda, J. Peters. Optimizing the Execution of Dynamic Robot Movements With Learning Control. *IEEE Transactions on Robotics* 35, 909-924, 2019.
- [4] S. Kawamura, F. Miyazaki, S. Arimoto, S. Is a local linear PD feedback control law effective for trajectory tracking of robot motion? *Proceedings. Proceedings of IEEE International Conference on Robotics and Automation*, 1335-1340 vol.3, 1988.

# A Recursive Dynamics Algorithm for Soft Robotic Manipulators Made of Viscoelastic Material

Makoto Iwamura<sup>1</sup>, Kento Hirata<sup>1</sup>, Yoshiki Maeda<sup>1</sup>, Kyuji Oto<sup>1</sup>

<sup>1</sup> Department of Mechanical Engineering  
Fukuoka University  
8-19-1 Nanakuma, Jonan, 814-0180 Fukuoka, Japan  
iwamura@fukuoka-u.ac.jp

## EXTENDED ABSTRACT

### 1 Introduction

In recent years, research and development of robots that exist in the same space as humans and can collaborate with humans have been actively carried out. If the body of a robot for nursing care or home use is made of a hard material, it may cause injury. Therefore, attempts have been made to make a robot with a soft body using rubber or resin. In order to accelerate such research on soft robotics, it is necessary to establish high-speed and stable simulation algorithm for robots containing viscoelastic bodies such as rubber and resin. So far, studies have been conducted to describe viscoelastic bodies by the finite element method and incorporate them into multibody dynamics analysis, but the theory is difficult and the calculation time is enormous. Therefore, in this study, we consider to approximate viscoelastic bodies with finite rigid body segments and connect them with joints and linear viscoelastic elements such as Voigt model and Maxwell model to approximate viscoelastic properties. The recursive dynamics algorithm [1] is used to speed up the calculation, and the generalization- $\alpha$  method [2] is used to stabilize the numerical integration. In particular, we propose a new method on how to incorporate the Maxwell model into recursive dynamics algorithm and generalization- $\alpha$  method. The effectiveness of the proposed method is confirmed by some numerical examples.

### 2 Recursive dynamics algorithm

As an example, consider a two-joint manipulator composed of rubber links as shown in Figure 1. If one rubber link is approximated by two rigid body segments, it can be modeled as shown in Figure 2. Generally, as shown in Figure 3, the relationship between the generalized velocity  $\mathbf{v}_i$  and the generalized acceleration  $\mathbf{a}_i$  of the adjacent body  $i$  and body  $i-1$  can be expressed as follows.

$$\mathbf{v}_i = \mathbf{D}_i \mathbf{v}_{i-1} + \mathbf{J}_i \dot{q}_i \quad (1)$$

$$\mathbf{a}_i = \mathbf{D}_i \mathbf{a}_{i-1} + \mathbf{J}_i \ddot{q}_i + \boldsymbol{\beta}_i \quad (2)$$

where  $q_i$  is the joint variable of the  $i$ -th joint of the model approximated by finite segments,  $\mathbf{D}_i$  is the transformation matrix,  $\mathbf{J}_i$  is the Jacobian matrix, and  $\boldsymbol{\beta}_i = \dot{\mathbf{D}}_i \mathbf{v}_{i-1} + \dot{\mathbf{J}}_i \dot{q}_i$ . On the other hand, the relation of the generalized force  $\mathbf{Q}_i^J$  transmitted through the joint  $i$  and the joint driving force  $\tau_i$  of the  $i$ -th joint can be expressed by the following equations.

$$\mathbf{Q}_i^J = \mathbf{M}_i \mathbf{a}_i + \mathbf{h}_i - \mathbf{Q}_i^g + \mathbf{D}_{i+1}^T \mathbf{Q}_{i+1}^J \quad (3)$$

$$\tau_i = \mathbf{J}_i^T \mathbf{Q}_i^J + \bar{Q}_i \quad (4)$$

where  $\mathbf{M}_i$  is the generalized mass matrix,  $\mathbf{h}_i$  is the centrifugal and Coriolis force, and  $\mathbf{Q}_i^g$  is the generalized force due to gravity. In addition,  $\bar{Q}_i$  is the force due to the linear viscoelastic element. In the case of the Voigt model in which the spring and damper are introduced in parallel as shown in Figure 4 (a), the following equation is obtained.

$$\bar{Q}_i(t) = k_i(q_i(t) - q_i^0) + c_i \dot{q}_i(t) \quad (5)$$

On the other hand, in the case of the Maxwell model in which the spring and damper are introduced in series as shown in Figure 4 (b), the following equation can be derived.

$$\bar{Q}_i(t) = e^{-\frac{k_i}{c_i}t} \left\{ \int_0^t e^{\frac{k_i}{c_i}\tau} k_i \dot{q}_i(\tau) d\tau - Q_i^0 \right\} \quad (6)$$

Here,  $k_i$  is the spring constant,  $c_i$  is the viscous damping coefficient, and  $Q_i^0 = \bar{Q}_i(0)$ . It is easy for the Voigt model, but it is not obvious how to incorporate it into the recursive dynamics algorithm and generalization- $\alpha$  method for the Maxwell model. In this paper, we propose a method of discretizing and incorporating it into calculations.

Inverse dynamics calculation can be conducted by first calculating equations (1) and (2) from  $i = 1$  to  $i = N$ , and then equations (3) and (4) from  $i = N$  to  $i = 1$ . By repeatedly using this inverse dynamics calculation, the generalized mass matrix  $\mathbf{M}$  and the centrifugal and Coriolis force  $\mathbf{h}$  of the equations of motion in minimal form

$$\mathbf{M}(\mathbf{q})\ddot{\mathbf{q}} + \mathbf{h}(\mathbf{q}, \dot{\mathbf{q}}) = \boldsymbol{\tau} \quad (7)$$

can be calculated efficiently.

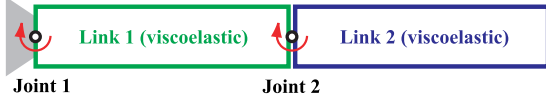


Figure 1: 2 link manipulator made of silicone rubber

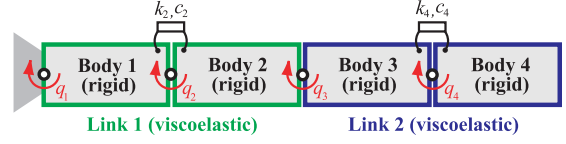


Figure 2: Finite segment approximation

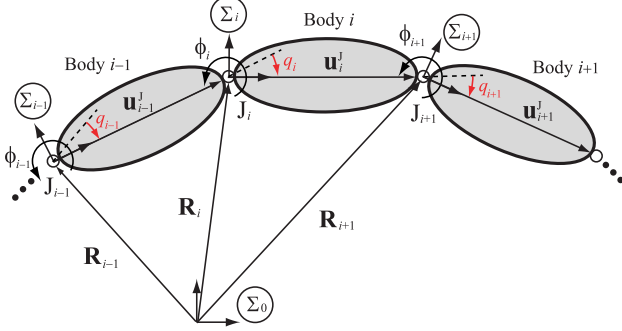


Figure 3: Relationship between neighboring bodies

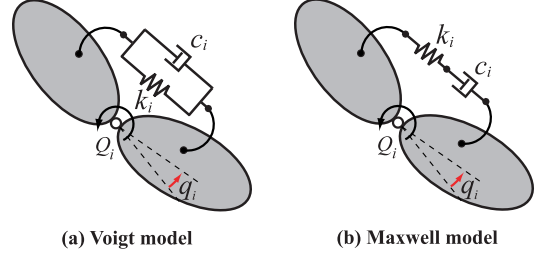


Figure 4: Viscoelastic dynamics model added to joints

### 3 Numerical integration method

Since robots including viscoelastic bodies are generally stiff systems, we use the generalized- $\alpha$  method, which is an implicit method with excellent stability. Divide the interval  $t \in [0, t_f]$  for which the solution should be found at equal intervals  $h$  such as  $0 = t_0 < t_1 < \dots < t_{p-1} < t_p = t_f$ . The value of  $\mathbf{q}(t)$  at time  $t_n$  is expressed as  $\mathbf{q}_n$ . When the generalized- $\alpha$  method is used, the residual of the equations of motion (7) at  $t = t_{n+1}$  can be expressed as follows.

$$\mathbf{e}(\mathbf{q}_{n+1}) \equiv \mathbf{M}(\mathbf{q}_{n+1})\ddot{\mathbf{q}}_{n+1}(\mathbf{q}_{n+1}) + \mathbf{h}(\mathbf{q}_{n+1}, \dot{\mathbf{q}}_{n+1}(\mathbf{q}_{n+1})) - \boldsymbol{\tau}_{n+1} \quad (8)$$

From the above equation, the Jacobian matrix of the residual  $\mathbf{e}$  with respect to  $\mathbf{q}_{n+1}$  can be calculated as follows.

$$\frac{\partial \mathbf{e}}{\partial \mathbf{q}_{n+1}} = \beta' \mathbf{M}(\mathbf{q}_{n+1}) + \gamma' \mathbf{D}'(\mathbf{q}_{n+1}) + \mathbf{K}'(\mathbf{q}_{n+1}) \equiv \mathbf{S}(\mathbf{q}_{n+1}) \quad (9)$$

where  $\mathbf{K}'$  and  $\mathbf{D}'$  are matrices defined as follows.

$$\mathbf{K}'(\mathbf{q}_{n+1}) \equiv \frac{\partial \mathbf{M}(\mathbf{q}_{n+1})}{\partial \mathbf{q}_{n+1}} \ddot{\mathbf{q}}_{n+1}(\mathbf{q}_{n+1}) + \frac{\partial \mathbf{h}(\mathbf{q}_{n+1}, \dot{\mathbf{q}}_{n+1}(\mathbf{q}_{n+1}))}{\partial \mathbf{q}_{n+1}}, \quad \mathbf{D}'(\mathbf{q}_{n+1}) \equiv \frac{\partial \mathbf{h}(\mathbf{q}_{n+1}, \dot{\mathbf{q}}_{n+1}(\mathbf{q}_{n+1}))}{\partial \dot{\mathbf{q}}_{n+1}} \quad (10)$$

Once the Jacobian matrix  $\mathbf{S}(\mathbf{q}_{n+1})$  is calculated,  $\mathbf{q}_{n+1}, \dot{\mathbf{q}}_{n+1}, \ddot{\mathbf{q}}_{n+1}$  at the time  $t = t_{n+1}$  can be obtained by repeating the following calculation until  $\mathbf{e}(\mathbf{q}_{n+1}) = \mathbf{0}$  is satisfied within the margin of error.

$$\mathbf{S}(\mathbf{q}_{n+1}^{(k)}) \Delta \mathbf{q}_{n+1}^{(k)} = -\mathbf{e}^{(k)}, \quad \mathbf{q}_{n+1}^{(k+1)} = \mathbf{q}_{n+1}^{(k)} + \Delta \mathbf{q}_{n+1}^{(k)}, \quad \dot{\mathbf{q}}_{n+1}^{(k+1)} = \dot{\mathbf{q}}_{n+1}^{(k)} + \gamma' \Delta \dot{\mathbf{q}}_{n+1}^{(k)}, \quad \ddot{\mathbf{q}}_{n+1}^{(k+1)} = \ddot{\mathbf{q}}_{n+1}^{(k)} + \beta' \Delta \ddot{\mathbf{q}}_{n+1}^{(k)} \quad (11)$$

Iterative calculations are required at each step, and the Jacobian matrix must be calculated each time. Here, we propose a method for calculating the Jacobian matrix at high speed and without approximation using the recursive dynamics algorithm, in order to shorten the calculation time. From equation (10), it can be seen that  $\mathbf{K}'$  and  $\mathbf{D}'$  can be expressed as follows.

$$\mathbf{K}'(\mathbf{q}_{n+1}) = \frac{\partial}{\partial \mathbf{q}} \{ \mathbf{M}(\mathbf{q}) \ddot{\mathbf{q}} + \mathbf{h}(\mathbf{q}, \dot{\mathbf{q}}) \} \Big|_{t=t_{n+1}} = \frac{\partial \boldsymbol{\tau}}{\partial \mathbf{q}} \Big|_{t=t_{n+1}}, \quad \mathbf{D}'(\mathbf{q}_{n+1}) = \frac{\partial}{\partial \dot{\mathbf{q}}} \{ \mathbf{M}(\mathbf{q}) \ddot{\mathbf{q}} + \mathbf{h}(\mathbf{q}, \dot{\mathbf{q}}) \} \Big|_{t=t_{n+1}} = \frac{\partial \boldsymbol{\tau}}{\partial \dot{\mathbf{q}}} \Big|_{t=t_{n+1}} \quad (12)$$

That is,  $\mathbf{K}'$  is the partial derivative of the inverse dynamics relation with respect to  $\mathbf{q}$ , and  $\mathbf{D}'$  is the partial derivative of the inverse dynamics relation with respect to  $\dot{\mathbf{q}}$ . Using this, we formulate an algorithm that calculates  $\mathbf{K}'$  and  $\mathbf{D}'$  strictly and at high speed based on the recurrence formula from (1) to (4) of inverse dynamics. At that time, since the calculation of  $\partial \bar{Q}_i / \partial q_i$  and  $\partial \bar{Q}_i / \partial \dot{q}_i$  are also required, a new calculation method is derived.

### References

- [1] M. Iwamura, H. Sugiyama and K. Sato. Recursive inverse and forward dynamics algorithms for flexible manipulators. Proceedings of the 6th Asian Conference on Multibody Dynamics, USB 9 pages, 2012.
- [2] M. Arnold and O. Bruls, Convergence of the generalized- $\alpha$  scheme for constrained mechanical systems. Multibody System Dynamics, 18: 185-202, 2007.

# Mathematical Model and Control Simulation of Hexapod Robot Locomotion in Tripod Gait

Krešimir Osman<sup>1</sup>, Trpimir Alajbeg<sup>2</sup>

<sup>1</sup>Zagreb University of Applied Sciences  
Department of Electrical Engineering  
Konavoska 2, 10000 Zagreb, Croatia  
kresimir.osman@tvz.hr

<sup>2</sup>Zagreb University of Applied Sciences  
Department of Electrical Engineering  
Konavoska 2, 10000 Zagreb, Croatia  
trpimir.alajbeg@tvz.hr

## EXTENDED ABSTRACT

The application of behavioural simulations (kinematic and dynamic model) in robotics have been quite popular in recent years. One of the important reasons is that it allows developers and researchers to predict, test and validate robotic performance before prototyping and production [1]. It also allows faster and easier improvement of management strategies, focused on safety and more cost-effectiveness.

Using knowledge from nature, i.e. by studying and investigating the locomotion of animals helped researchers develop different types of so-called bio-inspired robots [2]. Among these, the most convenient is the researching of arthropods that have six legs and thus simply maintain their stability (insects, centipedes, symphylans, millipedes etc.). They show quite a robustness of the system in case of damage to the legs. One of the typical examples of the development of robots from this group is the hexapod robot based on the anatomy and locomotion of insects.

Hence, researchers encounter the problem of operating such robotic systems, which are quite complex and have an increased number of degrees of freedom (DOF) of motion due to the performance of the legs of robots from multiple ankles (links) [2]. In practice, many commercial six-legged robots have already been carried out, which have found their application in many areas such as [3]: research in remote and inaccessible places (space, seabed, volcanoes, etc.), dangerous environments (like military operations), construction work, transport operations, etc.

Therefore, in hexapod robots, two typical systems at architectures and locomotions originating from spider insects (hexagonal hexapod) and cockroaches (rectangular hexapod) can be found in the literature [4]. In this paper, a robot configuration based on a rectangular hexapod system architecture is described. The hexapod robot is a type of mobile robot that achieves its locomotion using six legs (three on each side of chassis), of which at least three or more legs must be on the ground to achieve their stable condition.

When moving in nature, insects can use different types of gait. Inspired by this [5], the most common types of gait they can perform (4 typical walks) of hexapod robots are wave gait, tetrapod gait, transition gait and tripod gait. In this paper, a model of behaviour based on tripod gait is presented. The reason that tripod gait is the most interesting because of movement speed. It is the fastest gait of insects when they maintain their body in dynamic balance [6].

Figure 1 shows the simplified product architecture of a hexapod robot, while figure 2 shows model of one hexapod robot (observed) leg with all the joints and links. On this basis, kinematic analysis was done to obtain a mathematical model of the robot. The Denavit-Hartenberg (D-H) method [7] was used to establish the joint coordinate system of a hexapod robot for its one leg. Individual parameters on each joint and variables on joints (1 – hip joint, 2- knee joint and 3 - ankle joint) are defined, and the equation of motion for the leg is obtained. On each link of the open kinematic chain, right-wing orthonormal coordinate systems are systematically joined. As the final equation, a matrix equation is obtained, and the position of the top of the robot's leg relative to the coordinates of the robot's body. Solving the problem of inverse kinematics gives the values of the angles of rotation for each of the joints, i.e., the servo motors on them, for a given point in space at the observed robot leg.

When planning the trajectory of the movement of hexapod robots, the movement of the robot's leg in its stance (supporting) phase and swing (suspending) phase, and the transfer phase should be considered throughout the moving cycle. When performing the behaviour of the robot, the simulation was made for flat terrain. The simulation was performed using a combination of MATLAB Simulink tool and Simscape Multibody environment. The last one is very acceptable for block diagram modelling because it allows a block view of all sensors, bodies, system elements, joints and constraints using block components from the Simscape™ family. It also provides the possibility of 3D displaying the animation of the dynamics of the observed robot system. The control algorithm is derived using a PID controller on one robot leg (in each joint). The controller's parameters are adjusted on one leg of the robot, and after that, this is used to adjust the control on the other legs in this way. In joints 1 and 2 PID algorithm is based on position control [8] while in joint 3 is based on force control [8].

Equations for forward dynamics which represents the relationships between the system of coordinates of the robot base (global system) with the base of the robot leg (leg coordinate system) (1) - (3), obtained by the Denavit-Hartenberg method and homogeneous transformations:

$$p_x = \cos\theta_1(l_1 + l_2 \cdot \cos\theta_2 + l_3 \cdot \cos(\theta_2 - \theta_3)) \quad (1)$$

$$p_y = \sin\theta_1(l_1 + l_2 \cdot \cos\theta_2 + l_3 \cdot \cos(\theta_2 - \theta_3)) \quad (2)$$

$$p_z = d_1 + l_2 \cdot \sin\theta_2 + l_3 \cdot \sin(\theta_2 - \theta_3) \quad (3)$$

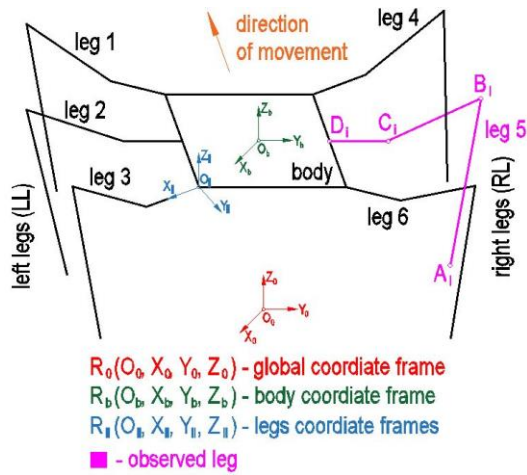


Figure 1: Product architecture of a hexapod robot

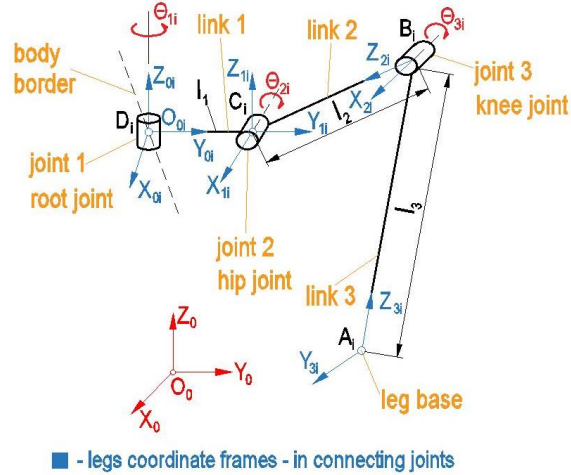


Figure 2: Model of a hexapod robot observed leg

In this paper, a development of mathematical model and the control algorithm of a hexapod robot during tripod gait locomotion is described. Simulation is performed using combination of MATLAB Simulink tool and Simscape Multibody environment. The intention is to take advantage of that, so that could be used in teaching laboratory exercises in one of the courses at the graduate study on Zagreb University of Applied Sciences. The mathematical model presented is derived according to a model based on rectangular hexapod design configuration, using PID controllers in each leg joint. During the conduct of the research it has been proven that a major drawback is use of a PID controller which is quite difficult to set their controller parameters. When developing a control algorithm, the simplest example of robot's usage locomotion on flat terrain is taken here.

Each leg has three joints, each joint contains a servo motor. In the starting position, angle in the joint A is set to value  $0^\circ$ , in the joint B to  $45^\circ$  and in joint C to value  $30^\circ$ . During robot moving, it is first planned to move legs 1, 3 and 5 (marked in Figure 1). After these legs touch the ground, the same movement is achieved by legs 2, 4 and 6 with the same amplitude and frequency of movement. In the presented simulation, the robot walk along a straight path of a certain distance was performed, and therefore the robot movement analysis was performed.

The development and application of another regulator based on adaptive control, as well as, its application for these robots on uneven terrains, has been presented as several directions for future research.

## Acknowledgments

The research presented in this paper is part of internal project „KO006-2020/1 - Establishment and equipping of laboratory for the course „Systems and Control Algorithms in Robotics" and „Mobile Robotics" at the Polytechnic Graduate Professional Study of Electrical engineering" supported by Zagreb University of Applied Sciences, Zagreb, Croatia.

## References

- [1] M. Shahriari. Design, Implementation and Control of a Hexapod Robot using Reinforcement Learning Approach", M.Sc. Thesis, Kish Island, Iran, 2013.
- [2] S. Mănoiu-Olaru and M. Nițulescu. Matlab Simulator for Gravitational Stability Analysis of a Hexapod Robot. The Romanian Review Precision Mechanics, Optics & Mechatronics, No. 39, 2011.
- [3] J. A. Tenreiro Machado and M. F. Silva. An Overview of Legged Robots. MME 2006 – International Symposium on Mathematical Methods in Engineering, Ankara, Turkey, 2006.
- [4] G. Carbone and M. Ceccarelli. Legged Robotic Systems", In: Cutting Edge Robotics ARS Scientific Book, Wien, pp. 553-576, 2005.
- [5] R. Campos, V. Matos, Cristina Santos. Hexapod locomotion: A nonlinear dynamical systems approach. IECON 2010 - 36th Annual Conference on IEEE Industrial Electronics Society
- [6] X. Duan, W. Chen, S. Yu and J. Liu. Tripod gaits Planning and Kinematics Analysis of a Hexapod Robot. 2009 IEEE International Conference on Control and Automation, Chistchurch, New Zealand, pp. 1850-1855, 2009.
- [7] R.P. Paul. Robot Manipulators: Mathematics, Programming and Control, The Computer Control of Robot Manipulators. The MIT Press, Cambridge Massachusetts and London, England, 1981.
- [8] Z. Kovačić, S. Bogdan, V. Krajčič. Osnove robotike. Graphis, Zagreb, Croatia, 2002.

**Section**

**OPTIMIZATION, SENSITIVITY ANALYSIS, AND PARAMETER IDENTIFICATION**

OPTIM-1-2



# Sensitivity Analysis for Thermohydrodynamic Models: Uncertainty Analysis and Parameter Estimation

Camilla Fiorini<sup>1</sup>, Bruno Després<sup>2</sup>, Maria Adela Puscas<sup>3</sup>

<sup>1</sup> Inria Rennes - Bretagne Atlantique  
Rennes, France  
camilla.fiorini@inria.fr

<sup>2</sup> Laboratoire Jacques-Louis Lions,  
Sorbonne Université, Paris, France  
bruno.despres@sorbonne-universite.fr

<sup>3</sup> CEA-Saclay,  
CEA/DES/ISAS/DM2S/STMF/LMSF,  
Université de Paris-Saclay, France  
maria-adela.puscas@cea.fr

## EXTENDED ABSTRACT

### Introduction

The sensitivity analysis (SA) studies are essential for many engineering applications, such as uncertainty quantification, optimal design, and to answer what if questions, i.e., what happens to the model's solution if the input parameters change [1]. The sensitivity variable itself is defined as the derivative of the state (i.e., the output of the model) with respect to the parameters of interest [2]. In the thermohydrodynamic models, the SA can be used to determine how the model response in a point is affected by a change in initial conditions or limits, or to any other physical parameter such as the viscosity, the heat capacity, thermal diffusivity, etc. The SA provides first-order estimates of average and variance of the velocity field when some parameters are uncertain [3].

### Sensitivity analysis

Let us consider the domain  $\Omega$  in Figure 1, the Navier-Stokes system (the state system) and the boundary conditions for this domain are:

$$\begin{cases} \partial_t \mathbf{u} - \nu \Delta \mathbf{u} + (\mathbf{u} \cdot \nabla) \mathbf{u} + \nabla p = \mathbf{f} & \Omega, t > 0, \\ \nabla \cdot \mathbf{u} = 0 & \Omega, t > 0, \\ \mathbf{u}(\mathbf{x}, 0) = 0 & \Omega, t = 0, \\ \mathbf{u} = -g(y)\mathbf{n} & \text{on } \Gamma_{in}, \\ \mathbf{u} = 0 & \text{on } \Gamma_w = \Gamma_{obst} \cup \Gamma_{top} \cup \Gamma_{bottom}, \\ (\nu \nabla \mathbf{u} - pI)\mathbf{n} = 0 & \text{on } \Gamma_{out}, \end{cases} \quad (1)$$

where  $\mathbf{u}$  is the velocity,  $p$  is the pressure,  $\mathbf{f}$  the external force and  $g(y)$  the prescribed inflow condition which depends on an uncertain parameter  $a$ . The sensitivity variable itself is defined as the derivative of the state with respect to the parameters of interest:

$$\mathbf{u}_a(\mathbf{x}, t; a) := \frac{\partial}{\partial a} \mathbf{u}(\mathbf{x}, t; a), \quad p_a(\mathbf{x}, t; a) := \frac{\partial}{\partial a} p(\mathbf{x}, t; a)$$

The first order sensitivity system of the state system (1) is:

$$\begin{cases} \partial_t \mathbf{u}_a - \nu \Delta \mathbf{u}_a + (\mathbf{u}_a \cdot \nabla) \mathbf{u} + (\mathbf{u} \cdot \nabla) \mathbf{u}_a + \nabla p_a = \mathbf{f}_a & \Omega, t > 0, \\ \nabla \cdot \mathbf{u}_a = 0 & \Omega, t > 0, \\ \mathbf{u}_a(\mathbf{x}, 0) = 0 & \Omega, t = 0, \\ \mathbf{u}_a = -g_a(y)\mathbf{n} & \text{on } \Gamma_{in}, \\ \mathbf{u}_a = 0 & \text{on } \Gamma_w, \\ (\nu \nabla \mathbf{u}_a - p_a I)\mathbf{n} = 0 & \text{on } \Gamma_{out}. \end{cases} \quad (2)$$

### Uncertainty propagation

The sensitivity can be used to give a first order estimate of the variance of the model output. In this context, a random parameter  $a$  with a known distribution, expected value  $\mu_a$ , and variance  $\sigma_a^2$  is considered in the model. This can be related to the boundary condition, viscosity, etc. Let  $X(\mathbf{x}, t; a)$  be a physical variable, whose expected value  $\mu_X$  and variance  $\sigma_X^2$  we want to estimate. Based on the Taylor expansion of  $X$ , one obtains the following first order estimates [3]:

$$\mu_X(\mathbf{x}, t) = E[X(\mathbf{x}, t; a)] \simeq X(\mathbf{x}, t; \mu_a) + E[(a - \mu_a)]X_a(\mathbf{x}, t; a) = X(\mathbf{x}, t; \mu_a), \quad (3)$$

$$\sigma_X^2(\mathbf{x}, t) = E[(X(\mathbf{x}, t; a) - \mu_X(\mathbf{x}, t))^2] \simeq E[(a - \mu_a)^2]X_a^2(\mathbf{x}, t; a) = \sigma_a^2 X_a^2(\mathbf{x}, t; a). \quad (4)$$

Therefore, with just two simulations, one of the state and one of the sensitivity, one can have first order estimates of the average and the variance of the output. However, since SA is based on Taylor expansions of the state variable with respect to the parameter of interest, these methods can be used only for random variables with a small variance.

## Numerical results

The domain used for the numerical simulations is the one in Figure 1, and the values of the parameters are:  $\ell = 0.7$ ,  $L = 2$ ,  $x_D = 0.4$ , and  $d = 0.1$ .

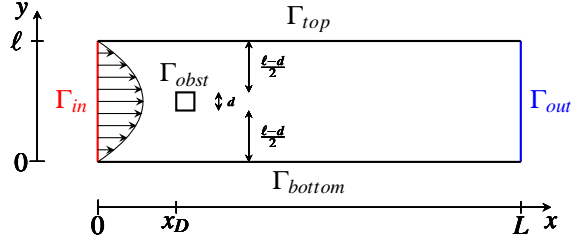


Figure 1: Domain

We consider the following parabolic inflow condition:  $g(y) = \frac{4A}{\ell^2}y(y-\ell)$ , where  $A$  is the maximal value of the inflow velocity, and it is the uncertain parameter (i.e.  $a = A$ ).  $A$  is a Gaussian random variable of average  $\mu_A$  and variance  $\sigma_A^2$ . We consider a small inflow velocity,  $\mu_A = 0.25$ , which corresponds to  $Re = 25$  and leads to a stationary solution.

For this test case, we were able to make a Monte Carlo approach as well: 1300 simulations of the state were necessary. In Figure 2, we show the 95% confidence intervals: in blue the confidence intervals are obtained with the average and variance estimated with SA, in red with Monte Carlo. For this test case, the first order approximations provided by the SA are more than satisfactory: with only two simulations, we obtain results comparable to the ones obtained with the Monte Carlo approach, which requires 1300 simulations.

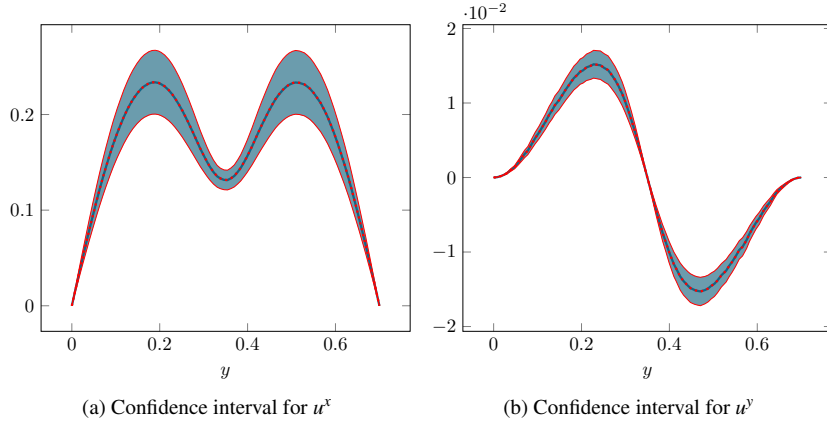


Figure 2: Confidence intervals of the velocity  $\mathbf{u}$  on the vertical cross section  $x = 1$ , with  $\alpha = 0.05$ . Comparison between Monte Carlo (in red) and the SA (in blue) approaches.

## Conclusions

We present an efficient computational strategy to deal with problems of uncertainty propagation for the Navier–Stokes equations based on sensitivity analysis. A classical test case of flow past a square-section cylinder is investigated in a steady regime. The sensitivity is used to estimate the variance of the velocity field, and 95% confidence intervals are computed. A detailed comparison with a Monte Carlo method is performed: the results of the sensitivity based method are extremely accurate, and the computational gain is significant.

## References

- [1] C. Chalons, R. Duvigneau, and C. Fiorini. Sensitivity analysis and numerical diffusion effects for hyperbolic PDE systems with discontinuous solutions. The case of barotropic Euler equations in Lagrangian coordinates. *SIAM Journal on Scientific Computing*, 40.6, A3955–A3981, 2018.
- [2] C. Fiorini, C. Chalons, and R. Duvigneau. A modified sensitivity equation method for Euler equations in presence of shocks. *Numerical Methods for Partial Differential Equations*, 36.4, 839–867, 2020.
- [3] C. Fiorini, B. Després, and M. A. Puscas. Sensitivity equation method for the Navier–Stokes equations applied to uncertainty propagation. *International Journal for Numerical Methods in Fluids*, 93.1, 71–92, 2020.

# On the Role of Adjoint Gradients in Time-Optimal Control Problems under Final Constraints

Daniel Lichtenecker<sup>1</sup>, Philipp Eichmeir<sup>2,3</sup>, Karin Nachbagauer<sup>2,4</sup>

<sup>1</sup> Technical University of Munich, Germany  
School of Engineering & Design  
Department of Mechanical Engineering  
Chair of Applied Mechanics  
daniel.lichtenecker@tum.de

<sup>2</sup>University of Applied Sciences  
Upper Austria, Campus Wels  
Stelzhamerstraße 23, 4600 Wels, Austria  
[philipp.eichmeir,karin.nachbagauer]@fh-wels.at

<sup>3</sup> Institute of Mechanics and Mechatronics  
Vienna University of Technology  
Getreidemarkt 9/E325, 1060 Wien, Austria

<sup>4</sup>Institute for Advanced Study  
Technical University of Munich  
Lichtenbergerstraße 2a, 85748 Garching, Germany

## EXTENDED ABSTRACT

### 1 Introduction

In this present work, the goal is to solve a time-optimal control problem regarding final constraints with a classical direct method, e.g. the Sequential Quadratic Programming (SQP), and then evaluate the respective optimality conditions based on an indirect optimization approach. Here, the adjoint method can be investigated for an efficient computation of the gradient of the cost functional. Moreover, the adjoint variables can be used to evaluate the optimality conditions regarding the Hamiltonian function. In the present paper, the time-optimal trajectory planning of a two-arm robot will be solved exemplarily by a static optimization and the optimality conditions regarding the Hamiltonian function will be evaluated by the adjoint variables. The application will show the easy access to the adjoint gradients and discusses the latter mentioned role of the adjoint variables in the optimality conditions.

Optimal control theory is based on the calculus of variations and deals with finding optimal trajectories for nonlinear dynamical systems, e.g. spacecrafts or multibody systems like robots. The works by Kelley [1] and Bryson and Ho [2] have to be mentioned as groundbreaking in the field of optimal control theory and serve as basis for extensive subsequent research. As a special class of time-optimal control problems considering final constraints one can cite the control of a robot arm designed in such a way that the time for a rest-to-rest maneuver becomes a minimum. Following an indirect approach, such problems can be transformed into a two-point boundary value problem, which usually can be solved by shooting methods or full collocation. Alternatively, a direct approach can be pursued, where the boundary value problem is posed as a nonlinear programming problem method see e.g. [3] for the time-optimal trajectory planning accounting for continuity required to respect technological limits of real robots. An alternative to the mentioned methods is offered by gradient methods, which are regarded as particularly robust with respect to initial controls. The pioneering work by Bryson and Ho [2] shows how the gradient can be computed straightforward using adjoint variables. With this gradient information optimal control problems can be solved iteratively by the use of nonlinear optimization routines.

### 2 Theory and Objective

A special class of time-optimal control problems for dynamic systems is solved by Eichmeir et al. [4] by the adjoint method, in which the final state of a system is given by a scalar transversality condition. In a more recent work [5], additional influence differential equations are introduced beside the adjoint system, in order to relate the control variations with the error in the final conditions. This coupling in the canonical (adjoint and influence) equations is summarized briefly here. Considering a nonlinear dynamical system of the form

$$\dot{\mathbf{x}}(t) = \mathbf{f}(\mathbf{x}(t), \mathbf{u}(t)) \text{ and } \mathbf{x}(t_0) = \mathbf{x}_0, \quad (1)$$

where  $\mathbf{u}(t) \in \mathbb{R}^m$  denotes the vector of control inputs and  $\mathbf{x}(t) \in \mathbb{R}^n$  the vector of state variables. The control has to be found such that the state variables at the final time  $t_f \in \mathbb{R}^+$  satisfy  $q$  given final conditions. The Hamiltonian for time optimal controls can be formulated using a penalty function  $P(\mathbf{x}(t), \mathbf{u}(t))$  introducing additional state and/or control constraints:

$$\mathcal{H}(\mathbf{x}(t), \mathbf{u}(t)) := 1 + P(\mathbf{x}(t), \mathbf{u}(t)) + \boldsymbol{\lambda}^\top \mathbf{f}(\mathbf{x}(t), \mathbf{u}(t)) \quad (2)$$

in which  $\boldsymbol{\lambda} = \boldsymbol{\lambda}(t) = (\mathbf{p}(t) + \mathbf{R}(t)\boldsymbol{\nu})$  exploits the decoupling of boundary conditions of the state and the adjoint equations [5] by introducing a set of so-called influence adjoint variables  $\mathbf{R}(t) \in \mathbb{R}^{n \times q}$  and adjoint variables  $\mathbf{p}(t) \in \mathbb{R}^n$ . Moreover,  $\boldsymbol{\nu} \in \mathbb{R}^q$  is a vector of multipliers to combine both set of adjoint variables. This decoupling within the multiplier  $\boldsymbol{\lambda}$  enables sequential integration of a new set of canonical equations forward and backward in time, depending on a putative optimal control history. Finally, the solution  $\mathbf{p}(t)$  and  $\mathbf{R}(t)$  of the canonical (adjoint and influence) equations are combined to determine the Hamiltonian in Eq. (2). Hence, the optimality conditions according to the Hamiltonian are evaluated in terms of the adjoint variables. The objective of the present work is the discussion of these optimality conditions regarding the minimum time solution derived by an alternative optimization approach, e.g. computed by a nonlinear programming strategy.

Here, one major criterion for solving optimal control problems using a discretization scheme is the parametrization of the control history  $\mathbf{u}(t)$ . In general, any control parametrization which maps a set of parameter values to the continuous control history, as

e.g. in the case of spline parametrization, can be used. In the special case where the control appears linearly in the underlying differential equation and therefore also in the Hamiltonian, the control which leads to the minimal operation time becomes a bang-bang structure. In this case, two different scenarios can occur: either the control has singular arcs or the control takes values of given bounds. Hence, the control  $\mathbf{u}(t)$  can be parameterized by  $\mathbf{z} = (z_1, \dots, z_N, t_f)^T$  in which  $N$  is the number of parameters to be identified and  $t_f$  is the final operation time. Possible parametrization may be spline parametrization or switching point optimization. These set of parameters can be optimized with a direct approach and in case of bang-bang controls, the optimal solution leads to roots in the switching function

$$h_i(t) = \mathbf{f}_{u_i}^T(\mathbf{p}(t) + \mathbf{R}(t)\boldsymbol{\nu}), \quad i = 1, \dots, m. \quad (3)$$

Note that the switching function is given in terms of the adjoint variables of the indirect approach and can now be used to evaluate the solution of the direct approach.

### 3 Example

The problem of trajectory planning of a robot arm in minimal time is transformed into a static parametric optimization problem by discretization of the control. Unknown quantities of the optimal bang-bang control for the joint torques  $u_1(t)$  and  $u_2(t)$  are the switching points and the final time for a rest-to-rest-maneuver of the tool center point (TCP) of the robot, see Fig. 1(a). The optimization is carried out with the SQP algorithm with the set of parameters  $\mathbf{z}$  with  $m = 2$ . The resulting drive signals are

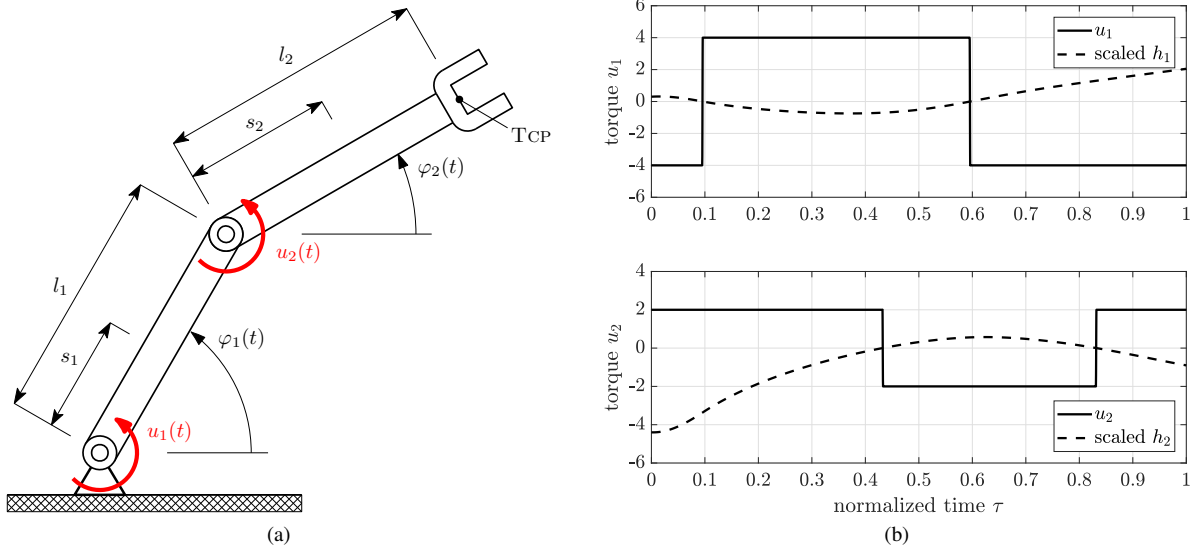


Figure 1: (a) Analyzed two-arm robot and (b) optimized bang-bang controls and associated switching function.

depicted in Fig. 1(b) in which the normalized time scale is used. One can observe that the switching points computed by the static optimization appear exactly at the times where the switching functions in Eq. (3) computed by the adjoint variables produce zeros. Note that the switching function has been evaluated with the result of the direct approach.

### Acknowledgments

Philipp Eichmeir acknowledges support from the Austrian Research Promotion Agency (FFG): 875421. Daniel Lichtenecker and Karin Nachbagauer acknowledge support from the Technical University of Munich – Institute for Advanced Study.

### References

- [1] H. J. Kelley, “Method of gradients,” pp. 206–254, Optimization Techniques with Applications to Aerospace Systems, Vol 5 of Mathematics in Science and Engineering, Academic Press, New York, 1962.
- [2] A. E. Bryson and Y. C. Ho, *Applied Optimal Control*. Hemisphere, Washington, DC, 1975.
- [3] A. Reiter, A. Müller and H. Gatringer, “On higher order inverse kinematics methods in time-optimal trajectory planning for kinematically redundant manipulators,” *IEEE Trans. Industr. Informatics*, vol. 14, no. 4, pp. 1681–1690, 2018.
- [4] P. Eichmeir, T. Lauß, S. Oberpeilsteiner, K. Nachbagauer, and W. Steiner, “The adjoint method for time-optimal control problems,” *J. Comput. Nonlinear Dynam.*, vol. 16, no. 2, 2020.
- [5] P. Eichmeir, K. Nachbagauer, T. Lauß, K. Sherif, and W. Steiner, “Time-optimal control of dynamic systems regarding final constraints,” *J. Comput. Nonlinear Dynam.*, vol. 16, pp. 1–11, 2021.

# Discrete Adjoint Approach for the Sensitivity Analysis of an Augmented Lagrangian Index-3 Formulation with Projections

Álvaro López Varela, Daniel Dopico Dopico, Alberto Luaces Fernández.

Laboratorio de Ingeniería Mecánica  
Universidade da Coruña  
C/ Mendizábal s/n, 15403, Ferrol, Spain  
[alvaro.lopez1,ddopico,aluaces]@udc.es

## EXTENDED ABSTRACT

### 1 Introduction

Different mechanical applications, as optimal control and design optimization, require the evaluation of the impact of different parameters in the response of a mechanical system. This variation can be measured through a sensitivity analysis.

The sensitivity analysis of the dynamics of multibody systems can be computed with different methods, from the simplest finite differences to the more complex analytical methods involving direct differentiation [1, 2] or the adjoint variable method [3]. In a sensitivity analysis, three key properties of the calculation must be considered: the accuracy, the computational time and the generality of the expressions for any multibody system. Some calculations like finite differences, could give poorly accurate solutions involving a high consumption of computational time, especially with a large set of parameters. On the other hand, analytical calculations are usually faster and more accurate, but a generalization is not always easy to implement.

The analytical sensitivities can be focused from two different points of view: the forward sensitivity calculations, for which the derivatives of the states must be calculated through the direct differentiation of the expressions of the dynamics; and the adjoint variable method, which only requires to calculate a set of new variables, namely, the adjoint variables.

Recently, the adjoint sensitivity analysis of an augmented Lagrange index-3 formulation with velocity and acceleration projections was developed in [3], considering the equations of motion as continuous in time. The continuous approach constitutes a general method to compute the sensitivity analysis of a multibody system, but it has as main drawbacks the complexity of the initialization of the adjoint variables and the presence of time derivatives of the mass and projection matrices.

In this work, a different approach based on the use of the discrete derivatives of the equations of motion to build the adjoint system of the augmented Lagrange index-3 formulation with projections is developed and tested in a benchmark model (five-bar). The computation of the discrete analytical approach has been implemented in the multibody system library MBSLIM for natural coordinates models.

### 2 Problem statement

Let us consider a multibody system modeled with  $\mathbf{q} \in \mathbb{R}^n$  dependent natural coordinates related by  $\Phi \in \mathbb{R}^m$  holonomic constraints. Applying the ALI3-P scheme, the following equations of motion are achieved:

$$\mathbf{M}\ddot{\mathbf{q}}^* + \Phi_q^T (\lambda^{*(i+1)} + \alpha\Phi) = \mathbf{Q}, \quad (1)$$

$$\lambda^{*(i+1)} = \lambda^{*(i)} + \alpha\Phi; i > 0, \quad (2)$$

where  $\mathbf{M} \in \mathbb{R}^{n \times n}$  is the mass matrix of the system,  $\Phi_q \in \mathbb{R}^{m \times n}$  is the jacobian matrix of the constraints,  $\mathbf{Q} \in \mathbb{R}^n$  is the vector of generalized forces and  $\lambda^* \in \mathbb{R}^m$  the Lagrange multipliers.

In this formulation, the fulfillment of the constraints in velocities and accelerations is imposed with velocity and acceleration projections:

$$(\bar{\mathbf{P}} + \varsigma\Phi_q^T\alpha\Phi_q)\dot{\mathbf{q}} = \bar{\mathbf{P}}\dot{\mathbf{q}}^* - \varsigma\Phi_q^T\alpha\Phi_t, \quad (3)$$

$$(\bar{\mathbf{P}} + \varsigma\Phi_q^T\alpha\Phi_q)\ddot{\mathbf{q}} = \bar{\mathbf{P}}\ddot{\mathbf{q}}^* - \varsigma\Phi_q^T\alpha(\Phi_q\dot{\mathbf{q}} + \dot{\Phi}_t), \quad (4)$$

where  $\bar{\mathbf{P}}$  is a symmetric projection matrix, and the superscript  $*$  indicates that the correspondent term is an unprojected magnitude.

Let us consider an objective function expressed as an integral in time:

$$\psi = \int_{t_0}^{t_F} g(\mathbf{q}, \dot{\mathbf{q}}, \ddot{\mathbf{q}}, \lambda, \rho) dt. \quad (5)$$

The sensitivity analysis of the objective function with respect to a set of parameters  $\rho \in \mathbb{R}^p$  can be computed applying the adjoint

method to the objective function using the equations solved in the dynamics, leading to the following Lagrangian:

$$\begin{aligned} \mathcal{L} = & \psi - \int_{t_0}^{t_F} \boldsymbol{\mu}^T (\mathbf{M}\ddot{\mathbf{q}}^* + \boldsymbol{\Phi}_q^T (\boldsymbol{\lambda}^* + \boldsymbol{\alpha}\boldsymbol{\Phi}) - \mathbf{Q}) dt - \int_{t_0}^{t_F} \boldsymbol{\mu}_{\Phi}^T \boldsymbol{\Phi} dt \\ & - \int_{t_0}^{t_F} \boldsymbol{\mu}_{\Phi}^T ([\bar{\mathbf{P}} + \boldsymbol{\zeta}\boldsymbol{\Phi}_q^T \boldsymbol{\alpha}\boldsymbol{\Phi}_q] \dot{\mathbf{q}} - \bar{\mathbf{P}}\dot{\mathbf{q}}^* + \boldsymbol{\Phi}_q^T \boldsymbol{\zeta}\boldsymbol{\alpha}\boldsymbol{\Phi}_t) dt - \int_{t_0}^{t_F} \boldsymbol{\mu}_{\Phi}^T ([\bar{\mathbf{P}} + \boldsymbol{\zeta}\boldsymbol{\Phi}_q^T \boldsymbol{\alpha}\boldsymbol{\Phi}_q] \ddot{\mathbf{q}} - \bar{\mathbf{P}}\ddot{\mathbf{q}}^* + \boldsymbol{\Phi}_q \boldsymbol{\zeta} \boldsymbol{\alpha} (\dot{\boldsymbol{\Phi}}_q \dot{\mathbf{q}} + \dot{\boldsymbol{\Phi}}_t)) dt. \end{aligned} \quad (6)$$

Observe that an index-3 formulation was used in the adjoint instead of the augmented Lagrange index-3 in order to avoid the Lagrange multipliers iterations, thanks to the lemma 4.3 presented in [3]. The resulting Lagrangian has 4 arrays of adjoint variables, correspondent to the index-3 part of the dynamics ( $\boldsymbol{\mu}$  and  $\boldsymbol{\mu}_{\Phi}$ ), and to the projections of velocities ( $\boldsymbol{\mu}_{\dot{\Phi}}$ ) and accelerations ( $\boldsymbol{\mu}_{\ddot{\Phi}}$ ).

The main change with respect to the continuous approach consists in the use of the discrete derivatives of the previous Lagrangian, applying a numerical integrator in order to express  $\dot{\mathbf{q}}^*$  and  $\ddot{\mathbf{q}}^*$  in terms of  $\mathbf{q}$ . This process eludes the integration by parts used in [3] which entails the addition of new terms at times  $t_0$  and  $t_F$  and which complicates the initialization of the adjoint variables. The application of the integrator expressions instead of an integration by parts has, however, as bigger drawback the appearance of these integrator expressions in the final adjoint equations.

The discrete adjoint equations are reached by means of considering subsequent steps of time and nullifying the terms multiplying the unknown sensitivities of the states generated during the derivation of (6). In this approach, instead of time integration of variables, an accumulative term from time  $t_i$  to time  $t_{i-1}$  appears, working as linkage among consecutive instants of time.

The non-existence of dynamic equations further than time  $t_F$  allows a much simpler initialization of all the adjoint variables than the continuous approach, with the only need of nullifying the accumulation terms previously commented. The same equations of any instant of time are used in this initialization process.

### 3 Numerical experiments

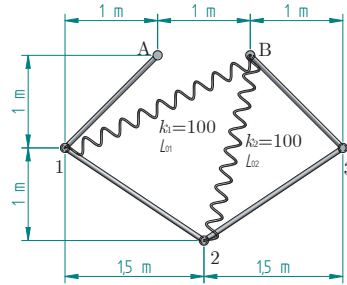


Figure 1: Five-bar mechanism

The test case solved in this work is the five-bar mechanism of Fig. 1 described in [4, 5], with the coefficients of two external actuator torques applied on the joints of the two bars attached to the fixed bar as sensitivity parameters, and with an objective function describing the error between the trajectory described by point  $\mathbf{r}_2$  and a reference set of values. This problem is presented as an optimal control test.

### Acknowledgments

The support of the Spanish Ministry of Economy and Competitiveness (MINECO) under project DPI2016-81005-P is greatly acknowledged. Furthermore, the first author would like to emphasize the acknowledgment for the support of MINECO by means of the doctoral research contract BES-2017-080727, co-financed by the European Union through the ESF program.

### References

- [1] D. Dopico, F. González, M. Saura, D. G. Vallejo. Forward sensitivity analysis of the index-3 augmented lagrangian formulation with projections. In Proceeding of the 8th ECCOMAS Thematic Conference on Multibody Dynamics. 2017.
- [2] D. Dopico, F. González, A. Luaces, M. Saura, D. García-Vallejo. Direct sensitivity analysis of multibody systems with holonomic and nonholonomic constraints via an index-3 augmented lagrangian formulation with projections. Nonlinear Dynamics, 2018. doi:10.1007/s11071-018-4306-y.
- [3] D. Dopico, A. Sandu, C. Sandu. Adjoint sensitivity index-3 augmented lagrangian formulation with projections. Mechanics Based Design of Structures and Machines, 2021. doi:10.1080/15397734.2021.1890614.
- [4] D. Dopico, Y. Zhu, A. Sandu, C. Sandu. Direct and adjoint sensitivity analysis of ordinary differential equation multibody formulations. Journal of Computational and Nonlinear Dynamics, 10(1):1–8, 2014. doi:10.1115/1.4026492.
- [5] D. Dopico, A. Sandu, C. Sandu, Y. Zhu. Sensitivity Analysis of Multibody Dynamic Systems Modeled by ODEs and DAEs., chapter 1, 1–32. Multibody Dynamics - Computational Methods and Applications. Springer, 2014. doi:10.1007/978-3-319-07260-9.

# Input Optimization For Flexible Multibody Systems Using The Adjoint Variable Method And The Flexible Natural Coordinate Formulation

Simon Vanpaemel<sup>1,2</sup>, Frank Naets<sup>1,2</sup>, Wim Desmet<sup>1,2</sup>

<sup>1</sup> Faculty of Mechanical Engineering  
KU Leuven, Division LMSD  
Celestijnenlaan 300, 3001 Leuven, Belgium  
simon.vanpaemel, frank.naets, Wim.Desmet@kuleuven.be

<sup>2</sup> DMMS Lab  
Flanders Make  
Oude Diestersebaan 133, 3920 Lommel, Belgium

## EXTENDED ABSTRACT

### 1 Introduction

In the field of input optimization problems, the focus lies on finding the kinematic (position, angle,...) or load (force/torque) input signal that minimize a predefined objective function. Often employed objective functions are energy consumption, time needed to transition between two predefined multibody configurations, following a predefined trajectory, etc... The design parameters are defined by the parametrization of the input signal, and in general results in a large design space for non-trivial input signals. Input optimization routines often employ sensitivity information in order to obtain faster convergence. However, the generation of this information comes at a cost, which depends on the employed sensitivity method. There exist a variety of methods, of which finite differences, direct differentiation (DDM) [1], the Adjoint Variable Method (AVM) [2] and automatic differentiation [3] are most notable. The efficiency and accuracy of these methods with respect to each other, depend heavily on the problem which needs to be optimized.

In this work, the authors focus on the AVM method for obtaining the sensitivity information for optimization problems in the field flexible multibody models. This method is highly accurate and the computational complexity is relatively independent to the size of the design space, making it highly suitable for problems with a relatively large amount of design parameters such as input optimization problems. However, the method also comes with the drawback of a high implementation complexity, and data-storage of the state vector from the forward simulation, that is used during during the backwards integration of the adjoint equations to obtain the adjoint variables. However, by properly choosing the underlying multibody formulation, several drawbacks of the adjoint method can be mitigated. Because, the structure of the equations of motion influences the resulting adjoint equations and the necessary Jacobians that need to be computed. Therefore, one of the key focus points of this work is the proposal to leverage on the Flexible Natural Coordinate Formulation's (FNCF) simple equation of motion structure. Literature on input optimization problems using the adjoint variable method and the well known Floating Frame of Reference (FFR) multibody formulation is yet available in [4, 5, 6].

### 2 Flexible natural coordinate formulation (FNCF)

By employing an appropriate (flexible) multibody formulation for which the terms in the adjoint equations drop out, or are of low complexity, the computational and implementation cost of computing the terms appearing in the adjoint equations every time-step, can be reduced. Therefore, the authors employ the FNCF[7]. The specific equation structure obtained through FNCF reduces the complexity of the AVM as the simulation derivatives can be readily obtained and are of limited order. This formulation combines the advantageous properties of the FFR method [8] and the Generalized Component Mode Synthesis (GCMS) method [9].

The FNCF method employs the generalized coordinates of the FFR method to describe the flexible deformation in a local frame, leading to a constant reduced stiffness matrix, hence no non-linear terms in the equations of motion related to a non-constant stiffness matrix, as is the case using GCMS. Furthermore, the FNCF method employs also the generalized coordinates of the GCMS method, that describe the rigid body motion and flexible deformation in a common inertial frame. The use of the GCMS generalized coordinates results in the drop-out of the gyroscopic forces, obtaining a constant reduced mass matrix. The generalized coordinates describing the flexible deformation in a local frame and in a common inertial frame are interdependent. These dependencies are taken into account by introducing the necessary algebraic constraint equations. It must be noted that the redundancy in the flexible coordinates is a disadvantage of this approach, as it leads to increased degrees of freedom. This leads to an increase in computational cost of the factorization during numerical integration and increased data-storage. The equations of motion using FNCF can be written as follows:

$$\begin{cases} \mathbf{M}\ddot{\mathbf{q}} + \frac{\partial \phi^T}{\partial \mathbf{q}} \boldsymbol{\lambda} = \mathbf{f}_{gra} - \mathbf{C}\dot{\mathbf{q}} - \mathbf{K}\mathbf{q} + \mathbf{f}_{ext} + \mathbf{f}_{int} \\ \phi = \mathbf{0} \end{cases} \quad (1)$$

where the system mass matrix  $\mathbf{M}$ , stiffness matrix  $\mathbf{K}$ , damping matrix  $\mathbf{C}$  and gravitational force  $\mathbf{f}_{gra}$  are constant in the equations using FNCF. The terms  $\mathbf{f}_{ext}$  and  $\mathbf{f}_{int}$  are respectively the generalized external and internal forces on the generalized coordinates  $\mathbf{q}$ . The constraint equations  $\phi$  have a quadratic dependence on the generalized coordinates, the associated Lagrange multipliers



are denoted by  $\lambda$ . Because of the properties of FNCF, various terms that appear in the adjoint equations such as  $\ddot{\mathbf{M}}$ ,  $\dot{\mathbf{M}}$ ,  $\frac{\partial \mathbf{M}}{\partial \mathbf{q}}$ ,  $\frac{\partial \mathbf{C}}{\partial \mathbf{q}}$ ,  $\frac{\partial \mathbf{K}}{\partial \mathbf{q}}$  and  $\mathbf{f}_{gra}$ , drop out. The simple kinematics of FNCF leads to first order partial derivatives  $\frac{\partial \mathbf{R}}{\partial \mathbf{q}}$  and  $\frac{\partial \mathbf{u}}{\partial \mathbf{q}}$  which are constant, and thus second order partial derivatives which are eliminated. Resulting in simple projection matrices from the forces onto the generalized coordinates. Furthermore, the first order derivatives of the constraint equations  $\frac{\partial \phi}{\partial \mathbf{q}}$  are linear in the generalized coordinates, second order derivatives  $\frac{\partial^2 \phi}{\partial \mathbf{q}^2}$  are constant terms.

### 3 Optimization process & results

The methodology is illustrated for an input optimization problem on a flexible slider-crank multibody mechanism. In this case, the torque delivered from the motor driving the crank will be optimized such that the resulting motor shaft's velocity matches a predefined (reference) signal as close as possible, as shown in Figure 1b. In order to assess the result of the optimization process, the reference velocity signal has been generated using a known torque input signal, meaning that the optimization process should be able to reproduce the torque signal, which is the case as illustrated in Figure 1a. Furthermore, a validation of the sensitivity information has been performed via a comparison with the finite differences approach.

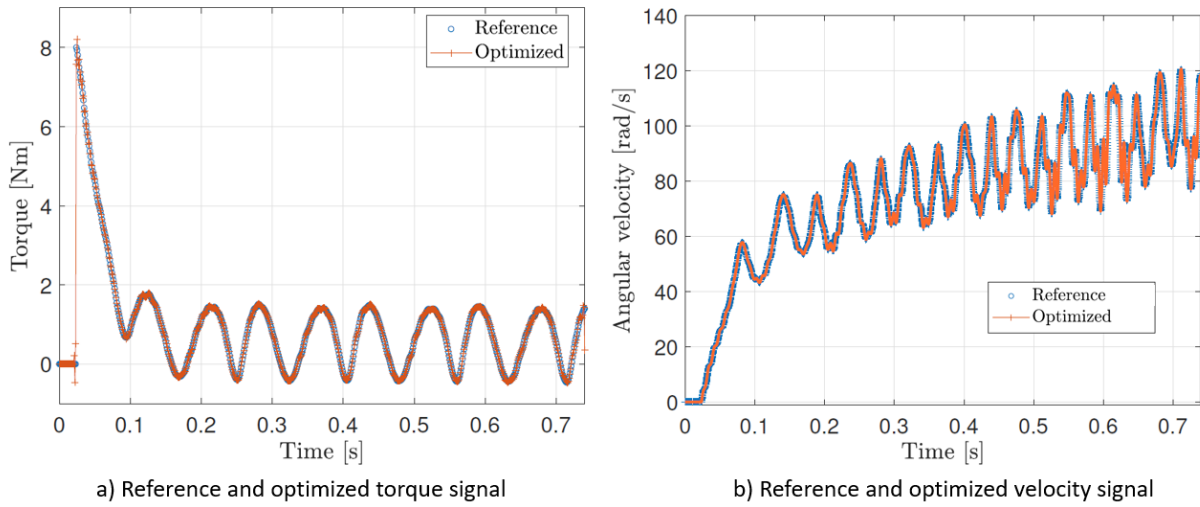


Figure 1: Reference and optimized time signals

### 4 Conclusion

This work illustrates the usage of AVM and FNCF for generating sensitivity information for input optimization problems of flexible multibody systems. The specific equation structure obtained through FNCF reduces the complexity of the AVM as the simulation derivatives can be readily obtained and are of limited order. The methodology has been illustrated on a flexible slider crank mechanism where a torque signal is found such that a predefined angular velocity signal is achieved.

### Acknowledgments

Internal Funds KU Leuven are gratefully acknowledged for their support.

### References

- [1] E. J. Haug, R. A. Wehage, and N. K. Mani, "Design sensitivity analysis of large-scale constrained dynamic mechanical systems," *Journal of Mechanical Design, Transactions of the ASME*, vol. 106, no. 2, pp. 156–162, 1984.
- [2] E. J. Haug, "Design Sensitivity Analysis of Dynamic Systems," in *Computer Aided Optimal Design: Structural and Mechanical Systems* (S. C. A. Mota, ed.), pp. 705–755, Springer Berlin Heidelberg, 1987.
- [3] C. H. Bischof, "On the Automatic Differentiation of Computer Programs and an Application to Multibody Systems," in *Solid Mechanics and its Applications*, pp. 41–48, Springer, Dordrecht, 1996.
- [4] S. Oberpeilsteiner, T. Lauss, K. Nachbagauer, and W. Steiner, "Optimal input design for multibody systems by using an extended adjoint approach," *Multibody System Dynamics*, vol. 40, no. 1, pp. 43–54, 2017.
- [5] T. Lauß, P. Leitner, S. Oberpeilsteiner, and W. Steiner, "Energy Optimal Manipulation of an Industrial Robot," vol. 43, no. 0, pp. 2–3, 2015.
- [6] D. I. T. Lauß, "Optimal Control of Multibody Systems using the Adjoint Variable Approach," no. July, 2019.
- [7] M. Vermaut, F. Naets, and W. Desmet, "A flexible natural coordinates formulation (FNCF) for the efficient simulation of small-deformation multibody systems," *International Journal for Numerical Methods in Engineering*, vol. 115, no. 11, pp. 1353–1370, 2018.
- [8] A. A. Shabana, *Dynamics of multibody systems*, vol. 9781107042. 2013.
- [9] J. Gerstmayr and J. A. C. Ambrósio, "Component mode synthesis with constant mass and stiffness matrices applied to flexible multibody systems," *International Journal for Numerical Methods in Engineering*, vol. 73, pp. 1518–1546, mar 2008.

# Shape Optimization In Time Variant System Through Multibody Dynamics Analysis

Koki Akeno, Rohit Arora and Hiroyuki Kanazawa

Machinery Research Department  
Research & Innovation Center  
Mitsubishi Heavy Industries, 676-0008, Hyogo, Japan  
[koki.akeno.xv](mailto:koki.akeno.xv), [rohit.arora.y8](mailto:rohit.arora.y8), [hiroyuki.kanazawa.57@mhi.com](mailto:hiroyuki.kanazawa.57@mhi.com)

## EXTENDED ABSTRACT

### 1 Introduction

Shape optimization of contact interface under dynamic loading using FEM analysis is computationally expensive [1]. On the other hand, multibody dynamics analysis tools have been widely used to analyze time variant phenomena and contact forces between interconnected parts in a system. In this paper we developed part shape optimization tool by combining multibody analysis software, a CAD modification software, and an optimization software and used it reduce the operating torque over whole time domain simulation.

### 2 Development and Evaluation of Part Shape Optimization Tool

In order to search optimized shape of a part with time variant boundary conditions, an optimization system is developed. Proposed part shape optimization system consists of 3 tools: a multibody dynamics (MBD) simulation software to numerically analyze the time variant phenomena, a 3D CAD modification tool to create a new CAD from shape parameters and an optimization software to calculate the new shape parameters from MBD analysis result.

To evaluate proposed method, a part shape optimization of main lever (figure 1) is conducted. In the given system, the opening degree of the dampers determined by the rotation angle of the main lever. For the MBD analysis, the main lever and the dampers on which the fluid force calculated by CFD is applied are modeled and analyzed with MSC.ADAMS. The dampers rotate according to the rotation angle of the main lever by moving the pin of the link connected to the damper in the slots of the main lever. The open source optimization tool DAKOTA [2] evaluates the objective function to minimize the average torque and calculate the shape parameters (length  $L_1$  and  $L_2$  of links) for next step. Then new CAD of the main lever which has slots corresponding to the parameters is created by Open Cascade and ADAMS model is updated.

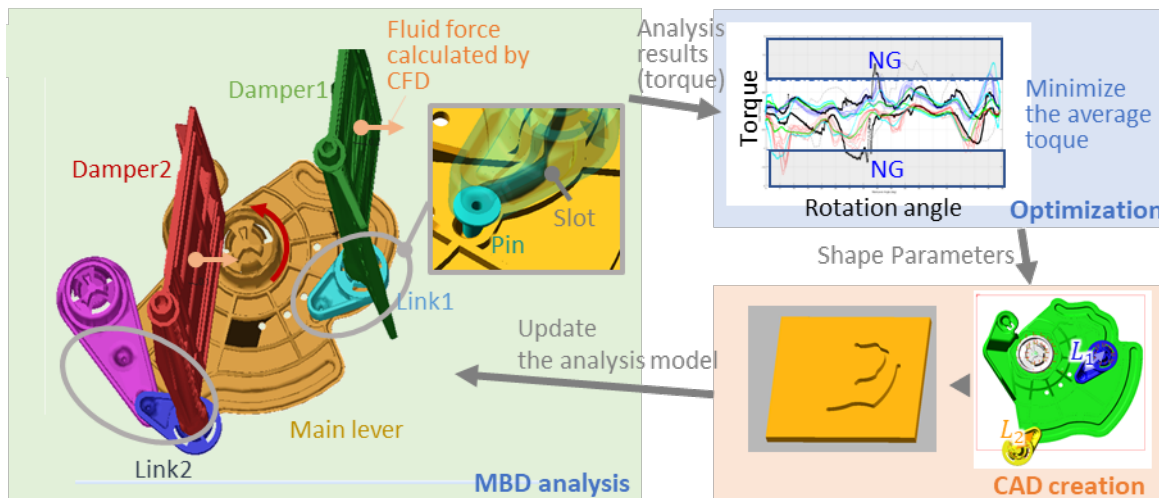
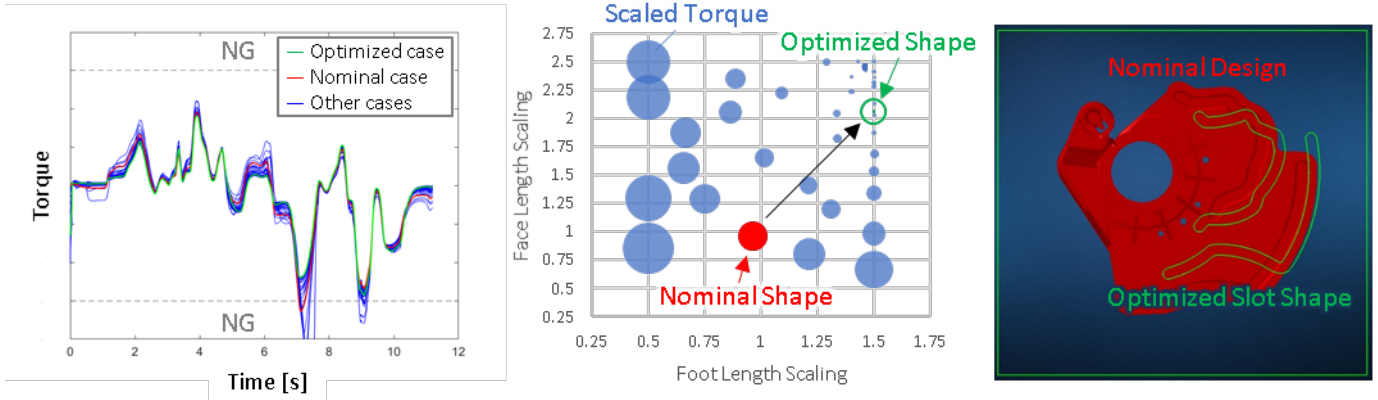


Figure 1: Part Shape Optimization Flow chert

### 3 Results

Figure 2 shows the time history of torque (a), average torque magnitude corresponds to 2 parameters used for optimization (b) and optimized slot shape (c). Time history of torque shows the torque of optimized design is smaller over the entire time domain and does not overshoot the NG area for design. And, optimized parameter combination and the optimized slot shape are obtained through the optimization loop.



(a) Time history of the torque (b) Scaled average torque corresponds to 2 parameters (c) Optimized slots shape

Figure 2: Slots Shape Optimization Results

## References

- [1] A. A. Nejat, A. Held, and R. Seifried, An Efficient Adjoint Sensitivity Analysis of Flexible Multibody Systems for a Level-set-based Topology Optimization, *Proceedings in Applied Mathematics & Mechanics*, Vol. 20, Issue 1, e202000066, 2021.
- [2] Adams, B.M., Bohnhoff, W.J., Dalbey, K.R., Ebeida, M.S., Eddy, J.P., Eldred, M.S., Hooper, R.W., Hough, P.D., Hu, K.T., Jakeman, J.D., Khalil, M., Maupin, K.A., Monschke, J.A., Ridgway, E.M., Rushdi, A.A., Seidl, D.T., Stephens, J.A., Swiler, L.P., and Winokur, J.G., "Dakota, A Multilevel Parallel Object-Oriented Framework for Design Optimization, Parameter Estimation, Uncertainty Quantification, and Sensitivity Analysis: Version 6.12 User's Manual," Sandia Technical Report SAND2020-12495, November 2020.

# Optimization of a Three Wheeled Tilting Vehicle.

Daniel Dopico Dopico, Álvaro López Varela, Alberto Luaces Fernández.

Laboratorio de Ingeniería Mecánica  
Universidade da Coruña  
C/ Mendizábal s/n, 15403, Ferrol, Spain  
[ddopico,alvaro.lopez1,aluaces]@udc.es

## EXTENDED ABSTRACT

### 1 Introduction

Three wheeled tilting vehicles are an alternative to common bicycles. The dynamics of such a vehicle can be made similar to the bicycle dynamics, nevertheless the system offers wider configuration and desing possibilities with a larger variety of behaviors. The simpler and safer strategy is to design the vehicle to mimic the “equivalent” bicycle dynamics, but even in this case the engineer must face additional design problems compared to a common bicycle design.

The steering optimal design of the tadpole tilting three wheeled vehicle multibody model shown in Figure 1 is not an easy task. The steering system should satisfy Ackerman’s steering condition, not only for null roll angles (the typical design for a car steering) but also for any combination of roll and steering angles. Moreover, the relation between the handlebar rotation and the wheels angles should be adjusted. In case we wish to mimic a standard bicicle behavior, this relation must be approximately equivalent to the single handlebar-wheel mount of a common bicycle.

In this work, the optimization of the mentioned vehicle, paying especial attention to the steering system is addressed. Several optimization problems are solved: first the kinematic design optimization of the steering; second the dynamic optimization of the steering, equivalent to the kinematic optimization but solved under dynamic conditions, making possible to desing the system to real-drive situations; third, the optimal design of the system, which can be used to program some maneuvers for the dynamical design optimization. All the optimizations performed are gradient-based, they are solved under the same general framework and rely on the multibody sensitivity equations using two approaches: direct sensitivity for optimal design and adjoint sensitivity for optimal control.

### 2 Kinematic problem statement

Let us consider a multibody system modeled with  $\mathbf{q} \in \mathbb{R}^n$  dependent coordinates related by  $\Phi \in \mathbb{R}^m$  holonomic constraints. Only  $d$  coordinates out of the full set of  $n$  are independent and they can be chosen as degrees of freedom of the system,  $\mathbf{z} \in \mathbb{R}^d$ . The kinematic equations at position level can be represented as:

$$\begin{bmatrix} \Phi_{\mathbf{q}}^{\{i\}} \\ \mathbf{B} \end{bmatrix} \Delta \mathbf{q}^{\{i+1\}} = \begin{bmatrix} -\Phi^{\{i\}} \\ \mathbf{0} \end{bmatrix}; \quad i = 0, 1, 2, \dots, \quad (1a)$$

$$\Delta \mathbf{q}^{\{i+1\}} = \mathbf{q}^{\{i+1\}} - \mathbf{q}^{\{i\}} \quad (1b)$$

$$\Phi^{\{i\}} = \Phi(t, \mathbf{q}^{\{i\}}, \boldsymbol{\rho}) \quad (1c)$$

Observe that the constraint equations depend on some design parameters, normally local coordinates of points or vectors defining the model. These parameters are of interest for the optimization to accomplish.

### 3 Dynamic problem statement

Let us consider a multibody system modeled with  $\mathbf{q} \in \mathbb{R}^n$  dependent natural coordinates related by  $\Phi \in \mathbb{R}^m$  holonomic constraints. Consider the dynamics of the system dependent on some parameters  $\boldsymbol{\rho} \in \mathbb{R}^p$ , being some of them design parameters, i.e., local coordinates of points, parameters related to masses or forces; while some others can be control function parameters affecting forces or rheonomic constraints. All of them, design parameters and optimal controls, are considered under the same framework.

The equations of motion for the system can be represented as:

$$\mathbf{M} \ddot{\mathbf{q}}^* + \Phi_{\mathbf{q}}^T (\boldsymbol{\lambda}^{*(i+1)} + \boldsymbol{\alpha} \Phi) = \mathbf{Q} \quad (2)$$

$$\boldsymbol{\lambda}^{*(i+1)} = \boldsymbol{\lambda}^{*(i)} + \boldsymbol{\alpha} \Phi; i > 0 \quad (3)$$

where  $\mathbf{M} \in \mathbb{R}^{n \times n}$  is the mass matrix of the system,  $\Phi_{\mathbf{q}} \in \mathbb{R}^{m \times n}$  is the jacobian matrix of the constraints,  $\mathbf{Q} \in \mathbb{R}^n$  is the generalized forces vector and  $\boldsymbol{\lambda}^* \in \mathbb{R}^m$  the Lagrange multipliers.

In this formulation, the fulfillment of the constraints in velocities and accelerations is imposed with velocity and acceleration projections:

$$(\bar{\mathbf{P}} + \varsigma \Phi_q^T \alpha \Phi_q) \dot{\mathbf{q}} = \bar{\mathbf{P}} \dot{\mathbf{q}}^* - \varsigma \Phi_q^T \alpha \Phi_t \quad (4)$$

$$(\bar{\mathbf{P}} + \varsigma \Phi_q^T \alpha \Phi_q) \ddot{\mathbf{q}} = \bar{\mathbf{P}} \ddot{\mathbf{q}}^* - \varsigma \Phi_q^T \alpha (\Phi_q \dot{\mathbf{q}} + \dot{\Phi}_t) \quad (5)$$

Where  $\bar{\mathbf{P}}$  is a symmetric projection matrix, and the superscript  $*$  indicates that the correspondent term is an unprojected magnitude.

#### 4 Optimization and optimal control problem statement

Let us consider a set of objective functions,  $\boldsymbol{\psi} \in \mathbb{R}^o$ , expressed as integrals in time:

$$\boldsymbol{\psi} = \int_{t_0}^{t_F} \mathbf{g}(\mathbf{q}, \dot{\mathbf{q}}, \ddot{\mathbf{q}}, \boldsymbol{\lambda}, \boldsymbol{\rho}) dt. \quad (6)$$

The sensitivity analysis of the objective functions with respect to the set of parameters  $\boldsymbol{\rho} \in \mathbb{R}^p$  can be computed by means of direct sensitivity or adjoint sensitivity methods and using the kinematic or the dynamic equations presented before [1, 2].

#### 5 Numerical experiments

The case study for optimal design and optimal control is the tilting three wheeled vehicle shown in Figure 1. The optimal design can be accomplished by means of a kinematic analysis in positions or by means of a dynamic analysis in order to better optimize for the service conditions of the vehicle.

The objective functions considered enforce the satisfaction of Ackerman's steering principle and the relation between the handlebar rotation and the effective steering angle. For the dynamic simulation, the degrees of freedom of the vehicle are predetermined and the optimization is carried out over this prescribed motion, but for the dynamic simulation, an optimal control function will be added to force the vehicle to fit the desired trajectory and speed, controlling the handlebar and pedals.

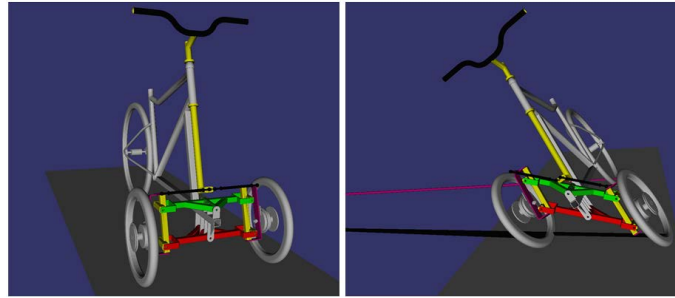


Figure 1: Three wheeled tilting vehicle.

#### 6 Conclusions

The present work proves that the approach proposed is a valid approach to improve the design of mechanical systems using kinematics or dynamics simulations. Moreover, the optimal control is also considered and both types of problems can be solved together under the same framework.

#### Acknowledgments

The support of the Spanish Ministry of Economy and Competitiveness (MINECO) under project DPI2016-81005-P is greatly acknowledged.

#### References

- [1] D. Dopico, F. González, M. Saura, D. G. Vallejo. Forward sensitivity analysis of the index-3 augmented lagrangian formulation with projections. In Proceeding of the 8th ECCOMAS Thematic Conference on Multibody Dynamics. 2017.
- [2] D. Dopico, A. Sandu, C. Sandu. Adjoint sensitivity index-3 augmented lagrangian formulation with projections. Mechanics Based Design of Structures and Machines, 2021. doi:10.1080/15397734.2021.1890614.

# A Gradient-Based Computation of Time Optimal Bang-Bang Controls

Philipp Eichmeir<sup>1,2</sup>, Karin Nachbagauer<sup>1,3</sup>, Wolfgang Steiner<sup>1,2</sup>

<sup>1</sup>University of Applied Sciences  
Upper Austria, Campus Wels  
Stelzhamerstraße 23, 4600 Wels, Austria  
[philipp.eichmeir,karin.nachbagauer,wolfgang.steiner]@fh-wels.at

<sup>2</sup>Institute of Mechanics and Mechatronics  
Vienna University of Technology  
Getreidemarkt 9/E325, 1060 Wien, Austria

<sup>3</sup>Institute for Advanced Study  
Technical University of Munich  
Lichtenbergerstraße 2a, 85748 Garching, Germany

## EXTENDED ABSTRACT

### 1 Introduction

Among all optimal control tasks, the computation of time optimal trajectories is the supreme discipline. If the control appears linear in the state equations and therefore also linear in the Hamiltonian, two cases can be considered for minimum time problems; either the control is singular or of the *bang-bang* type. In this article, we want to pay special attention to the latter, non-singular case, considering bounded (linear) inputs where only the switching points are unknown. We consider a nonlinear dynamical system of the form

$$\dot{\mathbf{x}}(t) = \mathbf{f}(\mathbf{x}(t), \mathbf{u}(t)), \quad \mathbf{x}(t_0) = \mathbf{x}_0. \quad (1)$$

where  $\mathbf{u}(t) \in \mathbb{R}^m$  denotes the vector of control inputs and  $\mathbf{x}(t) \in \mathbb{R}^n$  the vector of state variables. The initial states  $\mathbf{x}_0$  are specified and we are interested in problems where a control has to be found such that the state variables at the final time  $t_f$  satisfy the (auxiliary) conditions

$$\boldsymbol{\phi}(\mathbf{x}(t_f), t_f) = \mathbf{0}, \quad \boldsymbol{\phi} : \mathbb{R}^n \times \mathbb{R} \rightarrow \mathbb{R}^q, \quad (2)$$

and a cost functional of the form

$$J = \int_{t_0}^{t_f} [1 + \Pi(\mathbf{x}(t))] dt, \quad (3)$$

is minimized. Here,  $\Pi(\mathbf{x}(t))$  is a penalty function in order to introduce additional state constraints. The time optimal control can be obtained by solving a two-point boundary value problem which is usually hard to solve. Hence, we pursue an iterative method by computing the gradients of the cost functional  $J$  from Eq. (3) and of the function  $\boldsymbol{\phi}$  from Eq. (2) with respect to the control. This main idea is inspired by the gradient technique by Bryson and Ho [1].

### 2 Gradient Computation

A variation  $\delta u_i(t)$  of the bang-bang control  $u_i(t)$ , results from a variation of the switching times  $t = t_{i,1} \dots t_{i,N_i}$ , where  $N_i$  is the total number of switching points associated to  $u_i$ . Since either  $u_i = u_{i,\min}$  or  $u_i = u_{i,\max}$ , the difference between a disturbed control  $u_i^*(t)$  and the original signal  $u_i(t)$  is defined by the shift  $\delta t_{i,k}$  of the switching points as follows:

$$\delta u_i(t) = \begin{cases} \pm \bar{u}_i & \text{for } t \in [t_{i,k}; t_{i,k} + \delta t_{i,k}] \\ 0 & \text{otherwise,} \end{cases} \quad (4)$$

where  $\bar{u}_i = u_{i,\max} - u_{i,\min}$ . The negative sign of  $\bar{u}_i$  has to be taken if the control switches from  $u_{i,\min}$  to  $u_{i,\max}$  and the positive sign for a switch from  $u_{i,\max}$  to  $u_{i,\min}$  at  $t_{i,k}$ . The control has to be found such that the state variables at the final time  $t_f$  satisfy the given final conditions. In the present approach, a decoupling of the boundary conditions of the state and of the conventional adjoint equations is proposed by introducing new adjoint variables  $\mathbf{p}(t) \in \mathbb{R}^n$  and a set of so-called influence adjoint variables  $\mathbf{P}(t) \in \mathbb{R}^{n \times q}$  from which the variations of the cost functional and the auxiliary conditions

$$\delta \bar{J} = \sum_{i=1}^l \sum_{k=1}^{N_i} \pm \bar{u}_i \left( \mathbf{p}^T \mathbf{f}_{u_i} \right) \Big|_{t=t_{i,k}} \delta t_{i,k} + (1 + \Pi(\mathbf{x}(t_f))) \delta t_f \quad \delta \bar{\boldsymbol{\phi}} = \sum_{i=1}^l \sum_{k=1}^{N_i} \pm \bar{u}_i \left( \mathbf{P}^T \mathbf{f}_{u_i} \right) \Big|_{t=t_{i,k}} \delta t_{i,k} + \dot{\boldsymbol{\phi}}_f \delta t_f, \quad (5)$$

can be computed. Note that we have introduced  $\dot{\boldsymbol{\phi}}_f$  as the total time derivative of  $\boldsymbol{\phi}$  at  $t = t_f$ , and  $\mathbf{f}_{u_i}$  as the partial derivative of  $\mathbf{f}$  with respect to  $u_i$ . The variations show the direct influence of  $\delta t_{i,k}$  and  $\delta t_f$  on  $\delta J$  and  $\delta \bar{\boldsymbol{\phi}}$ . Therefore, the updates can be computed directly by

$$\delta t_f = -\kappa \left( 1 + \Pi(\mathbf{x}(t_f)) + \mathbf{v}^T \dot{\boldsymbol{\phi}}_f \right) \quad \text{and} \quad \delta t_{i,k} = \mp \kappa \bar{u}_i \left( \mathbf{f}_{u_i}^T \mathbf{p} + \mathbf{f}_{u_i}^T \mathbf{P} \mathbf{v} \right) \Big|_{t=t_{i,k}}, \quad (6)$$

where  $\kappa$  defines the update step size for  $t_f$  and  $t_{i,k}$ . The adjoint variables  $\mathbf{p}(t)$  can be computed by a linear time-variant final value problem which can be solved backwards in time. Analogously, the influence adjoint variables  $\mathbf{P}(t)$  have to be solved from one set of  $n$  ordinary differential equations for each component of the final condition  $\boldsymbol{\phi}(\mathbf{x}(t_f), t_f) = \mathbf{0}$ . The vector  $\mathbf{v} \in \mathbb{R}^q$  includes multipliers which are determined such that the variations  $\delta t_{i,k}$  and  $\delta t_f$  result in a better approximation of the constrained optimum. For an elaborate derivation of the algorithm see [2].

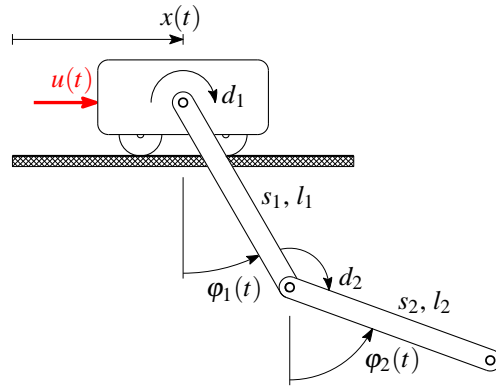


Figure 1: Cart double pendulum

### 3 Dynamic Model

In order to apply the proposed theory, we are looking for the excitation force  $u(t)$  of a cart which is required to swing up a double pendulum in the upper rest position in minimal time. The system under consideration is depicted in Fig. 1 and the results of the time optimal solution are summarized in Fig. 2.

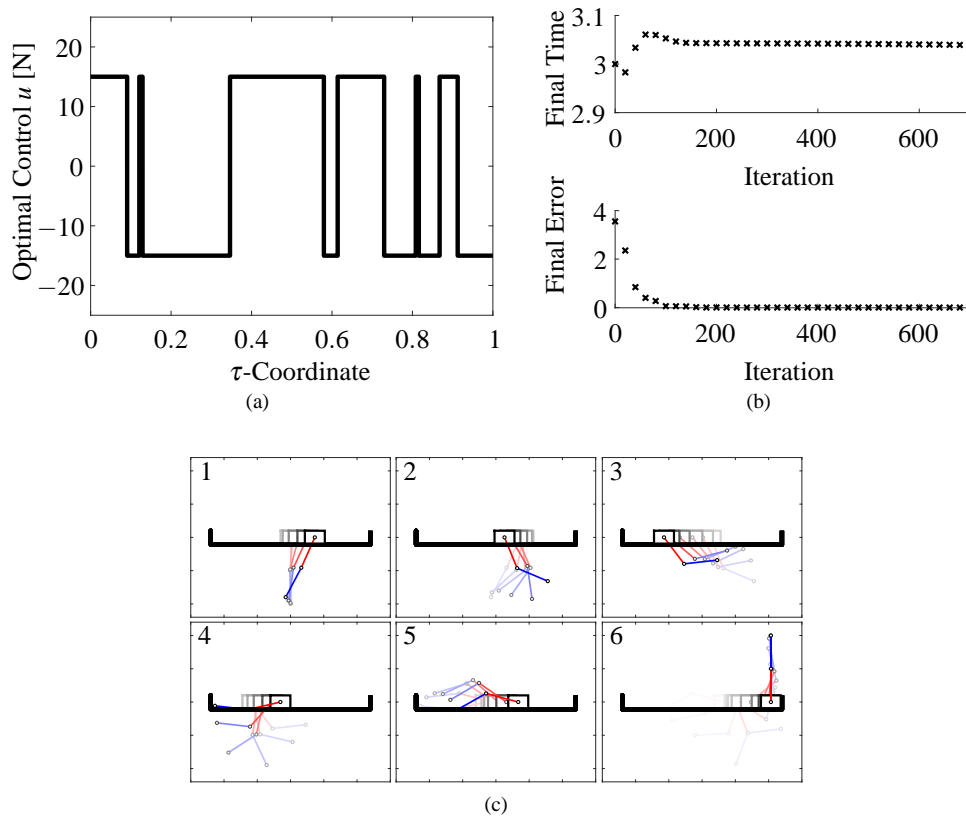


Figure 2: Results: (a) Time optimal bang-bang control (b) Convergence (c) Trajectory of the swing-up maneuver

### Acknowledgments

Philipp Eichmeir acknowledges support from the Austrian Research Promotion Agency (FFG): 875421. Karin Nachbagauer acknowledges support from the Technical University of Munich – Institute for Advanced Study.

### References

- [1] A.E. Bryson, Y.C. Ho. *Applied Optimal Control*. Hemisphere, Washington, DC, 1975.
- [2] P. Eichmeir, K. Nachbagauer, K. Sherif, T. Lauß, W. Steiner. *Time-Optimal Control of Dynamic Systems Regarding Final Constraints*. Journal of Computational and Nonlinear Dynamics, 2021.



# Topology Optimization Procedure for Flexible Multibody Systems with Augmented Standard Input Data

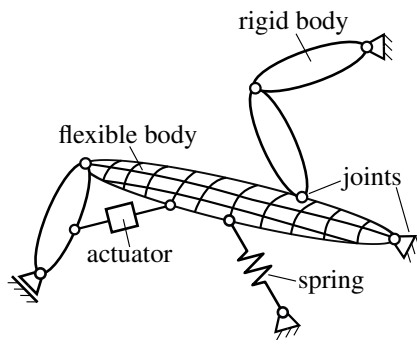
Alexander Held, Tobias Rückwald

Institute of Mechanics and Ocean Engineering  
Hamburg University of Technology  
Eißendorfer Straße 42, 21073, Hamburg, Germany  
{alexander.held,tobias.rueckwald}@tuhh.de

## EXTENDED ABSTRACT

### 1 Introduction

The method of flexible multibody systems is a powerful tool for the analysis of compliant mechanisms. The currently most widely used method to describe flexible bodies is the floating frame of reference approach. It is well suited to perform topology optimizations of flexible bodies since their deformations are approximated by global shape functions, which are often obtained from finite element models using model reduction techniques. These finite element models, however, can be directly reused in the formulation of topology optimization problems.



$$\begin{aligned}
 \mathbf{y}(t, \mathbf{x}), \mathbf{z}(t, \mathbf{x}) &\in \mathbb{R}^r && \text{(redundant position and velocity variables)} \\
 \boldsymbol{\lambda}(t, \mathbf{x}) &\in \mathbb{R}^{n_c} && \text{(Lagrange multipliers)} \\
 \mathbf{x} &\in \mathbb{R}^h && \text{(vector of design variables)} \\
 \mathbf{K}\mathbf{R} &:= \dot{\mathbf{y}} - \mathbf{Z}(\mathbf{y})\mathbf{z} = \mathbf{0} && \text{(kinematic relation)} \\
 \mathbf{E}\mathbf{M} &:= \mathbf{M}(\mathbf{y}, \mathbf{x})\dot{\mathbf{z}} - \mathbf{f}(t, \mathbf{y}, \mathbf{z}, \mathbf{x}) - \mathbf{C}^T\boldsymbol{\lambda} = \mathbf{0} && \text{(kinetic equations)} \\
 \mathbf{c}(t, \mathbf{y}, \mathbf{x}) &= \mathbf{0} && \text{(constraint equations).}
 \end{aligned}$$

Figure 1: Schematic representation (left) and system equations (right) of flexible multibody systems

A schematic representation of a flexible multibody system and the system equations are summarized in Fig. 1. Thereby,  $\mathbf{Z}$  is the kinematic matrix,  $\mathbf{M}$  the global mass matrix,  $\mathbf{f}$  comprises the generalized inertia forces, elastic forces, and the applied loads, and  $\mathbf{C}$  is the Jacobian matrix of the constraint equations  $\mathbf{c}$ .

### 2 Topology Optimization of Flexible Bodies

To find the optimal topology of a flexible body, the modified Solid Isotropic Material with Penalization (SIMP) approach suggested in [2] is used. In this approach, the design domain is discretized and the stiffness  $E_i$  and density  $\rho_i$  of each subdomain  $i$  is penalized by a continuous design variables  $x_i$  as shown in Fig. 2.

$$\rho_i(x_i) = \begin{cases} cx_i^q \rho_0 & \text{for } x_{\min} = 0.01 \leq x_i < 0.1, \\ x_i \rho_0 & \text{for } 0.1 \leq x_i \leq 1, \end{cases}$$

$$E_i(x_i) = x_i^p E_0$$

Figure 2: Material parameterization (left) of meshed design domain (right)

From the assembled mass matrix  $\bar{\mathbf{M}}(\mathbf{x})$  and stiffness matrix  $\bar{\mathbf{K}}(\mathbf{x})$  of the finite element model, global shape functions  $\boldsymbol{\Phi}(\mathbf{x})$  can be determined using, for instance, simple modal truncation.

### 3 Design Evaluation and Sensitivity Analysis of Flexible Multibody Systems

The integral compliance of the flexible body

$$\psi = \int_{t^0}^{t^1} \underbrace{\mathbf{q}^T \bar{\mathbf{K}} \mathbf{q}}_F dt \quad (1)$$

is taken as objective function in the optimization. Thereby,  $\mathbf{q}$  and  $\bar{\mathbf{K}}$  are the elastic coordinates and modally reduced stiffness matrix of the flexible body, respectively.

For efficient topology optimizations, the gradient  $\nabla\psi(\mathbf{x}) = d\psi/d\mathbf{x}$  of the criterion function (1) is required. However, its computation is tedious since the state variables, which follow from the solution of the system equations, depend not only on time but also on the design variables  $\mathbf{x}$ . Here, the adjoint variable method is used to efficiently compute  $\nabla\psi$  in two steps. Firstly, a system of adjoint differential equations

$$\begin{aligned}\dot{\mu} &= -\left(\frac{\partial \mathbf{K}\mathbf{R}}{\partial \mathbf{y}}\right)^T \mu + \left(\frac{\partial \mathbf{E}\mathbf{M}}{\partial \mathbf{y}}\right)^T (\mathbf{v} + \xi) + \left(\frac{\partial \ddot{\mathbf{c}}}{\partial \mathbf{y}}\right)^T \gamma - \frac{\partial F}{\partial \mathbf{y}}, \\ M\dot{\mathbf{v}} &= -\left(\frac{\partial \mathbf{K}\mathbf{R}}{\partial \mathbf{z}}\right)^T \mu - M\mathbf{v} + \left(\frac{\partial \mathbf{E}\mathbf{M}}{\partial \mathbf{z}}\right)^T (\mathbf{v} + \xi) + \left(\frac{\partial \ddot{\mathbf{c}}}{\partial \mathbf{z}}\right)^T \gamma,\end{aligned}\quad (2)$$

have to be set up and solved for the adjoint variables  $\mu$  and  $\mathbf{v}$ . Since the constraint equations are considered at acceleration level  $\ddot{\mathbf{c}} = \mathbf{o}$ , the adjoint system is an index-1 differential-algebraic equation. However, it turns out that the auxiliary variables  $\xi$  and  $\gamma$  can be computed in each time step by solving the system of linear equations

$$\begin{bmatrix} \mathbf{M} & \mathbf{C}^T \\ \mathbf{C} & \mathbf{o} \end{bmatrix} \begin{bmatrix} \xi \\ \gamma \end{bmatrix} = \begin{bmatrix} \mathbf{o} \\ -\mathbf{C}\mathbf{v} \end{bmatrix}.\quad (3)$$

A detailed derivation of the adjoint system (2) and (3) is given, for instance, in [1]. With the adjoint variables  $\mu$  and  $\mathbf{v}$ , and the auxiliary variables  $\xi$  and  $\gamma$ , the gradient can finally be computed as

$$\nabla\psi = \int_{t^0}^{t^1} \left[ \frac{\partial F}{\partial \mathbf{x}} - \left(\frac{\partial \mathbf{E}\mathbf{M}}{\partial \mathbf{x}}\right)^T (\mathbf{v} + \xi) - \left(\frac{\partial \ddot{\mathbf{c}}}{\partial \mathbf{x}}\right)^T \gamma \right] dt.\quad (4)$$

For the evaluation of Eq. (4), the derivatives of the system equations with respect to the design variables are required. However, their computation is not easy because the dependencies are deeply buried in the kinetic and constraint equations via the global shape functions. Therefore, a procedure is developed, which yields the gradient of SIMP parameterized multibody systems.

#### 4 Optimization Procedure

As shown in Fig. 4, three software tools are combined for the design evaluation and sensitivity analysis in the optimization procedure. The parameterized finite element model is generated, and modal analysis is performed with ANSYS MECHANICAL. Then the resulting system matrices and modal analysis results are exported to the Matlab toolbox RED, where the standard input data are computed that completely describe the flexible body, see [3]. Thereby, the standard input data are augmented by their design derivatives to allow the exact evaluation of Eq. (4). In this way, all information is available in the multibody toolbox DYNMANTO to perform the transient system analysis and adjoint sensitivity analysis. From the objective function  $\psi$  and its gradient  $\nabla\psi$ , an improved design is determined using a gradient-based optimization algorithm such as the Method of Moving Asymptotes. Then the next iteration starts until a stopping criterion is fulfilled.

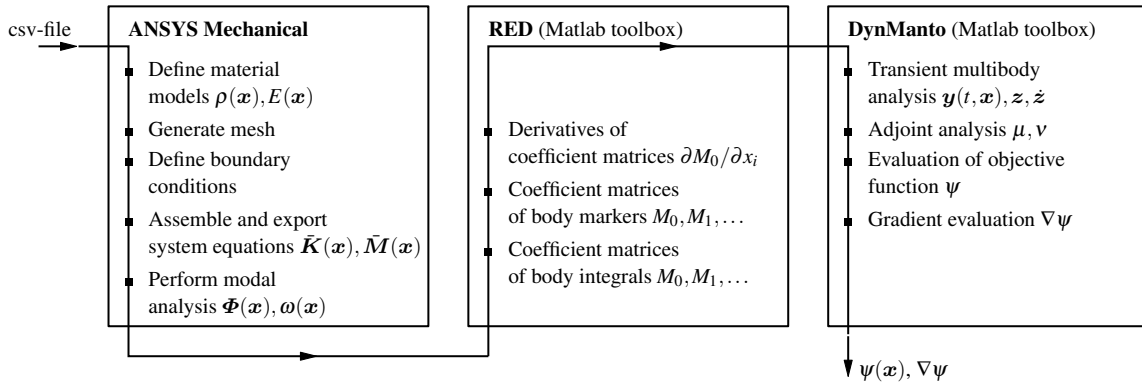


Figure 3: Process chain for design evaluation and analysis of flexible multibody system

#### References

- [1] A. Azari Nejat, A. Moghadas, A. Held. Adjoint sensitivity analysis of flexible multibody systems in differential-algebraic form. *Journal of Computers and Structures*, Volume 228, 2019.
- [2] N. Olhoff, J. Du,. Topological Design of Continuum Structures Subjected to Forced Vibration. In: 6th World Congresses of Structural and Multidisciplinary Optimization, 2005.
- [3] O. Wallrapp. Standard Input Data of Flexible Bodies for Multibody System Codes. Report IB 515-93-04, DLR, German Aerospace Establishment, Institute for Robotics and System Dynamics, Oberpfaffenhofen, 1993.

# On The Dynamics And Optimal Control Of Constrained Mechanical Systems

Simeon Schneider, Peter Betsch

Institute of Mechanics, Karlsruhe Institute of Technology, 76131 Karlsruhe, Germany  
simeon.schneider@kit.edu, peter.betsch@kit.edu

## EXTENDED ABSTRACT

### 1 Motivation

Optimal control covers a large field of applications, from optimal control of chemical or economic processes up to optimal control of satellites or robots. Often the general system to control contains many subsystems whose interaction with each other define the behaviour of the general system. In the case of mechanical multibody systems the choice of coordinates plays a crucial role. In particular, the choice of coordinates affects the specific form of both the equations of motion and the necessary optimality conditions. In the case of minimal coordinates the equations of motion take the form of nonlinear ordinary differential equations (ODEs) and numerical methods to solve related optimal control problems are well established. On the other hand, the choice of redundant coordinates facilitates the description of general multibody systems. Due to the presence of holonomic constraints the equations of motion take the form of differential-algebraic equations (DAEs). Numerical methods for optimal control problems with DAEs as state equations have not yet reached the level of maturity when compared to optimal control problems with ODEs as state equations. The aim of the present talk is shed further light on the solution of optimal control problems for constrained mechanical systems.

### 2 Multibody systems and boundary value problems

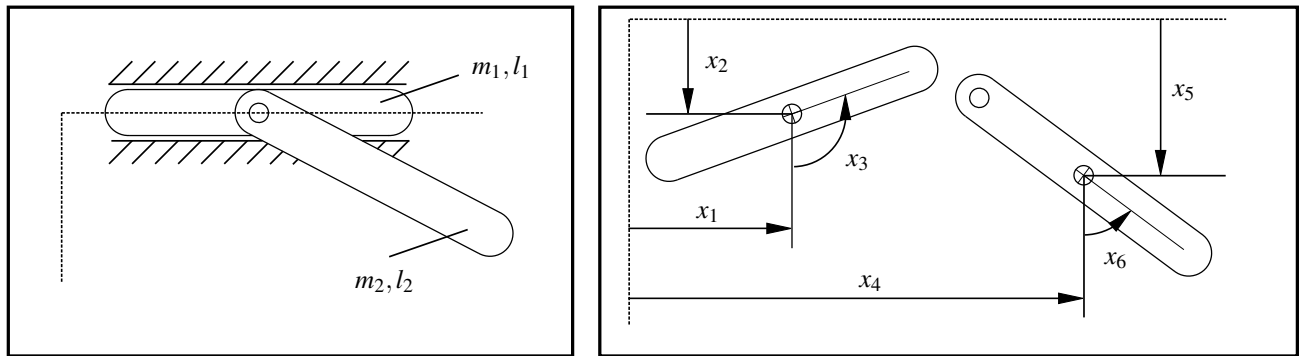


Figure 1: Physical pendulum on a slide taken from [1]

A simple but representative example of a multibody system is depicted in Figure 1, whose behaviour can be either described by using minimal coordinates  $\mathbf{q} = (x_1, x_6)$  or redundant coordinates  $\mathbf{x} = (x_1, x_2, x_3, x_4, x_5, x_6)$  along with the constraints

$$\begin{aligned} g_1(\mathbf{x}) &= x_2 = 0 \\ g_2(\mathbf{x}) &= x_3 = 0 \\ g_1(\mathbf{x}) &= x_1 - x_4 + \frac{l_2}{2} \sin(x_6) = 0 \\ g_1(\mathbf{x}) &= x_2 - x_5 + \frac{l_2}{2} \cos(x_6) = 0 \end{aligned}$$

The generalized coordinates  $(x_1, x_2, \dots, x_6)$  are depicted in Figure 1. They are used to describe the kinematics of the two rigid bodies constituting the planar 2-body system at hand. Livens principle [2] can be used to determine the equations of motion. To this end, we introduce the augmented action integral

$$S = \int_{t_0}^{t_f} L(\cdot) dt$$

In the case of minimal coordinates, the augmented Lagrangian  $L$  is given by

$$L(\mathbf{q}, \dot{\mathbf{q}}, \mathbf{v}, \mathbf{p}_m) = T(\mathbf{q}, \mathbf{v}) - V(\mathbf{q}) - \mathbf{p}_m^T (\mathbf{v} - \dot{\mathbf{q}})$$

while using redundant coordinates entails an augmented Lagrangian  $L$  of the form

$$L(\mathbf{x}, \dot{\mathbf{x}}, \mathbf{y}, \mathbf{v}, \mathbf{p}) = T(\mathbf{x}, \dot{\mathbf{x}}) - V(\mathbf{x}) - \mathbf{p}^T (\mathbf{v} - \dot{\mathbf{x}}) - \mathbf{y}^T \mathbf{g}(\mathbf{x})$$

In both cases  $T$  and  $V$  stand for the kinetic energy and the potential function, respectively. In Livens principle the relation between coordinates and velocities is considered as constraint which is enforced by means of Lagrange multipliers,  $\mathbf{p}_m$  and  $\mathbf{p}$ , respectively. In the case of redundant coordinates additional Lagrange multipliers arranged in vector  $\mathbf{y}$  take account of the holonomic constraints. Enforcing the stationary of the augmented action integral yields the equations of motion along with the boundary conditions

$$[\mathbf{p}_m \delta \mathbf{q}]|_{t_0}^{t_f} = 0 \quad \text{and} \quad [\mathbf{p} \delta \mathbf{x}]|_{t_0}^{t_f} = 0$$

respectively. Typically, end-point conditions are assumed to hold for the variations of the coordinates  $\delta \mathbf{q}$  and  $\delta \mathbf{x}$ , respectively. However, having in mind optimal control problems, we shall keep the boundary terms to investigate dynamical boundary value problems (BVP).

The controlled version of the equations of motion can be written in the form

$$\left. \begin{aligned} \dot{\mathbf{q}} &= \frac{\partial H(\mathbf{q}, \mathbf{p})}{\partial \mathbf{p}} \\ \dot{\mathbf{p}}_m &= -\frac{\partial H(\mathbf{q}, \mathbf{p})}{\partial \mathbf{q}} + \mathbf{u}_m \end{aligned} \right\} \dot{\boldsymbol{\alpha}} = \mathbf{f}(\boldsymbol{\alpha}, \mathbf{u})$$

for the choice of minimal coordinates. Here,  $H$  denotes the Hamiltonian and  $\mathbf{u}_m$  contains the control inputs conjugate to the two minimal coordinates. Similarly, for redundant coordinates we have

$$\left. \begin{aligned} \dot{\mathbf{x}} &= \frac{\partial H^y(\mathbf{x}, \mathbf{p}, \mathbf{y})}{\partial \mathbf{p}} \\ \dot{\mathbf{p}} &= -\frac{\partial H^y(\mathbf{x}, \mathbf{p}, \mathbf{y})}{\partial \mathbf{q}} + \mathbf{u} \\ \mathbf{0} &= \mathbf{g}(\mathbf{x}) \end{aligned} \right\} \dot{\boldsymbol{\beta}} = \mathbf{f}(\boldsymbol{\beta}, \mathbf{y}, \mathbf{u})$$

where  $H^y$  is an augmented Hamiltonian and  $\mathbf{u}$  is a vector with non-zero components associated with the two controls conjugate to  $(x_1, x_6)$ .

We now turn to the optimal control problem which can be formulated in a similar way as the dynamical problem considered above. Accordingly, we introduce the functional

$$\mathbb{S}^{OC} = \int_{t_0}^{t_f} \mathbb{L}^{OC}(\cdot) dt$$

where  $\mathbb{L}^{OC}$  is an augmented cost function. In the case of minimal coordinates we have

$$\mathbb{L}^{OC}(\boldsymbol{\alpha}, \mathbf{u}, \boldsymbol{\lambda}_m) = C(\boldsymbol{\alpha}, \mathbf{u}) - \boldsymbol{\lambda}_m^T (\dot{\boldsymbol{\alpha}} - \mathbf{f}(\boldsymbol{\alpha}, \mathbf{u}))$$

while for redundant coordinates

$$\mathbb{L}^{OC}(\boldsymbol{\beta}, \mathbf{u}, \mathbf{y}, \boldsymbol{\lambda}, \boldsymbol{\eta}) = C(\boldsymbol{\beta}, \mathbf{u}, \mathbf{y}) - \boldsymbol{\lambda}^T (\dot{\boldsymbol{\beta}} - \mathbf{f}(\boldsymbol{\beta}, \mathbf{u}, \mathbf{y})) - \boldsymbol{\eta}^T \mathbf{G}(\boldsymbol{\beta}, \mathbf{u}, \mathbf{y})$$

Here,  $C$  is the cost function to be minimized. Furthermore,  $\boldsymbol{\lambda}_m$  and  $(\boldsymbol{\lambda}, \boldsymbol{\eta})$ , respectively, are the adjoint variables. Note that the form of function  $\mathbf{G}(\boldsymbol{\beta}, \mathbf{u}, \mathbf{y})$  depends on the (differentiation) index of the underlying state DAEs. We refer to [3],[4] for more background on optimal control problems with DAEs as state equations.

It is worth noting that the optimal control problem yields a similar type of BVP as the dynamical problem based on Livens principle considered before. Of course, for both the optimal control problem and the dynamical problem, the solution of the respective BVP has to be independent of the choice of coordinates. That is, applying minimal coordinates or redundant coordinates should eventually yield equivalent solutions to the BVP under consideration. However, using redundant coordinates, poses additional challenges with regard to the proper handling of boundary terms and the optimality conditions. These issues will be further addressed in the talk.

## References

- [1] W. Blajer. An orthonormal tangent space method for constrained multibody systems. *Comput. Methods Appl. Mech. Engrg.*, 121 (1995), pp. 45-57.
- [2] G. H. Livens. On Hamilton's Principle and the Modified Function in Analytical Dynamics. *Proceedings of the Royal Society of Edinburgh.*, [Sess. 1918-19.], pp. 113-119.
- [3] T. Roubicek, M. Valasek. Optimal control of causal differential-algebraic systems. *J. Math. Anal. Appl.*, 269(2):616–641, 2002
- [4] M. Gerds. *Optimal Control of ODEs and DAEs*. De Gruyter, Berlin/Boston, 2012

# Nonlinear Optimal Control of Underactuated Mechanical Systems

Bálint Bodor<sup>1</sup>, László Bencsik<sup>2</sup>

<sup>1</sup> Department of Applied Mechanics  
Budapest University of Technology and Economics  
Budapest, 1111, Hungary  
bodor@mm.bme.hu

<sup>2</sup> MTA-BME Research Group on Dynamics of Machines and Vehicles  
Budapest, 1111, Hungary  
bencsik@mm.bme.hu

## EXTENDED ABSTRACT

### 1 Introduction

Underactuated mechanical systems have more degrees of freedom (DoF) than the number of control inputs. Typical examples include cranes and low-weight manipulators having flexible elements. The trajectory tracking control of these systems is addressed in our work. In case of underactuated systems the control force cannot be calculated as a solution of an inverse dynamics problem and the approaches based on computed torque control also face stability issues [1]. To overcome this problem, the authors proposed a linear optimal control approach in a previous work [2]. In order to gain higher accuracy of the controller an iterative nonlinear optimal control solution is presented in this paper.

### 2 The mechanical model and the control task

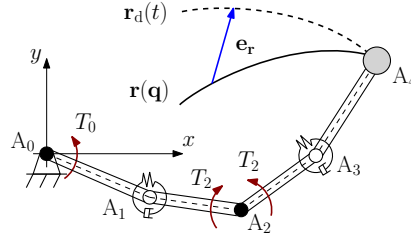


Figure 1: Mechanical model of a flexible RR manipulator

The mechanical model of an RR manipulator consisting of two flexible elements is shown in Fig. 1. The manipulator has two actuators in the joints  $A_0$  and  $A_2$  generating the torques  $T_0$  and  $T_2$  respectively, while the joints  $A_1$  and  $A_3$  are passive. The end-effector, which trajectory is to be prescribed, is located in the point  $A_4$ . To develop a model-based control algorithm, we introduce the set of dependent generalised coordinates  $\mathbf{q}(t)$  and the vector of the input torques  $\mathbf{u}(t)$ . Then the equation of motion is written in the following classical form

$$\mathbf{M}(\mathbf{q})\ddot{\mathbf{q}} + \mathbf{c}(\mathbf{q}, \dot{\mathbf{q}}) = \mathbf{H}(\mathbf{q})\mathbf{u}. \quad (1)$$

The goal is to find the control force  $\mathbf{u}(t)$ . Fig. 1 shows the trajectory tracking error  $\mathbf{e}_r = \mathbf{r}_d(t) - \mathbf{r}(\mathbf{q})$ , which is defined by the difference of the desired trajectory  $\mathbf{r}_d(t)$  and the realised trajectory  $\mathbf{r}(\mathbf{q})$ . The nonlinear finite horizon cost functional is defined as

$$J(\mathbf{q}, \mathbf{u}) = \int_{t_s}^{t_f} (\mathbf{e}_r^T \mathbf{W}_e \mathbf{e}_r + \mathbf{u}^T \mathbf{W}_u \mathbf{u}) dt, \quad (2)$$

with the error vector  $\mathbf{e}^T = [\mathbf{e}_r^T \dot{\mathbf{e}}_r^T]$ . The matrices  $\mathbf{W}_e$  and  $\mathbf{W}_u$  are the weights of the errors and the control inputs respectively. The goal of the optimal control problem is to find the inputs  $\mathbf{u}(t)$  and the optimal motion  $\mathbf{q}(t)$  of the system that minimises the cost functional in Eq. (2) while satisfying the equation of motion (1).

### 3 Iterative solution of the nonlinear optimal control problem

To obtain the solution of the optimization problem, the Euler-Lagrange equations are possible to derive for Eqs. (1)-(2). However, this approach results in a nonlinear boundary value problem that possesses huge computational demand to solve. Alternatively, an iteration is introduced in this work that is based on the minimization of the second-order expansion of the cost functional (2) and leads to a sequence of time-varying finite horizon LQR problems [3].

For the sake of simplicity the state variables  $\mathbf{x}^T = [\mathbf{q}^T \dot{\mathbf{q}}^T]$  and the optimisation variables  $\mathbf{y}^T = [\mathbf{x}^T \mathbf{u}^T]$  are defined. We approximate the cost functional (2) with a second order expansion around the  $k$ -th approximated solution  $\mathbf{y}_k(t)$

$$J(\mathbf{y}_k + \Delta \mathbf{y}_k) \approx J(\mathbf{y}_k) + \delta J|_{\mathbf{y}_k} \langle \Delta \mathbf{y}_k \rangle + \delta^2 J|_{\mathbf{y}_k} \langle \Delta \mathbf{y}_k \rangle, \quad (3)$$

where  $\delta J|_{\mathbf{y}_k} \langle \Delta \mathbf{y}_k \rangle$  is the first variation and  $\delta^2 J|_{\mathbf{y}_k} \langle \Delta \mathbf{y}_k \rangle$  is the second variation of the cost functional (2). The minimization of this second-order expansion (3) is equivalent to the solution of the following time-varying LQR problem

$$J^* \langle \Delta \mathbf{x}_k, \Delta \mathbf{u}_k \rangle = \int_{t_s}^{t_f} \left( \frac{1}{2} \begin{bmatrix} \Delta \mathbf{x}_k^T & \Delta \mathbf{u}_k^T \end{bmatrix} \begin{bmatrix} \mathbf{Q} & \mathbf{N} \\ \mathbf{N}^T & \mathbf{R} \end{bmatrix} \begin{bmatrix} \Delta \mathbf{x}_k \\ \Delta \mathbf{u}_k \end{bmatrix} + \begin{bmatrix} \mathbf{S}^T & \mathbf{T}^T \end{bmatrix} \begin{bmatrix} \Delta \mathbf{x}_k \\ \Delta \mathbf{u}_k \end{bmatrix} + (\Delta \mathbf{x}_k^T \mathbf{E} + \mathbf{V}) \Delta \dot{\mathbf{x}}_k \right) dt \quad (4)$$

with the linear constraint equation

$$\mathbf{A} \Delta \dot{\mathbf{x}}_k + \mathbf{B} \Delta \mathbf{x}_k + \mathbf{C} \Delta \mathbf{u}_k + \mathbf{D} = \mathbf{0}. \quad (5)$$

Finally, the iteration is performed as follows: first, an initial value  $\mathbf{x}_0, \mathbf{u}_0$  is assigned. Then in every iteration step the time-varying LQR problem (4)-(5) is solved numerically and the next approximation of the solution is computed by the equations

$$\mathbf{x}_{k+1} = \mathbf{x}_k + \Delta \mathbf{x}_k, \quad (6)$$

$$\mathbf{u}_{k+1} = \mathbf{u}_k + \Delta \mathbf{u}_k. \quad (7)$$

## 4 Results

The proposed algorithm was successfully applied to the manipulator shown in Fig. 1 during a linear interpolation task of the end-effector. The resulting motion is plotted on Fig. 2 by a stroboscopic view. Fig. 3 shows the trajectory tracking error and Fig. 4 shows the calculated input torques.

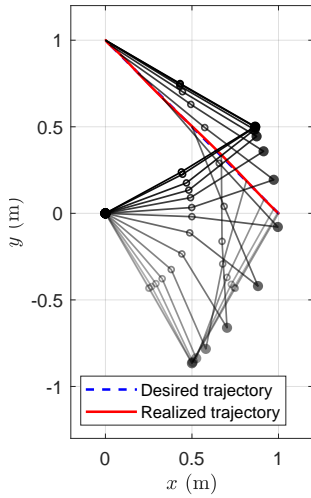


Figure 2: Stroboscopic view of the calculated motion

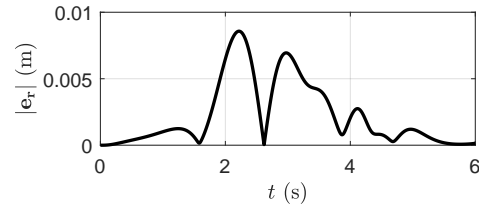


Figure 3: Trajectory tracking error during the motion

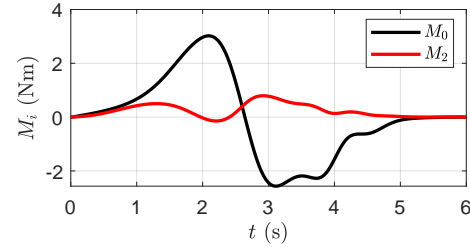


Figure 4: Calculated control input torques

## 5 Conclusion

The control of underactuated systems is still under investigation nowadays as they possess an internal dynamics which stability is not guaranteed by regular approaches. Therefore, a nonlinear optimal control approach was presented to manage this problem that results in a bounded motion of the system. Compared to other optimisation based controllers [4] from the literature, the advantage of this solution is that it does not require the discretization of the problem before generating an iteration that results in the optimal solution. Contrarily, the iteration is derived for the continuous-time states and control inputs first. Then the resulting continuous-time LQR problems are possible to solve with arbitrary numerical methods which results in low computational demand. In succeeding works the authors intend to exploit the opportunity of this property.

## References

- [1] W. Blajer., K. Kołodziejczyk. A case study of inverse dynamics control of manipulators with passive joints. *Journal Of Theoretical And Applied Mechanics*, 52(3), pages 793-801, 2014.
- [2] B. Bodor., A. Zelei, L. Bencsik. Predictive trajectory tracking algorithm of underactuated systems based on the calculus of variations. *Journal of Computational and Nonlinear Dynamics*, August 2021; 16(8): 081002., 2021.
- [3] F. L. Lewis., D. Vrabie, V. L. Syrmos. *Optimal control*. John Wiley & Sons, Inc., Hoboken, NJ, USA, 2012.
- [4] G. Bastos., O. Bröls. Analysis of Open-Loop Control Design and Parallel Computation for Underactuated Manipulators. *Acta Mech.*, 231(6), pages 2439–2456, 2020.

# Stability Chart of a Multiple Spring-Mass System Subjected to Delayed Collocated Control

Bence Szaksz, Gabor Stepan

Department of Applied Mechanics  
Budapest University of Technology and Economics  
Muegyetem rkp. 3., 1111 Budapest, Hungary  
szaksz@mm.bme.hu, stepan@mm.bme.hu

## EXTENDED ABSTRACT

### 1 Introduction

The control of elastic structures still poses challenges if the degree of freedom (DoF) of the system is increased, or if the time delay of the feedback control is not negligible. The stability analysis of elastic beams subjected to delayed follower force was investigated in [1], which was approximated by a lower DoF model since the analytical investigation of the continuum beam would have been too complex. The howling sound of a microphone-amplifier-loudspeaker system was modeled as longitudinal self-excited vibration of a beam subjected to delayed force feedback, first with a finite DoF approximation [2], then with a continuum beam [3]; a similar noise control system was investigated in [4].

The current study investigates the stabilization of an  $n$  DoF spring-mass system where the position and velocity of the first block are sensed and a delayed collocated feedback control force is applied at the same block (see Fig. 1).

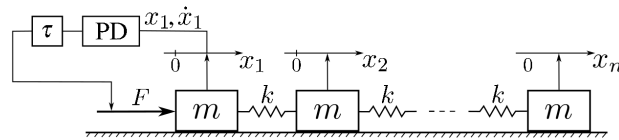


Figure 1: Mechanical model of an  $n$  DoF spring-mass system subjected to delayed collocated feedback.

### 2 Mechanical model

The dynamics of the  $n$  DoF system can be described by the governing equation

$$\mathbf{M}\ddot{\mathbf{x}}(t) + \mathbf{K}\mathbf{x}(t) = \mathbf{f}(\mathbf{x}(t - \tau), \dot{\mathbf{x}}(t - \tau)), \quad (1)$$

where  $\mathbf{x} = \text{col}[x_1, x_2, \dots, x_n]$  is the vector of the displacements of the blocks,

$$\mathbf{M} = \begin{bmatrix} m & 0 & 0 & \dots & 0 \\ 0 & m & \ddots & \ddots & \vdots \\ 0 & \ddots & \ddots & \ddots & 0 \\ \vdots & \ddots & \ddots & m & 0 \\ 0 & \dots & 0 & 0 & m \end{bmatrix} \quad \text{and} \quad \mathbf{K} = \begin{bmatrix} k & -k & 0 & \dots & 0 \\ -k & 2k & \ddots & \ddots & \vdots \\ 0 & \ddots & \ddots & \ddots & 0 \\ \vdots & \ddots & \ddots & 2k & -k \\ 0 & \dots & 0 & -k & k \end{bmatrix} \quad (2)$$

are the  $n \times n$  sized mass and stiffness matrices, respectively, while the delayed proportional-derivative (PD) control force takes the form

$$\mathbf{f}(\mathbf{x}(t - \tau), \dot{\mathbf{x}}(t - \tau)) = [-K_p x_1(t - \tau) - K_d \dot{x}_1(t - \tau), 0, \dots, 0]^T, \quad (3)$$

where  $\tau$  is the constant time delay. Introduce the dimensionless delay  $\alpha = \tau\sqrt{k/m}$ , the dimensionless proportional gain  $k_p = K_p \tau^2/m$ , and the dimensionless differential gain  $k_d = K_d \tau/m$ . The characteristic function  $D(\lambda)$  is the determinant of the corresponding tridiagonal matrix, which can be derived recursively with the help of the continuant, yielding

$$D(\lambda) = \left( \lambda^2 + (\lambda k_d + k_p) e^{-\lambda} \right) \sum_{l=0}^{n-1} \binom{n+l-1}{2l} \alpha^{2(n-l-1)} \lambda^{2l} + \sum_{l=1}^{n-1} \binom{n+l-2}{2l-1} \alpha^{2(n-l)} \lambda^{2l} = 0 \quad (4)$$

for the characteristic equation. The left hand-side of (4) is a quasi-polynomial with respect to the dimensionless characteristic exponent  $\lambda$ ; it has got infinitely many roots, finite number of which may be in the right-hand side of the complex plane.



### 3 Stability analysis

Static stability loss occurs when a real root crosses the imaginary axis through the origin, which corresponds to possible saddle-node bifurcation. Substituting  $\lambda = 0$  into the characteristic equation (4), the static D-curve can be found at  $k_p = 0$  (see the left panel of Fig. 2). The other possibility is that a pair of complex conjugate roots crosses the imaginary axis with nonzero imaginary part, which corresponds to possible Hopf bifurcation. Let us substitute  $\lambda = i\omega$  into Eq. (4), where  $\omega$  is the dimensionless angular frequency with which the system loses its stability. This yields the dynamic D-curve

$$k_p(\omega) = \frac{U_{2n-1}\left(\frac{\omega}{2\alpha}\right)}{U_{2n-2}\left(\frac{\omega}{2\alpha}\right)} \alpha \omega \cos(\omega), \quad k_d(\omega) = \frac{U_{2n-1}\left(\frac{\omega}{2\alpha}\right)}{U_{2n-2}\left(\frac{\omega}{2\alpha}\right)} \alpha \sin(\omega), \quad (5)$$

where  $U_j(y)$  is the  $j$ -th Chebyshev polynomial of the second kind. The dimensionless natural angular frequencies of the uncontrolled system can be found at

$$\omega_{n,l} = 2\alpha \cos\left(\frac{n-l}{2n}\pi\right), \quad l = 0, 1, 2, \dots, n-1, \quad (6)$$

from which  $\omega_{n,0} = 0$  corresponds to the translational motion and the others to the oscillating modes.

The left panel of Fig. 2 presents the stability chart of a 3 DoF system in the plane of the control parameters ( $k_p$ ,  $k_d$ ) for  $\alpha = 0.5$ ; the circled numbers represent the number of unstable characteristic roots in the disjunct domains. Increasing the dimensionless angular frequency  $\omega$ , the dynamic D-curve starts from the origin with  $\omega = \omega_{n,0} = 0$ ; then it has a singularity at  $\pm\infty$  and goes through the origin for the second time at  $\omega = \omega_{n,1}$ ; after this, it has another singularity at  $\pm\infty$  and goes through the origin again at  $\omega = \omega_{n,2}$ ; then it crosses the imaginary axis at  $\omega = \pi/2$  and starts spiraling outwards counterclockwise (see the blue curve in Fig. 2). The variation of the dimensionless delay  $\alpha$  or the DoF of the system alter the dynamic D-curve but it always starts from the origin, it has  $n-1$  singularities, and it goes through the origin  $n-1$  times when  $\omega = \omega_{n,l}$  with  $l = 1, \dots, n-1$ .

As it can be observed from the right panel of Fig. 2, the stabilizable domain shrinks and disappears with increasing the dimensionless delay  $\alpha$ , but it reappears again and again for larger  $\alpha$  values. Moreover, the largest applicable proportional gain can be found at the first reappearing stable domain.

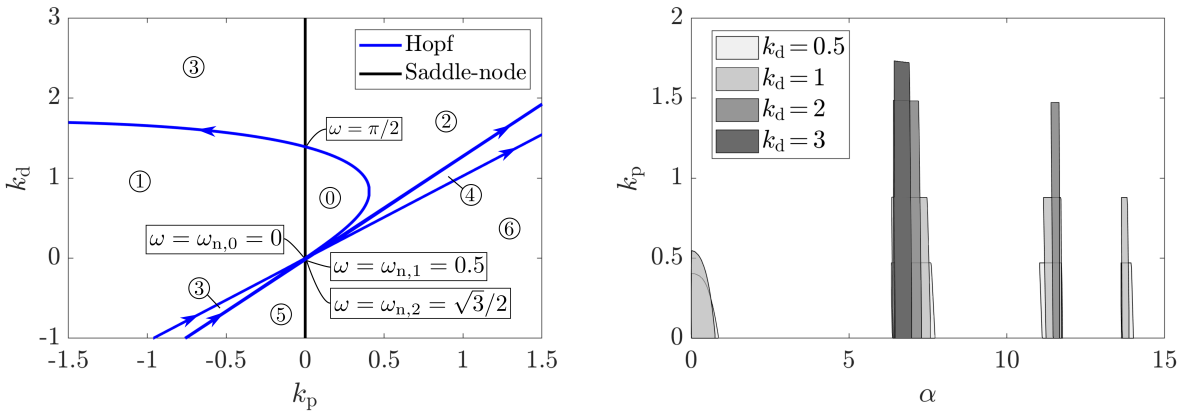


Figure 2: Stability charts of the 3 DoF system. The left panel presents the stability chart in the parameter plane ( $k_p, k_d$ ) for  $\alpha = 0.5$ ; the numbers represent the number of unstable characteristic roots. The right panel shows the stability chart in the plane of the dimensionless delay  $\alpha$  and the proportional gain  $k_p$  for different values of the differential gain  $k_d$ .

### 4 Conclusions

The study gives a closed form algebraic expression for the dynamic D-curves of a PD-controlled  $n$  DoF spring-mass system. A typical stability chart is presented, and it is shown that increasing the dimensionless delay, that is, increasing the time delay or the stiffness of the springs, the stable area disappears but it reappears again and again. Moreover, the largest proportional gain corresponds to the first reappearance of the stable region.

### References

- [1] Ma, H., Butcher, E. A. Stability of elastic columns with periodic retarded follower forces. *Journal of Sound and Vibration*, 286(4-5):849-867, 2005.
- [2] Kidd, M., Stepan, G. Delayed control of an elastic beam. *International Journal of Dynamics and Control*, 2.1:68-76, 2014.
- [3] Zhang, L., Stepan, G. Exact stability chart of an elastic beam subjected to delayed feedback. *Journal of Sound and Vibration*, 367:219-232, 2016.
- [4] Haraguchi, M., Hu, H. Y. Stability analysis of a noise control system in a duct by using delay differential equation. *Acta Mechanica Sinica*, 25.1:131-137, 2009.

**Section**

**EFFICIENT NUMERICAL ALGORITHMS**

REALTIME

# Reduced Order Interface Modelling for Haptic Simulation and Interfacing

Liam Kerr<sup>1</sup>, József Kövecses<sup>1</sup>

<sup>1</sup> Department of Mechanical Engineering and Centre for Intelligent Machines  
McGill University  
845 Rue Sherbrooke O., H3A0C3 Montréal, Canada  
liam.kerr@mail.mcgill.ca, jozsef.kovecses@mcgill.ca

## EXTENDED ABSTRACT

The use of haptic devices is becoming ubiquitous in simulators for operator training, virtual prototyping, and recreation, and for teleoperation of real-world robotic devices. The role of the haptic device in these applications is to convey the forces arising from interactions with a remote or virtual environment to the human operator, a process known as haptic rendering [1]. This is used, for example, to train machinery operators, astronauts, and medical professionals to perform tasks in their respective fields in a safe and cost-effective manner, while also improving learning curve and quality of work [2],[3]. Though haptic devices can be employed to interface with both real and simulated environments, in this work we focus on haptic devices interfacing with interactive virtual environments such as those in training simulators or video games.

Haptic interfacing is digital in nature, the control signal outputs must be computed based on inputs sampled at discrete time points, both from the virtual environment with which they are interacting and the haptic device itself. Haptic systems have to run at high frequencies to avoid instabilities caused by time delay and discretization error. Conversely, interactive simulations typically run at lower rates to smoothly display graphics while maximizing the available computation time between successive integration time steps. This discrepancy in frequency requirements can force the haptic system to extrapolate the environment behaviour when sampling between integration time steps. The most common method to achieve this is known as the zero-order-hold (ZOH), in which the last known state of the environment is assumed to remain constant until the next integration time step, regardless of potential changes in the behaviour of the continuous-time representation of the environment between the sampling points. Such time-history-based methods may yield a prediction of the environment state with no physical basis, resulting in a loss of information which can induce instabilities, chatter, and reduced rendering fidelity [3].

A clear parallel can be drawn between the notion of a haptic system running at a different frequency than the virtual environment with which it interfaces and the concept of multi-rate co-simulation, in which a system to be simulated is decomposed into multiple coupled subsystems which are integrated at different rates to accommodate different frequency requirements between the two subsystems. We hypothesize that a recently devised reduced-order modelling technique known as reduced interface modelling (RIM), developed in [4], [5], to improve the performance of multi-rate co-simulation, could help to improve the performance of haptic devices.

Reduced interface modelling was introduced for improving the performance of multi-rate co-simulations involving mechanical subsystems interacting with other subsystems of various nature. Consider the case of a single mechanical subsystem interacting with a single other subsystem with faster dynamics and shorter time scales, i.e., a hydraulic actuator. The method involves computing a reduced-order model of the mechanical subsystem by parameterizing its dynamics in terms of the local velocities at the interface between the mechanical subsystem and the other subsystem. This parameterization is obtained by reformulating the dynamics of the mechanical system such that the dynamics associated with the subspace defined by the local interface velocities can be factored out. This process is derived in detail in [4] and [5]. The reduced interface model is then transferred to the simulation unit integrating the other subsystem, which is integrated at a higher rate than the mechanical subsystem on account of its faster dynamics. The higher rate of integration requires that more than one integration step of the faster subsystem takes place for each integration step of the mechanical subsystem. The interface model allows the faster simulation unit to make a dynamics-based prediction of the state of the mechanical subsystem between its (longer) integration steps, rather than relying on an extrapolation function based on the time history of the state of the mechanical subsystem.

In this work, we implement the RIM technique to improve the performance of haptic simulation. To demonstrate the efficacy of this approach, we employ a driver-in-the-loop vehicle simulation, in which the driver interacts with a simulated vehicle through an impedance haptic steering wheel. Steering torque feedback is one of the most important indicators of both vehicle handling quality and limit performance. The reduction in steering effort as the tires reach maximum cornering potential is one of the main indicators of impending loss of grip, and the steering-force gradient has an influence on the overall handling quality of the vehicle [6]. Accordingly, it is imperative that steering torque feedback is accurately rendered by haptic steering wheels for driver training and human-in-the-loop testing of virtual vehicle prototypes. We use a multibody vehicle model  $\mathcal{V}$  running in a virtual environment interfacing with a haptic steering wheel  $\mathcal{H}$ . The vehicle model consists of five rigid bodies – one for each of the four wheels and one for the chassis – connected via bilateral constraints simulating revolute and prismatic joints. The interaction of the wheels with the ground is characterized by empirical tire models relating the vehicle state to the forces and moments acting on the tires.

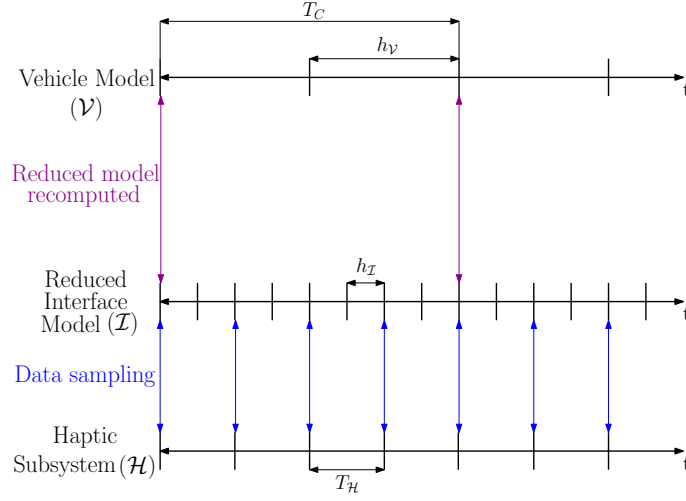


Figure 1: Timeline of events in haptic simulation implemented with RIM.

A single degree-of-freedom (DOF) reduced order interface model  $\mathcal{I}$  is computed at the beginning of each communication step, to represent the dynamics of the vehicle from the perspective of the haptic steering wheel. In this case, the local velocity which defines the interface between the haptic subsystem and vehicle subsystem, and which is used to define the subspace in which the interface dynamics are expressed, is the angular velocity about the steering axis. Note that the communication step may be equal to- or longer than the vehicle simulation integration step. At each communication point the reduced model is transferred to the haptic subsystem, which can integrate the reduced model at a rate higher than that of the full model, owing to the smaller number of dynamic equations in the reduced model. The haptic controller can then sample the state of the vehicle between integration steps of the full model using the reduced model which includes information about the dynamics of the vehicle. The timeline of these events is shown in Fig. 1, where the communication step size is  $T_C$ , the vehicle simulation integration step size is  $h_V$ , the reduced interface model step size is  $h_I$ , and the haptic controller sampling period is  $T_H$ . The details of the full vehicle model and reduced model, and the specifications of the haptic simulation will be addressed in the presentation, along with results of experiments investigating the stability and fidelity of the haptic rendering.

## Acknowledgments

This work was supported by the Natural Sciences and Engineering Research Council of Canada (NSERC) and CM Labs Simulations Inc. The support is gratefully acknowledged.

## References

- [1] K. Salisbury, F. Conti, F. Barbagli. Haptic rendering: Introductory concepts. *IEEE Computer Graphics and Applications*, 24(2): 24-32, 2004.
- [2] H. Culbertson, S. B. Schorr, A. M. Okamura. Haptics: The present and future of artificial touch sensation. *Annual Review of Control, Robotics, and Autonomous Systems*, 1:385-409, 2018.
- [3] K. Ghaffari Toiserkan. A unified framework for rendering stiff and dynamic virtual environments. PhD Thesis, McGill University, Montréal, 2014.
- [4] A. Peiret, F. Gonzalez, J. Kövecses, M. Teichmann. Multibody system dynamics interface modelling for stable multirate co-simulation of multiphysics systems. *Mechanism and Machine Theory*, 127:52-72, 2018.
- [5] J. Kövecses. Dynamics of mechanical systems and the generalized free-body diagram – part I: General formulation. *Journal of Applied Mechanics*, 75(6), 2008.
- [6] N. Kim, D. J. Cole. A model of driver steering control incorporating the driver's sensing of steering torque. *Vehicle System Dynamics*, 49(10):1575-1596, 2011.

# Rod-removal technique for flexible-rods in the framework of semi-recursive multibody formulation

Yongjun Pan<sup>1</sup>, Liming Huang<sup>1</sup>, Xinxin Yu<sup>2</sup>, Aki Mikkola<sup>3</sup>

<sup>1</sup> State Key Laboratory of Mechanical Transmission  
College of Mechanical and Vehicle Engineering, Chongqing University  
Chongqing, 400044, China  
yongjun.pan@cqu.edu.cn

<sup>2</sup> Department of Mechanical Engineering  
Lappeenranta University of Technology  
Lappeenranta, 53850, Finland  
[xinxin.yu, aki.mikkola]@lut.fi

## EXTENDED ABSTRACT

### 1 Introduction

A semi-recursive multibody formulation takes the advantages of relative coordinates and leads to numerically efficient approach to solve dynamics of complex systems. The efficiency of the semi-recursive multibody formulation can be further improved by employing the rod-removal technique. Efficiency enhancement is due to reduced number of constraint equations and, in part, reduced number of relative coordinates. In practice, slender rods are often part of multibody systems, for example, in vehicle suspensions and heavy machinery. Deformation of slender rods is often significant making it necessary to model a slender rod as a flexible body. In terms of computational efficiency and accuracy, it is important to be able to apply the rod-removal technique for flexible rods as well.

This paper presents a novel approach for modeling the flexible slender-rods using the framework of the rod-removal technique. The principle behind this method is to remove the flexible-rods and consider the variable-length constraint equations. When applying the flexible-rod removal technique, the rods-associated second-derivative-based inertial forces and velocity-dependent inertial forces and external forces must be calculated and assembled in the whole system. The stiffness equations of the removed flexible-rods, in turn, are formulated based on the beam finite elements. The finite element equations are combined with the multibody equations of motion to perform the simulation of rigid-flexible multibody system. A four-bar mechanism with a flexible middle-link is employed to verify the effectiveness of the presented flexible-rod removal technique. Finally, a rigid-flexible vehicle model is taken as an example to investigate the effects of flexible-rods towards vehicle dynamics, where different initial velocities and sprung masses are considered. The results reveal how the flexible-rods affect the vehicle dynamics, and prove that the effects must be taken into account especially during high-speed, heavy-load, and bumpy road conditions.

Combining the finite element equations of the flexible-rods and the equations of motion of the multibody system, the governing equations of the rigid-flexible multibody system can be finally expressed as:

$$\begin{cases} \bar{\mathbf{K}}\delta\bar{\mathbf{q}} = \delta\bar{\mathbf{P}}(\ddot{\mathbf{z}}) \approx \delta\hat{\mathbf{P}} \\ \mathbf{M}\ddot{\mathbf{z}} = \bar{\mathbf{P}}(\mathbf{z}, \dot{\mathbf{z}}, \delta\bar{\mathbf{q}}) \end{cases} \quad (1)$$

### 2 Simulation results

This section introduces a four-bar mechanism to verify the introduced flexible-rod removal technique. Three variations for the stiffness are considered. They are the original stiffness, the half stiffness, and the one-tenth stiffness. Figures 1 and 2 show the differences of flexible-rod removal technique with different stiffness in terms of relative coordinates and velocities. Note that the ADAMS results are regarded as the reference solutions for comparison. Furthermore, for the purpose of validation, the numerical results of flexible-rod removal technique are also compared with the rigid-rod removal technique and floating frame of reference formulation.

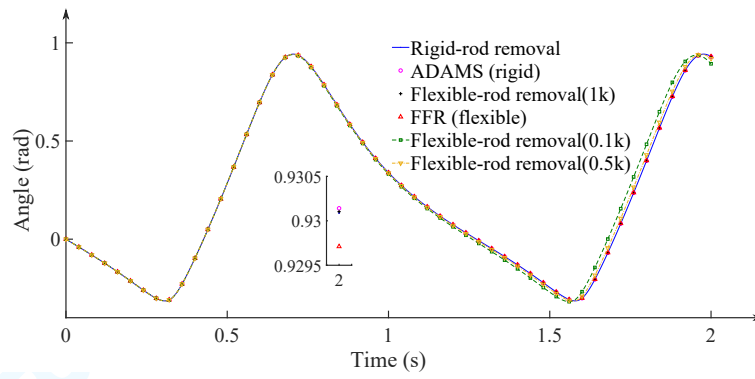
Figure 1 shows the responses of the relative angles when the rod-flexibility is considered. Figure 2 shows the responses of the relative angular-velocities when the rod-flexibility is considered. It can be seen that the numerical results close to the reference solutions. The stiffer the flexible-rod is, the closer the numerical results to the reference solution, as expected. Furthermore, the floating frame of reference formulation is implemented to verify the effectiveness of the flexible-rod removal technique.

### Acknowledgments

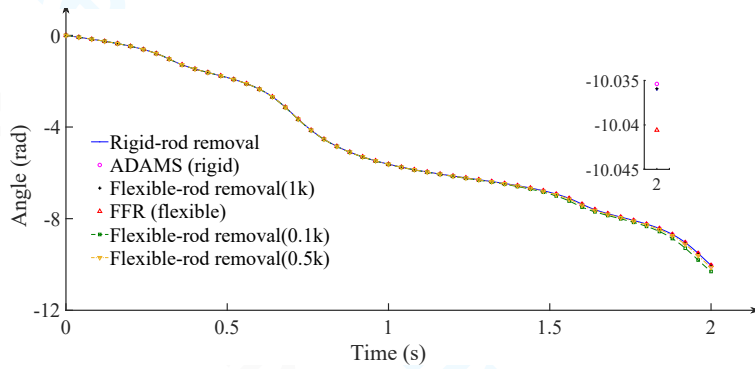
This work was supported by the National Natural Science Foundation of China (Project No.12072050).

### References

- [1] García de Jalón, J. and Álvarez, E. and de Ribera, F.A. and Rodríguez, I. and Funes, F.J. A Fast and Simple Semi-Recursive Formulation for Multi-Rigid-Body Systems. In: Ambrósio, Jorge A.C.(Ed.), Computational Methods in Applied Sciences, Vol.2 of Computational Methods in Applied Sciences, Springer Netherlands, pages 1-23, 2005.
- [2] Pan, Yongjun and Callejo, Alfonso and Bueno, José L. and Wehage, Roger A. and García de Jalón, Javier". Efficient and accurate modeling of rigid rods. Multibody System Dynamics, 40(1):23-42, 2017.

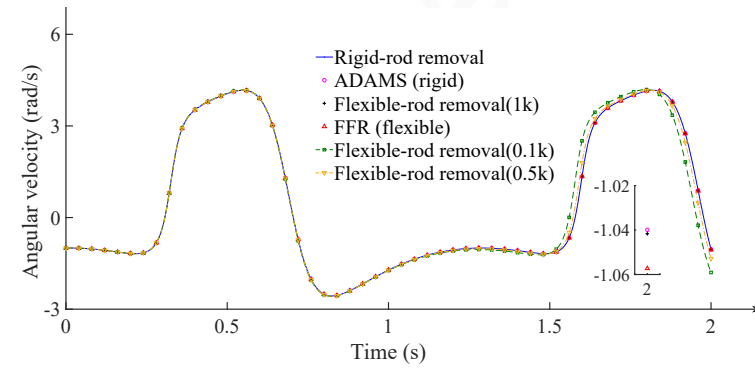


(a) angle  $z_1$

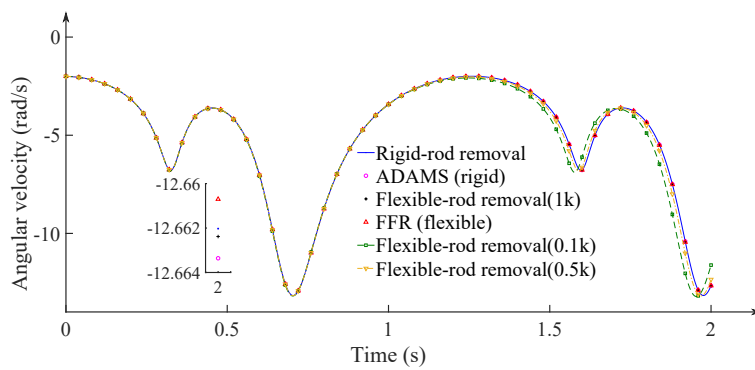


(b) angle  $z_3$

Figure 1: Angles of different formulations



(a) angular velocity  $\dot{z}_1$



(b) angular velocity  $\dot{z}_3$

Figure 2: Angular velocities of different formulations

# Enabling Artificial Intelligence Studies in Off-Road Mobility Through Physics-Based Simulation of Multi-Agent Scenarios

Aaron Young, Simone Benatti, Jay Taves, Asher Elmquist, Radu Serban, Dan Negrut,

<sup>1</sup> Department of Mechanical Engineering, University of Wisconsin - Madison  
Madison, Wisconsin, United States  
Email: {aryoung5, benatti, jtaves, amelmquist, serban, negrut}@wisc.edu

## EXTENDED ABSTRACT

### 1 Introduction

Computer simulation has been extensively used in the design and analysis of various automation aspects tied to on-road mobility, see for instance [1]. A similar statement cannot be made for off-road mobility owing to a smaller market and a set of stiff challenges brought along by the task at hand. However, a predictive simulation platform for off-road mobility analysis of autonomous agents (AAs) is very desirable since it can accelerate the engineering design cycle, reduce costs, perform more thorough testing, and produce more performant and safer designs. Simulation has its limitations, first of all related to the issue of simulation-to-reality transfer, which pertains to the failure of control policies derived in simulation to work well in the real world. Furthermore, models are difficult to set up and calibrate, the validation process can be tedious and time consuming. Open source simulation tools that are both predictive and expeditious are not readily available [2]. This contribution addresses this last point. It describes a simulation environment whose stated purpose is to allow the practitioner to gain insights into the operation of AAs (robots and autonomous wheeled or tracked vehicles) in off-road conditions with an eye towards: improving mechanical designs of AAs; and, producing and testing control policies that govern the operations of the AAs. The environment is demonstrated in conjunction with the design and assessment of a reinforcement learning policy that uses sensor fusion and inter-agent communication to enable the movement of mixed convoys of human-driven and autonomous vehicles. Policies are learned on rigid terrain and are subsequently shown to transfer successfully to hard (silt-like) and soft (snow-like) deformable terrains. The enabling simulation environment is developed from the high fidelity, physics-based simulation engine Chrono. The software stack and the Chrono simulator are both open source [3]. Relevant movies: [4].

### 2 Deriving Control Policies Through Simulation

Derived using an accurate simulation framework, control algorithms have been shown to bridge the sim-to-reality gap successfully. The use of vehicles with Level 1 and Level 2 autonomy has grown considerably and the automotive industry is making major strides in the transition to Levels 3 and 4 autonomy. The design of a robust controller that performs adequately in complex environments has proven difficult when aiming for a generalized policy. As opposed to traditional control approaches, such as Model Predictive Control (MPC), an emerging approach that has gained momentum in recent years is based on Machine Learning (ML). In the context of autonomous vehicles (AVs), deep reinforcement learning (DRL) has been very successful, as it displays the ability to learn and respond in complex scenarios without the need for preprocessed or labeled data.

The purpose of the simulation environment described is twofold. First, it is used to produce the data needed to design a control policy. Second, it is used for testing purposes. To this end, it exposes the control policy produced in a model-based or model-free approach to tests that gauge its correctness and robustness. In this contribution, five Chrono modules are employed: Chrono::Engine, Chrono::Vehicle, PyChrono, SynChrono and Chrono::Sensor. Vehicles are modeled using Chrono::Engine and Chrono::Vehicle and deployed on deformable terrain within the training/testing environment. Utilizing the Python interface to the C++ Chrono API called PyChrono and OpenAI Gym's supporting infrastructure, training is conducted in a GymChrono learning environment. The GymChrono-generated policy is subsequently deployed for testing in SynChrono, a scalable, cluster-deployable multi-agent testing infrastructure built on MPI. SynChrono facilitates inter-agent communication and maintains time and space coherence between agents. A sensor modeling tool, Chrono::Sensor, supplies sensing data that is used to inform agents during the learning and inference processes.

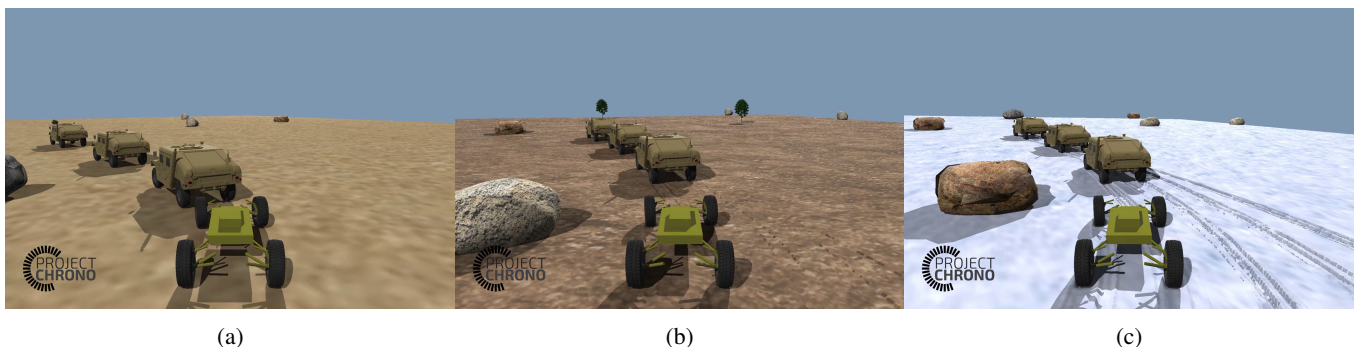


Figure 1: Still frames from attached third person camera: (a) rigid terrain; (b) SCM-Hard terrain; (c) SCM-Soft terrain.



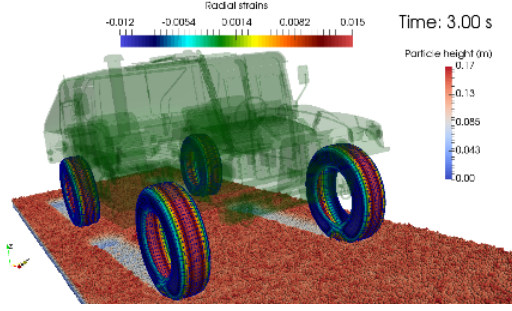


Figure 2: Chrono::Vehicle HMMWV with flexible tires navigating granular terrain demonstrating vehicle dynamics, flexible bodies, and parallel computing support.

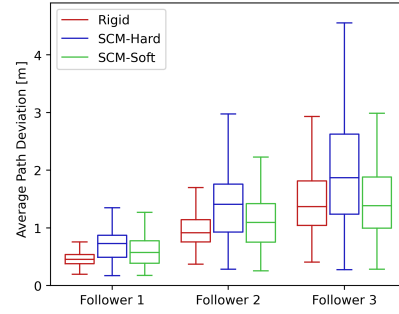


Figure 3: Average deviation in [m] between the leader and each subsequent follower on each terrain type tested in the 1L+3F configuration.

### 3 Technology demonstration

The goal of the demonstration, apart from showcasing the simulation infrastructure, is to enable a vehicle to move as part of a convoy. To train and subsequently test the derived policy, a four-vehicle convoy is constructed on either rigid or SCM deformable terrain. Up to three of the convoy vehicles use this policy while driving in a platoon. Thus, the possible scenarios are: three lead vehicles and one following vehicle (3L+1F), two lead and two followers (2L+2F), and one lead and three followers (1L+3F). The *lead* vehicles are programmed to follow a path defined by way-points; for all purposes, these can be considered human driven. A follower vehicle is autonomous and uses the learned policy to follow the vehicle in front of it. In doing so, it should (i) not crash into the vehicle ahead of it, and (ii) avoid hitting obstacles in the vicinity of the path. DRL is the chosen technique used to demonstrate the simulation capabilities; Proximal Policy Optimization (PPO) [5] is one of the most widely used algorithms for continuous state and action environments and is the algorithm of choice for this demonstration.

In order to perform a statistical analysis of the performance of the platooning policy, we define a set of six performance metrics that measure the deviations of a follower vehicle from that of the convoy leader and encode both lateral path deviation and deviations in the vehicle speed at a given location along the leader’s path. These metrics are defined in such a way as to allow comparisons between the performance of followers at different positions in the convoy, as well as across the three different terrain types considered here. Statistical results of one of the aforementioned metrics is shown in Figure 3.

### 4 Conclusion and Future Work

This contribution pertains to a simulation platform designed to facilitate the design and testing of control policies for AAs operating in off-road conditions. The platform draws on a physics-based simulation engine; has templates for wheeled and tracked vehicles; enforces space and time coherence for multiple vehicles being run in parallel by different processors; allows for human-in-the-loop scenarios; provides sensor simulation capabilities; has a bridge to ROS/ROS2; can simulate mobility on fully resolved, continuum, or SCM representations of the terrain; is open source; and is cluster deployable to support multi-AA mobility studies. This software framework is used here to design an RL-based control policy that allows AAs to follow in a convoy formation. The virtual environments used in testing differed in textures and colors from the ones used in the training, thus demonstrating robustness of the inferred policy that relies on inputs from an RGB camera sensor. Unsurprisingly, the fewer AAs in the platoon, the tighter the control policy managed to follow a prescribed path. Looking ahead, we plan to augment the sensing simulation support; improve scalability; and use this infrastructure to derive new control policies for off-road AA mobility.

### References

- [1] Dosovitskiy, A., Ros, G., Codevilla, F., Lopez, A., and Koltun, V., 2017. “CARLA: An open urban driving simulator”. In *Proceedings of the 1st Annual Conference on Robot Learning*, pp. 1–16.
- [2] Choi, H., Crump, C., Duriez, C., Elmquist, A., Hager, G., Han, D., Hearl, F., Hodgins, J., Jain, A., Leve, F., Li, C., Meier, F., Negrut, D., Righetti, L., Rodriguez, A., Tan, J., and Trinkle, J., 2021. “On the use of simulation in robotics: Opportunities, challenges, and suggestions for moving forward”. *Proceedings of the National Academy of Sciences*, **118**(1).
- [3] Tasora, A., Serban, R., Mazhar, H., Pazouki, A., Melanz, D., Fleischmann, J., Taylor, M., Sugiyama, H., and Negrut, D., 2016. “Chrono: An open source multi-physics dynamics engine”. In *High Performance Computing in Science and Engineering – Lecture Notes in Computer Science*, T. Kozubek, ed. Springer, pp. 19–49.
- [4] Project Chrono, 2020. Off-road AV simulations. <https://uwmadison.box.com/s/g1bpqxpomgyiomt2ydcpte35avr44vd>.
- [5] Schulman, J., Wolski, F., Dhariwal, P., Radford, A., and Klimov, O., 2017. “Proximal policy optimization algorithms”. *CoRR*, **abs/1707.06347**.

# Comparing Semi-recursive Multibody Formulations for Hydraulically Driven Mechanisms

Suraj Jaiswal<sup>1</sup>, Jarkko Rahikainen<sup>2</sup>, Qasim Khadim<sup>1</sup>, Jussi Sopanen<sup>1</sup>, Aki Mikkola<sup>1</sup>

<sup>1</sup> Department of Mechanical Engineering,  
Lappeenranta University of Technology,  
Yliopistontie 34, 53850 Lappeenranta, Finland  
[suraj.jaiswal, qasim.khadim, jussi.sopanen, aki.mikkola]@lut.fi

<sup>2</sup> Mevea Ltd.,  
Laserkatu 6, 53850 Lappeenranta, Finland  
jarkko.rahikainen@mevea.com

## EXTENDED ABSTRACT

### 1 Introduction

Simulation of complex mechanical systems, such as heavy machinery, can be performed using multibody dynamics. A semi-recursive method is an often-used computational approach within multibody dynamics. In this approach, closed-loop systems are modeled by incorporating loop-closure constraints in the dynamics of its open-loop equivalent. In the application of heavy machinery, the equations of motion are often coupled with models of other physical nature such as hydraulic actuators. The modeling of hydraulic actuators often leads to a numerically stiff system [1], and consequently, the time integration of coupled multibody models becomes cumbersome. However, this problem can be alleviated by a proper selection of a multibody formulation.

The objective of this study is to introduce and compare two semi-recursive multibody formulations in the framework of monolithically coupled hydraulic actuators. In the multibody formulations, the loop-closure constraints are incorporated using the index-3 augmented Lagrangian method with projections and the coordinate partitioning method [2]. Hydraulic actuators are modeled using the lumped fluid theory [3]. In the study, only a fixed step-size integrator is considered making the introduced methods suitable for real-time simulation. A case study of a hydraulically actuated quick-return mechanism is illustrated where the approaches are compared based on the work cycle, energy balance, constraint violation, and numerical efficiency.

### 2 Multibody system dynamics

In semi-recursive formulations, the equations of motion for an open-loop system with  $N_b$  bodies can be written as [1, 2]

$$\bar{\mathbf{M}}^\Sigma \ddot{\mathbf{z}} = \bar{\mathbf{Q}}^\Sigma, \quad (1)$$

where  $\ddot{\mathbf{z}} \in \mathbb{R}^{N_b}$  is the vector of relative joint accelerations,  $\bar{\mathbf{M}}^\Sigma$  is the mass matrix, and  $\bar{\mathbf{Q}}^\Sigma$  is the external force vector.

For a closed-loop system, a set of  $N_m$  loop-closure constraints,  $\Phi = \mathbf{0}$ , can be incorporated into the open-loop dynamics in many ways. In the index-3 augmented Lagrangian method with projections [2], the equations of motion for the closed-loop system can be written as

$$\left. \begin{aligned} \bar{\mathbf{M}}^\Sigma \ddot{\mathbf{z}} + \Phi_z^T \alpha \Phi + \Phi_z^T \lambda &= \bar{\mathbf{Q}}^\Sigma \\ \lambda^{(h+1)} &= \lambda^{(h)} + \alpha \Phi^{(h+1)} \end{aligned} \right\}, \quad (2)$$

where  $\Phi_z$  is the Jacobian matrix of  $\Phi$ ,  $\alpha$  is the penalty factor,  $\lambda$  is the vector of iterated Lagrange multipliers, and  $h$  is the iteration step. Here, the velocities and accelerations are corrected using projections after each integration step. For simplicity, the constraints are assumed to be holonomic and scleronomic in this study.

In the coordinate partitioning method [2], the relative joint velocities are mapped onto a set of independent relative joint velocities as  $\dot{\mathbf{z}} = \mathbf{R}_z \dot{\mathbf{z}}^i$ , where  $\dot{\mathbf{z}}^i \in \mathbb{R}^{N_f}$  are the independent relative joint velocities with  $N_f$  being the degrees of freedom, and  $\mathbf{R}_z \in \mathbb{R}^{N_b \times N_f}$  is a velocity transformation matrix. Accordingly, the equations of motion for the closed-loop system can be written as

$$\mathbf{R}_z^T \bar{\mathbf{M}}^\Sigma \mathbf{R}_z \ddot{\mathbf{z}}^i = \mathbf{R}_z^T (\bar{\mathbf{Q}}^\Sigma - \bar{\mathbf{M}}^\Sigma \mathbf{R}_z \dot{\mathbf{z}}^i) \Rightarrow \bar{\mathbf{M}}^\Sigma \ddot{\mathbf{z}}^i = \bar{\mathbf{Q}}^\Sigma, \quad (3)$$

where  $\ddot{\mathbf{z}}^i \in \mathbb{R}^{N_f}$  are the independent relative joint accelerations,  $\bar{\mathbf{M}}^\Sigma = (\mathbf{R}_z^T \bar{\mathbf{M}}^\Sigma \mathbf{R}_z)$ , and  $\bar{\mathbf{Q}}^\Sigma = [\mathbf{R}_z^T (\bar{\mathbf{Q}}^\Sigma - \bar{\mathbf{M}}^\Sigma \mathbf{R}_z \dot{\mathbf{z}}^i)]$ . This method assumes that redundant constraints and singular configurations do not exist. Here, the independent relative joint coordinates are identified using the Gaussian elimination with full pivoting to the Jacobian matrix.

### 3 Modeling of hydraulic actuators

In this study, the hydraulic pressures in a hydraulic circuit are computed using the lumped fluid theory [3]. In this approach, the hydraulic circuit is divided into discrete volumes, where the pressures are assumed to be equally distributed. The pressure,  $p_s$ , within a hydraulic control volume,  $V_s$ , can be written as

$$\dot{p}_s = \frac{B_{e_s}}{V_s} \sum_{k=1}^{n_f} Q_{s_k}, \quad (4)$$

where  $\dot{p}_s$  is the pressure build-up,  $B_{e_s}$  is the effective bulk modulus,  $Q_{s_k}$  is the incoming and/or outgoing volume flow rates, and  $n_f$  is the total number of volume flow rates associated to the control volume  $V_s$ .

#### 4 Test and results

In this study, the coupling of the semi-recursive multibody methods with the hydraulic actuators are performed in a monolithic approach. The force vectors in Eqs. (2) and (3) are incremented with the pressure variation equations shown in Eq. (4). The coupled systems are integrated using an implicit single-step trapezoidal rule. The numerical example is shown in Fig. 1.

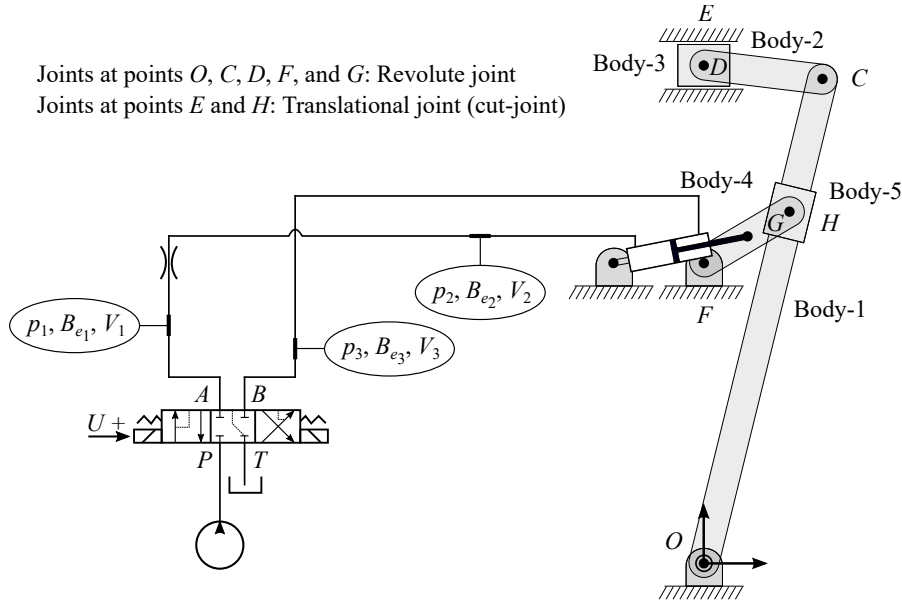


Figure 1: A hydraulically actuated quick-return mechanism

For the presented case study, the energy balance in both approaches showed a good agreement as shown in Fig. 2a, which is computed using the kinetic energy, potential energy, and actuator work. The augmented Lagrangian approach utilized a full set of coordinates, whereas identifying the independent coordinates in the coordinate partitioning approach is considered a relative drawback. The augmented Lagrangian approach can handle redundant constraints and singular configurations, whereas they are assumed to be non-existent in the coordinate partitioning approach. The augmented Lagrangian approach took 28.47 s of total integration time and is numerically more efficient than the coordinate partitioning approach (29.03 s) as shown in Fig. 2b. The poor numerical efficiency of the latter approach is attributed to the iterative solution of the position problem.

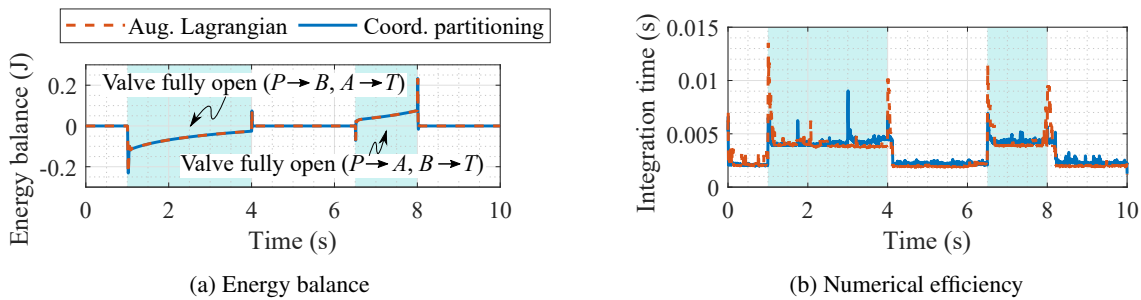


Figure 2: A comparison of energy balance and numerical efficiency with a time-step of 1 ms

#### 5 Conclusion

For the presented case study, the augmented Lagrangian approach had a number of advantages and was numerically more efficient compared with the coordinate partitioning approach.

#### References

- [1] J. Rahikainen, M. Kiani, J. Sopanen, P. Jalali, and A. Mikkola. Computationally efficient approach for simulation of multibody and hydraulic dynamics. *Mechanism and Machine Theory*, 130:435-446, 2018.
- [2] J. G. De Jalon and E. Bayo. *Kinematic and dynamic simulation of multibody systems: The real-time challenge*. Springer, Berlin, 1994.
- [3] J. Watton. *Fluid power systems: Modeling, simulation, analog, and microcomputer control*. Prentice Hall, New York, 1989.

# Assessment of Variable Step-Size Integration of Multibody Systems

Maurizio Ruggiu<sup>1</sup>, Francisco González<sup>2</sup>

<sup>1</sup> Dipartimento di Ingegneria Meccanica, Chimica e dei Materiali  
Università di Cagliari  
Via Marengo, 2, 09123 Cagliari, Italy  
maurizio.ruggiu@dimcm.unica.it

<sup>2</sup> Laboratorio de Ingeniería Mecánica  
University of A Coruña  
Mendizábal s/n, 15403 Ferrol, Spain  
f.gonzalez@udc.es

## EXTENDED ABSTRACT

### 1 Introduction

A considerable number of methods and algorithms for the simulation and analysis of Multibody System (MBS) Dynamics have been proposed since the early developments in this area were first published [1]. The performance of each approach depends on the characteristics of the problems to which it is applied, and so methods that are effective in the simulation of a certain type of mechanical system may be inefficient when applied to mechanisms with a different topology or subjected to other kinds of physical phenomena. Moreover, implementation techniques and the hardware platform used to execute the code, as well as the interaction between them, have a critical impact on the time elapsed in computations. For these reasons, selecting a MBS formalism for its application to a particular problem may prove challenging in some cases, particularly when efficiency constraints are imposed as a requirement.

Benchmark problems represent a useful tool to evaluate both the accuracy and efficiency of MBS codes. Ideally, benchmarks should be simple enough to enable their exact reproduction by any researcher or team interested in using them. At the same time, they must be nontrivial problems that provide interesting information about some aspect of the behaviour of the solution method [2]. In recent years, several initiatives have been put forward by MBS researchers to propose meaningful test problems that can be generally accepted as benchmarks by the community, e.g., [4, 5]. These examples illustrate the performance of MBS formulations and implementations when dealing with complex issues such as redundant constraints, singular configurations, flexibility, stiff problems, and contacts, to mention just a few.

Variable step-size integration methods are frequently used in MBS dynamics applications. In some cases, the step-size control solution is combined with the MBS formulation used to handle the equations of motion, e.g., [3]. This paper presents a benchmark problem particularly geared towards such integration methods.

### 2 Methodology

As benchmark problem, we propose a variation on the well-known slider-crank mechanism, which has already been used as benchmark in [4], shown in Fig. 1. The addition of an externally applied force  $f$  on point Q on the slider may give rise to the chaotic behaviour of the system under certain circumstances. This is exploited to test the correctness of variable-step solution approaches. At the same time, it poses a challenge regarding the determination of the reference solution of the problem.

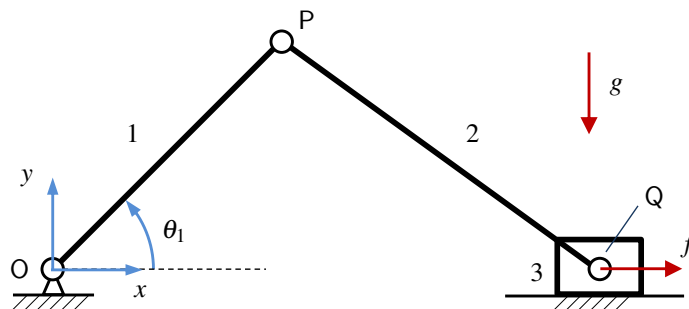


Figure 1: Slider-crank mechanism used as benchmark problem.

Three simulation cases are considered, as shown in Table 1, which details the lengths ( $L$ ), masses ( $m$ ), and moments of inertia ( $I_G$ ) of the links of the mechanism, as well as the angle of link 1 at time  $t = 0$ ,  $\theta_{1,0}$  and the initial velocity of the slider,  $\dot{x}_{Q,0}$ . It also specifies the expression of the force  $f$  applied on Q as a function of time. The system moves under gravity effects, with  $g = 9.81 \text{ m/s}^2$  acting along the negative y-axis.

Case 1 corresponds to the slider-crank benchmark problem in [4], which goes through a singular configuration when  $\theta_1 = \pi/2$ , and is used for comparison purposes. Cases 2 and 3 introduce the externally applied force  $f = 100 \sin(\pi t)$ , which causes numerical difficulties in the problem solution. Unlike cases 1 and 3, case 2 does not feature any singular configurations.

Table 1: Simulation cases

Case	$L_1$ (m)	$L_2$ (m)	$m_1$ (kg)	$m_2$ (kg)	$m_3$ (kg)	$I_{G,1}$ (kgm <sup>2</sup> )	$I_{G,2}$ (kgm <sup>2</sup> )	$\theta_{1,0}$ (rad)	$\dot{x}_{Q,0}$ (m/s)	$f$ (N)
1	1	1	1	1	0	1/12	1/12	$\pi/4$	-4	0
2	3	6	1.5	3	0.25	9/8	9	0	0	$100 \sin(\pi t)$
3	1	1	1	1	0	1/12	1/12	$\pi/4$	0	$100 \sin(\pi t)$

### Acknowledgments

F. González acknowledges the support of the Ministry of Economy of Spain through the Ramón y Cajal programme, contract RYC-2016-20222.

### References

- [1] O. A. Bauchau. Flexible multibody dynamics. Springer, Dordrecht, 2011.
- [2] M. González, F. González, A. Luaces, J. Cuadrado. A collaborative benchmarking framework for multibody system dynamics. *Engineering with Computers*, 26(1):1-9, 2010.
- [3] D. Dopico, E. Sanjurjo, J. Cuadrado, A. Luaces. A variable time-step and variable penalty method for the index-3 augmented Lagrangian formulation with velocity and acceleration projections. In *Proceedings of the ECCOMAS Thematic Conference on Multibody Dynamics*, Prague, Czech Republic, 2017.
- [4] IFToMM Technical Committee for Multibody Dynamics. Library of Computational Benchmark Problems. <https://www.iftomm-multibody.org/benchmark/>, accessed 2021.
- [5] O. A. Bauchau, P. Betsch, A. Cardona, J. Gerstmayr, B. Jonker, P. Masarati, V. Sonneville. Validation of flexible multibody dynamics beam formulations using benchmark problems. *Multibody System Dynamics*, 37(1):29-48, 2016.

**Section**  
**SLENDER STRUCTURES**

THREAD-1-2-3

# A One-Dimensional Model for Developable Flexible Elastic Strips with Isogeometric Discretisation

Benjamin Bauer<sup>1,2</sup>, Michael Roller<sup>1</sup>, Joachim Linn<sup>1</sup>, Bernd Simeon<sup>2</sup>

<sup>1</sup> Department of Mathematics for the Digital Factory  
Fraunhofer Institute for Industrial Mathematics

Fraunhofer Platz 1, 67663 Kaiserslautern, Germany  
[benjamin.bauer; michael.roller; joachim.linn]@itwm.fraunhofer.de

<sup>2</sup> Differential-Algebraic Systems Group  
Felix-Klein-Zentrum, TU Kaiserslautern

Gottlieb-Daimler-Straße 47, 67663 Kaiserslautern, Germany  
simeon@mathematik.uni-kl.de

## EXTENDED ABSTRACT

### 1 Introduction

Thin-walled elastic structures appear in numerous engineering applications. Flexible flat cables constitute a specific example of such slender flexible objects which are of particular interest in the development of consumer electronics and computer hardware. Besides their high flexibility with typically elastic behaviour and large width-to-thickness aspect ratio, most cables can be characterized geometrically as piecewise developable surface strips.

The increasing level of digitalisation of industrial processes in design, functional performance layout and virtual product realisation requires reliable software tools. These need to provide physically correct models, as well as efficient numerical methods to compute the behaviour of elastic structures in system operation.

Classical shell theories [1] represent thin objects by means of their centre surface and thereby constitute the state of the art for the application at hand. This dimensional reduction massively reduces both the number of involved degrees of freedom and numerical costs. A prominent candidate is the Kirchhoff-Love model which is especially suited to simulate large deformations of very thin-walled shell structures.

Isometric deformations with identically vanishing membrane energy density preserve the developability of the centre surface. The structural model introduced in the subsequent sections exploits this property and, thus, its stored energy function consists only of the shell bending energy. Moreover, developability allows for another dimensional reduction with the computational benefits mentioned above.

### 2 Previous Work on and with One-Dimensional Models

Over ninety years ago, Sadowsky [2] continued the idea of dimensional reduction and integrated the bending energy of a developable, infinitesimally narrow Kirchhoff-Love shell along the width dimension. His approach was pursued by Wunderlich [3], who explicitly wrote down the small width approximation term. This yields a one-dimensional integral to describe the elastic bending energy of the whole solid.

Computer graphics designs developable surfaces like paper sheets only through a curve [4]. This is because every developable surface can be represented as rectifying developable (RD), i.e. as envelope of rectifying planes of a geodesic. Let  $\phi$  and  $\gamma$  denote the parametrisations of surface and generator curve, respectively. Since all developable surfaces are ruled, the surface parametrisation then reads

$$\phi: [0, L] \times \left[-\frac{w}{2}, \frac{w}{2}\right], \quad (s, v) \mapsto \gamma(s) + v\mathbf{d}(s).$$

The director vector field  $\mathbf{d}$  spans the linear rulings in width dimension and, by definition via a Frenet frame, matches the Darboux vector divided by the Frenet curvature.

Recently, research came up with several one-dimensional models describing the mechanical behaviour of ribbons. Starostin and van der Heijden [5] utilised the described framework of RDs to compute the equilibrium state of a Möbius band. The book edited by Fosdick and Fried [6] provides a comprehensive overview of recent work on the subject.

### 3 Generalised Rectifying Developable Surfaces

In this contribution, we avoid issues associated with vanishing curvature and base our formulation on generalised rectifying developable surfaces (GRDs) of a relatively parallel framed [7] generator curve. The definition of these GRDs stems from three properties, which are characteristic for the RD: the surface itself is developable, the base curve is a geodesic within the surface and the straight rulings following the zero-curvature direction are non-parallel to the curve tangent. A system of nonlinear geometrical constraints arises and represents isometry in this transformation, which preserves developability according to the Gaussian theorem egregium

$$\kappa_G^\phi \equiv 0, \quad \kappa_g^\gamma \equiv 0, \quad \|\gamma \times \mathbf{d}\| > 0, \quad \|\dot{\gamma}\| \equiv 1, \quad (1)$$

where  $\kappa_G^\phi$  and  $\kappa_g^\gamma$  denote the Gaussian curvature of  $\phi$  and the geodesic curvature of  $\gamma$  within  $\phi$ .



We decompose the director vector field along the relatively parallel frame  $(\mathbf{t}, \mathbf{m}_1, \mathbf{m}_2)$  of the centre line  $\mathbf{d} = d_0\mathbf{t} + d_1\mathbf{m}_1 + d_2\mathbf{m}_2$ . This allows us to simplify the arising equations for the GRD (1) and to write them solely in the coefficient functions  $d_0, d_1, d_2$  and the curvatures of the relatively parallel frame  $k_1, k_2$ . Additionally, the elastic bending energy of a homogeneous isotropic shell with effective bending stiffness  $D$  reduces to a one-dimensional version along the generator curve analogously to [3]

$$\Xi = \frac{D}{2} \int_0^L (k_1 d_2 - k_2 d_1)^2 (d_0^2 + 1)^2 ds.$$

#### 4 Equilibrium State by Energy Minimisation

The outcome of our formulation is a nonlinear optimisation program with geometric constraints. In order to find the stable static equilibrium configuration, we minimise the elastic bending energy functional among feasible solutions satisfying the GRD-equations (1).

A penalty method addresses these complicated constraints and the resulting penalised objective is minimised by an interior point optimiser. The degrees of freedom for this optimisation procedure stem from an isogeometric discretisation [8] of the generator curve and the coefficient functions of the director within the local frame. The isogeometric basis functions yield the required smoothness and still allow to incorporate geometric boundary conditions directly on specific degrees of freedom. Gradient and Hessian matrix are computed by algorithmic differentiation [9], which provides code exact derivatives and, thus, avoids numerical inaccuracies inherent in finite differences.

#### 5 Results

This work elaborates the equivalence between a vanishing membrane energy and the geometrically justified constraints (1). Subsequently, we discuss the numerical behaviour of our approach at hand of benchmark strips clamped at both ends and, thereby, illustrate its feasibility. We stress susceptibility to high iteration numbers as a drawback, stability with respect to buckling as for symmetric boundary conditions (Figure 1, 2), and global convergence in form of large deformations coming from a plane strip (Figures 3) as advantages of our approach.

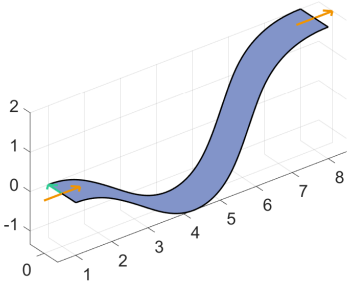


Figure 1: Equilibrium configuration under symmetric boundary conditions.

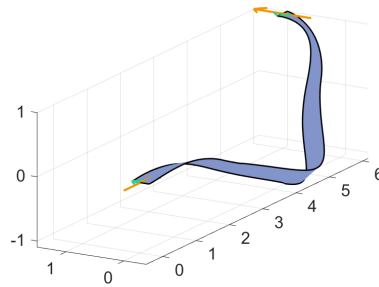


Figure 2: Example with non-planar centre curve.

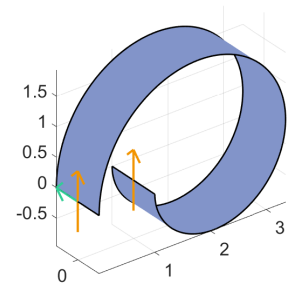


Figure 3: Circular equilibrium configuration after large deformation.

#### References

- [1] M. Bischoff, W.A. Wall, K.-U. Bletzinger, E. Ramm. Models and Finite Elements for Thin-walled Structures. Encyclopedia of Computational Mechanics, 172:59–137, 2004.
- [2] Sadowsky, M.: Ein elementarer Beweis für die Existenz eines abwickelbaren Möbiusschen Bandes und Zurückführung des geometrischen Problems auf ein Variationsproblem. Sitzungsberichte der Preussischen Akademie der Wissenschaften. Philosophisch-historische Klasse, 1930
- [3] Wunderlich, W.: Über ein abwickelbares Möbiusband. Monatshefte Mathematik, 66(3):276–289, 1962.
- [4] Bo, P., Wang, W.: Geodesic-Controlled Developable Surfaces for Modeling Paper Bending. Computer Graphics Forum, 26:3, 365–374, 2007.
- [5] Starostin, E.L.: Equilibrium Shapes with Stress Localisation for Inextensible Elastic Möbius and Other Strips. Journal of Elasticity, 119(1):67–112, 2015.
- [6] R. Fosdick, E. Fried. The Mechanics of Ribbons and Möbius Bands. Springer, Netherlands, 2016.
- [7] R. L. Bishop. There is More than One Way to Frame a Curve. American Mathematical Monthly, 82(3):246–251, 1975.
- [8] Piegl, L., Tiller, W.: The NURBS Book. Springer, Berlin, Heidelberg, 1995.
- [9] A. Griewank, A. Walther: Evaluating Derivatives, Principles and Techniques of Algorithmic Differentiation. SIAM (Second Edition), 2008.

# Effective Inelastic Bending Behavior of Multi-Wire Cables Using Finite Elements Accounting for Wire Contact

Muhammad Hawwash<sup>1,2</sup>, Vanessa Dörlich<sup>1</sup>, Joachim Linn<sup>1</sup>, Ralf Müller<sup>2</sup>, Roger Keller<sup>3</sup>

<sup>1</sup>Department Mathematics for the Digital Factory  
Fraunhofer Institute for Industrial Mathematics ITWM  
Fraunhofer Platz 1, D-67663 Kaiserslautern, Germany

[muhammad.hawwash, vanessa.doerlich, joachim.linn]@itwm.fraunhofer.de

<sup>2</sup>Chair of Applied Mechanics  
Technical University of Kaiserslautern

Gottlieb-Daimler-Straße, 67653 Kaiserslautern, Germany

[hawwash, ram]@rhrk.uni-kl.de

<sup>3</sup>Burckhardt Compression AG  
Franz Burckhardt Strasse 5, 8404 Winterthur, Switzerland  
roger.keller@burckhardtcompression.com

## EXTENDED ABSTRACT

In the development and manufacturing process of modern cars, cables and hoses are important system components, see Fig. 1. In automotive industry, virtual assembly planning and digital validation of system layouts require a fast and physically correct simulation of the mechanical behavior of cables and hoses. In this work, we present a modelling approach using a finite element (FE) model [1] for cables which can be used to investigate the effective inelastic constitutive behavior of abstract cables resulting from structural effects.

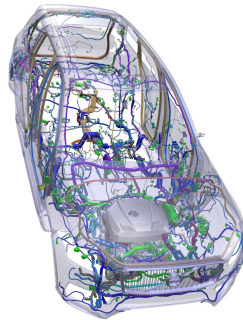


Figure 1: Overview of the system of cables and hoses in a car.

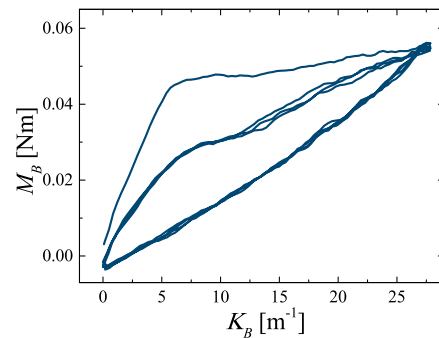


Figure 2: Experimental result of the pure bending of a cable specimen given as bending moment  $M_B$  vs. bending curvature  $K_B$  diagram [2].

Cyclic pure bending experiments on a simple cable specimen show that the effective mechanical response of cables is usually strongly nonlinear and inelastic [2], see Fig. 2. Presumably, material plasticity, damage and structural effects on the level of individual constituents such as contact and friction between wires occur in such experiments. In real experiments, material and structural effects can hardly be investigated separately with acceptable experimental effort. Cable models using finite elements on the level of wires provide an alternative approach to investigate such effects and their interplay. A commercial FEM tool [3]

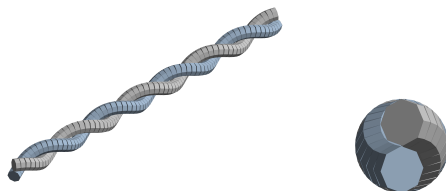


Figure 3: 3D FE model of the double wire strand with a wire helix angle of  $\alpha = 36^\circ$ .

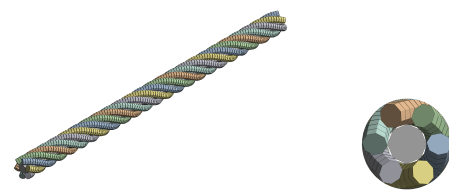


Figure 4: 3D FE model of the seven wire strand with a wire helix angle of  $\alpha = 36^\circ$ .

is used to model the pure bending of a cable. We model the cable as an abstract strand of intertwined wires starting at low model complexity. The intertwined wires are modelled as stress-free helices [4], one helix resembling one metallic wire. In this first step, the wires are modelled as materially elastic in order to avoid a superposition of material and structural inelasticity. The first model we investigate is a double wire strand consisting of two intertwined helices, see Fig. 3. The second simplified cable is modelled using seven wires with one straight wire in the middle and six helices in the outer layer, see Fig. 4. The radii of the core wire and the outer wires are not equal and defined such that there is only pairwise contact between the core and the outer wires.

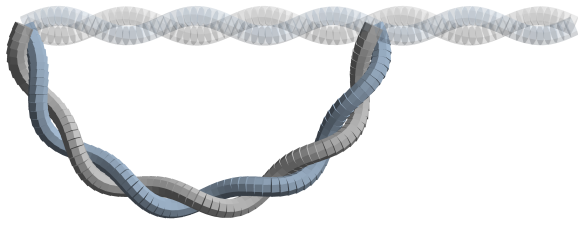


Figure 5: FE simulation of the pure bending experiment on a double wire strand, helix angle of  $\alpha = 36^\circ$

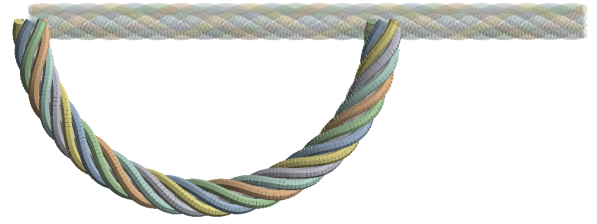


Figure 6: FE simulation of the pure bending experiment on a seven wire strand, helix angle of  $\alpha = 36^\circ$

Cables undergo large spatial deformations in applications. Therefore, we model the wires in our abstract cable model using finite beam elements with quadratic shape functions. The beam element is a one-dimensional line element in space and is defined by three nodes having six degrees of freedom per node: translations in  $x$ ,  $y$  and  $z$  directions and rotations about the  $x$ ,  $y$  and  $z$  axes [3]. In addition, contact between wires occurs and must be taken into account. We use the Coulomb friction model [3] provided in ANSYS to model contact between wires. In order to investigate the influence of friction on the effective mechanical response of the cable, simulations without and with friction, with varying friction coefficients have been performed. This modelling approach can furthermore be used to investigate the influence of different lay angles of the helix wires on the effective behaviour of the abstract cable model. Therefore, the pure bending simulation was performed using models with different wire helix angles as initial stress-free configuration.

The modelling approach presented in this work allows for versatile and detailed investigations of the effective mechanical response of wire strands as abstract cable models. We will show that it is useful for specific simulation experiments on cable-like structures to get a better understanding of the different material and structural inelastic effects which occur in real experiments performed on cables. While it is not simply possible to switch friction on and off in real experiments and measure the influence of friction on the effective behaviour, we can perform such investigations using the presented model.

## References

- [1] O. C. Zienkiewicz, R. L. Taylor, J. Z. Zhu. The finite element method: its basis and fundamentals, Elsevier, 2005.
- [2] V. Dörlich, J. Linn, S. Diebels. Flexible Beam-Like Structures - Experimental Investigation and Modeling of Cables. Advances in Mechanics of Materials and Structural Analysis. Advanced Structured Materials, vol 80. Springer, Cham., 2018.
- [3] ANSYS Mechanical User's Guide (2020 R2). <https://ansyshelp.ansys.com/>. August 31, 2021
- [4] E. Stanova, G. Fedorko, M. Fabian, S. Kmet, Computer modelling of wire strands and ropes Part I: Theory and computer implementation, Advances in Engineering Software, Volume 42, Issue 6, 2011.

# Stability of Coarse Grid Discretisations for Dissipative Systems: Numerical Experiments for a Test Problem

Denise Tumiotto, Martin Arnold

Institute of Mathematics  
Martin Luther University Halle-Wittenberg  
Theodor-Lieser-Str. 5, 06120 Halle (Saale), Germany  
denise.tumiotto@mathematik.uni-halle.de, martin.arnold@mathematik.uni-halle.de

## EXTENDED ABSTRACT

### 1 Introduction

Explicit solvers fail for stability reasons in the application to stiff or constrained problems. Classical implicit solvers in system dynamics like A-stable Runge-Kutta methods or Backward Differentiation Formula (BDF) are tailored to controlled systems that are designed to return rapidly to some nominal system configuration, e.g., by (very) stiff hydraulic force elements, [1]. In numerical analysis, this qualitative behaviour is studied by linear test problems such as  $\dot{y} = \lambda y$  with a parameter  $\lambda \in \mathbb{C}^-$ .

In the application to flexible multibody systems, these A- or A( $\alpha$ )-stable solvers tend to introduce an unphysical amount of numerical dissipation unless the time step size is reduced drastically. For larger time step sizes, the user controlled numerical damping in Newmark type integrators like the generalized- $\alpha$  method, [2], seems to be more favourable but again the stability analysis is based on a linear test problem:  $\ddot{x} + \omega^2 x = 0$ . In the nonlinear case, the methods are known to converge asymptotically with second order but there are no guaranteed error bounds for simulations with reasonable finite time step sizes.

Symplectic integrators are known to preserve an approximation of the Hamiltonian on long time intervals. The tools of backward error analysis are available to study their behaviour in the application to conservative mechanical systems. Favourable properties have been observed as well in the application to nonlinear multibody system models with material damping and other sources of dissipation such as friction or control structures.

In the present paper, we compare a symplectic integrator with a more classical integrator that is well approved in industrial applications and achieves its stability by numerical dissipation. Both integrators are applied to a simple but non-trivial test problem with material damping. The focus is on rather large time steps (i.e., far beyond the asymptotic limit) since we want to apply these methods in future research to geometrically exact beam models being discretized on coarse grids in space and time.

### 2 Test configuration and methods

As a test problem, we present the elastic pendulum, being defined as a flexible rod with one fixed end, subject to a gravitational field. We consider the planar pendulum in two configurations: the floating frame of reference, [3], and the rotational angles in two dimensions.

In the first configuration, the generalized coordinates which determine the position of the body are

- a)  $\theta \in \mathbb{R}$ , the angle between the global fixed frame and the floating frame
- b)  $\mathbf{q}_f \in \mathbb{R}^n$ , the vector of flexible coordinates describing the excitation of the first  $n$  eigenmodes

We assume that the origin of the floating frame and the fixed frame coincide and its position is fixed in time. The equations of motion are

$$\mathbf{M}(\mathbf{q})\ddot{\mathbf{q}} + \mathbf{D}(\mathbf{q})\dot{\mathbf{q}} + \mathbf{K}(\mathbf{q})\mathbf{q} = \mathbf{Q}_v(\mathbf{q}, \dot{\mathbf{q}}) + \mathbf{Q}_g(\mathbf{q}) \quad (1)$$

where the vector  $\mathbf{q} = (\theta, \mathbf{q}_f)$  collects the generalized coordinates,  $\mathbf{M}(\mathbf{q})$ ,  $\mathbf{D}(\mathbf{q})$ ,  $\mathbf{K}(\mathbf{q})$  are respectively the mass, the dissipation, and the stiffness matrix, and  $\mathbf{Q}_v(\mathbf{q}, \dot{\mathbf{q}})$ ,  $\mathbf{Q}_g(\mathbf{q})$  are the vectors of generalized forces.

In the second configuration, we model the elastic pendulum with a series of  $N$  rigid masses connected by torsional springs. The generalized coordinates are the corresponding angles each segment establishes with the vertical axes. The vector  $\boldsymbol{\alpha} \in \mathbb{R}^N$  collects the generalized coordinates. In this case the equations of motion are given by a combination of Cartesian coordinates and rotational angles, and may be reduced to

$$\mathbf{A}(\boldsymbol{\alpha})\ddot{\boldsymbol{\alpha}} = \mathbf{b}(\boldsymbol{\alpha}, \dot{\boldsymbol{\alpha}}) \quad (2)$$

by an algorithm with  $\mathcal{O}(N)$  complexity.

The integration in time is performed with two integrators: the implicit midpoint rule and the generalized- $\alpha$  method.

The former is a symplectic method, [4]. The second one is a numerical integrator with user-controllable numerical dissipation. The generalized- $\alpha$  method is part of the family of Newmark integrators and the numerical dissipation of the algorithm can be controlled via the parameter  $\rho_\infty \in [0, 1]$ . This method is widely used in simulating the dynamics of flexible bodies because the high frequencies cancel out. This property allows us to have a better look at the dynamics of the system itself.

### 3 Numerical results

The results in Figure 1 are obtained solving the elastic pendulum in the floating frame of reference configuration both with the implicit midpoint rule and the generalized- $\alpha$ . For the other set up, the results are qualitatively the same presented in the following. On the left hand side of Figure 1, a comparison between different values of  $\rho_\infty$  is presented. Decreasing the value of  $\rho_\infty$  causes an increase in the numerical dissipation, which can be easily seen in the plot for the conservative system. For the dissipative system, there are smaller oscillations, and the two solutions are more similar.

In the other two columns of Figure 1, in the conservative system, the implicit midpoint rule conserves almost exactly the total energy of the system, [4]. On the contrary, the generalized- $\alpha$  shows the dissipation effect that is due to the numerical dissipation. One can see that for the conservative system a bigger time step influences also the trend in energy dissipation.

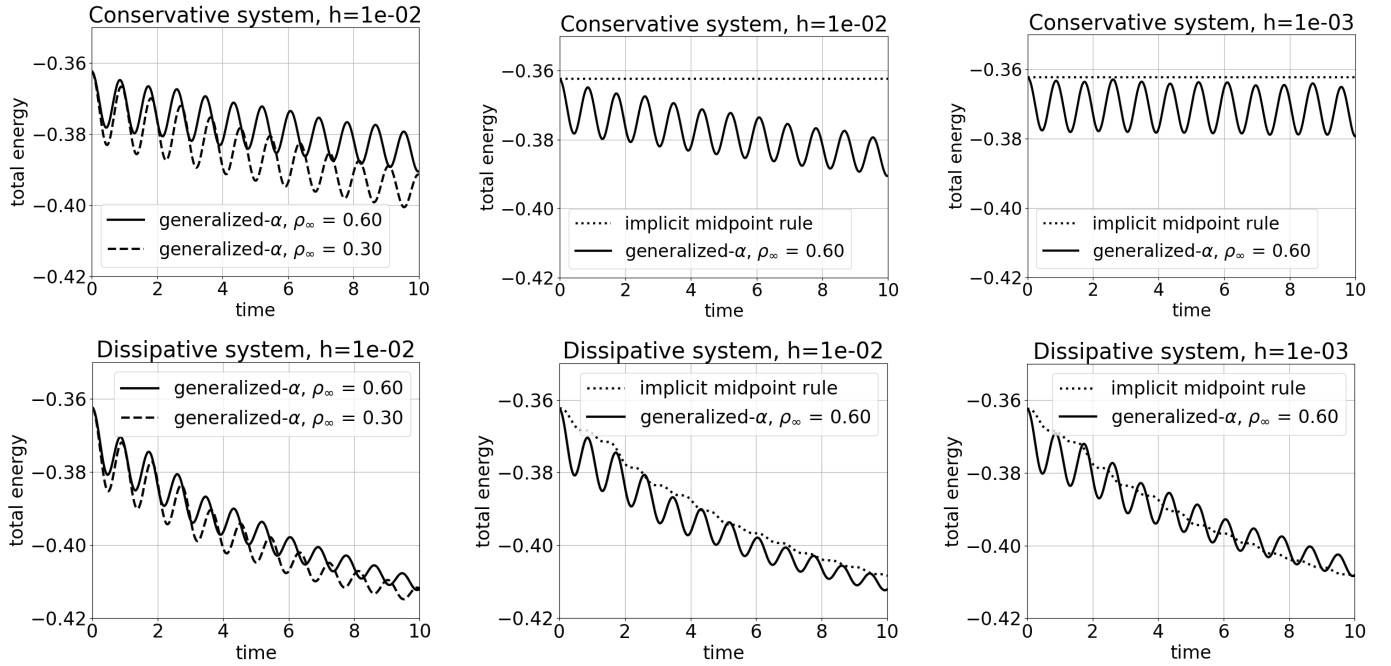


Figure 1: Energy trend over time. On the rows: conservative system, dissipative system. On the columns: large time steps  $h = 10^{-2}$ s, small time steps  $h = 10^{-3}$ s.

The second row of Figure 1 shows the solution for a dissipative system. Both methods reproduce the energy trend correctly, with smaller errors in the rightmost plot ( $h = 10^{-3}$ ). When solving dissipative systems with the generalized- $\alpha$ , increasing the time step size does not compromise the accuracy as in the conservative systems. Nevertheless, the implicit midpoint rule shows an overall better behaviour.

### Acknowledgements

This project has received funding from the European Union's Horizon 2020 research and innovation programme under the Marie Skłodowska-Curie grant agreement No 860124.



### References

- [1] M. Arnold, B. Burgermeister, C. Führer, G. Hippmann, G. Rill. Numerical methods in vehicle system dynamics: State of the art and current developments. *In Vehicle System Dynamics*, 49:1159-1207. 2011.
- [2] M. Géradin, A. Cardona. *Flexible multibody dynamics: a finite element approach*. Wiley, 2001.
- [3] A. A. Shabana. *Dynamics of multibody systems*. Cambridge university press, 2003.
- [4] E. Hairer, C. Lubich, G. Wanner. *Geometric numerical integration: structure-preserving algorithms for ordinary differential equations*. Springer, 2006.

# Dynamics of Axially Moving Beams with Transported Discrete Masses and Contact

Konstantina Ntarladima, Michael Pieber, Johannes Gerstmayr

Institute for Mechatronics  
Leopold-Franzens-Universität Innsbruck  
Technikerstraße 13, 6020 Innsbruck, Austria  
[konstantina.ntarladima, michael.pieber, johannes.gerstmayr]@uibk.ac.at

## EXTENDED ABSTRACT

In this paper we present a formulation for the investigation of the stability of axially moving beams with attached co-moving masses having contact with sheaves. Real-world applications of this study concern ropeway systems and conveyor belts. First, we present the numerical modeling of the system which is based on the Absolute Nodal Coordinate Formulation (ANCF), using the model of Gerstmayr and Irschik [1], but extended by an additional Eulerian coordinate to represent the axial motion of the beams [2]. Second, numerical experiments are conducted to investigate the impact of the co-moving discrete masses as well as of the contact with the sheaves on the dynamic response of the system.

### 1 Mathematical Formulation

In the developed Arbitrary Lagrangian Eulerian (ALE) formulation the Eulerian part consists of an independent coordinate. The

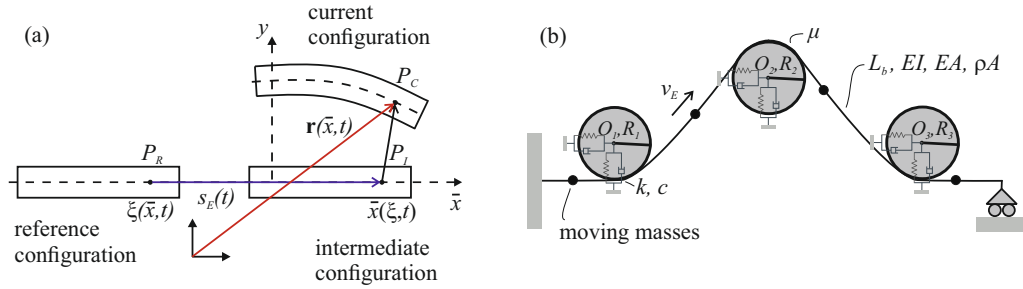


Figure 1: (a) Reference, intermediate and deformed configuration. (b) Mass-carrying axially moving beam in contact sheaves.

position of a point  $P_C$  in the current configuration, as shown in Fig. 1(a), is a function of the local coordinate  $\bar{x}$  in the intermediate configuration  $\bar{x} \in [0, L]$ ,  $\mathbf{r} = \mathbf{r}(\bar{x}, t)$ . The point  $P_R$  in the reference configuration, see Fig. 1(a), was placed in the point  $\xi(\bar{x}, t)$  and underwent an axial displacement,  $s_E$ , thus its position in the intermediate configuration,  $P_I$ , is  $\bar{x} = \xi + s_E(t)$ . The Eulerian velocity is the time derivative of the intermediate coordinate,  $v_E(t) = \dot{s}_E(t) = \partial \bar{x}(\xi, t) / \partial t$ . Therefore, the velocity of the point  $P_C$  also depends on axial velocity,  $v_E$ ,

$$\mathbf{v}(\bar{x}, t) = \frac{d}{dt}(\mathbf{r}(\bar{x}(\xi, t), t)) = v_E \mathbf{r}'(\bar{x}, t) + \frac{\partial \mathbf{r}}{\partial t}(\bar{x}, t), \quad (1)$$

in which we have used the notation  $(\cdot)' = \frac{\partial}{\partial \bar{x}}(\cdot)$ . The equations of motion for the axially moving beams [2] are developed based on extended Lagrange equations given as,

$$\frac{d}{dt} \frac{\partial T}{\partial \dot{\mathbf{p}}} - \frac{\partial T}{\partial \mathbf{p}} + \int_S \frac{\partial T'}{\partial \dot{\mathbf{p}}} \mathbf{v}_n \cdot \mathbf{n} dA - \int_S T' \frac{\partial \mathbf{v}_n}{\partial \dot{\mathbf{p}}} \cdot \mathbf{n} dA = \mathbf{Q}^T, \quad (2)$$

with the vector of generalized coordinates denoted as  $\mathbf{p} \in \mathbb{R}^9$ ,  $\mathbf{p} = [\mathbf{q}^T s_E]^T$ , in which  $\mathbf{q} \in \mathbb{R}^8$  is a vector of coordinates of the ANCF element,  $\mathbf{q} = [\mathbf{r}_1^T \mathbf{r}_1'^T \mathbf{r}_2^T \mathbf{r}_2'^T]^T$ . We interpolate the nodal positions,  $\mathbf{r}_1, \mathbf{r}_2$ , and slopes  $\mathbf{r}_1', \mathbf{r}_2'$  using shape functions of third order polynomial,  $\mathbf{S}$ , which are explicitly described in [2]. It follows that the time derivatives of  $\mathbf{p}$  can be written as  $\dot{\mathbf{p}} = [\dot{\mathbf{q}}^T \dot{s}_E]^T$ . Moreover, the kinetic energy,  $T$ , used in Eq. (2) can be written as,

$$T = \frac{1}{2} (\dot{\mathbf{q}}^T \mathbf{M} \dot{\mathbf{q}} + 2 v_E \dot{\mathbf{q}}^T \mathbf{M}_x \mathbf{q} + v_E^2 \mathbf{q}^T \mathbf{M}_{xx} \mathbf{q}), \quad (3)$$

in which we have made use of the mass matrix,  $\mathbf{M} = m \int_0^L \mathbf{S}^T \mathbf{S} d\bar{x}$ , and the inertia matrices  $\mathbf{M}_x = m \int_0^L \mathbf{S}^T \mathbf{S}' d\bar{x}$  and  $\mathbf{M}_{xx} = m \int_0^L \mathbf{S}^T \mathbf{S}'' d\bar{x}$ . The two integrals of Eq. (2) are computed over the boundary of the beam  $S$  where mass flows in or out. The vector  $\mathbf{v}_n$  is equal to  $\mathbf{v} - \mathbf{w}$ , namely to the velocity of non-material volume minus the velocity of the material volume. Finally, the vector of generalized forces is represented by  $\mathbf{Q} \in \mathbb{R}^9$ . We reach at two equations of motion, the first of which refers to the ANCF beam mesh,

$$\mathbf{M} \ddot{\mathbf{q}} + \dot{v}_E \mathbf{M}_x \mathbf{q} + 2 v_E \mathbf{M}_x \dot{\mathbf{q}} + v_E^2 (\mathbf{B}_x - \mathbf{M}_{xx}) \mathbf{q} = \mathbf{Q}_q, \quad (4)$$



while the second refers to the superimposed Eulerian coordinate  $s_E$ ,

$$\mathbf{q}^T \mathbf{M}_x^T \ddot{\mathbf{q}} + \dot{v}_E \mathbf{q}^T \mathbf{M}_{xx} \mathbf{q} + 2v_E \mathbf{q}^T \mathbf{M}_{xx} \dot{\mathbf{q}} + \frac{1}{2} v_E^2 \mathbf{q}^T \mathbf{B}_{xx} \mathbf{q} = Q_v, \quad (5)$$

in which we have made use of the matrices,  $\mathbf{B} = [m \mathbf{S}^T \mathbf{S}]_0^L$ ,  $\mathbf{B}_x = [m \mathbf{S}^T \mathbf{S}']_0^L$  and  $\mathbf{B}_{xx} = [m \mathbf{S}'^T \mathbf{S}']_0^L$ . For the detailed equation development we refer the reader to [2] and to the implementation in EXUDYN [3].

The dynamics of the discrete attached masses are introduced through a multibody dynamics approach using sliding joints. Furthermore, we consider a contact-friction condition between the axially moving beams and two dimensional circles which can represent sheaves in ropeway systems, see Fig. 1. The modeling of contact of the axially moving beams with the sheaves includes the computation of a normal and frictional force using a penalty-based algorithm according to which the contact normal force is proportional to the depth of penetration of the beam inside the surface of the sheave. More details about the contact modeling will be shown in the presentation.

## 2 Numerical Investigations

We consider the structure of Fig. 1(b) which consists of an axially moving rope, modeled by the above presented beam finite elements, co-moving discrete masses and sheaves. The beam has a fixed Lagrangian node on the left, but mass is moving along the beam at velocity  $v_E$ . In Fig. 2, results obtained for the case of axially moving beams with co-attached moving masses are shown. The thorough description of the example is given in a previous work of the authors [2]. In order to investigate the effects of discrete masses we define the mass factor,  $m_{DMF}$ , as the ratio of the mass of the discrete masses over the total mass of the system. For example, if  $m_{DMF} = 0.2$ , it follows that 20% of the mass of the system belongs to the discrete masses and 80% to the beam. We plot the deflection at the one quarter of the length of the beam as a function of the axial velocity and we observe that after a critical velocity the beam loses its stability through a Hopf bifurcation. In Fig. 2, the bifurcation diagrams of the beams are given for  $m_{DMF} = 0.75$  and 1 to 3 discrete masses, see Fig. 2(a), resp. 4, 8 and 16 discrete masses, see Fig. 2(b). It appears

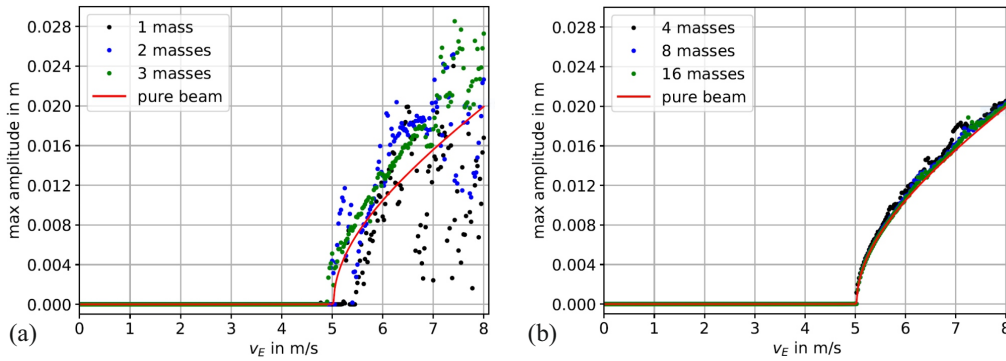


Figure 2: Bifurcation diagram of the beam with a fixed-fixed boundary condition as a function of the flow velocity with 75% mass attached on discrete masses ( $m_{DMF} = 0.75$ ) and number of masses between (a) 1 and 3 ( $n_m = 1 - 3$ ) and (b) 4, 8 and 16 ( $n_m = 4, 8, 16$ ).

that the response of the system converges to the continuous case with the full total mass attached to the beam ( $m_{DMF} = 0$ ) for increasing number of discrete masses. Having observed that the discrete masses appear to have similar effects on the stability of the system as continuously distributed mass, we investigate the impact of the contact with sheaves on the overall response of the system.

## Acknowledgments

This project has received funding from the European Union's Horizon 2020 research and innovation programme under the Marie Skłodowska-Curie grant agreement No 860124.



## References

- [1] J. Gerstmayr and H. Irschik. On the correct representation of bending and axial deformation in the absolute nodal coordinate formulation with an elastic line approach. *J. Sound and Vibration*, 318(3): 461-487, 2008.
- [2] K. Ntarladima, M. Pieber and J. Gerstmayr. Investigation of the stability of axially moving beams with discrete masses. In *Proceedings of ASME 2021 International Design Engineering Technical Conferences and Computers and Information in Engineering Conference*, 2021.
- [3] J. Gerstmayr, 2021. Exudyn – Flexible Multibody Dynamics Systems with Python and C++. <https://github.com/jgerstmayr/EXUDYN> (accessed on March 4, 2021).



# A Nonsmooth Approach to Frictionless Beam-to-Beam Contact

Armin Bosten<sup>1,2</sup>, Alejandro Cosimo<sup>1</sup>, Joachim Linn<sup>2</sup>, Olivier Brûls<sup>1</sup>

<sup>1</sup> Department of Aerospace and Mechanical Engineering  
University of Liège  
Allée de la Découverte 9, 4000 Liège, Belgium  
(a.bosten;a.cosimo;o.bruls)@uliege.be

<sup>2</sup> Department of Mathematics for the Digital Factory  
Fraunhofer Institute for Industrial Mathematics  
Fraunhofer Platz 1, 67663 Kaiserslautern, Germany  
joachim.linn@itwm.fraunhofer.de

## EXTENDED ABSTRACT

Thin and flexible structures such as cables and beams and their contact interactions play an important role in many engineering systems [1]. Even if beam models and general contact mechanics have been extensively studied in the literature, publications on beam-to-beam contact are scarce. Systems involving the contact of beams have many specificities which are generally linked to the slenderness of their constituents. These influence modeling and numerical methodology choices and include the following aspects. First, the multitude of possible contact configurations ie. contact being distributed along portions of finite length (line-to-line) or over regions short enough to be viewed as pointwise interactions (point-to-point). Some authors apply one single contact model to handle both situations in a unified manner [2, 3]. Contacts are treated as simple discrete forces, but their number and location need to be tuned carefully as soon as the contact location cannot be assimilated to a unique point. A sufficient number of contact points should be chosen to obtain accurate results without over-constraining the system. Other authors argue for a separate treatment [4], where distributed contact forces are assumed in a certain range of configurations and discrete forces otherwise. Second, due to the kinematic assumptions of beam models, distributed contact forces are discontinuous in space [5]. Third, the presence of buckling which limits the applicability of quasi-static solvers and thus, in the general case, calls for the need of dynamic simulation. For contact among beams that have some radial rigidity this means handling contact transitions with discontinuous velocities in time.

In the quest for robust simulation of complex beam assemblies including contact, each issue must be dealt with one by one. A non-smooth approach within the Finite Element Method is taken. Non-penetration is enforced via Lagrange multipliers. It differs from penalty methods in that constraints are verified exactly and the solution is independent of any arbitrary parameter. However, great care has to be taken in the choice of numerical method, which needs to be able to deal with the potential discontinuity of velocities in time or distributed contact forces in space. First efforts by the authors concentrated on a quasi-static mortar formulation for frictionless line-to-line beam contact [6]. It proves to be a convenient strategy for the modeling of beam-to-beam contact along portions of sufficient length. Indeed, over-constraining and the need for a  $C^1$  continuous representation of the beam center-line could be avoided. The method was found to be impractical when the length of the contact region becomes too small. Thus it was complemented by a point-to-point contact model and extended to the dynamic case. The time-integrator of choice is the non-smooth generalized- $\alpha$  (NSGA) scheme tailored to flexible multibody systems with vibrations and impacts. First introduced in [7], it is based on a smooth prediction that excludes impact contributions and two subsequent projection steps that impose non-penetration constraints first at position and then at velocity level. In this methodology a certain freedom remains in the definition of the smooth problem, which has an influence on convergence. A fully decoupled version with an improved behaviour for flexible systems and non-linear constraints was studied in [8]. Contact information may be included at the prediction stage by additionally imposing constraints at acceleration level, as done in [9]. In the case of contact among slender structures such as beams this is necessary to cope with typical tunneling effects.

Finally, all developments are made taking the  $SE(3)$  local frame approach [10]. The equations of motion are written on a Lie group and consistent time and spatial Lie group discretization schemes are applied. A formulation free of global parametrizations is obtained and locking effects are automatically avoided. Moreover, the contact elements conserve the interesting invariance properties present in the contact free case. At the symposium, progress made on modeling contact interactions among beams will be presented and it will be shown that the combination of all the previously mentioned concepts forms an appropriate framework for handling geometric non-linearities, discontinuities and complex contact configurations exhibited by cable assemblies. Two indicative examples are shown in figures 1 and 2.

## References

- [1] M. Arnold, O. Brûls, and J. Linn. Thread-Numerical modeling of highly flexible structures for industrial applications. *Mathematics with industry: driving innovation-ECMI Annual Report*, pages 20–25, 2019.
- [2] F. Bertails, F. Cadoux, G. Daviet, and V. Acary. A nonsmooth Newton solver for capturing exact Coulomb friction in fiber assemblies. *ACM Trans. Graph.*, 30:1–14, 2011.
- [3] D. Durville. Contact-friction modeling within elastic beam assemblies: an application to knot tightening. *Comput. Mech.*, 49:687–707, 2012.

- [4] C. Meier, M. J. Grill, W. A. Wall, and A. Popp. Geometrically exact beam elements and smooth contact schemes for the modeling of fiber-based materials and structures. *Int. J. Solids Structs.*, 154:124–146, 2018.
- [5] J-S. Chen. On the contact behavior of a buckled Timoshenko beam constrained laterally by a plane wall. *Acta. Mech.*, 222:225–232, 2011.
- [6] A. Bosten, A. Cosimo, J. Linn, and O. Brüls. A mortar formulation for frictionless line-to-line beam contact. *Multibody Syst. Dyn.*, under review.
- [7] O. Brüls, V. Acary, and A. Cardona. Simultaneous enforcement of constraints at position and velocity levels in the nonsmooth generalized- $\alpha$  scheme. *Comput. Methods Appl. Mech. Engrg.*, 281:131–161, 2014.
- [8] A. Cosimo, J. Galvez, F. J. Cavalieri, A. Cardona, and O. Brüls. A robust nonsmooth generalized- $\alpha$  scheme for flexible systems with impacts. *Multibody Syst. Dyn.*, 48:127–149, 2020.
- [9] O. Brüls, V. Acary, and A. Cardona. On the constraints formulation in the nonsmooth generalized- $\alpha$  method. In R. I. Leine, V. Acary, and O. Brüls, editors, *Advanced topics in non-smooth dynamics*, chapter 9, pages 335–374. Springer, Berlin, 2018.
- [10] V. Sonnevile, A. Cardona, and O. Brüls. Geometrically exact beam finite element formulated on the special Euclidean group  $SE(3)$ . *Comput. Methods Appl. Mech. Engrg.*, 268:451–474, 2014.

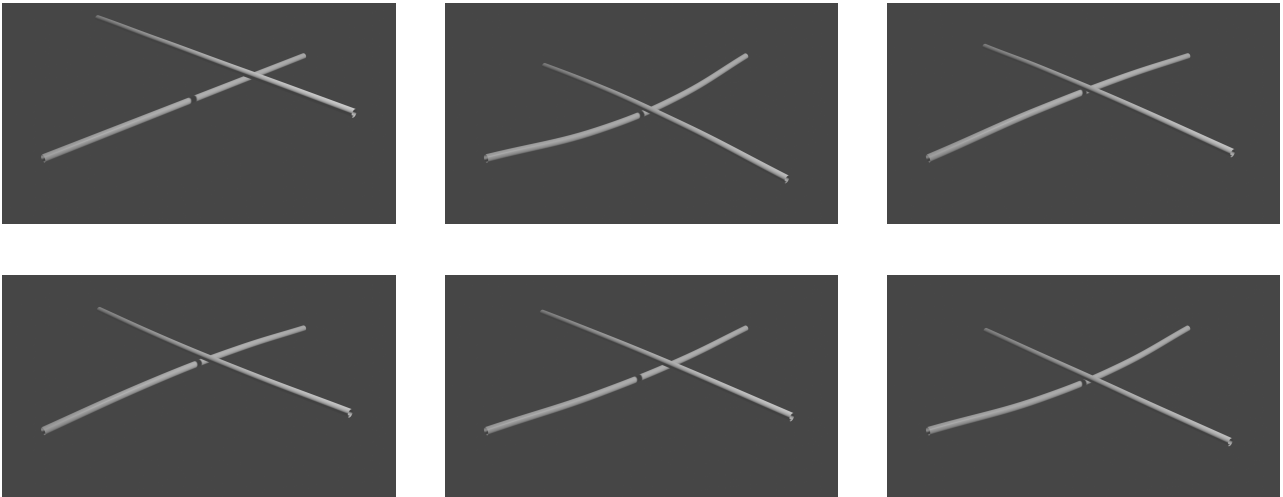


Figure 1: From top left to right bottom: The top beam is dropped onto the lower beam, which is clamped on both ends. A detachment effect may be observed.



Figure 2: Example of three fiber twisting with line-to-line contact.

# Tensegrity Based Spatial Serial Robots

Jan Zavřel<sup>1</sup>, Tomáš Kaňka<sup>1</sup>, Vojtěch Halamka<sup>1</sup>, Michael Valášek<sup>1</sup>, Zbyněk Šika<sup>1</sup>

<sup>1</sup>Faculty of Mechanical Engineering  
Czech Technical University in Prague  
Technická 4, 166 00, Praha 6  
Jan.Zavrel@fs.cvut.cz

## EXTENDED ABSTRACT

### 1 Introduction

Tensegrity is the name given to spatial mechanisms stabilized by a tension in their structure [1]. The tensegrity structure consists of rigid struts connected by flexible cables. The main advantage of tensegrity is a very good stiffness to weight ratio of the structure. Tensegrity is impact resistant and robust against damage of any of the components. The bars and cables of the structure are loaded only by axial forces, the bars by pressure and the cables by tension. Large nodes displacements are possible in tensegrity. Tensegrity is characterized by the ability to change equilibrium position with small energy demands on the controlling. The main disadvantages are the complex description of the internal dynamics, the nonlinear geometric behavior resulting from large deformations and the low damping of oscillations. The stiffness of tensegrity is determined by the geometry and prestress. However, the choice of geometry has a dominant effect on the overall stiffness of the structure.

On the basis of the mentioned properties of tensegrity structures, it can be concluded that their high stiffness and low mass predestines them for use as replacements for serial spatial robots [2]. However, motion control of tensegrity structures is not trivial with respect to their properties [3]. The tensegrity structure can be controlled by a PID controller, by advanced control methods such as H-infinity or Computed Torques Control (CTC), or by other methods.

### 2 Tensegrity spatial serial structure

First, there are modelled planar tensegrity structures (Fig. 1) as a replacement for planar serial mechanisms. The stiffness and its dependence on the cable connection structure and the number of cables were analyzed. The resulting structure is modelled by connecting identical parts (stages). In this way, the arm of any arbitrary length can be created.

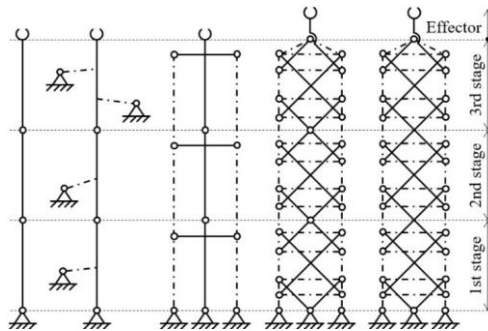


Figure 1: Sequence of design of planar manipulators, from left: classic serial robot, external driven structure, cross structure, hybrid structure, tensegrity structure.

When the spatial tensegrity structure is modelled, the individual stages can be formed by tensegrity prisms. Their designation is formed by the number of struts (S) and the number of cables (C).

By connecting such simple tensegrity structures (stages), a structure replacing the spatial serial robot mechanism can be obtained. Ideal solids are used to model the struts and the cables are replaced by a force actions dependent on the cable stiffness, its free length, prestressing with the inclusion of damping according to equation (1), where  $k_{ci}$  [N/m.m] is the specific cable stiffness per unit cable length and  $b_{ci}$  [Ns/m.m] is the damping coefficient per unit cable length of the  $i$ -th element.

$$F_{ci} = \frac{k_{ci}}{l_{cio}}(l_{ci} - l_{cio}) + \frac{b_{ci}}{l_{cio}} \frac{d}{dt}(l_{ci} - l_{cio}) \quad (1)$$

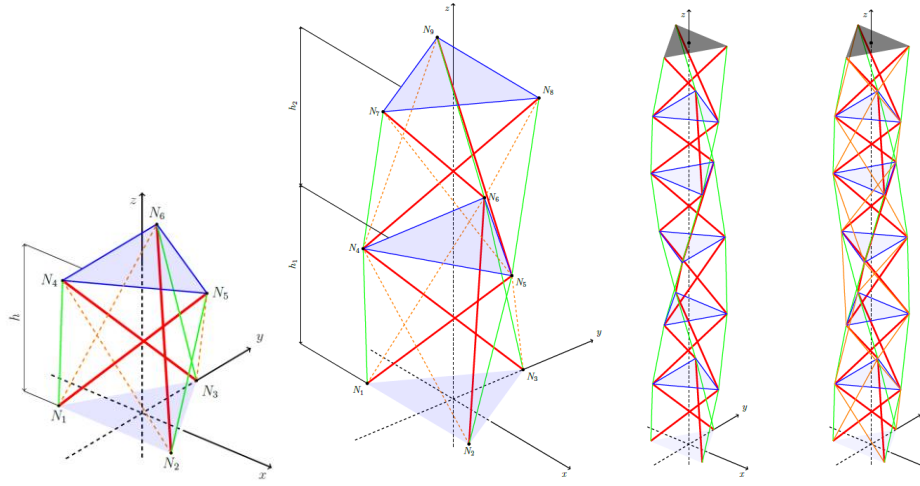


Figure 2: Tensegrity manipulator. On the left is the S3C6 stage of the manipulator and two levels connected together. On the right there are two tensegrity structures composed of six S3C6 levels (without diagonal cables and with diagonal cables).

### 3 Results of simulations

The aim is to analyze the control methods of tensegrity based spatial structures and the influence of the positioning capability based on different forms of tensegrity structure. The number and the method of connection of cables in the tensegrity structure (Fig. 2) is significant, as well as its internal prestress. It has a great influence on the positioning accuracy of the control [4]. The movement of the tensegrity structure along the specified spiral trajectory is realized by a PID controller (Fig. 3). The motion of a given structure and the quality of the control will be reflected in the resulting error.

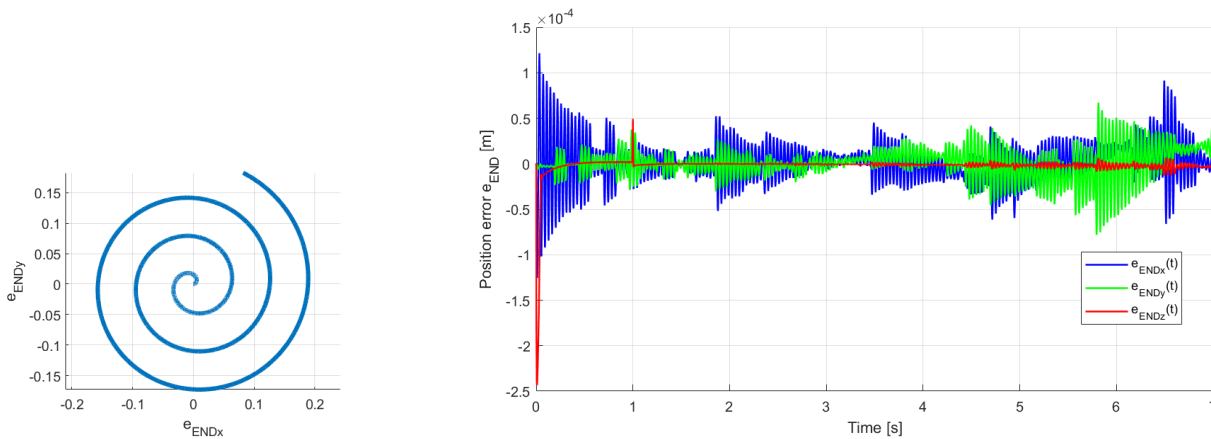


Figure 3: Desired spiral trajectory of the center of the platform of the tensegrity structure (left) and the position error (right).

Eigenfrequencies of tensegrity structure are also analyzed. Furthermore, the possibility of damping in the cables and the effect of the damping coefficient on the steady motion are analyzed as well.

### Acknowledgments

The work has been supported by the Czech Science Foundation project GA20-21893S "Mechatronic tensegrities for energy efficient light robots".

### References

- [1] Skelton, Robert E; De Oliveira, Mauricio C. Tensegrity systems. Springer, 2009.
- [2] Fadeyev, Denis; Zhakatayev, Altay; Kuzdeuov, Askat; Varol, Huseyin Atakan. Generalized dynamics of stacked tensegrity manipulators. IEEE Access. 2019, p. 63472-63484.
- [3] Wroldsen, Anders S; Oliveira, Mauricio C de; Skelton, Robert E. A discussion on control of tensegrity systems. In: Proceedings of the 45th IEEE Conference on Decision and Control. 2006, p. 2307-2313.
- [4] Oppenheim, Irving J; Williams, William O. Vibration of an elastic tensegrity structure. European Journal of Mechanics-A/Solids. 2001, 20(6), p. 1023-1031.

# Analysis of Beam-to-Beam Contact Using Mortar Method

Jan Tomec<sup>1</sup>, Gordan Jelenić<sup>2</sup>

<sup>1</sup> Faculty of Civil Engineering  
University of Rijeka  
Radmile Matejčić 3, 51000 Rijeka, Croatia  
jan.tomec@uniri.hr

<sup>2</sup> Faculty of Civil Engineering  
University of Rijeka  
Radmile Matejčić 3, 51000 Rijeka, Croatia  
gordan.jelenic@uniri.hr

## EXTENDED ABSTRACT

### 1 Introduction

While modern contact mechanics in 3D continuum largely focus on the mortar method [1, 2], beam-to-beam contact development somehow lags behind these developments, with some exceptions such as ABC method [3]. In order to fill this gap, a new frictionless mortar method for beam-to-beam contact has been developed. It is based on a line-to-line type formulation with distributed contact force represented by a Lagrange multiplier field.

### 2 Beam-to-beam contact

A beam-to-beam contact describes interaction between two bodies that can be represented by beam theory. In a more general case, these two bodies can be viewed as segments of one or more beams and in this way refer to both the contact between the two beams as well as self-contact in either of them. In what follows, these two segments will be simply referred to as beam (1) and beam (2). Individual beam geometry is described by its centreline  $\mathbf{x}^{(i)}(s^{(i)})$  in a deformed configuration. The contact is enforced by the following contact conditions

$$\begin{aligned} \text{non-penetration condition} & \quad g \geq 0, \\ \text{positive pressure condition} & \quad F_N \leq 0, \\ \text{zero-work condition} & \quad F_N g = 0, \end{aligned}$$

where  $g$  denotes the gap and  $F_N$  the contact force. These conditions apply to each individual point on the beam surface. For the contact-geometry definition the shear deformation is neglected and the cross-section is assumed to remain perpendicular to the centreline. This assumption, together with the assumption of circular cross-section, simplifies the gap function as it now depends solely on the position of the two centrelines. It is justified by the fact that the shear deformation only marginally changes the distance between the two beams.

### 3 Mortar method

The contribution of frictionless contact to the total energy of the system can be defined by the contact potential [4]

$$\Pi_N = \int_{\Gamma_c} \lambda g ds \approx \int_{\Gamma^{(1)}} \lambda g ds^{(1)}, \quad (1)$$

where  $\lambda$  and  $g$  are Lagrange multiplier and gap respectively. The true integration domain of the contact potential is the actual contact segment  $\Gamma_c$  where the two surfaces intersect. It is approximated by the centreline of one beam  $\Gamma^{(1)}$ , making it the non-mortar side of the contact. Non-mortar side is also the carrier of the Lagrange multiplier field  $\lambda$  representing the distributed contact force which is equal and opposite on the two sides of the contact and is therefore not necessary to compute twice.

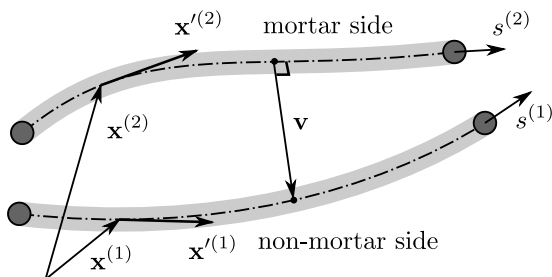


Figure 1: Geometry of mortar contact

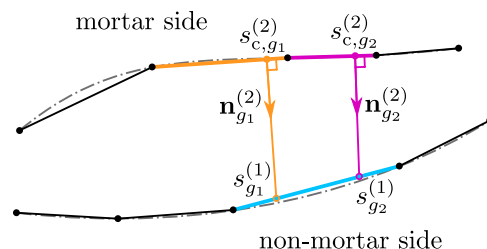


Figure 2: Mortar element

The gap function is defined as the shortest path from the mortar-side centreline to some point on the centreline on the non-mortar side (see Figure 1) reduced by the beams thickness

$$g = \mathbf{v}^T \mathbf{n}^{(2)} - \rho^{(1)} - \rho^{(2)}, \quad (2)$$

where constants  $\rho^{(1)}$  and  $\rho^{(2)}$  are cross-section radii of the respected beams. Following the virtual work principle, the variation of discrete contact potential (1) is

$$\delta \Pi_N^e = \int_0^{L^{(1)}} \lambda \left( \delta \mathbf{x}^{(1)} - \delta \mathbf{x}^{(2)} \right) \cdot \mathbf{n}^{(2)} ds^{(1)} + \int_0^{L^{(1)}} \delta \lambda g ds^{(1)}, \quad (3)$$

where the first term is associated with the virtual contact work and the second is the weak form of the non-penetration condition. A standard finite-element procedure follows with the linearisation of equation (3), insertion of the Lagrange polynomial interpolation of displacement and Lagrange multiplier field and assembly of the global system of equations. Finite-element discretization defining a mortar element is shown on Figure 2. Gauss quadrature is used for numerical integration. Not all non-mortar side element integration points need to be paired with a same mortar element, but the established pairs should remain constant during the balance search within the Newton-Raphson algorithm to preserve a second-order convergence rate.

#### 4 Discussion

A series of numerical experiments has been conducted on three different test cases, each targeting some aspects of frictionless beam-to-beam contact. The patch test has been performed to check the non-penetration condition and establish validity of the method. In contrast to penalty methods, the Lagrange multiplier approach guarantees exact solution with zero gap within the machine numerical precision. Due to the weak fulfilment of the non-penetration condition, sliding over elements does not lead to any loss of convergence. Example of two twisting cantilever beams forming a helix has served to test the distributed contact force. The resulting contact force is  $C^0$  continuous and converges with the increased number of elements. The last experiment is an example of self contact (Figures 3 and 4). A ring clamped on one end has been twisted in the shape of number 8. Self contact has been detected and shown to cause no instability in the solution.

Surprisingly, the method has proved to be rather independent of the number of integration points. Only a few of them have been sufficient for all test cases (usually double the number of nodes on an element). Although not as numerically efficient as some existing formulations, i.e. [3], it can address a wide range of different applications free from the choice of the penalty parameter. These tests prove that the mortar method is not only an effective formulation for beam-to-beam contact but also provides a lot of space for improvements and future research.



Figure 3: Twisting of a ring

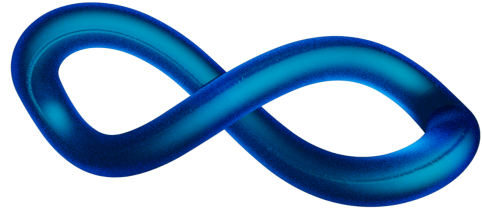


Figure 4: Final deformed shape

#### Acknowledgments

This work has received funding from the European Union's Horizon 2020 research and innovation programme under the Marie Skłodowska-Curie grant agreement No 860124.

#### References

- [1] F. B. Belgacem, P. Hild, L. Patrick. Approximation du problème de contact unilatéral par la méthode des éléments finis avec joints. *Comptes Rendus de l'Académie des Sciences - Series I - Mathematics*, 324(1):123–127, 1997.
- [2] M. A. Puso, J. M. Solberg. A dual pass mortar approach for unbiased constraints and self-contact. *Computer Methods in Applied Mechanics and Engineering*, 367, 2020.
- [3] C. Meier, W. Wall, A. Popp. A unified approach for beam-to-beam contact. *Computer Methods in Applied Mechanics and Engineering*, 315:972-1010, 2017.
- [4] P. Wriggers, J.C. Simo. Note on Tangent Stiffness for Fully Nonlinear Contact Problems. *Communications in Numerical Methods in Engineering*, 1:199-203, 1985.

# First Steps in Data Based Constitutive Modelling of Inelastic Effects in Composite Cables Using Preisach Hysteresis Operators

Davide Manfredo<sup>1,2</sup>, Vanessa Dörlich<sup>1</sup>, Joachim Linn<sup>1</sup>, Martin Arnold<sup>2</sup>

<sup>1</sup> Fraunhofer ITWM

Fraunhofer Platz 1, 67663 Kaiserslautern, Germany  
[davide.manfredo,vanessa.doerlich,joachim.linn]@itwm.fraunhofer.de

<sup>2</sup> Institute of Mathematics

Martin Luther University Halle-Wittenberg  
Theodor-Lieser-Str. 5, 06120 Halle (Saale), Germany  
martin.arnold@mathematik.uni-halle.de

## EXTENDED ABSTRACT

Electric cables, as those shown in Fig. 1a, are complex objects due to their multi-material composition and their geometric properties. Consequently, different internal interaction effects occur and lead to an observed effective inelastic deformation behaviour of such cables. Cyclic bending experiments [1, 2] show open hysteresis loops with noticeable difference between the first load cycle and the following ones, as shown in Fig. 1c. In the framework of continuum mechanics, such deformation effects are modelled using suitable constitutive equations for specific material behaviour. In the presented work, we aim at modelling the observed behaviour on an abstract level using hysteresis operators. The choice of this mathematical framework has been motivated by the ability of such operators to describe hysteresis phenomena with enough generality and without the need of a priori assumptions on the material behaviour.

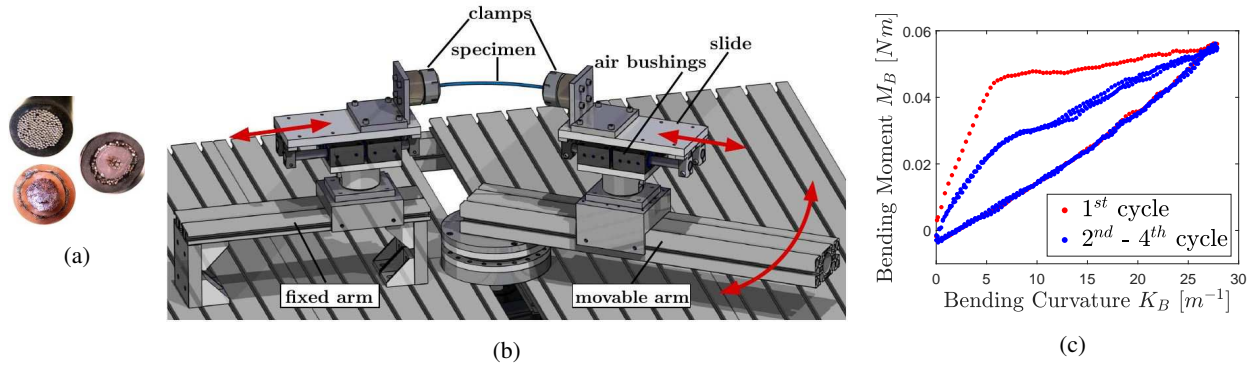


Figure 1: (a) Cross sections of different electric cables. (b) Pure bending test rig. (c) Bending moment vs. bending curvature diagram measured in a pure bending experiment.

As shown in [3, 4], hysteresis operators are a well-studied topic with a variety of applications, mainly hysteresis effects arising from electric and magnetic phenomena. The Preisach operator  $\mathcal{P}$  plays a major role in modelling the input-output relation in hysteresis behaviours and can be expressed as a superposition of relay operators  $\mathcal{R}_{s-r,s+r}$  multiplied by a suitable kernel function  $\omega(r,s)$ , which is assumed to vanish for large values of  $|s|$  and  $r$ ,

$$w(t) = \mathcal{P}[v](t) = \int_0^{+\infty} \int_{-\infty}^{+\infty} \omega(r,s) \mathcal{R}_{s-r,s+r}[v](t) ds dr. \quad (1)$$

In particular,

- $v(t)$  and  $w(t)$  are respectively the input and the output function, the plot of the input function used in this case is shown in Fig. 3a,
- $s$  and  $r$  are the coordinates of the Preisach plane,
- $\mathcal{R}_{s-r,s+r}[v(t)] \in \{\pm 1\}$ , equals  $+1$  or  $-1$  if  $v(t)$  crosses the threshold value  $s+r$  from below or  $s-r$  from above, respectively, and is interpreted as a switch operator between the values  $-1$  and  $+1$ , with switching interval of width  $2r$  and centered in  $s$ . In Fig. 2, the diagram of the relay operator for  $s=0$  and  $r=0.5$  is shown.

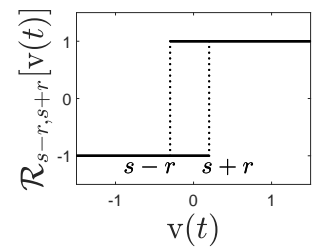


Figure 2

The definition of the Preisach plane occurs naturally from the definition of the Preisach operator and can be determined recursively. This definition entails that the interface between the two regions that form a partition of the Preisach plane automatically carries the total memory information present in the system at time  $t$  (Fig 3b). It should be noted that Preisach hysteresis operators



provide a model for causal response (see [4]), such that the output value  $w(t)$  at time  $t$  depends only on inputs  $v(t')$  at past times  $t' \leq t$ . Thus, hysteresis loops can be computed by integrating a suitable kernel function over a domain included in the Preisach plane.

Here, data collected from different bending experiments [1] are utilised for a first approach. A mathematical formulation of the problem is introduced, and a first attempt is made to mathematically determine the hysteresis behaviour that describes the relation between input and output. In Fig. 1c the experimental results for a pure bending experiment on a simple cable are shown. Fig. 3c shows the simulation result obtained from the kernel function  $\omega(r,s)$  that has been determined by a fit to the data.

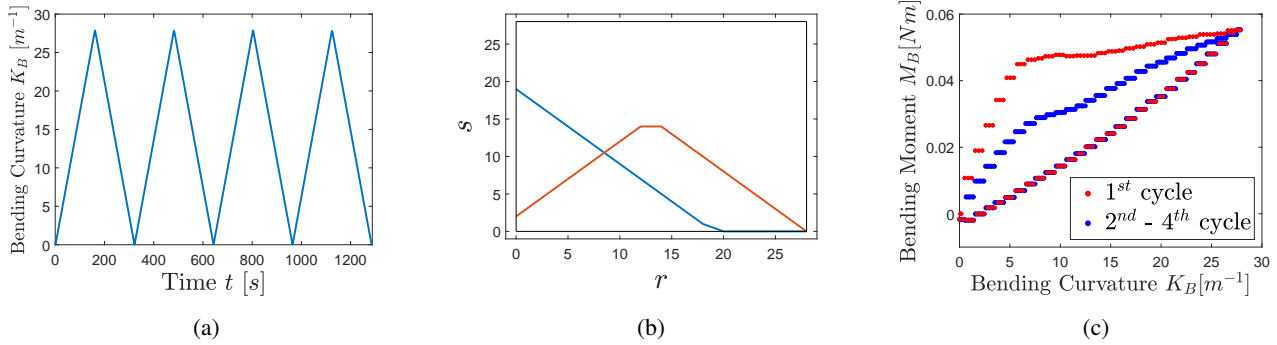


Figure 3: (a) Curvature vs. time. (b) Domain (black rectangle) included in the Preisach plane with two examples of interface lines between the sub-regions of such domain. (c) Estimated plot of bending moment vs. curvature obtained by means of the hysteresis operator.

In this contribution, starting from the input scalar function (e.g. bending curvature), the Preisach plane is recursively defined and the identification of a suitable kernel function is achieved by means of a least squares method, in a way that the integration of such kernel function over the Preisach plane results in the output (e.g. bending moment) measured during the experiments [5, 6]. Moreover, observations and comments regarding the kernel functions are made comparing different kernel functions derived from different experiments.

Finally, an outlook on the possibility of including the presented method into a Cosserat rod model [7] is presented, with the idea of utilizing this approach to formulate a versatile constitutive model, aiming at its application in the simulation of deformation of cables.

## Acknowledgements

This project has received funding from the European Union's Horizon 2020 research and innovation programme under the Marie Skłodowska-Curie grant agreement No 860124.



## References

- [1] V. Dörlich, J. Linn, S. Diebels, Flexible Beam-Like Structures - Experimental Investigation and Modeling of Cables, in H. Altenbach, F. Jablonski, W. Müller, K. Naumenko, P. Schneider (eds) *Advances in Mechanics of Materials and Structural Analysis. Advanced Structured Materials*, vol 80, *Springer International Publishing*, 2018, pp 27 - 46.
- [2] V. Dörlich, J. Linn, S. Diebels, Bending of Viscoplastic Cables, in *PAMM. Proc. Appl. Math. Mech.* 17, 2017, pp. 293 – 294.
- [3] M. Brokate, J. Sprekels, *Hysteresis and Phase Transitions*, *Springer-Verlag New York*, 1996, viii+357 pp.
- [4] A. Visintin, *Differential Models of Hysteresis*, *Springer-Verlag Berlin Heidelberg*, 1994, vii+407 pp.
- [5] M. E. Shirley, R. Venkataraman, On the Identification of Preisach Measures. *Proceedings Volume 5049, Smart Structures and Materials 2003: Modeling, Signal Processing, and Control*, (2003).
- [6] K.-H. Hoffmann, J. Sprekels, A. Visintin, Identification of Hysteresis Loops, *Journal of Computational Physics*, Volume 78, Issue 1, September 1988, pp. 215-230.
- [7] J. Linn, T. Hermansson, F. Andersson and F. Schneider, Kinetic aspects of discrete Cosserat rods based on the difference geometry of framed curves In: Valasek, M., et al. (eds.) *Proceedings of the ECCOMAS Thematic Conference on Multibody Dynamics 2017*, pp. 163–176 (2017).

# Nonlinear Cosserat Rod Statics Using Homogenized Constitutive Properties of Multi-Layered Cross-Sections

Martina Stavole, Sigrid Leyendecker,

Institute of Applied Dynamics  
Friedrich-Alexander-Universität Erlangen-Nürnberg  
Immerwahrstrasse 1, 91058 Erlangen, Germany  
martina.stavole@fau.de  
sigrid.leyendecker@fau.de

## EXTENDED ABSTRACT

### 1 Introduction

Composite materials are widely used in engineering applications. However, their constitutive properties are not easy to define due to the complex behaviour of the mixed materials. In order to analyse composite beam cross-sections, several techniques are presented in the literature. In particular, computational approaches [1], such as finite element methods, are popular for analyzing such problems, since even the simple multi-material cross-sectional study cases are complex to solve with theoretical procedures. Nevertheless, an analytical determination of effective stiffness properties of composite beam cross-sections, based on the model of directed curves in linear theory of rods, is shown in [2,3]. This work focuses on the homogenization of the mechanical properties of circular multi-layered cross-sections obtained through [2] and the comparison of results in terms of displacements and rotations of beams studied in the linear and the nonlinear case.

### 2 Characterisation of composite circular cross-sections

Multi-layered beams are composite structures and they can be composed of numerous layers of different materials. In [2], two-layers piecewise homogeneous sandwich beams made of isotropic materials, shown in Figure 1, are studied. The cross-section is divided in a core and a face, characterized by different material parameters and welded together in such a way that no separation can occur during deformation.

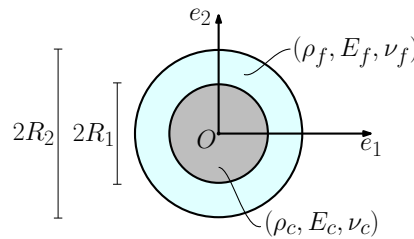


Figure 1: Circular sandwich cross-section

The authors investigate the mechanical behaviour of composite elastic beams using the theory of directed curves, a Cosserat-type model for thin rods. In other words, rods are modeled as deformable curves defined by a position vector and a triad of directors attached to every point along the curve, and the triad describes the rotations of cross-sections during deformation as previously done in [3]. They derive the constitutive equations for elastic composite rods in the linear case and obtain the effective extensional, bending, shear and torsion stiffness properties of thin rods by comparing the solutions of some extension, bending and torsion problems for directed curves with the corresponding results obtained for three-dimensional rods. In the particular case of isotropic materials for circular sandwich cross-sections, the effective stiffness properties are expressed as a combination of material parameters and geometry of layers [2]. These values are used as inputs in the stiffness matrices in (1) for the geometrically exact beam model.

### 3 Homogenization of the constitutive properties of a three-dimensional Cosserat beam model

We consider a static three-dimensional Cosserat beam model (adapted from [5] to the static case) of homogeneous material, and assume that the beam's planar cross-section is constant along the beam and remains rigid when the beam deforms. The equilibrium equations are derived from the Lagrangian function (consisting of the deformation energy only) by applying the Hamilton principle to the action integral [4]. The matrices of elasticity coefficients of the beam are defined as follow:

$$\mathbf{C}^\Gamma := \text{Diag}(GA \ GA \ EA) \quad \text{and} \quad \mathbf{C}^K := \text{Diag}(EI \ EI \ GJ). \quad (1)$$

where  $A$  is the cross-sectional area of the rod,  $I$  is the principal moment of inertia of the circular cross-section,  $J = 2I$  is the polar moment of inertia,  $E$  is Young's modulus,  $G = E/[2(1 + \nu)]$  is the shear modulus, and  $\nu$  is Poisson's ratio.

#### 4 Comparison of the homogenized effective stiffnesses in the linear and nonlinear case

Maximum deflection and rotation are evaluated from the analytical solutions for benchmark problems for directed curves, as in [2-3]. For our study, those results are compared to the numerical ones obtained from the nonlinear Cosserat rod model using by homogenized effective stiffness coefficients. The comparison shows that for small loads results in terms of deflections and rotations are the same and, while increasing the load magnitude, results in the linear and nonlinear frames diverge.

#### 5 Conclusion and discussion

This work represents a comparison of the linear model from [2] and a nonlinear Cosserat beam model for the case of multi-material layered cross-sections. In future, this process will be useful to study more complex inhomogeneous cross-section models of beams in cases relevant for medical device operation, i.e. endoscopes. Indeed, the characterisation of effective properties for inhomogeneous cross-sections will be validated through an experimental campaign in collaboration with Fraunhofer ITWM (Germany). For this purpose, MeSOMICS (Measurement System for the Optically Monitored Identification of Cable Stiffness) will be used to investigate effective stiffness parameters of thin rod samples with multi-layered cross-section, by carrying out bending, torsion and elongation experiments.

#### Acknowledgments

This project has received funding from the European Union's Horizon 2020 research and innovation under the Marie Skłodowska-Curie grant agreement No.860124.



#### References

- [1] U. K. Chakravarty. On the modeling of composite beam cross-sections. Elsevier, Composites Part B: Engineering, 42(4):982-991, 2011
- [2] M. Birsan, D. Pietras, T. Sadowski. Determination of effective stiffness properties of multilayered composite beams. Continuum Mechanics and Thermodynamics, 1-23, 2021
- [3] M. Birsan, H. Altenbach, T. Sadowski. et al.. Deformation analysis of functionally graded beams by the direct approach. Composites Part B: Engineering, 43(3):1315-1328, 2012
- [4] J. E. Marsden, M. West. Discrete mechanics and variational integrators. Acta Numerica, 10:357-514, 2001
- [5] S. Leyendecker, P. Betsch, P. Steinmann. Objective energy-momentum conserving integration for the constrained dynamics of geometrically exact beams. Computer Methods in Applied Mechanics and Engineering, 195(19-22):2313–2333, 2006

# Velocity-based Elements in the Analysis of Post-critical Behaviour of Spatial Frames

Sudhanva Kusuma Chandrashekhara, Dejan Zupan<sup>1</sup>,

<sup>1</sup> Faculty of Civil and Geodetic Engineering  
University of Ljubljana  
Jamova 2, 1000 Ljubljana, Slovenia  
skusuma@fgg.uni-lj.si; dejan.zupan@fgg.uni-lj.si

## EXTENDED ABSTRACT

### 1 Introduction

In the non-linear stability analysis of structures undergoing complex deformation, the precise prediction of the behaviour of the structure in the post-buckling regime poses a serious challenge for the numerical procedure. This problem has typically been studied by considering the geometrical non-linearities within the static equilibrium equations. Near the critical points of the equilibrium path, the load-deflection characteristics are dynamic in nature. This often results in requirements of short time intervals to simulate the quasi-static load increment close to the critical point. Further, at the critical points, the structures are exhibiting also snap-through and snap-back behaviours, which requires time-dependent load relaxation. In addition, the incremental time step, i.e., adaptive step size can be used in the path-following constraint equation by replacing the arc-length parameter by time. For this purpose, we have extended the velocity based finite-element formulation of spatial beams with the modified arc-length path following control additionally equipped with adaptive step size. The crucial idea of the proposed formulation is to employ velocities in fixed frame description and angular velocities in moving frame description as the primary unknowns. Such model therefore allows standard additive interpolation to be fully consistent with the configuration space, direct application of path-following constraint in the tangent space and elegant extension of path-following controls to rotational degrees of freedom.

### 2 Methodology

The present beam formulation is based on  $2^{nd}$  order approximation of governing equations in time with the implicit midpoint time integration. Among various possibilities, the quaternion algebra is employed for the parametrization of rotations, however, the primary unknowns of the iterative scheme are chosen to be velocities and angular velocities. It was already shown that such approach is computationally advantageous when choosing standard additive-type interpolation functions for the primary unknowns when expressed in suitable reference frames. Standard Galerkin-type finite-element method is employed for the spatial discretization, see [1] for further details. The final discrete governing equations of a three-dimensional beam are given by:

$$\int_0^L \left[ \rho A \left( v^{[n+1]} - v^{[n]} \right) P_i + h \bar{n} P'_i - h \bar{n}^{[n+1/2]} P_i \right] dx - h \delta_i \bar{f} = 0 \quad (1)$$

$$\int_0^L \left[ J_\rho \left( \Omega^{[n+1]} - \Omega^{[n]} \right) P_i + h \bar{\Omega} \times J_\rho \bar{\Omega} P_i - h K^{[n+1/2]} \times \bar{M} P_i + h \bar{M} P'_i - h P_i \right. \\ \left. \left( \hat{q}^{*[n+1/2]} \circ r^{[n+1/2]} \circ \hat{q}^{[n+1/2]} \right) \times \bar{N} - h \left( \hat{q}^{*[n+1/2]} \circ \tilde{m}^{[n+1/2]} \circ \hat{q}^{[n+1/2]} \right) P_i \right] dx - h \delta_i \bar{H} = 0. \quad (2)$$

The superscript denotes the time at which a particular quantity is evaluated,  $h = t_{n+1} - t_n$  is the time step, and time  $t_{n+1/2} = t_n + h/2$  denotes the mid-time between  $t_n$  and  $t_{n+1}$ . The system of equations is clearly non-linear and is therefore solved in an iterative manner using Newton-Raphson method. For that purpose, we express all the quantities of the beam with velocities and angular velocities at the middle of the time step:

$$v^{[n+1/2]} = \bar{v} = \frac{1}{2} \left( v^{[n]} + v^{[n+1]} \right), \quad \Omega^{[n+1/2]} = \bar{\Omega} = \frac{1}{2} \left( \Omega^{[n]} + \Omega^{[n+1]} \right). \quad (3)$$

E. g., for the configuration variables, we assume

$$r^{[n+1/2]} = r^{[n]} + \frac{h}{2} \bar{v}, \quad \hat{q}^{[n+1/2]} = \hat{q}^{[n]} \circ \exp \left( \frac{h}{4} \bar{\Omega} \right). \quad (4)$$

The objective in the stability analysis of structures is to obtain the equilibrium states at various load levels. The equilibrium states trace the load-displacement responses where the applied load is a function of a unique load parameter. Thus, in equilibrium equations (1)–(2) discrete loads are expressed in the following form

$$\begin{bmatrix} \delta_i \bar{f} \\ \delta_i \bar{H} \end{bmatrix} = \bar{\lambda} p, \quad (5)$$

where  $p$  is a constant vector of external reference point forces and moments and  $\bar{\lambda} = \frac{1}{2} (\lambda^{[n]} + \lambda^{[n+1]})$  is the load factor at the mid time. The time dependent load-displacement response of a structure can now be represented using the tangent vector,  $[\dot{r}, \dot{\lambda}]^T$  while the additional equation relating the unknowns is given by the following generalized arc-length control equation

$$\xi(\dot{r}, \dot{\lambda}) = \dot{r}^T W \dot{r} + \dot{\lambda}^2 p^T H p - 1 = 0. \quad (6)$$

However, from the perspective of velocity-based beam formulation the path-control equation can be conveniently expressed as

$$h^2 \left[ \frac{\bar{v}}{\Omega} \right]^T W \left[ \frac{\bar{v}}{\Omega} \right] + (\lambda^{[n+1]} - \lambda^{[n]})^2 p^T H p = h^2, \quad (7)$$

where  $W$  and  $H$  are arbitrary symmetrical scaling matrices representing various arc-length schemes. The above quadratic discrete path-control equation is added to the governing equations and solved simultaneously with them.

### 3 Numerical example

We demonstrate the applicability of the method on a right angle cantilever frame subjected to an in-plane loading as presented in [3]. The geometrical and material properties are:  $E = 71240$  MPa,  $\nu = 0.31$ , length of each arm  $L = 240$  mm. Width of the cross section  $b = 30$  mm and slenderness ratio of  $1/50$  are taken. The in-plane load of  $P_x = 1.2$  N is applied at the tip. The results are obtained using a mesh of 25 elements of order 5. Due to the high slenderness of the cross section, the frame buckles laterally, which can be observed in the figure.

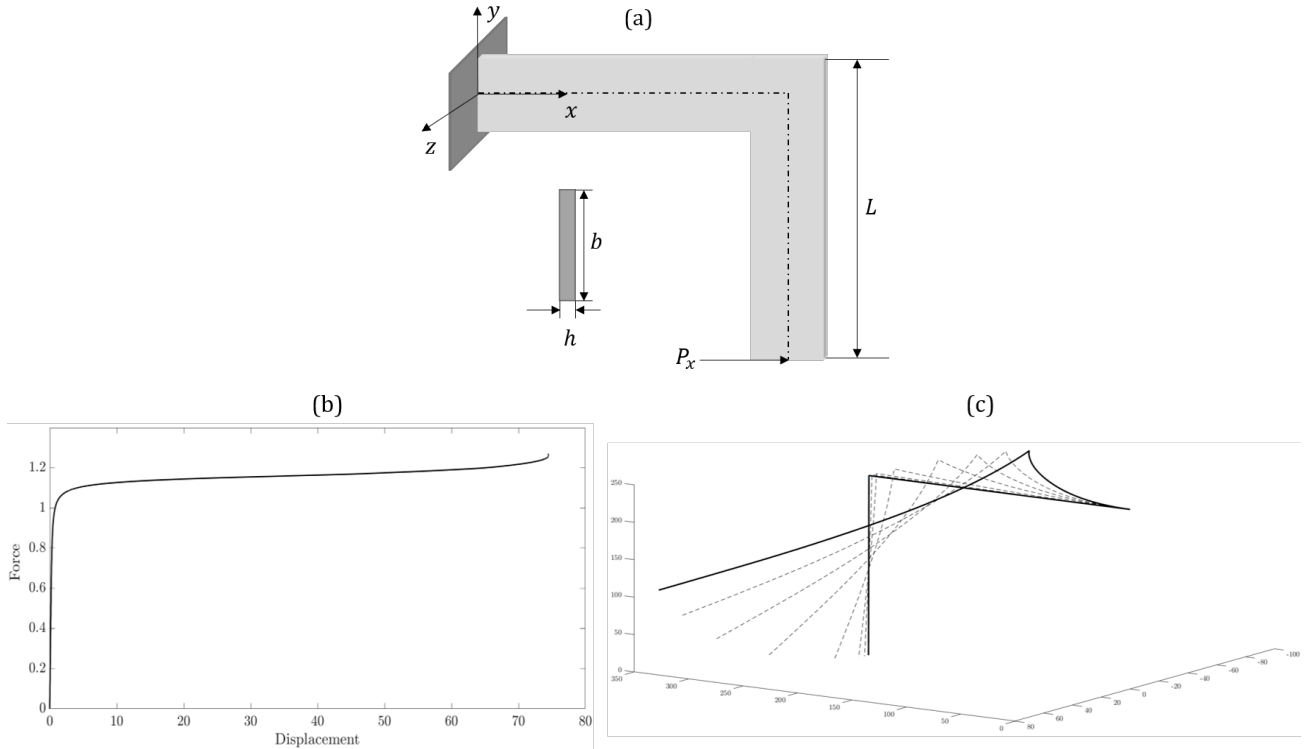


Figure 1: Lateral buckling of a right angle cantilever frame (a), the load-displacement curve (b), and the deformed shapes (c).

### Acknowledgments

This work was supported by the European Union's Horizon 2020 research and innovation programme under the Marie Skłodowska-Curie grant agreement No. 860124. The support is gratefully acknowledged.

### References

- [1] E. Zupan and D. Zupan, "On conservation of energy and kinematic compatibility in dynamics of nonlinear velocity-based three-dimensional beams", *Nonlinear Dynamics*, vol. 95, no. 2, pp. 1379-1394, 2018.
- [2] E. Zupan and D. Zupan, "Third-order Time Integration Scheme for Structural Dynamics", in *The Eleventh International Conference on Advanced Engineering Computing and Applications in Sciences*, Barcelona, Spain, 2017, pp. 56-62.
- [3] J. Simo and L. Vu-Quoc, "A three-dimensional finite-strain rod model. part II: Computational aspects", *Computer Methods in Applied Mechanics and Engineering*, vol. 58, no. 1, pp. 79-116, 1986.

# Modeling The Rotary Inertia of Sheaves with The Arbitrary Lagrangian-Eulerian Modal Approach

José L. Escalona, Narges Mohammadi

Dept. of Mech. and Manufacturing Eng.  
University of Seville  
Camino de los Descubrimientos s/n,  
41092, Sevilla, Spain  
[escalona] [narges] @us.es

## EXTENDED ABSTRACT

### 1 Introduction

The Arbitrary Lagrangian-Eulerian Modal (ALEM) approach is a discretization method recently developed [1, 2] for the dynamic analysis of reeving systems. The main properties of this method are:

- It is a systematic method that can be used to automatically build the equation of motion of reeving systems
- It models the wire rope flexibility in the axial and transverse directions and the twist
- Thanks to the ALE approach, it results in computationally efficient modeling equations that requires a small number of finite elements (see Fig. 1 (a) and (b))
- The resulting equations of motion (EOM) include a minimum set of constraint equations due to the wire rope to rigid body interactions

In this work, an improvement in the formulation is described that reduces to zero this set of constraint equations while accounting for the rotary inertia of the deviation sheaves.

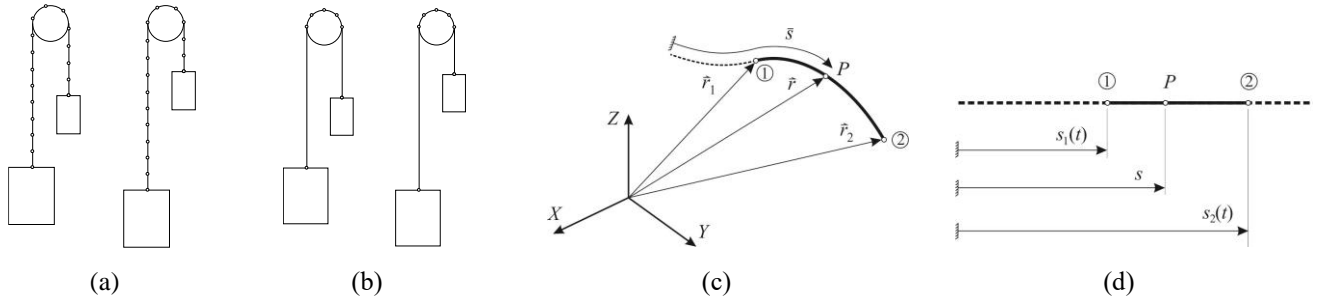


Figure 1: ALEM formulation: (a) Reeving system modeled with Lagrangian FEM and (b) modeled with ALE-FEM, (c) ALEM element in arbitrary position in space and (d) in reference straight position

### 2 Modeling rope to sheave interaction

Figure 2 shows the ALEM elements  $j$  and  $k$  whose ends 2 and 1, respectively, are tangent to a sheave that is rigidly connected to the rigid body  $i$ . In the ALEM formulation, the rope to sheave contact is not modeled so far. It is not needed to analyze the overall dynamics of the reeving system. The connectivity condition  $s_{j2} - s_{k1} = 0$  excludes the rope segment in contact with the sheave of the system model. The element to sheave interaction was modeled [1, 2] using the following kinematic constraints:

$$\begin{aligned} \mathbf{r}_{j2} - (\mathbf{R}^i + \mathbf{A}^i \bar{\mathbf{u}}_{i2}^i) &= \mathbf{0} \\ \mathbf{r}_{k1} - (\mathbf{R}^i + \mathbf{A}^i \bar{\mathbf{u}}_{i1}^i) &= \mathbf{0} \\ (F_{ax}^{j2}(\mathbf{q}^j) - F_{ax}^{k1}(\mathbf{q}^k))R_s - M_m(t) &= 0 \end{aligned} \quad (1)$$

where the two first equations force the end nodes to be located at the pre-defined tangent points of the sheave. The last equation is a time-dependent constraint that guarantee that the torque due to the axial load different equals the externally applied force to the sheave. The two first equations are linear in terms of the ALEM nodal coordinates (they can be eliminated of the EOM) and the last equation is a non-linear constraint that must be accounted for in the EOM using, for example, the Lagrange multiplier technique. Clearly, this last equation neglects the effect of the rotary inertia of the sheave, that uses to be very small in comparison with other inertia effects in reeving systems. In the following section, an alternative approach that avoids this non-linear constraint is proposed.

### 3 Rope to sheave interaction considering rotary inertia of the sheave

The alternative formulation for the rope to sheave interaction requires to add as a generalized coordinate of the reeving system

the angle  $\alpha_s$  rotated by the sheave. That way, the third constraint in Eq. (1) can be substituted with the following no slip condition:

$$s_{j2} - (s_{j20} - \alpha_s R_s) = 0 \quad (2)$$

This is a linear constraint that can be accounted for in the EOM eliminating the nodal coordinate  $s_{j2}$  of the EOM. That way, the rope total inertia and the sheave rotary inertia are considered while the EOM are simplified at the expense of increasing the size of the system with 1 dof per sheave.

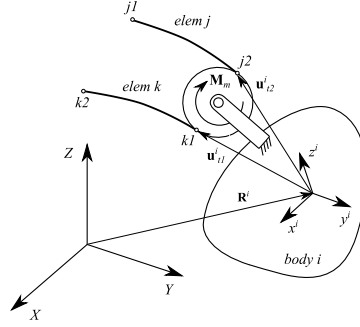


Figure 2: ALEM elements tangent to a sheave

#### 4 Example

Figure 3 (a) shows the model of an elevator with elastically supported motor and a compensating rope under the cabin and counterweight. The deviation sheave at the bottom has been modeled with and without considering the rotary inertia. The deviation sheave is loaded with a spring to have a static pre-tension of 1 kN. Figures 2 (b) and (c) show the tension on the drive and compensation ropes, respectively, during the elevator ride. As it can be observed, the inertia of the deviation sheave has a small effect of the tension of the drive sheaves. In the deviation sheaves, when rotary inertia is not considered, the tension on ropes *c* and *d* is equal, as imposed with the third equation in Eq. (1). When rotary inertia is considered, tension is different in both segments. However, the difference is not only due to the rotary inertia. This is clear because at the initial and final instants, when the system is not moving, tensions are different. The reason for this tension difference is that the ALEM method considers linear interpolation of the axial deformation of the ropes. Thus, the tension is assumed to be constant. However, due to the inertia and gravity forces of the ropes, the tension is actually space dependent. These results show that it would be desirable to develop new ALEM element that consider axial strain that vary along the element. This is the next development of this formulation.

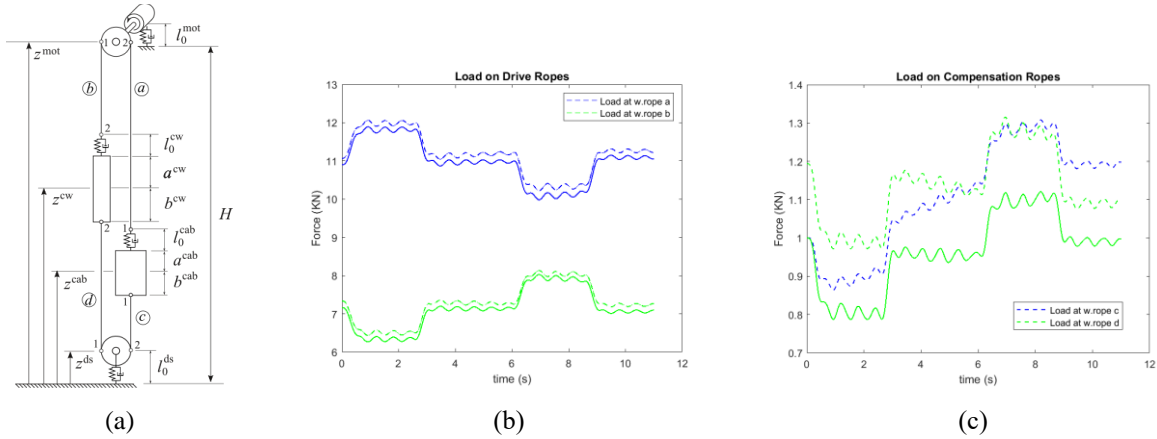


Figure 3: (a) Elevator model, (b) tension on drive ropes and (c) tension on compensating ropes. In the plots, solid lines do not consider sheave rotary inertia and dashed lines do consider it

#### Acknowledgments

This research was funded by European Union's Horizon 2020 research and innovation program under the Marie Skłodowska-Curie project No. 860124 (THREAD).

#### References

- [1] Escalona, J.L, "A discretization method for the flexible multibody simulation of reeving systems", Mechanism and Machine Theory, 112, 2017.
- [2] Escalona, J.L, Orzechowski, G, Mikkola, A, "Flexible multibody modeling of reeving systems including transverse vibrations", Multibody System Dynamics, 44, 2018.



# Optimized Tensegrity Structures for the Usage in Robotics

Michal Hajžman, Radek Bulín, Martin Hrabáčka, Pavel Polach, Miroslav Byrtus

Faculty of Applied Sciences  
University of West Bohemia  
Technická 8, 301 00 Pilsen  
Czech Republic  
mhajzman@kme.zcu.cz

## EXTENDED ABSTRACT

### 1 Introduction

Conventional robotic manipulators are designed mainly as (quite) rigid elements coupled by suitable kinematical joints that are driven by active drives. The most common robots have the well known serial structure. They have good ratio between the built-up space and the effective workspace [1]. Their main drawbacks are typically the low effective stiffness, low damping and in particular, the unfavorable ratio between stiffness and mass. On the other hand there exist structures with more favourable properties for particular applications. Such structures could be various tensegrity systems, which are defined as a structure whose integrity is maintained by tension in its design elements [2]. They are commonly composed of struts (rigid elements, bars, rods) and cables (fibers, strings, etc.). It is an interesting idea to use these tensegrity units instead of common rigid elements and study their effects on the manipulators' performance. The aim of this paper is to introduce the methodology for the optimization of tensegrity structures which are suitable for the further usage in the design of various robotic manipulators based on multibody system dynamics.

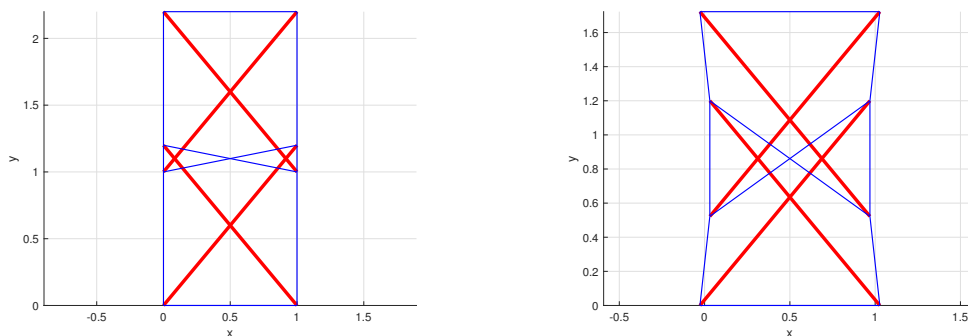


Figure 1: Initial (left) and deformed (right) configuration of a basic planar tensegrity (struts are denoted by red colour while cables are denoted by blue colour)

### 2 Methodology

Since the main motivation is to replace typical rigid and massive elements of serial manipulators by suitable tensegrity structures (see Figure 1 for a typical planar example of class 1 tensegrity unit), the elementary step of the design is to find the basic tensegrity with optimal properties with respect to planned manipulator working conditions. It means that it is necessary to

- determine the overall structure of the manipulator (i.e. the number of tensegrity units and joints between them),
- design basic dimensions of the tensegrity units considering the working space,
- find the proper topology of the tensegrity unit and determine the prestress of its cables,
- optimize other possible parameters (stiffness, masses etc.) in order to obtain prescribed properties.

This approach was implemented in an in-house software in MATLAB system and it allows to automatically find suitable tensegrity structural units. One of the most important methods used during the process is the form finding by the adaptive force density method [3], which is basically a numerical method proposed to achieve the required rank deficiency of the equilibrium matrix characterizing a tensegrity. The parameters of tensegrities are optimized also with respect to possible load cases in order to obtain the structure which can be loaded in different directions based on a considered robot operation.

Afer the run of the introduced procedure, it is necessary to verify and possibly improve the dynamic behaviour using a complex multibody model of the tensegrity unit. The tool for the automatic generation of the SIMSCAPE multibody models using the previously found topology and other parameters was also created (see Figure 2 for the example of a generated basic tensegrity

model). These models can be easily combined together with standard kinematical joints and chosen driving elements and complex dynamics of the proposed tensegrity manipulator can be investigated. The methodology was developed for both, planar and spatial structures. Design, control and simulation results of the motion of a serial tensegrity structure without special joints were shown by the authors of [4]. It is planned to incorporate also the active tensegrity structures with embedded actuators.

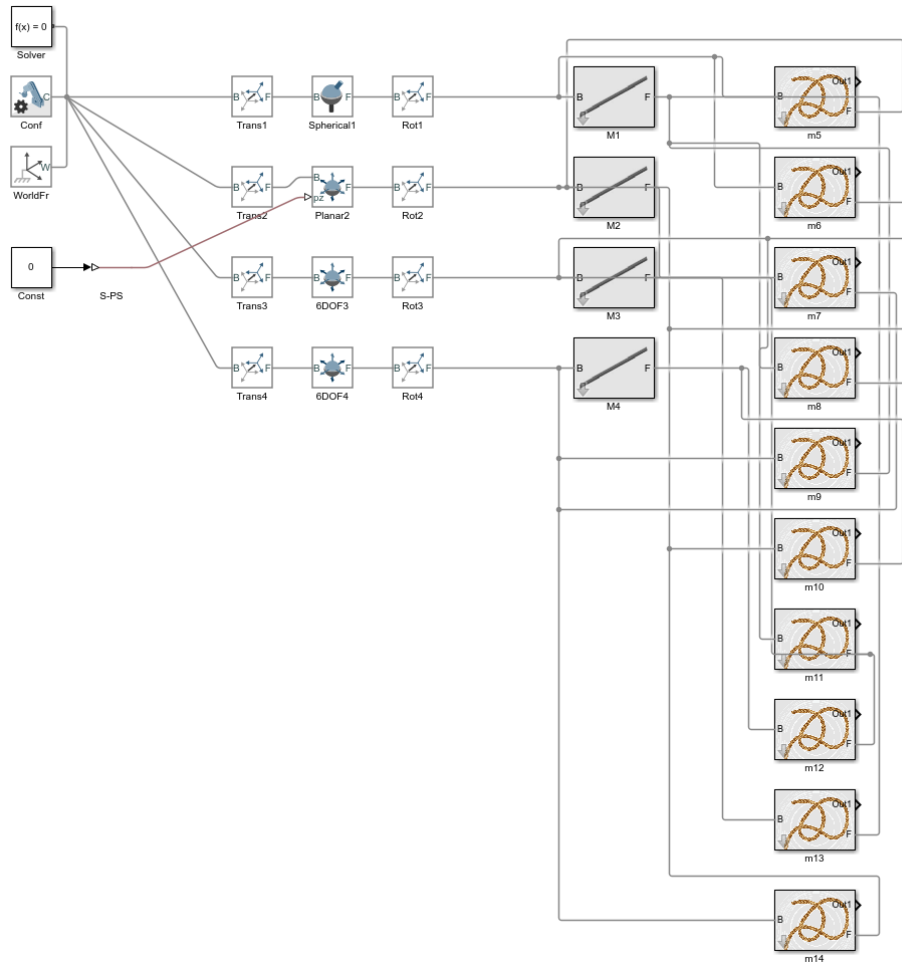


Figure 2: Realization of the model of a basic tensegrity unit in SIMSCAPE

### 3 Results and conclusions

This paper deals with the methodology for the optimized tensegrity structures design for the development of robotic manipulators. The in-house software for the automatic solution of this task was created based on the proposed methodology. The replacement of classical serial robot by light active tensegrity mechanism can significantly improve its stiffness/mass ratio and bring completely new possibilities of controllability and observability by internal actuators and sensors. The great benefit of active tensegrities is that we can reach a high level of force control within the structure. The low authority control (vibration suppression) can be combined with the high authority motion control and force control. The possibility of temporary relaxation of potentially colliding tendons can enlarge the reachable workspace.

#### Acknowledgments

The work has been supported by the Czech Science Foundation project GA20-21893S “Mechatronic tensegrities for energy efficient light robots”.

#### References

- [1] N. Vahrenkamp, T. Asfour. Representing the robot’s workspace through constrained manipulability analysis. *Autonomous Robots*, 38: 17–30, 2015.
- [2] B.S. Gan. *Computational Modeling of Tensegrity Structures*. Springer, Cham, 2020.
- [3] J.Y. Zhang, M. Ohsaki. Adaptive force density method for form-finding problem of tensegrity structures. *International Journal of Solids and Structures*, 43: 5658–5673, 2006.
- [4] J. Zavřel, T. Kaňka, V. Halamka, M. Valášek, Z. Šika. Tensegrity Based Spatial Serial Robots. In *ECCOMAS Thematic Conference on Multibody Dynamics*, 2021. Budapest, Hungary.

# Realistic parameters for dynamic simulation of composite cables using a damped Cosserat rod model

Dominik Jungkenn<sup>1</sup>, Fabio Schneider<sup>1</sup>, Fredrik Andersson<sup>2</sup> and Joachim Linn<sup>1</sup>,

<sup>1</sup> Fraunhofer Institute for Industrial Mathematics ITWM

Department Mathematics for the Digital Factory (MDF)

Fraunhofer Platz 1, 67663 Kaiserslautern, Germany

(dominik.jungkenn, fabio.schneider, joachim.linn)@itwm.fraunhofer.de

<sup>2</sup> Fraunhofer Chalmers Research Centre for Industrial Mathematics FCC

Department Geometry and Motion Planning

Chalmers Science Park ,41288 Gothenburg, Sweden

fredrik.andersson@fcc.chalmers.se

## EXTENDED ABSTRACT

### 1 Motivation

In today's automotive industry, an early stage digital validation has become the standard procedure in product development. This includes the validation of flexible parts such as cables and hoses. The variety of electronics used in modern vehicles has made the cable system one of the central parts when it comes to safety and function of the product. So far the simulation based validation of cables and hoses using the IPS software family has focused on the basic functionality of the vehicles, namely the proper design of moving parts (such as doors, lids or the suspension linkage and steering) as well as the validation of production processes (mountability by hand and robotic applications). With the relatively new Durability and Dynamics module (introduced in 2018) we extended the field of application for our software by simulations of products in operation. This change of objective is followed by the need for different simulation approaches.

### 2 Cable model

For slow motions like opening or closing doors and lids a quasistatic approach yields the best trade-off between accuracy and speed. In this approach we utilize a geometrically non-linear Cosserat rod model and combine it with a linear material model [1]. This approach leads to a minimization problem for the potential energy, which is (among others) determined by the elastic energy:

$$\mathcal{V} = \int_0^L (\Gamma_1 \ \Gamma_2 \ \Gamma_3) \begin{pmatrix} GA_1 & & \\ & GA_2 & \\ & & EA \end{pmatrix} \begin{pmatrix} \Gamma_1 \\ \Gamma_2 \\ \Gamma_3 \end{pmatrix} + (K_1 \ K_2 \ K_3) \begin{pmatrix} EI_1 & & \\ & EI_2 & \\ & & GJ_T \end{pmatrix} \begin{pmatrix} K_1 \\ K_2 \\ K_3 \end{pmatrix} ds \quad (1)$$

Here, the material strain and curvature measures are denoted as  $\mathbf{\Gamma}$  and  $\mathbf{K}$ , respectively, and the *effective stiffness parameters* of the cables need to be determined for practical applications in cable simulation:

$$[GA_1], [GA_2], [EA], [EI_1], [EI_2] \text{ and } [GJ_T] \quad (2)$$

These parameters are obtained using the MeSOMICS machine, a highly automated measurement setup that has been developed at ITWM [2].

The kinematics of suspension linkage will (among others) undergo very fast motions in operation. As a consequence inertial effects play a considerable role in the motion of cables and hoses that are attached to these parts of the vehicle. In order to validate these kinds of scenarios, we have to move from the quasistatic to a transient simulation approach. Here we assume a Kelvin-Voigt-type material to take damping effects into account [3]. Therefore, we additionally consider dissipative energy terms in the system:

$$\mathcal{D} = \int_0^L (\dot{\Gamma}_1 \ \dot{\Gamma}_2 \ \dot{\Gamma}_3) \begin{pmatrix} \eta_{GA_1} & & \\ & \eta_{GA_2} & \\ & & \eta_{EA} \end{pmatrix} \begin{pmatrix} \dot{\Gamma}_1 \\ \dot{\Gamma}_2 \\ \dot{\Gamma}_3 \end{pmatrix} + (\dot{K}_1 \ \dot{K}_2 \ \dot{K}_3) \begin{pmatrix} \eta_{EI_1} & & \\ & \eta_{EI_2} & \\ & & \eta_{GJ_T} \end{pmatrix} \begin{pmatrix} \dot{K}_1 \\ \dot{K}_2 \\ \dot{K}_3 \end{pmatrix} ds \quad (3)$$

The dissipative energy is affecting the strain and curvature rates  $\dot{\mathbf{\Gamma}}$  and  $\dot{\mathbf{K}}$ . This leads to an extended set of parameters needed. In addition to the above mentioned effective stiffness parameters we need to obtain the *effective viscous parameters*:

$$[\eta_{GA_1}], [\eta_{GA_2}], [\eta_{EA}], [\eta_{EI_1}], [\eta_{EI_2}] \text{ and } [\eta_{GJ_T}] \quad (4)$$

These parameters can be further reduced by applying a theoretically deduced value for critical damping in case of tensile and shearing load cases (see [4] and [5]). Torsional and bending damping have to be investigated experimentally.

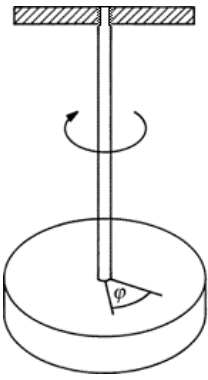


Figure 1: Measurement scheme for torsional oscillations

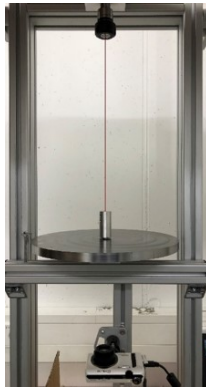


Figure 2: Experimental Setup for torsion oscillations

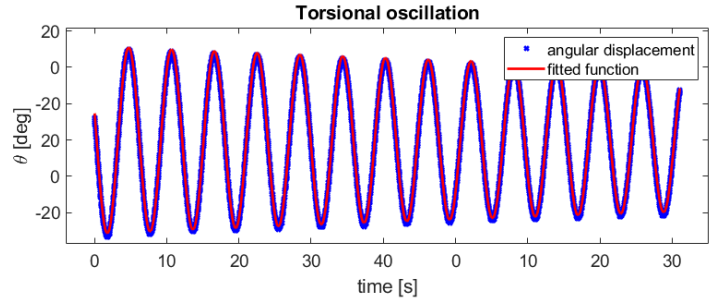


Figure 3: Extracted data from an example measurement

### 3 Experiment

Two experimental prototypes (similar to the stiffness measurements) have been setup and are being tested at ITWM. One is a dynamic torsion test, following the standard torsional pendulum test for measuring the torsional stiffness of plastics [6] (see Fig. 1, 2 and 3). The other setup is a dynamic bending test (see Fig. 4, 5 and 6). In both tests the specimen are fixed on one end. The free end is deflected mechanically and after releasing the decaying free oscillation is recorded using a high speed camera. Our preliminary results are promising and indicate that the Kelvin-Voigt-type material model is suited to simulate dynamic behavior of cables and hoses. Fitting the extracted motion data yields a damping value  $[\eta_G J]$  (or  $[\eta_E I]$ ) as well as a dynamic stiffness parameter  $[GJ]_{\text{dyn}}$  (or  $[EI]_{\text{dyn}}$ ). The obtained parameters can conveniently be used as effective mechanical properties within the frame work of our simulation software.

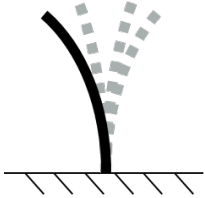


Figure 4: Measurement scheme for bending oscillations



Figure 5: Screenshot from a recorded motion video

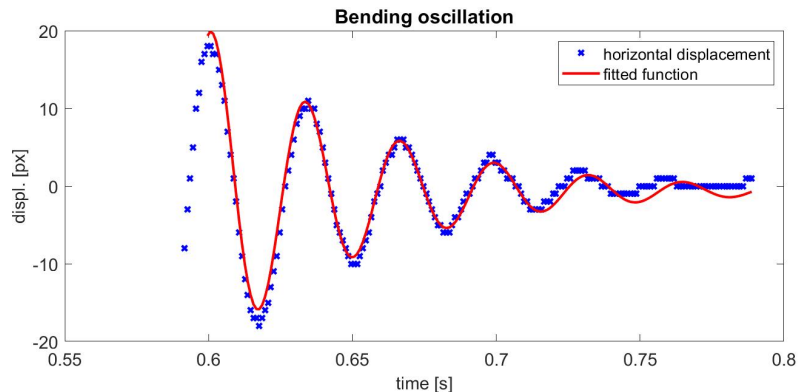


Figure 6: Extracted data from an example measurement

### References

- [1] J. Linn, T. Hermannsson, F. Andersson, F. Schneider. Kinetic aspects of discrete Cosserat rods based on the difference geometry of framed curves. Proceedings of ECCOMAS Thematic Conference on Multibody Dynamics, pp.163-176, Prague, 2017
- [2] MeSOMICS Homepage: [www.mesomics.eu](http://www.mesomics.eu)
- [3] H. Lang, J. Linn, M. Arnold. Multibody dynamics simulation of geometrically exact Cosserat rods. Multibody System Dynamics, 25(3):285-312, 2011
- [4] F. Schneider, Y. Kunz, J. Linn, V. Dörlich, F. Andersson. Kelvin-Voigt Damping Parameters for cosserat rod dynamics. ECCOMAS Multibody Dynamics Conference, Duisburg, 2019
- [5] H. Lang, S. Leyendecker, J. Linn. Numerical experiments for viscoelastic Cosserat rods with Kelvin-Voigt damping. Proceedings of ECCOMAS Thematic Conference on Multibody Dynamics, pp.453-462, Zagreb, 2013
- [6] Kunststoffe - Bestimmung dynamisch-mechanischer Eigenschaften - Teil 2: Torsionspendel-Verfahren DIN EN ISO 6721-2:2019-09

# On the Modelling of Flexible Slender Structures Guided Through Narrow Space

Radek Bulín<sup>1</sup>, Štěpán Dyk<sup>1</sup>, Michal Hajžman<sup>1</sup>

<sup>1</sup> NTIS - New Technologies for the Information Society  
Faculty of Applied Sciences  
University of West Bohemia  
Technická 8, Pilsen, 301 00, Czech Republic  
{rbulin, sdyk, mhajzman} @ntis.zcu.cz

## EXTENDED ABSTRACT

### 1 Introduction

Long and slender flexible body can be a part of various mechanical systems. This type of bodies is characterized by one dominant dimension, which by its size prevails over other dimensions. Typical representatives of long slender bodies are beams, cables, ropes, pipelines or offshore risers. Due to the slenderness, these bodies are prone to loss of stability when axially loaded, thus they should be supported or guided during their motion. General examples of such slender bodies guided through narrow space can be found in drilling industry, medical applications, guided cable installations and others. A specific example of such system can be found in nuclear reactors, where long thin control rods (CR) are guided by guide thimbles (GT) to the active zone in order to control or completely stop the nuclear reaction.

In this paper, computational approaches suitable for modelling of guided long slender structure motion are briefly summarized. Then, a benchmark simulation of a long thin beam described by absolute nodal coordinate formulation guided through rigid elbow pipe are shown. The practical application is then shown on a problem of nuclear reactor control rod emergency drop.

### 2 Overview of suitable modelling approaches

Since the flexible slender structures can perform large motions inside the guidance, the approaches used in flexible multibody systems dynamics can be successfully used for their modelling. The most common approach for modelling of flexible bodies within multibody systems is the floating frame of reference formulation (FFRF) [1], which is in its classical form suitable for small deformations problems. The main advantage of FFRF lies in the possible usage of component mode synthesis and thus fast and efficient simulations. Other approaches suitable for slender beam structures are finite segment method or rigid finite elements method, which are based on the flexible body division into small rigid segments interconnected by elastic elements. These approaches may also lead to fast simulations, but in case of more curved guiding tubes they would require more segments to properly describe bending properties of a flexible body, which can, on the other hand, decrease the time efficiency. Another suitable approach is the geometrically exact beam formulation [2], which is both accurate and effective. Last but not least, the popular absolute nodal coordinate formulation (ANCF) of finite elements [1] can be used for modelling of slender flexible bodies guided through narrow space. This approach is suitable for large deformation problems, that can be advantageous in problems of more curved guiding tubes. One of the main disadvantage of ANCF lies in the nonlinear formulation of elastic forces, that can lead to time consuming numerical integration, but several works have been published that are dedicated to ANCF efficiency increase [3, 4].

### 3 Benchmark simulation

A new benchmark problem for a beam and a curved pipe dynamic interaction testing is proposed in this paper. In a benchmark simulation of a flexible slender structure, the ANCF thin beam [5] was used for modelling of 1 m length slender beam with radius 0.01 m. The beam moves inside a curved rigid pipe and a vertical force 30 N is applied on its upper end. The inner radius of

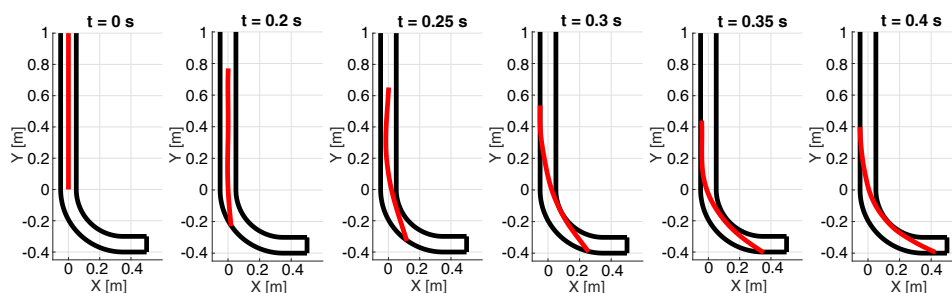


Figure 1: The snapshots of the slender beam center-line (red) and its limited space (black)

pipe is 0.015 m. The Young's modulus is set as  $1e9$  Pa, material density of the beam is  $7800 \text{ kg/m}^3$ . The interaction between the beam and pipe was modelled using Hunt-Crossley's contact model and smoothed Coulomb friction model [6]. In Figure 1, the flexible beam center-line shape in discrete time steps is shown together with the boundaries, that guides the beam motion. This simple benchmark simulation can be used to verify the model efficiency and accuracy and can serve also as a standard example of a flexible slender structure guided through narrow space.

#### 4 Control rod drop model

The practical application of described methodology is shown on the nuclear reactor CR drop problem. In case of emergency, the CRs fall down to the active zone of nuclear reactor to stop the reaction. The CR moves inside the water filled GT that can be slightly deformed by operating conditions. In order to successfully stop the nuclear reaction, the CR should fall down about 4 meters in the limited time 3.5 s (VVER 1000 type of reactor). Due to the GT deformation (*C* or *S* shape of deformation commonly occur), the CR may get stuck, which is very dangerous condition for the nuclear power safety.

This particular problem is represented by a long thin rod modelled by ANCF thin beam elements, that is moving inside a thimble modelled by classical beam finite elements. Both interacting bodies are considered as flexible and other external effects, such as water flow are considered. In Figure 2, the schematics of the problem is shown and the time histories of the CR tip vertical position and velocity for various maximal GT *S* shape deformations are shown. The model helps to predict the limit GT deformation for safe nuclear power plant operation. Also various other phenomena, such as the influence of operational vibrations or seismic excitations on the CR drop time can be further studied.

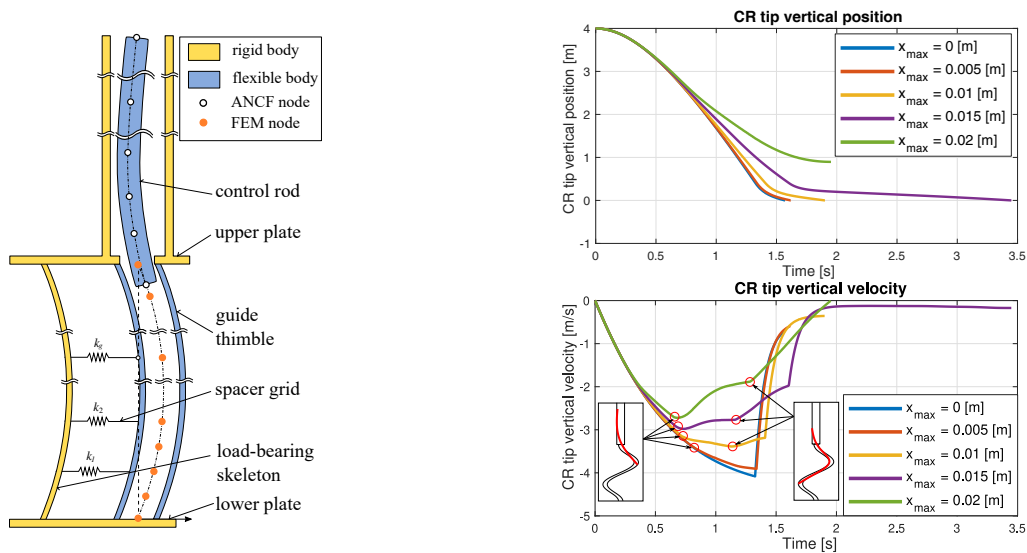


Figure 2: Scheme of the CR drop model and the CR tip vertical position and vertical velocity for various maximal deformation of the GT

#### Acknowledgments

The work was supported from European Regional Development Fund-Project "Research and Development of Intelligent Components of Advanced Technologies for the Pilsen Metropolitan Area (InteCom)" (No. CZ.02.1.01/0.0/0.0/17\_048/0007267)

#### References

- [1] A. A. Shabana. Dynamics of multibody systems, Fifth edition. Cambridge University Press, Cambridge, 2020.
- [2] I. Romero. A comparison of finite elements for nonlinear beams: the absolute nodal coordinate and geometrically exact formulations. *Multibody System Dynamics*, 20:51-68, 2008.
- [3] R. Bulín, M. Hajžman. Efficient computational approaches for analysis of thin and flexible multibody structures. *Nonlinear Dynamics*, 103(3):2475-2492, 2021.
- [4] D. García-Vallejo, J. Mayo, J.L. Escalona, J. Domínguez. Efficient evaluation of the elastic forces and the Jacobian in the absolute nodal coordinate formulation. *Nonlinear Dynamics*, 35:313-329, 2004.
- [5] J. Gerstmayr, A.A. Shabana. Analysis of thin beams and cables using absolute nodal co-ordinate formulation. *Nonlinear Dynamics*, 45:109-130, 2006.
- [6] R. Bulín, S. Dyk, M. Hajžman. Nonlinear dynamics of flexible slender structures moving in a limited space with application in nuclear reactors. *Nonlinear Dynamics*, 104(4):3561-3579, 2021.

# Modeling of Spiral Strands Using 1D Finite Strain Beam Model: Role of Frictional Contact Interactions in the Bending Behavior

Mohammad-Ali Saadat, Damien Durville

MSSMat Laboratory  
CentraleSupélec, CNRS UMR8579, Université Paris-Saclay  
3 Rue Joliot Curie, 91190 Gif-sur-Yvette, France  
[mohammad-ali.saadat, damien.durville]@centralesupelec.fr

## EXTENDED ABSTRACT

### 1 Introduction

The spiral strands are widely employed in different applications; therefore, having a tool to predict their behavior is of great importance. Many theoretical models are available in the literature since the early fifties, which could be categorized into two main types, namely the semi-continuous and discrete formulations. There are also different articles regarding the numerical simulation of spiral strands. Most of these articles either use full 3D FEM simulation [1], or an altered version of FEM, e.g., concise finite element model [2].

In this paper, a finite element simulation of spiral strands using 1D finite strain beam model [3], focusing on the role of frictional contact and residual stresses on the bending behavior, is presented. It is well known that the spiral strands exhibit a nonlinear behavior in bending [4], due to the frictional contact interactions between wires. According to the literature, the bending stiffness of these strands varies between a maximum, corresponding to the state where all the wires are stuck together, and a minimum, where all the wires are sliding. The presence of both residual stresses and intralayer contact due to the manufacturing process is suggested to explain why the maximum bending stiffness is reached in case of bending without external tensile load, in line with the experimental results. In order to have high bending stiffness in case of bending without external tensile load, in the absence of detailed knowledge of the residual stresses induced by the different phases of the manufacturing process, a simplified method for modeling these stresses is presented. Finally, through several numerical examples, the proposed numerical scheme is verified against bending experimental results.

### 2 Kinematically enriched beam model

The position vector for any material particle,  $\xi$ , of the beam with a curvilinear abscissa  $\xi_3$  is written as a first order Taylor expansion with respect to the transverse coordinates  $\xi_1$  and  $\xi_2$  in the cross section as:

$$\mathbf{x}(\xi, t) = \mathbf{r}(\xi_3, t) + \xi_1 \mathbf{g}_1(\xi_3, t) + \xi_2 \mathbf{g}_2(\xi_3, t) \quad (1)$$

where  $\mathbf{r}$  is the position of the center of the cross section, and  $\mathbf{g}_1$  and  $\mathbf{g}_2$  are the two section directors. Since the section directors are unconstrained, plane deformations of the cross section could be captured, and each node has 9 degrees of freedom. The Green-Lagrange strain tensor could be written based on the 3 above kinematic vectors, and a full 3D elasticity law is used.

For the formulation of contact between two beams, intermediate geometries are used to consider both parts of beams in contact symmetrically. The contact elements are defined at discrete points of the intermediate geometries, for each pair of particles candidate to contact.

### 3 Residual stresses due to manufacturing process

The spiral strands exhibit hysteretic behavior, which in case of elastic behavior of individual wires, is solely due to the frictional contact interactions between different wires. According to the literature, the bending stiffness varies between two limit cases, namely the full slip and full stick states.

Due to the helical geometry of spiral strands, the wires' tensile forces produce a contact pressure that could prevent the wires from sliding. Therefore, the tensile stresses of the wires directly affect the contact pressure, and consequently, the bending stiffness of the strands. The high bending stiffness of unstressed spiral strands [5], suggests the presence of residual stresses which dramatically affect the bending stiffness. However, based on experimental and numerical evidence, the maximum bending stiffness could not be achieved by having only interlayer contact.



In the present study, the residual stresses are modeled by considering residual bending strains for all wires, which after relaxation of the strand without external loads, will cause pretension in the wires. This pretension induces a contact pressure between wires, that prevents them from sliding. Moreover, to have a very high initial bending stiffness as observed in the experiment, a small alteration in the nominal configuration, in order to force intralayer contact, has been made. The parameters of the strand, which has been studied here and in [3], are given in Table 1.

Layer	No. of wires	Wire diameter, nominal configuration [mm]	Wire diameter, altered configuration [mm]	Young's Modulus [GPa]	Lay angle [°]
Core	1	4.4	4.38	210	-
1	6	4.4	4.29	210	10.15
2	12	4.4	4.39	210	12.6
3	18	4.4	4.42	210	13.96
4	24	4.4	4.43	210	14.23
5	30	4.4	4.43	210	15.4

Table 1: Parameters of the 5-layer spiral strand

#### 4 The bending behavior of spiral strands

The force-deflection diagram of the spiral strand above for a three-point bending test is shown in Figure 1. As it can be seen, if no residual stress is present, all the wires act independently, and the force-displacement curve corresponds to the minimum bending stiffness. Moreover, one notices that even if the cable has residual stresses, the interlayer contact is not enough to achieve a very high bending stiffness. Therefore, to get a behavior similar to the experiment, it is necessary to account for the presence of intralayer contact, which could be achieved by a small alteration in the nominal configuration.

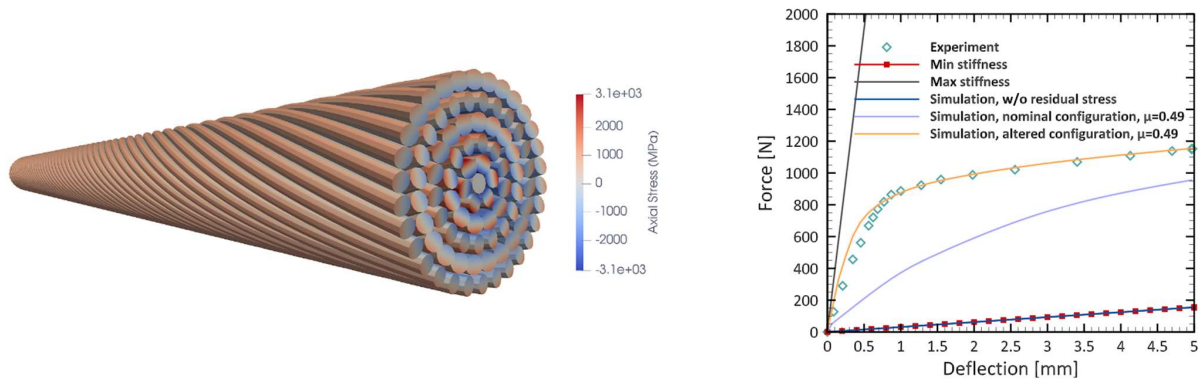


Figure 1: The axial stress caused by the residual stresses (left) and the force-deflection diagram of the three-point bending test (right) for a 5-layer spiral strand

#### Acknowledgments

This work has received funding from the European Union's Horizon 2020 research and innovation programme under the Marie Skłodowska-Curie grant agreement No 860124.

#### References

- [1] R. Judge. and Z. Yang. and SW. Jones. and G. Beattie. Full 3D finite element modelling of spiral strand cables. *Construction and Building Materials*, 35:452:459, 2012.
- [2] WG. Jiang. and JL. Henshal. and JM. Walton. A concise finite element model for three-layered straight wire rope strand. *International Journal of Mechanical Sciences*, 42:63:86, 2000.
- [3] D. Durville. Contact-friction modeling within elastic beam assemblies: an application to knot tightening. *Computational Mechanics*, 49:687:707, 2012.
- [4] K. Papailiou. The rope bending with a variable bending stiffness due to the internal friction, the tensile force and the rope warping (Doctoral dissertation, ETH Zurich, Zurich, Switzerland), 1995.
- [5] Z. Chen. and Y. Yu. and X. Wang. and X. Wu. and H. Liu. Experimental research on bending performance of structural cable, 96:279-288, 2015.

**Section**

**VEHICLE DYNAMICS AND AEROSPACE APPLICATIONS**

VEH-1-2-3

# Simplified mechanical model for balancing a motorbike with steering at zero speed

András Szabó<sup>1</sup>, Hanna Zs. Horváth<sup>1</sup>, Dénes Takács<sup>2</sup>

<sup>1</sup> Department of Applied Mechanics  
Budapest University of Technology and Economics  
H-1111 Budapest, Műegyetem rkp. 3, Hungary  
szaboandras97@gmail.com, hanna.horvath@mm.bme.hu

<sup>2</sup> MTA-BME Research Group on Dynamics of Machines and Vehicles  
H-1111 Budapest, Műegyetem rkp. 3, Hungary  
takacs@mm.bme.hu

## EXTENDED ABSTRACT

### 1 Introduction

In the development of autonomous vehicles, engineers are facing fascinating but complex tasks. The localization of the vehicle, the detection of the surrounding objects, the decision making, motion planning, and finally, the motion control of the vehicle provide challenges. These challenges are even more complicated when the automated vehicle is a motorcycle. The investigations of bicycles and motorcycles are very complex due to the fact that no in-plane mechanical models can accurately describe the dynamics of these vehicles. However, the governing equation of the required spatial nonholonomic models cannot be handled analytically [1, 2, 3]. To overcome this problem, we present a simplified mechanical model of a motorcycle, by which a linear feedback controller is designed to stabilize the unstable vertical equilibrium at zero longitudinal speed using the steering system.

### 2 Mechanical model

The simplified mechanical model is shown in Figure 1. When the tilting angle  $\varphi$  and the steering angle  $\delta$  of the motorcycle are small, the pitch motion is negligible (see [4]). Hence, the crank mechanism in panel (b) is a possible simplified model of the vehicle. The contact point  $P_1$  of the front wheel is modeled as a rotary joint, while the contact point  $P_2$  of the rear wheel can move along the  $X$ -axis when the front wheel is steered. The plane of motion of the crank mechanism (marked with blue) can tilt with the tilting angle  $\varphi$  around the  $X$ -axis capturing the tilting motion of the motorcycle. The angle between the two arms of the crank mechanism is the steering angle  $\delta$ . The internal steering torque is marked with  $M$ . Using the geometric parameters of the vehicle shown in panel (a), the trail  $e$ , the wheelbase  $a + b - e$  and the height  $h$  of the centre of gravity determine the lengths of the rods of the crank mechanism.

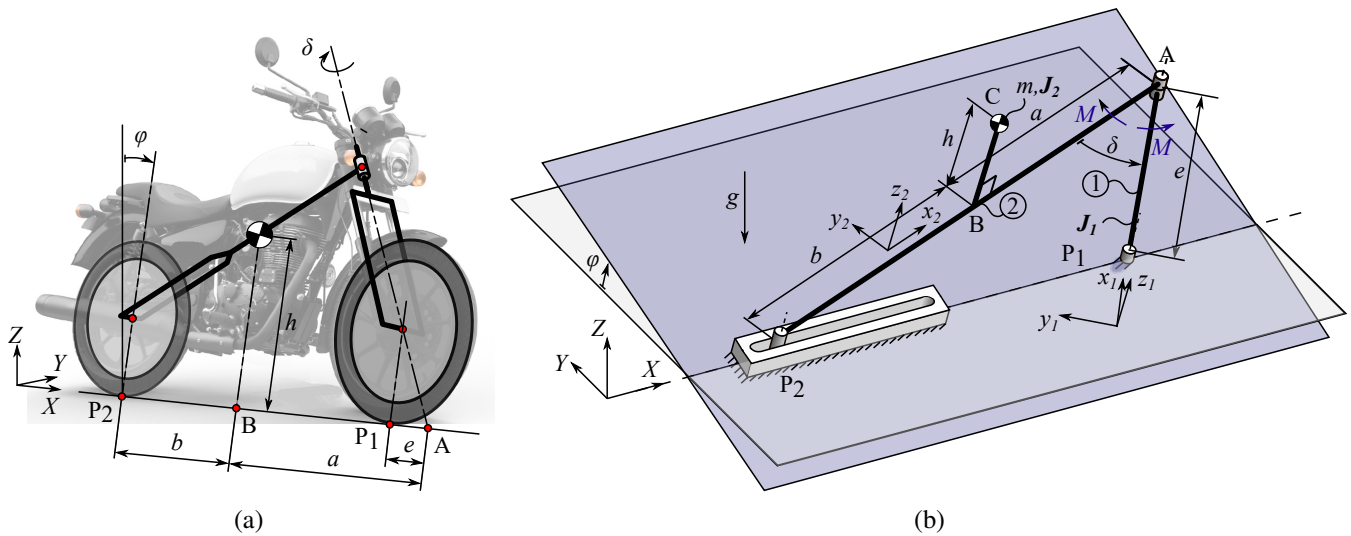


Figure 1: The geometry of the motorbike (a) and the simplified mechanical model (b).

The equations of motion of this two degree-of-freedom mechanical model can be derived using the Lagrangian equation of the second kind. After linearization around the equilibrium  $\varphi \equiv 0$ ,  $\delta \equiv 0$ , we obtain:

$$\begin{bmatrix} \frac{J_{P_1}^{z_1}(a+b)^2 + (J_C^{z_2} + mb^2)e^2}{(a+b-e)^2} & -\frac{mebh}{a+b-e} \\ -\frac{mebh}{a+b-e} & J_{P_1}^{x_1} + J_C^{x_2} + mh^2 \end{bmatrix} \begin{bmatrix} \ddot{\delta} \\ \ddot{\varphi} \end{bmatrix} + \begin{bmatrix} 0 & \frac{mgeb}{a+b-e} \\ \frac{mgeb}{a+b-e} & -mgh \end{bmatrix} \begin{bmatrix} \delta \\ \varphi \end{bmatrix} = \begin{bmatrix} M \\ 0 \end{bmatrix}, \quad (1)$$

where  $m$  is the mass of the vehicle,  $J_{P_1}^{x_1}$  and  $J_{P_1}^{z_1}$  refer to the mass moments of inertia of the steered fork-wheel system about  $x_1$  and  $z_1$  axes with respect to the point  $P_1$  (see Figure 1(b)), respectively.  $J_C^{x_2}$  and  $J_C^{z_2}$  are the mass moments of inertia of the motorcycle body about  $x_2$  and  $z_2$  axes with respect to the center of gravity C.

### 3 Balancing with steering

The unstable vertical equilibrium position of the motorcycle can be stabilized by using the steering mechanism. This paper investigates the applicability of a PD controller in detail with and without feedback delay  $\tau$ . The controller actuates through the steering torque, namely, a lower level control of the steering servo creates the steering torque, while the desired steering angle  $\delta_{\text{des}}$  is calculated by the higher level controller:

$$M = -K_{p\delta}(\delta - \delta_{\text{des}}) - K_{d\delta}\dot{\delta}, \quad \text{and} \quad \delta_{\text{des}} = -K_{p\phi}\varphi(t - \tau) - K_{d\phi}\dot{\varphi}(t - \tau), \quad (2)$$

where  $K_{p\delta}$ ,  $K_{d\delta}$ ,  $K_{p\phi}$  and  $K_{d\phi}$  are the proportional and differential control gains corresponding to the steering angle and the roll angle respectively.

First, the linear stability of the closed-loop system was checked for the zero time delay case, and the stability boundaries were found analytically using the Liénard-Chipart stability criterion [5]. Stability charts were drawn in the  $K_{p\phi} - K_{d\phi}$  plane using realistic, small scale vehicle model parameters, see dashed curves in Figure 2. The linearly stable domain is shaded with light blue color. Closed form formulas can be determined for the upper and lower limits of the lower level control parameters at which vertical position of the motorcycle is stabilizable.

Since the accurate measurement of the tilting angle requires filtering, a non-negligible time delay is introduced in the system. Considering this feedback delay, the stability boundaries were identified using semi-discretization [6]. Even a small value of the delay scales and shifts the stable region significantly in the stability diagram, see the dark blue domain in Figure 2.

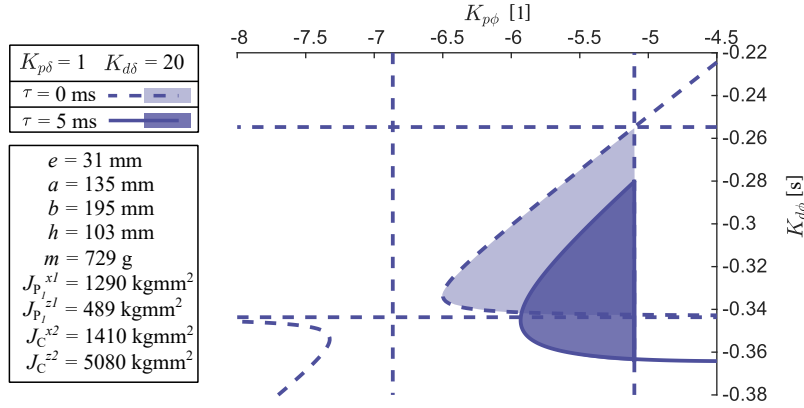


Figure 2: The stability chart.

### 4 Conclusion

A simplified mechanical model was constructed to design steering controller for balancing a motorcycle at zero longitudinal speed. It was shown that the hierarchical linear feedback controller is capable of stabilizing the vertical position of the motorcycle when the control gains are chosen appropriately and the feedback delay is small enough. The experimental validation of the results is the task of future work, for which a small scale experimental rig is already designed and manufactured.

### Acknowledgments

The research reported in this paper has been supported by the National Research, Development and Innovation Office under grant no. NKFI-128422.

### References

- [1] J. P. Meijaard, J. M. Papadopoulos, A. Ruina, and A. L. Schwab. Linearized dynamics equations for the balance and steer of a bicycle: a benchmark and review. *Proceedings of the Royal Society A*, 463:1955–1982, June 2007.
- [2] R. S. Sharp, S. Evangelou, and D. J. N. Limebeer. Advances in the modelling of motorcycle dynamics. *Multibody System Dynamics*, 12(3):251–283, 2004.
- [3] Manfred Plöchl, Johannes Edelmann, Bernhard Angrosch, and Christoph Ott. On the wobble mode of a bicycle. *Vehicle System Dynamics*, 50(3):415–429, mar 2012.
- [4] Jason Moore. *Human Control of a Bicycle*. PhD thesis, 08 2012.
- [5] F. Gantmacher. *Lectures in analytical mechanics*. MIR Publishers, Moscow, 1975.
- [6] Tamas Insperger and Gabor Stepan. *Semi-discretization*, pages 39–71. Springer New York, 2011.

# Handling Evaluation of Tractor-semitrailer with Split Fifth Wheel Coupling Undergoing an ISO Double Lane Change Manoeuvre

Ajith Jogi<sup>1</sup>, Sujatha Chandramohan<sup>2</sup>, Sabyasachi Dash<sup>3</sup>

<sup>1</sup>Department of Mechanical Engineering  
Indian Institute of Technology Madras  
Chennai, India -600036  
ajithjogi@gmail.com

<sup>2</sup>Department of Mechanical Engineering  
Indian Institute of Technology Madras  
Chennai, India -600036  
sujatha@iitm.ac.in

<sup>3</sup>Department of Mechanical Engineering  
National Institute of Technology Trichy  
Tiruchirappalli, India -620015  
sabyadash21@gmail.com

## EXTENDED ABSTRACT

### 1 Introduction

Tractor-semitrailers are articulated freight carrying vehicles, where a portion of the trailer's load is supported by the tractor. Usually, these are lengthy vehicles making them difficult to manoeuvre in congested roads, since the space required to take the turn increases with wheelbase. Off-tracking is a metric used to measure this turning space and is defined as the radial distance between the trajectory of the front and rearmost axles of a vehicle during the turning manoeuvre. Many researchers, including Jindra [1], and Choi et al. [2] have worked on the modelling of off-tracking. Steering the semitrailer axle is one of the effective methods for reduction of off-tracking; however, it includes a complex system to control the steering, which makes it expensive. Jogi and Chandramohan [3] have developed a new hitch mechanism, termed Split fifth wheel coupling (SFWC) which reduces the off-tracking by a significant margin. SFWC is a passive mechanism without the inclusion of complex systems.

It is necessary to evaluate the handling performance of the tractor-semitrailer with SFWC to ensure its safe operation. Double lane change (DLC) manoeuvre is one of the handling evaluation methods, wherein the vehicle swiftly changes its lane and comes back to its original lane to avoid an obstacle. There are various kinds of DLC specifications which have been compared with each other by Peng and Yang [4]. ISO DLC is one of the standards for such tests. ADAMS /Car tool is capable of performing the simulations of closed-loop ISO DLC test and provides good results [5].

#### 1.1. SFWC

The Conventional fifth wheel coupling (CFWC) consists of a turntable fixed to the chassis of the tractor. It receives the kingpin of the semitrailer, forming a joint which serves not only as an articulation point, but also as the point of vertical load transfer from the semitrailer to the tractor. Figure 1 (a) shows the conceptual model of the tractor-semitrailer with CFWC. On the other hand, SFWC being a novel off-tracking reduction mechanism, the articulation point and the point of vertical load transfer have been separated by a certain distance. It consists of two sub-units: cylindrical joint and roller mechanism, as shown in Figure 1 (b). The former takes care of articulation, whereas the latter allows the vertical load transfer from the semitrailer to the tractor even when the vehicle is articulating.

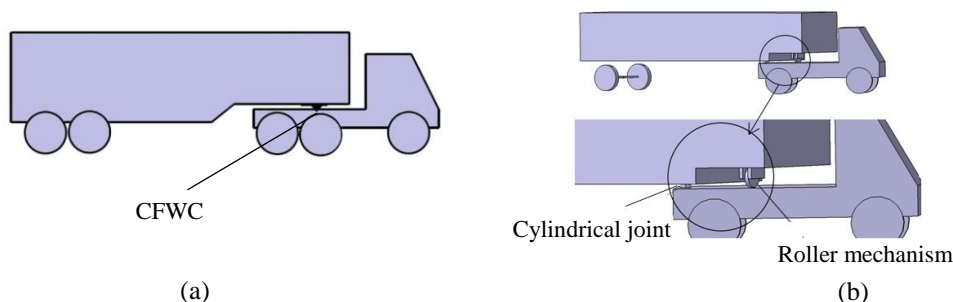


Figure 1. Conceptual model of the tractor-semitrailer with (a) CFWC (b) SFWC (Courtesy: Jogi and Chandramohan [7]).

### 2 Methodology

In the present work, a multi-body virtual prototype is built using the ADAMS Car tool. Initially, the Conventional fifth wheel coupling (CFWC) model is built as per the specifications of AASHTO Standard Design Interstate Tractor-Trailer WB-62. Using the template builder option, CFWC model is modified into SFWC, by adding a roller mechanism and curved track as shown in Figure 2. To evaluate the handling performance of the vehicle with SFWC, it is simulated for closed-loop ISO double lane change (DLC) manoeuvre. Five speeds are chosen for the study: 20 kmph to 60 kmph with an interval of 10 kmph. The actual length of the ISO DLC course is 170 m; however, to study the behaviour of the vehicle after finishing the course, the vehicle is run for an additional distance of about 130 m. The simulation data are used to plot the trajectory, yaw rate response, lateral acceleration response and articulation angle response of both the vehicle models. To understand the relative performance of the tractor-semitrailer with SFWC, the results of both models are compared with each other and useful conclusions are drawn.

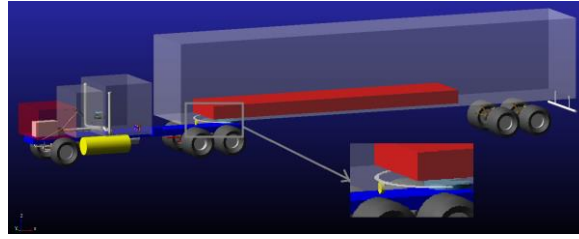


Figure 2: ADAMS CAR model of the tractor-semitrailer with SFWC

### 3 Results and discussion

The SFWC model traces the target path pretty well at lower speeds; however, it is a little unstable at higher speeds when compared to the CFWC model as shown in Figure 2. The behaviour of both vehicles changes significantly between 40 and 50 kmph. The lateral acceleration response explains that the DLC is a very dynamic manoeuvre and can generate rapid rates of change of lateral acceleration. Interestingly, for speeds below 40 kmph, the lateral acceleration experienced by the semitrailer of the SFWC vehicle is less compared to that of the CFWC vehicle. One should note that the DLC manoeuvre is highly dependent on the driver's steering input. The default driver model present in ADAMS/ Car tool is optimized for the tractor-semitrailer with CFWC. Hence, the actual steering input to be given to SFWC vehicles may vary. In the present study, the performance of the tractor-semitrailer with SFWC is on par with that of CFWC at speeds below 50 kmph. The vehicle's inability to trace the ISO DLC path is more pronounced at higher speeds. With the development of stability control systems like ESC, optimized for tractor-semitrailer with SFWC, their performance would improve.

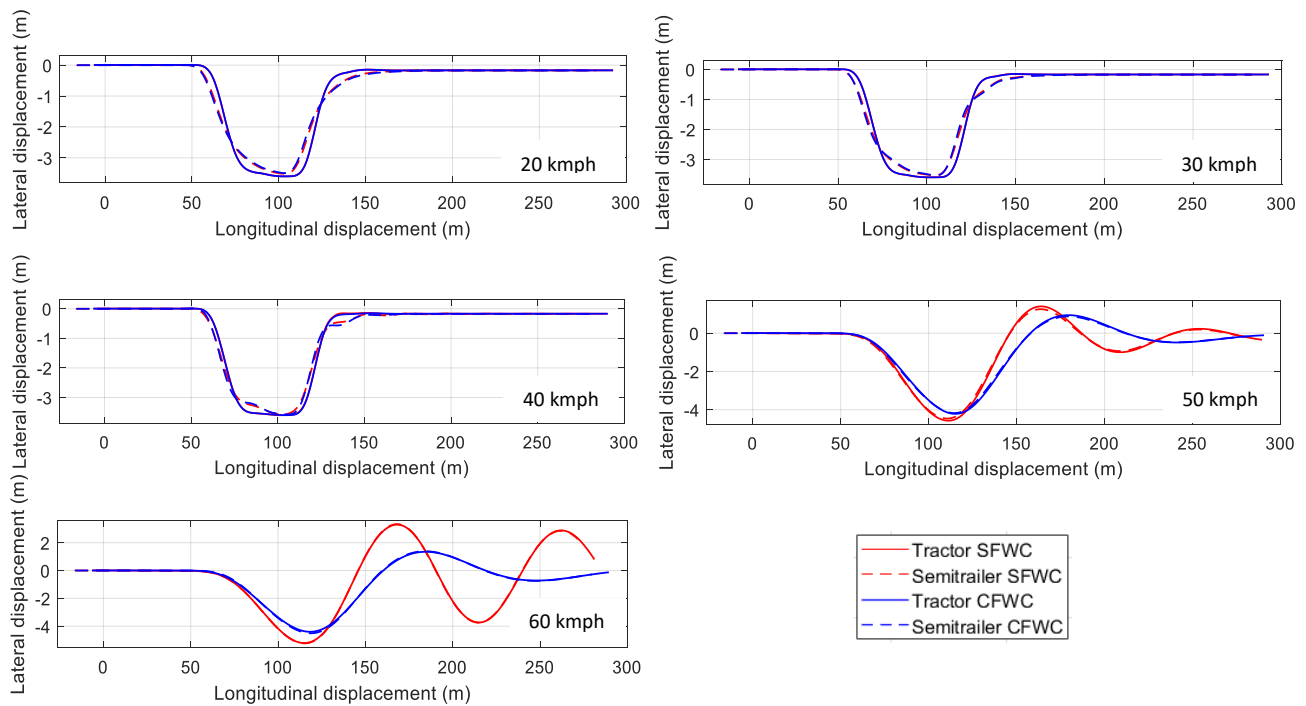


Figure 2: Trajectory of the tractor-semitrailer with SFWC and CFWC at various speeds

### References

- [1] F. Jindra, Off-tracking of tractor-trailer combinations. *J. Automob. Eng.* 96–101, 1963.
- [2] J. Choi, J. Baek, S. Lee, W. Kang, Offtracking model on horizontal curve sections. *Eastern Asia Society for Transportation Studies*, vol. 3, No. 1, 2001.
- [3] A. Jogi, S. Chandramohan, Kinematic analysis of tractor-semitrailer with split fifth wheel coupling during low speed turning maneuvers, *SAE Int. J. Commer. Veh.* 10(2): 2017, doi:10.4271/2017-01-1554, 2017.
- [4] Y. Peng, X. Yang, Comparison of various double lane change manoeuvre specifications, *Vehicle System Dynamics*, 50:7, 1157-1171, DOI: 10.1080/00423114.2012.659741, 2012.
- [5] N. Khettou, D. Trifkovic, S. Muzdeka, Using modelling and simulation to predict dynamics of converted ground vehicle, *Defence Science Journal*, Vol. 66, No. 5, pp. 509-516, DOI : 10.14429/dsj.66.9783, 2016.

## Development of Steering Laws to Assist the Driving of a 4-Wheel Steering Vehicle

Louis DAMBACHER<sup>1</sup>, Benjamin BOUDON<sup>1</sup>, Nicolas BOUTON<sup>1</sup>, Roberto LOT<sup>2</sup>, Nicolas LALANDE<sup>3</sup>, Roland LENAIN<sup>4</sup>

<sup>1</sup> Université Clermont Auvergne, CNRS

SIGMA Clermont, Institut Pascal  
63000 Clermont-Ferrand, France

[louis.dambacher,  
benjamin.boudon, nicolas.bouton]  
@sigma-clermont.fr

<sup>2</sup> Departement of industrial Engineering

University of Padova

35131 Padova, Italy

roberto.lot@unipd.it

<sup>3</sup> Airbus Helicopters

Aéroport de Marseille Provence

13700 Marignane, France

nicolas.lalande.as@gmail.com

<sup>4</sup> French National Institute

for Agriculture, Food,  
and Environment (INRAE)

63170 Aubière, France

roland.lenain@inrae.fr

### EXTENDED ABSTRACT

#### 1 Context

The field of 4-wheel steering (4WS) vehicles has been gaining in interest since the improvement of on-board electronics in vehicles. The further exploitation of the 4WS vehicle may indeed allow improving the driving comfort, agility and safety. The 4WS systems on the market for premium cars do not make a full use of the two steering axles. The use of actuated rear steering axle is often under-exploited, as it consider only the improvement of vehicle dynamics [1] without increasing maneuverability (crabway motion, parallel steering) that is achievable by a manual driver. This paper is related to the field of assisted ground vehicles and more specifically to the field of 4WS systems. The work proposed in this paper aims at modelling and simulating a 4WS vehicle in order to compute observation and control strategy for assisting a driver to control a 4WS vehicle easily and safely.

#### 2 State of art

In previous works, very advanced dynamic representations can be found [2]. But the large number of parameters makes them difficult to use for control. In the opposite case, simple kinematic models have been developed for control purposes [3]. However, these models are not representative of various phenomena, in particular: the lack of grip, the vehicle inertia, or the load transfer phenomenon. In this paper we will use hybrid approaches allowing the use of simplified models adapted in real time by observers [4]. These approaches are used in mobile robotics [5] on autonomous robots. The challenge here is to control the rear axle according to the driver's command.

#### 3 Proposed approach

The tool developed to test the different control laws, in view of the implementation on vehicle, is a MATLAB/Simulink simulator represented on figure 1. It is composed of several main blocks:

- Vehicle model : The evolution equations of the dynamic model adapted to the control are implemented. The only inertia considered is the inertia of the vehicle chassis. Lateral slippage is modelled by a linear relationship between the lateral slip forces ( $F_F, F_R$ ) and the drift angles ( $\beta_f, \beta_r$ ). The coefficient linking these two variables is the cornering stiffness  $C_e$ .
- Geometric model : The yaw rate set point  $\dot{\theta}_{target}$  is calculated. It is the result of a purely geometric modelling of a "bicycle" model of the vehicle in a rolling without slipping condition.
- Control law : The steering law operating on the rear steering gear is implemented. This is aimed at limiting the impact of slippery ground on the user's high-speed driving. Specifically, the purpose of this control is to make the 4-wheel-steered vehicle behave like a 2-wheel-steered vehicle on non-slippery ground, such as asphalt. The control law is based on a backstepping strategy.
- Observer : The cornering stiffness ( $C_e$ ) is calculated based on the speed of the vehicle ( $u$ ), the steering angles ( $\delta_f, \delta_r$ ) and the measurement of the vehicle's yaw rate ( $\dot{\theta}_{mes}$ ). This observer is based on a first order exponential decrease of the observation error and a MIT Rule [6].

More sophisticated vehicle models can be placed in this simulator to validate the control laws already developed and to take into account the maintaining of stability in the development of new control laws.



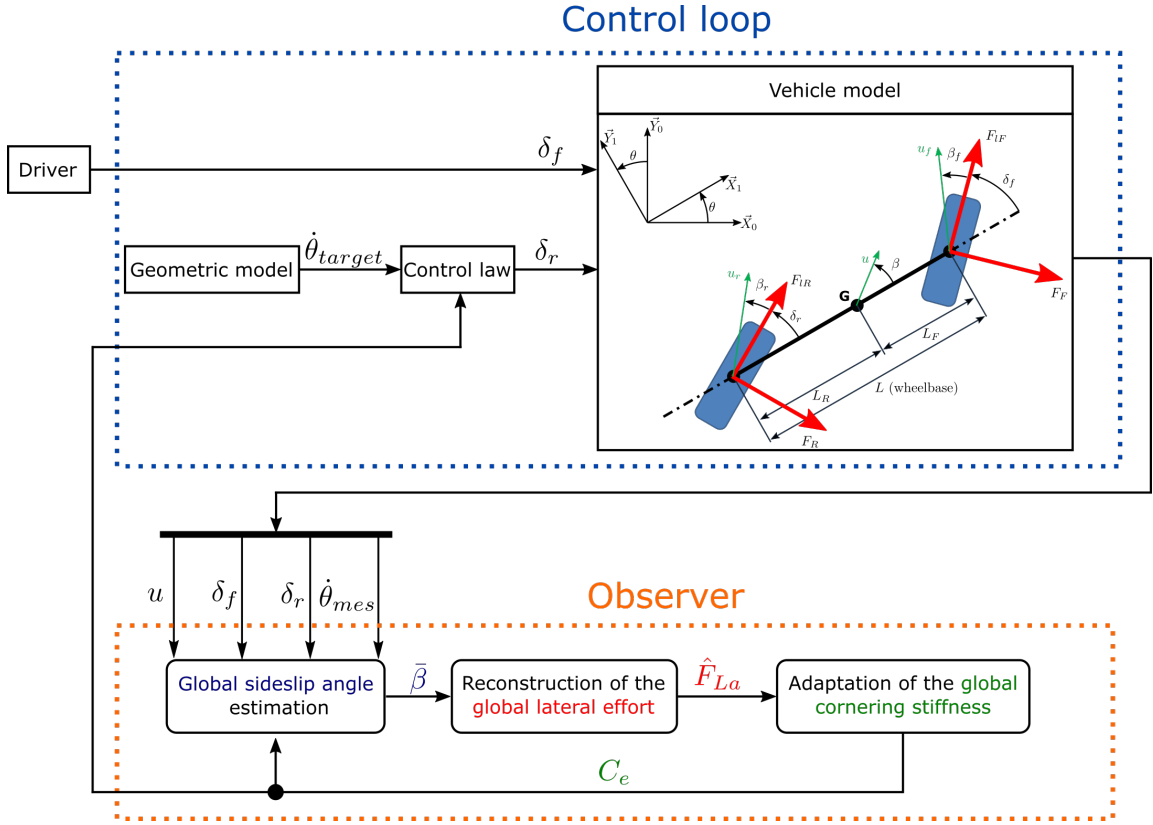


Figure 1: Global control scheme

$\delta_f / \delta_r$	Front / rear steering angle
$u$	Speed of the vehicle's centre of gravity in the yaw plane
$\dot{\theta} / \dot{\theta}_{target} / \dot{\theta}_{mes}$	Real / set point / measured yaw rate

#### 4 Results and perspectives

This approach provides a simulation that is representative of a real vehicle and allows the implementation of initial control laws to optimise the behaviour of a manually steered 4WS vehicle. The first results allow the regulation of a target yaw rate given by the front steering angle through adaptive approaches. These results will be extended to other criteria, such as space requirement, control of the radius of curvature, and relative position of the vehicle, independently of its orientation. This requires real-time simulations with the driver integrated. This will be done on Gazebo by adding new commands for the driver.

#### Acknowledgments

This work was sponsored by a public grant overseen by the French National Research Agency as part of the “Investissements d’Avenir” through the IMobS3 Laboratory of Excellence (ANR-10-LABX-0016) and the IDEX-ISITE initiative CAP 20-25 (ANR-16-IDEX-0001).

#### References

- [1] H. Sato, H. Kawai, M. Isikawa, H. Iwata, and S. Koike, “Development of four wheel steering system using yaw rate feedback control,” *SAE Technical Papers*, 1991.
- [2] N. Dal Bianco, R. Lot, and M. Gadola, “Minimum time optimal control simulation of a GP2 race car,” *Proceedings of the Institution of Mechanical Engineers, Part D: Journal of Automobile Engineering*, vol. 232, no. 9, pp. 1180–1195, 2018.
- [3] C. Samson, “Control of Chained Systems Application to Path Following and Time-Varying Point-Stabilization of Mobile Robots,” *IEEE Transactions on Automatic Control*, vol. 40, no. 1, pp. 64–77, 1995.
- [4] N. Bouton, *Stabilité dynamique des véhicules légers tout-terrain*. PhD thesis, 2009.
- [5] C. Cariou, R. Lenain, B. Thuilot, and M. Berducat, “Automatic guidance of a four-wheel-steering mobile robot for accurate field operations,” *Journal of Field Robotics*, vol. 26, no. 6-7, p. 15, 2009.
- [6] K. Astrom and B. Wittenmark, *Adaptive Control Second Edition*. New-York: Addison-Wesley, 1994.

# Multibody Dynamic Approach to Risk Analysis of Autonomous Driving Test Scenario

Sheng-peng Zhang<sup>1</sup>, Ji-yoon Choi<sup>2</sup>, Sung-hyuk Won<sup>2</sup>, Dong-hoe Heo<sup>2</sup>, Tae-oh Tak<sup>1\*</sup>

<sup>1</sup>Faculty of Mechanical and Biomedical Engineering  
Kangwon National University  
Chuncheon city, Kangwon-do, 24341, Korea  
zsp363527125@gmail.com, totak@kangwon.ac.kr

<sup>2</sup>Faculty of Mechanical and Biomedical Engineering  
Kangwon National University  
Chuncheon city, Kangwon-do, 24341, Korea  
jiyoon0246@gmail.com, 3385ws@kangwon.ac.kr, gjeh22@naver.com

## EXTENDED ABSTRACT

Recently autonomous driving vehicles with more than level 3 are widely developed, and some of them are available on the market. In the development of autonomous vehicles, one of the most critical issues is how to guarantee safety of the vehicle in real-world traffic environments. Various methods on the safety assessment have been developed, such as scenario-based method, function-based method, and real-world testing. In any cases, test scenarios that can adequately represent complex and dynamic traffic situations play a key role in verifying performance of autonomous vehicles. This work focuses on development of a novel risk analysis method of autonomous driving test scenarios based on Analytic Hierarchy Process(AHP) method [1] in multibody vehicle dynamics settings.

The risk analysis methods include both deterministic and probabilistic approaches [2]. The first one assesses the risk through computing quantitative risk indicators, on the other hand, the probabilistic approach estimates risk-taking uncertainty of vehicle motion, for example, the collision risk probability can be obtained by the ratio of collision position between two vehicles using the Gaussian distribution. However, these studies do not consider enough motion variables for the host vehicle (HV) and surrounding vehicles (SV), such as the relative position, orientation, and velocity, which make them less representative for dynamic and interactive nature of traffic situations. In this study, risk analysis of autonomous driving test scenarios, where risk is quantified by the relative positions, orientations, and velocities of HV and SVs modeled with multibody vehicle dynamics is performed. Additionally, in order to improve conventional AHP method, optimal solution between motion characteristics and risk index of test scenarios are used instead of subjective evaluation of comparison matrices values by scenario designer, which makes conventional AHP method more dependent to use cases.

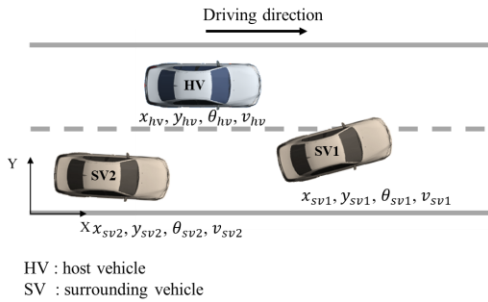


Figure 1: Test scenario construction for multi-vehicles

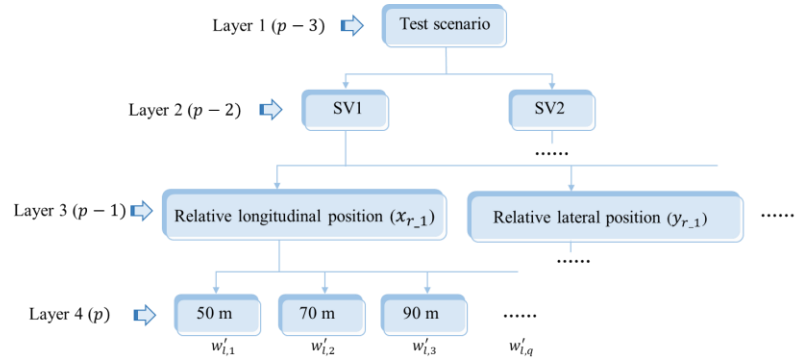


Figure 2: Hierarchy model of test scenario

As shown in Figure 1, the motion variables of HV and SVs modeled by multibody method are represented, by longitudinal position, lateral position, yaw angle, and driving velocity ( $x, y, \theta, v$ ), respectively with respect to X-Y global reference frame. In order to represent the relative motion variables between HV and SVs, the hierarchy model of test scenario shown in Figure 2 is built, where test scenario is defined as the top layer of the objective in hierarchy model, and subsequent layers of SVs, motion variables, and their values. Each layer plays a dominant role with its subsequent layer, and the relationship of layer-to-layer is transferred from top to bottom in the hierarchy model. In the Figure 2,  $p$  represents number of layers and  $w'_{p,q}$  is priority importance value calculated by AHP method.

The comparison matrix  $A_{l,q}$  between dominant layer and subsequent layer in the hierarchy model is generated by judging the relative importance of elements in pairs shown as equation (1) [1].

$$A_{l,q} = \begin{bmatrix} 1 & a_{1,2} & \dots & a_{1,q_j} \\ 1/a_{1,2} & 1 & \dots & \dots \\ \dots & \dots & 1 & a_{q_i,q_j} \\ 1/a_{1,q_j} & \dots & 1/a_{q_i,q_j} & 1 \end{bmatrix} \quad q_i, q_j \in [1, \dots, n]; l \in [(p-1), (p-2), (p-3)] \quad (1)$$

where  $A_{l,q}$  is the matrix of dominant layer which is the  $q$ -th factor in layer  $l$ ,  $a_{q_i,q_j}$  represent the pairwise comparison value between the two factors in the  $q_i$ -th row and the  $q_j$ -th column,  $n$  is number of factors in the subsequent layer for matrix  $A_{l,q}$ . Based on the comparison matrix  $A_{l,q}$ , the priority importance values  $w$  are determined by solving the eigenvalue problem shown as in equation (2). Priority importance values  $w$  are obtained by an approximation method, which is computed by normalized comparison matrix.

$$A_{l,q} w = \lambda_{max} w \quad (2)$$

where  $\lambda_{max}$  defines principal eigenvalue of matrix  $A_{l,q}$ ,  $w$  is priority importance values of matrix  $A_{l,q}$ .

In order to obtain all priority importance values in a test scenario, the priority importance values of individual comparison matrices are combined into the same reference frame. The combined values in the last layer are defined as “priority importance index”. The priority importance index  $w'_{p,q}$  represents  $w_{p,q}$  of individual comparison matrix comparing to layer 1 shown in Fig. 2. There is only one path from  $w'_{p,q}$  to layer 1, and the transfer path is recorded as  $R_{p,q}$ . And each one's priority importance value is  $w_k^{R_{p,q}}$ . Therefore, the priority importance index comparing to layer 1 can be obtained as

$$w'_{p,q} = \prod_{k=2}^p w_k^{R_{p,q}} \quad k \in [1, \dots, (p-1), p] \quad (3)$$

A test scenario is generated by the elements of  $q$  in the layer  $(p-1)$  in Figure 2 (such as, from the “relative longitudinal position” in layer 3 to “50m” in layer 4). Therefore, the risk index ( $RI$ ) of test scenarios can be calculated according to equation (4).

$$RI = \sum_{m=1}^{i'_{(p-1)}} (w'_{p,q})_{m,n} \quad (4)$$

where  $p$  represents number of layers,  $m$  defines number in the order of elements in the layer  $(p-1)$ ,  $n$  is of that number in the order of elements in the next layer of element  $m$ ,  $(w'_{p,q})_{m,n}$  defines priority importance index in layer  $p$ ,  $i'_{(p-1)}$  is elements number in the layer  $(p-1)$ .

Because it is difficult to determine the value of the comparison matrices of AHP in equation (1) by the scenario designer, optimal solution of comparison matrices values is calculated from the correlation coefficient ( $r$ ) [3] between relative motion characteristics and risk index of test scenarios using particle swarm optimization (PSO) method. The minimum relative distance and minimum relative velocity between vehicles body boundary are used to represent as the relative motion characteristics between host vehicle and surrounding vehicle.

A cut-in scenario is used to verify as an example of the proposed risk analysis method. In order to generate the dangerous cut-in scenarios, the motion variables including the relative longitudinal position (9m, 14m, and 19m), relative lateral position (3.75m, 3.25m, and 2.75m), cut-in angle (4deg, 5deg, and 6deg), and relative longitudinal velocity (8.3m/s, 5.6m/s, and 2.7m/s) are defined to induce the collision scenarios. Thus,  $3^4 = 81$  cut-in test scenarios are generated, including 25 collisions and 56 non-collisions. Figure 3 shows the correlation between risk index and the minimum relative distance (left) and minimum relative velocity (right) of relative motion characteristics for conventional AHP and the proposed AHP. The result shows the correlations coefficient of AHP method in minimum relative distance and minimum relative velocity are -0.904 and 0.925, and the correlations coefficient of the proposed AHP method in minimum relative distance and minimum relative velocity are -0.957 and 0.938, respectively. The results demonstrate that minimum relative distance of relative motion characteristics decreases with increasing risk index, and the minimum relative velocity of relative motion characteristics increases with increasing risk index.

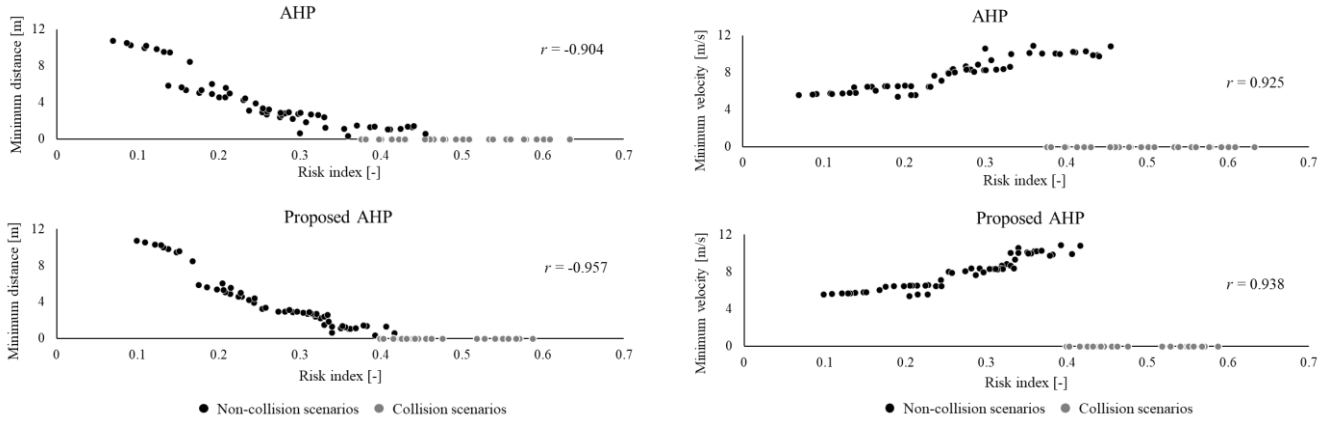


Figure 3: Correlation between risk index and minimum relative distance (left) and minimum relative velocity (right) of vehicle body boundary.

This study proposes a novel risk analysis method of autonomous driving test scenarios, where risk is quantified by the relative position, orientation, and velocity between host and surrounding vehicles. A new analytic hierarchical model is proposed, which uses the optimal solution between motion variables and risk index of test scenarios instead of subjective evaluation of relative motion variables in test scenario by scenario designer. The performance of AHP and improved AHP models are compared in the cut-in test scenarios example, and the results demonstrate that the proposed risk analysis method can better predict the risk for test scenarios.

## References

- [1] T. L. Saaty, "Axiomatic foundation of the analytic hierarchy process," *Management science*, vol. 32, pp. 841-855, 1986.
- [2] H. Huang, X. Zheng, Y. Yang, J. Liu, W. Liu, and J. Wang, "An integrated architecture for intelligence evaluation of automated vehicles," *Accident Analysis & Prevention*, vol. 145, p. 105681, 2020.
- [3] A. G. Asuero, A. Sayago, and A. Gonzalez, "The correlation coefficient: An overview," *Critical reviews in analytical chemistry*, vol. 36, pp. 41-59, 2006.

# Modeling and Simulation of a High-speed Maglev Vehicle on an Infinite Elastic Guideway

Georg Schneider<sup>1</sup>, Patrick Schmid<sup>1</sup>, Florian Dignath<sup>2</sup>, Peter Eberhard<sup>1</sup>

<sup>1</sup> Institute of Engineering and Computational Mechanics  
University of Stuttgart  
Pfaffenwaldring 9, 70569 Stuttgart, Germany  
[georg.schneider, patrick.schmid, peter.eberhard]@itm.uni-stuttgart.de

<sup>2</sup>thyssenkrupp Transrapid GmbH  
Moosacher Str. 58, 80809 Munich, Germany  
florian.dignath@thyssenkrupp.com

## EXTENDED ABSTRACT

### 1 Introduction

Currently, a new high-speed maglev (magnetic levitation) train with a maximum speed of more than 600 km/h is under development at the Chinese rolling stock manufacturer CRRC Qingdao Sifang Co., Ltd. A prototype of the future vehicle has already been presented to the public. The new high-speed maglev train aims to close the gap between current high-speed railway technology with top speeds of 300 to 350 km/h and aircraft traveling with speeds around 900 km/h. Therefore, the new maglev train offers a notable alternative for short- to medium-haul flights regarding economic and ecologic aspects. For safety and ride comfort aspects, a perfectly rigid guideway would be desirable. However, with increasing stiffness requirements, the production costs for the guideway girders are also increasing. Therefore, a tradeoff is required providing acceptable costs on the one hand and a degree of girder elasticity that can be handled by the control system also at high speeds on the other hand. Simulations and analyses with suitable models taking into account the dynamical behavior of the coupled system of guideway, vehicle, magnet, and controller offer valuable contributions for finding such a tradeoff.

### 2 State of the Art

The dynamic interaction of maglev vehicles and their pillared track is investigated in numerous publications focusing on different aspects. Some focus on the bending of an elastic beam representing the guideway but simplify the vehicle by a point mass or single constant force. Others have a detailed vehicle model, but the guideway is modeled by rigid elements. In [1], these approaches are combined with a rigid multibody vehicle crossing a single elastic guideway element. The simulation results show that for high speeds the elastic deformation of the beam causes a disturbance that influences the vehicle dynamics for several seconds after the vehicle has left the elastic guideway element. Thus, to predict the coupled system dynamics during a ride on a periodically pillared track, a model is required that allows the vehicle to travel a longer distance, including multiple elastic guideway elements. The idea of a guideway of infinite length represented by a finite number of guideway elements is discussed in [2] but not elaborated in detail. Furthermore, a more detailed vehicle model is desirable as, for example, described in [3, 4].

### 3 Simulation Model

In this contribution, the multibody systems approach is used to set up a two-dimensional model of a maglev vehicle moving with constant velocity along an infinite elastic guideway, mapping the heave-pitch motions and vertical guideway bending. Figure 1 shows a visualization of the coupled system. Based on the model from [1], the track model is extended to represent a pillared, elastic guideway of infinite length by applying and implementing the theoretical concept of moving model boundaries described in [2]. To do so, the complete infinite track is represented by a small number of identical single-span Euler-Bernoulli beam elements, which are used repeatedly. Once the vehicle passed an element, this element is taken away from the rear end of the currently considered track segment (behind the vehicle) and added at the front end of the currently considered track segment (in front of the vehicle). So the model boundaries, given by the rear and front end of the currently considered track segment, are shifted along the track together with the moving vehicle. The number of required beam elements depends on the number of elements coupled by the moving vehicle.

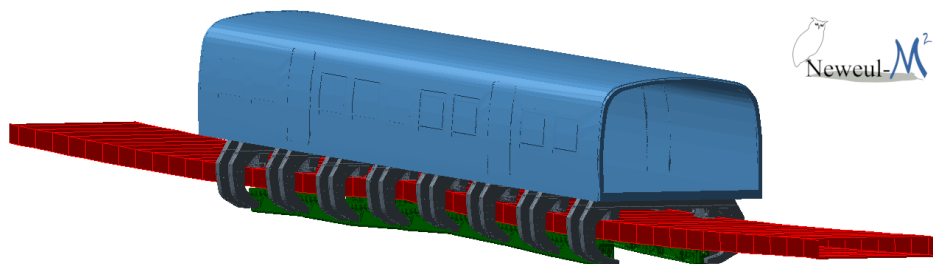


Figure 1: Elastic multibody system with a rigid multibody vehicle traveling on a guideway modeled by an infinite series of periodically repeating flexible beams.

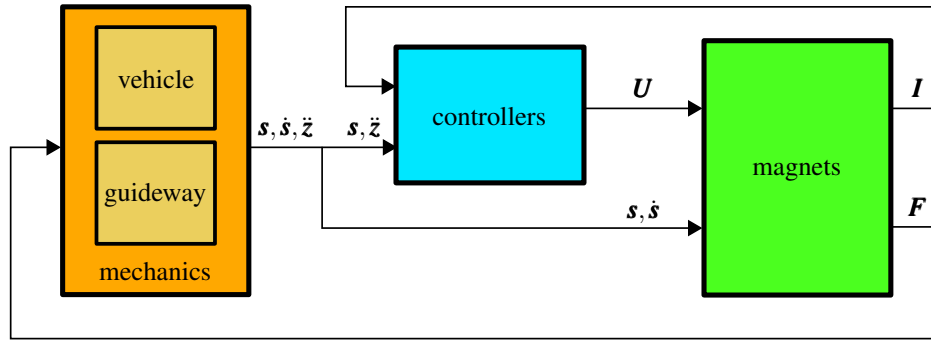


Figure 2: Basic scheme of coupled model in Simulink with vectors of air gaps  $\mathbf{s}$ , air gap velocities  $\dot{\mathbf{s}}$ , magnet accelerations  $\ddot{\mathbf{z}}$ , voltages  $\mathbf{U}$ , currents  $\mathbf{I}$ , and magnet forces  $\mathbf{F}$ .

Regarding the vehicle mechanics, the model used in [1] is replaced by a more detailed one based on the descriptions in [3, 4], representing a section of the maglev vehicle Transrapid. It consists of rigid bodies for the car body, levitation chassis, and levitation magnets. The bodies are coupled by the primary suspension between magnets and levitation chassis and by the secondary suspension between levitation chassis and car body, resulting in more than 20 degrees of freedom.

The mechanical equations of motion for the vehicle and one guideway element are obtained in symbolic form from the Matlab-based multibody simulation toolbox Neweul-M<sup>2</sup> [5]. In Simulink, they are coupled with the electromagnet models from [6], taking into account the effects of magnetic reluctances, fringing and leakage flux, magnetic saturation, and eddy currents, and with the magnet controller presented in [7], representing an offset-free nonlinear model predictive control scheme. Thus, vehicle and guideway are coupled by the electromagnet forces. Figure 2 shows the basic scheme of the coupled components in Simulink. The arrangement of the available beam elements to form the currently considered track segment is also implemented in Simulink.

#### 4 Results

The novelty of this contribution is the infinite elastic guideway formed by a repeating sequence of a few beam elements combined with a detailed model of a Transrapid maglev vehicle. To the best of the authors' knowledge, such a coupled system has not been modeled and investigated yet. With this model, the vehicle moving along the elastic track over a longer distance with different velocities is simulated. Thereby, the interaction of vehicle and guideway is analyzed in a dynamic situation, in which the vehicle dynamics are already affected by the bending of the previously passed guideway elements at the moment when the vehicle enters the next guideway element.

#### References

- [1] G. Schneider, X. Liang, F. Dignath, and P. Eberhard. Simulation of the Maglev Train Transrapid Traveling on a Flexible Guideway Using the Multibody Systems Approach. In A. Kecskeméthy and F. Geu Flores, editors, *Multibody Dynamics 2019. ECCOMAS 2019. Computational Methods in Applied Sciences*, Vol. 53, pp. 503–510, Cham: Springer, 2020.
- [2] K. Popp, W. Schiehlen. *Ground Vehicle Dynamics*. Springer, Berlin/Heidelberg, 2010.
- [3] N. Hägele, F. Dignath. Vertical dynamics of the Maglev vehicle Transrapid. *Multibody System Dynamics*, Vol. 21, No. 3, pp. 213–231, 2009.
- [4] M. Dellnitz, F. Dignath, K. Flaßkamp, M. Hessel-von Molo, M. Krüger, R. Timmermann, Q. Zheng. Modelling and Analysis of the Nonlinear Dynamics of the Transrapid and Its Guideway. In M. Günther et al. (Eds.) *Progress in Industrial Mathematics at ECMI 2010, Mathematics in Industry*, No. 17, pp. 112–123, Springer, Berlin/Heidelberg, 2012.
- [5] T. Kurz, P. Eberhard, C. Henninger, W. Schiehlen. From Neweul to Neweul-M<sup>2</sup>: Symbolical Equations of Motion for Multibody System Analysis and Synthesis. *Multibody System Dynamics*, Vol. 24, No. 1, pp. 25–41, 2010.
- [6] P. Schmid, G. Schneider, F. Dignath, X. Liang, and P. Eberhard. Static and Dynamic Modeling of the Electromagnets of the Maglev Vehicle Transrapid. *IEEE Transactions on Magnetics*, Vol. 57, No. 2, pp. 1–15, 2021.
- [7] P. Schmid, P. Eberhard. Offset-free Nonlinear Model Predictive Control by the Example of Maglev Vehicles. Accepted for publication at the 7th IFAC Conference on Nonlinear Model Predictive Control, Bratislava, July 11-14, 2021.

# Analysis of the Dynamic Behavior of a Counterbalance Forklift Truck Through Multibody Modelling and Simulation

Marco Pinelli<sup>1,2</sup>, Monica Giovannucci<sup>2</sup>, Alberto Martini<sup>3</sup>

<sup>1</sup> School of Engineering  
University of Bologna  
V.le del Risorgimento 2  
40136 Bologna, Italy  
marco.pinelli5@studio.unibo.it

<sup>2</sup> Toyota Material Handling  
Manufacturing Italy SpA  
Via Persicetana Vecchia 10,  
40132 Bologna, Italy  
monica.giovannucci@toyota-industries.eu

<sup>3</sup> DIN – Dept. of Industrial Engineering  
University of Bologna  
V.le del Risorgimento 2,  
40136 Bologna, Italy  
alberto.martini6@unibo.it

## EXTENDED ABSTRACT

Counterbalance forklift trucks (FLT) represent a very common equipment for material handling in industrial applications. Usually, the vertical compliance of their suspension systems is mainly provided by tires, since they are not equipped with elastic elements and/or shock absorbers, with the vehicle being supported at three points (namely, the two front wheels and the pivot of the rear axle, which determine the stability triangle). In addition, solid rubber tires or cushion tires are adopted for most applications. These features cause the behavior of FLT during motion to be significantly affected by ground irregularities, hence safety issues and high dynamic loads possibly being experienced. Accordingly, new FLT prototypes manufactured by Toyota Material Handling Manufacturing Italy S.p.A. (Bologna, Italy), which promoted this research, must be verified with rigorous experimental campaigns to assess the actual vehicle response and measure the dynamic stresses that its main components may undergo during operation. Such tests are costly and time consuming, also because numerous transducers (typically strain gauges rosettes) are needed to monitor complex components properly.

This study aims at developing a multibody model to predict the dynamic loads experienced by a FLT that hits a steel plate obstacle when running in straight line at constant high speed, which is one of the most critical testing conditions in the manufacturer's verification protocols. In particular, the final objective is implementing reliable numerical tools to achieve an accurate estimate of the dynamic stresses acting on the FLT main components (in particular, the chassis), hence possibly reducing the need for experimental tests. To the Authors' best knowledge, most of the studies on FLT dynamics available in the literature dealt with the topic of vehicle stability [1], whereas only few works aimed at developing predictive models to help the structural and durability design of FLT components [2]. The results presented in [3] have been exploited to develop a new model that takes into account the load handling assembly dynamics.

The studied vehicle is an electric FLT characterized by a total mass of about 6 tons and a load capacity of 2.5 tons. The front axle is driven by an electric motor while steering is located in the rear axle. The FLT is equipped with two couples of wheels, with a bigger radius for the front axle tires. The load handling assembly (forks, fork positioner and mast) includes two actuation systems: two hydraulic cylinders (referred to as tilt cylinders) act symmetrically between the chassis and the mast (one on each side) and control the mast tilting angle; one further hydraulic cylinder controls the fork positioner lifting (and the mast extension) through a transmission chain.

Experimental tests were conducted to characterize the behavior of the studied FLT in the condition of interest. The FLT was equipped with six accelerometers and two load cells. Two piezoelectric accelerometers were placed on the left and right sides of the chassis, near the wheel hubs of the front axle, with vertical measuring axis: these accelerations are the reference signals for the comparison with the numerical model. One piezoelectric accelerometer was placed on the rear part of the chassis, laying on the vehicle vertical-longitudinal plane and close to the rear axle pivot, for measuring vertical acceleration as well. One triaxial MEMS accelerometer was placed on the frame under the operator seat, for monitoring the accelerations along the longitudinal, vertical and lateral directions, respectively. Two piezoelectric accelerometers were installed on the left and right sides of the mast, above each tilt cylinder joint. The two load cells were placed in the mast/tilt cylinders connections, replacing the joint pivots and measuring the axial forces exerted by the tilt cylinders (referred to as tilt forces). Signals were acquired with a sampling frequency of 1 kHz. A low-pass filter (cutting frequency 50 Hz) has been applied in the post processing, since no relevant frequency content was observed above 20 Hz. Two loading conditions were tested: the unloaded FLT (referred to as NL condition); the FLT loaded at about 80% of its capacity (WL). Five passages on the obstacle at constant velocity were carried out for each loading condition. The mast was kept tilted by 8° backwards, with the forks close to the ground.

Figure 1 shows the analysis in frequency domain of the acceleration signal acquired from the left-front axle (LFA). A major resonance at about 5 Hz that can be related to the bounce mode of the vehicle (front and rear axle appear in phase by applying a narrow pass band filter to the signals) is observed. The signal appears to be significantly affected also by the dynamics of the mast. Indeed, the other frequencies excited between 8 and 13 Hz are reasonably related to the response of the load handling assembly. Out-of-plane phenomena appear negligible.

A numerical model of the complete FLT (Figure 1) is implemented by using the multibody software RecurDyn (FunctionBay, Seongnam, South Korea). The model accuracy is evaluated in terms of its capability to correctly predict two measured quantities that are deemed essential for assessing properly the FLT dynamics, according to the manufacturer's knowhow: (i) vertical acceleration of the front axle, in terms of amplitude and location of the highest peak (generated by the impact with the obstacle), and of frequency content; (ii) tilt force, in terms of amplitude and location of the highest peaks, and of frequency content. All the FLT parts are modelled as rigid bodies. Their mass properties are assigned based on both CAD geometries and experimental



measurements. Contact ground-to-surface functions between ground and wheels are set. However, the actual tire compliance is modeled by using a nonlinear lumped-stiffness parameter acting between each wheel and the corresponding axle, estimated from the static load-deflection curve provided by the tire manufacturer. The lifting actuator is modeled with as a nonlinear spring that generates a null force when the fork positioner assembly rebounds. The tilt cylinders are modeled with a single linear spring acting on the FLT vertical-longitudinal plane of symmetry: the corresponding stiffness has been estimated with a dedicated test to measure the frequency content of the tilt forces generated by a load rapidly moving downward. The load in the WL condition is a rigid block supported by the forks through contact functions. The static load on the four wheels and the static tilt force computed with the model closely match the measured ones (error below 1.5 %).

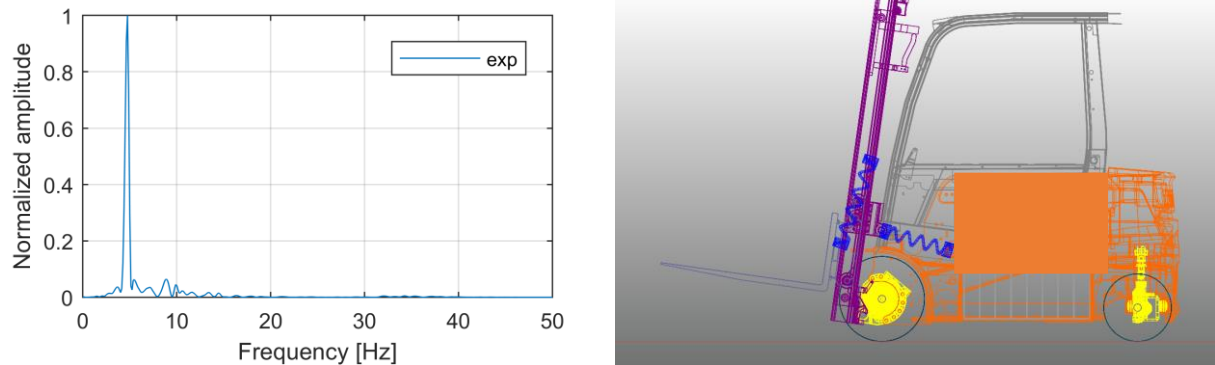


Figure 1: Normalized Power Spectral Density of the LFA acceleration (left) and numerical model (right)

Simulations of the vehicle dynamics are performed by prescribing the motion of the driving wheels, through velocity functions. Figure 2 shows the comparison between the measured data and the numerical results (normalized with respect to the measured maximum value) concerning the NL case, for the LFA acceleration and the tilt force. Both quantities are matched satisfactorily by the current model, in terms of amplitude, main resonance and general damping.

A further model updating is ongoing to improve the accuracy for the WL condition. The focus is on refined models for the compliance of tires and tilt cylinders, as well as for the load/forks interaction. These are deemed as the key aspects to be investigated, since the presence of the load may emphasize nonlinear effects related to them.

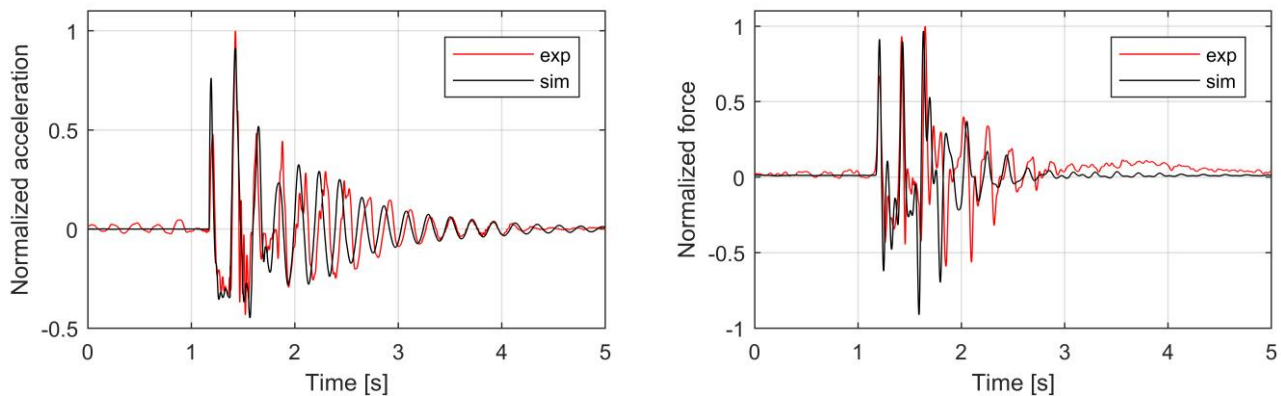


Figure 2: Experimental (exp) vs. numerical (sim) results, NL condition, LFA acceleration (left) and tilt force (right)

## Acknowledgments

EnginSoft (Trento, Italy) is gratefully acknowledged for operative cooperation and support.

## References

- [1] J. Rebelle, P. Mistrot, R. Poirot. Development and validation of a numerical model for predicting forklift truck tip-over. *Vehicle System Dynamics*, 47(7): 771-804, 2009.
- [2] I. Doçi, V. Imeri. Dynamic Analysis of Forklift during Load Lifting using Modeling and Simulations. *International Journal of Current Engineering and Technology*, 3(2):342-347, 2013.
- [3] A. Martini A, G.P. Bonelli, A. Rivola. Virtual Testing of Counterbalance Forklift Trucks: Implementation and Experimental Validation of a Numerical Multibody Model. *Machines*, 8(2):26, 2020.



# Reversing a Truck-Full Trailer Combination in the Presence of Feedback Delay

Levente Mihályi<sup>1</sup>, Illés Vörös<sup>2</sup>, Balázs Várszegi<sup>1</sup>, Dénes Takács<sup>2</sup>

<sup>1</sup> Department of Applied Mechanics  
Budapest University of Technology and Economics  
H-1111 Budapest, Műegyetem rkp. 3, Hungary  
levente.mihalyi10@gmail.com  
varszegi@mm.bme.hu

<sup>2</sup> MTA-BME Research Group on Dynamics of Machines and Vehicles  
H-1111 Budapest, Műegyetem rkp. 3, Hungary  
illes.voros@mm.bme.hu  
takacs@mm.bme.hu

## EXTENDED ABSTRACT

### 1 Introduction

Nowadays, with continuous advances in the development of autonomous vehicles, research in the field of vehicle dynamics has become even more significant. As the level of automation develops, the applied control algorithms, and the increasing computational resources allow the vehicle to operate in such formerly avoided parameter ranges where the nonlinear properties of the vehicle system become relevant, e.g., see [1, 2]. These enhanced motion control systems allow also the realization of complex path-following tasks that could not be or could hardly be done by human drivers [3]. Reversing a truck with one or more trailers is one such challenge.

In this paper, the straight-line reverse motion is investigated in case of a truck-full trailer combination. This vehicle system contains two articulated joints, which makes the control of the reversing to be a complicated task for human drivers. The kinematic model of the vehicle is presented and a linear feedback controller is designed taking into account the feedback delay in the control loop.

### 2 Mechanical model

The single track kinematic model of the truck-full trailer combination is presented in Fig. 1. The vehicle system is modeled by the three rods, which are denoted by the encircled numbers in the figure: 1 represents the truck; 2 is the drawbar that creates the coupling between the truck and the trailer; and 3 denotes the trailer. At points F, R, T<sub>2</sub> and T<sub>3</sub>, rigid wheels are considered, i.e. the side slip of the tires is neglected and the rolling direction of the wheels are described by four kinematic constraints. The longitudinal speed of the towing vehicle is set to be equal to the constant value  $V$ .

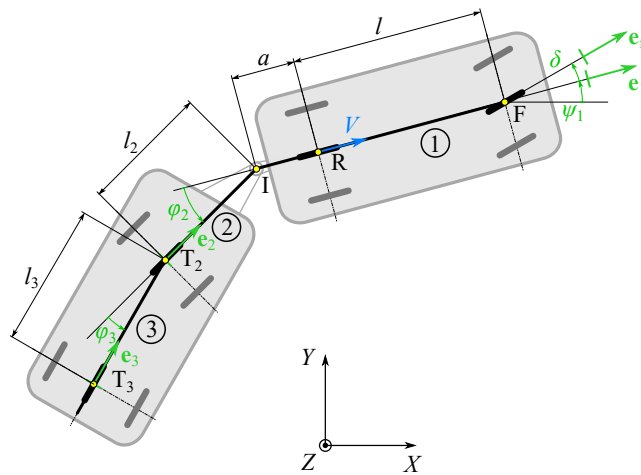


Figure 1: Mechanical model of the truck-full trailer combination

The motion of the system is described by five generalized coordinates:  $X_R, Y_R$  are the coordinates of the rear axle center point R;  $\psi_1$  is the yaw angle of the towing vehicle;  $\phi_2$  and  $\phi_3$  denote the relative yaw angles of the drawbar and the trailer, respectively;  $\delta$  is the steering angle of the front wheel of the towing vehicle.

Considering all the kinematic constraints and the dynamics of the steering mechanism, the equations of motion of the system can be obtained as

$$\begin{aligned} \dot{X} &= V \cos \psi_1, \quad \dot{Y} = V \sin \psi_1, \quad \dot{\psi}_1 = \frac{V}{l} \tan \delta, \quad \dot{\phi}_2 = -\frac{V}{l \cdot l_2} (l \sin \phi_2 + (l_2 + a \cos \phi_2) \tan \delta), \\ \dot{\phi}_3 &= -\frac{1}{l_3} (V \sin(\phi_2 + \phi_3) + a \psi_1 \cos(\phi_2 + \phi_3) + l_2(\psi_1 + \phi_2) \cos \phi_2) - (\psi_1 + \phi_2), \quad \dot{\delta} = \omega, \quad \dot{\omega} = \frac{T}{J}, \end{aligned} \quad (1)$$

where  $J$  is the mass moment of inertia of the steering system and  $T(t) = -k_p(\delta(t) - \delta_{\text{des}}(t)) - k_d\dot{\delta}(t)$  refers to the steering torque that realizes the desired steering angle  $\delta_{\text{des}}$ . In this study, the desired steering angle is calculated based on the linear feedback that maintains the straight-line reverse motion ( $V < 0$ ) of the vehicle system along the  $X$ -axis:

$$\delta_{\text{des}}(t) = -P_Y Y(t - \tau) - P_{\psi_1} \psi_1(t - \tau) - P_{\varphi_3} \varphi_3(t - \tau), \quad (2)$$

where  $\tau$  is the feedback delay,  $P_Y$ ,  $P_{\psi_1}$  and  $P_{\varphi_3}$  are the control gains.

### 3 Control

The equations of motion linearized around the straight-line reverse motion can be given via the state-space representation  $\dot{\mathbf{x}}(t) = \mathbf{A}\mathbf{x}(t) + \mathbf{B}\mathbf{u}(t - \tau)$  with  $\mathbf{u}(t) = \mathbf{K}\mathbf{x}(t)$ . One can prove that the control law (2) maintains the controllability and the observability of the system. Based on the characteristic equation, the linear stability of the closed-loop system can be analyzed using the D-subdivision method [4]. A stability chart is shown in Fig. 2, where the gain of the lateral position is fixed at  $P_Y = 2 \text{ rad/m}$ , and the stable parameter regions of the other two control gains are depicted for different feedback delays. Different shades of blue denote the linearly stable region of control gains for various amounts of time delay. As shown, even if the feedback delay is relatively large, the straight-line reverse motion can still be stabilized.

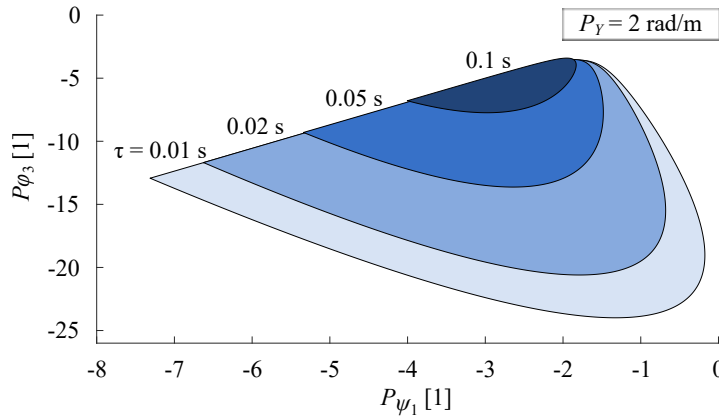


Figure 2: Stability chart in the plane of control gains  $P_{\psi_1}$  and  $P_{\varphi_3}$  for different amounts of time delay for different time delays. Parameter values:  $V = -0.3 \text{ m/s}$ ,  $l = 0.24 \text{ m}$ ,  $a = 0.05 \text{ m}$ ,  $l_2 = 0.2 \text{ m}$ ,  $l_3 = 0.25 \text{ m}$ ,  $J = 10^{-6} \text{ kgm}^2$ ,  $k_p = 3 \cdot 10^{-4} \text{ Nm}$ ,  $k_d = 1.7321 \cdot 10^{-5} \text{ kgm}^2/\text{s}$

### 4 Conclusion

A linear feedback controller is designed to stabilize the straight-line reverse motion of a truck-full trailer system. It is shown that utilizing the lateral position, the yaw angle of the towing vehicle and the relative angle of the trailer and the drawbar ensures the linear stability of the system even in the presence of time delay. In our study, we also validate our results via numerical simulations and laboratory experiments, moreover, we realize the general path-following of the vehicle system in reverse motion.

### Acknowledgments

The research reported in this paper has been supported by the National Research, Development and Innovation Office under grant no. NKFI-128422.

### References

- [1] Della Rossa, F., Mastinu, G. and Piccardi, C., "Bifurcation analysis of an automobile model negotiating a curve", *Vehicle System Dynamics* 50, 1539–1562 (2012)
- [2] Goh, J. Y., Goel, T. and Christian Gerdes, J. (November 21, 2019). "Toward Automated Vehicle Control Beyond the Stability Limits: Drifting Along a General Path.", *ASME. J. Dyn. Sys., Meas., Control*. February 2020; 142(2): 021004. <https://doi.org/10.1115/1.4045320>
- [3] D. Tilbury, R. M. Murray and S. Shankar Sastry, "Trajectory generation for the N-trailer problem using Goursat normal form" in *IEEE Transactions on Automatic Control*, vol. 40, no. 5, pp. 802-819, May 1995, doi: 10.1109/9.384215.
- [4] Insperger T., Stépán G. "Semi-discretization for time-delay systems: stability and engineering applications", Springer, New York, USA, 2011. <https://doi.org/10.1007/978-1-4614-0335-7>

# Flexible Multibody Dynamic Analysis for a 23-g Flapping Wing Micro Aerial Vehicle

JaeWon Choi<sup>1</sup>, DuHyun Gong<sup>1</sup>, Byeong-Uk Im<sup>1</sup>, SangJoon Shin<sup>2</sup>

<sup>1</sup>Department of Aerospace  
Engineering  
Seoul National University  
Seoul, 08826, Republic of Korea  
[yewowon, zpslem, goody147]@snu.ac.kr

<sup>4</sup> Institute of Advanced Aerospace  
Technology  
Seoul National University  
Seoul, 08826, Republic of Korea  
ssjoon@snu.ac.kr

## EXTENDED ABSTRACT

### 1 Introduction

An insect-type flapping wing micro aerial vehicle (FWMAV) has a unique flight mechanism for maneuver. First, it uses two flexible wings to generate the aerodynamic forces. The flexibility of the wings should be considered because it affects the performance, such as thrust and power. Second, there are no control surfaces and tail wings. Thus, additional device should be utilized for producing the control forces for maneuver and stability.

In this abstract, 23-g insect-type FWMAV is to be simulated by finite element (FE)-based multibody dynamics. In order to consider its flexibility, the geometrically exact beam (GEB) element [1, 2] will be adopted. Also, the variational asymptotic methods-based analysis is conducted for the cross-sectional properties of the corresponding beam [3, 4]. The additional devices are modeled by simplifying the detailed configuration and by implementing the operation principle. The aerodynamic coefficients such as lift and drag are estimated by a prediction model [5] and Peters' two-dimensional unsteady aerodynamics [6, 7]. To reflect the environment of thrust experiment, where FWMAV is connected to a load cell, fixed boundary conditions are imposed for the simulation.

### 2 Present insect-type FWMAV

The present 23-g insect-type FWMAV is capable of generating the aerodynamic forces by its two flexible wings during the flapping motion with an amplitude of  $\pm 80^\circ$ . Also, a trailing edge control (TEC) device is embedded for control forces. TEC device consists of three rotary actuators and several joints. The roots of the main wings are connected to the joints through a linkage. Regarding its operation, receiving the control signal, the torque of the actuator is transmitted to the linkage and twists both wings. In such manner, the twist angle of the both wings will vary during the flapping motion and generates an asymmetrical aerodynamic force, which results in control force. Specifications of the present FWMAV are described in Table 1.

Table 1: Specifications of the present FWMAV

<i>Classification</i>	<i>Value</i>	<i>Classification</i>	<i>Value</i>
Total weight	23 [g]	Control method	Trailing edge control
Wing span	125 [mm]	Flapping amplitude	$\pm 80$ [ $^\circ$ ]
Aspect ratio	4.12	Linkage operation angle	$\pm 9$ [ $^\circ$ ]

### 3 Simulation methodology

In order to simulate the present FWMAV, FE-based multibody dynamic analysis, DYMORE [1, 2], will be adopted. The schematic diagram of the fluid-structure interaction (FSI) analysis is shown in Figure 1. Starting with the prescribed motions as initial condition, displacements and velocities at the current time step are obtained. Then the aerodynamic loads will be estimated by reflecting the updated displacement and velocity of the wing. As a result, the estimated aerodynamic forces will become a revised input to the structural analysis at next time step.

The structural model is divided into flexible multibody dynamics and rigid body motion. To consider the nonlinear flexible behaviors of the main wings, GEB elements are employed along with the cross-sectional properties obtained by the commercial software VABS [3, 4]. Each wing is discretized into 125 spanwise stations. The connectivity between the wing and the fuselage consists of four kinematic constraints under the relative rotating motion [8]. To represent TEC modeling, rigid body elements are employed for linkages and connected to the fuselage by three individual revolute joints to implement pitching, rolling, and yawing motion.

The aerodynamic model in the present framework provides the steady and unsteady aerodynamic loads as shown in Figure 1. The air station is located at 25% chord length and discretized into 125 ones in the spanwise direction. To obtain the steady aerodynamic load, the lift and drag coefficients are obtained by reference to Taha et al. [5]. Also, the unsteady aerodynamic load is estimated by using Peters' unsteady aerodynamic model [6, 7].

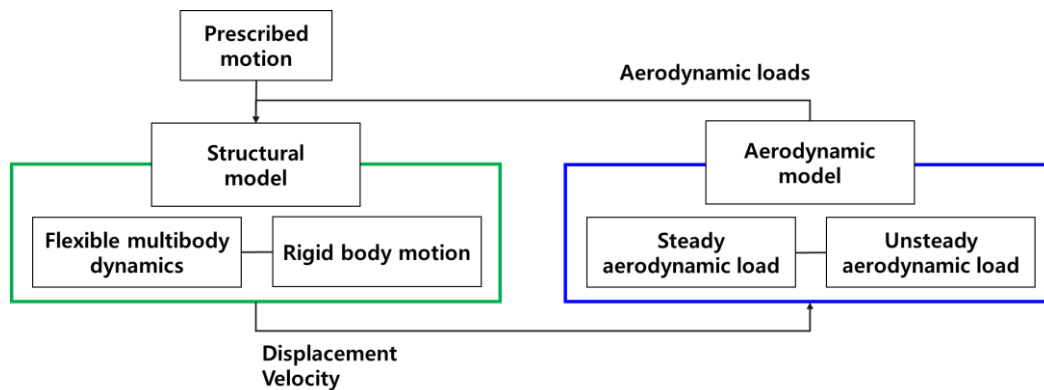


Figure 1: Schematic diagram of the FSI framework

#### 4 Results and conclusion

The present analysis is validated against the thrust measurement experiment. For comparison, the numerical simulation is performed at a flapping frequency of 12 Hz. The average thrust of the numerical simulation is estimated 17.4gf, which shows good agreements with the experimental result of 17.8gf. On the other hands, the adequacy of the control mechanism is evaluated. The estimated control forces show an increasing tendency in terms of the control inputs within the linkage operation angle of  $\pm 9^\circ$ . Therefore, it is concluded that the present control device is capable of generating adequate control forces during the flight.

In the future, the present numerical framework will be applied to obtain the non-dimensional aerodynamic derivatives to design of a proportion - integration - derivation (PID) controller. Then, the numerical simulation regarding the attitude adjustment will be conducted by the present numerical framework.

#### Acknowledgments

This research was supported by a grant to Bio-Mimetic Robot Research Center Funded by Defense Acquisition Program Administration, and by Agency for Defense Development (UD190018ID).

#### References

- [1] O. A. Bauchau. DYMORE User's Manual. December, 2006.
- [2] C. E. S Cesnik, and D. H. Hodges. VABS: A New Concept for Composite Rotor Blade Cross-Sectional Modeling. Journal of the American Helicopter Society, 42:27-38, 1997.
- [3] W. Yu, and D. H. Hodges. Generalized Timoshenko Theory of the Variational Asymptotic Beam Sectional Analysis. Journal of the American Helicopter Society, 50:46-55, 2005.
- [4] W. Yu, and D. H. Hodges. Generalized Timoshenko Theory of the Variational Asymptotic Beam Sectional Analysis. Journal of the American Helicopter Society, 50:46-55, 2005.
- [5] H. E. Taha, M. R. Hajj, and P. S. Beran. State-space representation of the unsteady aerodynamics of flapping flight. Aerospace Science and Technology, 34:1-11, 2014.
- [6] D. A. Peter, M. A Hsieh, and A. Torrero. A State-Space Airloads Theory for Flexible Airfoils. Journal of the American Helicopter Society, 52:329-342, 2007.
- [7] D. A. Peter. Two-dimensional incompressible unsteady airfoil theory—An overview. Journal of Fluids and Structures, 24:295-312, 2008.
- [8] O. A. Bauchau, and J. Rodriguez. Modeling of Joints with Clearance in Flexible Multibody Systems. International Journal of Solids and Structures, 39:41-63, 2002.

# Numerical Analysis of the Linearization of the Railway Multibody Equations of Motion with Moving Reference Frames

Javier F. Aceituno<sup>1</sup>, José L. Escalona<sup>2</sup>

<sup>1</sup>Mechanical and Mining Engineering Department  
University of Jaén  
Avda. de la Universidad s/n, Edificio Departamental  
D-044, 23700, Linares, Jaén, Spain.  
jaceitun@ujaen.es

<sup>2</sup>Mechanical and Manufacturing Engineering Department  
University of Seville  
Camino de los Descubrimientos s/n,  
41092, Sevilla, Spain.  
escalona@us.es

## EXTENDED ABSTRACT

### 1 Introduction

This work presents a multibody formulation for railway vehicles that applies linearization at vehicle kinematics and equations of motion. The proposed formulation is greatly linearized because it adopts multiple moving reference frames and relative body-track frame coordinates as shown in Fig. 1, against other formulations that employ relative-track frame coordinates [1] or absolute coordinates [2]. This is, each vehicle body has its own track frame that follows the vehicle movement keeping its longitudinal x-axis tangent to the trajectory followed.

In this context, one of the main advantages of relative body-track frame coordinates is that vehicle-bodies and vehicle to track interactions depend on their relative position with respect to the track, which in most scenarios result in relative-small generalized coordinates. For this reason, the kinematic and dynamic linearization can be applied with little loss of accuracy and important gained in computational efficiency. However, it has an important drawback that is the need of curvilinear coordinates for the description of the each moving frame.

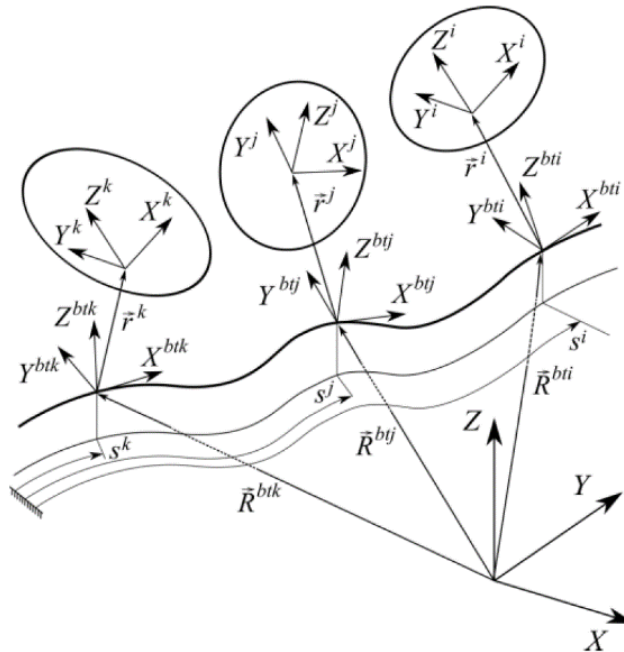


Figure 1: Kinematics of the bodies of a railway vehicle with relative body-track frame coordinates

### 2 Method description

The proposed formulation presented in this work describes the vehicle as a set of open-chain mechanisms (see Fig. 2) and applies linearization at those rotational matrices when the relative-small angle assumption can be adopted between bodies that comprise the same chain and between different chains.

In addition, using symbolic computation to formulate the equations of motion, the velocity transformation matrices used to account for the generalized mass matrices and forces are also linearized taking advantage of the use of relative body-track frame coordinates.

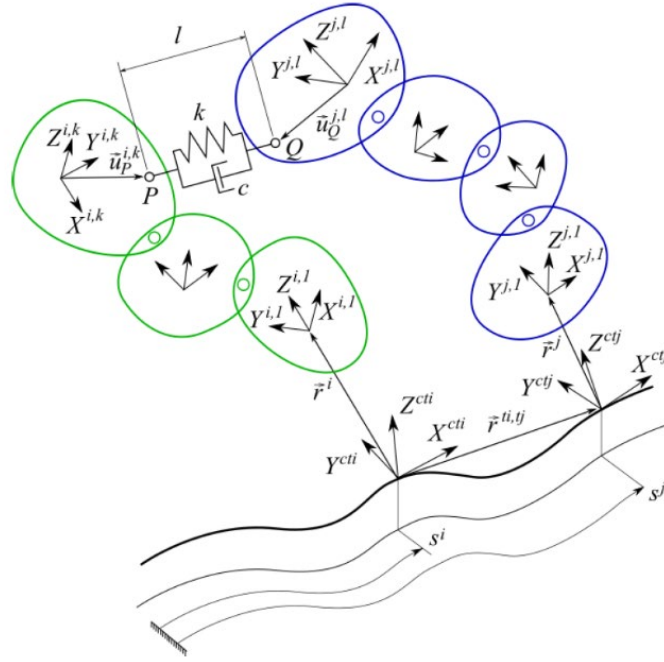


Figure 1: The railroad vehicle as a set of open-chain mechanisms

### 3 Numerical results

Numerical results of a railway vehicle with the proposed formulation are compared to those obtained using a non-linearized formulation in terms of accuracy and computational efficiency during a 1-km track length case study. In both simulations, relative body track frame coordinates and reference frames remain the same. Also, track geometry, suspension forces and wheel-rail contact forces, which for this work the simplified wheel-rail KEC-method [3] is used (2-dimensional wheel-rail constraint Knife-edge Equivalent Contact method), remain the same to emphasize the role of the proposed linearization.

### Acknowledgments

This work is supported by the Andalusian Regional Government, in Spain, under the PAIDI 2020 program with project reference P18-RT-1772. This support is gratefully acknowledged.

### References

- [1] Escalona, J. L., & Aceituno, J. F. (2019). Multibody simulation of railway vehicles with contact lookup tables. *International Journal of Mechanical Sciences*, 155, 571-582.
- [2] Shabana, A. A., Zaazaa, K. E., & Sugiyama, H. (2007). *Railroad vehicle dynamics: a computational approach*. CRC press.
- [3] Escalona, J. L., Aceituno, J. F., Urda, P., & Balling, O. (2020). Railway multibody simulation with the knife-edge-equivalent wheel-rail constraint equations. *Multibody System Dynamics*, 48(4), 373-402.

# Influence of the Friction Model on the Dynamics of Railway Freight Vehicles

Pedro Millan, João Pagaimo, Jorge Ambrósio<sup>1</sup>, Hugo Magalhães, Pedro Antunes<sup>1,2</sup>

<sup>1</sup>IDMEC, Instituto Superior Técnico  
University of Lisbon  
Address, 1044-001 Lisbon, Portugal  
{pedro.millan, joao.pagaimo,  
jorge.ambrosio}@tecnico.ulisboa.pt

<sup>2</sup>Institute of Railway Research  
University of Huddersfield  
Address, HD1 3DH Huddersfield, UK  
{h.magalhaes, p.antunes}@hud.ac.uk

## EXTENDED ABSTRACT

### 1 Introduction

One of the mechanical characteristics of the general railway freight vehicles is their friction damped suspensions, which are not only a cheaper construction but also sturdy and with reduced maintenance costs. The multibody modelling of this type of vehicles requires features that are seldom available in commercial multibody codes but which are well matured in different multibody dynamics approaches. In all these vehicles the existence of clearances between the mechanical components of the suspension elements is required not only to ensure a construction with economical tolerances and adjustments but also to provide the friction characteristics required for the damping of the suspensions. The need to consider the clearance joints in the vehicle model also requires the use of suitable normal contact force and friction models to allow for a realistic representation of the relative kinematics between the mechanical elements. In this work the clearance joint models proposed by Ambrosio et al. [1] are used to represent the relevant mechanical joints of the freight vehicle elements. In the process of using this methodology, the study of impact of different friction models, as those reviewed by Marques et al. [2] on the system performance is carried. The methodologies suggested in this work are applied to the study of the dynamics of a freight train composed by a locomotive and two wagons.

### 2 Methods

General railway vehicles are commonly modelled by using perfect kinematic joints and specialized force elements to represent the kinematic restrictions between mechanical elements. The unified clearance joint formulations, proposed by Ambrosio et al. [1] are used in this work to represent most of the clearance joints in the vehicles suspension systems depicted in Fig. 2. The modified Kelvin-Voight normal contact force model [1,3] is used to represent the normal contact forces for all clearance joints. The friction in the clearance joints, or in the contact elements of the vehicle suspensions, plays a critical role in the vehicle dynamics. Among the different friction force models explored by Marques et al. [2] in their work the Amontons-Coulomb model with Threfal smoothing, representing the simplest static friction model, the Akay and Bengisu model, which already includes some representation of stiction, and the Gonthier friction model, which is a dynamic friction model based on the concept of bristle deformations, are tested here. The application to the dynamics of a freight train, shown in Fig. 1, allows to understand the importance not only of considering models that are able to represent the importance of static and dynamic friction coefficients, Stribeck velocity or local deformations on the vehicle dynamics

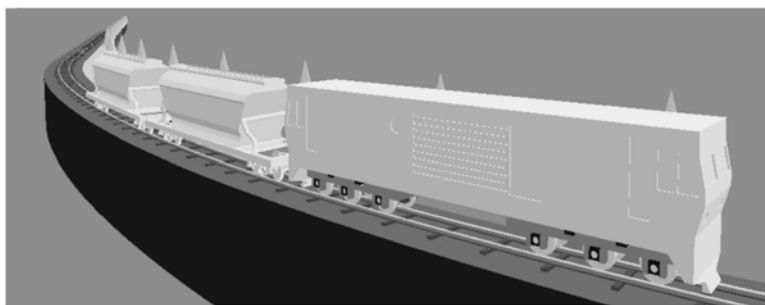


Figure 1: Simulation scenario of a freight train made of a locomotive and two wagons.

### 3 Models and Results

The models of a diesel freight locomotive with friction damping and of a wagon are developed, leading to the models outlined in Fig.2. Particular relevance is given to the modelling of the mechanical elements responsible for the friction damping of the suspensions, labeled in Fig. 2 as friction surfaces. The freight train, composed of a locomotive and two wagons is studied in a realistic scenario in which they are operated in a mountainous track with metric gauge. Preliminary results show rather small variation on the vehicle dynamic response as a function of the suspension friction characteristics. It is observed that larger differences in the dynamic response occur due to the stick-slip transition in the contact elements of particular components in the transition between track segments with constant radius and transition curves. Moreover, it is observed that the efficiency of the computational simulations depends greatly on the transition velocity, or Stribeck velocity, used in each of the friction models.



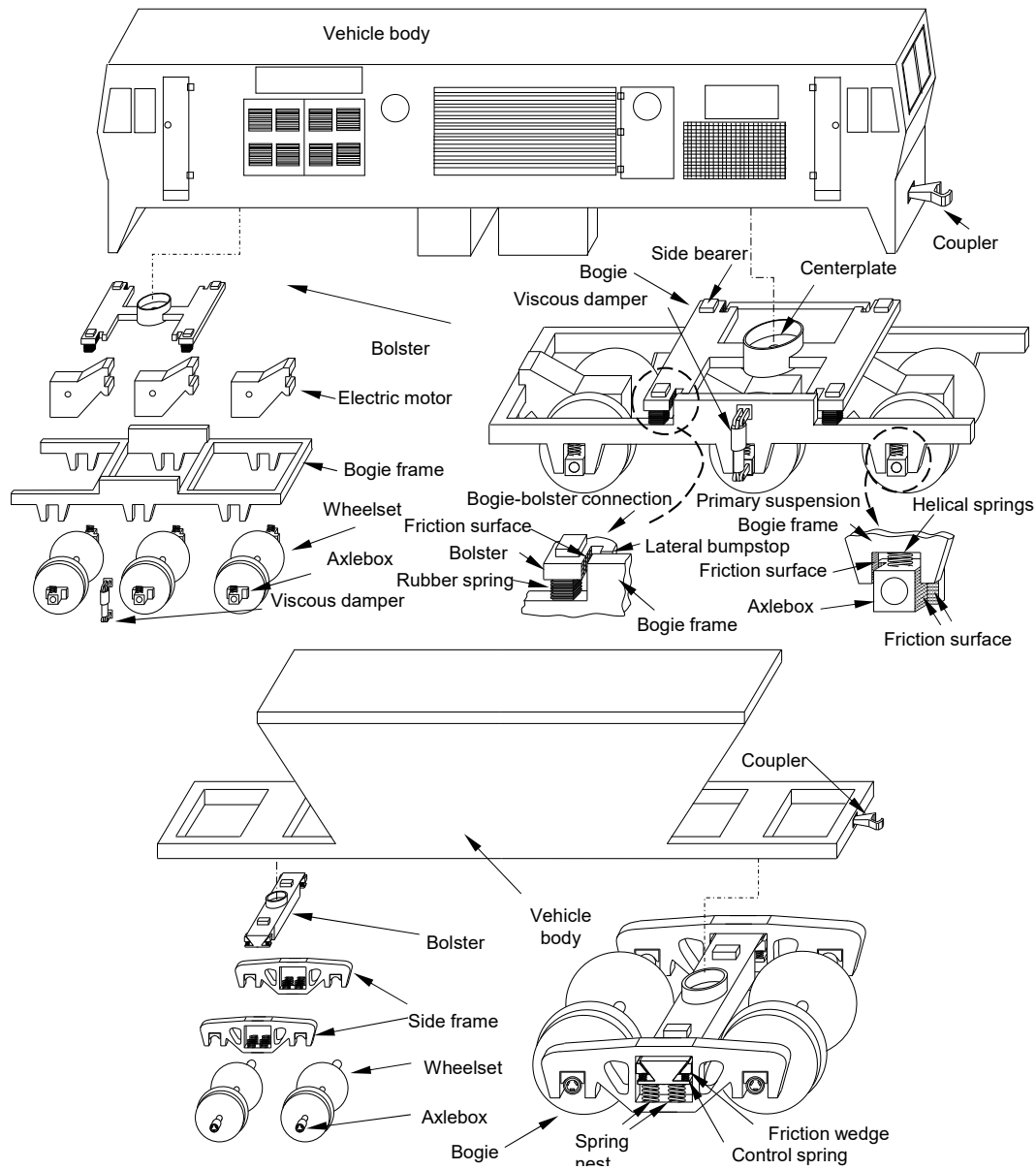


Figure 1: Exploded views of a railway locomotive and freight vehicle highlighting the friction elements used for the suspension friction damping

#### 4 Preliminary Conclusions

The modelling features provided by the clearance joints are instrumental for the realistic modelling of freight railway vehicles, in which the friction damping of the suspensions plays a major role in their dynamics. It is observed that different friction models play a role in the vehicle dynamics in particular conditions. It is expected that, when operating in tracks with irregularities, the importance of representing the stick-slip transition in the contacting elements is reduced..

#### Acknowledgments

The work reported in this paper has a fundamental input from the Shift2Rail JU under the project LOCATE (Locomotive bOgie Condition mAinTenance) with the grant n°881805. This work was supported by FCT, through IDMEC, under LAETA project number UIDB/50022/2020.

#### References

- [1] Ambrósio J, Pombo J. A unified formulation for mechanical joints with and without clearances/bushings and/or stops in the framework of multibody systems. *Multibody Syst Dyn.* 2018;42:317–345.
- [2] Marques F, Flores P, Pimenta Claro JC, et al. A survey and comparison of several friction force models for dynamic analysis of multibody mechanical systems. *Nonlinear Dyn.* 2016;86:1407–1443.
- [3] Flores P, Ambrósio JAC, Claro J. P, et al. *Kinematics and Dynamics of Multibody Systems with Imperfect Joints.* Springer, Dordrecht, The Netherlands, 2008.

# Multi-Stage MBS and FE Simulation Strategy to Design a Safe Motorcycle

Steffen Maier<sup>1</sup>, Jörg Fehr<sup>1</sup>

<sup>1</sup> Institute of Engineering and Computational Mechanics  
University of Stuttgart  
Pfaffenwaldring 9, 70569 Stuttgart, Germany  
[joerg.fehr, steffen.maier]@itm.uni-stuttgart.de

## EXTENDED ABSTRACT

Motorcycle accidents are inherently chaotic and often have serious or fatal consequences for the riders involved. The complex nature of these accidents hinders the development of effective protection mechanisms for the riders as well as the repeatable investigation of the coherence of a motorcycle and a motorcyclist's equipment design with accident consequences. Common strategies used in the vehicle development process of passenger cars for occupant protection break down the accident event into several individual problems. Thus, in experiments and simulations, the interaction of the vehicle with the accident opponent and the behavior of the occupants within the vehicle interior are often considered separately. Full-vehicle laboratory crash tests or simulations of new products are rarely carried out during the design process but rather at the very end of the development to ultimately prove the occupant protection for vehicle approval or to evaluate occupant safety for consumer ratings. Such a breakdown is usually not possible when investigating accidents involving current conventional motorcycles, e.g., in collisions with passenger cars. Here, the passenger interacts with the motorcycle and the opponent, as well as the road and road-side structures. A safety concept that restrains a motorcyclist to a motorcycle and protects the rider from the accident environment therefore not only has the advantage of potentially improving passive safety, which must be proven, but by separating the occupant from the accident environment this enables more systematic investigation methods. Such an investigation strategy, based on multi-stage multibody systems (MBS) and finite element (FE) methods, will be explained and demonstrated in this work using a concept of a novel passive safety system for motorcycles.

The novel safety concept, shown in Figure 1, consists of a newly designed motorcycle body, seat belts, multiple surrounding airbags, foam leg impact protectors and side impact structure. The concept envisages that in the event of an accident, the rider is restraint to the motorcycle by two thigh belts. This causes the rider's upper body to rotate around the belt restraint. The surrounding airbags then decelerate the upper body rotation in a controlled manner and protect the rider from hard contacts with accident opponent, the road, and road-side structures. The foam leg impact protectors absorb the impact of the legs on the motorcycle cockpit and the side impact structure protects the lower extremities laterally. For the design of the involved safety systems and the investigation of their protective performance in representative accident scenarios, simulation driven design methods are needed as an alternative to costly experimental methods. To be able to try many different solutions efficiently, models with varying levels of complexity and computing effort and that capture different aspects of accident are necessary.

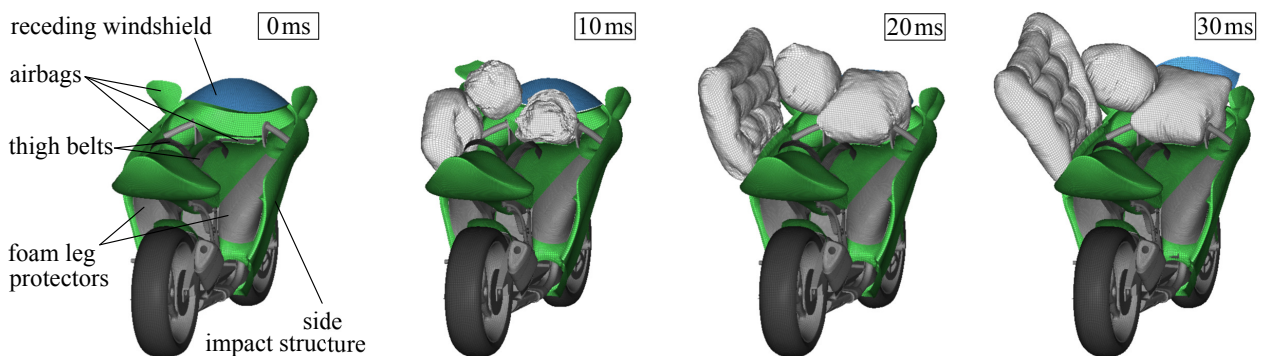


Figure 1: Safety systems of the novel safety concept for motorcycles. A video of the safety concept is shown in [1].

This work outlines the procedure of a virtual simulation-based product design consisting of three successive development stages with a continuously increasing level of detail and expected fidelity shown in Figure 2. In the first stage of the simulation strategy the motorcycle, the airbags, the belts, and a rider surrogate are modelled in a combined MB and FE approach in the MADYMO software environment [2]. The MB motorcycle model replicates (i) rotating wheels, (ii) front and rear suspension, (iii) front fork steering and (iv) front fork impact deformation with coupling and contact characteristics based on fitted simulation models of full-scale crash tests of conventional motorcycles [3]. In the second stage, the motorcycle cockpit is modelled further detailed in the FE LS-Dyna software environment with now also deformable cockpit surfaces that include the foam impact protectors [4]. To replicate the crash dynamics, the multi-axial rigid body motions of the MB simulations are applied as prescribed motions for the motorcycle and car's outer bodies where the car's body geometry acts solely as reaction surfaces for the airbags. The third

stage is a full FE representation of the motorcycle, the already tuned passive safety systems, a rider surrogate, and an accident opponent in LS-Dyna. The motorcycle's structurally relevant components that determine the crash behaviour are deformable. The front and rear suspension, rotating wheels and front fork steering are modelled with joints.

**Stage 1:** Motorcycle interaction with accident opponent and dummy response with MB models | **Stage 2:** Detailing the driver interaction with motorcycle components in FE environment | **Stage 3:** Full FE representation of motorcycle, dummy and accident opponent

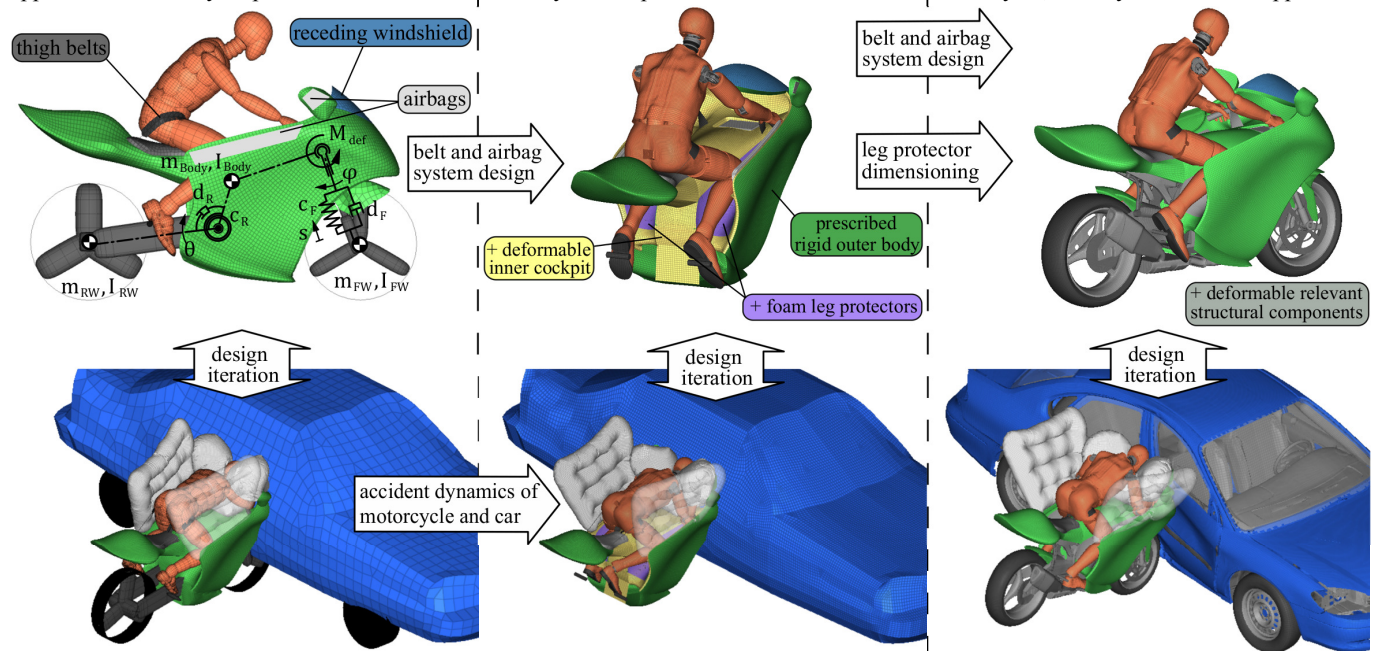


Figure 2: Numerical research strategy

The first stage MB approach features low complexity and low numerical costs while capturing the essential physics of the collision. This represents a numerically efficient way to tune and improve the safety system, i.e., adapting the properties, shapes and locations of the safety components. The third stage full FE approach aims to fully represent the interaction of the collision to accurately predict the performance of the finalized design by replicating every structural component of the vehicles in great detail. However, this is bought by a challenging model generation and significantly increased computational efforts. The advantages of the second stage partial FE approach using MB-vehicle interaction of the numerical strategy presented here are the successive methodological model generation and gradually increased level of detail and expected fidelity while significantly reducing computation time compared to a full FE model representation. Among others, this offers the possibility to consider a larger variance of accident scenarios or occupant diversity or to enable very complex and numerically expensive investigations with FE human body models.

The shown numerical research strategy outlines a novel procedure in virtual motorcycle accident research and passive safety equipment development that is very similar to common strategies in the development process of passenger cars for occupant protection. It shows clear advantages regarding a systematic model generation approach and step-by-step validation of individual components with reduced computational effort and model complexity. The strategy enabled the virtual design and dimensioning of a novel safety system with little time and resources. Although the procedure is presently applied only under the conditions of a novel safety system for motorcycles, the application of similar procedures in virtual research for conventional two-wheelers are highly desirable.

## References

- [1] S. Maier: Sicheres Motorrad - Ein Projekt des Technologietransferprogramms. <https://www.youtube.com/watch?v=4NAfxN19fE4>, 2020 (in German).
- [2] S. Maier, L. Doléac, H. Hertneck, S. Stahlschmid, J. Fehr. Evaluation of a Novel Passive Safety Concept for Motorcycles with Combined Multi-Body and Finite Element Simulations. Proceedings of IRCOBI Conference, IRC-20-38, pages 250-265. Munich, Germany, 2020.
- [3] A. Berg, P. Rücker, H. Bürkle, R. Mattern, D. Kallieris. Prüfverfahren für die passive Sicherheit motorisierter Zweiräder. Berichte der Bundesanstalt für Straßenwesen, Tech. Rep. 49, Bergisch Gladbach, Germany, 2011.
- [4] S. Maier, L. Doléac, H. Hertneck, S. Stahlschmid, J. Fehr. Finite Element Simulations of Motorcyclist Interaction with a Novel Passive Safety Concept for Motorcycles. Proceedings of IRCOBI Conference, online, 2021.

# Optimization of Flapping Wing Dynamics for Martian Atmosphere via DMOC Approach

Zdravko Terze, Viktor Pandža, Marko Kasalo, Dario Zlatar

<sup>1</sup>Faculty of Mechanical Engineering and Naval Architecture  
University of Zagreb

Ivana Lučića 5, 10000 Zagreb, Croatia

[zdravko.terze, viktor.pandza, marko.kasalo, dario.zlatar]@fsb.hr

## EXTENDED ABSTRACT

### 1 Introduction

NASA's Ingenuity Mars Helicopter has recently performed the first powered controlled flight on another planet. However, in spite of success of this mission, rotary wing solution might not be the optimal technology for flying in thin Martian atmosphere. The low density of the atmosphere (only 1% of the Earth's) forces the aircraft to fly at low Re numbers, which significantly deteriorates the performance of a rotary wing [1]. On the other hand, insects fly very efficiently at the same Reynolds numbers, with great aerial capabilities, which makes the insect-type aircraft a promising concept for Mars exploration [2]. To this end, the novel optimization algorithm for development of insect-type aerial vehicle, capable of flight in Martian atmosphere, is proposed.

### 2 Method

The novel optimization algorithm combines Discrete Mechanics and Optimal Control (DMOC) approach with quasi-steady aerodynamical model [3]. The basic assumption of the quasi-steady aerodynamic model is that the aerodynamic forces are inherently time independent which means that the aerodynamic forces directly depend only on kinematic variables [4]. This simplification, combined with adequate experimental data, results in the aerodynamical model with a good ratio of accuracy and computational efficiency. The utilized quasi-steady model encompasses three main aerodynamic phenomena, namely, lift enhancement due to stable leading edge vortex during stroking motion, lift enhancement due to rapid pitching rotation at the end of the stroking motion, and added mass effect. On the other hand, DMOC is a direct transcription method, for optimal control problems in mechanics, in which discretization of the Lagrange-d'Alembert principle results in the time stepping equations that are implemented as equality constraints in the constrained nonlinear optimization problem [5]. This leads to the "natural" discrete description of the inherently continuous problem, which means that the domain of the objective function is not constrained with some predefined set of parametric functions. This approach is not constrained by the user input and can yield any solution that respects the physical laws, in other words, optimal solution can be obtained without an excellent initial guess.

The flapping-wing vehicle is modeled as a system of three rigid bodies based on the morphological characteristics of the fruit fly (lat. *Drosophila melanogaster*). In order to achieve sufficient lift force wings are uniformly scaled with various scaling numbers. Furthermore, wings have two rotational degrees of freedom, one for stroking and one for pitching motion. Both motions are discretized with 100 points, which means that the optimization problem has 200 variables. The goal of optimization is to minimize energy consumption, that is, to find the most efficient flapping pattern for hovering in the Martian atmosphere.

The *discrete constrained nonlinear optimal control problem* is stated in the following form:

$$\min_{u_d} J_d(q_d, u_d), \quad (1a)$$

$$s. t. \quad p_k + D_1 L_d(q_k, q_{k+1}) + f_d^-(q_k, q_{k+1}, u_k) = 0, \quad (1b)$$

$$p_{k+1} - D_2 L_d(q_k, q_{k+1}) - f_d^+(q_k, q_{k+1}, u_k) = 0, \quad (1c)$$

$$p^0 + D_1 L_d(q_0, q_1) + f_d^-(q_0, q_1, u_0) = 0, \quad (1d)$$

$$p^T - D_2 L_d(q_{N-1}, q_N) - f_d^+(q_{N-1}, q_N, u_{N-1}) = 0, \quad (1e)$$

$$h(q_k, q_{k+1}, u_k) \leq 0, \quad (1f)$$

with  $k = 1, \dots, N - 1$ . Equation (1a) represents objective function, equations (1b) and (1c) represent laws of physics, equations (1d) and (1e) represent initial and final conditions respectively, while (1f) represents externally imposed constraints.



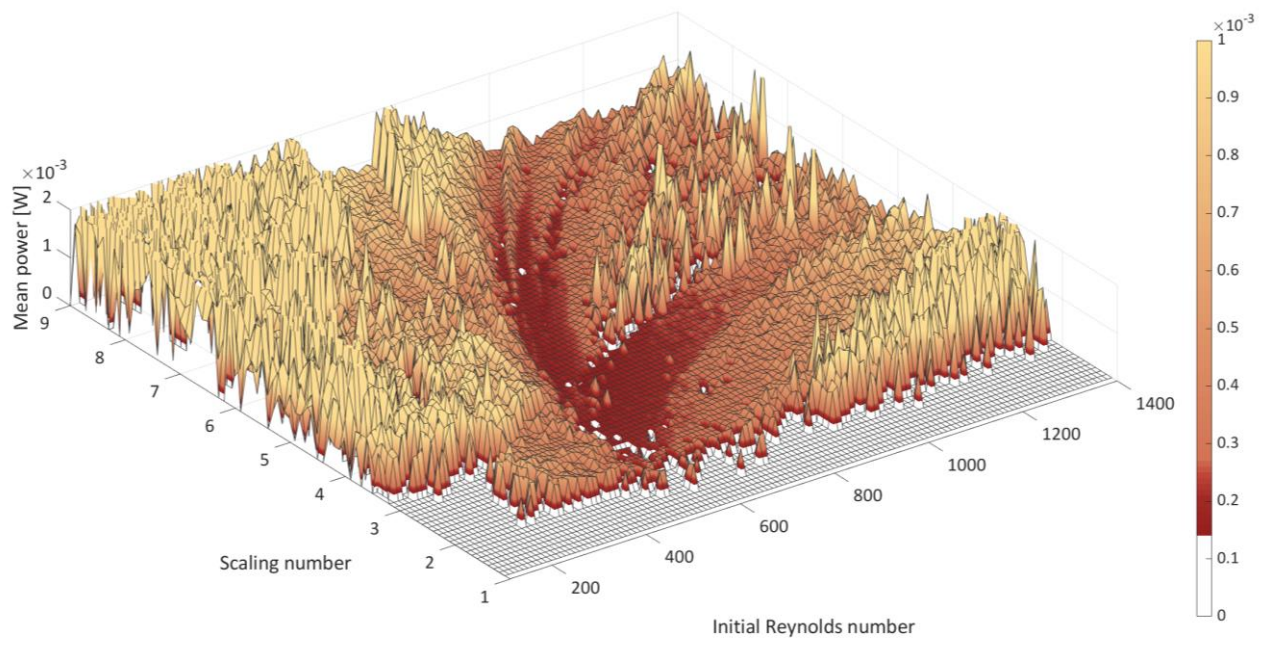


Figure 1: Mean power required for standstill hovering at different combinations of scaling factor and initial Reynolds number

### 3 Results

Optimizations were performed for 10400 different combinations of wing scaling factors (1 to 9) and experimentally validated initial Reynolds numbers (100 to 1400) [6]. For each feasible combination of wing scaling factor and Reynolds number, the mean power required for hovering in Martian atmosphere is reported, see Figure 1. The optimal combination was found for wings uniformly scaled by scaling factor  $n=4.2$ , while flying in the conditions resulting in mean Reynolds number  $Re=631$ . The algorithm found different energy-efficient flapping patterns for a wide range of scaling factors, thus providing notable insights into the physics of flapping flight on Mars and valuable directions for the design and control of Mars flapping wing aerial vehicles.

### 4 Conclusion

Results of the numerical experiment indicate that the developed optimization algorithm can be successfully used for computationally efficient optimization of design and dynamics of an insect-type flapping aerial vehicle for Mars exploration purposes — where higher fidelity fluid-structure coupled procedures fail to deliver because of computational non-efficiency. The next natural step, in the development process of the presented algorithm and research of flapping flight on Mars, is to expand the existing aerodynamic model with forward flight features.

### Acknowledgments

This work has been fully supported by Croatian Science Foundation under the project IP-2016-06-6696.

### References

- [1] Koning, Witold J. F., Johnson, Wayne, and Grip, Håvard F. “Improved Mars Helicopter Aerodynamic Rotor Model for Comprehensive Analyses.” *AIAA Journal* Vol. 57 No. 9 (2019): pp. 3969–3979. DOI 10.2514/1.J058045.
- [2] Terze, Zdravko, Pandža, Viktor, Kasalo, Marko, and Zlatar, Dario. “Discrete mechanics and optimal control optimization of flapping wing dynamics for Mars exploration.” *Aerospace Science and Technology* Vol. 106 (2020): p. 106131. DOI 10.1016/j.ast.2020.106131.
- [3] Terze, Zdravko, Pandža, Viktor, Kasalo, Marko, and Zlatar, Dario. “Optimized flapping wing dynamics via DMOC approach.” *Nonlinear Dynamics* Vol. 103 No. 1 (2021): pp. 399–417. DOI 10.1007/s11071-020-06119-y.
- [4] Sane, Sanjay P. and Dickinson, Michael H. “The aerodynamic effects of wing rotation and a revised quasi-steady model of flapping flight.” *Journal of Experimental Biology* Vol. 205 No. 8 (2002): pp. 1087–1096. DOI 10.1242/jeb.205.8.1087.
- [5] Ober-Blöbaum, Sina, Junge, Oliver, and Marsden, Jerrold E. “Discrete mechanics and optimal control: An analysis.” *ESAIM: Control, Optimisation and Calculus of Variations* Vol. 17 No. 2 (2011): pp. 322–352. DOI 10.1051/cocv/2010012.
- [6] Lentink, David and Dickinson, Michael H. “Rotational accelerations stabilize leading edge vortices on revolving fly wings.” *The Journal of experimental biology* Vol. 212 Pt 16 (2009): pp. 2705–2719. DOI 10.1242/jeb.022269.

# Adaptive techniques for Kalman filter estimation based on multibody models

Antonio J. Rodríguez<sup>1</sup>, Emilio Sanjurjo<sup>1</sup>, Miguel Ángel Naya<sup>1</sup>

<sup>1</sup> Laboratorio de Ingeniería Mecánica  
University of A Coruña  
Rúa Mendizábal s/n, Ferrol 15403, Spain  
[antonio.rodriquez.gonzalez,emilio.sanjurjo,miguel.naya]@udc.es

## EXTENDED ABSTRACT

### 1 Introduction

Estimation techniques have become a useful method for increasing the available information of a particular system. From a reduced set of sensors and a model of the system, not-sensed variables can be estimated. In most cases, the estimator belongs to Kalman filter family. The filter corrects the possible drift between model and real system based on a reduced set of sensor measurements.

The Kalman filter assumes that the system is linear and that the noises of the measurements and the system are gaussian white noise and with known statistical properties. None of these assumptions are usually fulfilled in real applications: most systems are non-linear and their statistical properties are hard to obtain. This is the case when a multibody model is employed to represent the system. To deal with non-linear systems, several filters have been proposed [1]. From them, the error extended Kalman filter (errorEKF) stands out as one of the best in terms of accuracy and efficiency [2]. The determination of the statistics of the sensors and system (also known as covariance noise matrices) is typically based on a trial-and-error procedure. However, it is important to have knowledge on the statistics, since wrong values can be turned into estimation errors and divergence issues.

As a solution to this difficulty, Adaptive Kalman filters (AKF) are proposed. The most popular approaches rely on the innovation sequence of the filter, that is, the difference between the real and estimated measurements. From the Kalman filter theory, for the true value of the covariance noise matrices, the innovation sequence must be white noise. Based on the previous principle, several methods have been developed such as the maximum likelihood estimation [3], Sage-Husa filter [4] or variational Bayesian estimation [5]. The maximum likelihood looks for the covariance matrices which result in the maximum probability of observing a certain innovation sequence. The Sage-Husa filter is based on the maximum a posteriori principle, which is similar to find the maximum likelihood weighting the most recent estimations. The variational Bayesian, instead of giving a unique value for the matrices, estimates a probability density function.

From the previous methods, only the maximum likelihood has proven to be capable of estimating the measurement noise covariance matrix (MNCM) and process (system) noise covariance matrix (PNCM). Although Sage-Husa filter can theoretically estimate both matrices, it has shown stability issues when both matrices are estimated at the same time. With respect to the variational Bayesian, it is only used for estimating the MNCM, since it assumes that the PNCM is known. This constitutes an important limitation, since an acceptable value of the MNCM can be obtained from the manufacturer of the sensors. Meanwhile, it is difficult to be certain with any initial guessing of the PNCM.

Adaptive Kalman filters are traditionally employed in navigation problems. Hence, it is necessary to address its combination for multibody-based state estimation and evaluate its performance. Due to the a priori benefits of the maximum likelihood, this work presents an extended Kalman filter combined with the maximum likelihood approach for estimating the covariance noise matrices.

### 2 Methodology

The performance of the proposed filter is evaluated in terms of robustness and accuracy. For that purpose, two mechanisms are modeled: a four-bar linkage (Figure 1a) and a five-bar linkage (Figure 1b). Each mechanism is modeled in natural coordinates and using the augmented Lagrangian of index-3 (ALI3P) [6] as formulation to solve the motion of the mechanism. Since all the tests are performed in a simulation environment, three multibody models are employed. The first one is considered as the *real mechanism*. The sensor measurements are obtained from this model. The second multibody model acts as a *model* of the *real mechanism*. In order to replicate a real situation, modeling errors are introduced. Finally, the third model is the *model* combined with the proposed filter, which would correct the errors based on the information provided by the measurements taken from the *real mechanism*.

The accuracy of the filter is evaluated through a batch of tests with different initial values of the covariance noise matrices. The filter is expected to estimate an adequate value of the covariance noise matrices and lead to a solution with the same magnitude of error with independence of the initial covariance values. During these tests, the mechanism is only affected by the gravity force. To asses the robustness of the filter, a torsional spring is added to the crank. After some seconds, the spring breaks simulating a failure on a real machine. The filter should re-adapt its estimation on the covariance matrices to the new scenario in order to keep the accuracy on the estimations.

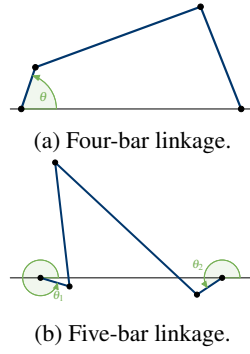


Figure 1: Mechanisms employed in this work.

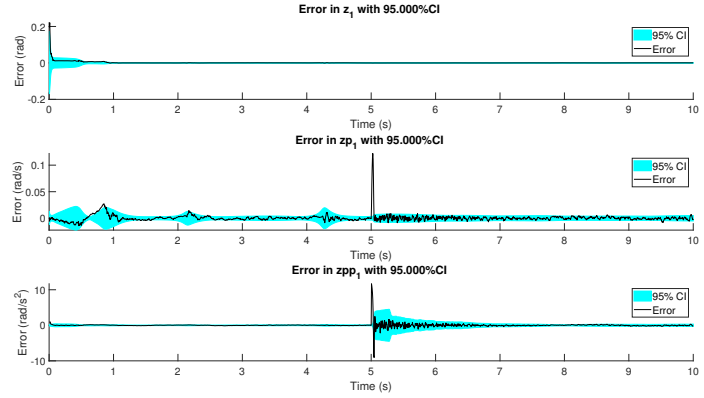


Figure 2: Error and confidence interval of the position, velocity and acceleration of the crank angle in the four-bar linkage during the robustness test.

### 3 Results

The results show that the proposed filter can be used to estimate the values of the process noise covariance matrix. However, the algorithm showed divergence issues when estimating also the measurement noise covariance matrix in some scenarios. Nevertheless, the estimation of the MNMCM did not improve the accuracy of the state estimation.

Regarding the accuracy, the proposed filter converged to a solution which minimizes the error of the estimations with independence of the assumptions for the initial covariance matrices. With respect to the robustness, it showed to provide accurate estimations even with unexpected changes in the real system, tracking the effects of the new scenario quickly.

These conclusions can be extracted from Figure 2, where it can be seen how the confidence interval becomes wider when the spring breaks, keeping the error in the estimations under a confidence interval of 95%, showing accuracy and reliability in the estimations. It means that when the AerrorEKF-FE detects the new scenario, it increases the values of the PNCM giving more relevance to the sensor measurements in order to track the new state of the system. Once that the *observer* tracks the new scenario of the *real mechanism*, the covariances are reduced.

However, the computational cost of the proposed adaptive filter is higher than the errorEKF-FE. The additional cost of estimating the process noise covariance matrix implies that the filter requires about the double of time per time-step to perform the estimations.

Finally, this work shows the benefits of adaptive Kalman filtering based on multibody models. In most applications, the process noise covariance matrix can not be known and, hence, the accuracy and stability of the filter is compromised. With adaptive methods, the process noise covariance matrix can be estimated increasing the accuracy and robustness of the estimator.

### Acknowledgments

This research was partially financed by the Spanish Ministry of Science, Innovation and Universities and EU-EFRD funds under the project "Técnicas de co-simulación en tiempo real para bancos de ensayo en automoción" (TRA2017-86488-R), and by the Galician Government under grant ED431C2019/29.

### References

- [1] E. Sanjurjo, M.Á. Naya, J.L. Blanco-Claraco, J.L. Torres-Moreno, A. Giménez-Fernández. Accuracy and efficiency comparison of various nonlinear Kalman filters applied to multibody models. *Nonlinear Dynamics*, 88:1935–1951, 2017.
- [2] A.J. Rodríguez, E. Sanjurjo, R. Pastorino, M.Á. Naya. State, parameter and input observers based on multibody models and Kalman filters for vehicle dynamics. *Mechanical Systems and Signal Processing*. 155:107544, 2021.
- [3] A.H. Mohamed, K.P. Schwarz. Adaptive Kalman Filtering for INS/GPS. *Journal of Geodesy*, 73:193-203, 1999.
- [4] Z. Luo, Z. Fu, Q. Xu. An Adaptive Multi-Dimensional Vehicle Driving State Observer Based on Modified Sage–Husa UKF Algorithm. *Sensors*, 20:6889, 2020.
- [5] C. Shan, W. Zhou, Y. Yang, Z. Jiang. Multi-Fading Factor and Updated Monitoring Strategy Adaptive Kalman Filter-Based Variational Bayesian. *Sensors*, 21:198, 2021.
- [6] J. Cuadrado, D. Dopico, M.Á. Naya, M. González. Penalty, Semi-Recursive and Hybrid Methods for MBS Real-Time Dynamics in the Context of Structural Integrators. *Multibody System Dynamics*, 12:117-132, 2004.



# Survey of the Use of Multibody Simulations in the Development of Trolleybuses

Pavel Polach, Michal Hajžman

Research and Testing Institute Pilsen  
Tylova 1581/46, CZ-301 00 Pilsen, Czech Republic  
{polach; hajzman}@vzuplzen.cz

## EXTENDED ABSTRACT

### 1 Introduction

This contribution presents a survey of the use of multibody simulations in the trolleybus development performed by the authors of the paper (trolleybus is similar in its design to a bus, it differs in some design elements – traction motor, pantographs, etc. – and thus in the distribution of unsprung masses). These are especially simulations of driving along an uneven road surface, simulations of a slow front impact against a concrete wall, design of the rear body stabilizer bar of an articulated trolleybus, simulations of the fall of a standing passenger against the trolleybus composite doors. Results of these simulations were generally confirmed by experimental measurements. [1]

### 2 Simulations with multibody models of the trolleybuses

In the case of trolleybuses (generally road vehicles of public transport), multibody models of empty and fully loaded vehicles are generally created. For both model weight variants of relative simply multibody model and multibody model with the detailed kinematics of the axles suspension are generally created (see Figure 1). Generation of relatively simple multibody models and an effort to improve them are important because they shorten significantly the computing time and can reveal mistakes in detailed models.

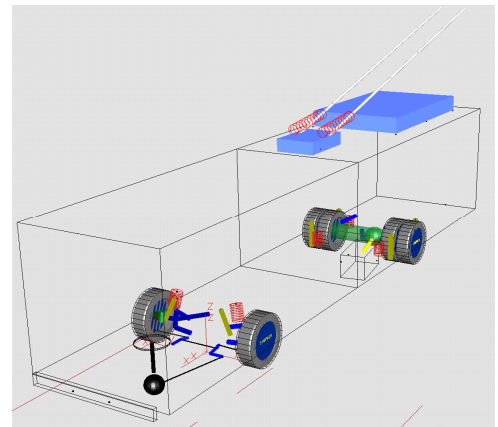


Figure 1: Real trolleybus ŠKODA 21 Tr and visualization of its multibody model (in SIMPACK software)

The results of the simulations with multibody models of trolleybuses are used especially as input data for the calculation of stresses of bodywork and chassis parts using FEM programs, in the field of fatigue life assessment of dynamically loaded parts of vehicle structures, for the improvement of driving properties of vehicles, for the evaluation of the suitability and design of the used axles suspension elements (air springs and shock absorbers) and for the improvement of the ride safety and driving comfort of a driver and passengers.

### 3 Simulations of driving along an uneven road surface

Driving along an uneven road surface can reveal a lot about the vehicle's vertical dynamic properties and about the suitability of the applied axles suspension elements. Especially time histories of relative deflections of springs, relative velocities in the shock absorbers, stress acting in the axles radius rods or radius arms, and acceleration in various points in the vehicle interior are the monitored quantities (e.g. [2]). On the basis of the relative deflections of springs, relative velocities in shock absorbers, and stress acting in radius rods or radius arms it is possible to determine the time histories and the extreme values of the forces acting in those suspension elements of axles, which can be utilized in connection with the suitable numerical methods for the stress analysis of structures, for the prediction of fatigue life of bodywork and chassis parts of the tested vehicle. In order to evaluate the vertical dynamic properties of the vehicle when driving along the uneven road surface, it is necessary to know the surface characteristics, i.e. statistical properties of unevennesses of the surface or direct its geometry. The geometry of the uneven surface profile of the run through the section is known in test polygons. Test tracks, which are created by distributing artificial vertical unevennesses (obstacles) on the road surface, are also often used. An artificial test track created according to the internal methodology was used for test drives with real trolleybuses and for simulations with multibody models (e.g. [1]).

#### **4 Simulations of slow front impact against the concrete wall**

The front impact against a concrete wall at the running speed of 5 km/h is one of the tests which are used for the verification of properties of public transport vehicles required by their operators. In practice, a slow front impact may occur e.g. during arrival in the vehicles depot. Due to that impact, a permanent deformation of the vehicle structure should not occur. This requirement was a starting point for the proposal of the new design of a front wall of the ŠKODA trolleybuses which a new type of bumper was used. The dynamic deformation load characteristic of the bumper was determined at laboratory tests. The simulations of a slow front impact were carried out with the trolleybuses multibody models. Time histories and extreme values of the bumper deformation, the acceleration in the front wall of the trolleybuses, and the total force transferred to the front wall of the trolleybuses were the monitored quantities during slow front impact simulations. The simulations results served as input data for the FEM calculation of the trolleybuses structure deformation.

#### **5 Design of the rear body stabilizer bar of an articulated trolleybus**

In the course of the ŠKODA articulated trolleybus modernization a different type of the articulation and the driving axles were used in its construction among others. During test drives with the real modernized trolleybus focused on the vehicle driving stability considerable rolling of the rear body appeared during all the driving manoeuvres. Test manoeuvres consisted in severe changing the right lane to the left one and immediate severe returning to the right lane. Test drives with both empty and loaded trolleybus were stopped at lower speeds than the requirements of their operators are, considering the problematic behaviour of the vehicle. Using the rear body stabilizer was chosen as a suitable constructional solution for reducing the roll angle of the rear body of the modernized trolleybus. A torsional lateral stabilizer of the trolleybus rear body made of the steel bar of a circular cross section was considered in the design. A suitable diameter of the bar was determined on the basis of simulations results that were performed with the multibody models of the trolleybus. The monitored quantities were, like in the case of experimental measurements, time histories and extreme values of the angle of mutual position of the trolleybus front and rear bodies, the rear body roll angle, and the lateral acceleration of the rear body above the rear axle. On the basis of the results of the documented test drives simulations the optimum diameter of the steel rod used for the stabilizer bar making was proposed. The suitability of the complete structural design of the rear body stabilizer of the trolleybus for improving its driving stability was confirmed at operation of real trolleybuses.

#### **6 Simulations of the fall of a standing passenger against the trolleybus doors**

In the framework of a so-called “plastic program” ŠKODA manufacturer introduced composite doors into the trolleybuses of its production program. Verification of the applicability of their structural design was carried out by means of both experimental tests on the real composite doors prototype and computer simulations. Before introducing composite doors into vehicles in series production it is necessary to carry out operational, fatigue life and strength tests and impact force resistance tests. In tests of doors resistance against the impact force, it is necessary to determine the maximum dynamic force which should be transferred by the doors. The force was determined during the simulation with the multibody models of the trolleybuses with a standing passenger (passenger is modelled using alaska/Dynamicus human body model). In the multibody models the computed doors stiffness is realized by a spring-damper element, which is active only in case of a passenger – doors contact. In order to determine the time history and the extreme force acting on the doors, which was excited by the fall of a standing passenger, an unexpected avoidance manoeuvre in various driving speeds and with various front wheels angles were simulated. The following “parameters” of the passenger were changed: distance from the doors, mass, and height. In the simulations a quick response of the passenger was not considered. Otherwise back or shoulder impact was considered. Simulations results served as input data for the FEM calculation of the composite doors stresses and as the basis for experimental tests on their real prototype. On the basis of the simulations results the construction of steel guide brackets of the mechanism for shutting the doors was optimized. The correctness of the results of the simulation was confirmed by means of tearing the guide bracket out on the real prototype of doors.

#### **7 Conclusions**

The contribution presents examples of multibody simulations with trolleybuses, the results of which were used to improve the technical properties of these vehicles. Based on the requirements of their manufacturers and operators to improve other technical properties, it is of course possible to perform other types of simulations.

#### **Acknowledgments**

The contribution has originated in the framework of institutional support for the long-time conception development of the research institution provided by the MIT of the Czech Republic to Research and Testing Institute Pilsen.

#### **References**

- [1] P. Polach. Utilization of Multibody Simulations at Buses and Trolleybuses Development. Habilitation thesis, University of West Bohemia, Pilsen, 2020. (in Czech)
- [2] T. D. Gillespie, S. M. Karamihas. Simplified models for truck dynamic response to road inputs. *International Journal of Heavy Vehicle Systems*, 7:52-63, 2000.

# Surface Error Correction of a Mesh Deployable Reflector

Pietro Davide Maddio<sup>1</sup>, Pietro Salvini<sup>1</sup>, Rosario Sinatra<sup>2</sup>, Alessandro Cammarata<sup>2</sup>

<sup>1</sup> University of Rome "Tor Vergata"

Department of Enterprise Engineering

Via del Politecnico 1, 00133 Rome, Italy

pietro.davide.maddio@uniroma2.it;

salvni@uniroma2.it;

<sup>2</sup> University of Catania

DICAR

Via S. Sofia 64, 95123 Catania, Italy

rosario.sinatra@unict.it; alessandro.cammarata@unict.it

## EXTENDED ABSTRACT

### 1 Introduction

In recent decades, Large Deployable Reflectors (LDR) have attracted the attention of several aerospace companies due to their wide applications. LDR systems are commonly used as mesh reflectors for large aperture space antennas in aerospace applications since they provide affordability while guaranteeing at the same time a high gain and a high directivity. These types of reflectors are appropriate for the majority of applications where very large apertures are required such as, for example, space missions that include communications, synthetic aperture radar, radiometry, radio astronomy, and navigation.

The key features that characterize the geometry of LDR systems are closely connected with volume constraints of launch vehicles, mainly because of budget problems [1]. Deployable mesh reflectors are composed of rigid bodies, deformable components, mechanical joints, and control actuators which allows for achieving a complete transition between the initial stowed configuration to the final deployed configuration.

The fundamental problems for the correct functioning of an LDR system are, therefore, the proper deployment of the folding mechanism and the form-finding of the cable net which serves as support for the metal mesh. To maintain excellent reflective qualities and meet the prescribed bandwidth requirements, the reflector surface must be as close as possible to the shape of a paraboloid.

Most of the methods used in the literature define the best surface of the reflector as the one passing through the nodes of the cable system of the front net [2]. In this case, the *RMS* error depends on the distance between the nodes of the front net with respect to the desired working surface. In this work, however, we want to focus on the amount of energy that hits the feed, thus investigating the best topology of the net that guarantees a greater concentration of the incident rays directed towards the focus of the paraboloid.

### 2 Surface error correction algorithm

To improve the performance of the reflector, the best-fit paraboloid that minimizes the *RMS* error needs to be found. For convenience of analysis, the two-dimensional model will first be illustrated.

As shown in Fig. 1(a), taking into consideration a prime-focus antenna, where the focus is positioned in the centre of the reflector, the incident rays parallel to the *y*-axis are reflected on the surface of the reflector and then directed towards the feed. The point  $P_{Ci}$  represents the centre of the *i*-th line segment of the polygonal. Figure 1(b) shows an enlargement around the feed, which highlights how the incident rays coming from the points  $P_{Ci}$  are not directed exactly on the focus *F*, but are distant from it by a quantity  $d_i$ .

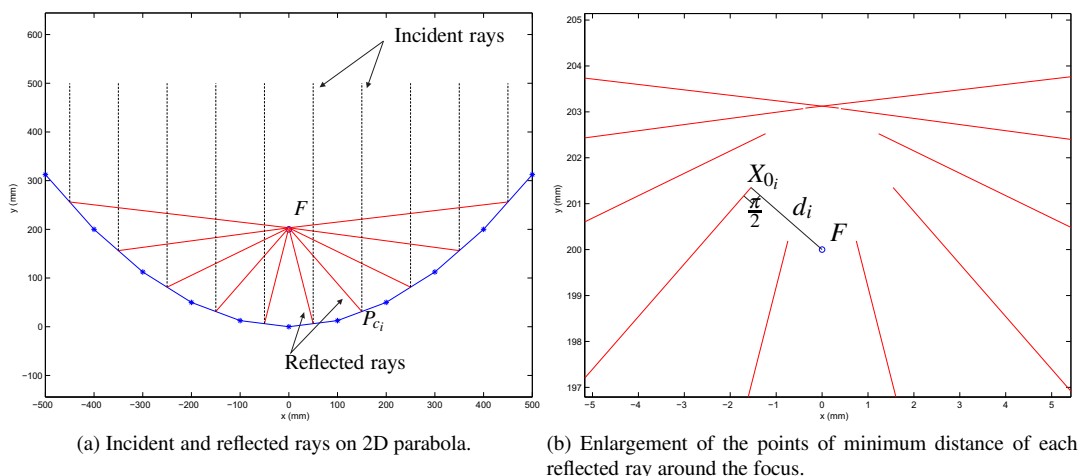


Figure 1: A two-dimensional parabola.

To determine this quantity, we need to calculate the minimum distance between the focus and each reflected ray coming from all line segments of the polygonal chain. From a geometric point of view, the distance of a point from a line is defined as the line segment perpendicular to the line which has the point itself and a point on the line as extremes. To find the point of minimum distance  $X_0$  we need to solve the following system of equations:

$$\begin{bmatrix} \mathbf{1} & -\mathbf{v}_r \\ \mathbf{v}_r^T & 0 \end{bmatrix} \begin{bmatrix} \mathbf{x}_0 \\ \lambda \end{bmatrix} = \begin{bmatrix} \mathbf{p}_c \\ \mathbf{v}_r^T \mathbf{F} \end{bmatrix} \quad (1)$$

where  $\mathbf{1}$  is an identity matrix of order 3,  $\mathbf{p}_c$  is the position vector of  $P_{ci}$  and  $\mathbf{v}_r$  is the vector of the reflected ray. The latter vector is calculated using the law of reflection.

What described for the two-dimensional model can be even extended in the three-dimensional model. Unlike the 2D model, the polygonal chain is replaced by the surface reflector consisting of the cable net system, whose nodes are located on the paraboloid surface. Here, for the *RMS* error evaluation, the vertices of the triangular facets and their centroid are considered. As can be seen from Fig. 1(b) of the 2D model, the net topology having the nodes located on the ideal parabola does not guarantee the best energy contribution to the feed. Hence, the best-fit paraboloid can be achieved thanks to the formulation of an optimization algorithm which, by varying the position of the nodes of the cable net, minimizes the distance of each reflected ray with respect to the focus of the paraboloid. The optimization problem can be summarized as follows:

$$\begin{aligned} &\text{Find} && \mathbf{x}, \mathbf{y}, \mathbf{z} \\ &\min && e_{RMS} \\ &\text{subject to} && \mathbf{x}_v = \mathbf{x}_v^0, \mathbf{y}_v = \mathbf{y}_v^0, \mathbf{z}_v = \mathbf{z}_v^0 \end{aligned} \quad (2)$$

where  $\mathbf{x}, \mathbf{y}, \mathbf{z}$  represent the coordinates of the nodes of the cable net,  $e_{RMS}$  is the RMS of the  $d_i$  distances,  $\mathbf{x}_v, \mathbf{y}_v, \mathbf{z}_v$  the coordinates of the nodes located on the ring truss and  $\mathbf{x}_v^0, \mathbf{y}_v^0, \mathbf{z}_v^0$  their initial position.

### 3 Numerical simulation

To demonstrate the validity of the proposed method, the best topology of an offset-feed reflector is proposed. The set of points located in the left part of the Fig. 2 demonstrates how the reflected rays are located in a very small area near the feed.

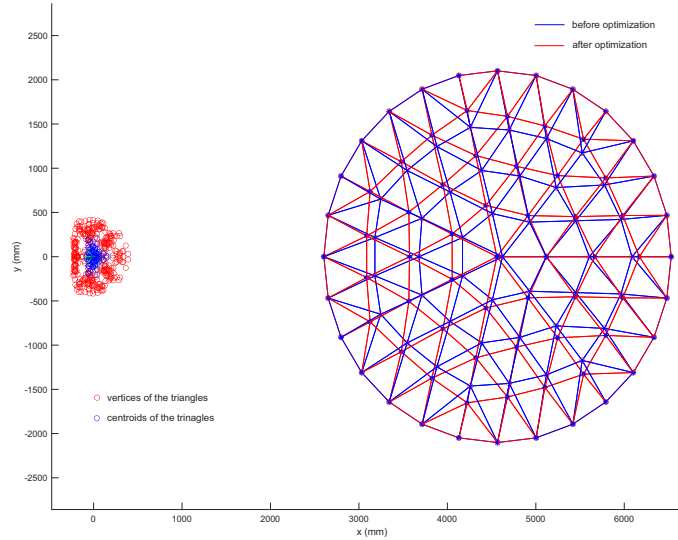


Figure 2: The topology of the cable net of an offset reflector before and after optimization, and the points of minimum distance with respect to the focus.

### 4 Conclusions

An optimization algorithm to find the best surface of a mesh deployable reflector has been proposed. The numerical results confirm the validity of the method, unlike those proposed in the existing literature, finding the best cable net topology that maximizes the energy contribution of the reflector.

### References

- [1] Puig L, Barton A, Rando N. A review on large deployable structures for astrophysics missions. *Acta Astronautica*. 2010 Jul 1;67(1-2):12-26.
- [2] Tang Y, Li T, Wang Z, Deng H. Surface accuracy analysis of large deployable antennas. *Acta Astronautica*. 2014 Nov 1;104(1):125-33.

# Model Order Reduction for Elastic Multibody Systems with Fast Rotating Flexible Bodies

Lennart Frie<sup>1</sup>, Oliver Dieterich<sup>2</sup>, Peter Eberhard<sup>1</sup>

<sup>1</sup> Institute of Engineering and Computational Mechanics  
University of Stuttgart  
Pfaffenwaldring 9, 70569 Stuttgart, Germany  
{lennart.frie,peter.eberhard}@itm.uni-stuttgart.de

<sup>2</sup> Airbus Helicopters Germany GmbH  
Dynamics and Vibrations  
Industriestr. 4, 86607 Donauwörth, Germany  
oliver.dieterich@airbus.com

## EXTENDED ABSTRACT

### 1 Introduction

Elastic multibody systems (EMBS) are often used to describe coupled mechanical systems. High complexity of those systems and increasing demands on detail make the use of model order reduction (MOR) inevitable. MOR aims at generating reduced models that allow numerically efficient evaluations with a small approximation error in the space of interest. Classical reduction approaches for EMBS, e.g. the Craig-Bampton-Method [1], reduce the single bodies separately with modal MOR and build the reduced system basis by assembling the reduced bodies. However, this method can neither account for the interaction between the different bodies and the dynamics induced by the coupling nor is it able to regard viscous damping or gyroscopic terms. Nevertheless, Craig-Bampton and modal truncation are still state of the art. Input-output based MOR techniques, as e.g. Krylov subspace methods, instead are often better suited for coupled systems [2]. This contribution extends existing MOR methods to EMBS with fast rotating bodies. Improved reduction schemes are applied by the use of the powerful software packages MatMorembs [3] and Neweul-M<sup>2</sup> [4] which were developed in previous projects and are enhanced for the reduction of fast rotating bodies or viscous damping, respectively. Furthermore, the applicability to an industrial use case, a helicopter model with non-rotating flexible airframe, shown in Figure 1, and rotating main rotor, is demonstrated.

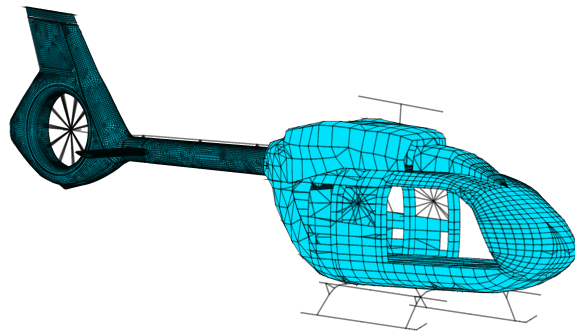


Figure 1: Finite element mesh of a helicopter airframe structure, available at Airbus Helicopters [5]

### 2 Description of flexible multibody systems with rotating bodies

The motion of an EMBS caused by external forces  $\mathbf{f}$  can be described with the floating frame of reference approach [6]. Its advantage is that the degrees of freedom can be divided into nonlinear rigid body motions  $\mathbf{q}_r$  and small linear deformations  $\mathbf{q}_e$ . The elastic degrees of freedom frequently result from a discretization of the elastic bodies with finite elements (FE) so that  $\mathbf{q}_e = [\mathbf{q}_e^1, \mathbf{q}_e^2, \dots, \mathbf{q}_e^K]^T$  describes the displacements of the FE-nodes for a system with  $K$  elastic bodies. The equation of motion of the system then reads

$$\mathbf{M}\ddot{\mathbf{q}} + \mathbf{D}\dot{\mathbf{q}} + \mathbf{K}\mathbf{q} = \mathbf{f}. \quad (1)$$

Here,  $\mathbf{M}, \mathbf{D}, \mathbf{K} \in \mathbb{R}^{N \times N}$  are the mass, damping and stiffness matrix, respectively, and  $\mathbf{q} \in \mathbb{R}^N$  denotes the generalized coordinates  $\mathbf{q} = [\mathbf{q}_r, \mathbf{q}_e]^T$  of a system with  $K$  bodies. If a body underlies fast rotations, nonlinear gyroscopic terms  $\mathbf{G}(\dot{\mathbf{q}})$  in  $\mathbf{D} = \mathbf{D}_1 + \mathbf{G}$  and geometric stiffness  $\mathbf{K}_{\text{geo}}(\dot{\mathbf{q}})$  in  $\mathbf{K} = \mathbf{K}_1 + \mathbf{K}_{\text{geo}}$  cannot be neglected and are added to the linear damping and stiffness matrix,  $\mathbf{D}_1$  and  $\mathbf{K}_1$ , of the elastic bodies. Also the mass matrix  $\mathbf{M} = \mathbf{M}(\mathbf{q}, \dot{\mathbf{q}})$  becomes state dependent because of the rigid body motions. For mechanical systems, linear MOR is popular and shall also be applied in this work. The nonlinearity in the rotating system, caused by geometric stiffness and gyroscopic effects, prevents direct application of linear MOR. Thus, linearization of the system around a steady state  $\mathbf{q}_s$  with  $\dot{\mathbf{q}}_{e,s} = \ddot{\mathbf{q}}_{e,s} = \mathbf{0}$  is necessary. The elastic deformation of a body  $k$  underlying a fast, constant rotation  $\omega^k$  can be determined with

$$\mathbf{q}_{e,s}^k = \left( \mathbf{K}_1^k + \mathbf{K}_{\text{geo}}^k(\omega^k) \right)^{-1} \mathbf{f}^k. \quad (2)$$

For small deviations  $\Delta \mathbf{q}$  and  $\bar{\mathbf{q}} = \mathbf{q}_s + \Delta \mathbf{q}$  with  $\mathbf{q}_s = [\mathbf{q}_{r,s}, \mathbf{q}_{e,s}]^T$  then

$$\mathbf{M}_s \bar{\mathbf{q}} + \mathbf{D}_s \bar{\mathbf{q}} + \mathbf{K}_s \bar{\mathbf{q}} = \mathbf{f} \quad (3)$$

holds. Here,  $\mathbf{M}_s(\mathbf{q}_s, \dot{\mathbf{q}}_s)$ ,  $\mathbf{D}_s(\mathbf{q}_s, \dot{\mathbf{q}}_s)$  and  $\mathbf{K}_s(\mathbf{q}_s, \dot{\mathbf{q}}_s)$  are constant and linear MOR can be applied.

### 3 Projection based model order reduction

The linearized equation of motion (3) can be rewritten as linear time invariant system

$$\begin{aligned} \mathbf{M}_s \ddot{\mathbf{q}} + \mathbf{D}_s \dot{\mathbf{q}} + \mathbf{K}_s \mathbf{q} &= \mathbf{B} \mathbf{u}, \\ \mathbf{y} &= \mathbf{C} \mathbf{q}. \end{aligned} \quad (4)$$

Here,  $\mathbf{B} \in \mathbb{R}^{N \times b}$  and  $\mathbf{C} \in \mathbb{R}^{c \times N}$  are the input and output matrices and  $\mathbf{u} \in \mathbb{R}^b$  und  $\mathbf{y} \in \mathbb{R}^c$  are the system inputs and outputs. The dimension  $N$  is usually high and system evaluations are numerically expensive. The goal of MOR is to approximate the full order system with

$$\tilde{\mathbf{q}} \approx \mathbf{V} \tilde{\mathbf{q}} \quad (5)$$

in a low dimensional subspace  $\mathcal{V} = \text{span}\{\mathbf{V}\}$ . Plugging (5) into (4) and left multiplying  $\mathbf{V}^T$  yields the reduced model

$$\begin{aligned} \underbrace{\mathbf{V}^T \mathbf{M}_s \mathbf{V}}_{\tilde{\mathbf{M}}} \ddot{\tilde{\mathbf{q}}} + \underbrace{\mathbf{V}^T \mathbf{D}_s \mathbf{V}}_{\tilde{\mathbf{D}}} \dot{\tilde{\mathbf{q}}} + \underbrace{\mathbf{V}^T \mathbf{K}_s \mathbf{V}}_{\tilde{\mathbf{K}}} \tilde{\mathbf{q}} &= \underbrace{\mathbf{V}^T \mathbf{B}}_{\tilde{\mathbf{B}}} \mathbf{u}, \\ \tilde{\mathbf{y}} &= \underbrace{\mathbf{C} \mathbf{V}}_{\tilde{\mathbf{C}}} \tilde{\mathbf{q}}. \end{aligned} \quad (6)$$

The choice of  $\mathbf{V}$  is the key problem in MOR by projection since the reduced system dimension should be  $n \ll N$  on the one hand and the approximation error in time and frequency domain is required to be small on the other. Classical approaches try to find such  $\mathbf{V}$  by taking selected eigenmodes as its columns, for instance the Craig-Bampton method, other component mode synthesis and modal truncation. Yet, other methods based on Gramian matrices or Krylov subspaces [5] are often more appropriate for EMBS with interacting elastic bodies. This is because the eigenvalue problem does not consider any excitation of the system whereas the bodies are indeed excited by the moving interfaces. Another drawback of the modal approaches in the case of fast body rotations is that the system eigenmodes become complex caused by the gyroscopic terms. By contrast, input-output based methods do take into account if and where the system is excited and at which point the displacements should be predicted.

### 4 Numerical example

The described reduction methods are applied and compared for a helicopter in steady flight. The system consists of a rotating elastic main rotor coupled with an elastic airframe. The rotation and the resulting effects influence the system dynamics as well as the interaction between both bodies. A proper subspace therefore depends on the rotor speed. If the coupling of the bodies is not considered during the reduction important modes, e.g. rotor-shaft-bending modes, are ignored. Current state of the art is the representation of main rotor inertia by an equivalent rotor mass. This work aims to find a more appropriate solution by modeling the system as EMBS, applying input-output based MOR techniques and comparing the size of the reduced systems as well as the approximation errors.

### Acknowledgments

This research is done within the framework of the EVOLVE (FKZ 20A1902C) research project funded by the German Federal Ministry of Economics and Energy.

Gefördert durch:



Bundesministerium  
für Wirtschaft  
und Energie

aufgrund eines Beschlusses  
des Deutschen Bundestages

### References

- [1] Craig, R.; Bampton, M.: Coupling of Substructures for Dynamic Analyses. AIAA Journal, Vol. 6, No. 7, pp. 1313–1319, 1968.
- [2] Holzwarth, P.; Eberhard, P.: Input-Output Based Model Reduction For Interconnected Systems. In Oñate, E.; Oliver, J.; Huerta, A. (Eds.): Proceedings of the 5th European Conference of Computational Mechanics, Barcelona, 2014.
- [3] Fehr, J.; Grunert, D.; Holzwarth, P.; Fröhlich, B.; Walker, N.; Eberhard, P.: Morembs—A Model Order Reduction Package for Elastic Multibody Systems and Beyond. In Keiper, W.; Milde, A.; Volkwein, S. (Eds.): Reduced-Order Modeling (ROM) for Simulation and Optimization: Powerful Algorithms as Key Enablers for Scientific Computing, pp. 141–166. Cham: Springer International Publishing, 2018.
- [4] Kurz, T.; Eberhard, P.; Henninger, C.; Schiehlen, W.: From Neueul to Neueul-M<sup>2</sup>: Symbolical Equations of Motion for Multibody System Analysis and Synthesis. Multibody System Dynamics, Vol. 24, No. 1, pp. 25–41, 2010.
- [5] Fröhlich, B.; Hose, D.; Dieterich, O.; Hanss, M.; Eberhard, P.: Uncertainty Quantification of Large-Scale Dynamical Systems Using Parametric Model Order Reduction. submitted, 2020.
- [6] Schwertassek, R.; Wallrapp, O.: Dynamik flexibler Mehrkörpersysteme (in German). Braunschweig: Vieweg, 1999.



**Author index**

Aarts, Ronald	107, 188
Aceituno, Javier F.	304
Achleitner, Johannes	117
Acosta Suñé, Raül	81
Akaki, Tomohiro	100
Akeno, Koki	231
Akhadkar, Narendra	89
Al Yahmedi, Amur Salim	23
Al-Ouakad, Hassan	23
Alazard, Daniel	185
Aller, Felix	214
Alves da Silva, Wallyson Thomas	133
Ambrósio, Jorge	40, 123, 306
Amirouche, Farid	166
Andersson, Fredrik	281
Antali, Máté	77
Antunes, Pedro	306
Arbatani, Siamak	212
Arnold, Martin	261, 271
Arora, Rohit	100, 231
Askari, Ehsan	148
Bait Bahadur, Issam	23
Balogh, Tamas	198
Bauer, Benjamin	257
van den Bedem, Henry	36
Belotti, Roberto	113
Benatti, Simone	250
Bencsik, László	241
Bentefrit, Mohamed	73
Berendsen, Dustin	188
Betsch, Peter	119, 135, 154, 162, 239
Bettega, Jason	206
Bijalwan, Ashutosh	129
Björkenstam, Staffan	50
Bodor, Bálint	241
Borchsenius, Fredrik	158
Boscariol, Paolo	200
Boschetti, Giovanni	204
Bosten, Armin	265
Bottero, Francisco	102
Boudon, Benjamin	190, 292
Bouton, Nicolas	190, 292
Bouzgarrou, Chedli	190
Bowling, Alan	44
Brouwer, Dannis	107
Brüls, Olivier	69, 85, 168, 265
Bulín, Radek	279, 283
Byrtus, Miroslav	279
Cabello, Mario	65
Cammarata, Alessandro	121, 316
Cardona, Alberto	69, 85
Carricato, Marco	111
Castaño, David	25
Castejón Sisamón, Cristina	95
Cavalieri, Federico	69, 85



Cera, Mattia	152
Chandramohan, Sujatha	290
Chen, Junpeng	42
Chen, Xiyu	36
Cho, Michael	44
Choi, JaeWon	302
Choi, Ji-yoon	294
Cirelli, Marco	152
Colantonio, Lorenzo	91
Corral Abad, Eduardo	95
Cosimo, Alejandro	69, 85, 168, 265
Costa, João	123
Crevecoeur, Guillaume	148
Cuadrado Aranda, Francisco Javier	102
Cuadrado, Javier	15, 25, 65
Dambacher, Louis	292
Dambly, Valentin	137
Dang, Thu-Thuy	190
Dash, Sabyasachi	290
Dehombreux, Pierre	91
Desmet, Wim	73, 229
Després, Bruno	223
Detrembleur, Christine	58
Devigne, Olivier	168
Di Castro, Mario	183
Di Leva, Roberto	111
Dieterich, Oliver	318
Dignath, Florian	296
Docquier, Nicolas	81
Dopico Dopico, Daniel	142, 227, 233
Durville, Damien	285
Dwarshuis, Koen	107
Dyk, Štěpán	283
Dörlich, Vanessa	50, 259, 271
Eberhard, Peter	296, 318
Eichmeir, Philipp	172, 225, 235
Ellenbroek, Marcel	107, 115
Elmqvist, Asher	250
Escalona, Jose Luis	277, 304
Eugster, Simon	67
Ezati, Mahdokht	19
Fehr, Jörg	308
Fiedler, Bodo	127
Finozzi, Antonio	185
Fiorini, Camilla	223
Fisette, Paul	58, 81, 98
Flores, Paulo	63
Font Llagunes, Josep Maria	38, 56
Frie, Lennart	318
Frączek, Janusz	150, 179
Gamper, Hannes	183
Gattringer, Hubert	111, 164, 183, 208
Gerstmayr, Johannes	105, 263
Giovannucci, Monica	298
Gismelseed, Sarra Abbasher	23
Gismeros Moreno, Raúl	95
Gnad, Daniel	164

Gong, DuHyun	302
González Varela, Francisco Javier	102, 204, 254
Gonçalves, Sérgio	34
Grube, Malte	127
Gufler, Veit	117
Guigon, Louis	190
Guo, Jianqiao	42
Géradin, Michel	140
Gómez García, María Jesús	95
Habib, Giuseppe	144
Hag, Yashar Shabbouei	194
Hajžman, Michal	91, 181, 279, 283, 314
Hakansson, Nils	32
Halamka, Vojtěch	267
Handroos, Heikki	194
Harant, Monika	50, 52, 214
Havas, Vince	77
Hawwash, Muhannad	259
Held, Alexander	125, 237
Heo, Dong-hoe	294
Hinneken, Simon	58, 98
Hirata, Kento	218
Hogan, S. John	77
Horváth, Hanna Zs.	288
Houdek, Václav	181
Hrabačka, Martin	279
Hu, Haiyan	131
Huang, Dengpeng	109
Huang, Liming	248
Huynh, Hoai Nam	137
Im, ByeongUk	302
Inkol, Keaton A	54
Insperger, Tamas	30, 48, 198, 210
Iwamura, Makoto	218
Jaiswal, Suraj	194, 252
Jane, Marcel	38
Jelenić, Gordan	269
Jogi, Ajith	290
Jungkenn, Dominik	281
Jörgl, Matthias	208
Kanazawa, Hiroyuki	100, 231
Kasalo, Marko	310
Kaňka, Tomáš	267
Kecskemethy, Andres	71, 177
Keller, Roger	259
Kerr, Liam Peter	246
Khadim, Qasim	194, 252
Kim, Jae Yeon	170
Kim, Soo Jin	170
Kinon, Philipp L.	162
Kovacs, Balazs	210
Krivošej, Jan	202
Kusuma Chandrashekhara, Sudhanva	275
Kövecses, József	61, 212, 246
Lalande, Nicolas	292
Lankarani, Hamid M.	32, 63
Leine, Remco I.	11, 67, 83

Lenain, Roland	292
Leyendecker, Sigrid	36, 50, 109, 273
Lichtenecker, Daniel	225
Linn, Joachim	50, 257, 259, 265, 271, 281
Lot, Roberto	292
Luaces Fernández, Alberto	227, 233
Lugrís Armesto, Urbano	15, 25, 102
Luthi, Adrien	183
López Varela, Álvaro	227, 233
López-Lombardero, Mario	65
Maceira Muñños, Diego	102
Maciąg, Paweł Wojciech	179
Maddio, Pietro Davide	121, 316
Madorell Batlle, Queralt	56
Maeda, Yoshiki	218
Magalhães, Hugo	306
Mahaudens, Philippe	58
Maier, Steffen	308
Malafosse, Pierre	190
Malczyk, Paweł	146, 150, 156, 179
Manfredo, Davide	271
Mangoni, Dario	87
Margetts, Rebecca	190
Marques, Filipe	63
Martini, Alberto	298
Masarati, Pierangelo	160
Matikainen, Marko K.	194
McColloch, Andrew	44
McPhee, John	19, 54
Menegaldo, Luciano L.	28
Meneses Alonso, Jesús	95
Michaud, Florian	25
Mihályi, Levente	300
Mikkola, Aki	13, 194, 248, 252
Millan, Pedro	123, 306
Mohammadi, Narges	277
Molnar, Csenge A.	30
Mombaur, Katja	52, 214
Moreau, Emile	98
Moreira, Pedro S.	28
Mueller, Andreas	183
Munoz, Jose J.	129
Müller, Andreas	111, 164, 208
Müller, Katharina	71
Müller, Ralf	259
Nachbagauer, Karin	225, 235
Naets, Frank	73, 75, 229
Nagy, Dalma J.	48
Nakagawa, Atsushi	100
Naya Villaverde, Miguel Ángel	102, 312
Negrut, Dan	12, 250
Ntarladima, Konstantina	263
Näf, Matthias Basil	52
Osman, Krešimir	220
Oto, Kyuji	218
Pagaimo, João	123, 306
Palomba, Ilaria	113

Pamies-Vila, Rosa	38
Pan, Yongjun	248
Pandža, Viktor	310
Patko, Dora	17
Peeters, Jari	75
Peiret Gimenez, Albert	38, 56, 61
Pennestri', Ettore	152
Pere, Balázs	79
Phillips, James R.	166
Pieber, Michael	263
Pikuliński, Maciej	146
Pinelli, Marco	298
Pinto, Dafne P.	28
Piva, Giulio	204
Polach, Pavel	279, 314
Porwal, Gitesh	89
Preiswerk, Pascal V.	83
Puscas, Maria Adela	223
Pätzold, Matthias	175
Pérez-Soto, Manuel	15
Quental, Carlos	40
Rabiei, Manoochehr	44
Rahikainen, Jarkko	252
Raison, Maxime	98, 216
Raoofian, Ali	61
Remírez, Adrián	65
Ren, Gexue	42
Reymundo, Pedro	32
Richiedi, Dario	200, 204, 206
Rivière-Lorphèvre, Édouard	137
Robuschi, Nicolò	87
Rodríguez Frade, Borja	102, 204
Rodríguez González, Antonio Joaquín	102
Rodríguez, Antonio J.	312
Rogovchenko, Yuriy	175
Roller, Michael	50, 257
Rostamian, Rouben	133
Roupa, Ivo	34
Ruggiu, Maurizio	254
Rusinek, Rafal	46
Rückwald, Tobias	125, 237
Saadat, Mohammad Ali	285
Sailer, Simon	11, 67
Salvini, Pietro	316
Sanchez, Eliana	85
Sandu, Adrian	142
Sandu, Corina	142
Sanfedino, Francesco	185
Sanjurjo Maroño, Emilio	15, 102, 312
Schilder, Jurnan	115
Schmid, Patrick	296
Schneider, Fabio	281
Schneider, Georg	296
Schneider, Simeon	239
Seifried, Robert	125, 127
Sequeira, Mariana	40
Serban, Radu	250

Serfőző, Dániel	79
Shen, Huiping	177
Shin, SangJoon	302
Šika, Zbyněk	202, 267
Silva, Miguel Tavares	34
Simeon, Bernd	257
Simões, Francisca	40
Sinatra, Rosario	121, 316
Sonneville, Valentin	140
Sopanen, Jussi	252
Sridhar, Aditya	188
Stavole, Martina	273
Steiner, Wolfgang	172, 235
Stépán, Gábor	243
Ströhle, Timo	119
Stépán, Gábor	77
Sun, Chiyu	177
Sun, Jialiang	131
Szabó, András	288
Szaksz, Bence Mate	243
Szilagyi, Attila	133
Tahedl, Michael	158
Tak, Tae-oh	294
Takata, Tomoshige	100
Takács, Dénes	288, 300
Taras, Andreas	158
Tasora, Alessandro	87
Taves, Jay	250
Teichmann, Marek	61, 212
Terze, Zdravko	310
Ther, Tamas	93
Tian, Qiang	42, 131
Tomec, Jan	269
Toussaint, Baptiste	216
Trevisani, Alberto	204, 206
Tumiotto, Denise	261
Valdes y Beck, Vanessa	154
Valentini, Pier Paolo	152
Valášek, Michael	196, 267
Vanpaemel, Simon	229
Várkonyi, Péter L.	93
Várszegi, Balázs	198, 300
Velichkova, Hristiana	127
Verlinden, Olivier	91, 137, 181
Vermaut, Martijn	73, 75
Verulkar, Adwait	142
Vidoni, Renato	113, 117
Vilas-Boas, João Paulo	40
Vyhlídal, Tomáš	202
Vörös, Illés	300
Wang, Jing	42
Wasmer, Paul	135
Wehrle, Erich	113, 117
Weremczuk, Andrzej	46
Wieck, Jan Christian	127
Wojtyra, Marek	63, 156
Woliński, Łukasz	63

Won, Sung-hyuk .....	294
Yoo, Wan Suk .....	170
Young, Aaron .....	250
Yu, Xinxin .....	248
Zaier, Riadh .....	23
Zajcsuk, Liliána .....	21
Zana, Roland Reginald .....	192
Zanoni, Andrea .....	160
Zapata, Luis .....	75
Zauner, Christian .....	208
Zavřel, Jan .....	267
Zelei, Ambrus .....	17, 21, 192
Zhakatayev, Altay .....	175
Zhang, Sheng-peng .....	294
Zhou, Ping .....	160
Zlatař, Dario .....	310
Zupan, Dejan .....	275
Zwölfer, Andreas .....	105







Budapest, 2021